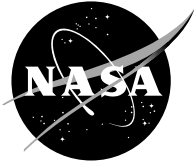


NASA/CP—2004-212735



Proceedings of the 15th Space Photovoltaic Research and Technology Conference

June 2004

The NASA STI Program Office . . . in Profile

Since its founding, NASA has been dedicated to the advancement of aeronautics and space science. The NASA Scientific and Technical Information (STI) Program Office plays a key part in helping NASA maintain this important role.

The NASA STI Program Office is operated by Langley Research Center, the Lead Center for NASA's scientific and technical information. The NASA STI Program Office provides access to the NASA STI Database, the largest collection of aeronautical and space science STI in the world. The Program Office is also NASA's institutional mechanism for disseminating the results of its research and development activities. These results are published by NASA in the NASA STI Report Series, which includes the following report types:

- **TECHNICAL PUBLICATION.** Reports of completed research or a major significant phase of research that present the results of NASA programs and include extensive data or theoretical analysis. Includes compilations of significant scientific and technical data and information deemed to be of continuing reference value. NASA's counterpart of peer-reviewed formal professional papers but has less stringent limitations on manuscript length and extent of graphic presentations.
- **TECHNICAL MEMORANDUM.** Scientific and technical findings that are preliminary or of specialized interest, e.g., quick release reports, working papers, and bibliographies that contain minimal annotation. Does not contain extensive analysis.
- **CONTRACTOR REPORT.** Scientific and technical findings by NASA-sponsored contractors and grantees.

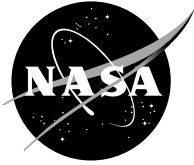
- **CONFERENCE PUBLICATION.** Collected papers from scientific and technical conferences, symposia, seminars, or other meetings sponsored or cosponsored by NASA.
- **SPECIAL PUBLICATION.** Scientific, technical, or historical information from NASA programs, projects, and missions, often concerned with subjects having substantial public interest.
- **TECHNICAL TRANSLATION.** English-language translations of foreign scientific and technical material pertinent to NASA's mission.

Specialized services that complement the STI Program Office's diverse offerings include creating custom thesauri, building customized databases, organizing and publishing research results . . . even providing videos.

For more information about the NASA STI Program Office, see the following:

- Access the NASA STI Program Home Page at <http://www.sti.nasa.gov>
- E-mail your question via the Internet to help@sti.nasa.gov
- Fax your question to the NASA Access Help Desk at 301-621-0134
- Telephone the NASA Access Help Desk at 301-621-0390
- Write to:
NASA Access Help Desk
NASA Center for Aerospace Information
7121 Standard Drive
Hanover, MD 21076

NASA/CP—2004-212735



Proceedings of the 15th Space Photovoltaic Research and Technology Conference

Proceedings of a conference held at and sponsored by
NASA Glenn Research Center
Cleveland, Ohio
June 10–12, 1997

National Aeronautics and
Space Administration

Glenn Research Center

June 2004

Contents were reproduced from author-provided
presentation materials.

Note that at the time of research, the NASA Lewis Research Center
was undergoing a name change to the
NASA John H. Glenn Research Center at Lewis Field.
Both names may appear in this report.

Available from

NASA Center for Aerospace Information
7121 Standard Drive
Hanover, MD 21076

National Technical Information Service
5285 Port Royal Road
Springfield, VA 22100

Available electronically at <http://gltrs.grc.nasa.gov>

TABLE OF CONTENTS

Message from the Program and Publications Chairman	vii
Plenary Session: <i>Invited Papers</i>	
SPACE SOLAR CELL R&D ACTIVITIES IN JAPAN Masafumi Yamaguchi, Toyota Technological Institute	1
UPDATE ON EUROPE'S SPACE PHOTOVOLTAIC PROGRAMME Lothar Gerlach and Klaus P. Bogus, European Space Agency	11
RUSSIAN ACTIVITIES IN SPACE PHOTOVOLTAIC POWER MODULES WITH CONCENTRATORS Vyacheslav M. Andreev and Valeri D. Romyantsev, Ioffe Physico-Technical Institute	19
SPACE PHOTOVOLTAICS SURVIVABILITY RESEARCH AT THE NAVAL RESEARCH LABORATORY Robert J. Walters, Naval Research Laboratory	31
ENERGY GENERATION TECHNOLOGY AT THE PHILLIPS LABORATORY Dean Marvin, The Aerospace Corp.....	37
Session 1: <i>Multibandgap Cells</i> <i>Invited Papers</i>	
PERFORMANCE TRADE-OFFS FOR MBG USING DIFFERENT BANDGAP PAIRS P.A. Iles, C.L. Chu, and L. Kilmer, TECSTAR/ASD; and M.L. Timmons and P. Sharps, Research Triangle Institute	65
PROGRESS IN THE MULTIJUNCTION SOLAR CELL MANTECH PROGRAM David N. Keener, Phillips Laboratory; Dean Marvin, The Aerospace Corporation; and David J. Brinker and Henry B. Curtis, NASA Lewis Research Center.....	77
Session 2: <i>Solar Cells</i> <i>Invited Papers</i>	
HIGH BEGINNING-OF-LIFE EFFICIENCY p/n InP SOLAR CELLS Richard W. Hoffman, Jr., Navid S. Fatemi, Victor G. Weizer, and Phillip P. Jenkins, Essential Research, Inc.; Steven A. Ringel, The Ohio State University; David A. Scheiman, NYMA Setar; and David M. Wilt and David J. Brinker, NASA Lewis Research Center	85
HYDROGEN PASSIVATION OF INTERSTITIAL Zn DEFECTS IN HETEROEPITAXIAL InP CELL STRUCTURES AND INFLUENCE ON DEVICE CHARACTERISTICS S.A. Ringel and B. Chatterjee, The Ohio State University	93
PASSIVATING WINDOW/FIRST LAYER AR COATING FOR SPACE SOLAR CELLS Mircea Faur and Maria Faur, SPECMAT, Inc.; S.G. Bailey, D.J. Flood, D.J. Brinker, S.A. Alterovitz, and D.R. Wheeler, NASA Lewis Research Center; G. Mateescu, Case Western Reserve University; and C. Goradia and M. Goradia, Cleveland State University	103
LIGHT WEIGHT, THIN-FILM Si HETEROJUNCTION SOLAR CELLS W.A. Anderson, B. Jagannathan, and E. Klémentieva, State University of New York at Buffalo	113
NOVEL Si SOLAR CELL FOR SPACE POWER APPLICATIONS Henry Brandhorst and Hayden Hontgas, Space Power Institute, Auburn University	119

PLASMA-ENHANCED PULSED LASER DEPOSITION OF WIDE BANDGAP NITRIDES FOR SPACE POWER APPLICATIONS G.E. Triplett, Jr., and S.M. Durbin, Florida A&M University, Florida State University.....	123
<i>Session 3: Thermophotovoltaics</i>	
<i>Invited Papers</i>	
InGaAs/InP MONOLITHIC INTERCONNECTED MODULES (MIM) FOR THERMOPHOTOVOLTAIC APPLICATIONS David M. Wilt, NASA Lewis Research Center; Navid S. Fatemi, Phillip P. Jenkins, Victor G. Weizer, and Richard W. Hoffman, Jr., Essential Research, Inc.; David A. Sheiman, NYMA, Inc.; and Christopher S. Murray and David R. Riley, Westinghouse Electric Corporation.....	131
MODELING OF $\text{In}_{0.52}\text{Ga}_{0.48}\text{As}/\text{In}_x\text{Ga}_{1-x}\text{As}$ ($x>0.6$) MULTIQUANTUM WELL THERMOPHOTOVOLTAIC CONVERTER I. Serdiukova and A. Freundlich, University of Houston.....	139
<i>Session 4: Flight Experiments</i>	
<i>Invited Papers</i>	
THE ROSSI X-RAY TIMING EXPLORER (XTE) SOLAR ARRAY ANOMALY Edward M. Gaddy, Robert Kichak, and Lee Niemeyer, Goddard Space Flight Center; and Richard Stegeman, Jackson and Tull.....	151
IN-ORBIT PERFORMANCE OF HS-376HP GaAs/Ge SOLAR ARRAYS Richard E. Daniel, Steven W. Geib, Joseph S. Powe, and Joel A. Schwartz, Hughes Space and Communications Company.....	161
SCARLET SOLAR ARRAY SYSTEM STUDY FOR HIGH POWER GEO SPACECRAFT Brian R. Spence, P. Alan Jones, Mike I. Eskenazi, and David M. Murphy, AEC-Able Engineering Company, Inc.....	169
BALLOON AND LEAR JET TESTING OF SCARLET MODULES AND CELLS Michael I. Eskenazi and David M. Murphy, AEC-Able Engineering Company, Inc.; Bruce E. Anspaugh and Robert L. Mueller, Jet Propulsion Laboratory; Dave J. Brinker, NASA Lewis Research Center; and Mark J. O'Neill, ENTECH, Inc.....	177
<i>Session 5: Environmental Effects</i>	
<i>Invited Papers</i>	
CONTRIBUTION OF LOW ENERGY PROTONS TO THE DEGRADATION OF SHIELDED GaAs SOLAR CELLS IN SPACE G.P. Summers, Naval Research Laboratory, University of Maryland Baltimore County; S.R. Messenger and E.A. Burke, SFA, Inc.; and M.A. Xapsos and R.J. Walters, Naval Research Laboratory.....	191
DEGRADATION PROPERTIES OF LARGE FLUENCE IRRADIATED SPACE SILICON BSR CELLS Tadashi Hisamatsu and Sumio Matsuda, National Space Development Agency of Japan (NASDA); and Tetsuya Nakao and Yusuke Matsumoto, Advanced Engineering Services (AES) Corporation.....	199
THE EFFECT OF LARGE SOLAR PROTON EVENTS ON GaAs SOLAR CELL EFFICIENCY M.A. Xapsos, Naval Research Laboratory; S.R. Messenger, SFA, Inc.; R.J. Walters, Naval Research Laboratory; G.P. Summers, University of Maryland; and E.A. Burke, SFA, Inc.....	211

EVIDENCE FOR ENHANCED UV DEGRADATION TO CRACKED COVERSLIDES Andrew Meulenber, Matra Marconi Space; and J. Brower, M. Kruer, and C.M.C. Toporow, TRW	217
NASCAP MODELING OF GEO SATELLITES—SPACECRAFT CHARGING IS BACK! R. Chock, D.C. Ferguson, and D.B. Snyder, NASA Lewis Research Center	223
<i>Session 6: Calibration and Characterization</i>	
<i>Invited Papers</i>	
SOLAR CELL CALIBRATION AND MEASUREMENT TECHNIQUES Sheila Bailey, Dave Brinker, and Henry Curtis, NASA Lewis Research Center; Phillip Jenkins, Essential Research, Inc.; and Dave Scheiman, NYMA, Inc.	231
MEASUREMENT OF N-TYPE 6H SiC MINORITY-CARRIER DIFFUSION LENGTHS BY ELECTRON BOMBARDMENT OF SCHOTTKY BARRIERS S.M. Hubbard and M. Tabib-Azar, Case Western Reserve University; S. Bailey, G. Rybicki, and P. Neudeck, NASA Lewis Research Center; and R. Raffaele, Florida Institute of Technology.....	237
<i>Session 7: Photovoltaics for Planetary Surfaces</i>	
<i>Invited Papers</i>	
HIGH CONCENTRATING GaAs CELL OPERATION USING OPTICAL WAVEGUIDE SOLAR ENERGY SYSTEM T. Nakamura and J.A. Case, Physical Sciences, Inc.; and M.L. Timmons, Research Triangle Institute.....	243
SPACE QUALIFICATION TEST OF a-SILICON SOLAR CELL MODULES Q. Kim, RA. Lawton, S.J. Manion, J.O. Okuno, R.P. Ruiz, D.T. Vu, and S.A. Kayali, Jet Propulsion Laboratory; and F.R Jeffrey, Iowa Thin Film Technologies.....	257
EXPLORING PV ON THE RED PLANET: MARS ARRAY TECHNOLOGY EXPERIMENT AND DUST ACCUMULATION AND REMOVAL TECHNOLOGY Geoffrey A. Landis, Ohio Aerospace Institute; Cosmo Baraona, NASA Lewis Research Center; David Scheiman, NYMA, Inc.; and David Brinker, NASA Lewis Research Center.....	267
<i>Workshop Summary:</i>	
Low Bandgap, High Bandgap and Alternative Conversion Devices and Technology Navid S. Fatemi, Essential Research, Inc.; and Alex Freundlich, University of Houston	147

Foreword

On behalf of the entire conference committee, I would like to thank you for your participation in the 15th Space Photovoltaic Research and Technology (SPRAT XV) Conference. We hope that it was an informative and enjoyable experience for all of the participants.

In an effort to make the information presented at the conference available to the you in as timely a manner as possible, we have had an “express” volume of the conference proceedings printed. In this volume you will find all of the papers and workshop summaries that were available at the time of printing.

This publication will be followed by a more thorough “official” publication of the conference proceedings. The official publication will include all of the papers presented at the conference, workshop summaries, and The Irving Weinberg Award presentation.

Please do not hesitate to contact me if there is information that you need urgently that is not contained in this volume.

Eric B. Clark
15th SPRAT Conference Publications Chairman
216-433-3926
eric.clark@lerc.nasa.gov

SPACE SOLAR CELL R&D ACTIVITIES IN JAPAN

Masafumi Yamaguchi
Toyota Technological Institute
Tempaku, Nagoya 468, Japan

In this paper, space solar cell R&D activities in Japan are briefly described. The terrestrial R&D program of multi-junction solar cells, in the New Sunshine project of MITI (Ministry of International Trade and Industry) in Japan is also reviewed. Up to now, monolithically grown InGaP/GaAs 2 junction solar cells have reached the highest efficiency achieved in Japan of 30.3% at AM1.5 (1-sun). The mechanical stacked 3-junction cells of monolithically grown InGaP/GaAs 2-junction cells and the InGaAs cells have reached 33.3% at AM1.5 (1-sun).

This paper also reports our recent results for high-efficiency InGaP/GaAs tandem cells and their radiation-resistance. The world-record efficiency of 26.9% at AM0 has also been attained with InGaP/GaAs 2 junction solar cells. Irradiation effects of 1-MeV electrons on InGaP single-junction solar cells and InGaP/GaAs 2-junction solar cells fabricated on GaAs substrates have been examined in comparison with those of GaAs and InP cells. Superior radiation-resistance of InGaP cells compared to GaAs cells has been found in terms of solar cell properties and minority-carrier diffusion length. Moreover, minority-carrier injection-enhanced annealing (light illumination or forward bias) of radiation damage to InGaP single-junction cells and InGaP/GaAs 2-junction cells has also been observed. The superior radiation resistance of InGaP materials is thought to be attributed to the fact that the migration energy (annealing temperature) of radiation-induced defects is lower than that in GaAs and is also related to the minority-carrier injection-enhanced annealing of defects.

These results show the great potential of InGaP/GaAs tandem solar cells for space applications.

I. SPACE SOLAR CELL R&D ACTIVITIES IN JAPAN

Space solar cell R&D works have been conducted mainly in NASDA (National Space Development Agency of Japan), ISAS (Institute of Space and Astronautical Science), JAERI (Japan Atomic Energy Research Institute), Sharp Corp., and Toyota

Technological Institute.

NASDA is promoting development of high-efficiency thin Si space solar cells in cooperation with Sharp Corp. and is organizing the Research Committee for Radiation Damage of Solar Cells to clarify the severe degradation of Si solar cells used in the Engineering Test Satellite-VI (ETS-VI) launched in 1994. As part of this collaboration, the following R&D works are conducting: ISAS is studying radiation damage and impurities in Si solar cells and materials using PL (photo-luminescence). JAERI is working on in-situ monitoring of radiation damage to Si solar cells. Sharp Corp. is developing high-efficiency thin Si space solar cells and is working on radiation damage to advanced Si cells.

Toyota Tech. Inst. is studying radiation damage to Si, InGaP cells and InGaP/GaAs tandem cells by using DLTS (deep-level transient spectroscopy) and solar cell properties in collaboration with NASDA and Japan Energy Corp., and has proposed a mechanism for the anomalous behavior of Si solar cells under high-fluence electron and proton irradiations. Figure 1 compares experimental data for short-circuit current degradation in Si solar cells after 1-MeV electron irradiation with modeled results which consider (a) degradation of only the minority-carrier diffusion length L , (b) degradation of L and carrier removal, and (c) degradation of L , carrier removal, and depletion width broadening [1]. We have also found minority-carrier injection-enhanced annealing phenomena for radiation damage to InGaP/GaAs tandem solar cells.

II. TERRESTRIAL MULTI-JUNCTION CELL PROGRAM IN JAPAN [2]

The super-high efficiency solar cell project started in FY 90. The objectives of the projects are conversion efficiencies about twice the 90 year values at the laboratory level by the beginning of the 21st century and production of such efficiency cells by 2010. Some subprogrammes are carried out by Japanese production companies and are technically and scientifically supported by universities and the Electrotechnical laboratory.

Figure 2 shows chronological improvements in the efficiencies of various solar cells developed in Japanese projects.

Multi-junction solar cells show potential for super-high efficiency cells with efficiencies of 36~40% due to their wide-band photo-response, although the theoretical target efficiency for single-junction GaAs or InP cells is 27~28%. Concentrator operation of 2-junction cells and 3-junction cells are promising for obtaining super-high efficiency more than 40%.

Thin-film compound solar cells fabricated on inexpensive substrates would be useful in terms of low-cost cells. The fabrication of III-V compound cells on Ge or Si substrates shows promise as an approach for achieving this. In addition, concentrator operation of solar cells is also effective not only in improving efficiency

but also in lowering cost by reducing the cell size per unit output by a factor of 100 to 1000 (almost equal to the concentration ratio) as shown in Fig. 3 [3]. Another cost analysis [4] of solar cell modules that suggests concentrator operation is promising for cost reduction.

As described above, it is necessary to improve conversion efficiency by using a multi-junction structure, reduce costs by using thin-film technology on inexpensive substrates such as Si and Ge, and reduce material and process costs for the widespread application of III-V compound solar cells.

Based on the above mentioned background, the Japanese R&D program of super high efficiency solar cells started at FY 1990 under support by MITI, NEDO and PVTEC. Five companies namely, Hitachi, Hitachi Cable, Sumitomo Electric Industries, Japan Energy and Oki Electric Industries are developing the program. The proposed structures and materials of the solar cells are AlGaAs/GaAs/Si(Ge), InGaP/GaAs/Si(Ge), and super lattice structure solar cells as shown in Fig. 4.

Up to now, monolithically grown InGaP/GaAs 2 junction solar cells have reached the highest efficiency achieved in Japan of 30.3% at AM1.5 (1-sun). Figure 5 shows a schematic cross-section and I-V characteristics of a high-efficiency InGaP/GaAs tandem solar cell fabricated by Japan Energy Corp. [5]. More recently, the mechanical stacked 3-junction cells of monolithically grown InGaP/GaAs 2-junction cells and the InGaAs cells have reached 33.3% at AM1.5 (1-sun) following joint work of Japan Energy Corp. and Sumitomo Electric Corp.

As a by-product of these results, the same cells are being developed for space applications.

III. InGaP/GaAs TANDEM SOLAR CELLS WITH WORLD-RECORD EFFICIENCY OF 26.9% AT AM0

An InGaP/GaAs tandem cell which consists of an optically thin InGaP top cell and a GaAs bottom cell has great potential to provide a high conversion efficiency for space applications. Since both the lattice parameters and generated current of these cells has been matched in this combination, a two-terminal monolithic tandem cell can be successfully obtained by using a tunnel junction for the inter-cell connection. Efficiencies of 25.7% (1-sun, AM0) GaInP/GaAs tandem cells have already been reported [6] and some efforts have been made to put this type cells into commercial production for space applications [7]. Some studies on radiation resistance of the tandem cell have been done and a high efficiency of 19.6% at EOL has been obtained [8].

Recently, a world record efficiency of over 30% under one-sun AM1.5 global conditions for the InGaP/GaAs tandem solar cell has been attained [5]. This paper also reports AM0 I-V characteristics of InGaP/GaAs tandem solar cells and their

radiation resistance. The characteristics of the tandem cells after 1 MeV electron irradiation and minority-carrier injection-enhanced annealing of radiation damage have been investigated. In addition, the optimal cell design for current matching at EOL is predicted.

InGaP/GaAs cell layers were grown on a GaAs substrate by the metalorganic chemical vapor deposition (MOCVD) method. Silane and diethylzinc were used as n-type and p-type dopants, respectively. The lattice mismatch between an InGaP epitaxial layer and a GaAs substrate was reduced to 500 ppm, and the photoluminescence energy of InGaP layers was 1.88eV. The carrier concentrations of the p-InGaP and p-GaAs base layer were 1.5×10^{17} and 1.0×10^{17} cm⁻³, respectively. The n-type emitter thicknesses were 0.05 and 0.1 μ m, respectively. The minority carrier lifetime in the p-InGaP base layer and the recombination velocity at the interface between the AlInP window layer and the n-InGaP emitter were estimated to be around 10-50 ns and 5800 cm/s, respectively, using the time-resolved photoluminescence technique. The top and bottom cells were connected by an InGaP tunnel junction.

A world-record efficiency of 26.9% ($V_{oc}=2.451V$, $I_{sc}=67.4mA$, $FF=88.1\%$) under AM0, 28 °C conditions, which has been measured at NASDA using a one light source simulator, has been obtained for 4 cm² InGaP/GaAs tandem cells, as shown in Fig. 6.

IV. RADIATION-RESISTANCE OF InGaP/GaAs TANDEM SOLAR CELLS

1 MeV electron irradiation at normal incidence was carried out using an electron accelerator at room temperature. Electron fluences ranged from 3×10^{14} to 1×10^{16} cm⁻², with an electron flux density of about 10^{12} cm⁻²s⁻¹. The AM1.5G solar simulator with 100mW/cm² was used for measurement of I-V curves and injection of minority carriers after irradiation.

Figure 7 shows the radiation resistance of InGaP/GaAs tandem cells against 1 MeV electron irradiation with fluences in the range from 3×10^{14} to 1×10^{16} cm⁻², in comparison with those of InP, InGaP and GaAs-on-Ge solar cells. The radiation resistance of our tandem cell observed is similar to a GaAs-on-Ge cell. The remaining factor of V_{oc} , I_{sc} , FF and η is thought to be mainly attributed to large degradation in the GaAs bottom cell with a highly doped base layer. Figure 8 shows the change in spectral response of the tandem cells before and after electron irradiation. Larger degradation in the GaAs bottom cells compared to that in the InGaP top cells is confirmed.

Figure 9 shows the maximum power recovery due to light illumination at various temperatures. The ratios of maximum power after injection P_1 to maximum power before irradiation P_0 are shown as a function of injection time. The recovery ratio increases with an increase in ambient temperature within the operating range for

space use. Such a remarkable recovery of a tandem cell is thought to be caused by the photoinjection-enhanced annealing of radiation damage to the InGaP cell. In fact, minority-carrier injection annealing of InGaP cells in this temperature range has been observed by the authors [9,10] and Chiang et al [11], and that of GaAs cells have occurred at higher temperatures (150-200 °C) [12]. Therefore, the results show that InGaP/GaAs tandem solar cells under device operation conditions have superior radiation-resistant properties.

Figure 10 shows the temperature dependence of the injection-enhanced annealing rate A^* due to injection (forward bias) and photo annealing for InGaP/GaAs tandem solar cells, in comparison with the injection annealing rate A^* and the thermal annealing rate A for InGaP single-junction cells, determined from forward bias and thermal annealing of solar cell properties, for radiation-induced defects in InGaP.

Although the radiation-induced defects in InGaP have an annealing rate of the order of 10^{-12} s^{-1} at room temperature as shown in Fig. 10, under minority-carrier injection, the defect annealing shows a large enhancement factor of 6-7 orders of magnitude. On the other hand, in the case of InGaP/GaAs tandem solar cells, the radiation-induced defects in InGaP top cell layer are thought to be annihilated under forward bias and light illumination conditions but those in the GaAs bottom cell layer still remain. Therefore, the forward bias injection annealing rate for InGaP/GaAs tandem cells is a factor of 2 lower than that for InGaP single junction cells. For InGaP/GaAs tandem cells, the photo-injection annealing rate is a factor of 3 lower than the forward bias injection annealing rate because the current density of $\sim 15 \text{ mA/cm}^2$ produced by a light injection intensity of 100 mW/cm^2 is much less than the density of the carrier-injection measurements (100 mA/cm^2). The enhancement of defect annealing in the InGaP top cell layer under minority-carrier injection conditions is thought to occur as a result of the nonradiative electron-hole recombination processes [12] whose energy E_R enhances the defect motion. As shown in Fig. 10, the thermal activation energy E_A (1.1eV) of the defect is reduced to E_I (0.48-0.54eV) by an amount E_R (0.56-0.62eV), and thus the electronic energy from a recombination event can be channeled into the lattice vibration mode which drives the defect motion: $E_I = E_A - E_R$. However, further studies are necessary to clarify the mechanism of the minority-carrier injection-enhanced annealing phenomena and the origin of the radiation-induced defects.

Next, the optimal cell design for current matching at EOL has been examined. The photo-current generated under AM0 illumination in both top and bottom cells as a function of the InGaP base layer thickness was investigated for the tandem cell before and after electron irradiation of 10^{15} cm^{-2} , as shown in Fig. 11. The photo-currents were determined from the integration of the AM0 spectral response. Minority carrier lifetime in p-InGaP and p-GaAs base layers at both BOL and EOL were estimated to be 10ns and 0.2ns for InGaP, and 10ns and 0.04ns for GaAs, respectively, which were fitted by numerical simulation. Also, the dependence of the photo-current on

the InGaP base layer thickness was calculated, as shown in Fig. 11. The calculated I_{sc} of the tandem cell at EOL as a function of the InGaP base layer thickness is also plotted in Fig. 11. It is found that the tandem cell I_{sc} does not agree with the photocurrent of the GaAs bottom cell, which is lower than that of the InGaP top cell.

Figure 12 illustrates the calculated I-V curves of an InGaP cell, a GaAs cell and a tandem cell, at EOL. When the minority carrier lifetime is low, most of the photocurrent in any cell (the GaAs cell in the case of the InGaP/GaAs tandem cell) is generated in the depletion region and the photocurrent is therefore bias dependent. This effect is expressed in the analysis of the equivalent circuit of the illuminated diode as an effective increase in shunt resistance. When the shunt resistance of the GaAs bottom cell is small, the tandem cell I_{sc} is greater than the photocurrent in the GaAs. Therefore, the current matching point of the InGaP base layer thickness at EOL is found to be around $0.2\mu\text{m}$.

SUMMARY

Space solar cell R&D activities in Japan has been briefly described and the R&D program of multi-junction solar cells in the New Sunshine project of MITI in Japan has also been reviewed. Up to now, monolithically grown InGaP/GaAs 2 junction solar cells have reached the highest efficiency achieved in Japan of 30.3% at AM1.5 (1-sun). The mechanically stacked 3-junction cells of monolithically grown InGaP/GaAs 2-junction cells and InGaAs cells reached 33.3% at AM1.5 (1-sun).

The world-record efficiency of 26.9% at AM0 were also attained with InGaP/GaAs 2 junction solar cells. Irradiation effects of 1-MeV electrons on InGaP single-junction solar cells and InGaP/GaAs 2-junction solar cells fabricated on GaAs substrates were examined in comparison with those of GaAs and InP cells. Superior radiation-resistance of InGaP cells compared to GaAs cells was found in terms of solar cell properties and minority-carrier diffusion length. Moreover, minority-carrier injection-enhanced annealing (light illumination or forward bias) of radiation damage to InGaP single-junction cells and InGaP/GaAs 2-junction cells was also observed. The superior radiation resistance of InGaP materials is thought to be attributed to the fact that the migration energy (annealing temperature) of radiation-induced defects is lower than that in GaAs and is also related to the minority-carrier injection-enhanced annealing of defects.

These results show great potential of InGaP/GaAs tandem solar cells for space applications.

REFERENCES

- [1] M. Yamaguchi, S.J. Taylor, S. Matsuda and O. Kawasaki, "Mechanism for the anomalous degradation of Si solar cells induced by high fluence 1MeV electron irradiation", *Appl. Phys. Lett.*, **68**, pp.3141-3143 (1996).
- [2] M. Yamaguchi and S. Wakamatsu, "Super-High Efficiency Solar Cell R&D Program in Japan", *Proc. 25th IEEE Photovoltaic Specialists Conference*, (IEEE, New York, 1996) pp.9-11.
- [3] M. Yamaguchi, T. Warabisako and H. Sugiura, "Chemical Beam Epitaxy as a Breakthrough Technology for Photovoltaic Solar Energy Applications", *J. Crystal Growth*, **136**, pp.29-36 (1994).
- [4] R.A. Whisnant, J.A. Hutchby, M.L. Timmons, R. Venkatasubramanian and J.S. Hills, "Silicon and GaAs/Ge Concentrator Power Plants: A Comparison of Cost of Energy Produced", *Proc. 1st World Conference on Photovoltaic Energy Conversion*, (IEEE, New York, 1994) pp.1103-1106.
- [5] T. Takamoto, E. Ikeda, H. Kurita and M. Ohmori, "High Efficiency InGaP/GaAs Tandem Cells", *Appl. Phys. Lett.* **70**, pp.381-383 (1997).
- [6] K. A. Bertness, S.R. Kurtz, D.J. Friedman, A.E. Kibbler, C. Krammer and J.M. Olson, "High-Efficiency GaInP/GaAs Tandem Solar Cells for Space and Terrestrial Applications", *Proc. 1st World Conference on Photovoltaic Energy Conversion*, (IEEE, New York, 1994) pp. 1671-1678.
- [7] Y.C.M. Yeh, C.L. Chu, J. Krogen, F.F. Ho, G.C. Datum, S. Billets, J. M. Olson and M.L. Timmons, "Production Experience with Large Area, Dual Junction Space Cells", *Proc. 25th IEEE Photovoltaic Specialists Conference*, (IEEE, New York, 1996) pp.187-190.
- [8] S.R. Kurtz, K.A. Bertness, D.J. Friedman, A.E. Kibbler, C. Kramer and J.M. Olson, "19.6% Electron-Irradiated GaInP/GaAs Cells" *Proc. 1st World Conference on Photovoltaic Energy Conversion*, (IEEE, New York, 1994) pp.2108-2111.
- [9] M. Yamaguchi, T. Okuda and S.J. Taylor, "Minority-carrier injection-enhanced annealing of radiation damage to InGaP solar cells", *Appl. Phys. Lett.*, **70**, pp.2180-2182 (1997).
- [10] M. Yamaguchi, T. Okuda, S.J. Taylor, T. Takamoto, E. Ikeda and H. Kurita, "Superior radiation-resistant properties of InGaP/GaAs tandem solar cells", *Appl. Phys. Lett.*, **70**, pp.1566-1568 (1997).
- [11] P.K. Chiang, P.S. Vijayakumar and B.T. Cavicchi, "Large Area GaInP/GaAs Tandem Cell Development for Space Power Systems", *Proc. 23rd IEEE Photovoltaic Specialists Conference*, (IEEE, New York, 1993) pp.659-664.
- [12] D.V. Lang, L.C. Kimerling and S.Y. Leung, "Recombination-enhanced annealing of the E1 and E2 defect levels in 1-MeV-electron-irradiated n-GaAs", *J. Appl. Phys.* **47**, 3587 (1976).

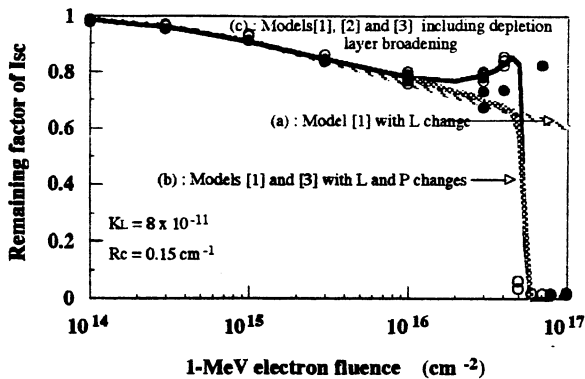


Fig. 1. Comparison of experimental data for short-circuit current degradation of Si solar cells with 1-MeV electron irradiation with modeled results which consider (a) degradation of only the minority-carrier diffusion length L , (b) degradation of L and carrier removal, and (c) degradation of L , carrier removal, and depletion width broadening.

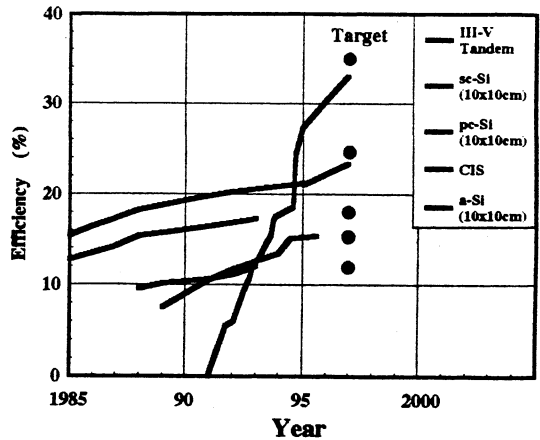


Fig. 2. Chronological improvements in the efficiencies of various solar cells developed in Japanese projects.

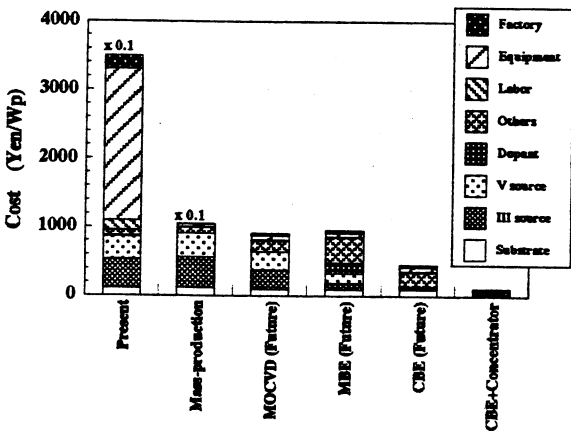


Fig. 3. Cost estimates for 2-junction cells monolithically integrated with III-V compound cell and Si cell, fabricated using CBE, MOCVD and MBE.

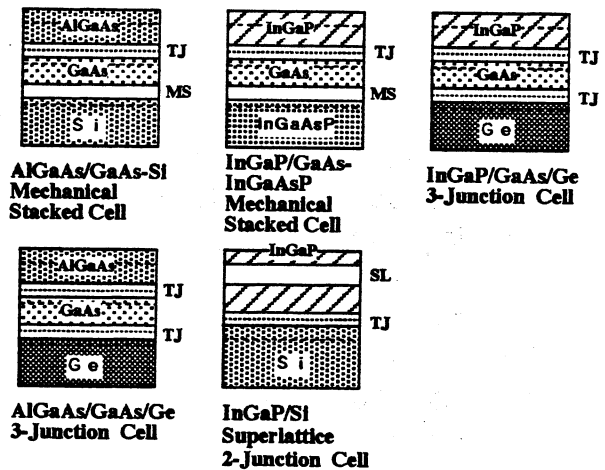


Fig. 4. Schematic cross section of multi-junction solar cells proposed in the New Sunshine Program in Japan.

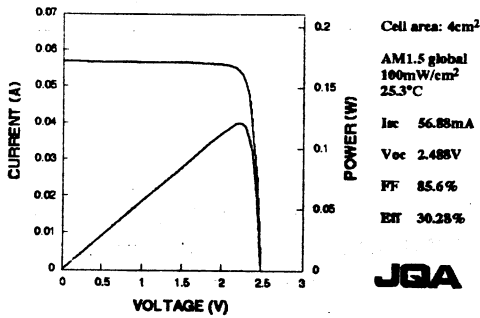
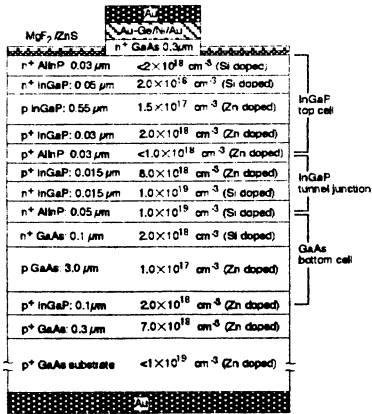


Fig. 5. A schematic cross section of and I-V characteristics of a high-efficiency InGaP/GaAs 2-junction solar cells.

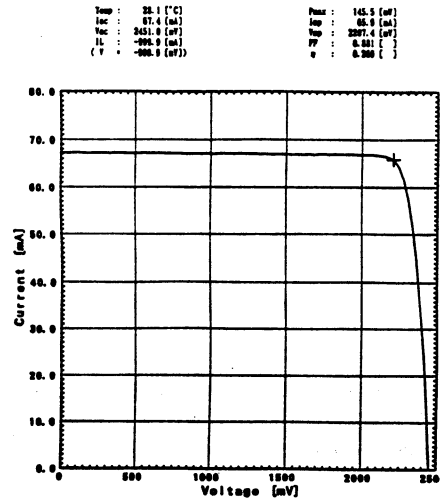


Fig. 6. AM0 I-V characteristics of a high-efficiency InGaP/GaAs tandem solar cell with a world-record conversion efficiency of 26.9%.

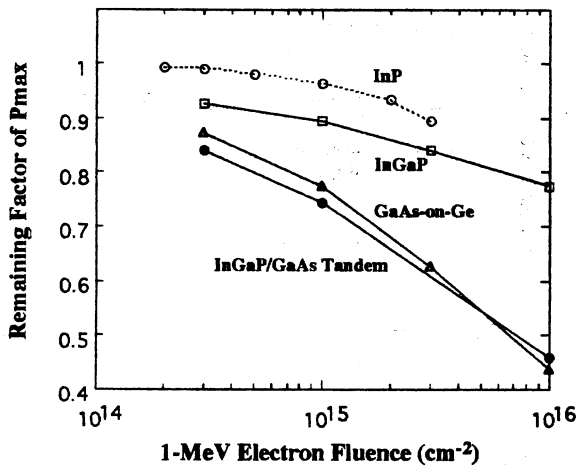


Fig. 7. Radiation resistance of InGaP/GaAs tandem cells against 1 MeV electron irradiation, in comparison with that of InP, InGaP and GaAs-on-Ge solar cells.

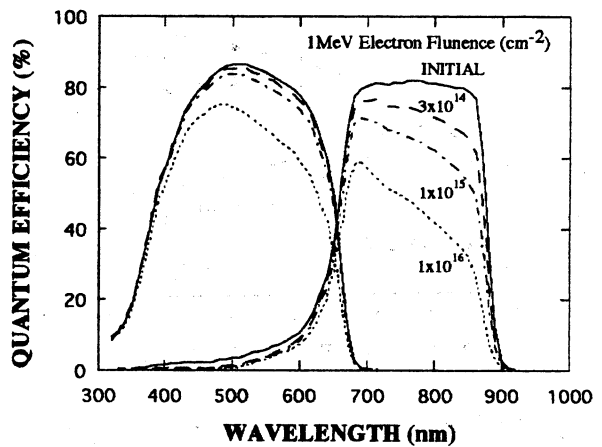


Fig. 8. Change in spectral response of the tandem cells before and after 1 MeV electron irradiation.

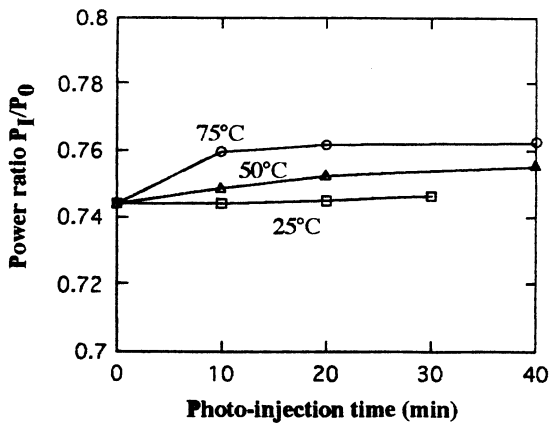


Fig. 9. The maximum power recovery due to light illumination at various temperatures.

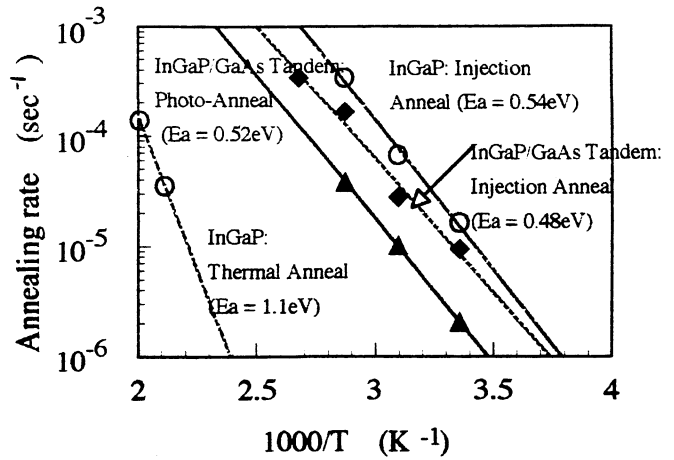


Fig. 10. Temperature dependence of the injection-enhanced annealing rates due to injection (forward bias) and photo-injection, for radiation damages to InGaP/GaAs tandem solar cells.

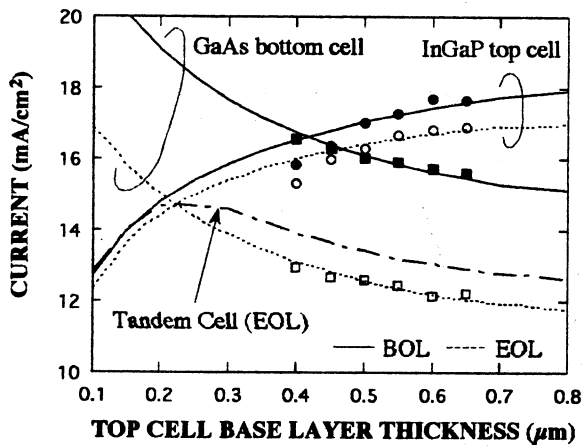


Fig. 11. The photo-current generated under AM0 illumination in both top and bottom cell as a function of the InGaP base layer thickness, before and after electron irradiation of 10^{15} cm^{-2} .

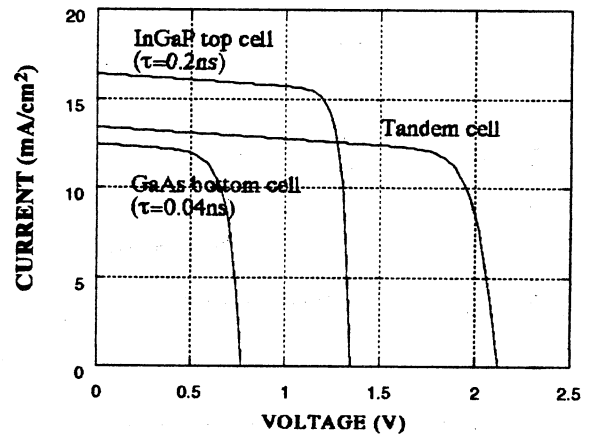


Fig. 12. Calculated I-V curves of an InGaP cell, a GaAs cell and a tandem cell, at EOL.

UPDATE ON EUROPE'S SPACE PHOTOVOLTAICS PROGRAMME.

Lothar Gerlach, Klaus P. Bogus
European Space Agency
European Space Research Centre
Noordwijk, The Netherlands

SUMMARY

The current space PV technology development programme of ESA is described. The programme is closely coupled to the European space mission scenario for the next 10 year period and has as main objective to make the most effective use of the limited resources available for technology in the present economical climate. This requires a well-balanced approach between concentration on very few options and keeping the competition alive if more than one promising technology exists.

The paper describes ESA's main activities in the areas of solar array technology, solar cell technology, solar cell assembly technology, and special test and verification activities including the in-orbit demonstration of new technologies.

INTRODUCTION

Europe has had a very successful record in the field of space photovoltaics and has achieved a competitive position in the world market. For a large variety of European spacecraft systems photovoltaic solar generators are the exclusive source of electrical power and additionally, Europe has succeeded in exporting solar arrays across the Atlantic (e.g. IUE, Hubble Space Telescope, CTS-Hermes, INTELSAT and GLOBALSTAR).

The main purpose of the space photovoltaic technology development programme is to maintain the high standard of European solar array technology by carefully modernising the existing concepts in a step-wise approach. The smooth introduction of new technologies into flight programmes is achieved by close cooperation between technologists and project engineers.

The close coupling of the technology programme to the European mission scenario for the next 10 years is perfectly in line with the approach described above and leads to a fast application cycle of new technologies. A disadvantage of this approach is the resulting low priority for globally attractive new technologies which are not directly required in the ESA mission scenario with its limited scope.

DETAILS OF ESA'S SPACE PV TECHNOLOGY PROGRAMME

The programme is described in the 7 tables below according to a systematic division into solar array technology, solar cell technology, assembly technology, technology verification activities and supplementary activities.

The first column of each table contains the technology activity title, the second column indicates the present status of the activity. "Proposed" stands for a new activity which is not yet accepted in the budget planning, after acceptance it turns into "planned", and after initiation into "running". The 3rd column identifies the frame-programme under which the activity is funded: "Basic" is the general basic TRP(Technological Research Programme) of ESA, "ASTP" is the acronym for applied supporting

technology programmes of the Telecommunications satellite area, "GSTP" standing for the general supporting technology programme of ESTEC for all ESA missions and "ARTES" is special supporting programme on advanced research in telecommunication systems. Additionally, several of the national activities in the ESA-member states are harmonised with ESA and run under common management arrangements. Schedule indications can be found in the 4th column. The last column contains summary descriptions.

SOLAR ARRAY TECHNOLOGY

ESA's Solar Array Technology is based on a two main design concepts: Advanced lightweight rigid panel arrays and advanced flexible blanket arrays. With both concepts a high degree of maturity and flight experience has been accumulated in recent flight programmes: OLYMPUS-1, HST and ERS-1 are operating very successfully with flexible blanket arrays, whereas EURECA, HIPPARCOS and the ECS/MARECS satellites are supplied with rigid panel arrays.

The solar array technology development aims at the improvement of the present lightweight carbon-fibre face-sheet panels for specific future telecom-missions. Since the technology requirements are generally very mission specific it has become general practice do these developments within the corresponding flight programmes and not in generic technology programmes.

Unfortunately EUROPE has presently no new programme requiring flexible blanket solar arrays so that this technology which has already reached a high degree of maturity, can not be further improved.

The development of alternative concepts was limited to studies on concentrator arrays (SARA-Louvre, Holographic Dispersive).

SOLAR CELL TECHNOLOGY

This part of the programme comprises two main elements: Further improvement of silicon solar cells and follow-on development of GaAs solar cells:

- Hi-ETA silicon cells with 16-17% efficiency have been pre-developed and are now approaching the pilotline production stage.
- Further improvement towards 18% efficiency are under pre-development using advanced passivation and optical confinement
- a demonstration of a 20% efficiency silicon cell is foreseen in a basic R&D study on small area, low quantity samples
- GaAs and GaAs-on-Ge cells have been pre-developed in Italy, Great-Britain and Germany.
- The next step is a pilotline production of GaAs-on-Ge cells: 1996 - 1998.
- In parallel two contracts have been awarded to elaborate the potential of cost savings in silicon and GaAs wafer production.
- Further improvements of III-V-compound cells are expected in the area of ultra-thin (superstrate supported) GaAs cells and multi-junction/tandem cells.
- For deep space missions (Jupiter distance) GaAs and silicon cells have been developed in Italy and Germany. At such extreme conditions these LILT (Low Intensity Low Temperature) solar cells have efficiencies of 25%. The Type Approval test on these cells has been started.
- For the potential mission to Mercury ESA issued an Invitation To Tender to study the feasibility if solar cells in general are a credible candidate for the power generation at these extreme operating conditions. HIHT (High Intensity-High Temperature) solar cells would have a worst case operating temperature of about 400 deg.C.

SOLAR CELL ASSEMBLY TECHNOLOGY

This part of the Programme covers :

- the development of improved Aluminum solar cell interconnectors (ATOX-resistant, low-cost)
- the development of ultrasonic welding for Si- and GaAs cells (long cycling life, low-cost)
- advanced cover-glass bonding (Direct Electrostatic bonding, Teflon Pre-preg bonding)
- Infra-red reflective coatings on cover-glasses (improved efficiency through lower Temp.)
- Development of integrated solar cell modules (GaAs-thin film and Silicon superstrate concepts).

TECHNOLOGY VERIFICATION TESTS

Apart from the activities performed at SPASOLAB (ESA's solar cell laboratory in Madrid), the main activities are related to the investigation of space environmental effects on solar arrays. This includes investigation of synergistic effects, thermal cycle induced fatigue, UV and atomic oxygen effects, micro meteoroid impact effects and particle radiation damage in solar cells. Except for radiation effects these activities are concentrating on extending the investigations from the Post-flight investigation programmes on the retrieved HST and EURECA solar arrays.

Extensive radiation damage investigations are required for two different reasons: One is the evaluation of new solar cells (e.g. advanced GaAs and Hi-ETA silicon cells), the other the planning of missions in different orbits (e.g. the new Telecom-missions in high-inclination, medium altitude orbits with equivalent fluences of more than $10E16$ One-MeV-electrons /sqcm).

SOLAR GENERATOR TECHNOLOGY PROGRAMME

STATUS OF CURRENT ACTIVITIES

1. **ARRAY SYSTEM DEVELOPMENT**
2. **ASSEMBLY TECHNOLOGY**
3. **COMPONENT TECHNOLOGY**
4. **TECHNOLOGY VERIFICATION TESTS**
5. **SUPPLEMENTARY ACTIVITIES**



ESTEC
L. GERLACH, XPG
K. BOGUS, XPG
SPRAT, 10 JUNE 97

SOLAR GENERATOR TECHNOLOGY PROGRAMME

1. ARRAY SYSTEM DEVELOPMENT

Title:	Status:	Programme:	Details/Contents:
* ADVANCED RIGID PANEL ARRAYS	running @ FSS	ARTES (HARMO)	ARAFOM , HOTBIRD+ (GSR(AS),MARK-3 (DSS))
* SYSTEM ANALYSIS & ASSESS. NOVEL CELLS	running @DSS	BASIC	Evaluation of new cell types on array level (ASCA Study)



ESTEC
L. GERLACH, XPG
K. BOGUS, XPG
SPRAT, 10 JUNE 97

SOLAR GENERATOR TECHNOLOGY PROGRAMME

2. ASSEMBLY TECHNOLOGY

* ALUMINIUM INTERC. TECHNOLOGY	last phase@DSS	BASIC	Development of ultrasonically welded alu-interconnectors
* INT. ELEV. VOLTAGE MODULE TECHN.	complete@ASE	BASIC	Pre-development of integrated GaAs ultrathin modules with diodes
* I-R-REFLECTING COATING	suspended@PST	ASTP-4	Reduction of operating temperature by reflector on cover-glass
* TEFLON-BONDING	complete@PST	ASTP-4	Teflon bonded cell-assemblies (with esd-protection)
* CMO-COVER GLASS	started@PST	ARTES	Development of CMO-glass for high radiation missions



ESTEC
L. GERLACH, XPG
K. BOGUS, XPG
SPRAT, 10 JUNE 97

SOLAR GENERATOR TECHNOLOGY PROGRAMME

3. COMPONENT TECHNOLOGY-A

- | | | | | |
|---|---|--|----------------|---|
| * | GaAs-Ge SOLAR-CELL INDUSTRIALISATION | running@ ENE
running@ CISE | ARTES-
TEPP | Set-up of GaAs- MOCVD-
Production on GERMANIUM |
| • | PRE-INDUSTRIAL DEV. OF GE-PRODUCTION | running@ U.M. | ARTES-
TEPP | Large-scale Ge-Substrate
Manufacturing |
| * | LILT SOLAR CELLS | complete@ASE/CISE | BASIC | Dev. of cells with 25%-eff.
In deep space (ROSETTA) |
| * | THIN-FILM CELLS | complete@UAM/CASA
running@IPE-Stuttg. | ASTP-4
P.O. | Pre-development of CIS-cells
System-assessment
CIS-Cell Adaptation to Space |



ESTEC
L. GERLACH, XPG
K. BOGUS, XPG
SPRAT, 10 JUNE 97

SOLAR GENERATOR TECHNOLOGY PROGRAMME

3. COMPONENT TECHNOLOGY-B

- | | | | | |
|---|--|------------------|--------|---|
| * | PILOTLINE HI-ETA SILICON CELLS | running@DSS/ASE | GSTP-1 | End-development of 16%
Cells incl. Pilot Production |
| * | ADVANCED LIGHW. GAAS CELLS | running@DSS | GSTP-1 | Cascade/tandem cells;>23%
& Ultra-thin tandem cells |
| * | GE-SUBSTRATES FOR GaAs CELLS | completed@ENE/UM | GSTP-1 | Development of improved substrates
for GaAs-Ge-Cells |
| * | LOW-COST SOLAR CELL PRODUCTION METHODS | running@FCM | TRP | Dev. of low-cost GaAs-wafer technology |
| * | LOW-COST SI-SOLAR CELL PRODUCTION METHODS | running@ ASE | TRP | Cost Reduction in Si-Solar Cell
Manufacturing |



ESTEC
L. GERLACH, XPG
K. BOGUS, XPG
SPRAT, 10 JUNE 97

SOLAR GENERATOR TECHNOLOGY PROGRAMME

3. COMPONENT TECHNOLOGY-C: NEW START

•	CASCADE SOLAR CELLS ON GE SUBSTRATES	TRP	III/97
•	CASCADE SOLAR CELLS WITHOUT GE SUBSTRATE	TRP	III/97
•	DEV. & QUALIFICATION OF CASCADE SOLAR CELLS	TRP	IV/98
•	HIHT-SOLAR CELL FOR NEAR-SUN MISSIONS	GSTP-2	I/97
•	CASCADE SOLAR CELLS: COMPLEM. DEV.	GSTP-2	IV/97
•	FLIGHT DEMONSTRATION OF ADV. GaAs-Ge Cells	GSTP-2	III/97
•	ASSEMBLY & INTEGRATION OF ADV. GaAs-BASED CELLS	GSTP-2	III/97
•	DEV. & QUAL. OF ULTRA-THIN SILICON SOLAR CELLS	GSTP-2	IV/97



ESTEC
L. GERLACH, XPG
K. BOGUS, XPG
SPRAT, 10 JUNE 97

SOLAR GENERATOR TECHNOLOGY PROGRAMME

4. TECHNOLOGY VERIFICATION TESTS

•	p ⁺ AND e ⁻ RADIATION	running@Various	P.O.	p ⁺ & e ⁻ tests of novel cells
•	SPASOLAB	running@INTA	INFRA-STR.	Type approval tests (PSS-01-604)
•	ARCHIMEDES	running@Various	P.O.	p ⁺ & e ⁻ tests of novel cells for missions with high flux



ESTEC
L. GERLACH, XPG
K. BOGUS, XPG
SPRAT, 10 JUNE 97

SOLAR GENERATOR TECHNOLOGY PROGRAMME
5. SUPPLEMENTARY ACTIVITIES

- **EQUATOR -S SOLAR CELL EXPERIMENT** running @ MPI-EP TDP Flight evaluation of NOVEL Solar cells
- **CHARACTERISATION OF GAAS/GE SURFACES** running @ NMRC Infrastruct. Diagnostics on GaAs/Ge Solar Cells
- **PORTABLE SUN SIMULATOR** planned IV/97 GSTP -2 Mini-flasher for field Tests
- **SOLAR DYN POWER EXPERIMENT (SDPS)** planned III/97 GSTP-2 Flight Demonstration of European sub-assemblies



ESTEC
L. GERLACH, XPG
K. BOGUS, XPG
SPRAT, 10 JUNE 97

RUSSIAN ACTIVITIES IN SPACE PHOTOVOLTAIC POWER MODULES WITH CONCENTRATORS¹

Vyacheslav M.Andreev and Valeri D.Rumyantsev

Ioffe Physico-Technical Institute,

St.Petersburg, 194021 Russia

Abstract

Space concentrator modules with point- and line-focus Fresnel lenses and with reflective parabolic troughs have been developed recently at Ioffe Physico-Technical Institute. PV receivers for these modules are based: on the single junction LPE and MOCVD AlGaAs/GaAs solar cells characterized by AM0 efficiencies of 23.5-24% at 20-50 suns and 24-24.7% at 50-200 suns; on the mechanically stacked tandem AlGaAs/GaAs-GaSb cells with efficiency of 27-28% at 20-100 suns. MOCVD AlGaAs/GaAs cells with internal Bragg reflector have shown a higher radiation resistance as compared to a traditional structure. Monolithic two-terminal tandems AlGaAs (top)-GaAs (bottom) for space application and GaSb (top) - InGaAsSb (bottom) for TPV application are under development as well.

Introduction

Concentrator concept in space provides potentially higher PV conversion efficiency and inherent protection from radiation effects at reduced cost. Optimal III-V materials and their combinations can be used for fabrication of the solar cells in this case to obtain the best output parameters of the PV modules. As to the sunlight concentrators for these modules, so they can be based on the refractive or reflective optical elements. An attractive feature of the refractive concentrator approach is a more "natural" module design. Here solar cells are placed on the bottom plate of the module which at the same time serves as a heat sink. A potential advantage of the reflective concentrator approach is an extremely high optical efficiency (if silver coating is used) and better radiation stability. That is why both these approaches are under development at the Ioffe Institute.

Solar Cells

The first heterostructure solar cells based on AlGaAs system were developed at Ioffe Physico-Technical Institute in 1969-1970 [1,2]. LPE method was used to grow those heterostructures. Many efforts had been done in the field of LPE technique, so that LPE is known to be a relatively inexpensive and effective method for production of the single-junction AlGaAs/GaAs SCs. LPE method have shown up to now the best crystal quality parameters of the epitaxial AlGaAs layers realized with more or less simple equipment.

¹ This work was supported, in part, by the US National Aeronautics and Space Administration and by the US Department of Defense.

Last years low-temperature LPE had been promoted successfully at Ioffe Institute in respect to fabrication of multilayer AlGaAs/GaAs SCs [3]. In particular, the crystallization rates of high quality layers as low as 0.1-1 nm/s in temperature range 550-400 C had been demonstrated - the rates of the same order of magnitude as in MBE and MOCVD. Both free electrons and free holes concentrations can be varied in epitaxial layers within a wide range. That is why LPE can be used for the growth of the monolithic tandem AlGaAs (top)-GaAs (bottom) SC heterostructures with tunnel junction. In the case when AlGaAs-layers are not photoactive, for example, in the case of the single-junction AlGaAs/GaAs SCs with internal Bragg reflector, MOCVD method is used successfully by us for the heterostructure growth.

An alternative to the monolithic tandems is a mechanical stack of two individual SCs, for instance, based on GaAs and GaSb materials [4]. This approach is under development at Ioffe Institute as well. A simple Zn diffusion method is used for GaSb subcell fabrication. At the same time narrow-gap monolithic two-terminal tandems GaSb (top) - InGaAsSb (bottom) could give an increase in net efficiency for space and especially for TPV applications. Such heterostructures are grown by LPE method.

Module Design And Fabrication

Two types of concentrator modules have been designed and manufactured for flight experiments. The first one is based on 4x4 Fresnel lens panel [5] (see Figure 1) and the second is based on the reflective parabolic troughs [6] (see Figure 2). An optical efficiency of 93% for parabolic trough concentrators has been achieved and misorientation curves suitable for space application have been realized in these modules. Diamond-like carbon layers provided an effective corrosion protection of the Ag-coatings of the mirrors: no reduction of the optical efficiency was measured in parabolic trough mirrors during 15 months of their usage in the ordinary indoor conditions. AM0 power density value of 230-235 W/m² and specific power 70-75W/kg have been predicted in the arrays based on developed parabolic trough concentrators and linear receivers. Also, the module with ENTECH linear Fresnel lens as a solar concentrator [4] has been developed and measured [7] (see Figure 3). In the latter case the secondary optical elements - quartz cylindrical lenses have been introduced on the front surfaces of the 4x4 mm solar cells. These elements are characterized by a very high optical efficiency providing an additional radiation resistance, 1.5x increased concentration ratio and more wide misorientation range (see Figure 4).

High efficiency (23.4-24.7%, AM0, 20-100 suns) single junction AlGaAs/GaAs solar cells (see Figures 5 and 6) have been designed and manufactured for the modules with concentrators (parabolic troughs and Fresnel lenses). Linear receivers (see Figure 3) with an efficiency of 18.5-19% have been manufactured on the basis of the radiation stable solar cells with internal Bragg reflector. The employment of the Bragg reflector allowed us to increase the internal quantum yield in the long-wavelength range of the spectrum and to use a thinner n-GaAs base layer. Radiation resistance under 1 MeV and 3.75 MeV irradiation was increased in these cells owing to an improvement in the radiation stability of the long-wavelength spectral response (see Figures 7 and 8). Mechanically stacked GaAs-GaSb tandem cells with an efficiency of 28-29% at 100 suns have been fabricated for the linear receivers as well.

Advanced Cells and TPV Devices

The heterostructure AlGaAs/GaAs cells with extremely thin both AlGaAs window layer (4-5 nm) and GaAs surface layer (2-3 nm) have been proposed and developed [8] regarding to improvement the cell ultraviolet sensitivity and especially for operation as the betavoltaic cells. In such a device the surface built-in electric field, which, in fact, reduces the height of the protective barrier in a very thin AlGaAs window layer, is accumulated in a heavily doped transparent enough GaAs front layer. This provides a suppression of the fundamental loss mechanism consisting in the tunnelling of the generated hot electrons from absorbing p-GaAs region to the surface states through or over the surface AlGaAs barrier.

Monolithic two-terminal two-junction Al_{0.35}Ga_{0.65}As/GaAs solar cells (see Figure 9) have been designed and manufactured by low-temperature LPE. Connecting tunnel diode (see Figure 10) was prepared by LPE

method for the first time providing n-type (Te) and p-type (Ge) dopant concentrations as high as 10^{20}cm^{-3} . Figure 11 shows the spectral response curves for such a tandem cell. The following parameters have been achieved in one of the best samples: $V_{oc}=2.53\text{ V}$, $FF=0.81$ at 50 suns (AM0, 25°C ; see Figure 12). Current densities under one sun AM0 illumination correspond to 15.3 mA/cm^2 in the GaAs subcell and 14.2 mA/cm^2 in the $\text{Al}_{0.35}\text{Ga}_{0.65}\text{As}$ subcell. The combination of high sensitivities of both AlGaAs and GaAs subcells in one tandem cell will allow us to achieve the efficiency values comparable with those obtained in InGaP-GaAs monolithic tandem solar cells.

Thermophotovoltaic devices based on GaSb and InGaAsSb have been fabricated by LPE and Zn diffusion methods. The maximum efficiency of 11.3% was measured in GaSb cells under 70 suns AM0 illumination (no GaAs filter). 1 sun AM0 current density of 45 mA/cm^2 and $V_{oc}=0.46\text{ V}$ at 3.15 A/cm^2 have been achieved in these cells. Lattice matched $\text{In}_x\text{Ga}_{1-x}\text{As}_y\text{Sb}_{1-y}/\text{GaSb}$ heterostructures were grown by LPE from a Sb-riched melt. Band-gap energy of InGaAsSb cells was in the range 0.52-0.6 eV, which provides a long-wavelength edge of photosensitivity of 2150-2350 nm in TPV devices.

Monolithic two-terminal tandem GaSb-InGaAsSb ($E_g=0.56\text{ eV}$) thermophotovoltaic devices with connecting tunnel GaSb diode have been developed and fabricated (see Figures 13 and 14). Theoretical studies have indicated that current matching the top (GaSb) and bottom (InGaAsSb) subcells in tandem TPV devices can be reached in the case of bottom subcell band-gap energies 0.6-0.55 eV for the black-body emitter temperatures of 1100-1500°C, respectively. External quantum yields as high as 80% in the wavelength range 800-1600 nm (top cell) and about 75% in the range 1800-2100 nm (bottom cell) have been measured in tandem cells (see Figure 15). The magnitudes of the $V_{oc}=0.61\text{ V}$ and $FF=0.75$ have been achieved in one of the tandem TPV devices characterized by a high photoresponse up to wavelength of 2150 nm.

Radiation Resistance Results

1 MeV, 2 MeV and 3.75 MeV electron and 6.7 MeV proton irradiation tests have been carried out on AlGaAs/GaAs, GaSb, InGaAs and InGaAsSb cells. GaAs-based cells with the junction depth of 0.4-0.5 μm are characterized by a good radiation resistance, comparable to the best published data [9,10]. GaSb- and InGaAs-based cells have shown radiation resistance similar to the ordinary GaAs-based cells. An improvement in radiation resistance has been achieved in AlGaAs/GaAs solar cells with internal Bragg reflector. In particular, a high stability of the long-wavelength part of the spectral response curve took place even after 3.75 MeV irradiation with the electron fluence of 10^{16}cm^{-2} (see Figure 7). This result has been obtained owing to reduction of the photoactive n-GaAs base layer thickness up to 1.5 μm when the p-n junction depth was in the range of 0.3-0.4 μm . $\text{Al}_{0.35}\text{Ga}_{0.65}\text{As}$ -based top cells in tandems have also demonstrated the higher radiation resistance, than in ordinary GaAs based solar cells.

References

- [1] Zh.I.Alferov, V.M.Andreev, N.S.Zimogorova, D.N.Tret'akov "Photoelectric Properties of the Heterojunctions AlGaAs-GaAs", *Fiz. i Tekhn. Polupr.* 3(1969) 1633 (in Russian). Translated into English in *Sov. Phys. Semiconductors*, 3(1969)
- [2] Zh.I.Alferov V.M.Andreev, M.B.Kagan et al. "Solar Converters on the Base of the Heterojunctions pAlGaAs-nGaAs", *Fiz. i Tekhn. Polupr.* 4(1970) 2378 (in Russian). Translated into English in *Sov. Phys. Semiconductors*, 4(1970)
- [3] V.M.Andreev, V.P.Khvostikov, V.R.Larionov, V.D.Rumyantsev, M.Z.Shvarts "Multilayer AlGaAs/GaAs Heterostructure Solar Cells for Concentrator Modules", *Proc. of the 12th European PV Solar Energy Conf.*, Amsterdam 11-15 April, 1994.
- [4] M.Piszczor, M.O'Neill, L.Fraas. "A novel space photovoltaic module using a linear Fresnel lens and a line-focus tandem cell receiver", *Proc. of the 23rd IEEE Photovoltaic Specialists Conference*, Louisville, USA, 1993, pp. 1386-1391.

- [5] V.A.Grilikhes, V.D.Rumyantsev, M.Z.Shvarts. "Indoor and Outdoor Testing of Space Concentrator AlGaAs/GaAs Photovoltaic Modules with Fresnel Lenses". *Proc. of the 25th IEEE PVSC*, Washington, DC, May 13-17, 1996, pp.345-348.
- [6] V.M.Andreev, V.D.Rumyantsev "A³B⁵ based solar cells and concentrating optical elements for space PV modules". *Solar Energy Materials and Solar Cells*, 44 (1996), pp.319-332.
- [7] V.M.Andreev, V.M.Lantratov, V.D.Rumyantsev, M.Z.Shvarts. "Development of PV Receivers for Space Line-Focus Concentrator Modules". *Proc.of the the 25th IEEE PVSC*, Washington, DC, May 13-17, 1996, pp. 341-344.
- [8] V.D.Rumyantsev, V.P.Khvoostikov, S.V.Sorokina, A.M.Mintairov, P.G.Peevski "Spectral behavior of AlGaAs/GaAs heterophotocells with extremely thin (2-8 nm) window layers.", *Proc. of the 23rd Int. Symp. on Compound Semicomd.*, St.Petersburg, September 23-27, 1996.
- [9] G.P.Summers, R.J.Walters, M.A.Xapsos, "A new approach to damage prediction for solar cells exposed to different radiations", *Proc. of the First WCPEC*, Hawaii, December 5-9, 1994, pp. 2068-2075
- [10] R.J.Walters, S.R.massenger, H.L.Cotal, G.P.Summers, P.R.Sharps, M.L.Timmons, P.Iles, Y.C.M.Yeh, "Radiation responce of InGaP/GaAs single and dual-junction splar cells", *Technical Digest of the International PVSEC-9*, Miyazaki, Japan, November 11-15, 1996, pp.619-620.

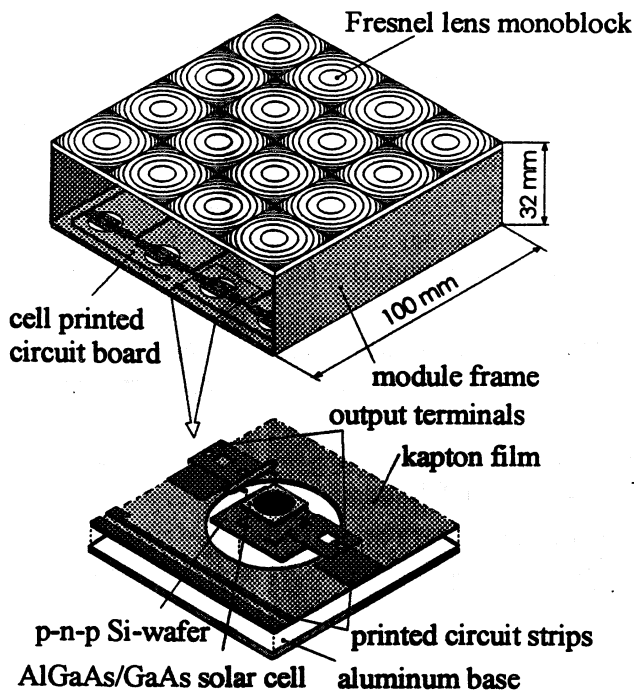


Fig.1. Point-focus Fresnel lens panel PV module conceptual design.

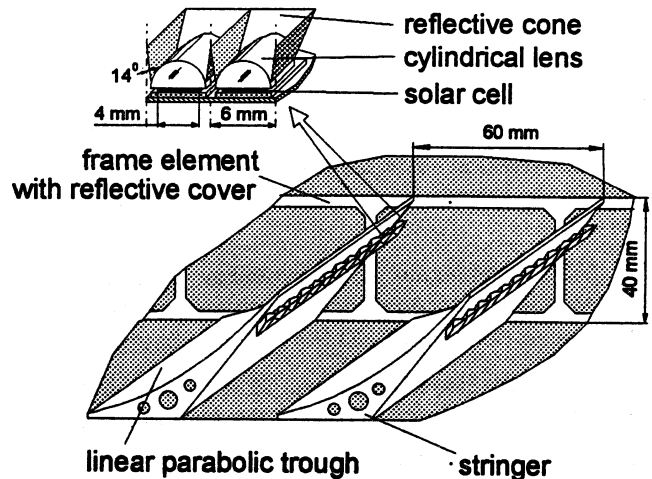


Fig.2. Conceptual design of a concentrator array with linear parabolic troughs.

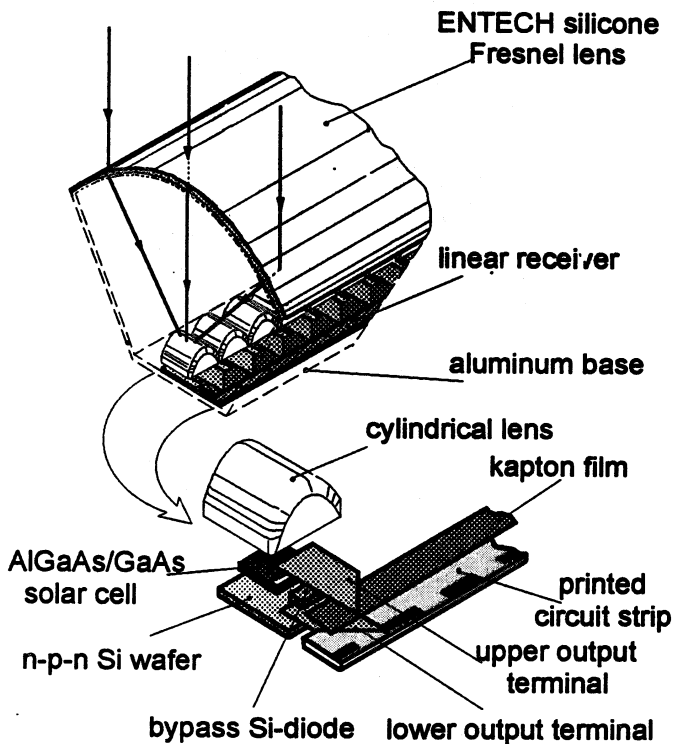


Fig.3. Line-focus Fresnel lens PV module conceptual design. Linear receiver is shown as well.

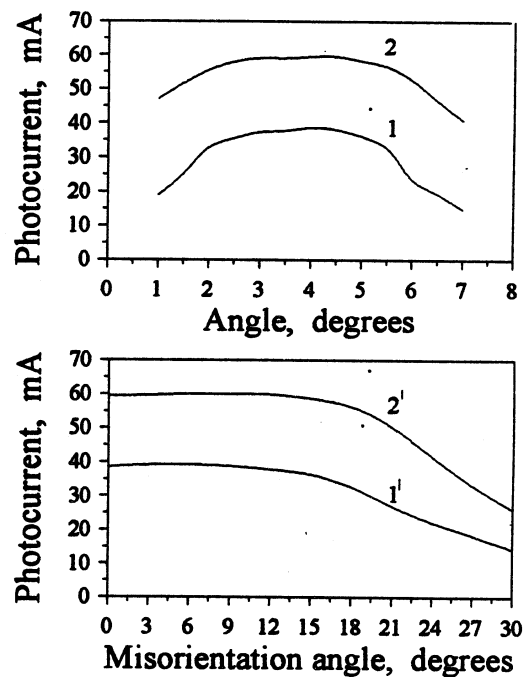


Fig.4. Misorientation curves of a module based on ENTECH line-focus Fresnel lens and developed string-type AlGaAs/GaAs receiver: a - for rotation around the axis parallel to the focal line; b - the same for the perpendicular axis. 1,1' - curves measured before bonding the secondary cylindrical lenses; 2,2' - the same after bonding the secondary lenses.

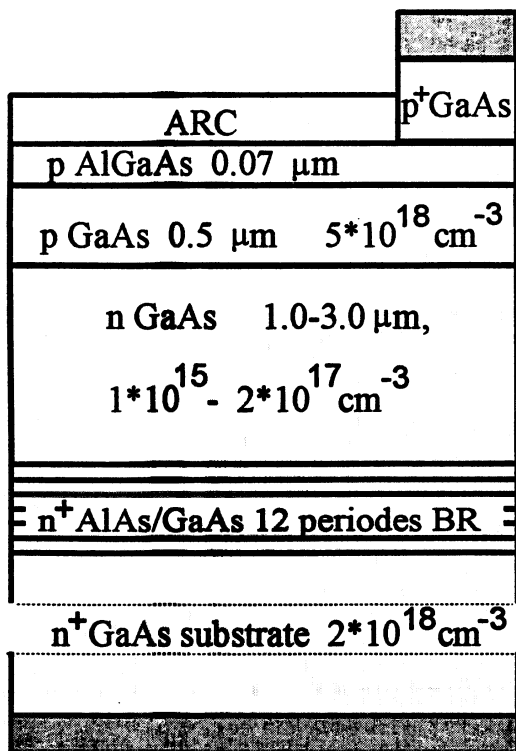


Fig.5. Schematic structure of the solar cell with Bragg reflector (BR).

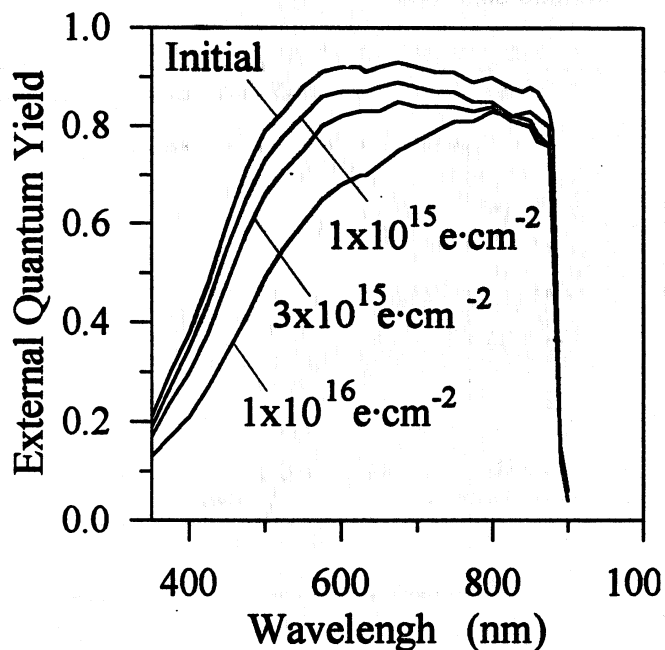


Fig.7. External quantum yield of the SC with Bragg reflector as a function of 3.75 MeV electron fluence.

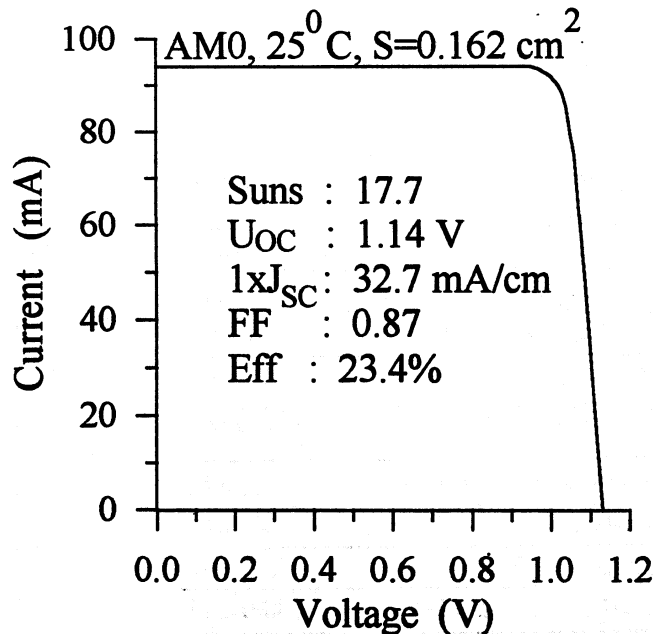


Fig.6. I-V curve of a 23.4% efficient solar cell with Bragg reflector.

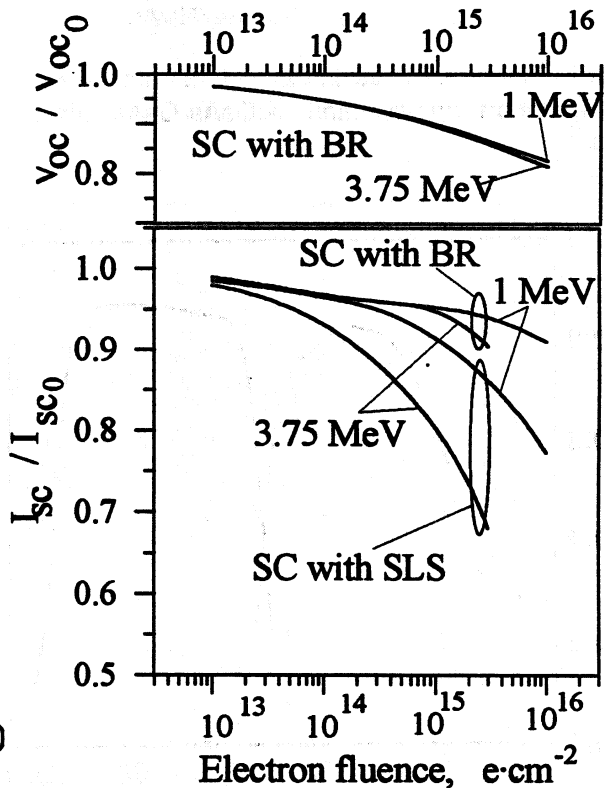


Fig.8. Open circuit voltage and short circuit current variations in the SC with Bragg reflector (BR) and with a superlattice structure (SLS) instead of BR (no long-wavelength reflection of light) after 1 MeV or 3.75 MeV electron irradiations.

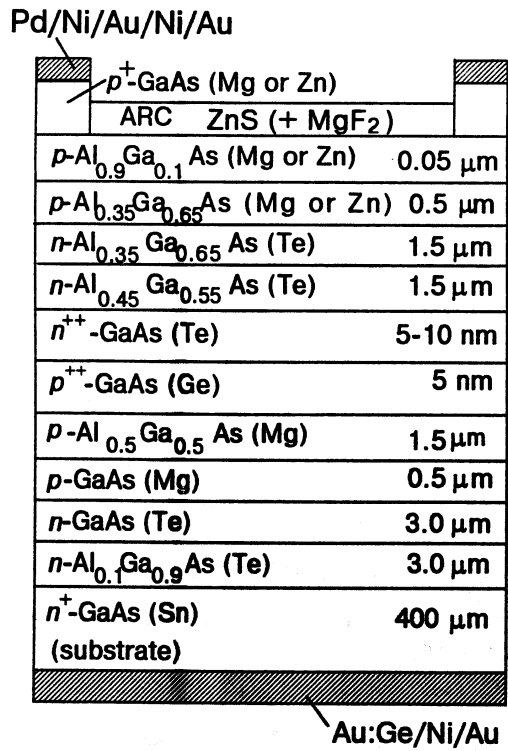


Fig.9. Schematic structure of a monolithic two-junction two-terminal AlGaAs-GaAs solar cell.

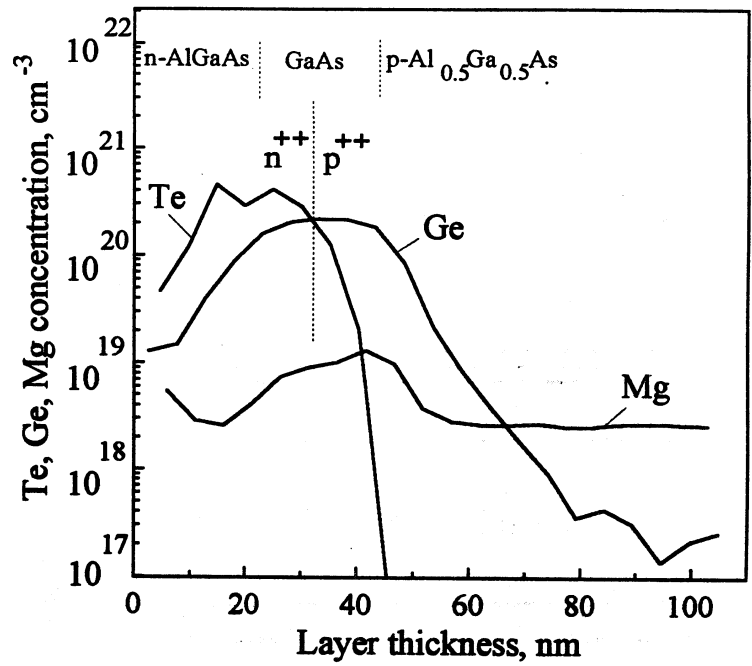


Fig.10. SIMS profiles of dopant elements across the tunnel junction layers in the AlGaAs-GaAs cascade solar cells.

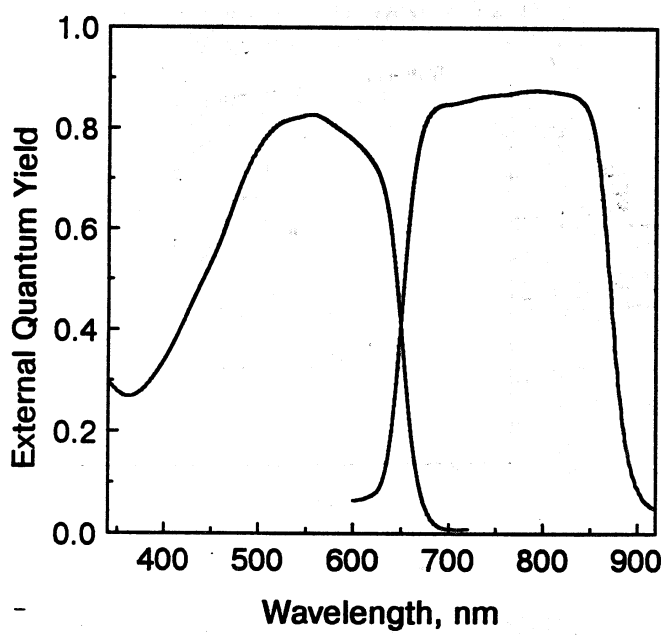


Fig.11. Spectral responses of the AlGaAs- and GaAs-subcell in two-terminal tandem solar cells.

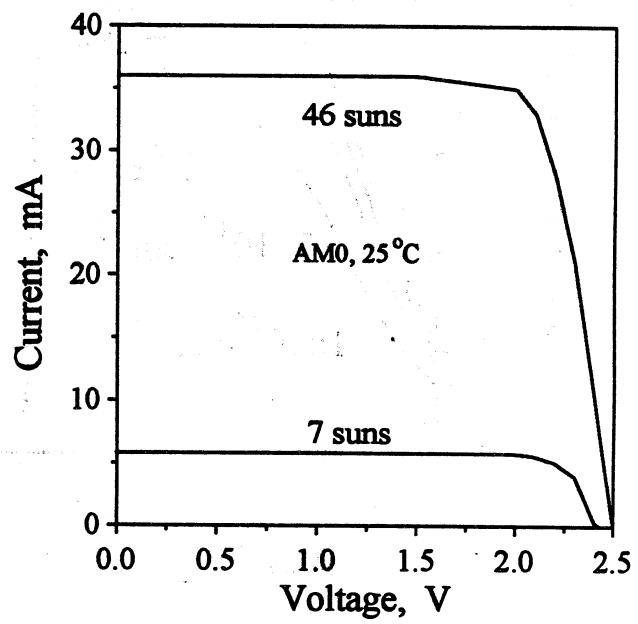


Fig.12. Illuminated I-V characteristics of the AlGaAs-GaAs two-terminal cascade solar cell.

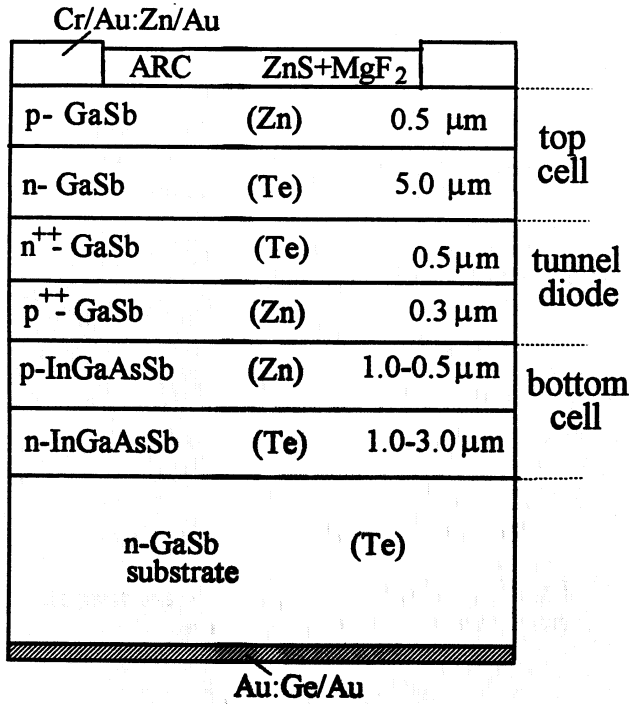


Fig.13. Schematic diagram of the monolithic two-junction two-terminal GaSb-InGaAsSb solar cell.

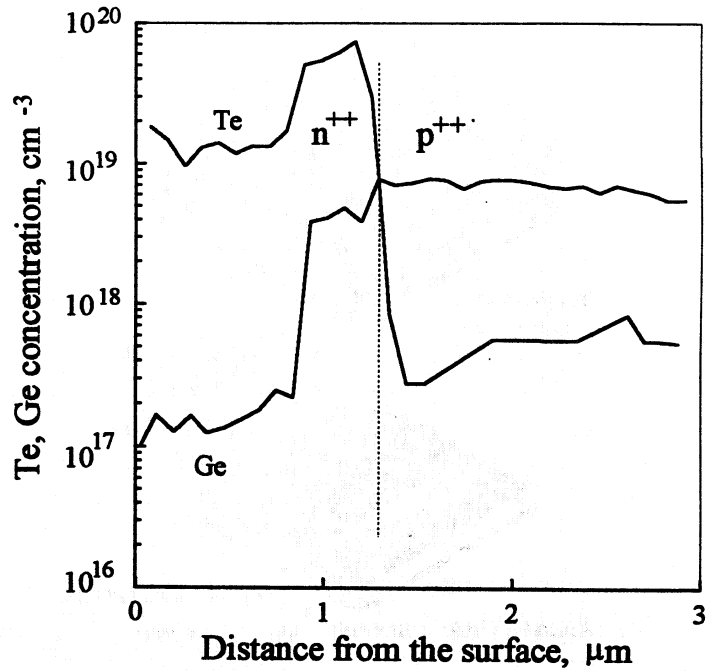


Fig.14. SIMS profiles for Te and Ge dopants in the GaSb-based tunnel diodes for GaSb-InGaAsSb tandem TPV device.

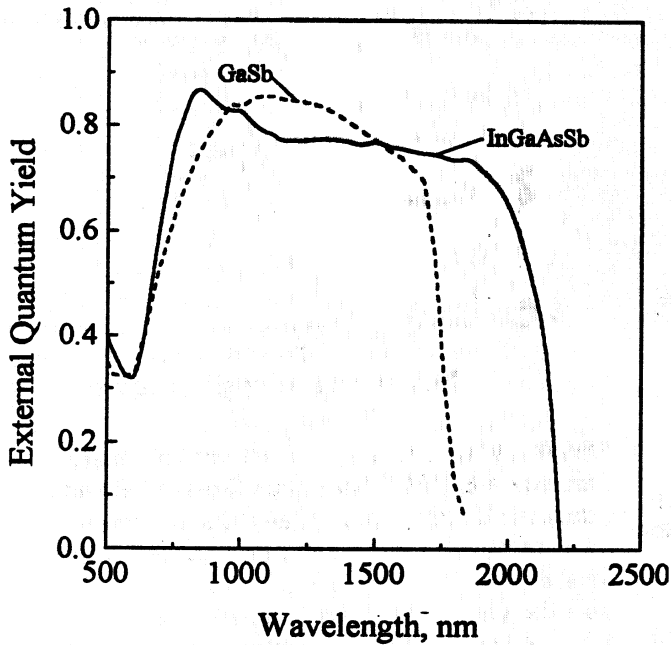


Fig.15. Spectral responses of GaSb- and InGaAsSb-based solar cells with ZnS+MgF₂ antireflection coating.

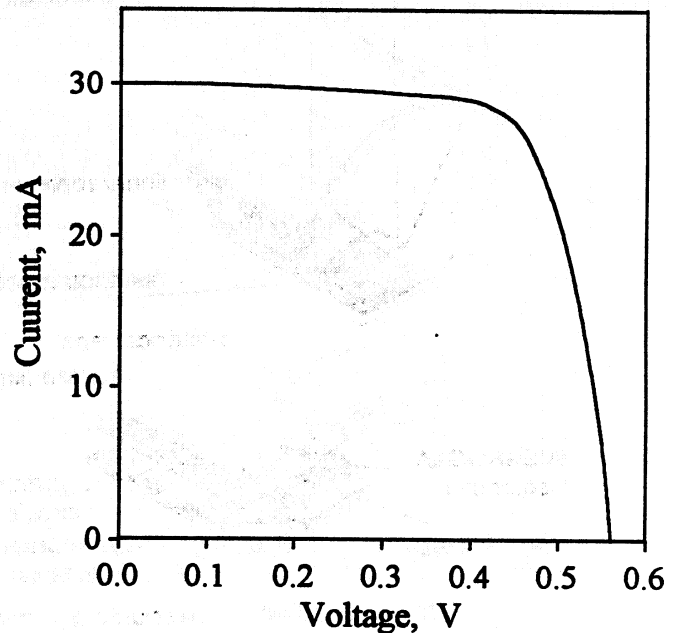


Fig.16. Illuminated I-V characteristic of the tandem GaSb-InGaAsSb ($E_g=0.56$ eV) TPV device.

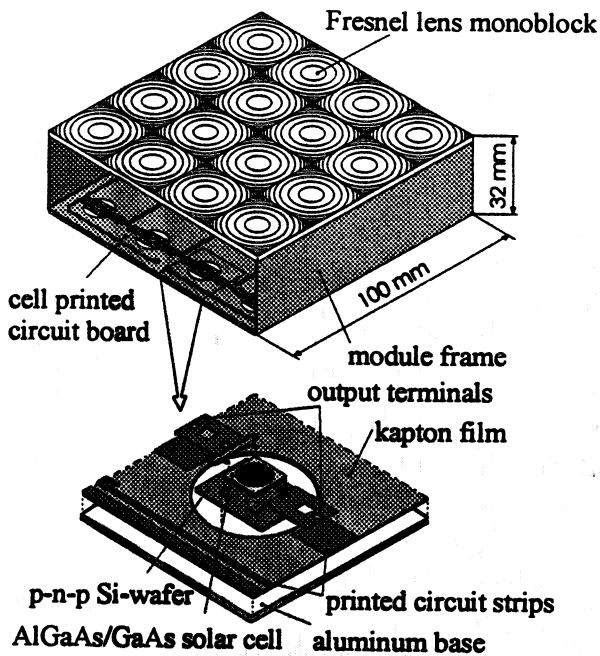


Fig.1. Point-focus Fresnel lens panel PV module conceptual design.

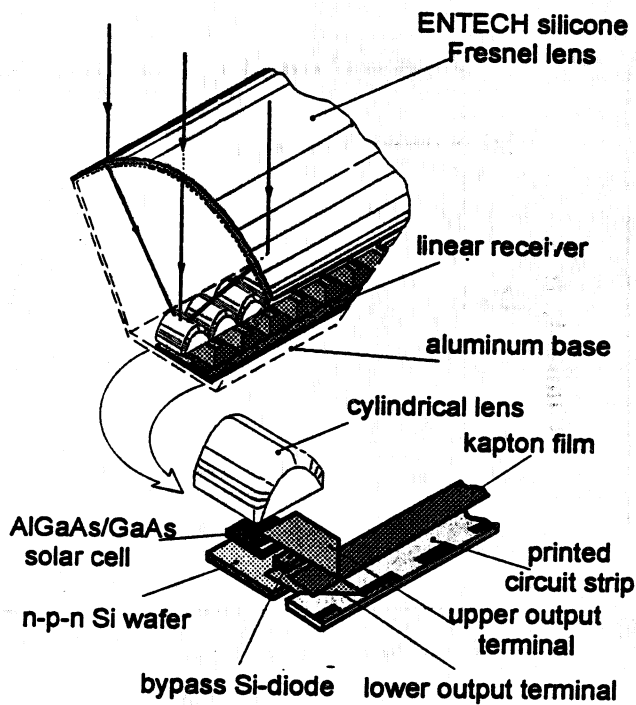


Fig.3. Line-focus Fresnel lens PV module conceptual design. Linear receiver is shown as well.

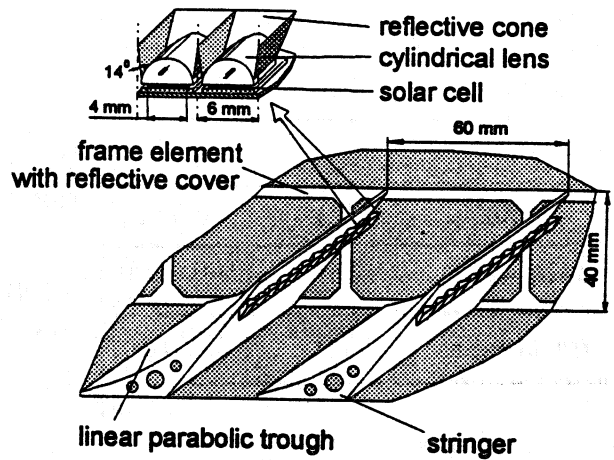


Fig.2. Conceptual design of a concentrator array with linear parabolic troughs.

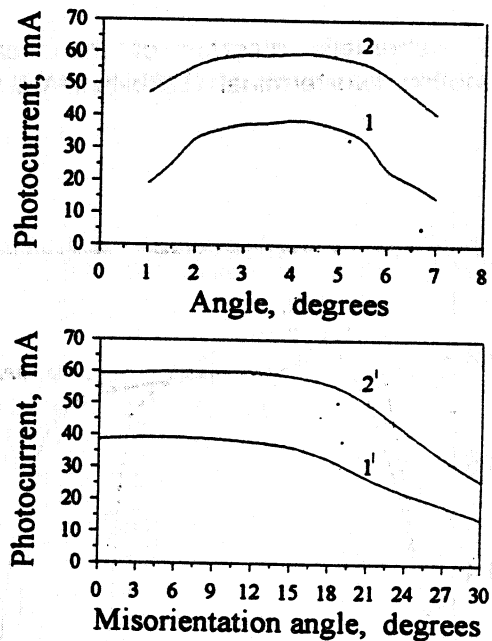


Fig.4. Misorientation curves of a module based on ENTECH line-focus Fresnel lens and developed string-type AlGaAs/GaAs receiver: a - for rotation around the axis parallel to the focal line; b - the same for the perpendicular axis. 1,1' - curves measured before bonding the secondary cylindrical lenses; 2,2' - the same after bonding the secondary lenses.

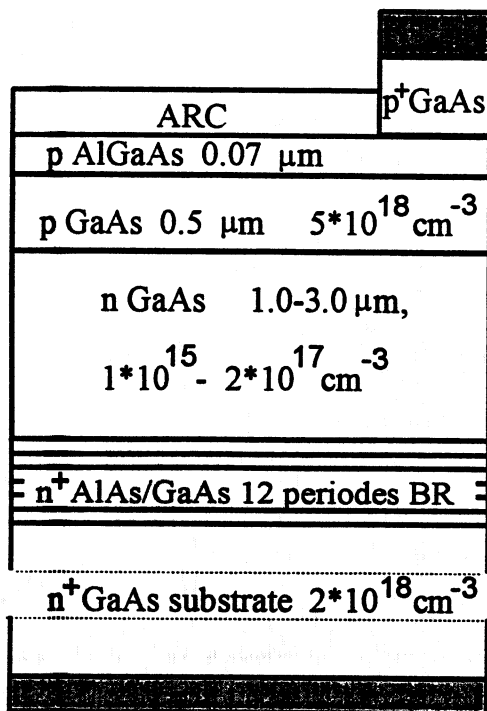


Fig.5. Schematic structure of the solar cell with Bragg reflector (BR).

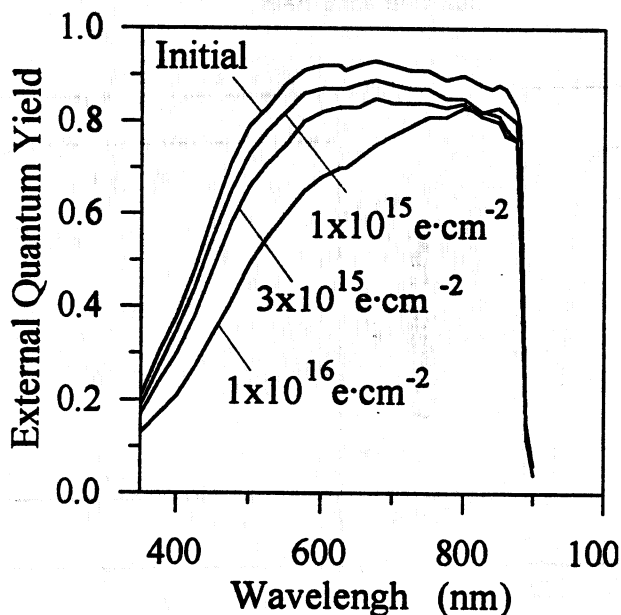


Fig.7. External quantum yield of the SC with Bragg reflector as a function of 3.75 MeV electron fluence.

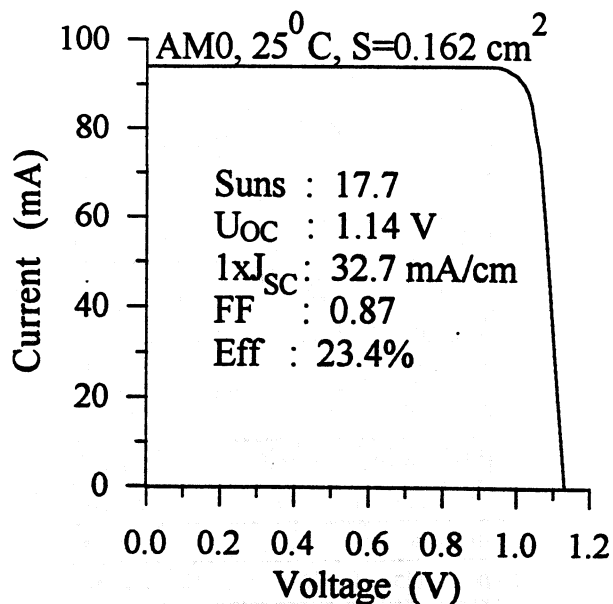


Fig.6. I-V curve of a 23.4% efficient solar cell with Bragg reflector.

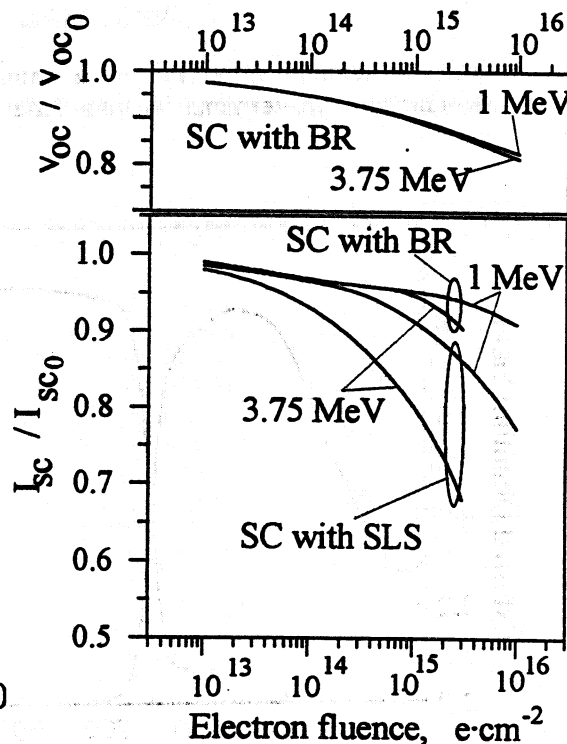


Fig.8. Open circuit voltage and short circuit current variations in the SC with Bragg reflector (BR) and with a superlattice structure (SLS) instead of BR (no long-wavelength reflection of light) after 1 MeV or 3.75 MeV electron irradiations.

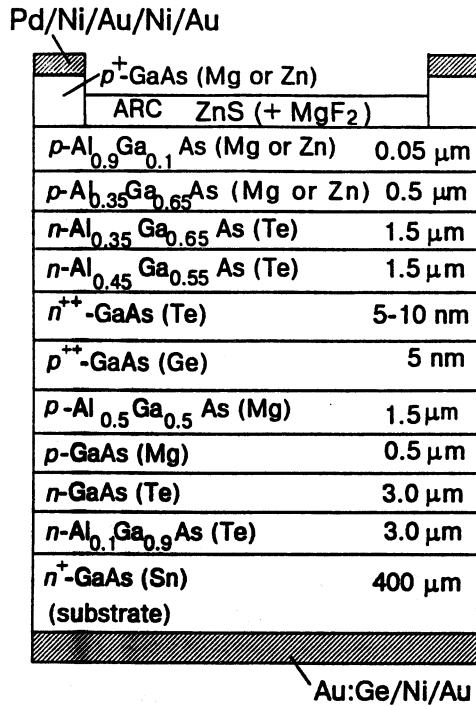


Fig.9. Schematic structure of a monolithic two-junction two-terminal AlGaAs-GaAs solar cell.

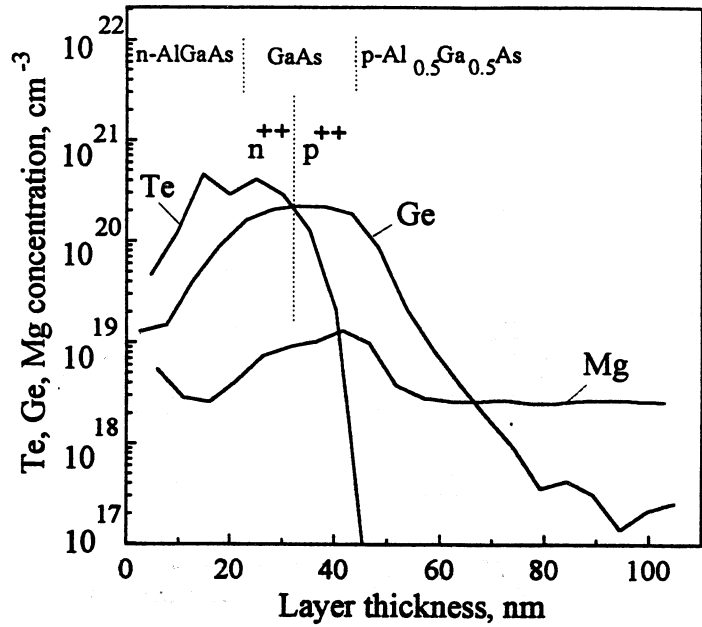


Fig.10. SIMS profiles of dopant elements across the tunnel junction layers in the AlGaAs-GaAs cascade solar cells.

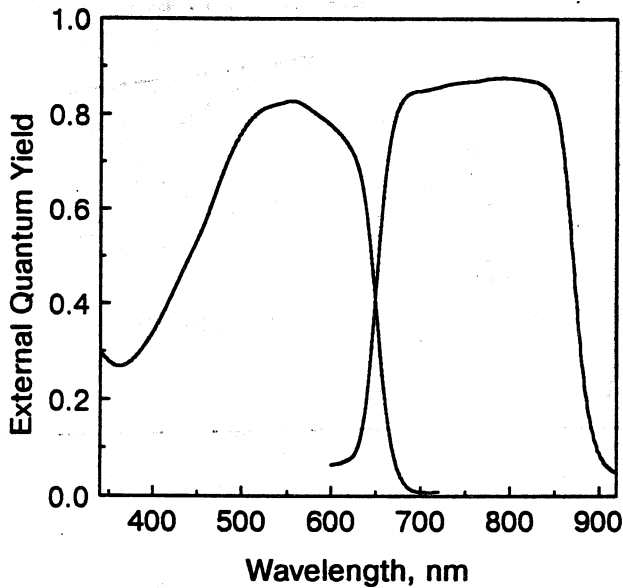


Fig.11. Spectral responses of the AlGaAs- and GaAs-subcell in two-terminal tandem solar cells.

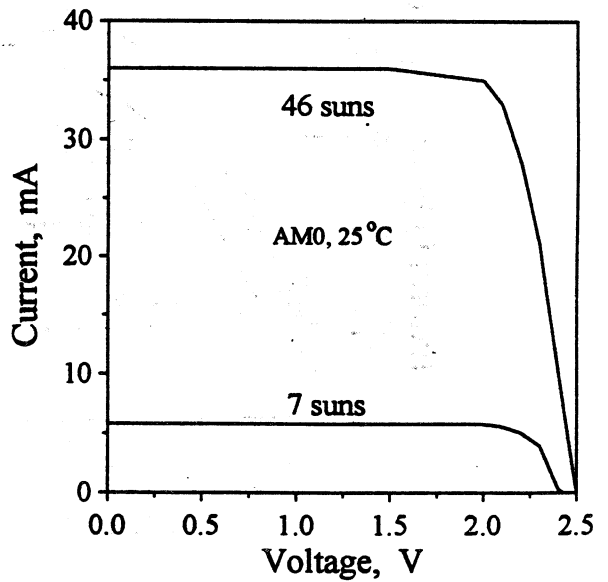


Fig.12. Illuminated I-V characteristics of the AlGaAs-GaAs two-terminal cascade solar cell.

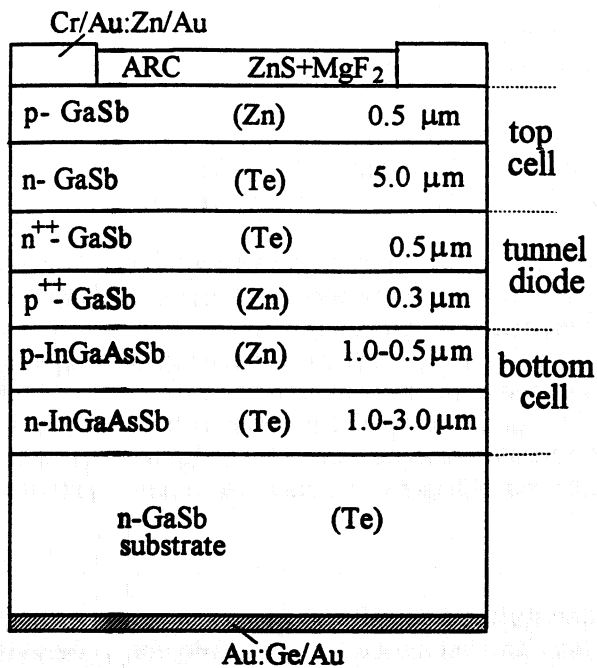


Fig.13. Schematic diagram of the monolithic two-junction two-terminal GaSb-InGaAsSb solar cell.

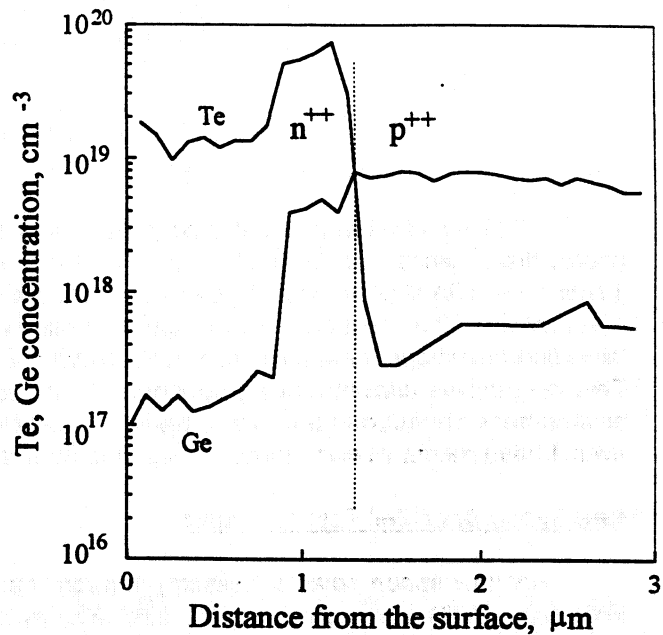


Fig.14. SIMS profiles for Te and Ge dopants in the GaSb-based tunnel diodes for GaSb-InGaAsSb tandem TPV device.

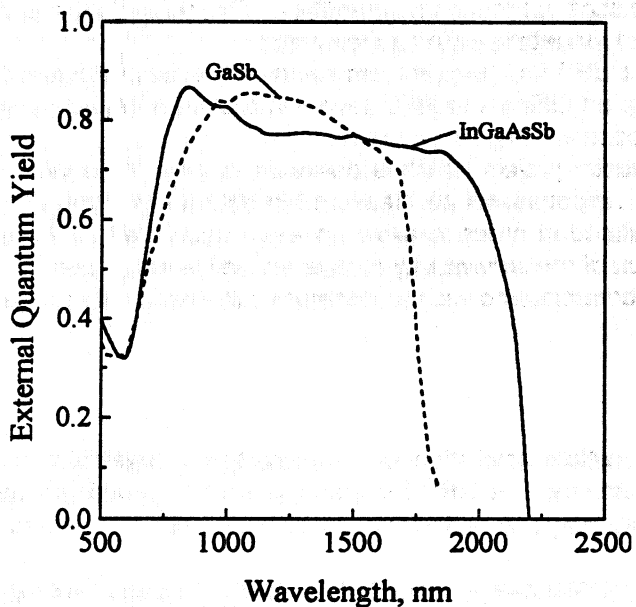


Fig.15. Spectral responses of GaSb- and InGaAsSb-based solar cells with ZnS+MgF₂ antireflection coating.

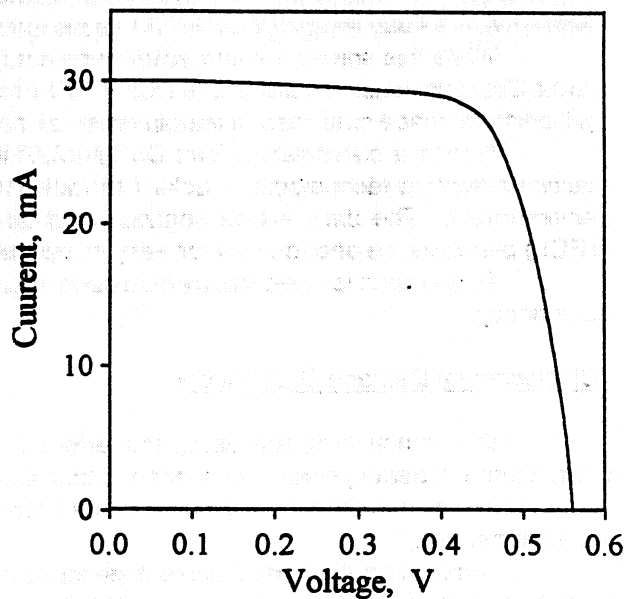


Fig.16. Illuminated I-V characteristic of the tandem GaSb-InGaAsSb ($E_g=0.56$ eV) TPV device.

**SPACE PHOTOVOLTAICS SURVIVABILITY RESEARCH AT
THE NAVAL RESEARCH LABORATORY**

Robert J. Walters

*Naval Research Laboratory, Code 6615, Washington, DC 20375
ph: 202-767-2533, fax: 202-404-8076, e-mail: rwalters@ccf.nrl.navy.mil*

The Naval Research Laboratory (NRL) has been conducting research on the radiation response of space photovoltaic devices since the 1960's. The response of many types of solar cells from crystalline Si to dual-junction InP/InGaAs to various types of particle irradiation such as electrons, protons, and alpha particles has been studied. The research also includes an analysis of the space radiation environment, and new techniques have been developed that allow accurate predictions of the on-orbit performance of a given solar cell technology. This research is currently being expanded to include not only the natural environment but also the weapons environment of neutrons and flash x-rays. In addition, considerable advances in the area of solar flare proton events have recently been made. This paper summarizes the highlights and latest achievements in these areas.

New Space Solar Cell Testing Project

A new space solar cell testing program has been established at NRL which emerged out of the UHF Follow-On (F/O) Satellite Program. UHF F/O is a Navy Communication Satellite Program. Because of the addition of the Global Broadcast System (GBS), the final three UHF F/O satellites required more power with a reduced weight margin. To address this, it was proposed to use a new solar cell technology, i.e. dual-junction (DJ) InGaP/GaAs solar cells. However, not enough data was available to determine the radiation survivability of these cells. In particular, the response of these cells in a weapons environment had never been tested, and there was a major disagreement over whether these cells could be qualified with the existing data and analytical calculations. Furthermore, the proper testing procedures and analysis techniques could not be agreed upon. This controversy along with several other factors lead to the decision to revert back to the older, standard Si cell technology which has proven survivability characteristics but reduced capabilities. This required the addition of a solar panel to each wing of the UHF F/O spacecraft to meet the power requirements.

While this solved the immediate problem for UHF F/O, the problem clearly still exists for future Navy and other DoD missions. Therefore, the UHF F/O Program Office and NRL have established a project in which NRL will perform space qualification measurements of space photovoltaic devices.

This is a coordinated, joint DoD/NASA/Industry project which is designed to be a three year project to qualify emerging technologies. Solar cell radiation response will be measured in both the natural and weapons environment. The data will be analyzed and tabulated in order to allow an easy calculation of the end-of-life (EOL) performance and to allow for easy comparison of the survivability of different cell technologies.

This project is open to any interested collaborators who wish to generate survivability data on a new cell technology.

Displacement Damage Dose Model

The concept of analyzing the effect of particle irradiation on semiconductor materials in terms of displacement damage dose has been under development at NRL for many years [1-3], and the model has recently been recognized as a powerful tool for analyzing the performance of solar cells in a space radiation environment [4,5].

Displacement Damage Dose is given by the product of the calculated nonionizing energy loss (NIEL) and the particle fluence. By plotting solar cell degradation data in terms of displacement damage dose, data measured under irradiation by particles of different energies all fall on the same curve. This curve is termed the characteristic curve for the given cell technology. The usefulness of the model lies in the fact that the characteristic curve can be determined from a single set of monoenergetic degradation data, but the characteristic curve, combined with the calculated NIEL values, can then be used to predict the cell response to irradiation by any particle energy, even irradiation by a spectrum of particles as found in the space environment.

An example of this technique is shown in Figure 1. The degradation of the maximum power (P_{max}) of n^+p InP/Si solar cells under irradiation by protons of various energies is plotted as a function of displacement damage dose. All of the data fall on the characteristic curve, independent of the particle energy. Therefore, the characteristic curve can be used to predict the cell response to irradiation by protons of essentially any energy. Furthermore, since the characteristic curve can be determined from a single data set, it is now necessary to perform only one proton irradiation measurement to fully characterize the cell response to irradiation by a spectrum of protons.

This model is also very useful in analyzing the radiation spectrum of a given earth orbit, the effect of low energy protons in the earth's radiation environment, and the effect of solar proton events on earth satellites. These topics are addressed by other papers from NRL in this conference [6,7].

Cell Response at high fluences - effects of carrier removal

During NRL's development of homoepitaxial n^+p InP/InP solar cells with Spire Corp. around 1991, it was observed that the radiation response of the cells displayed an interesting dependence on the initial cell base dopant level [8,9]. The open circuit voltage (V_{oc}) was seen to degrade more rapidly in cells with a lower base dopant level while the short circuit current (I_{sc}) degraded less rapidly in lightly doped cells. These effects tend to cancel each other so that the degradation of P_{max} is essentially independent of the initial cell base dopant level. About the same time, this same mechanism was observed by NREL in n^+p GaAs solar cells [10].

This behavior was explained through an analysis of the effects of carrier removal. The defects induced in the p-type cell base by the irradiation cause compensation which reduces the majority carrier concentration. This causes the depletion region width to increase which has two effects. First, a wider depletion region results in a larger recombination dark current which degrades V_{oc} . Second, a wider depletion region results in more light being absorbed in an electric field region which enhances the carrier collection efficiency and, hence, I_{sc} . Therefore, cells with initially low base dopant levels, which more readily show the effects of carrier removal, show more rapid degradation in voltage but less rapid degradation in current. The power, being essentially the product of these two, degrades at a constant rate independent of the base dopant level.

Recently, this subject has been revisited by NRL in the development of InP/Si cells and TTI and NASDA in Japan studying Si and diffused-junction InP solar cells. In these recent studies, higher fluence levels have been achieved which have shown a catastrophic failure mechanism in the cells when carrier removal becomes so severe that the base is type converted, the junction is destroyed, and the current drops to zero (Fig. 2).

The cell response in the fluence range just below failure is quite interesting. The current is seen to increase significantly, in fact to a value above the BOL value. The cell voltage continues to degrade in this fluence range, but the increase in current is so large that the power is seen to remain nearly constant. This has been termed the "plateau" region, and the entire sequence has been referred to as "plateau and plummet".

InP/InGaAs/Ge Dual Junction Solar Cells

For about the past 10 years, NRL and the National Renewable energy laboratory (NREL) have been developing homoepitaxial InP/InGaAs tandem solar cells for space applications. The best cells produced were $2 \times 2 \text{ cm}^2$ cells with 1 sun, AM0 efficiencies $\sim 22\%$. In 1995, NRL began a one year project to transition this cell to

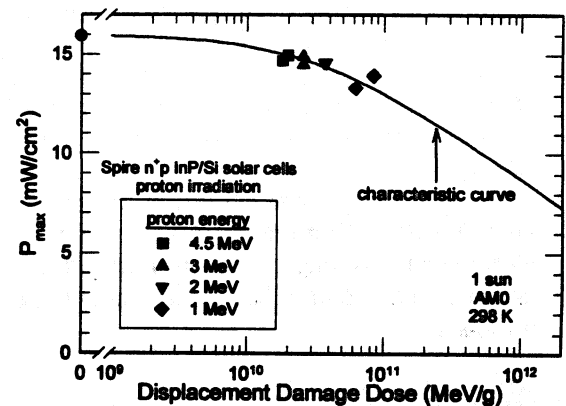


FIGURE 1: The degradation of InP/Si solar cells analyzed in terms of displacement damage dose

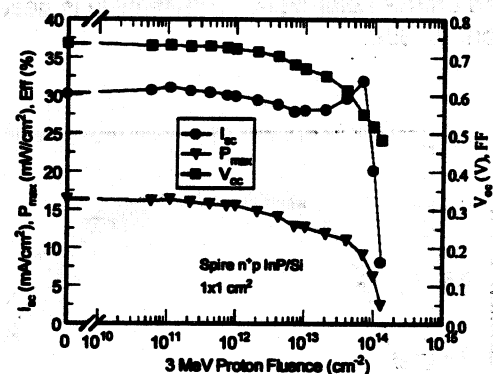


FIGURE 2: The degradation of InP/Si solar cells under high fluence irradiation showing plateau and plummet.

resistance than the n^+p cells at high fluences (Fig. 6). If the BOL efficiency of the p^+n cells is increased, then this advantage may appear at lower fluences.

Another advantage of the p^+n structure is related to heteroepitaxial growth on Si wafers. Si is an n-type dopant in InP. During MOCVD growth, Si atoms from the substrate diffuse into the epitaxial layers inducing an n-type layer at the rear of the cell. In n^+p InP/Si cells, this necessitates a tunnel junction at the cell/substrate interface. However, no such tunnel junction is needed in the p^+n structure, so the heteroepitaxial growth is simpler.

Recently, researchers at Essential Research have grown p^+n InP/InP cells with efficiencies $\sim 17\%$ [11]. This is a significant improvement, and it is anticipated that higher efficiencies may soon be achieved. With BOL efficiencies this high, it is likely that the advantages of the p^+n structure in a radiation environment may be realized. To this end, NRL is working with Essential Research to measure the radiation response of the improved p^+n cells.

InP/Si Solar Cells

It is now well known that the superior radiation resistance of InP/Si solar cells make them an excellent candidate for high radiation space missions [12,13]. Spire has grown $2 \times 4 \text{ cm}^2$ cells with BOL efficiencies $\sim 13\%$, 1 sun, AM0 which show essentially no degradation under irradiation by 1 MeV electron fluences as high as $1 \times 10^{16} \text{ cm}^{-2}$ (Fig. 7). With this performance, the InP/Si cells outperform even the DJ InGaP/GaAs cells in a radiation environment.

The mechanism for the radiation response of these cells has been studied [14]. Through measurements such as quantum efficiency (Fig. 8) combined with dark current measurements (Fig. 9), it has been determined that at low fluence levels, the cell degradation is caused primarily by a decrease in the minority carrier diffusion length which causes the diffusion dark current to increase which degrades V_{oc} . At higher fluences, the degradation mechanism due to carrier removal dominates as described above.

At present, the InP/Si program is funding Spire to fabricate a power panel for the STRV research satellite based on InP solar cells. The satellite is destined for a high radiation transfer orbit, and the expected launch date is Spring 1999.

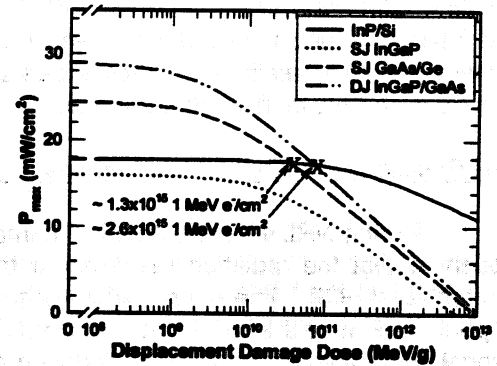


FIGURE 7: Comparison of the radiation response of InP/Si cells with other cell technology.

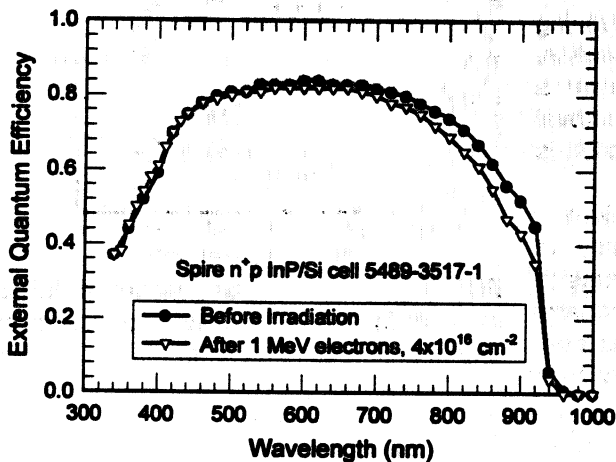


FIGURE 8: Degradation of the external quantum efficiency of an InP/Si under electron irradiation.

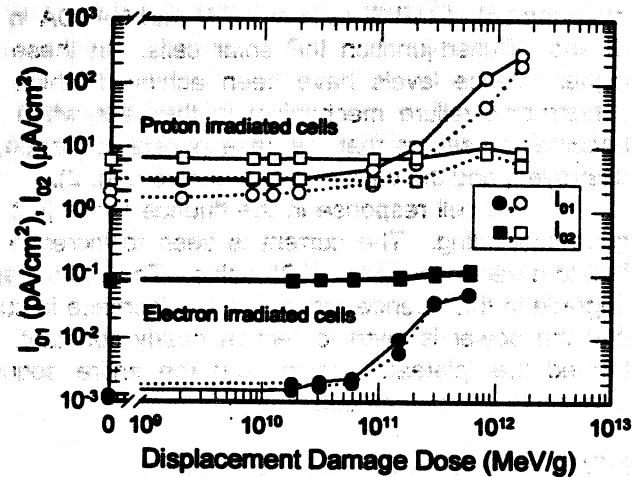


FIGURE 9: Increase in the junction dark current parameters due to proton and electron irradiation of InP/Si solar cells.

a heteroepitaxial version grown on Ge substrates. A team consisting of NRL, Tecstar, NREL, and RTI was assembled for the project. The significant achievements of the project were improvements design and structure of the individual cell components. In particular, improved lattice matching grade schemes were developed and alternate p-type dopants to Zn with lower diffusion constants were studied.

At the end of the 1 year project, the team was ready to fabricate the full tandem structure. However, no follow-on funding for the project could be obtained.

InGaP/GaAs Single and Dual Junction Solar Cells

The InGaP/GaAs dual junction cell technology has made significant advances in BOL efficiencies and is quickly gaining a place in the space photovoltaic market. However, there is still a significant lack of radiation response data on these cells. NRL has been studying p⁺n cells, both single junction InGaP and dual junction produced by Tecstar. The degradation under 1 MeV electron and 3 MeV proton irradiation has been measured and analyzed in terms of displacement damage dose model (Fig. 3). The basic mechanisms of the cell degradation are also under study through quantum efficiency (Fig. 4), dark current (Fig. 5), and other measurements.

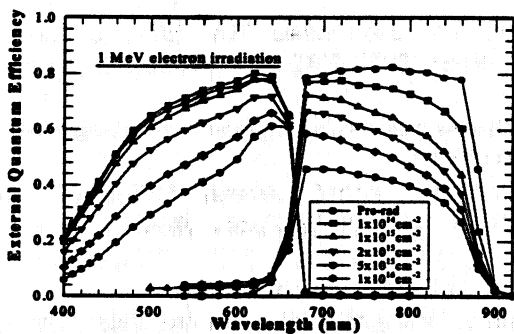


FIGURE 4: Degradation of the external quantum efficiency of a DJ InGaP/GaAs solar cell under electron irradiation.

p⁺n InP/InP

In the development of InP solar cells, the focus has been on n⁺p cells. This is the case because there has, as yet, been no suitable passivation scheme developed for InP, so the cell emitter must be made very thin for optimum current collection. In InP, thin, heavily doped n-type layers are easier to grow than p-type, so it has not been possible to achieve the high efficiencies of the n⁺p cells with the p⁺n structure. However, the p⁺n structure has certain advantages. The radiation-induced defects in InP do not act to compensate n-type material, so the p⁺n cells do not show carrier removal. Because of this, the p⁺n cells show better radiation

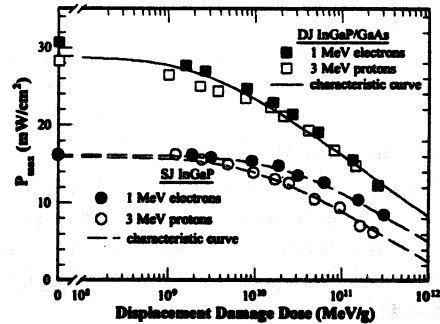


FIGURE 3: Degradation of single and dual junction InGaP/GaAs cells under electron and proton irradiation analyzed in terms of displacement damage dose.

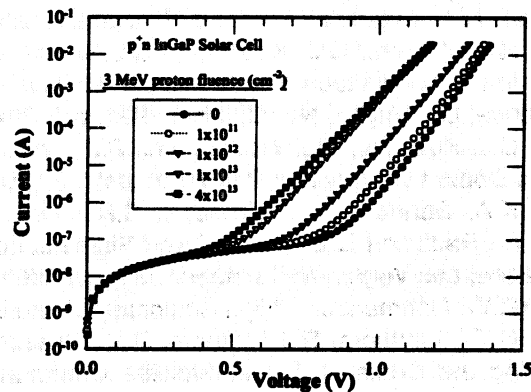


FIGURE 5: Increase in the junction dark current of SJ InGaP solar cell under proton irradiation.

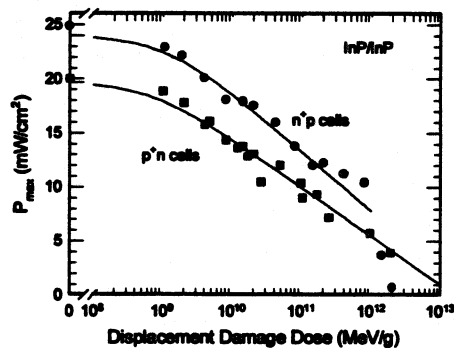


FIGURE 6: Comparison of the degradation of n⁺p and p⁺n InP/InP solar cells. Because the p⁺n cells are not affected by carrier removal, they may show better radiation resistance.

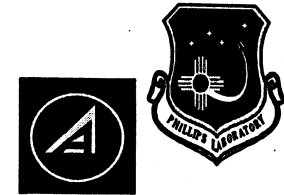
References

1. G.P. Summers, E.A. Burke, and M.A. Xapsos, "Displacement Damage Analogs to Ionizing Radiation Effects", *Radiation Measurements* 24 (1), 1-8 (1995).
2. G.P. Summers, E.A. Burke, P. Shapiro, S.R. Messenger, and R.J. Walters, "Damage Correlation in Semiconductors Exposed to Gamma, Electron, and Proton Radiations", *IEEE Trans. Nuc. Sci.* 40, 1300-1306 (1993).
3. G.P. Summers, R.J. Walters, M.A. Xapsos, E.A. Burke, S.R. Messenger, P. Shapiro, and R.L. Statler, "A New Approach to Damage Prediction for Solar Cells Exposed to Different Radiations", *IEEE Proc. 1st World Conference on Photovoltaic Energy Conversion*, Waikoloa Hawaii, Dec., 1994, p. 2068-2073.
4. M. Yamaguchi, T. Takamoto, S.J. Taylor, R.J. Walters, G.P. Summers, D.J. Flood, and M. Ohmori, "Correlations for Damage in Diffused Junction InP Solar Cells Induced by Electron and Proton Irradiation", *J. Appl. Phys.* 81 (9), (1997).
5. S.G. Bailey, R. Chock, H.B. Curtis, "Accurate On-Orbit Solar Cell Performance Using the Environmental Work Bench and Radiation Damage Models", *Proc. 9th Photovoltaic Science and Engineering Conference*, Miyazaki, Japan, p.627, Nov. (1996)
6. G.P. Summers, S.R. Messenger, E.A. Burke, M.A. Xapsos, and R.J. Walters, "Contribution of Low Energy Protons to the Degradation of Shielded GaAs Solar Cells in Space", this conference.
7. M.A. Xapsos, S.R. Messenger, R.J. Walters, G.P. Summers, and E.A. Burke, "The Effect of Large Solar Flares on GaAs Solar Cell Efficiency", this conference.
8. R.J. Walters, C.J. Keavney, S.R. Messenger, G.P. Summers, and E.A. Burke, "The Effect of Dopant Density on the Radiation Resistance of MOCVD InP Solar Cells", *Proc. 22nd IEEE Photovoltaic Specialists Conference*, Las Vegas, NV, October 1991, p 1588-1592.
9. C.J. Keavney, R.J. Walters, and P.J. Drevinsky, "Optimizing the Radiation Resistance of InP Solar Cells: Effect of Dopant Density and Cell Thickness", *J. Appl. Phys.* 73, 60-70 (1996).
10. K.A. Bertness, B.T. Cavicchi, S.R. Kurtz, J.M. Olson, A.E. Kibbler, and C. Kramer, "Effect of Base Doping on Radiation Damage in GaAs Single-Junction Solar Cells", *Proc. 22nd IEEE Photovoltaics Specialists Conference*, Las Vegas, NV, October 1991, p 1582-1587.
11. R.W. Hoffman, Jr., "High Beginning-of-Life Efficiency p/n InP Solar Cells", this conference.
12. G.P. Summers, R.J. Walters, S.R. Messenger, and E.A. Burke, "Role of Radiation-hard Solar Cells in Minimizing the Costs of Global Satellite Communication Systems", *Progress in Photovoltaics: Research and Applications* 4, 147-154 (1996).
13. S. Wojtczuk, P. Colter, N.H. Karam, H.B. Serreze, G.P. Summers, and R.J. Walters, "Radiation-hard, Lightweight 12% AM0 BOL InP/Si Solar Cells", *IEEE Proc. 25th Photovoltaic Specialist Conf.*, Washington, DC, May 1996, p.151-155.

Page intentionally left blank



**United States Air Force
PHILLIPS LABORATORY**



Energy Generation Technology at the Phillips Laboratory

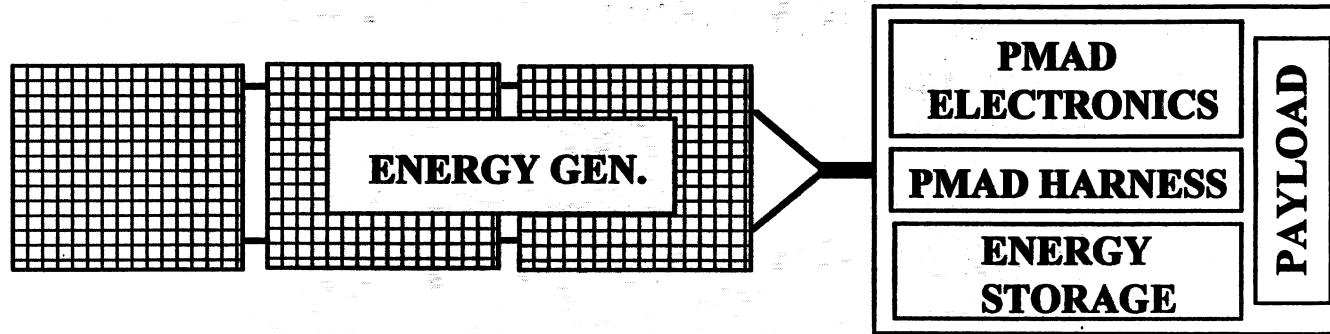
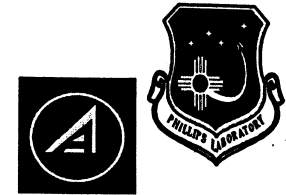
15th Space Photovoltaic Research and Technology Conference

**Dr. Dean Marvin - The Aerospace Corp.
Mr. Ralph James - Space Power Branch Chief**

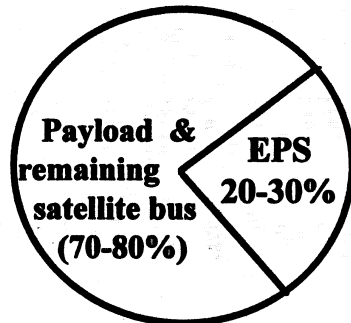
10 June 1997



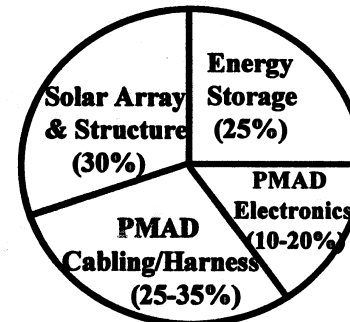
Satellite Electric Power System (EPS) Mass Budget



Satellite Mass*



EPS Mass*



TECHNICAL CHALLENGE: INCREASE EPS SPECIFIC POWER (W/KG) TO ENABLE GREATER PAYLOAD MASS AND POWER AND/OR USE OF SMALLER LAUNCH VEHICLES

* Data averaged from Milstar, DSCSIII, DSP, and GPS satellites.



Space Power Technology at PL

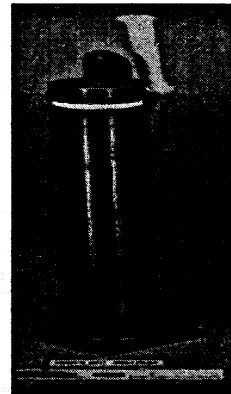


Solutions: advanced technologies to achieve 15+ w/kg, <\$5000/w, 7-10 yrs MMD LEO, 10-15 yrs MMD GEO

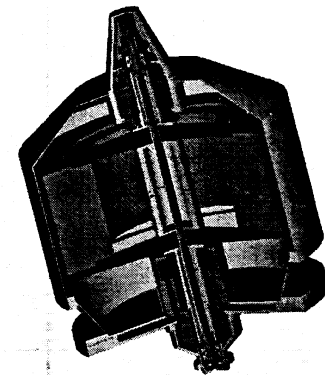
Energy Generation: increase efficiency from 18% to > 30%

Energy Storage: increase energy density from 25 w-hr/kg to >50 w-hr/kg

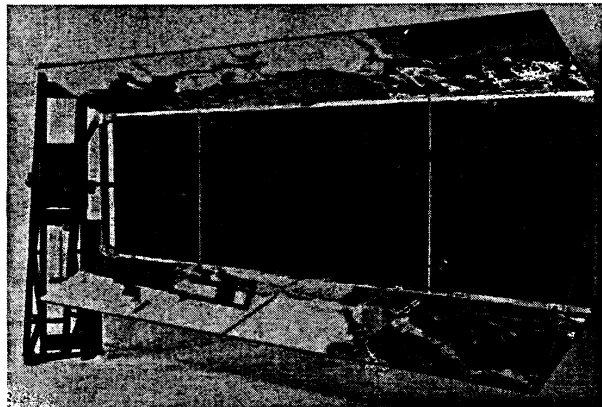
Power management & Distribution (PMAD): increase voltage from 28 V to >70 V



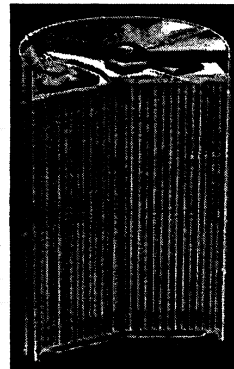
Sodium Sulfur



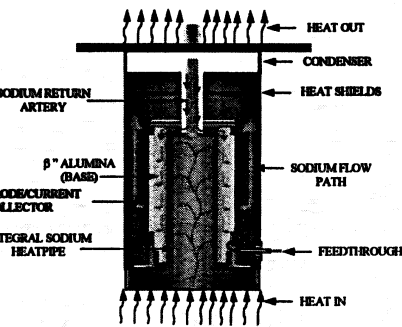
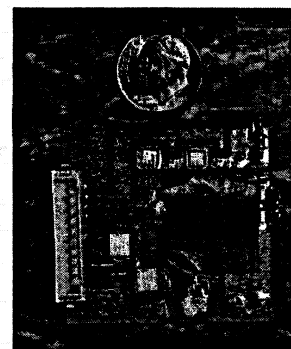
Fly Wheel



SOLAR ARRAYS



Lithium Ion



Solar Thermal AMTEC

PMAD



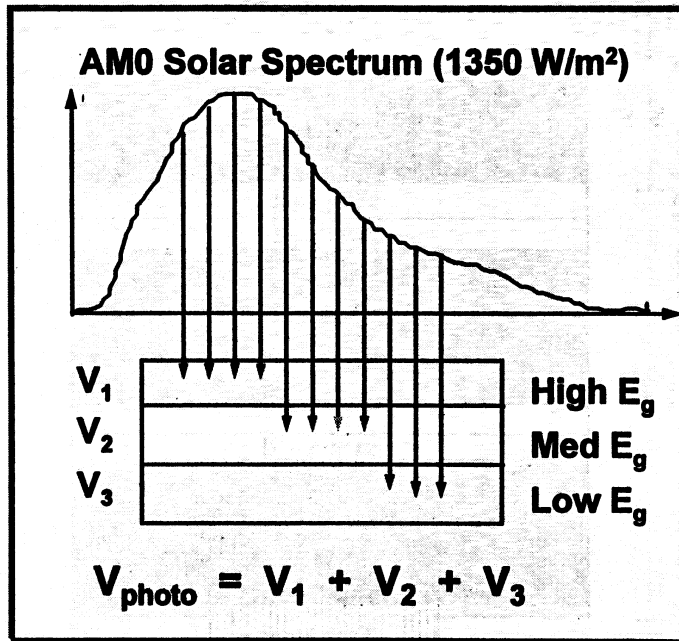
Solar Cell Performance Trends



	GaAs	MJ-1995	MJ-1997	MJ-1999
Eff	18%	20-22%	24%	25%
Size	4x4.8cm	2x2cm	2x2cm	4x4.8cm
p/p₀	0.75	0.775	0.79	0.79
Normalized Cost	1	10	2-3	1.15



Multijunction Solar Cell Benefits

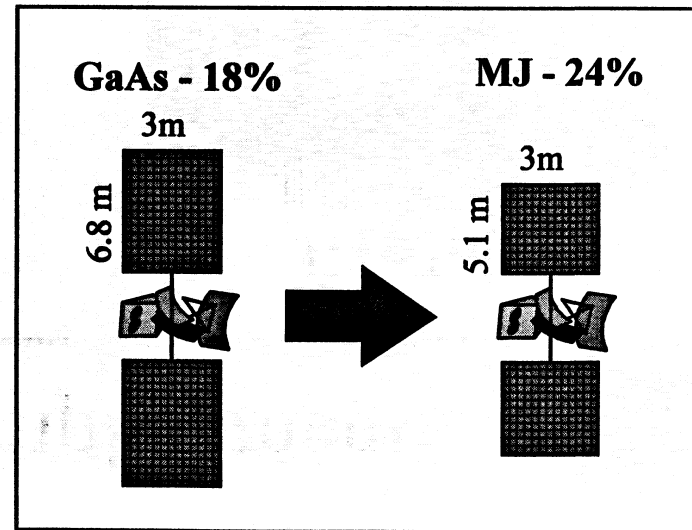


Significance/Impacts

- Reduced array area and system cost
- Baseline energy generation solution for new systems
- Cost effective, drop-in replacement for GaAs cells in upgraded systems

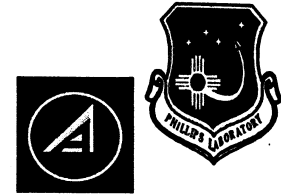
Technical Challenges

- Lattice matched semiconductors with desired bandgaps
- Feasibility of high yield, large area MOCVD growth
- Temperature coefficients and radiation effects

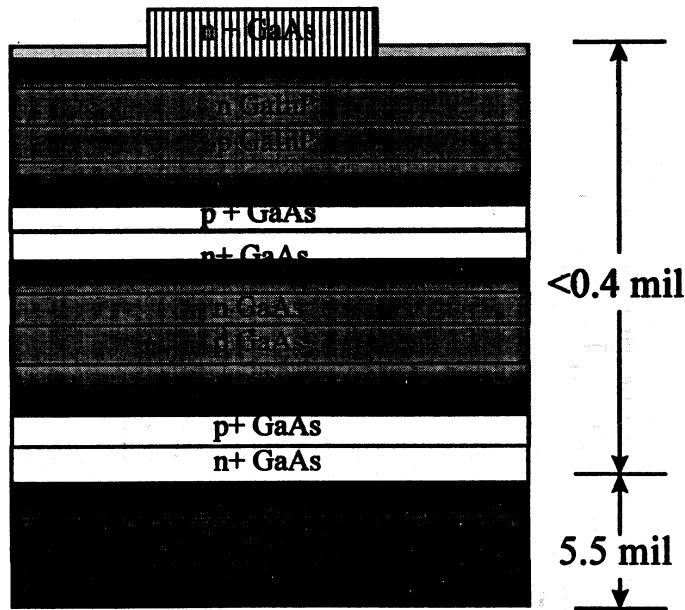




ManTech Accomplishments

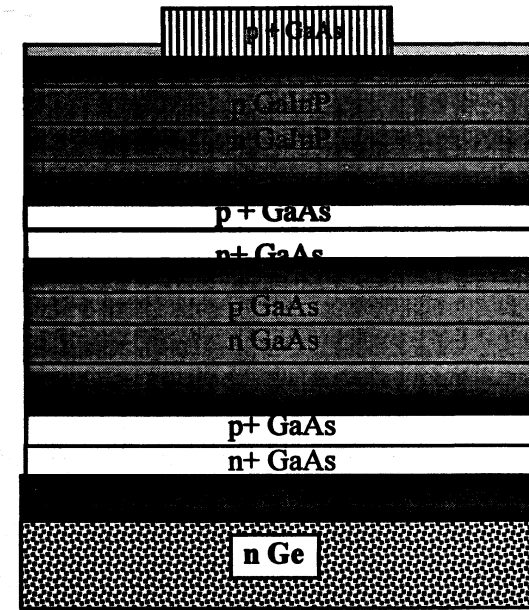


Spectrolab



- 25.5% 3J cell efficiency demonstrated (24.2% avg for 150 cells)
- 24.3% large area cell efficiency demonstrated
- 65% yield of $\geq 23\%$ efficiency cells (206 out of 317)

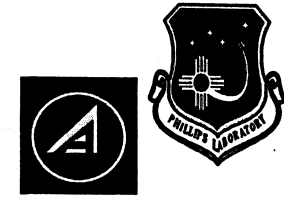
TECSTAR



- 24.1%, 2x2cm, 2J demonstrated (22.5% avg for 150 cells)
- 22.1%, 4x4.15cm, 2J demonstrated (21.8% avg)
- 38% yield of $\geq 22\%$ efficiency cells (229 out of 608)



ManTech Payoffs



Payoffs over GaAs/Ge

- Increase W/kg by 33%
- Decrease \$/W by 15%

Subsystem Impacts

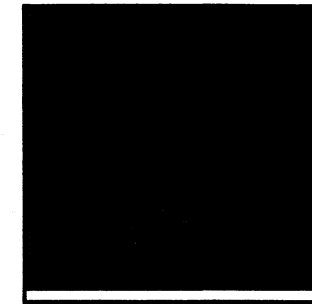
- Smaller, lighter arrays
- Lighter supporting structure
- More compact stowage

Cost Impacts

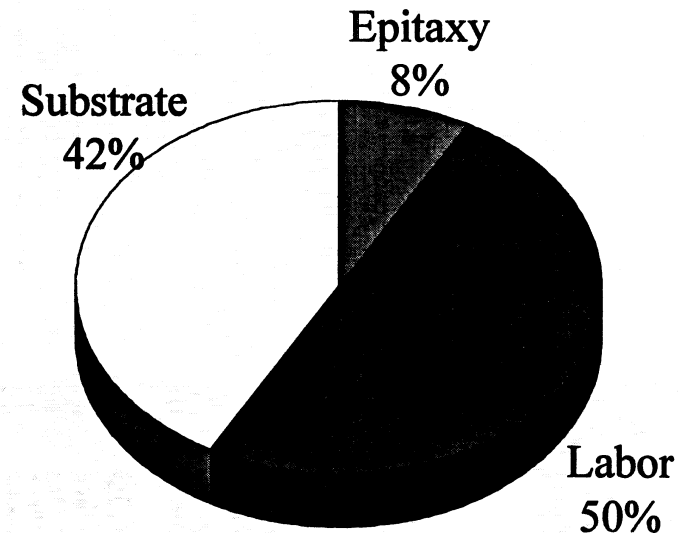
- Lower parts count
- Reduced power system cost
- Lower assembly labor cost



2x2cm

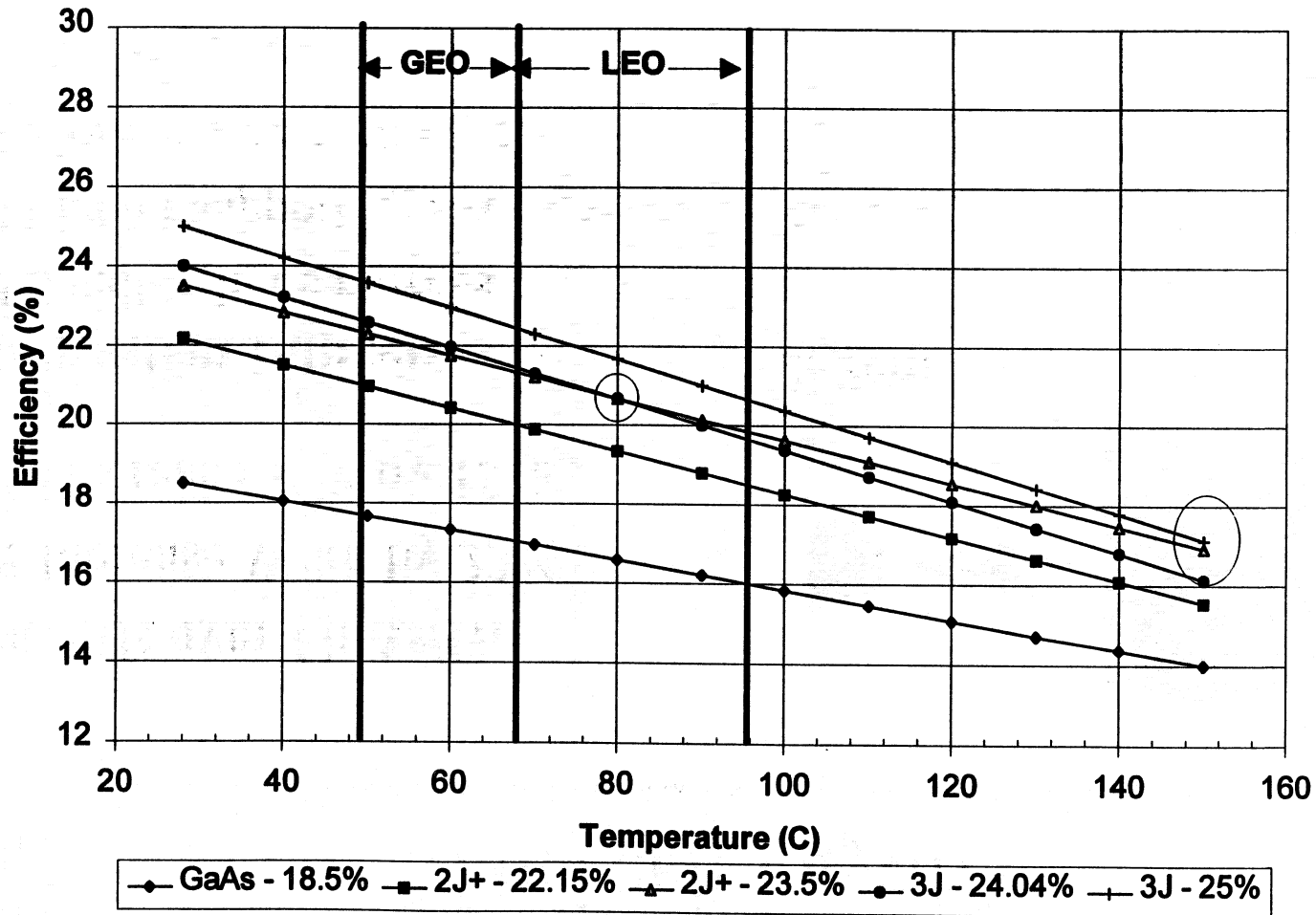


4x4cm



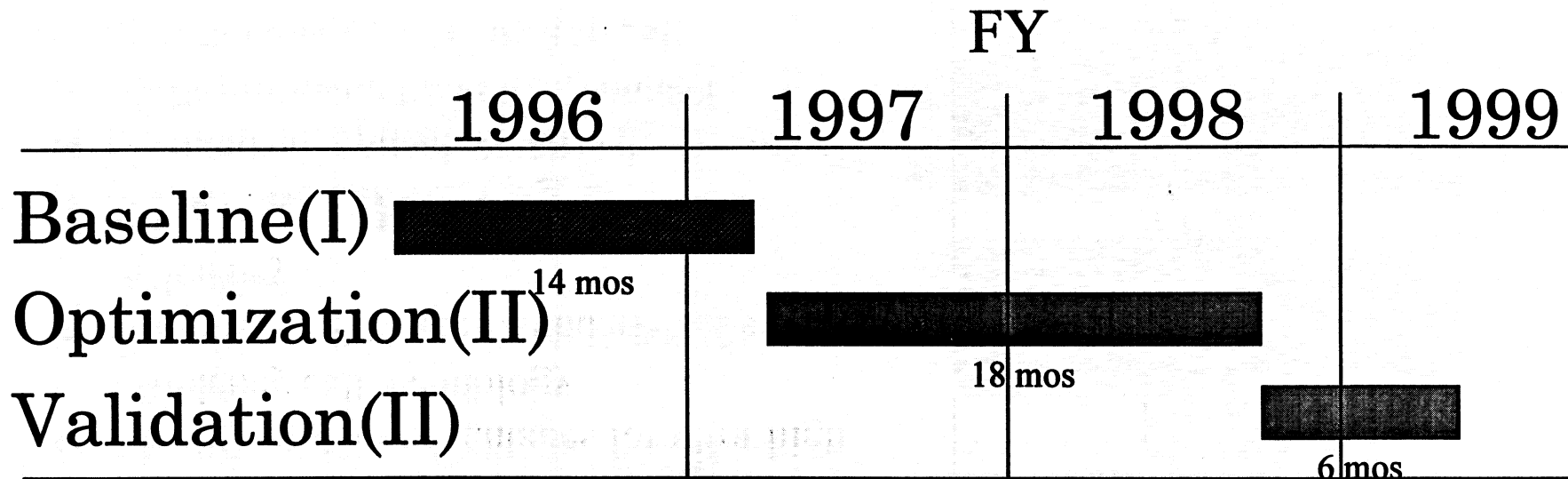


Mission Temperature Effects





ManTech Program Schedule



- Two Phase I contracts -- Spectrolab and TECSTAR
- Funding limitations would have forced downselect process after Phase I
- SBIRS Low supporting Phase II with \$1 million (FY97)
- Phase II -- Spectrolab, exercise option
TECSTAR, cost share de-scoped Phase II



RTI 4-Junction Solar Cell

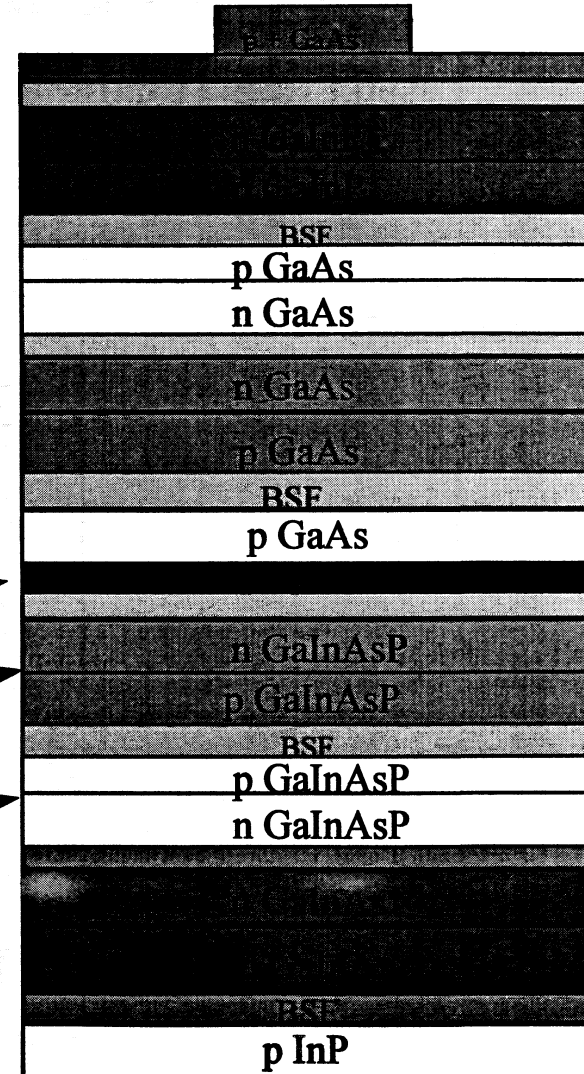


Objectives

- Demonstrate a mechanically-stacked, four-junction solar cell with 31-36% efficiency
- Identify system advantages for ultra-high efficiency cell technology
- Investigate the outer boundaries of solar cell efficiency

Technical Challenges

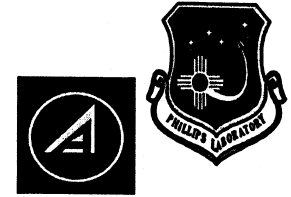
- Mechanical, optical, electrical properties of metal bond interconnect
- Material quality of GaInAsP cell
- Electrical properties and material quality of GaInAsP tunnel diode
- Integration of components into single structure



Note: Drawing not to scale

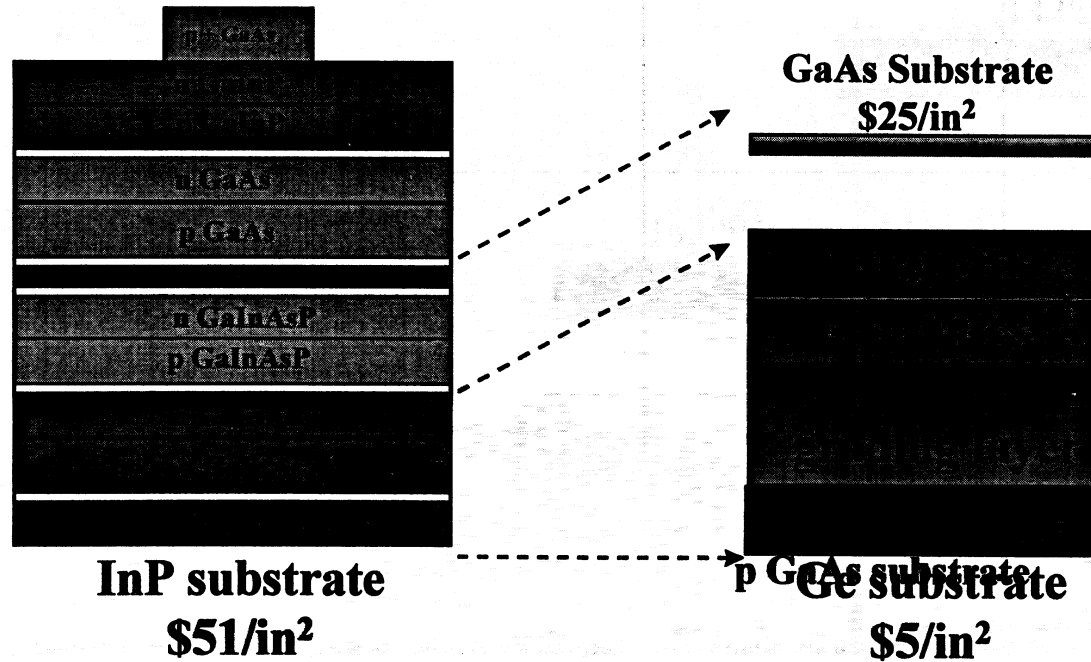


4J Cell Cost Issues



Overall cell cost driven by substrate cost

4J Cell - 35% AM0 efficiency

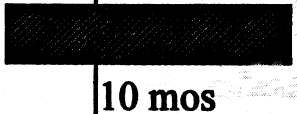



Cost modeling to define long term approach



4 Junction Cell Programmatic



	FY		
	1996	1997	1998
Modeling & Feasibility			
Concept Demonstration			


- Research Triangle Institute, \$480K total program
- \$100K cut in FY97 will cause slow down in FY98
- One of two 30% cell programs at RTI



Lightweight Flexible Solar Array




THIN FILM PHOTOVOLTAICS




- CIS (8% Efficiency)
- Efficient Stowage Volume
- Lightweight Flexible Blanket


SMART MECHANISMS



SMA RETENTION DEVICE




- Shockless/Controlled Deployment
- Low Mass
- Part Count Reduction
- Resetability



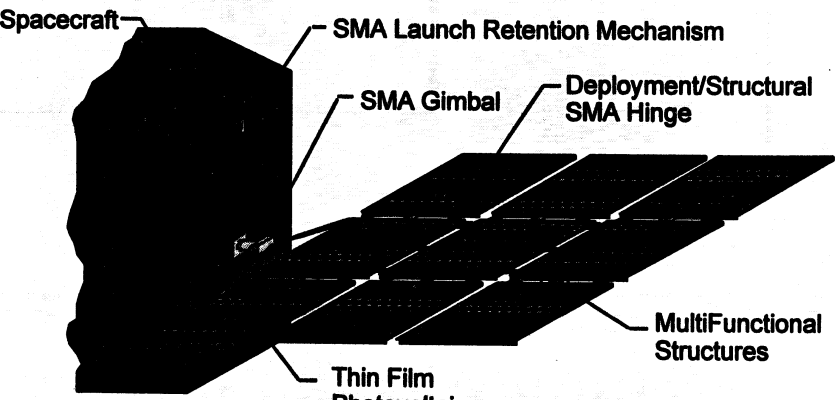
SMA GIMBAL **SMA HINGE**

MULTIFUNCTIONAL STRUCTURES



- Cableless Power Bus
- Integrated Power Management
- Lightweight Interconnects (>30% Reduced Mass)

LIGHTWEIGHT FLEXIBLE SOLAR ARRAY DEVELOPMENT



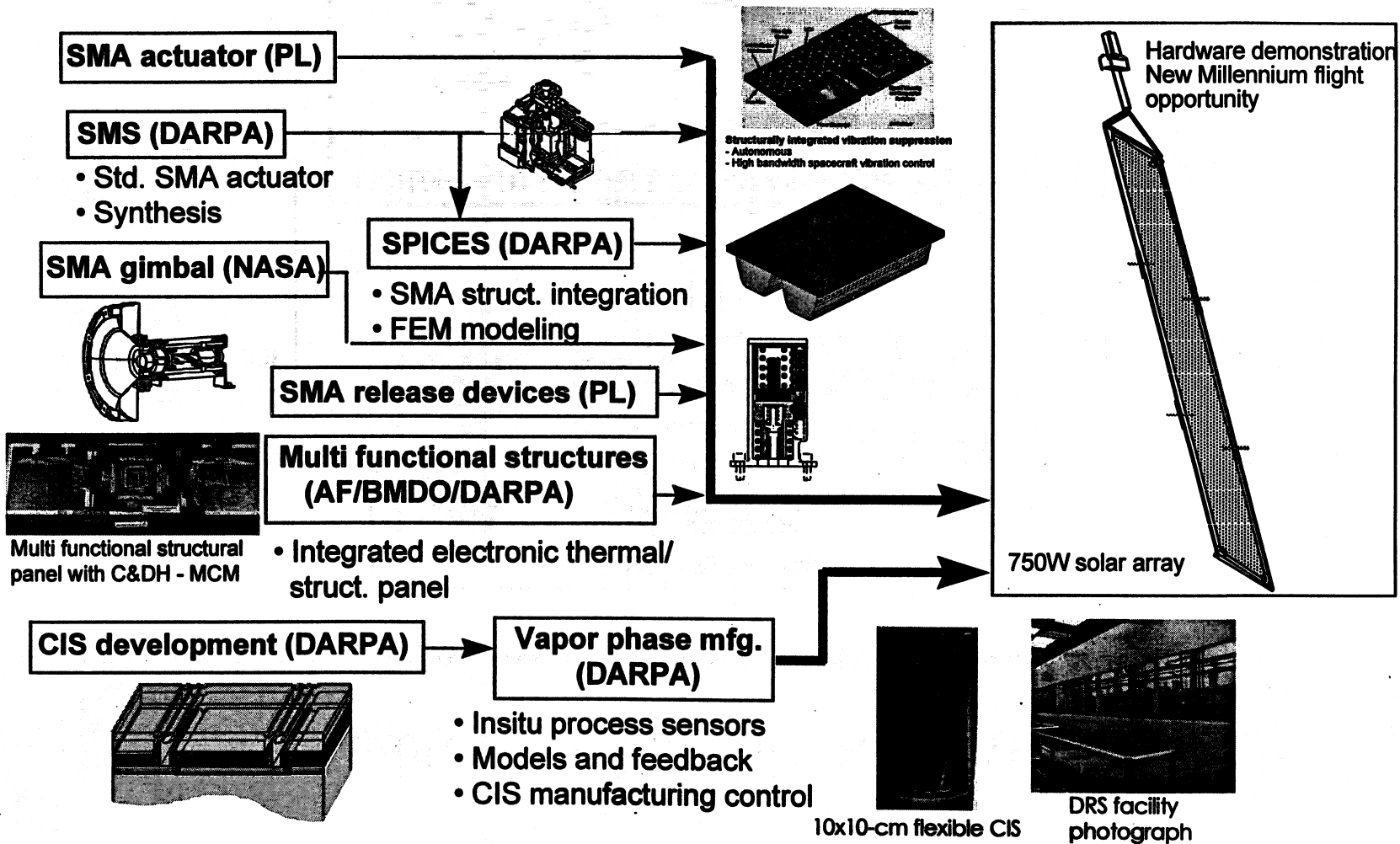
Spacecraft — SMA Launch Retention Mechanism — SMA Gimbal — Deployment/Structural SMA Hinge — MultiFunctional Structures — Thin Film Photovoltaics

- > 100 W/kg
- Stowage Volume < 0.15 m³
- Controlled Deployment

Partners:
PL
NASA Langley
Lockheed Martin



LWFSA Roadmap

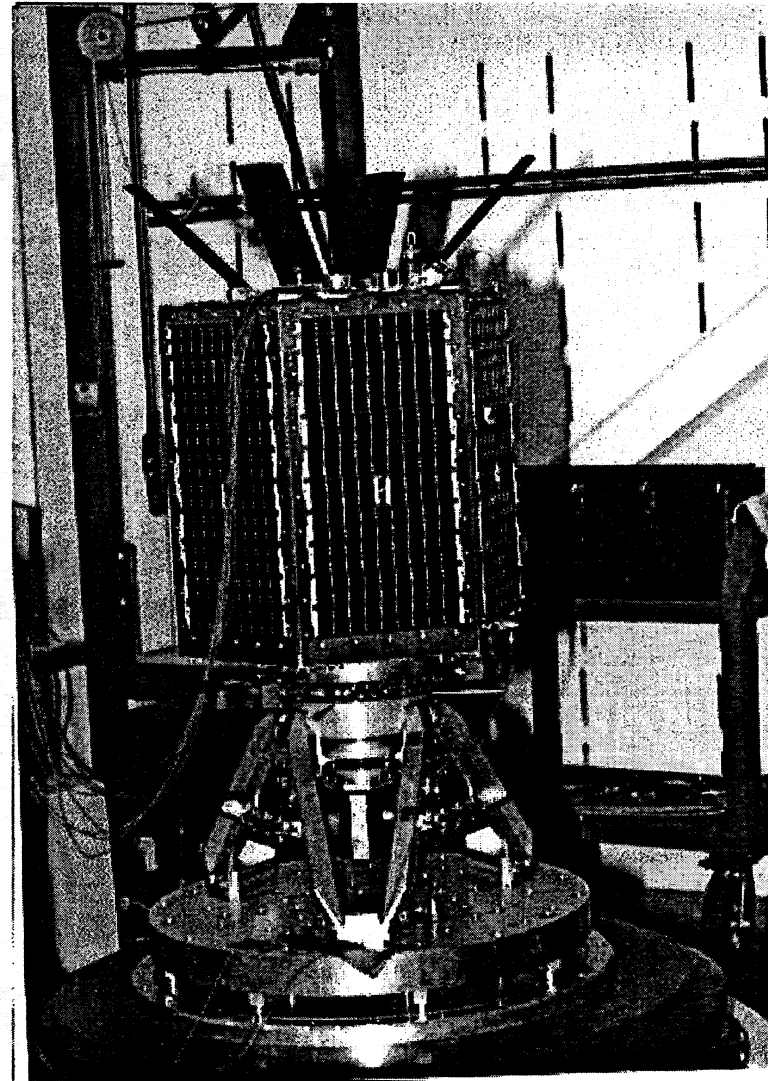




MightySat I ASCE Configuration



- 6 composite substrate side panels (20% MJ, 80% GaAs), one top panel (100% GaAs)
- TECSTAR dual junction cell technology
- One string of 18 multijunction cells in series per panel
 - 2x2 cm cells, 6 mil fused silica coverglass
 - 22% lot average efficiency
 - 1/8 of panel power output
- Two temperature sensors per panel (1 MJ, 1 GaAs)





MightySat ASCE Status



FY97	1Q			2Q			3Q			4Q		
	O	N	D	J	F	M	A	M	J	J	A	S
TASKS												
Spacecraft I&T	████████████████████											
Operations Rehearsals							████████████████████					
Operations/Data Collection												
Final Report												
MILESTONES												
Spacecraft delivery to GSFC							◆					
Launch							???					

- Minor panel modifications needed as a result of initial fit check (wiring, corner thickness)
- Spacecraft I&T complete -- spacecraft ships 20 May
- Two coverglasses damaged during spin balancing -- no impact on panel performance
- Current launch, STS-88, delayed due to Space Station payloads
- Currently working data reduction algorithms



STRV-2 Multijunction Solar Cell Experiment

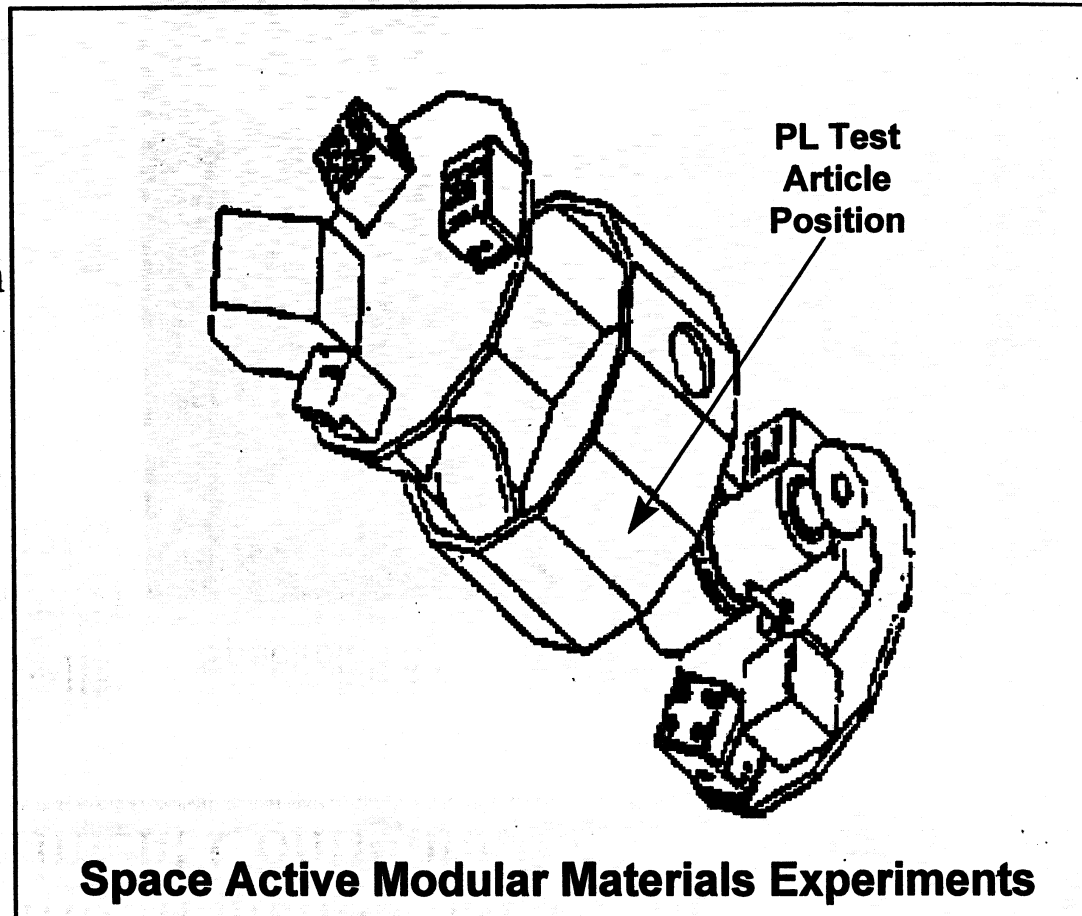


■ STRV-2 is BMDO funded payload platform

■ SAMMES collects data from

- solar cells (5 channels of IV)
- sun sensor
- AD590 temperature sensors
- calorimeters
- atomic oxygen actinometer

■ PL test article attached to SAMMES Solar Photovoltaic Module

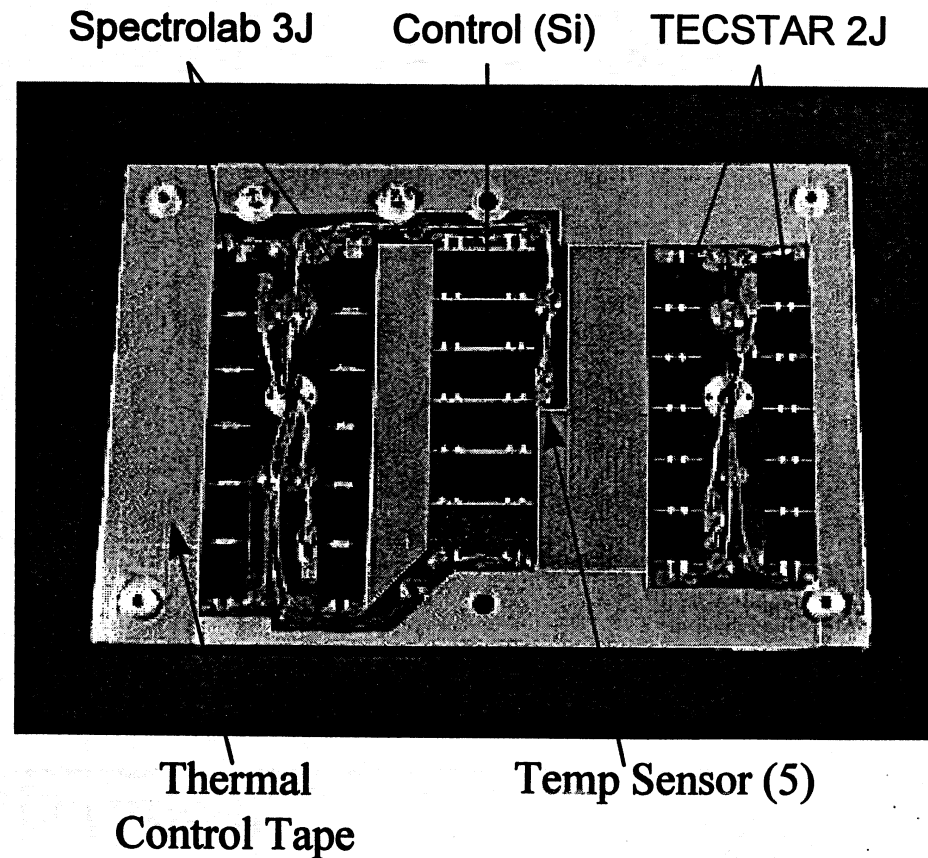




STRV-2 Multijunction Solar Cell Experiment Configuration



- Two types of multijunction cells
 - Spectrolab triple junction (20-22%)
 - TECSTAR dual junction (20-22%)
- One control string (Silicon)
- ELV launch (TSX-5) in mid-1998
 - 450 x 1600 km, 75 deg inclination
 - 1 year mission
- Data collection
 - I-V traces on all strings
 - String Temperature
 - Calorimetry





STRV 1c/d Flight Experiment



■ Mission/Objective

- One year mission on GEO Transfer Orbit (high radiation dose)
- Collect I-V data to measure on-orbit performance
- Observe on-orbit radiation degradation coefficients

■ Component Description

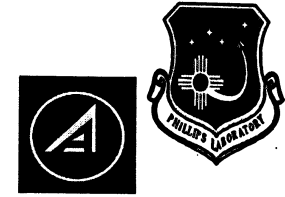
- Nine experiment slots available
- Four 24-26%, 2x2 cm, GaInP₂/GaAs/Ge ManTech cells Spectrolab Inc.
- Two 2x2 cm, GaInP₂/GaAs//GaInAsP/InGaAs cells (or components)
- Three CIS modules

■ Schedule

- Late 1998 flight
- GaAs primary power panels delivered early 1998

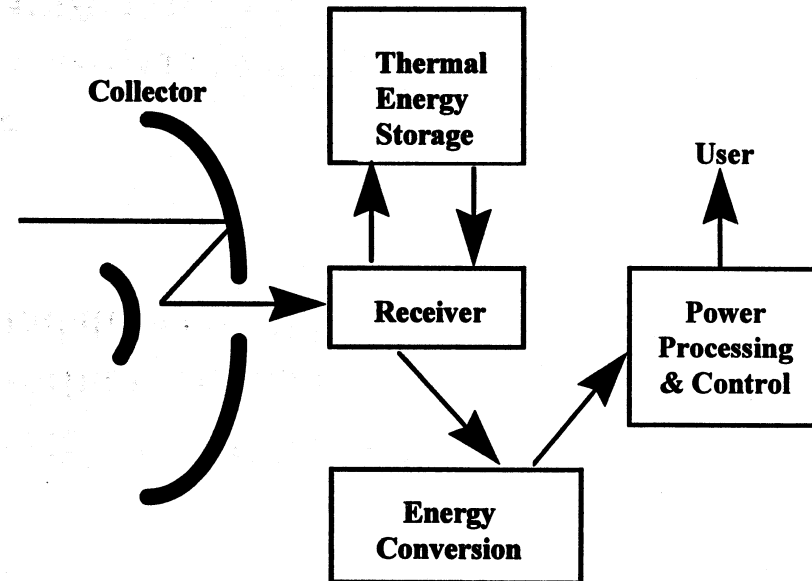


Alkali Thermal to Electric Conversion (AMTEC)



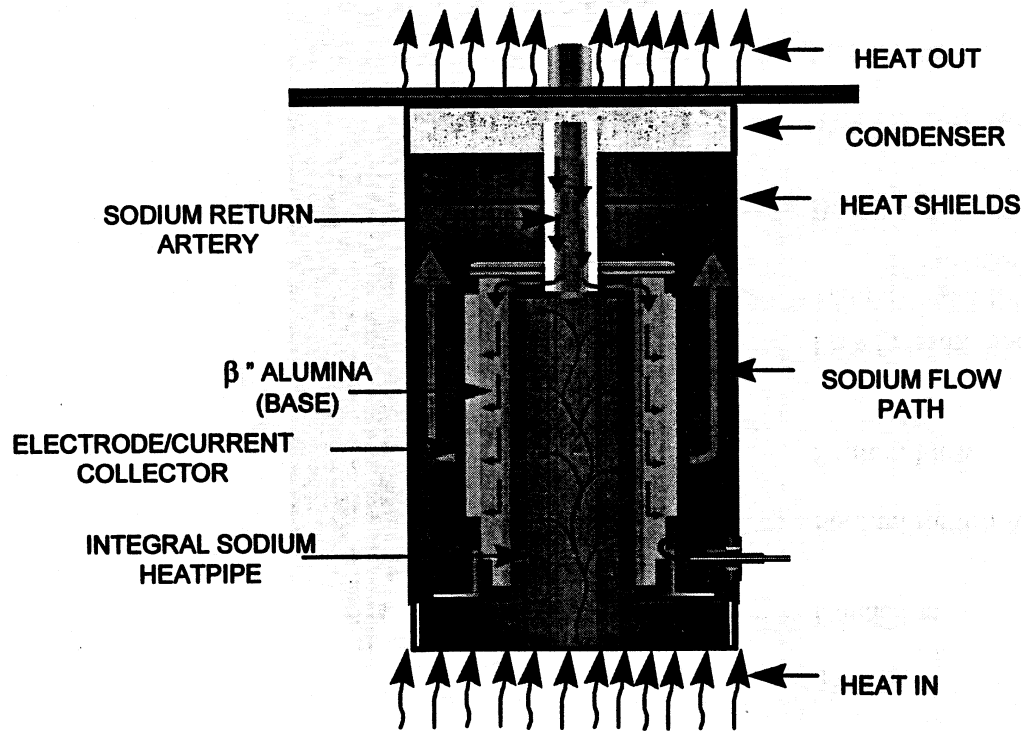
Solar Thermal AMTEC Converter

- Replaces solar cells and batteries
- Capable of 35-40% conversion efficiency
- 20 W/kg at system level possible
- Inherent radiation hardness
- Source neutral - can use solar, radioisotope, or fossil fuel energy.





AMTEC Development Activities

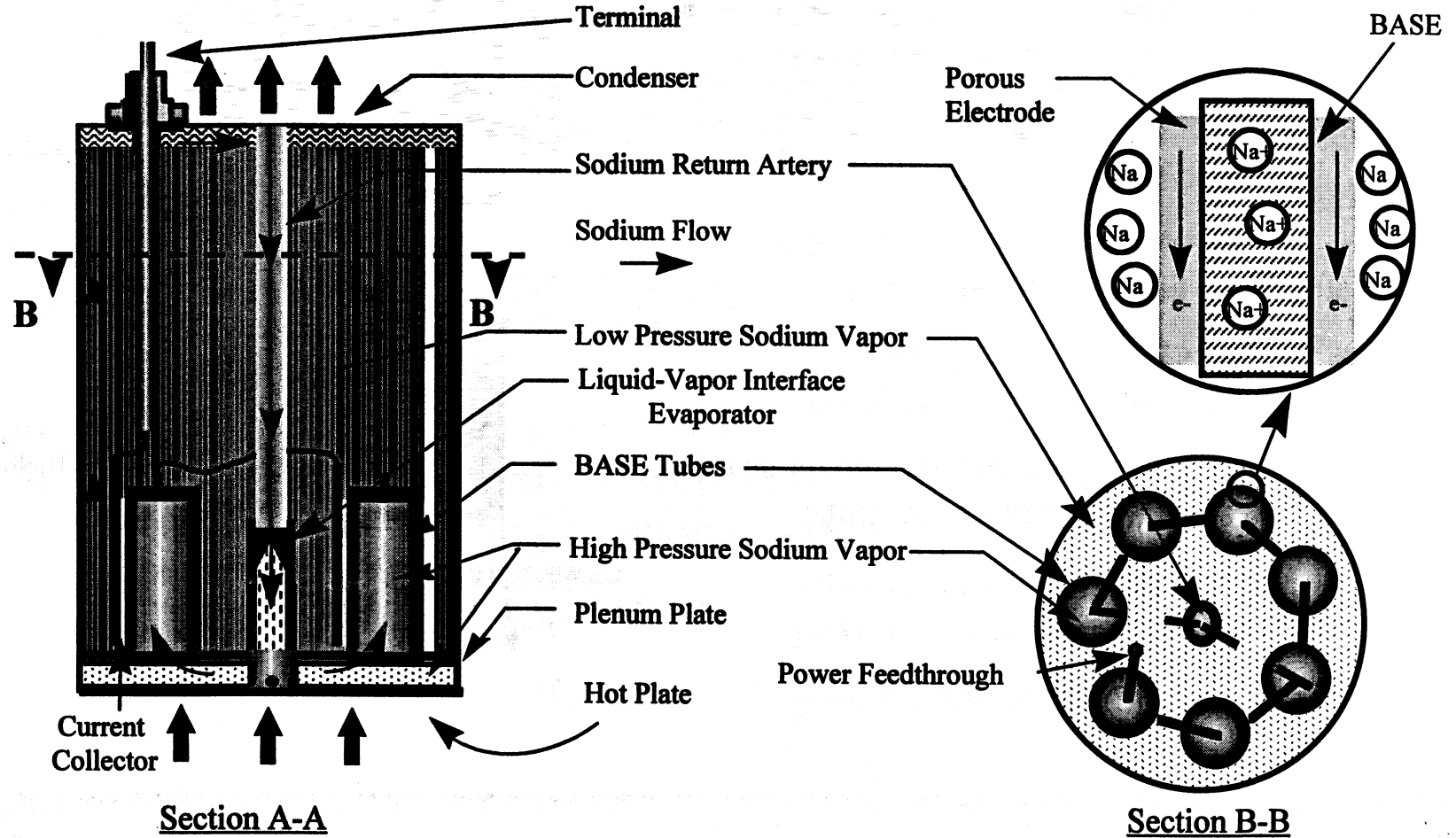
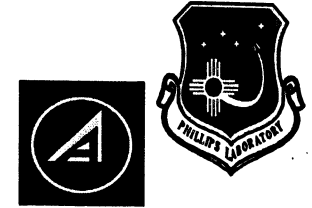


Supporting Activities

- Advanced Modular Power Systems contracted to design and fabricate cells
- Multi-tube cell performance characterization at PL
- Fabrication of cell with flat-plate electrodes using thin BASE (3Q FY98).
- Thin β'' alumina electrolyte for 50% higher cell energy density at Creare
- System studies at Rocketdyne and Lockheed-Martin
- AMTEC chosen as converter for NASA Pluto Express advanced radioisotope system.
- Flight experiment on STS-88 (1Q FY98).

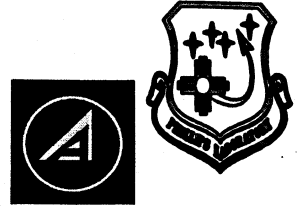


Multitube AMTEC Cell



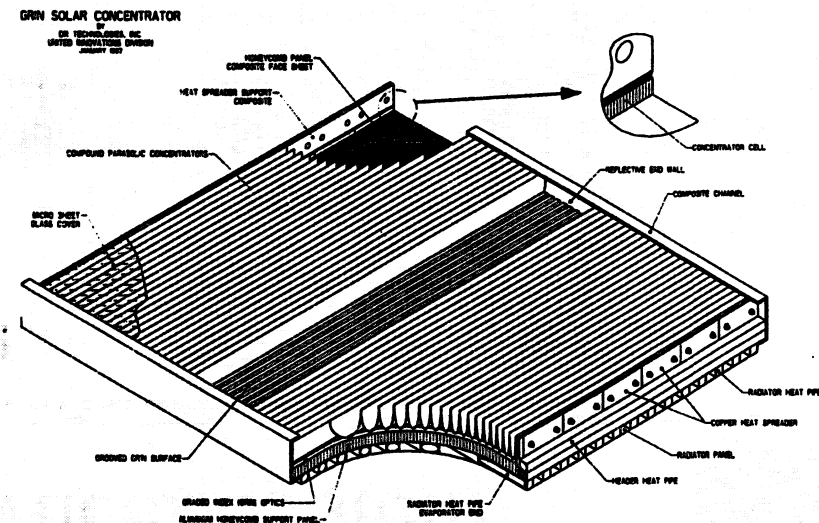
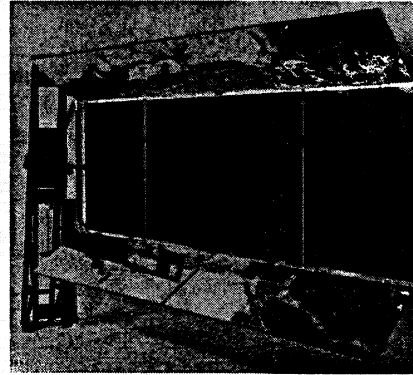


Solar Array New Start



Concentrator Arrays

- Resistant to radiation effects
- Potentially lower cost due to lower parts count
- Astro-Aerospace Channel Array
 - Light weight, high stiffness, reflector concept
 - 80 W/kg, 1.5X ratio, 30° pointing
- AEC-Able SCARLET
 - Linear Fresnel refractive system
 - 50 W/kg, 7X ratio, 2° pointing
 - Flight on SSTI/Lewis spacecraft
- United Innovations Graded Index
 - Graded refractive index glass
 - 70 W/kg, 200X ratio, 10° pointing



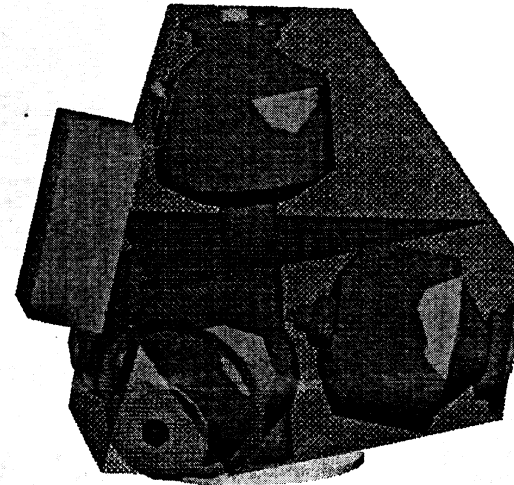
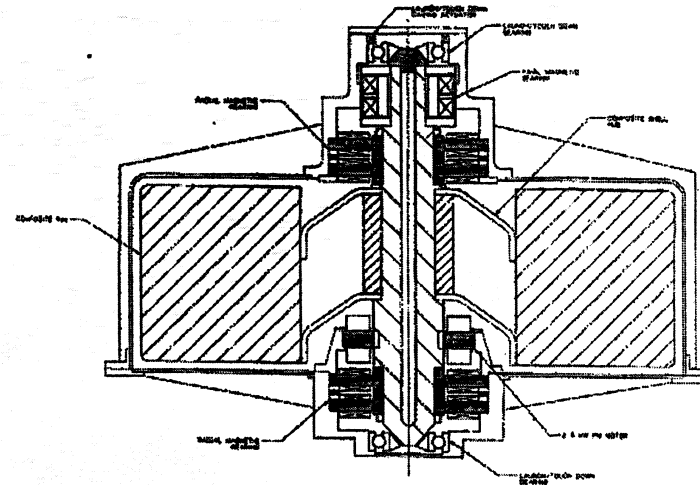


LEO Flywheel System



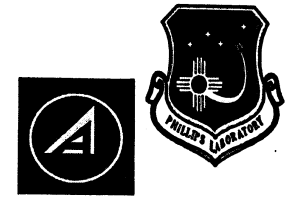
• Integrated Power and Attitude Control System

- 30 Whr/kg in LEO (complete)
- 50% total volume decrease compared with conventional ACS system, parts of PMAD, and NiH₂ battery system combined
- High discharge rate for pulsed applications
- Key issues are rotor design, magnetic bearing efficiency, and control electronics
- Technology development programs
 - SatCon; prototype 3 wheel system providing 8 kWhr storage, 10 yr life
 - Testing at NASA Lewis (FY 98)
 - Applied Materials Technology/Penn State; fault diagnostics, rotor design
- Proposal for flight demonstration on Space Station (FY 01)
- Joint flywheel program with NASA LeRC





Merits of IPACS



Integrated Power and Attitude Control System

- High specific energy, specific power
- Very long cycle life
- No capacity degradation
- High efficiency, charge & discharge
- Low “self-discharge” rate
- Capability to incorporate attitude control
- Replace some PMAD components



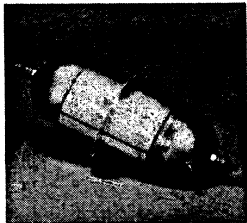
Flywheel Weight Savings



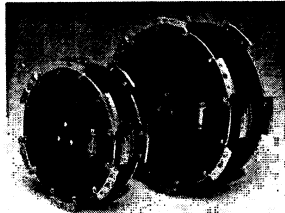
Energy Storage

Attitude Control

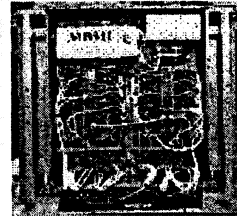
Power Management and Distribution



+



+



=

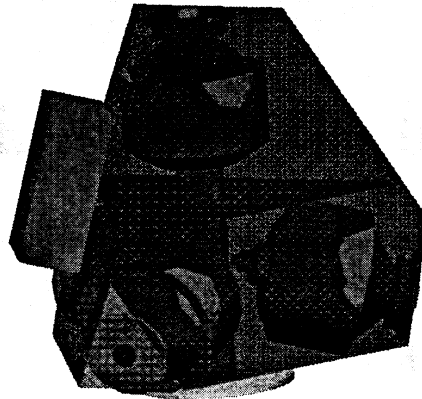
X kg

NiH2 Batteries
Thermal Control
Cell Switching

Reaction Wheels
or
Control Moment Gyros

Charge/Discharge units
Shunt Regulators
Voltage Regulators

Integrated Power and Attitude Control (IPACS) System



= **1/6 to 1/7X**



Energy Generation Program Summary



- **ManTech solar cells with 24-26% efficiency that are cost-effective**
- **Ultra-high efficiency solar cells with 35% efficiency**
- **Lightweight flexible solar array program**
- **Non-PV, non-electrochemical generation and storage**
- **Concentrator solar array new start**
- **Integrated energy storage/ACS with long cycle life and high rate capability**

Page intentionally left blank

PERFORMANCE TRADE-OFFS FOR MBG CELLS USING DIFFERENT BANDGAP PAIRS ¹

P.A. Iles, C.L. Chu and L. Kilmer
TECSTAR/ASD, City of Industry, CA 91745-1002
M.L. Timmons, P. Sharps
Research Triangle Institute, R.T. Park, NC 27709

BACKGROUND

Present GaInP₂/GaAs cells grown on Ge (or GaAs) substrates have demonstrated high efficiency. However, the individual bandgaps (1.85 eV, 1.42 eV respectively) are not the optimum match to convert the AMO spectrum efficiently, although by reducing the thickness of the GaInP₂ cell, good efficiencies have been achieved.

Within the III-V alloys, modeling shows that several dual junction cells, comprising different bandgap pairs, could give higher efficiency.

This paper outlines the modeling used, the bandgap pairs selected, and projections for the AMO efficiency assuming that the effects of lattice mismatch associated with the bandgap pairs can be reduced. We also present preliminary data on I-V performance for the selected top and bottom cells and for some full cascade cells. We have included some characterization results to check the bandgaps and lattice strain, to check how closely the fabricated cells conform to the model.

Note

In order to use continuous access to an MOCVD reactor dedicated to this project, we decided to scan across the bandgap (and lattice constant) range, rather than use systematically increasing lattice mismatch of selected bandgap pairs, to check the main problem areas in characterization and cell performance. We also prepared one set of Ge substrates with a thin GaAs seeding layer to cover all the MOCVD runs; in retrospect, these substrates may have reduced the quality of the ternary compounds grown on these substrates.

MODELING

Estimates for Optimum Bandgap Combinations

To estimate the optimum bandgap combinations we used the following format, based on the bandgap versus lattice constant plot for III-V alloys, shown in Figure 1.

- 1) We varied the y value in Ga_yIn_{1-y}As from 1.0 (GaAs) down to 0.6, using approximate Δy increments of 0.05.
- 2) For these different y-values, we computed the Ga_yIn_{1-y}As energy gap from the expression $E_g = 0.36 + 1.064y$ and the lattice constant a_0 from Vegard's Law, where a_0 scales linearly with composition, between the a_0 -value for GaAs = 5.6532\AA , and the a_0 -value
- 3) For these selected y-values, using Vegard's Law, we estimated the x values in Ga_xIn_{1-x}P which gives the same a_0 value as the GaInAs alloys.
- 4) Using the expression $E_g = 1.351 + 0.643x + 0.78x^2$, we calculated the E_g -values corresponding to the various x-values in Ga_xIn_{1-x}P.

¹Funded under SBIR Contract NAS3-2764 from NASA-Lewis Research Center

The results of these computations are given in Table 1, where bandgap pairs A through I are listed, with their corresponding x and y values, along with the lattice-mismatch with respect to Ge or GaAs.

Table 1 also shows a column of theoretical AM0 efficiency values as a function of bandgap pair values, taken from Fan (1) or Wanlass (2). For reference in the table, we have included the bandgap pair J, the InP/InGaAs combination.

Figure 2 shows the theoretical AM0 efficiency for the selected Eg-pairs where the abscissa is the lattice mismatch wrt Ge (Curve A). The points plotted do not give a smooth curve because the Eg-pairs were selected from compounds which were on the tie-lines for the ternary compounds GaInAs and GaInP. The figure does not include the degrading effects of lattice-mismatch. The determination of the trade-off between practical efficiency and lattice-mismatch effects is the purpose of this study.

In Figure 2, curve B shows estimates of how practical efficiency values, again not corrected for lattice-mismatch, will vary for the cells with different Eg-pairs. We have used the practical efficiency $\approx 25.5\%$ achieved for cells comprising $\text{Ga}_{0.5}\text{In}_{0.5}\text{P}$ and GaAs, grown monolithically, to draw the curve B.

Also in Figure 2 are two "estimated" curves, showing the trends in practical efficiency, when lattice-grading is used (curve C), or when no grading is used (curve D). This study is intended to provide data to determine practical curves like C and D.

EXPERIMENTAL DATA

Cell Growth

Three sets of cells were MOCVD-grown at RTI, mostly on GaAs/Ge substrates, namely:

- $\text{Ga}_x\text{In}_{1-x}\text{As}$ structures, where the lattice-grading structures were as shown in Figure 3.
- $\text{Ga}_y\text{In}_{1-y}\text{P}$ cells grown on the buffer (lattice-grading) layers of $\text{Ga}_z\text{In}_{1-z}\text{As}$, where the x values were selected from the modeling, to give lattice-match to the corresponding z-values. Figure 4 shows the layer scheme,
- Tandem cells - $\text{Ga}_y\text{In}_{1-y}\text{P}$ cells grown on $\text{Ga}_x\text{In}_{1-x}\text{As}$ cells, using buffer layers of $\text{Ga}_z\text{In}_{1-z}\text{As}$, where the x and y values correspond to theoretical lattice match composition. Figure 5 shows the layer scheme.

In previous tests, RTI established that an effective tunnel junction could be formed in lattice-mismatched GaInAs over the range of z-values used in this study.

Cell Fabrication

RTI had grown a GaInAs cap layer with the same x-value as the selected composition, on all the cell structures. We decided to use a "universal" cap-etch solution and the same front side metallization for all the structures, and we did not experience any problems resulting from this choice.

Some of the wafers (not always those involving the greatest lattice-mismatch) were bowed, and to reduce the chance of breakage the processing sequence was more complex.

Cell Testing

Tables 2, 3 and 4 summarize the I-V data for the various runs.

For these tables, we used the I-V data for the best cell of the four cells obtained from the starting substrates. We have also applied an AR coating gain of 33% to I_{sc} (and to efficiency).

We note that in Table 2, the GaInAs samples grown on GaAs substrates had significantly better performance than samples grown on Ge substrates. Our decision to complete all the runs in close sequence did not allow the possibility of optimizing the GaAs seeding layer on the Ge, or even in optimizing the various layer growths on GaAs substrates. When we plotted the trend in the I-V parameters in Table 2 versus lattice-mismatch, we found that V_{oc} (and CFF) decreased steadily as expected, but that J_{sc} also decreased, not as expected. These

reduced J_{sc} values indicated either substrate and seeding layer deficiencies, and/or ineffective lattice grading layers. The J_{sc} decrease showed that practical losses offset the theoretical increase at the lower bandgaps. The tandem structures also give significantly lower CFF (and V_{oc}) values than the single cell structures, indicating that the lattice-mismatch was more severe for the more complex structures, especially when GaInP layers were used.

In a later section we will give some conclusions on the cell I-V data, and also on the characterization methods tried.

Characterization

X-Ray Diffraction

We used double crystal X-ray diffraction to attempt to evaluate the degree of strain and of lattice-mismatch. Some of our X-ray results on the GaInAs cells are shown in Figures 6 through 10.

Figure 6 shows the diffraction pattern for sample #6-3464 ($Ga_{0.95}In_{0.05}As$ layers grown on a GaAs substrate) The GaAs peak is very narrow, showing little strain. The GaInAs peak is probably that shown at -400 arc-sec and its width indicates some residual strain. Using Vegard's Law for $y = 0.935$, the mismatch is around +0.47% and the peak at -400 arc-sec suggests that RTI has obtained some lattice-grading. The weak X-ray peak at +1488 arc-sec could indicate a growth anomaly, such as variable Ga/In ratios or superlattices in the grown layers.

Figures 7 through 10 are diffraction figures for GaInAs samples grown on Ge substrates, with a thin seeding layer of GaAs. Figures 7, 8, 9 and 10 show the plots obtained for 10%, 15%, 20% and 25% In content. Because the Ge substrates are deliberately misoriented from the (100) orientation, the tests often show different results for plots made at +8° and -8° from the horizontal orientation. In principle the In (or Ga) content can be estimated from the average of these 2 plots; however we observe it is not always clear which peak shows the layer with the required composition. In some cases, extra peaks, possibly caused by the grading layers are observed.

We also had one sample (6-3776, with 25% In content) characterized outside with triple crystal X-ray diffraction. The triple crystal instrument could provide both diffraction space maps as well as rocking curves, without the need for alignment to change the optics.

Figure 11 shows a slice taken through a diffraction space map. Figure 12 shows the same plot overlaid with a simulation plot for $Ga_xIn_{1-x}As$ layers where x varies from 0.95 to 0.75. The measured peak is close to $x = 0.88$ ($1-x = 0.12$) but the individual layers do not show clearly.

We concluded that although X-ray data could provide some insight, we could not obtain quantitative resolution of the various layers. We do not plan extensive X-ray evaluation of the later growth sets.

Quantum Efficiency (QE)

We use QE measurements to show the spectral response of the cells, and also to determine the bandgap from the response near the cut-off wavelength. We are completing these bandgap measurements for all three sets of cells.

Other Characterization Methods

Microscopic examination of the surface layers did not show systematic increase in growth-generated surface defects. We are also defining etchants to use to show the dislocation density in the grown layers over the composition range of the structures.

CONCLUSIONS

Overall we conclude that growth on Ge substrates, possibly because of the GaAs seeding layer obtained in a single growth, gives lower cell performance than growth on GaAs substrates.

The target compositions (x or y values) were not always obtained (the measured bandgaps differed from the target values).

Also there are indications that the lattice grading layers did not reduce strain sufficiently, particularly for the GaInP layers or for the tandem cell structures which are relatively complex.

As mentioned above, this indicates that our rapid scan approach was not as successful as a systematic iterative program.

We can conclude from this scan, that it is essential to optimize the substrate quality and to systematically refine the lattice-grading procedures, in order to determine if the deleterious lattice-mismatch effects can be reduced to allow the optimum bandgap pairs to give higher efficiency.

Our X-ray results also showed that in addition to dislocation counts, we need other characterization methods to assess the lattice-strain. At present the detailed trend of the I-V parameters is the best indicator, and we are investigating a wide range of the cell properties (especially dark diode characteristics) to use as indicators.

We are completing characterization of cells in all three growth sets.

REFERENCES

- 1) J.C.C. Fan, B-S Tsaur and B.J. Palm "Conference Proceedings of the 16th IEEE PVSC, 1983, P. 692
- 2) M. Wanlass "Photonics Spectra" November 1992, P. 159

Table 1

Estimates for AM0 Efficiency for Several Bandgap Pairs

Pair	E_g values (eV)	x in $Ga_xIn_{1-x}P$	y in $Ga_xIn_{1-y}As$	Theoretical AM0 Eff (%)	Lattice Mismatch to Ge (%)	Lattice Mismatch to GaAs (%)
A	1.9 1.42	.53	1.0	28.6	0	-0
B	1.89 1.37	.52	.95	29.2	+0.35	+0.36
C	1.865 1.32	.50	.90	29.8	+0.70	+0.72
D	1.825 1.265	.47	.85	30.2	+1.05	+1.076
E	1.80 1.21	.455	.80	30.8	+1.40	+1.44
F	1.77 1.16	.43	.75	31.0	+1.75	+1.80
G	1.73 1.11	.40	.705	31.6	+2.09	+2.12
H	1.70 1.06	.375	.65	31.7	+2.47	+2.51
I	1.65 1.02	.34	.62	31.1	+2.69	+2.725
J	1.35 0.75	0	.47	24	+3.75	+3.8

Table 2
I-V Data For Ga₂In_{1-x}As Cells

RTI Growth #	Structure	Target Values			Measured Values			
		In Content (1-x)	Eg (eV)	Eff (%)	Voc (mV)	Jsc (mA/cm ²)	CFF (%)	Eff (%)
-	Control GaAs/Ge	0	1.42	18.8	1020	32	78	18.8
6-3464	GaInAs/GaAs	0.05	1.37	18.6	938	34.1	77.7	18.4
6-3741	GaInAs/Ge	0.05	1.37	18.6	790	16.5	74.8	9.2
6-3742	GaInAs/Ge	0.05	1.37	18.6	903	17.8	79.2	9.4
6-3747	GaInAs/Ge	0.10	1.32	18.3	830	16.5	75.9	7.7
6-3751	GaInAs/Ge	0.15	1.265	17.8	813	12.2	70.1	5.2
6-3773	GaInAs/Ge	0.20	1.21	17.3	514	12.4	69.6	3.2

Table 3
I-V Data for Ga₂In_{1-y}P Cells (on Ga₂In_{1-z}As Layers)

RTI Growth #	Structure	Target Values				Measured Values			
		(1-y)	(1-z)	Eg (eV)	Eff (%)	Voc (mV)	Jsc (mA/cm ²)	CFF (%)	Eff (%)
6-4028	GaInP on GaInAs Grading layers	0.48	0.05	1.89	18.15	1077	13.0	73.5	7.7
6-4039		0.50	0.10	1.865	18.35	816	14.35	75.4	6.65
6-4040		0.53	0.15	1.825	18.5	799	14.63	6.9	6.0
6-4029		0.545	0.20	1.80	18.7	879	14.9	62.1	6.0
6-4042		0.57	0.25	1.77	18.9	786	16.0	75	6.9

Table 4
I-V Data for Ga₂In_{1-y}P on Ga₂In_{1-x}As Cells (on Ge Substrates)

RTI Growth #	Structure	Target Values				Measured Values			
		(1-y)	(1-x)	Eg (eV)	Eff (%)	Voc (mV)	Jsc (mA/cm ²)	CFF (%)	Eff (%)
6-4040	GaInP/GaInAs tandem cells on GaInAs grading layers	0.48	0.05	1.89	26.0	1634	12.75	55.7	8.5
6-4045		0.50		1.865	26.5	1718	13.4	54.3	9.2
-		0.10	0.53	1.32	26.9	890	14.35	49.6	4.7
6-4044			0.15	1.265					

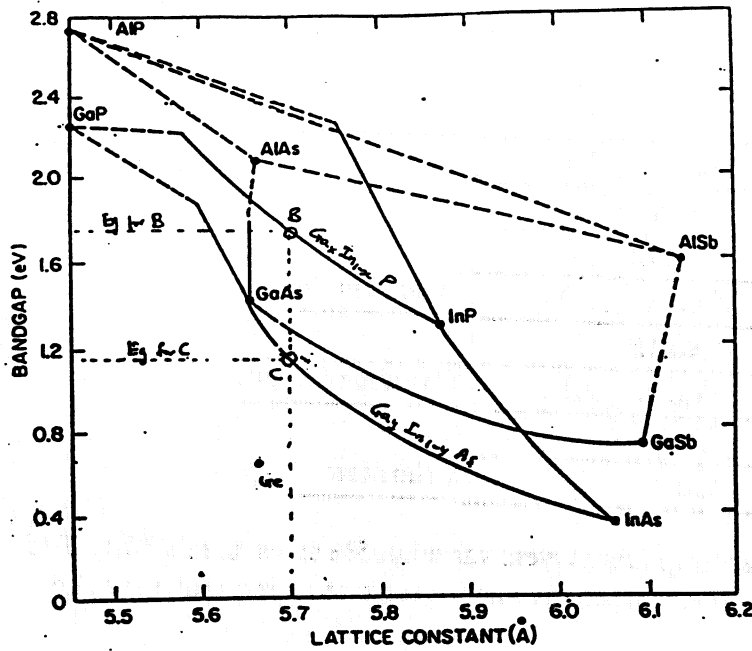


Figure 1
Bandgap versus Lattice Constant (III-V Alloys)

The GaInP and GaInAs tie-lines are shown. B and C are typical bandgap pairs.

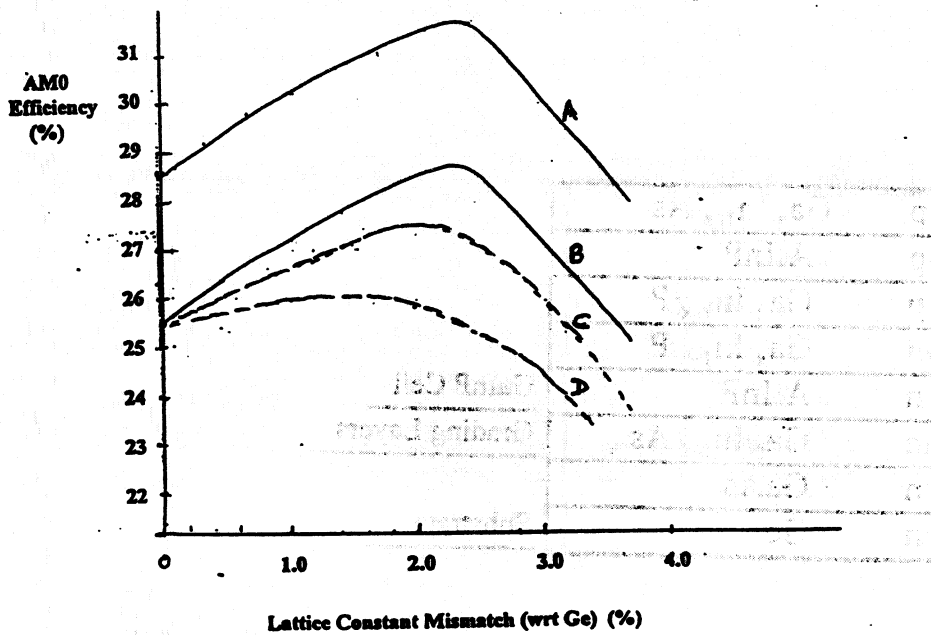
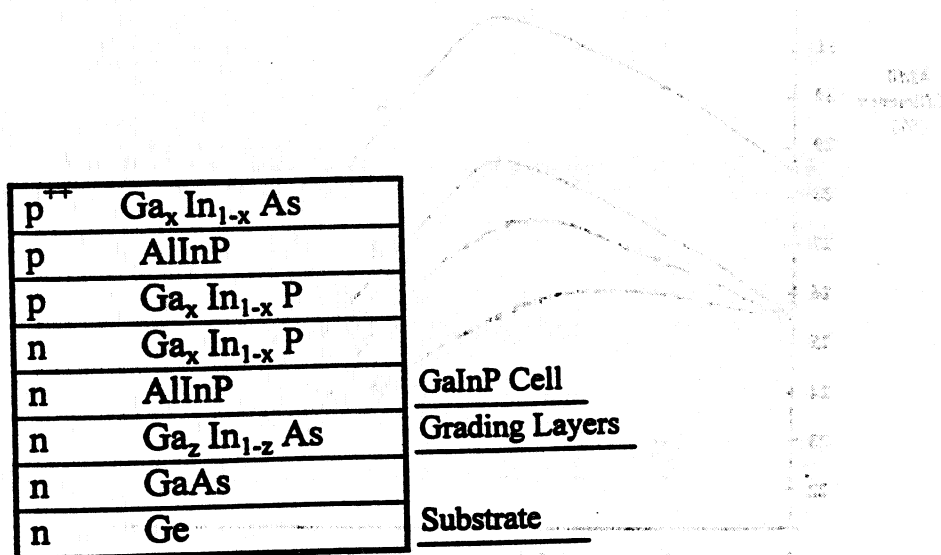


Figure 2
AMO Efficiency versus Lattice Constant Mismatch
(For Selected Bandgap Pairs)

p ⁺⁺	Ga _y In _{1-y} As	
p	GaInP	
p	Ga _y In _{1-y} As	GaIn As Cell
n	Ga _y In _{1-y} As	
n	GaInP	Grading Layers
n	Ga _z In _{1-z} As	
n	GaAs	Substrate
n	Ge	

z values in grading layers varied in 5% steps from 0.95 to 0.75
y values selected to give lattice match to appropriate z-value

Figure 3 Layer Sequence for Ga_yIn_{1-y}As Cells



z values in grading layers varied in 5% steps from 0.95 to 0.75
x values selected to give lattice match to appropriate z-value

Figure 4 Layer Sequence for Ga_xIn_{1-x}P Cells

p ⁺⁺	Ga _y In _{1-y} As	GaInP Cell
p	AlInP	
p ⁺	Ga _x In _{1-x} P	
n	Ga _x In _{1-x} P	
n	AlInP	
n ⁺⁺	Ga _y In _{1-y} As	Tunnel Junction
p ⁺⁺	Ga _y In _{1-y} As	
p ⁺	GaInP	
p ⁺	Ga _y In _{1-y} As	GaInAs Cell
n	Ga _y In _{1-y} As	
n	GaInP	
n	Ga _z In _{1-z} As	Grading Layers
n	GaAs	
n	Ge	Substrate

x- and y-values selected to give lattice-match to appropriate z-values

Figure 5 Layer Sequence for Tandem Cell

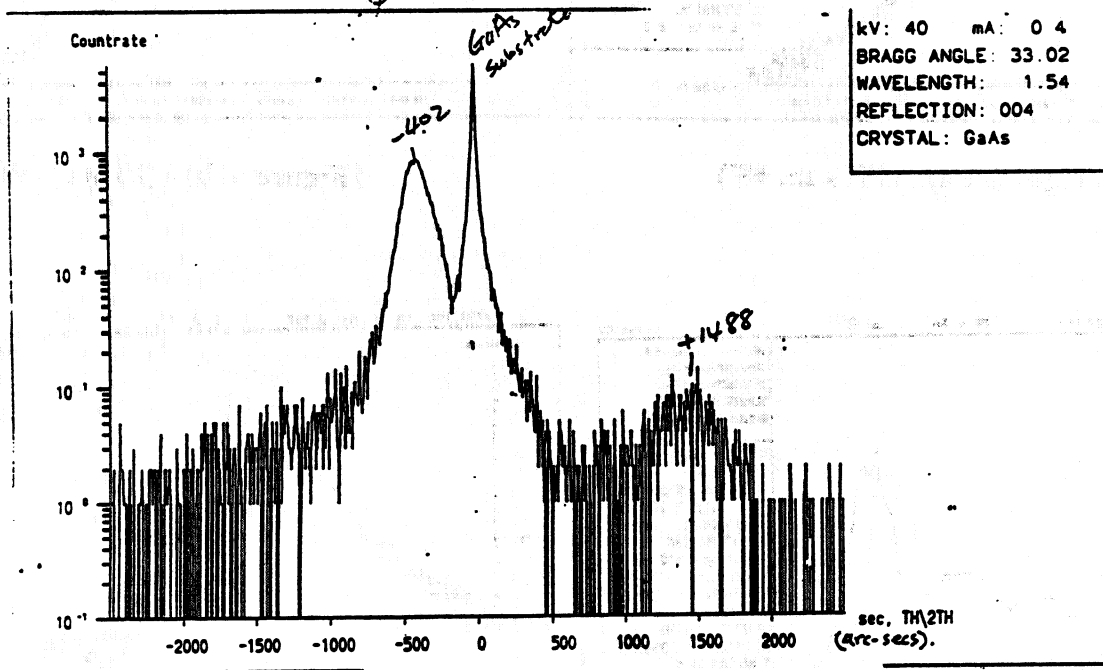


Figure 6

X-Ray Diffraction for RTI #6-3464

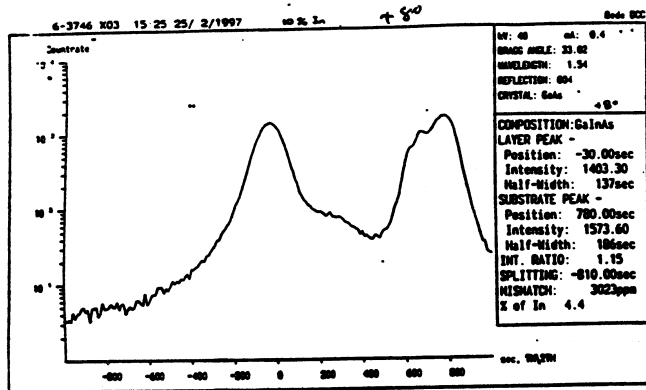


Figure 7 (10% In, +8°)

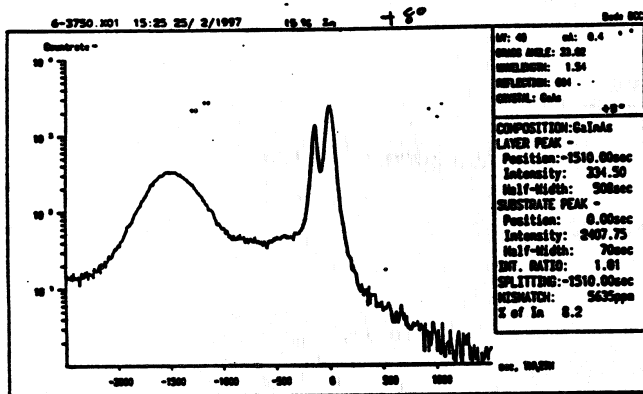


Figure 8 a) - (15% In, +8°)

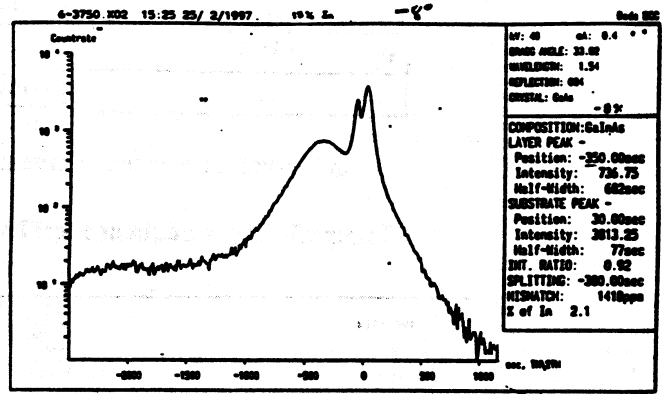


Figure 8 b) - (15% In, -8°)

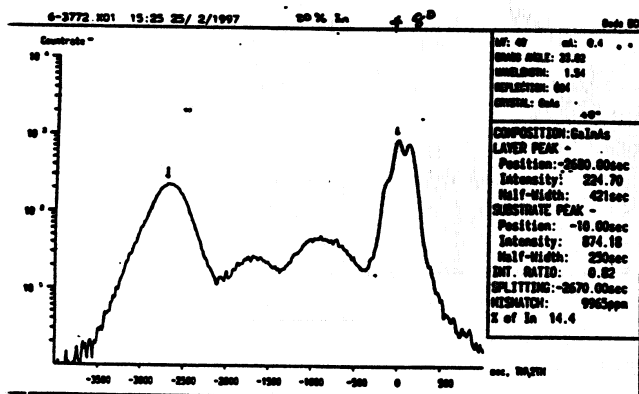


Figure 9 (a) - (20% In, +8°)

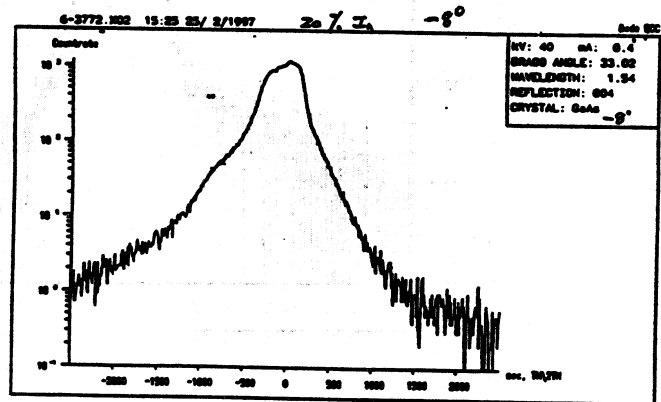


Figure 9 b) - (20% In, -8°)

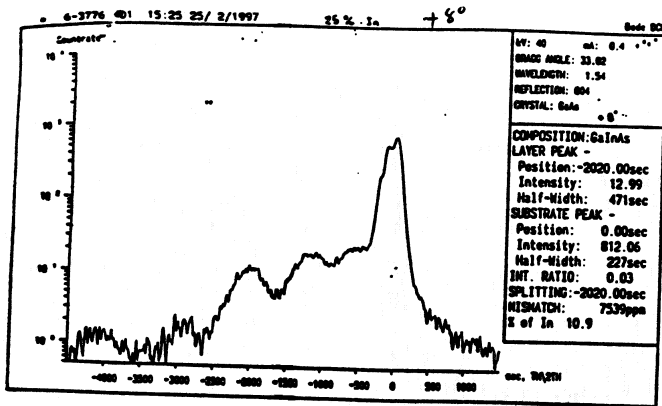


Figure 10 a) - (25% In, +8°)

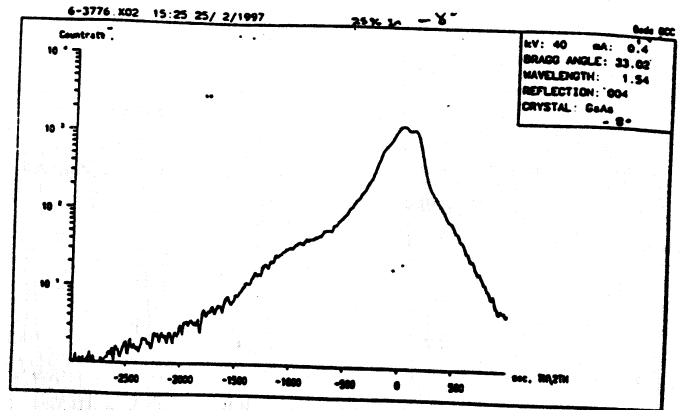


Figure 10 b) - (25% In, -8°)

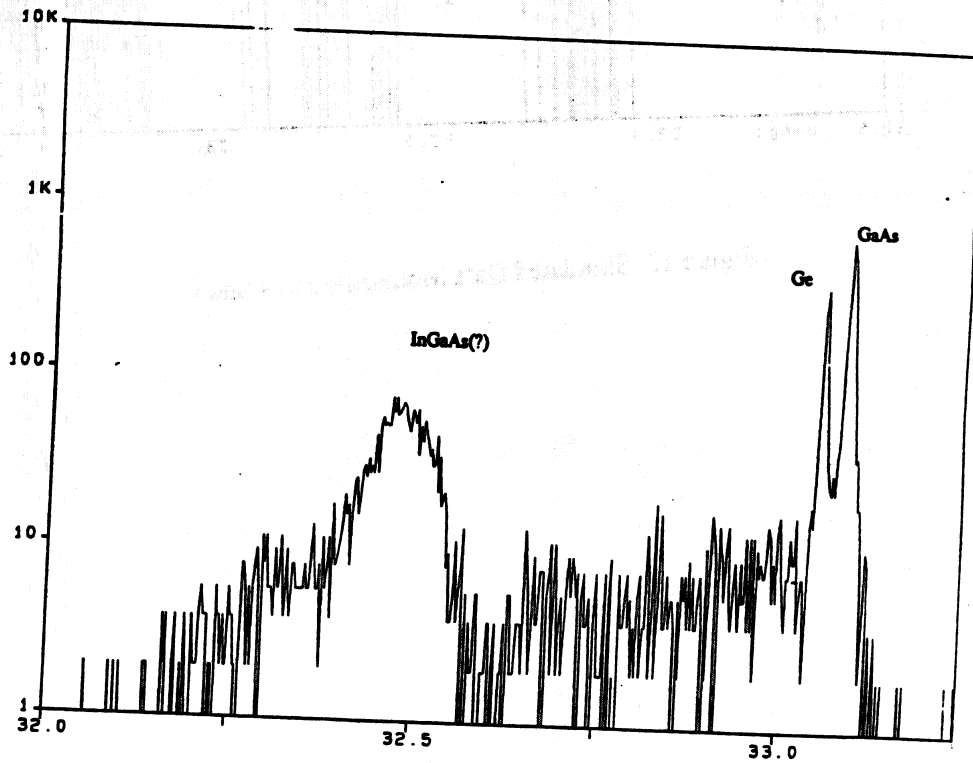


Figure 11 Section of Diffraction Space Map through the Substrate Maximum

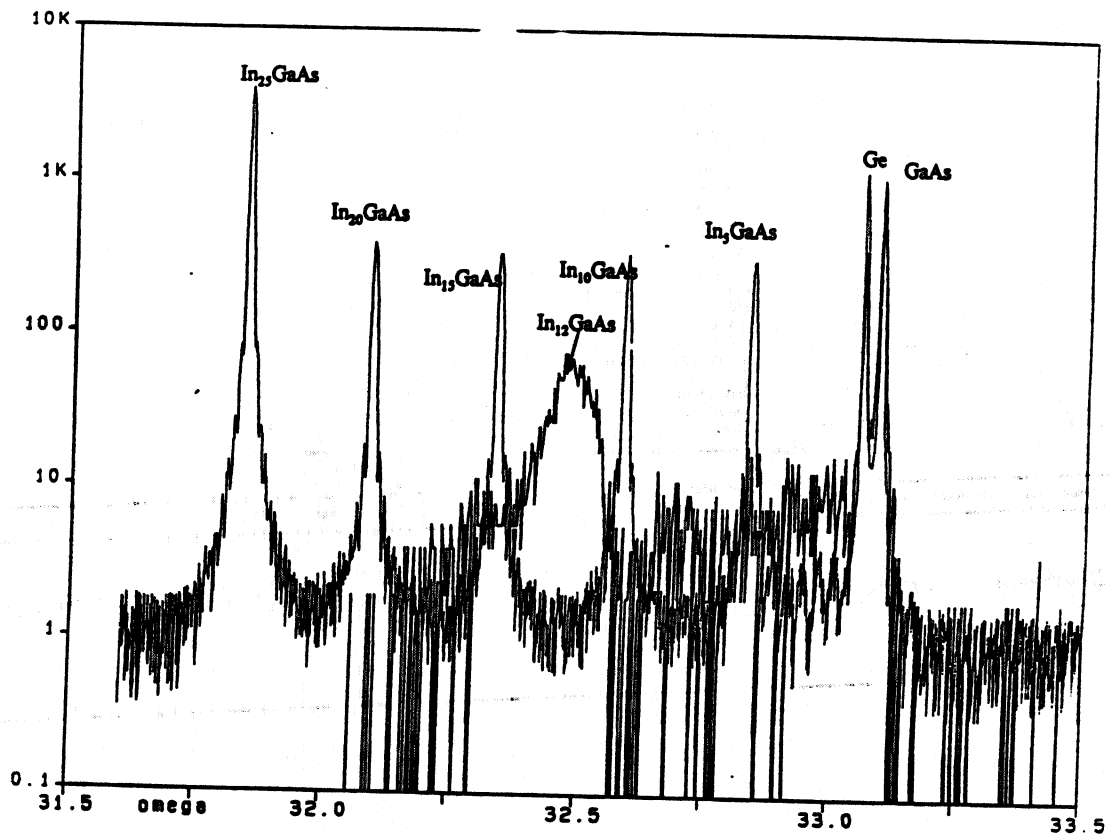


Figure 12 Simulated Data Modeled In% as Shown

PROGRESS IN THE MULTIJUNCTION SOLAR CELL MANTECH PROGRAM

Captain David N. Keener
Phillips Laboratory, Albuquerque, NM

Dr Dean Marvin
The Aerospace Corporation, Albuquerque, NM

David J. Brinker and Henry B. Curtis
NASA Lewis Research Center, Cleveland, OH

Introduction

The development of GaInP₂/GaAs/Ge multijunction solar cells has progressed rapidly since the early 1990s under various U.S. government programs. In early 1995, with the demonstration of >20% efficiency, 2x2cm, dual and triple junction GaInP₂/GaAs/Ge solar cells, the successful laboratory development of multijunction solar cells was completed. Then, in September 1995, the joint Wright Laboratory/Phillips Laboratory/NASA Lewis Multijunction Solar Cell Manufacturing Technology (ManTech) Program began to improve multijunction cell performance and scale them up to production size and quantity to support Air Force and commercial satellite programs. The first milestone of the program has been reached and the purpose of this paper is to present the results of the program so far.

The objectives of the Multijunction Solar Cell ManTech Program are to increase GaInP₂/GaAs/Ge lot average cell efficiency to 24-26%, increase the cell size to $\geq 16\text{cm}^2$ while maintaining high efficiency, and limit the per cell costs to $\leq 1.15\text{X}$ state-of-the-art GaAs/Ge cells. Advanced manufacturing technology and process control techniques such as in-situ process monitoring and real time process feedback are being used to optimize multijunction solar cell growth processes to achieve these goals.

Another objective of the program is for production multijunction solar cells to be available as a drop-in replacement for arrays currently using GaAs/Ge technology. Therefore, the program requirements call for ManTech multijunction solar cells to have the same physical qualities as GaAs/Ge cells including thickness, mass, radiation resistance, and contact strength (See Table 1). Having characteristics similar to GaAs/Ge cells should minimize concerns about inserting multijunction cell technology into new or upgraded space systems. Also, as a drop-in replacement, multijunction cells offer the benefit of increased power for a given solar array size or reduced solar array mass for a given power level.

Overall, the program cost and performance objectives carry the potential to increase solar array specific power (W/kg) by 33%, reduce array size by 25%, and decrease array cost per watt (\$/W) by 15% or more over GaAs/Ge cells. Additional mass and cost savings in the spacecraft attitude control subsystems and payloads will be realized as a result of increased solar cell efficiency. All of these sizable savings are working together to position GaInP₂/GaAs/Ge multijunction solar cells as the next state-of-the-art solar cell technology.

Table I - Multijunction ManTech Program Requirements

Parameter	Requirement
Lot Average Efficiency (bare, glass optimized AR coating)	24%
p/p ₀ @ 1x10 ¹⁵ 1MeV electrons	0.75
Cell Area	16 cm ²
Thickness	5.5 mil
Contact Integrity, Ag/Kovar weld	>300g w/ <0.2% loss

Two experienced space solar cell manufacturers, Spectrolab, Inc and TECSTAR/Applied Solar are working with the government team to meet the program goals, which consist of two phases. The Baseline Definition phase focused on cell performance improvements in 2x2 cm cells, and was completed in December 1996. The Optimization and Validation phase, which will focus on manufacturing process optimization, began in May 1997. Phase II, which runs for 24 months, will culminate with a 16,000 cm² production demonstration as a primer for full scale production of multijunction solar cells.

This paper will discuss progress made in Phase I of the program and give an overview of Phase II but will focus on side-by-side testing results collected by Phillips Laboratory and NASA Lewis on Phase I deliverable cells from both vendors. Cell performance, pre- and post-radiation, and temperature coefficient results on initial production multijunction solar cells will be presented and discussed. The data shows that this technology meets the objectives of the program, and that, in the interim before a new solar simulation standard becomes widely available, the measurement techniques being used by the major space solar cell manufacturers are providing adequate testing results for solar array design.

Phase I Discussion

Several material systems for high efficiency photovoltaic energy conversion have been investigated, but at this point, the GaInP₂/GaAs/Ge material system, which is being pursued in this program, is considered the most mature and manufacturable. The current design builds on GaAs/Ge technology by monolithically integrating three materials with different bandgaps into a single cell structure to take advantage of a greater portion of the solar spectrum and achieve higher efficiencies than single junction cells. Small area GaInP₂/GaAs tandem cells have been shown to be capable of near 26% efficiency [1] at 1-sun, AM0 conditions, and with this in mind, the goals of the Multijunction Solar Cell ManTech Program were set at a challenging level for the production environment.

Phase I of the program was the Baseline Definition phase, which was intended to improve cell performance and identify the best cell design to be transitioned to production in Phase II. At the beginning of Phase I, Spectrolab and TECSTAR were both manufacturing 20-22% efficiency dual and triple junction cells [2,3], the relationships between current matching, radiation resistance, and temperature coefficient were beginning to be documented, and it was unclear whether the dual or triple junction cell would be the best baseline cell for Phase II. Therefore, both vendors entered the program pursuing parallel dual and triple junction cell developments anticipating a downselect to one primary technology before the end of Phase I. However, the specific approaches taken by Spectrolab and TECSTAR did diverge shortly after the start of Phase I.

For dual junction cells, the approach was identical; p/n GaInP₂/GaAs structures. The approaches differ in the formation of the triple junction cell using the Ge substrate. Spectrolab reverses the cell polarity, and uses an n/p junction in the Ge substrate to form the third cell, and TECSTAR forms a controlled n/n AlGaAs/Ge heterointerface at the Ge substrate, which gives the cell a voltage boost. In this paper, cell structures are named according to the number of n/p or p/n junctions contained in the cell. Therefore, the Spectrolab active germanium cell is called a triple junction, and the TECSTAR active germanium cell a dual junction-plus.

The results of experimental studies, optimizations, and baseline production runs in Phase I were used to define the baseline design for Phase II. Specifically, work centered on understanding the effect of the Ge substrate quality, junction characteristics, and lattice orientation on the overall cell efficiency and attempts to increase the bandgap of the GaInP₂ top cell for increased cell voltage and efficiency. This work led to several very encouraging results including lot average efficiencies of 24.2% and 22.4% and best cell efficiencies of 25.5% and 24.1% at Spectrolab and TECSTAR respectively [4,5]. However, the Phase I baseline production demonstrations also indicated that for GaInP₂/GaAs/Ge in the manufacturing environment, the voltage boost from the Ge substrate is probably needed to meet the 24% lot average efficiency requirement of the program, and each vendor has selected a form of active germanium cell for the primary baseline design. Table 2 summarizes the baseline cell structures and major results of the Phase I program.

Table II - Summary of major Phase I results

	Spectrolab	TECSTAR
Baseline cell decision	n/p triple junction	p/n dual junction-plus
Polarity choice reasoning	Identical 2J and 3J processes Projected radiation resistance	Direct extension of GaAs/Ge line Control of Ge interface voltage
Ge cell formation	n/p Ge junction	n/n AlGaAs/Ge heterointerface voltage boost
Best dual junction cell efficiency	23.7%	22.8%
Best triple junction cell efficiency	25.5%	24.1% (dual junction-plus)
Best large area cell efficiency	24.3% (13.78 cm ²)	22.1% (16.6 cm ²)
Lot average of Phase I deliverables	24.2%	22.4%

At the end of Phase I, Spectrolab and TECSTAR each delivered 150 multijunction solar cells for evaluation by Phillips Laboratory and NASA. The purpose of the joint testing program was to verify the Phase I results with a direct side-by-side comparison of the cells from each vendor and to investigate the scope of the problem of accurate multijunction cell measurements and correlation with other testing systems. The test program included near AM0 Langley plot and I-V curve traces on the NASA Lewis Learjet aircraft as well as pre- and post- radiation performance and temperature coefficient measurements at Phillips Lab and NASA.

Learjet Cell Performance Measurements

Solar simulator measurements of multijunction solar cells are the subject of much user community discussion because a standard testing method has not yet been adopted. The objective of Learjet testing of Phase I ManTech cells was to test cells from each vendor side by side in a near-AM0 environment to remove simulator error from the discussion of the results. Cells from each contractor were flown on the Learjet, and Langley Plot Isc data as well as I-V curves at 25°C and 70°C were collected. The Isc results compared favorably with contractor provided data, and I-V curves showed fill factors from 0.8-0.85 with no evidence of significant current mismatch between the top and middle cells. Tables 3 and 4 show Learjet Isc results for the cells flown, and the results show reasonable agreement between contractor data collected on modified X-25 and dual source Hoffman simulators and the NASA data. The Learjet results do not reduce the need for a standard test method for multijunction solar cells, but they do indicate that, in the meantime, the individual contractor testing methods are making reasonably accurate cell measurements.

Table III - Comparison of TECSTAR and Learjet Isc Data

Cell	TECSTAR I_{sc}	Lear I_{sc}	% Diff
1	64.1	63.27	-1.295
2	63.8	62.52	-2.006
3	64.2	63.79	-0.639
4	60.6	61.49	1.469
5	60.9	62.84	3.186
6	62.7	62.02	-1.085
7	60.4	Unreliable data	N/A

Table IV - Comparison of Spectrolab and Learjet Isc Data

Cell	Spectrolab I_{sc}	Lear I_{sc}	% Diff
1	61.6	61.73	0.211
2	62.4	62.37	-0.048
3	63.9	63.39	-0.798
4	63.4	62.23	-1.845
5	61.9	62.27	0.598
6	63.6	63.10	-0.786
7	63.0	61.45	-2.460

Radiation Degradation Results

Spacecraft solar array sizing is done based on the expected solar cell efficiency at the end of the required mission lifetime in a given orbit. This method ensures that full power is available for the mission at end-of-life (EOL). As a drop-in replacement for GaAs/Ge solar cells, it is desirable for multijunction solar cells to have radiation performance similar to or better than GaAs/Ge cells. The radiation requirement for cells manufactured under the ManTech Program is $p/p_0 \geq 0.75$ after 1×10^{15} 1MeV electrons/cm², which is a common benchmark for GaAs/Ge cells [6]. GaInP₂/GaAs tandem cells have been documented with better radiation characteristics than single junction GaAs/Ge [7] due to EOL current match configurations and the slower degradation rate of GaInP₂ [8]. To verify and independently document the radiation performance of production cells manufactured for the ManTech Program, Phillips Laboratory and NASA Lewis each measured the pre- and post-radiation performance of a group of cells from each contractor. Phillips Laboratory measured the relative radiation degradation on a group of ten cells using a dual source simulator, and NASA measured a group of five cells with a combination of an X-25 simulator and the Learjet. Cells for each group were selected from the group of 150 deliverable cells so that efficiencies over the range delivered were represented. The ten cells from Spectrolab had a BOL current mismatch of approximately 1% with the GaInP₂ top cell current limiting, and the TECSTAR cells measured were current matched for best BOL performance. The irradiations were performed by Dr Bruce Anspaugh of JPL, and the cells received 1×10^{15} 1MeV electrons/cm² in a single dose. Tables 5 and 6 list the average radiation degradation results for the cells measured by Phillips Lab and NASA.

Table V - Average Radiation Degradation Results, Spectrolab Cells

	Phillips	NASA Lewis
Voc	0.906	0.918
Isc	0.872	0.888
FF	0.971	0.979
p/p₀/Eff	0.766	0.797

Table VI - Average Radiation Degradation Results, TECSTAR Cells

	Phillips	NASA Lewis
Voc	0.920	0.932
Isc	0.834	0.833
FF	0.984	0.995
p/p₀/Eff	0.754	0.772

The results from NASA are 2-4% higher than the Phillips Laboratory results probably due to differences in simulator calibration methods for EOL cells. The dual source simulator was calibrated at EOL with the same standards used for BOL, a GaInP₂ cell and a filtered GaAs/Ge cell. This method does not take into account changes in spectral response of the cells after radiation, but the smooth spectrum of the simulator is expected to keep this error small.

At NASA, an irradiated cell was reflown on the Learjet and became a secondary standard for the X-25 simulator. This cell was then used to calibrate the X-25 simulator to collect the other post-radiation data, but some error in the measurement may still be introduced by the spectrum of the X-25. The error investigation for these results is still ongoing and will be reported in the future.

Overall, the results of this testing shows that both types of multijunction cells being developed in the ManTech Program meet the requirement for radiation resistance. Also, the radiation resistance of GaInP₂/GaAs/Ge cells is shown to be as much as 6% better at this fluence than single junction GaAs/Ge cells. Future cell irradiations will include higher electron fluences, proton irradiation, and possibly annealing studies.

Temperature Coefficient Results

Temperature coefficient data are also important for sizing solar arrays according to the expected cell efficiency at the array operating temperature, which is determined by several factors including the mission orbit, spacecraft structure, and thermal control system. For GaInP₂/GaAs/Ge multijunction solar cells, temperature coefficients are related to the amount of voltage activity in the germanium substrate. For instance, the Spectrolab n/p Ge bottom cell produces more voltage than the TECSTAR AlGaAs/Ge heterointerface, and therefore, larger temperature coefficients for the Spectrolab cells were expected. However, when a cell reaches a temperature where the Ge activity goes to zero, the triple junction cell will assume the temperature coefficient of the analog pure dual junction cell. Phillips Laboratory and NASA Lewis made pre- post-radiation temperature coefficient measurements for Voc, Isc, Pmax, and efficiency on two groups of cells. At Phillips Laboratory, five cells were tested at 28°,40°C, and 60°C with three trials at each temperature. All of the data (45 data points) were plotted together to calculate a linear trend line through the data whose slope is the temperature coefficient. and NASA calculated temperature coefficient similarly. As expected, the Spectrolab cells exhibited larger temperature coefficients at BOL and EOL. Tables 7 and 8 summarize the BOL and EOL temperature coefficient data collected by Phillips Laboratory and NASA.

Table VII - BOL Temperature Coefficient Data

	Spectrolab		TECSTAR	
	Phillips Laboratory	NASA	Phillips Laboratory	NASA
Voc (mV/C)	-6.9	-6.4	-5.9	-5.2
Isc (mA/cm ² -C)	0.01	0.01	0.004	0.007
Pmax (mW/cm ² -C)	-0.087	-0.085	-0.073	-0.065
Eff (abs %/C)	-0.064	-0.062	-0.054	-0.047

Table VIII - EOL Temperature Coefficient Data

	Spectrolab	TECSTAR
Voc (mV/C)	-7.3	-5.6
Isc (mA/cm ² -C)	0.01	0.01
Pmax (mW/cm ² -C)	-0.087	-0.05
Eff (abs %/C)	-0.051	-0.036

The implications of these data are in the relative benefits of triple junction and dual junction-plus cell technology for various operating temperatures. Figure 1 extrapolates BOL efficiency temperature coefficient trends based on data collected by Phillips Laboratory and NASA to illustrate the trade space around the triple junction and dual junction-plus cell structures, and three things should be noted. First, the actual Phase I data shows that the triple junction structure, even with a higher temperature coefficient, currently has a small efficiency advantage over the dual junction-plus structure to greater than 150°C. Second, at the projected Phase II BOL lot average efficiencies of 25% for triple junction cells and 23.5%

for dual junction-plus cells, the previous trend will continue to hold true. Lastly, the triple junction cell loses its efficiency advantage at about 80°C in the case where the dual junction-plus efficiency increases more than the triple junction during Phase II. This illustration assumes that the temperature coefficients remained constant with cell efficiency improvements, which is a reasonable approximation for the purpose of this discussion. As multijunction cells approach full production in Phase II, this trade space will be updated to reflect the most current results.

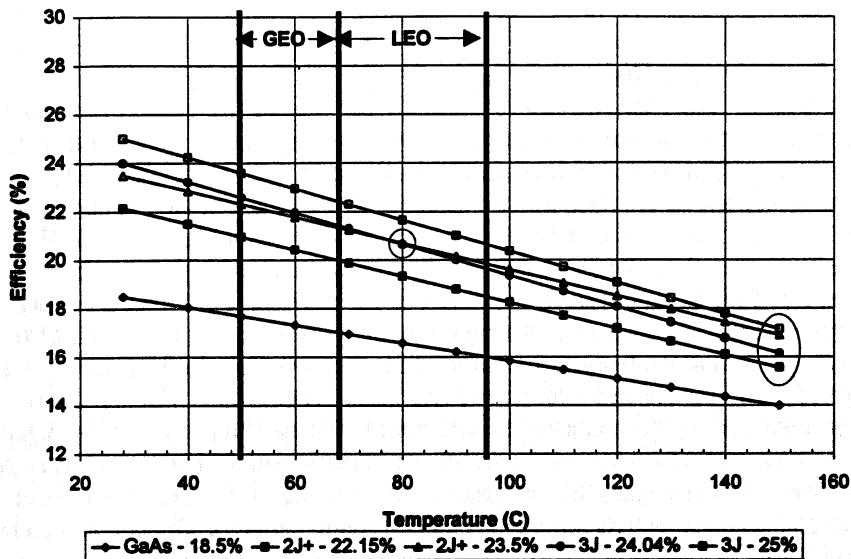


Figure 1 - BOL Temperature Coefficient Extrapolations Based on ManTech Results

Phase II Program Overview

Phase II of the Multijunction Solar Cell ManTech Program will build on the success of Phase I by reducing the manufacturing cost of multijunction cells while maintaining high efficiency. The objectives of Phase II are to produce large area cells with a cell-to-cell cost $\leq 1.15X$ GaAs/Ge cells while maintaining high efficiency. Achieving this goal will require improvements in process control and yield so that the main cost increases over GaAs/Ge cells is in material and reactor run time. Increasing cell size from 4cm² to 16cm² will also result in large solar array cost savings by reducing the parts count of a given solar array by 4 times not including array size savings due to higher efficiency cells.

To reach the cost objective of Phase II, the program is continuing cell growth process improvements including better temperature uniformity control, in-situ, real time process monitoring and control, and design of experiments to identify the critical parameters in the growth process. Some cell optimizations will also occur to push cell efficiencies to the highest level possible, but the baseline established in Phase I will essentially be the product transitioned at the end of Phase II.

Conclusions

The Multijunction Solar Cell Program is bringing high efficiency, large area, cost effective GaInP₂/GaAs/Ge solar cells to full production to meet the spacecraft power demands of future spacecraft systems. In Phase I of the program, baseline multijunction solar cell designs have been developed at two domestic vendors, and small scale production demonstrations have shown up to 24.2% lot average efficiencies. The cells also have demonstrated similar physical characteristics and better radiation performance than GaAs/Ge cells. Phase II of the program will focus on increasing multijunction cell size and yield while maintaining high efficiency to reduce solar array cost per watt (\$/W) by more than 15%. Together, the Multijunction Solar Cell ManTech Program has positioned high efficiency multijunction solar cell technology to be the next mass produced, state-of-the-art, space solar cell technology.

References

[1] J.M. Olson, S.R. Kurtz, A.E. Kibbler, and P. Faine. "Recent Advances in High Efficiency GaInP/GaAs Tandem Solar Cells." Proc. 21st IEEE Photovoltaic Specialists Conf. (New York, 1990). Vol. 1, p. 24.

[2] P.K. Chiang, D.D. Krut, and B.T. Cavicchi. "The Progress of Large Area GaInP/GaAs/Ge Triple-Junction Cell Development at Spectrolab." Proc. 14th Solar Photovoltaic Research and Technology Conf. (Cleveland, 1995). pp 47-56.

[3] Y.C.M. Yeh and C.L. Chu. "Status of Multijunction Solar Cells." Proc. 14th Solar Photovoltaic Research and Technology Conf. (Cleveland, 1995). pp 57-64.

[4] P.K. Chiang et. al. "Experimental Results of GaInP/GaAs/Ge Triple Junction Cell Development for Space Power Systems." Proc. 25th IEEE Photovoltaic Specialists Conf. (Washington D.C., 1996). p. 183.

[5] Y.C.M. Yeh et. al. "Production Experience With Large Area Dual Junction Space Cells." Proc. 25th IEEE Photovoltaic Specialists Conf. (Washington D.C., 1996). p. 187.

[6] B.A. Anspaugh. GaAs Solar Cell Radiation Handbook. JPL Publication 96-9.

[7] M. Yamaguchi et. al. "Radiation Resistance of InGaP Solar Cells." Proc. 25th IEEE Photovoltaic Specialists Conf. (Washington D.C., 1996). p. 163.

[8] Sarah Kurtz, K.A. Bertness, et al. "Design of High-Efficiency, Radiation-Hard, GaInP/GaAs Solar Cells." Proc. 13th Solar Photovoltaic Research and Technology Conf. (Cleveland, 1994). pp 181-186.

High Beginning-of-Life Efficiency p/n InP Solar Cells

Richard W. Hoffman, Jr., Navid S. Fatemi, Victor G. Weizer, and Phillip P. Jenkins
Essential Research, Inc., Cleveland, OH 44135

Steven A. Ringel
The Ohio State University, Columbus, OH 43210

David A. Scheiman
NYMA Setar, Cleveland, OH 44135

David M. Wilt and David J. Brinker
National Aeronautics and Space Administration, Lewis Research Center, Cleveland, OH 44135

Introduction

It is well known that high efficiency InP solar cells have excellent radiation hardness.^[1-3] The record efficiency for InP that Keavney achieved in 1990 still stands. In fact, the n/p configuration has consistently demonstrated conversion efficiency records, independent of the substrate material (see Table I). Because of a high surface recombination velocity value and the fact that no lattice matched surface passivation window layers have been identified, the design of the n/p configuration cells have an extremely thin emitter region (~30 nm). They depend on good current collection from the base region for their high performance where the strongest wavelength conversion tends to be in the red to far red region of the spectrum, the same region which suffers the largest loss upon radiation damage due to minority carrier lifetime degradation. Even though this cell configuration has demonstrated very good radiation hardness, thick emitter p/n diffused junction cells have demonstrated even better radiation resistance.^[4] However, the testing of the p/n configuration has been limited to cells of lower quality as judged by their beginning of life (BOL) air mass zero (AM0) efficiency values typically below 15%. The emitter structures in these cells, which must be thick relative to emitters in the n/p configuration for sheet resistance considerations, have been ineffective and therefore, the p/n configuration cells have suffered from poor blue response, low short circuit current density (J_{sc}) and moderate efficiencies.^[5,6]

Table I - Highest reported AM0 efficiencies for InP cells on various substrates.

Substrate	Configuration	Efficiency, (%)	Source
InP	n/p	19.1	Spire Corp. ^[7]
InP	p/n	15.9	Arizona State ^[8]
GaAs	n/p	13.7	NREL ^[9]
Si	n/p	13.0	Spire Corp. ^[10]

We recently reported on p/n InP cells which had AM0 efficiencies above 16%.^[11] These cells were fabricated using a new Ag-Zn front contact system^[12] which eliminated the necessity of an InGaAs p-type contact layer employed in early p/n epitaxial InP cells. Diffusion of Zn during the time it takes to grow the InGaAs layer caused the loss of junction depth control in these early cells.^[13] The Ag-Zn metallurgy allowed ohmic contact formation to the p-type InP without degrading junctions as thin as 100 nm. It was believed that cells fabricated without the InGaAs layer would have better junction depth control, since less opportunity for Zn diffusion existed, and therefore higher conversion performance was expected.

InP structures were grown by organo-metallic vapor phase epitaxy (OMVPE) under typical low pressure conditions. We used PH_3 , AsH_3 , SiH_4 , trimethylgallium, trimethylindium, diethylzinc and hydrogen in our home-built reactor. InP and InGaAs layers were grown at 620°C , a total pressure of 150 torr and a V/III ratio of 100. Standard reverse photolithography and vacuum resistive evaporation techniques were used to form the contacts. A dual layer anti-reflection coating (ARC) consisting of MgF_2/ZnS and optimized for the AM0 spectrum was also deposited by vacuum resistive evaporation. Cell with areas of 0.36 cm^2 and 1.0 cm^2 were fabricated on the same wafer, defined by mesa etching and had grid shadowing of 6% and 5% respectively. Cell performance was measured after various steps of processing.

Results and Discussion

We fabricated p/n InP cells with efficiencies exceeding 17.6% under AM0, one sun, 25°C test conditions. A summary of the cell performance data is presented in Table II. Many cells had efficiency values above 17%. A peak cell efficiency of 17.64% was obtained from a 0.36 cm^2 area cell. The corresponding I-V curve for this cell is shown in Figure 2. We were also able to achieve nearly the same performance from cells which were 1.0 cm^2 in area as demonstrated by the I-V curve in Figure 3.

Table II - Results of p/n InP solar cells tested under AM0, one sun, 25°C at NASA LeRC.

Cell	J_{sc} (mA/cm^2)	V_{oc} (mV)	FF (%)	Efficiency (%)	Area (cm^2)
393-1A	34.9	854	79.2	17.3	1.0
393-1C	35.2	850	77.5	17.0	1.0
393-2C	35.8	854	77.9	17.4	1.0
393-3A	35.2	855	79.7	17.5	1.0
393-3C	35.0	855	79.9	17.5	1.0
393-3D	34.8	854	81.1	17.6	0.36

In Figure 4 we show a comparison of the external quantum efficiency of our p/n cell to the external quantum efficiency measured from the previous record p/n cell from the literature. Our p/n InP cells have excellent blue response, significantly higher than the blue response of the previous record p/n cell while maintaining approximately equivalent red response. In Figure 5 is a comparison of the external quantum efficiency of our p/n InP cell to the internal quantum efficiency of the record n/p cell. Our p/n cell has a significantly higher blue response, even though the emitter region of the p/n cell is almost an order of magnitude thicker than the emitter region used in the record n/p cell. We do, however, observe a significantly lower red response for the p/n cell compared to the record n/p cell, a result of lower minority carrier diffusion length in the n-type base than the p-type base. However, it was precisely in this wavelength region where the n/p cell lost current collection when exposed to radiation due to the reduction of minority carrier diffusion length in the base. The p/n cells of the present work may provide better radiation resistance since they depend less strongly on the long wavelength current collection for high device performance.

Even though cells fabricated with Ag-Zn contacts exhibited an AM0 conversion efficiency above 16%, they suffered from other anomalous behavior. Interesting aging effects were observed where the cells improved with age, mostly through improvement to J_{sc} values. In addition, a reversible photo-degradation was observed where the J_{sc} value decreased 6% per hour upon exposure to the AM0, one-sun light in a X-25 solar simulator. We did, however, report an encouraging result from these cells, in that they demonstrated the possibility of very good quantum efficiency in the blue region of the light spectrum as compared to the n/p configuration.

In the present work, we report on the fabrication of high performance p/n InP solar cells, which directly resulted from improved growth of p-type InP. Through our understanding of the mechanisms involved in Zn doping of InP, we have gained better control of the OMVPE growth process, and have achieved record efficiencies for p/n InP solar cells under AM0, 25°C test conditions. These cells exhibit excellent blue response and are believed to demonstrate improved radiation resistance compared to n/p InP cells.

Experiment

We have returned to the conventional p/n InP cell design seen in Figure 1 where we used p-type InGaAs lattice matched to InP under the Au-Ge front contact grid fingers. In previous work^[11] we reported significant p-type dopant passivation due to conditions under which the samples were cooled to room temperature after growth. Under normal OMVPE growth, the samples are cooled to room temperature, or at least to 300-400°C in a partial pressure of appropriate hydride gas (PH₃ for phosphides, AsH₃ for arsenides). The unexpected passivation resulted from the rapid, deep diffusion of atomic hydrogen, available from the cracking of hydride gasses or organo-metallic vapors, which formed a complex with substitutional, active Zn, thus deactivating p-type majority carriers. To avoid this passivation effect, the p/n InP junctions were cooled from the growth temperature flowing only H₂ through the reactor, however, In droplets appeared on the InP surface due to loss of phosphorus. To prevent the surface decomposition during cool-down, we deposited lattice matched InGaAs on the InP cell structure and then cooled the structures under H₂. We then removed the InGaAs between the fingers after front contact formation, thus protecting the InP surface throughout cell processing.

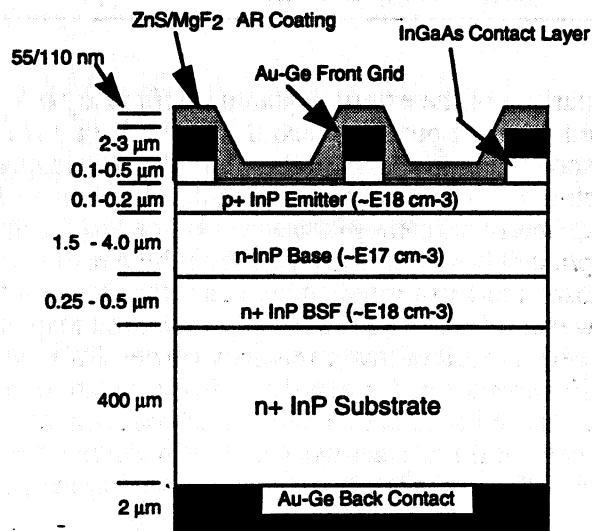


Figure 1 - Conventional p/n InP solar cell design employing InGaAs p-type contact layer under grid fingers.

Cell : 393-3D
 Date : 23 Apr 1997
 Reference Cell : A-181
 Area : .36 cm²
 Temperature : 25°C
 Air Mass Zero

I_{sc} = 12.535 mA
 V_{oc} = 854.7 mV
 I_{mp} = 11.93 mA
 V_{mp} = 728.4 mV
 P_{max} = 8.688 mW
 F.F. = 81
 Eff. = 17.64 %

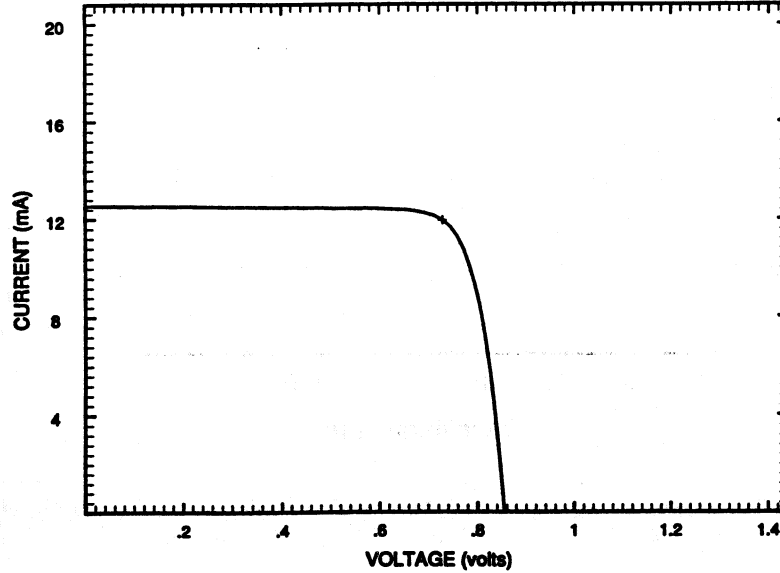


Figure 2 - I-V curve from the highest performance p/n InP cell, (0.36 cm² area) taken under AM0, 25°C, one-sun conditions.

Cell : 393-3A
 Date : 23 Apr 1997
 Reference Cell : A-181
 Area : 1 cm²
 Temperature : 25°C
 Air Mass Zero

I_{sc} = 35.215 mA
 V_{oc} = 855.7 mV
 I_{mp} = 33.45 mA
 V_{mp} = 718.1 mV
 P_{max} = 24.02 mW
 F.F. = 79.7
 Eff. = 17.57 %

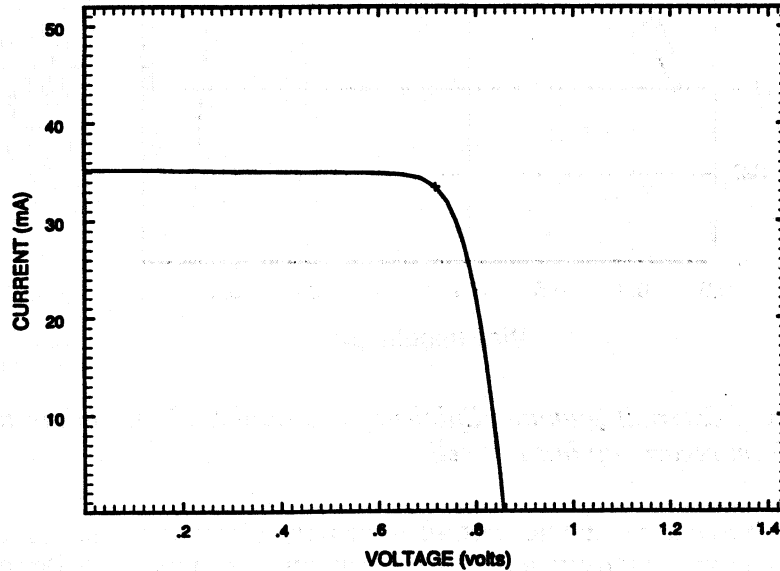


Figure 3 - I-V curve from the best 1.0 cm² area, p/n InP solar cell under AM0, 25°C, one-sun conditions.

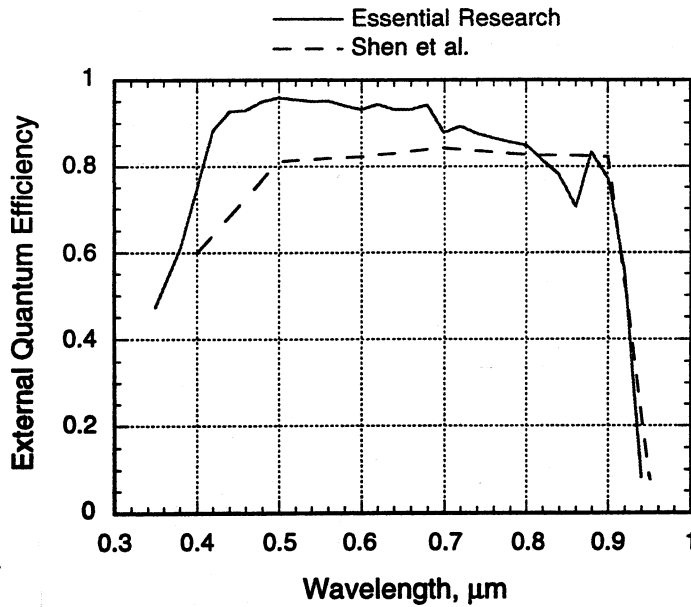


Figure 4 - Comparison on external quantum efficiency of our p/n InP cell to the previous record p/n cell.

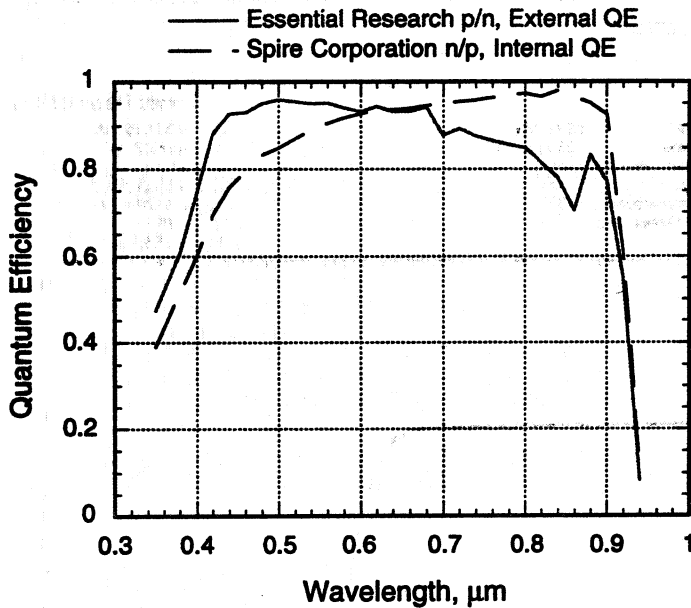


Figure 5 - Comparison of External Quantum Efficiency of p/n InP/InP cell to internal quantum efficiency from record n/p InP/InP cell.

Our previous p/n cells showed a reversible photo-degradation effect where the J_{sc} value was reduced by 6% per hour during exposure to AM0, one-sun intensity light.^[11] After removal from the solar simulator and resting in laboratory environment for a period of several days, the cells recovered to their pre-exposed performance level. We subjected cells from our present work to a

one hour AMO light soak and did not observe any significant change in measured cell performance. An example of the light soaking results (on a cell without ARC) are seen in Table III.

Table III - Stability of p/n InP cells under light soaking in AMO, one-sun conditions at 25°C.

Soak Time (min.)	J _{sc} (mA/cm ²)	V _{oc} (mV)	FF (%)	Efficiency (%)
0	25.2	854	79.5	12.5
60	25.0	853	79.7	12.4

Carrier passivation is a common occurrence in semiconductors when specifically introduced for defect passivation^[14], however, it was an unexpected observation in our OMVPE grown p-type InP. As an example of the significance of the effect, we designed an experiment where four identical samples of Zn doped InP were grown by OMVPE. Each sample was 2 μm thick and differed only by the gas composition exposure during cooling from the 620°C growth temperature to 300°C. One sample was cooled only in hydrogen, one was cooled in a mixture of hydrogen and phosphine, another in diethylzinc and hydrogen and the last sample was cooled in phosphine, diethylzinc and hydrogen. Below 300°C all samples were cooled in hydrogen. Carrier concentration depth profiles were measured using a Poloran® C-V instrument. The C-V measurement of carrier concentration measures the active net dopant concentration. The results of profiling are shown in Figure 6. In the figure, the carrier concentration of the sample cooled in hydrogen is relatively flat for over 1 μm depth. The value of carrier concentration was nearly identical to the concentration of Zn as determined by SIMS measurement on other similarly doped samples. The samples cooled in the phosphine mixture and in the diethylzinc mixture both show similar reduction of carriers from 4 x 10¹⁸ carriers/cm³ to 1.5 x 10¹⁸ carriers/cm³ due to hydrogen uptake. The phosphine cooled sample was affected slightly stronger than the diethylzinc exposed sample. Both phosphine and diethylzinc liberate atomic hydrogen when decomposed at elevated temperature. The sample cooled in the mixture of phosphine, diethylzinc and hydrogen showed a very large passivation effect, roughly an order of magnitude reduction of carrier concentration at the surface which also extends well into the InP layer. The additional passivation observed in this sample was explained by the fact that small amounts of organo-metallic compounds can enhance the cracking of hydride gasses^[15], thus liberating a higher concentration of atomic hydrogen. The evidence for diffusion of hydrogen is seen most easily in this sample by the increase in carrier concentration with depth (straight line on a logarithmic plot).

The improvement in observed cell performance of the p/n InP cells resulted from a full understanding of the OMVPE growth of Zn doped p-type InP and, therefore, better control of the p-type InP properties. The p-type carrier passivation effects are directly related to the previously observed aging and light soaking performance anomalies. The effect of carrier passivation on cell performance is further demonstrated in Figure 7. In this figure we compare I-V curves from two cells which have identical structures. They differ only in the method used to cool the structures from the OMVPE growth temperature. Both samples were capped with InGaAs prior to cooling. One structure, labeled AsH₃ + H₂ on the figure, was cooled to 300°C while a mixture of 0.7 torr partial pressure arsine and hydrogen flowed through the reactor. Below 300°C this sample was cooled in hydrogen to room temperature. The other structure, labeled H₂, was cooled with only hydrogen flowing in the reactor. The effect of the resulting carrier passivation due to trapped hydrogen during cooling was evidenced by a comparison of the performance results. The J_{sc} values were not affected by the carrier passivation in the emitter, which means that the minority carrier lifetime was already sufficiently large in the p-type emitter so that reducing the emitter doping, thus increasing minority carrier lifetime, did not change the carrier collection. It did,

however, significantly affect the V_{oc} and FF values, which can be understood by the following. A reduction in the emitter doping normally entails a drop in V_{oc} , and in turn, a decrease in FF. A further decrease in FF can also occur because of the increase in the emitter sheet resistance due to a reduction in the emitter doping.

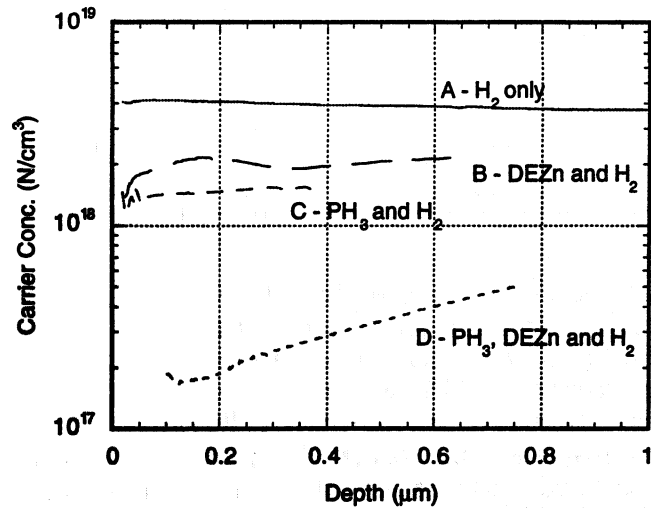


Figure 6 - Carrier passivation as a function of sample cooling conditions from OMVPE growth temperature^[11]. Curve A cooled in hydrogen, B in diethylzinc and hydrogen, C in phosphine and hydrogen, and D in phosphine, diethylzinc and hydrogen.

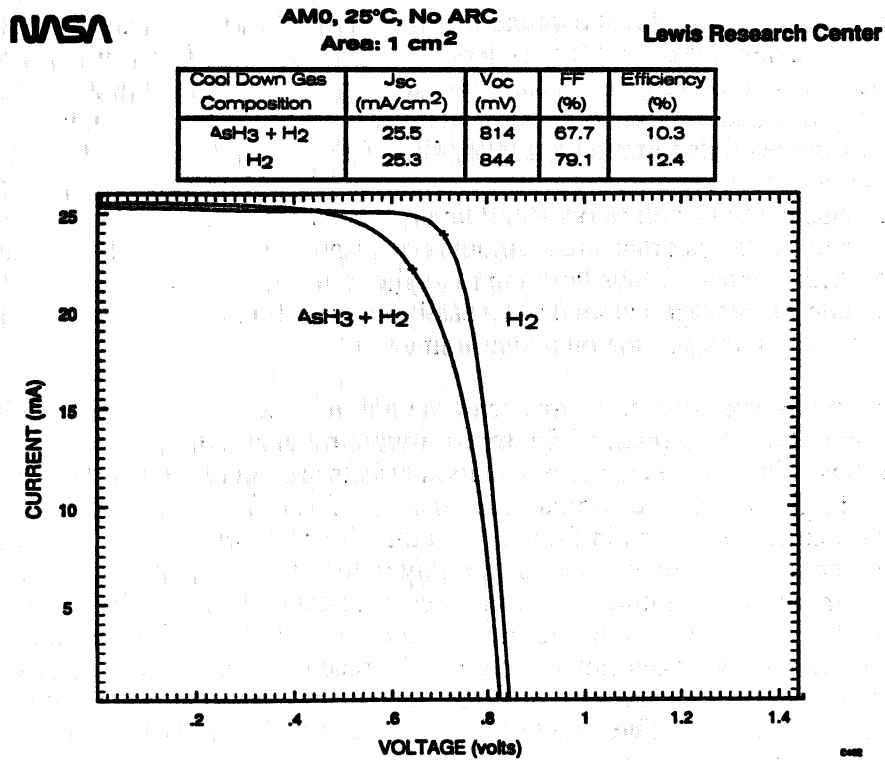


Figure 7 - Demonstration of the carrier passivation effect due to cooling gas composition in p-type InP on p/n solar cell performance.

We believe that the conversion efficiency of the p/n cells can readily be improved to the mid 18% level. Efficiencies as high as 19% may also be achievable. Further, it is believed that these high efficiency p/n cells will not suffer as much performance loss due to radiation exposure as the n/p configuration cells since a majority of the current from the p/n cells now originates from the blue response of the emitter region, whereas the largest loss in performance of the n/p cells due to radiation damage occurs in the collection of long wavelength light. This loss is due to the reduction of the minority carrier diffusion length in the base of the n/p cell.

Conclusions

We have achieved a new record efficiency of 17.6%, (AM0) for a p/n InP homo-epitaxy solar cell. In addition, we have eliminated a previously observed photo-degradation of cell performance, which was due to losses in J_{sc} . Cells soaked in AM0 spectrum at one-sun intensity for an hour showed no significant change in cell performance. We have discovered carrier passivation effects when using Zn as the p-type dopant in the OMVPE growth of InP and have found a method to avoid the unexpected effects which result from typical operation of OMVPE cell growth.

This work was supported by the NASA Lewis Research Center under the SBIR contract NAS3-27677. George Rybicki is the technical monitor of this contract.

References

- [1] A. Yamamoto, M. Yamaguchi and C. Uemura, *Appl. Phys. Lett.*, **44** (1984) 611.
- [2] I. Weinberg, C.K. Swartz, and R.E. Hart *Proc. of the 18th IEEE Photovoltaic Specialist Conference* p.1722 (1985).
- [3] R.J. Walters, S.R. Messenger, G.P. Summers, E.A. Burke and C.J. Keavney, *Proc. of the 22nd IEEE Photovoltaic Specialist Conference* p.1560 (1991).
- [4] M. Faur, M. Faur, D.J. Flood, I. Weinberg, C. Goradia, M. Goradia and C. Vargas-Aburto, *Proc. of the 23rd IEEE Photovoltaic Specialist Conference* p.1437 (1993).
- [5] P.R. Sharps, M.L. Timmons, S.R. Messenger, H.L. Cotal, G.P. Summers and P.A. Illes, *Proc. of the 25th Photovoltaic Specialist Conference* p.175 (1996).
- [6] H. Cotal, S.R. Messenger, R.J. Walters and G.P. Summers, *Proc. of the 25th Photovoltaic Specialist Conference* p.219 (1996).
- [7] C.J. Keavney, V.E. Haven, and S.M. Vernon, *Proc. of the 21st IEEE Photovoltaic Specialist Conference* p. 141 (1990).
- [8] K.Y. Choi, C.C. Shen and B.I. Miller, *Proc. of the 19th IEEE Photovoltaic Specialists Conference* p. 255 (1987).
- [9] M.W. Wanlass, T.J. Coutts, J.S. Ward and K.A. Emery, *Proc. of the 22nd Photovoltaic Specialist Conference* p.159 (1991).
- [10] S.J. Wojtczuk, N.H. Karam, P. Gouker, P. Colter, S.M. Vernon, G.P. Summers, R.J. Walters and R. Statler, *1st World Conference on Photovoltaic Energy Conversion* p. 1705 (1994).
- [11] R.W. Hoffman, Jr., N.S. Fatemi, P. Jenkins, D.A. Scheiman, S.A. Ringel, W.C. Davis, V.G. Weizer, D.M. Wilt and D.J. Brinker, *Proc. of the 25th Photovoltaic Specialist Conference* p.171 (1996).
- [12] N.S. Fatemi, V.G. Weizer, D.M. Wilt and R.W. Hoffman Jr., *Proc. of the 1st World Conference on Photovoltaic Energy Conversion* p.2129 (1994).
- [13] S.J. Wojtczuk, N.H. Karam, P. Gouker, P. Colter, S.M. Vernon, G.P. Summers, R.J. Walters and R. Statler, *Proc of the 1st World Conference on Photovoltaic Energy Conversion* p.1705 (1994).
- [14] For example see S.A. Ringel and B. Chatterjee, "Hydrogenation of Compound Semiconductors," in *Topics in Applied Vacuum Science & Technology*, ed. by S.J. Pearton (Research Signpost Publications, India, 1997).
- [15] N. Buchan, C.A. Larsen and G. B. Stringfellow, *Appl. Phys. Lett.* **51** (1987) 1024.

HYDROGEN PASSIVATION OF INTERSTITIAL Zn DEFECTS IN HETEROEPITAXIAL InP CELL STRUCTURES AND INFLUENCE ON DEVICE CHARACTERISTICS¹

S.A. Ringel and B. Chatterjee
The Ohio State University
Department of Electrical Engineering
Columbus, OH 43210

ABSTRACT

Hydrogen passivation of heteroepitaxial InP solar cells is of recent interest for deactivation of dislocations and other defects caused by the cell/substrate lattice mismatch that currently limit the photovoltaic performance of these devices. In this paper we present strong evidence that, in addition to direct hydrogen-dislocation interactions, hydrogen forms complexes with the high concentration of interstitial Zn defects present within the p⁺ Zn-doped emitter of MOCVD-grown heteroepitaxial InP devices, resulting in a dramatic increase of the forward bias turn-on voltage by as much as 280 mV, from ~ 680 mV to ~ 960 mV. This shift is reproducible and thermally reversible and no such effect is observed for either n⁺p structures or homoepitaxial p⁺n structures grown under identical conditions. A combination of photoluminescence (PL), electrochemical C-V dopant profiling, SIMS and I-V measurements were performed on a set of samples having undergone a matrix of hydrogenation and post-hydrogenation annealing conditions to investigate the source of this voltage enhancement and confirm the expected role of interstitial Zn and hydrogen. A precise correlation between all measurements is demonstrated which indicates that Zn interstitials within the p⁺ emitter and their interaction with hydrogen are indeed responsible for this device behavior. Excess interstitial Zn defects are shown to introduce deep donor states detected by PL measurements that partially compensate the desired emitter acceptor doping and likely provide recombination centers that together act to reduce the device voltage. We find that hydrogenation completely deactivates these donor states and that this passivation effect is thermally stable at 400 °C, the temperature at which Zn acceptors can be fully reactivated. This results in an increase in the emitter acceptor concentration by a factor of 2-3 after hydrogenation plus acceptor reactivation annealing since the compensating donor states remain deactivated. The thermal stability of this interstitial Zn passivation was found to be intermediate between Zn acceptor passivation and deep dislocation state passivation, partially reactivating after annealing at a temperature of 500 °C and completely reactivating above 550 °C, as determined by PL measurements. We find that as the interstitial Zn donor state is reactivated by progressively higher temperature annealing, both the emitter doping and diode turn-on voltage systematically return to their original as-grown values, indicating the direct impact of interstitial Zn on device characteristics.

1. INTRODUCTION

Hydrogenation of heteroepitaxial InP solar cells grown on substrates such as Si, Ge or GaAs is of recent interest as an approach to deactivate the electrical activity of dislocations within the InP device regions that arise from the large lattice mismatch between InP and the underlying substrate. [1,2] In previous work, we have extensively characterized this process and have shown that deep levels associated with dislocations are strongly passivated by hydrogen introduced in a post-growth plasma hydrogenation treatment.[3,4] Deep level

¹ Work supported by NASA grant no. NAG3-1461 and by subcontract to Essential Research via NASA SBIR contract SBIR96-NAS327677-1

concentrations were measured to decrease from near $1 \times 10^{15} \text{ cm}^{-3}$ to the low 10^{12} cm^{-3} range after hydrogenation. This passivation was found to exhibit very strong thermal stability, with minimal deep level reactivation occurring up to anneal temperatures approaching 600 C, and was correlated with orders of magnitude suppression of reverse bias leakage currents of heteroepitaxial InP diodes. Similar deep level passivation and reverse current suppression characteristics were also observed for both n-p and p-n cell structures.[5] However, in contrast to the reverse characteristics and deep level passivation, the forward bias I-V characteristics upon hydrogenation and annealing exhibited quite different behavior, which is summarized by dark I-V data in Figure 1. Comparison of the heteroepitaxial p-n and n-p structures (Figures 1a and 1b) reveals a dramatic increase in the forward bias turn on voltage, V_{TO} , for the former with no such effect for the latter. Based on the fact that dislocations are similarly passivated for both structures as verified by Deep Level Transient Spectroscopy (DLTS) measurements, this voltage enhancement is unlikely to be directly related to dislocation passivation. Moreover, figure 1a shows that there are significant differences in the dependence of the forward and reverse bias characteristics on post-hydrogenation annealing temperature even for the same p-n diode which indicates a different mechanism is controlling the forward current and reverse leakage characteristics. Taken together, these observations suggest that a process other than dislocation passivation is present within hydrogenated, heteroepitaxial p-n InP cell structures that also has a dramatic effect on device characteristics. It also implies that an additional and significant benefit can be realized by hydrogen passivation of heteroepitaxial p-n cells which are inherently limited by the performance of the p-type emitter.

The obvious difference in these cell structures is the presence of a high Zn concentration within the MOCVD-grown p-type emitter of the p-n configuration. Zn doping is a convenient but difficult dopant to control in MOCVD growth, particularly when ultra-sharp and high concentrations are needed, such as in a typical p-emitter layer, due to the propensity for Zn to diffuse in InP. In addition, high Zn doping is known to lead to high concentrations of Zn atoms incorporated as interstitial defects (Zn_i) which contribute deep donor bandgap states, rather than as desired substitutional defects which contribute shallow acceptor levels.[6] In an earlier paper, we have shown that the presence of dislocations within heteroepitaxial Zn-doped InP substantially increases the presence of interstitial Zn (Zn_i) by a dislocation gettering mechanism.[7] Since interstitial Zn atoms introduce deep donors in the InP bandgap, we suspect that they may play a role in the observed dark I-V shift. Therefore, in this paper we explore this possibility by conducting a controlled set of experiments to elucidate the presence of interstitial Zn and its possible interaction with hydrogen, in order to explain the observed device I-V characteristics.

2. EXPERIMENTAL

InP solar cell structures having a p-n configuration were grown by MOCVD on both GaAs and InP substrates to directly compare the effects of hydrogen and interstitial Zn defects with and without the presence of dislocations. A schematic of the device structures is shown in Figure 2. The target emitter and base doping concentrations in all cases are $2 \times 10^{18} \text{ cm}^{-3}$ and $1 \times 10^{17} \text{ cm}^{-3}$, respectively, with an emitter thickness of 0.15 μm . All structures were grown by low pressure metalorganic chemical vapor deposition (MOCVD) using trimethyl In and phosphine for InP growth with silane and diethyl Zn providing n-type (Si) and p-type (Zn) doping, respectively. Complete details of the growth procedure have been reported elsewhere.[8] For the p-n structures, identical Zn and Si doping profiles were targeted for all heteroepitaxial and homoepitaxial structures so that the latter can provide a "control" sample set for comparison. Additional n-p cell structures were also investigated for additional confirmation of the results.

Post-growth hydrogenation was performed using a 13.56 MHz parallel plate plasma reactor. Immediately prior to hydrogenation, a thin, H-permeable protective SiN_x coating was deposited onto the InP surface to avoid preferential loss of phosphorous and surface degradation due to sustained exposure to the H-plasma. Hydrogenation was performed using a substrate temperature of 250 °C at a plasma power density of 0.08 W/cm^2 for 2 hours at a total pressure of 750 mTorr. After plasma hydrogenation, acceptor and donor dopant atoms were reactivated by a 5 minute 400 °C anneal in flowing nitrogen followed by chemical removal of the protective silicon nitride cap. We have previously shown this to result in extensive passivation of deep levels associated with dislocations and other extended defects throughout the entire depth of the InP devices coupled with complete reactivation of the desired dopants. Details of the process have been described in earlier publications.[2-4] For samples selected for thermal stability studies after the dopant reactivation step, additional heat treatments for 5

minutes in flowing nitrogen at either 500 °C or 600 °C, depending on the particular experiment, were performed prior to nitride cap removal. For device testing, mesas were etched to define device areas and ohmic contacts were formed to the p-n junctions by electron beam evaporation using Ag-Zn and AuGeNi for p-type and n-type InP surfaces, respectively. Samples were characterized using a combination of electrochemical C-V dopant profiling, photoluminescence (PL), dark I-V and SIMS measurements at all stages of the hydrogenation and annealing process to monitor changes within the material.

3. RESULTS AND DISCUSSION

3.1. Comparison of Dark I-V Characteristics

As mentioned above, Figure 1 depicts a representative set of the I-V characteristics observed for heteroepitaxial p-n and n-p InP cell structures, along with homoepitaxial InP/InP p+n device to provide a comparison for the p-n structure without the presence of dislocations. After receiving the hydrogenation plus 400 °C dopant reactivation anneal, the reverse characteristics of both heteroepitaxial configurations displayed similar improvement in the reverse leakage current, and subsequent higher temperature annealing demonstrated a similar reactivation behavior. The temperatures at which the reverse leakage current reactivation are observed track the deep level reactivation associated with the dissociation of hydrogen-dislocation deep state complexes previously measured by DLTS.[4] In fact, results of Arrhenius analysis of the reverse current activation as a function of temperature were also previously found to match the dominant deep state in each case, indicating the correlation between dislocation-related deep states and reverse leakage current.

However, the forward I-V behavior between the two configurations deviate considerably. The optimum 2 hour hydrogen exposure plus 400 °C dopant reactivation anneal increases the forward bias turn on voltage (V_{TO}) by ~ 280 mV for the p-n structure, from 680 mV to 960 mV. We have also found that the magnitude of this shift is proportional to the duration of the hydrogen exposure, with saturation occurring beyond 2 hours. No such effect is observed for the n-p heteroepitaxial case and a negligibly small increase is observed for the homoepitaxial p-n structure. It is useful to note that the forward I-V characteristics for the homoepitaxial and heteroepitaxial p-n structures after hydrogenation are now very similar in terms of V_{TO} . This important similarity will be discussed later. Additional inspection of figure 1a reveals that, even for the same p-n diode, there are clear differences in the reactivation of the reverse and forward bias characteristics. Both the reverse leakage current and forward injection/diffusion current characteristics are markedly improved by the hydrogenation plus 400 °C dopant reactivation process, with current reduction in the former and a positive voltage shift in the latter. After a 500 °C anneal, the reverse current magnitude is retained at the passivated value, while the forward I-V has begun to shift back toward its original characteristic prior to passivation. Incremental annealing at higher temperatures results in a progressive recovery to the original forward I-V behavior. No such annealing dependence is observed for the reverse bias characteristics, which instead are quite stable up to temperatures in excess of 550 °C. This observation, coupled with our earlier results which correlated the reverse leakage current directly to dislocation-related current generation, suggests a different process is likely to be responsible for the observed dependence of the forward bias characteristics on post hydrogenation annealing.

3.2. Effects of Hydrogenation and Annealing on Emitter Doping and Zn Distribution

A series of experiments were performed to investigate whether Zn was involved in the observed I-V behavior. Zn is a likely suspect for device instabilities due to its high diffusion coefficient and its propensity to occupy interstitial sites within InP. Figure 3 shows the results of electrochemical C-V dopant profiling of p-n heteroepitaxial and homoepitaxial structures that have undergone the hydrogen processes described in the caption. The as-grown emitter doping concentration for the heteroepitaxial sample is slightly lower than its homoepitaxial counterpart for identical DEZn flow conditions, which we have consistently observed when comparing identically grown homoepitaxial and heteroepitaxial Zn doped InP layers. In an earlier paper we showed this to result from a higher concentration of Zn_i defects in the heteroepitaxial layer which will lower the hole concentration by competing with the desired incorporation of Zn as substitutional acceptors and by compensating the p-type material through the introduction of deep donor bandgap states.[7] Immediately after hydrogenation and prior to any reactivation anneal, the emitter acceptor concentration reduces by more than two orders of magnitude for both cases, as expected. The donors within the base are not passivated by hydrogen as seen by the unchanged dopant concentration in the base of both structures. A subsequent 400 °C anneal is

expected to reactivate the shallow acceptors to recover their as-grown concentration, and this does occur for the homoepitaxial sample. However, we consistently find that the net acceptor concentration within the heteroepitaxial devices are actually reactivated to values that are a factor of 2-3 larger than their as-grown concentration. This is clearly observed in figure 3. In fact, this concentration now closely matches that of the homoepitaxial sample. Further annealing at progressively higher temperatures results in a systematic decrease in the emitter doping concentration, eventually reaching the as-grown value after a 5 minute anneal at temperatures in excess of 550 °C.

These observations closely track the evolution of the dark I-V characteristics as a function of hydrogenation and annealing. To investigate whether a redistribution of the Zn profile can explain these observations, SIMS measurements were performed on the same sample matrix. The results are summarized by the series of SIMS profiles in figure 4. Only the Zn and H profiles were plotted here, although In, P, Si, C and O were also profiled. From this figure, it is clear that the Zn dopant profile is not significantly affected by either the hydrogenation process or the subsequent annealing at the temperatures used here. Quantitative variations in the average Zn concentration within the emitter are within a few percent over this sample matrix, whereas the acceptor concentration as measured by CV varied by a factor of ~ 2. A similar disparity is also evident by comparing the as-grown heteroepitaxial and homoepitaxial samples where a factor of ~ 2 change is observed for CV acceptor concentration but SIMS indicates a comparable total Zn dopant concentration. At this time, it is instructive to note that the hydrogen profile closely tracks the Zn profile, implying a possible connection between the two that will become evident later. In the next section, we provide evidence that the source of this discrepancy between acceptor concentration and total Zn doping is the presence of a high concentration of interstitial Zn (Zn_i) defects.

3.3. Effect of Passivation on Photoluminescence Spectra and Evidence for Passivation of Interstitial Zn

Figures 5 and 6 show low temperature PL spectra measured on homoepitaxial and heteroepitaxial samples processed as described above. All PL measurements were performed under the same conditions (temperature, incident laser intensity, etc.) so that meaningful comparisons can be made. A brief description of the features within the PL spectra is necessary prior to discussing connections to the earlier observations. The conduction band to acceptor (C-A) peak (and its phonon replica) is a signature of n -type InP and typically dominates p -InP PL spectra.[6,7] For n -InP however, the dominant feature is a band to band (B-B) peak with no C-A peak expected. This has been confirmed by performing PL measurements on individual epilayers. Since here PL is performed directly on the device structures, the PL linescans shown in figures 5 and 6 are actually composites of the PL emission from the 0.15 μ m thick p^+ emitter and the underlying n -type base region, although the emitter is expected to be the dominant contributor due to the strong absorption of the 488 nm PL excitation source within the surface region of the InP samples.

We first discuss differences in the *as-grown* PL spectrum of each figure, which leads to two important, initial observations. First, the overall magnitude of the PL spectra for the homoepitaxial *as-grown* sample in figure 5 is about a factor of 40 larger in magnitude than the PL spectra for the heteroepitaxial *as-grown* sample in figure 6. This is expected as the overall material quality of the homoepitaxial samples are superior to that of the heteroepitaxial samples. Second, while the overall PL spectrum is reduced for the heteroepitaxial sample, the quality of the emitter and base layers, as characterized by the B-B and C-A peak intensities respectively, appear to have degraded differently upon direct comparison between the *as-grown* spectra. The C-A peak, which is a signature of the PL emission from the Zn-doped emitter, is much larger than the B-B peak due to PL emission from the n -type base for the homoepitaxial sample, indicating that the majority of the PL response is from the emitter layer, as expected based on absorption of the excitation laser light. In contrast, for the *as-grown* heteroepitaxial PL spectrum in figure 6, the C-A peak is actually suppressed relative to the B-B peak, suggesting that a larger fraction of the overall PL emission is emanating from the n -type base. The reason for this is clear upon further inspection of figures 5 and 6 where a broad PL emission centered near 1.25 eV is also evident. This feature is easily detected in the heteroepitaxial *as-grown* sample and results from a donor-acceptor (D-A) transition between Zn_i donor-like levels and Zn substitutional acceptor levels. This D-A peak is generally observed for Zn doping concentrations in excess of mid 10^{17} cm^{-3} range for InP. In some earlier work, we have shown that the D-A intensity is greatly enhanced for heteroepitaxial samples as compared to identically doped homoepitaxial samples that was explained as a Zn_i gettering phenomena due to dislocation strain fields, which ultimately increases the Zn_i concentration at the expense of substitutional Zn.[7] This difference is clear from figures 5 and 6 where the D-A peak for the homoepitaxial sample is evident only in the magnified inset in figure 5.

From these PL studies, the Zn_i concentration as indicated by D-A peak intensities was estimated to be as much as 50% of the total Zn concentration for Zn doping in the 10^{18} cm^{-3} concentration range. Therefore, a large concentration of Zn_i defects within the heteroepitaxial p⁺ emitter here is certainly expected. Therefore, due to the presence of both dislocations and Zn dopants, the heteroepitaxial p⁺ emitter undergoes a severe degradation that is not shared by the n-type base, hence the observed suppression of the C-A peak in the as-grown heteroepitaxial PL spectrum.

Now that the Zn_i defect has been discussed via the observation of the D-A PL peak, and the general features of the PL spectra have been described, the effects of hydrogenation and post-hydrogenation annealing on the PL characteristics can be considered. After the 2 hour hydrogen exposure and the 400 °C dopant reactivation anneal, the C-A and B-B peaks increase in intensity as seen in figures 5 and 6, whereas the D-A peak is completely suppressed by hydrogen incorporation. Since the concentration of shallow Zn acceptors have been fully reactivated according the CV data shown earlier, the D-A peak suppression can only be due to the deactivation (effective elimination) of the Zn_i donor states. To our knowledge, this is the first direct evidence of Zn_i passivation in any III-V semiconductor, and indicates a different passivation mechanism for Zn in its interstitial form versus Zn in its substitutional acceptor form since the latter is fully reactivated by the same 400 °C anneal. A detailed and quantitative study of the Zn_i passivation process and properties in both heteroepitaxial and homoepitaxial InP is the subject of a publication in progress.

PL measurements were performed after subsequent higher temperature anneals in order to compare with the doping and I-V behavior already discussed. Both figures 5 and 6 show that the D-A peak is partially reactivated by a 500 °C anneal, and is fully reactivated after a 600 °C anneal for both heteroepitaxial and homoepitaxial device structures. This evolution of the PL spectra precisely tracks both the evolution in the Zn acceptor concentration shown in figure 3 and the forward bias I-V characteristics shown in figure 1, providing a remarkable correlation between the D-A PL peak behavior, the emitter doping behavior and the device forward I-V characteristics. This is strong evidence for the direct involvement of interstitial Zn in the heteroepitaxial p⁺n device behavior.

3.4 Comparison of I-V, Dopant Profiling and Photoluminescence results: Impact of H-Zn Interactions

Taken together, the data described above leads to the following model. The high concentration of Zn_i defects within the heteroepitaxial Zn-doped emitter is passivated by hydrogen, along with Zn acceptors as well as deep dislocation states. A 400 °C reactivates only the Zn acceptors, leaving dislocation states and the deep donor states associated with interstitial Zn passivated. The deactivation of the deep donors eliminates their ability to compensate the shallow Zn acceptor levels, effectively increasing the electrically active Zn acceptor concentration. This is confirmed by the SIMS data which showed no change in the total Zn concentration, which is the sum of the substitutional acceptor and interstitial donor concentrations. At higher annealing temperatures, the Zn_i donors become reactivated as the H- Zn_i complex (the exact form of which is currently under investigation) dissociates. This then begins to re-compensate the Zn acceptors, ultimately reducing the emitter doping concentration back to the original as-grown value. Hence, the PL, SIMS and CV data are consistent with each other and the variation of acceptor doping is completely explained by the passivation and reactivation of Zn_i donor-like defect states.

The trend in passivation and thermal reactivation of Zn_i defects is also consistent with the forward I-V data of figure 1. An increase in the emitter doping after hydrogenation plus the 400 °C dopant reactivation anneal due to reduced compensation will translate into an increase in the fundamental built in voltage of the pn junction, consistent with the increase in the turn on voltage, V_{TO} , shown by the I-V data of the heteroepitaxial p⁺n device in figure 1a. However, some simple calculations show the increase in the ideal built in voltage expected for this factor of 2-3 increase in emitter doping is only ~ 30 mV, not nearly enough to explain the observed 280 mV increase. Another possibility is a reduction in recombination current and/or increase in shunt resistance. This is highly plausible since the measured value of V_{TO} is far less than the theoretical built in voltage for InP and voltage loss through a parallel path can be expected, especially for highly defective material having low carrier lifetimes and since the likelihood of excess interstitial Zn incorporated within the depletion region is high. Whether the source of the recombination is related to interstitial Zn defects, and if hydrogen effectively suppresses this recombination current is currently under investigation. Nevertheless, it is clear from these results that Zn_i and H- Zn_i interactions have a direct impact on heteroepitaxial p⁺n InP device characteristics, and given the temperature range at which these complexes dissociate, such interactions may also be an issue for typical MOCVD growth of InP where Zn is used as a dopant.

4. Conclusions

In this paper we have shown that a high concentration of interstitial Zn defects are present within the emitter of p'n heteroepitaxial InP solar cell structures, and have demonstrated that they are efficiently passivated by post-growth hydrogenation. Interstitial Zn defects were shown to be responsible for the low turn-on voltages characteristic of heteroepitaxial p'n InP diodes, and were also shown to compensate the desired maximum emitter doping concentration. Post-growth hydrogenation was found to efficiently deactivate the deep donors associated with the interstitial Zn defects, displaying a thermal stability in excess of the common Zn acceptor passivation. Thus, the beneficial effects of the Zn_i passivation can be realized. We find this to be directly responsible for a factor of 2-3 increase in the maximum acceptor doping achievable in the heteroepitaxial p' emitter, as well as a remarkable increase in the device voltage output, with an increase from 680 mV to 960 mV being observed for the forward bias turn-on dark voltage. This is an important technological result if it can be sustained in an actual operating solar cell (currently under investigation) since the emitter and V_{oc} in general limit the performance of heteroepitaxial p'n InP cells.

5. References

1. R. K. Jain and D. J. Flood, "Influence of the Dislocation Density on the Performance of Heteroepitaxial InP Solar Cells", IEEE Trans Elec. Devices, vol. 40, pp. 128-134, 1993.
2. S.A. Ringel, "Hydrogen-Extended Defect Interactions in Heteroepitaxial InP Materials and Devices," Sol. State Electron. 41, pp. 359-380, 1997.
3. B. Chatterjee and S. A. Ringel, "Hydrogen Passivation and its Effects on Carrier Trapping by Dislocation in InP/GaAs Heterostructures", J. Appl. Phys. vol. 77, pp. 3885-3898, 1995.
4. B. Chatterjee, S. A. Ringel, R. Sieg, R. Hoffman, and I. Weinberg, "Hydrogen Passivation of Dislocation in InP on GaAs Heterostructures", Appl. Phys. Lett. vol. 65, pp. 58-61, 1994.
5. B. Chatterjee, S. A. Ringel, and R. Hoffman, "Hydrogen Passivation of n'p and p'n Heteroepitaxial InP Solar Cell Structures", Progress in Photovoltaics, vol. 4, pp. 91-100, 1996.
6. G. J. Van Gurp, T. Van Dongen, G. M. Fontijn, J. M. Jacobs, and D. L. A. Tjaden, "Interstitial and Substitutional Zn in InP and InGaAsP", J. Appl. Phys. vol. 65, pp. 553-560, 1988
7. R. M. Sieg, B. Chatterjee, and S. A. Ringel, "Evidence for Enhanced Zn Interstitial Concentration in Strain-Relaxed Heteroepitaxial InP", Appl. Phys. Lett. vol. 66, pp. 3108-3110, 1995.
8. R. W. Hoffman, N. S. Fatemi, D. M. Wilt, P. Jenkins, D. J. Brinker, and D. A. Scheiman, "High Efficiency InP Solar Cells from Low Toxicity TBP and TMIn by OMVPE", Proc. 1st IEEE World Conf. Photovoltaic Energy Conv. Pp. 1882-1885, 1994.

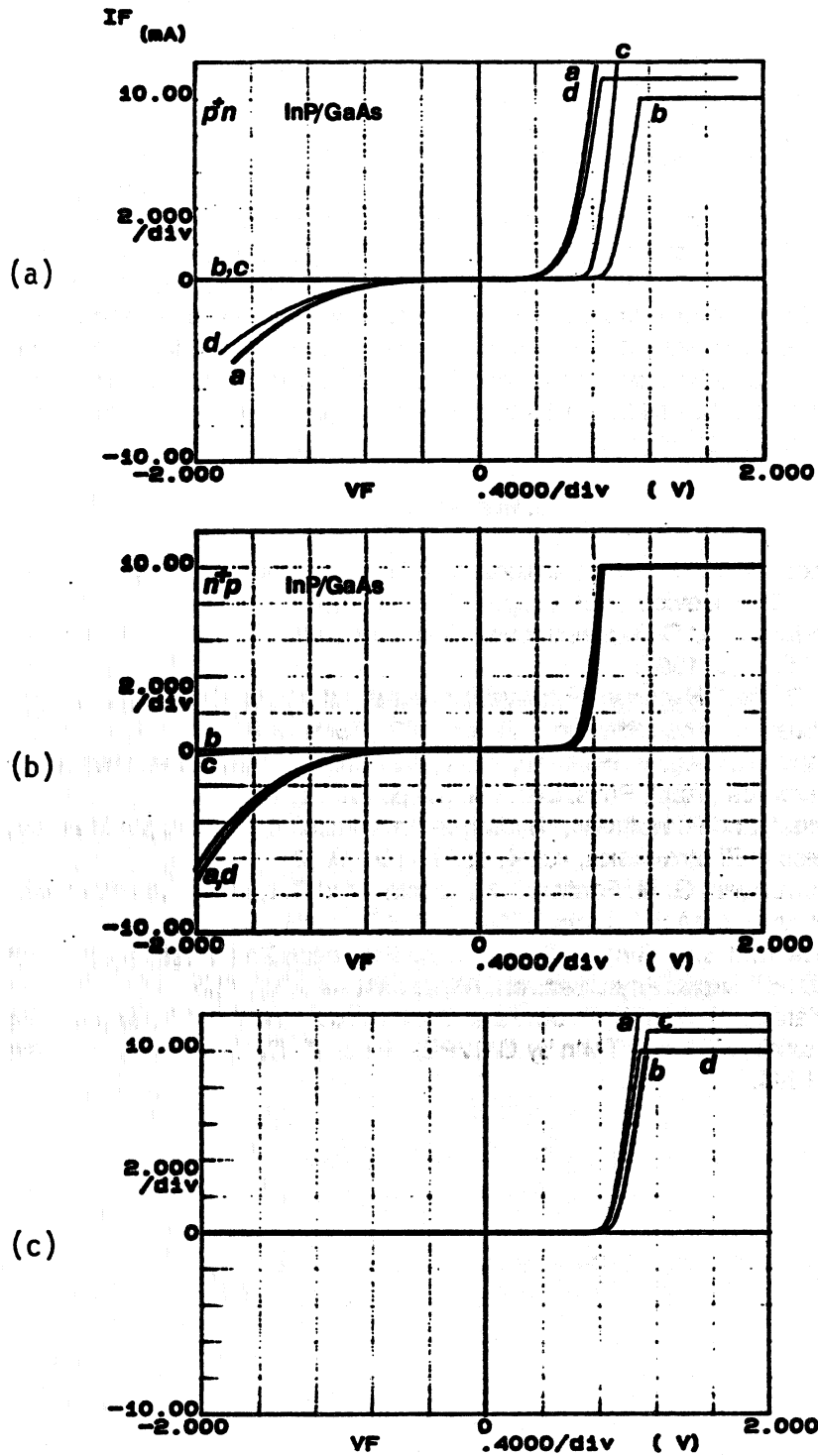


Figure 1. Dark I-V characteristics of (a) heteroepitaxial p^+n , (b) heteroepitaxial n^+p and (c) homoepitaxial p^+n InP cell structures. In each case, the labels a-d correspond to the following conditions; as-grown, hydrogenation + 400 °C dopant reactivation anneal, hydrogenation + 500 °C anneal and hydrogenation + 600 °C anneal, respectively. The magnitude of the forward bias shift in figure 1(a) is 280 mV.

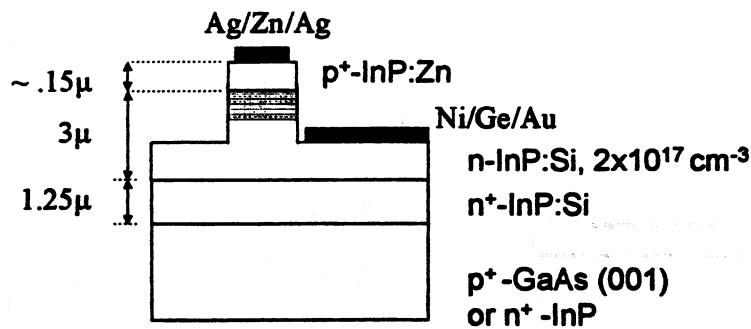


Figure 2. Schematic of the p+n device structures used in this study.

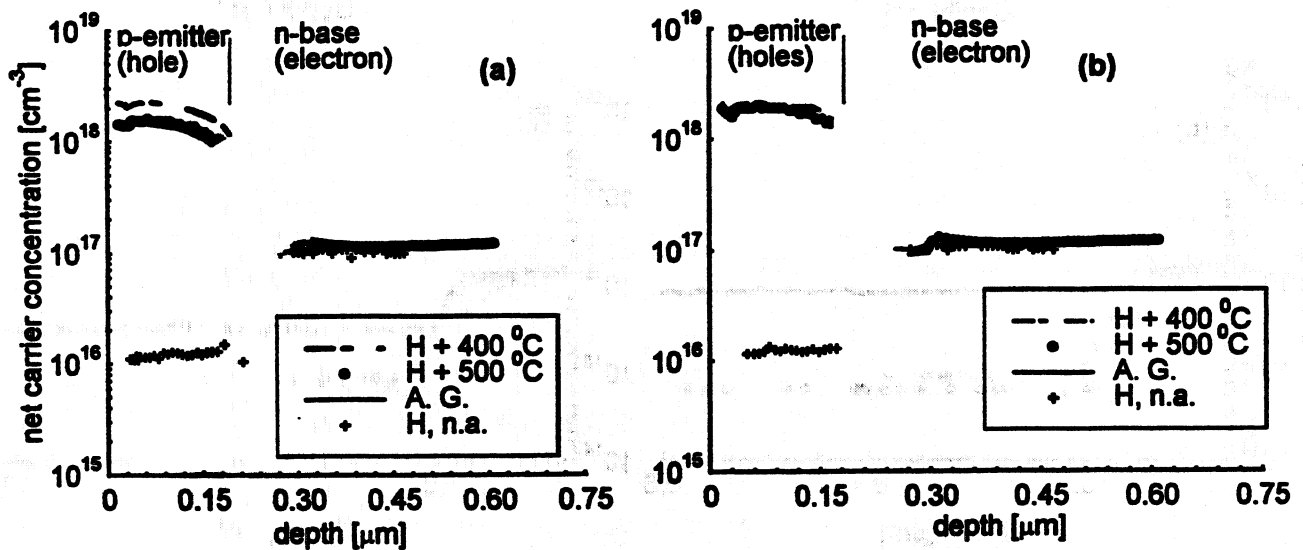


Figure 3. Electrochemical C-V dopant profiles measured for (a) heteroepitaxial and (b) homoepitaxial p+n InP structures for as-grown, after hydrogenation with no anneal, after hydrogenation + 400 °C dopant reactivation anneal and after hydrogenation + 500 °C anneal, as indicated. The increase in emitter doping concentration is clearly observed for figure 3a after the optimum passivation process. Note that the donors in the n-type base are not passivated by hydrogen, as expected.

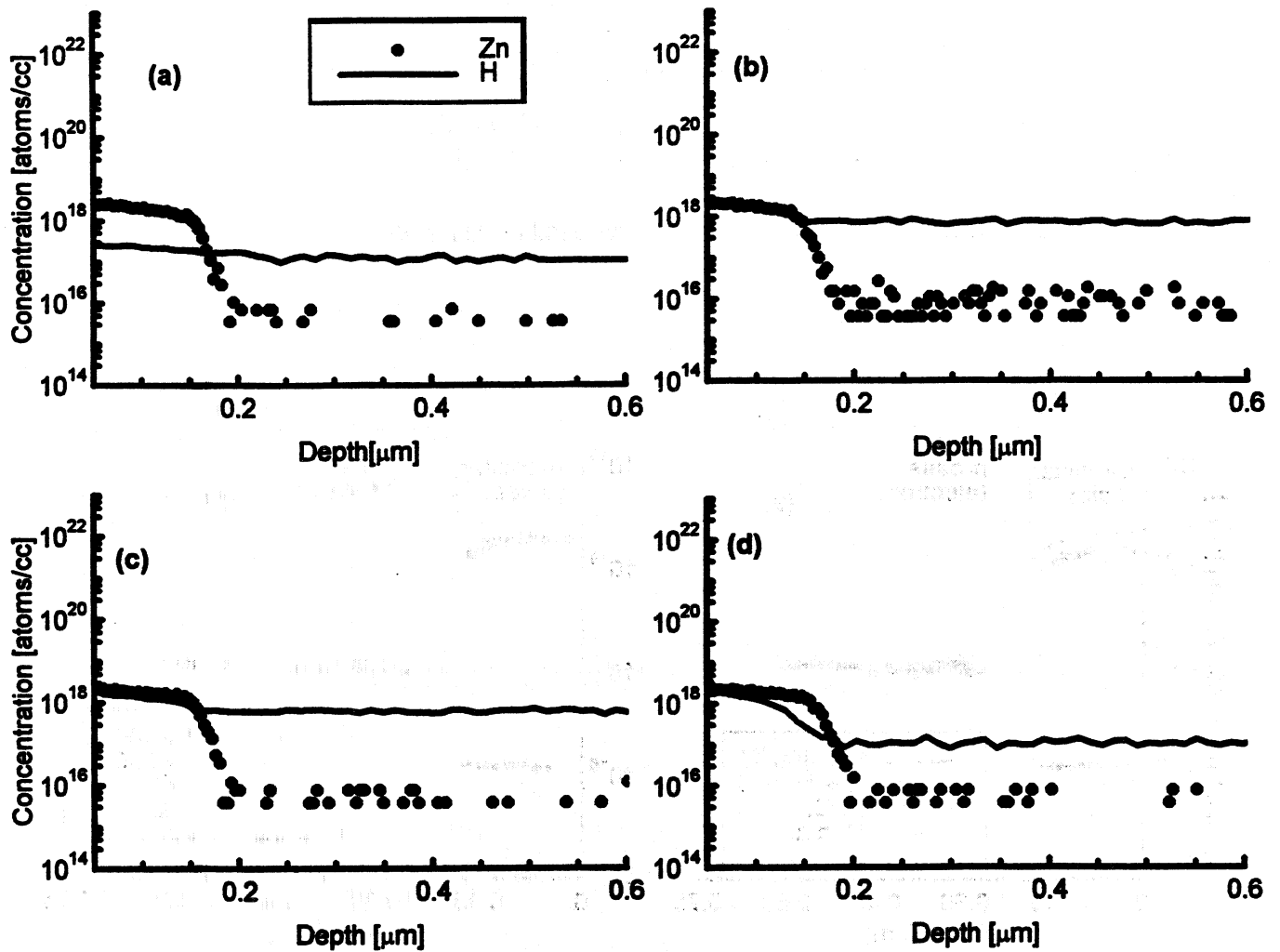


Figure 4. SIMS profiles for the heteroepitaxial p^+n structures indicating the distribution of Zn and H for (a) as-grown samples, (b) after hydrogenation + 400 °C annealing, (c) after hydrogenation + 500 °C annealing, and (d) after hydrogenation + 600 °C annealing. The evolution of hydrogen is evident for case (d).

PASSIVATING WINDOW/FIRST LAYER AR COATING FOR SPACE SOLAR CELLS

Mircea Faur and Maria Faur
SPECMAT, Inc., North Olmsted OH 44070, c/o NASA LeRC and CSU

S.G. Bailey, D.J. Flood, D.J. Brinker, S.A. Alterovitz and D.R. Wheeler
NASA LeRC, Cleveland OH 44135

G. Mateescu
Case Western Reserve University, Cleveland OH 44106

C. Goradia and M. Goradia
Cleveland State University, Cleveland OH 44115

ABSTRACT

Chemically grown oxides, if well designed, offer excellent surface passivation of the emitter surface of space solar cells and can be used as effective passivating window/first layer AR coating.

In this paper, we demonstrate the effectiveness of using a simple room temperature wet chemical technique to grow cost effective passivating layers on solar cell front surfaces after the front grid metallization step. These passivating layers can be grown both on planar and porous surfaces. Our results show that these oxide layers: (i) can effectively passivate the front surface, (ii) can serve as an effective optical window/first layer AR coating, (iii) are chemically, thermally and UV stable, and (iv) have the potential of improving the BOL and especially the EOL efficiency of space solar cells. The potential of using this concept to simplify the III-V based space cell heterostructures while increasing their BOL and EOL efficiency is also discussed.

INTRODUCTION

For space solar cells light- and radiation-induced effects are known to adversely affect the solar cell performance. An important degradation mechanism is known to be the generation of fast surface states at the emitter/first layer antireflective (AR) coating interface. It is a common practice to use physical vapor deposition to deposit the AR coating. For simple solar cell structures (e.g. Si and InP-based homojunction cell structures), the layers of the AR coating are deposited directly onto the emitter surface. This approach is known to destroy the stoichiometry of the emitter layer. It introduces additional defects at the emitter/AR coating interface. Physical vapor deposition of the AR coating is also known to adversely affect the performance of TPV cells.

The application of theoretical and experimental advances in the physics of semiconductor heterostructures to space solar cells has resulted in the fabrication of the large variety of high efficiency heterostructure space solar cells known today. However, increasing the number of layers of the heterojunction cells may have a negative impact not only on cost but on the functionality of these cells under the space radiation environment. This is especially true for cells designed for high radiation orbits. Simply put, the more

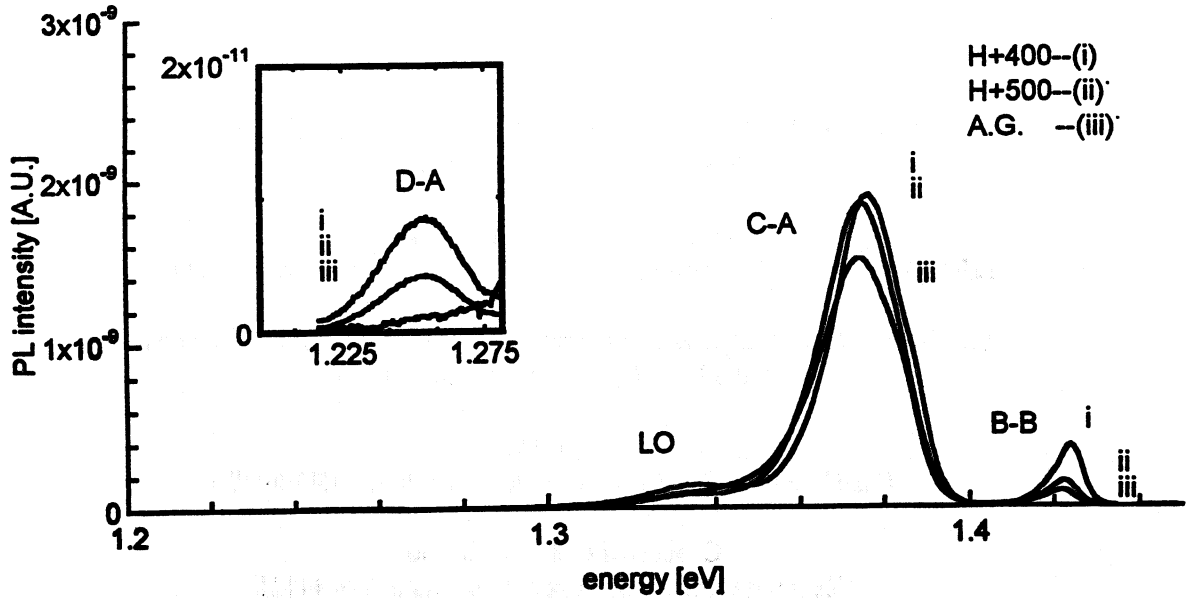


Figure 5. Photoluminescence spectra of homoepitaxial p⁺n InP solar cells structures that were hydrogenated for 2 hours and then annealed at the indicated temperatures. An as-grown PL spectrum is shown for comparison and the inset indicates the presence of a very small D-A peak.

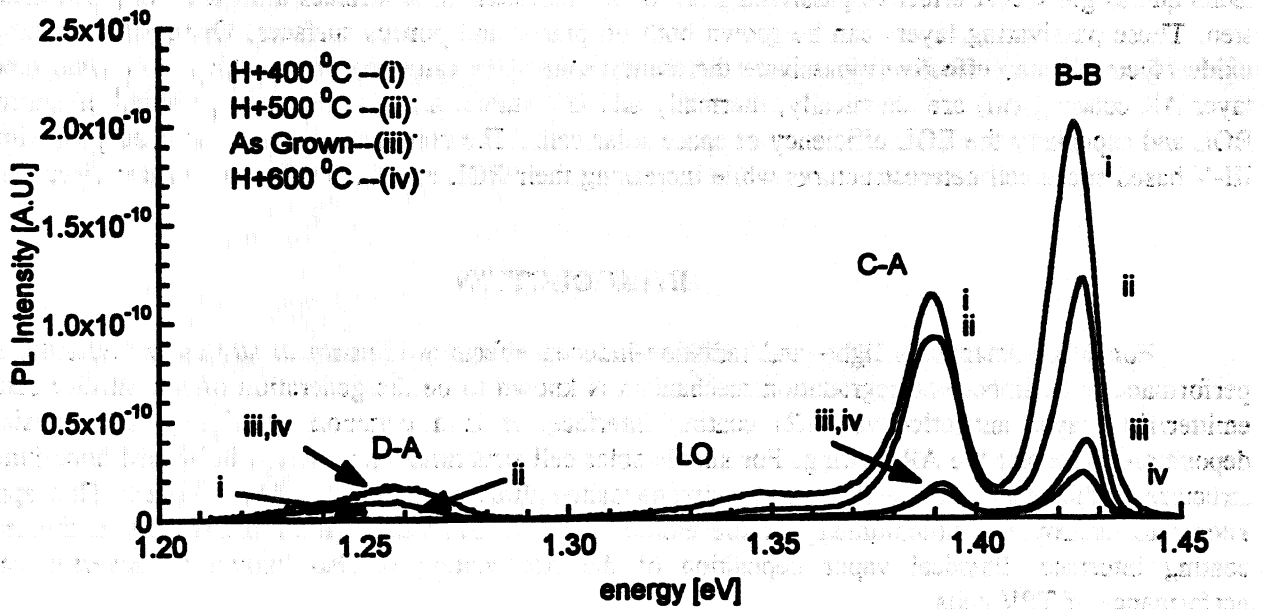


Figure 6. Photoluminescence spectra of heteroepitaxial p⁺n InP solar cells structures that were hydrogenated for 2 hours and then annealed at the indicated temperatures. An as-grown PL spectrum is shown for comparison. Note that the D-A peak is clearly pronounced in this case.

layers these heterostructure cells have, the larger the chance of degradation under the space environment. Therefore, it is highly desirable to reduce the number of layers of heterostructure space solar cells, as for example, by eliminating the passive window layer.

High efficiency III-V based space solar cells often use a window layer grown on the surface of the emitter prior to depositing the layers of the AR coating. This window layer partially passivates the emitter front surface and reduces the surface recombination velocity at the surface, thereby improving the cell performance. Although current epitaxial growth techniques (e.g. MOCVD, MBE) are capable of producing abrupt, atomically sharp heterojunction interfaces, lattice matched window layers (e.g. AlGaAs, InAlP, GaInP₂ and AlInP₂) grown by epitaxy, increase the cost and reduce the yield of finished cells. Based on the results presented in this paper, we suggest that replacing the presently used window layers with stable, ultrawide bandgap, chemically grown oxide layers can decrease the fabrication cost and increase the yield of space solar cells, while increasing both the BOL and EOL efficiencies.

Chemical oxides grown by a simple, yet reproducible wet chemical growth technique, which are of interest for replacing the above window layers, have ultrawide bandgap, e.g. 6.8 eV for In(PO₃)₃ grown on InP [1]. These oxides are transparent in the useful region of the spectra, and bandgap values larger than 5 eV should help to minimize the Fermi-level pinning effect and the oxide/semiconductor interface electrical instability.

One of the early criticisms about chemically grown oxides, still very much widespread within the semiconductor device community, is that they are thermally and electrically unstable [2]. Based on our published data on oxides grown on InP [e.g. 3-11] and preliminary unpublished data (oxides grown on Si, Ge, and GaAs), part of which are summarized in this paper, we are confident that through a relatively short R&D effort these oxides can be stabilized for any space solar cell. Using this approach, record high V_{OC} and J_{sc} values have been measured under AM0, 25°C conditions at NASA LeRC at 890 mV for a diffused junction p⁺n InP cell and at 55.5 mA/cm² for a diffused junction n⁺pp⁺ Ge cell, respectively.

RESULTS AND DISCUSSION

InP Solar Cells

While developing the technology of the low cost fabrication of high efficiency, radiation resistant thermally diffused p⁺n InP solar cells at NASA-LeRC/CSU, using chemically grown In(PO₃)₃-rich oxide for surface passivation and as a first layer AR coating, we have been able to consistently and reproducibly obtain world record high open circuit voltage (V_{OC}) values of 885 to 890 mV (AM0, 25 °C measured at NASA LeRC). We showed that the origin of the instability of chemically grown oxides on InP surfaces was the presence of In-rich oxide layer on the top of the P-rich In(PO₃)₃ interfacial oxide layer.

The fact that these thermally diffused cells had larger V_{OC} values than those of any other InP solar cells, including cells made by epitaxial techniques, proves that if the chemical growth process is well designed, the simple to apply and reproducible chemical oxidation technique offers a good surface passivation of InP surfaces. In fact, presently, we are not aware of any other window layer material for the InP based cell which offers a better surface passivation and, therefore, a better blue collection efficiency than that obtained using the simple P-rich chemical oxide on a diffused junction homostructure.

In Figure 1 is shown a typical external quantum efficiency plot of a diffused junction p⁺n(Cd,S)InP cell. The AM0, 25°C V_{OC} of this cell was 887.6 mV, using only a chemically grown P-rich In(PO₃)₃ oxide

layer as an AR coating. From low frequency EG-V measurements, we recorded a surface state density minimum (N_{SS}) at the Cd-diffused p+-InP/passivating layer interface as low as $2 \times 10^{10} \text{ cm}^{-2}\text{eV}^{-1}$, which is lower than other previously published values. Such a low N_{SS} value is in excellent qualitative agreement with the high measured V_{OC} and blue response values of these cells. Even after irradiating the cells with 10^{13} cm^{-2} , 3 MeV protons and with energetic α particles with $1.06 \times 10^{17} \text{ cm}^{-2}$ equivalent 1 MeV electrons, by using these $\text{In}(\text{PO}_3)_3$ -rich chemical oxides as passivating layer, the drop in the blue response was significantly lower compared to cells without this oxide layer. This means that the chemically grown P-rich oxide/InP interface is stable even after exposing the cell to such extreme radiation environments. The cells had also a very good UV stability and a higher radiation tolerance and better annealing properties under working conditions compared to any other InP cell structures.

The main optoelectronic characteristics of this chemically grown P-rich $\text{In}(\text{PO}_3)_3$ oxide include: (i) high transparency, with an estimated bandgap of 6.8 eV over the visible range of the solar spectrum, (ii) lower than 27% blue reflectivity and average surface reflection of 25% (for an oxide thickness of about 40 nm), and (iii) an average refractive index over 300 to 1000 nm wavelength range of 1.496 with a very small extinction coefficient. These properties, combined with its excellent passivating properties mentioned above, make this chemical oxide very attractive, indeed, for use as the first layer AR coating. Based on experimental ellipsometry and reflectivity data, we demonstrated that the reflectance of the InP cells can be reduced to less than 4% (not including the reflection from the grid metallization) by designing a three-layer AR coating using the P-rich $\text{In}(\text{PO}_3)_3$ oxide as the first layer, Al_2O_3 , ZnS or Si_3N_4 as the second layer and MgF_2 as the third layer. The proposed three-layer AR coatings designs shown in Figure 2 are optimized for minimum current loss of the p+n InP solar cell under AM0 light spectrum.

GaAs Solar Cells

Our very preliminary data show that using a simple room temperature wet chemical technique, under development at SPECMAT, good quality passivating layers can be grown on GaAs-based surfaces. Although not yet known conclusively, apparently these oxide layers are made up of a top layer which is a mixture of Ga_2O_3 and GaAsO_4 and an interfacial layer, which should be rich in a stable $\text{Ga}(\text{AsO}_3)_3$ oxide, probably mixed with some As_2O_5 component. We have not yet tested these oxides on any GaAs-based solar cells.

Compared to the InP cells, the GaAs-based space solar cells are at a much more advanced stage of development. GaAs based heterostructures also have good lattice matched window layers. Hence, it will be particularly interesting to test the effect of replacing the window layer with chemically grown As-rich layer on BOL and EOL efficiencies of these high efficiency GaAs-based solar cells.

Germanium Cells

Wet chemical oxides grown on Ge surfaces are known to be the worst in terms of their passivating properties and stability. Here, we demonstrate that it is possible to stabilize the chemically grown passivating oxides even in the worst case scenario, namely, Ge cells with front surfaces covered with a chemically formed porous Ge.

Under a 6 month Phase I Clean Car Initiative, awarded to CSU, we fabricated planar n^+pp^+ Ge cells. Due to their very good performance parameters (e.g. a record high short circuit current density of 55.5 mA/cm^2 , measured at NASA LeRC under AM0, 25°C conditions on a 1 cm^2 n^+pp^+ Ge cell with no AR coating except for a thin chemically grown passivating layer), these cells appear to have good potential for high efficiency, low cost TPV applications.

In Fig. 3 is shown the EC-V net majority carrier concentration depth profiling of the front n^+p junction of an optimized $n^+pp^+Ge(As,In)$ diffused structure. We used electrochemical characterization techniques for the step-by-step diffusion process optimization. The AM0, 25°C short circuit current density of a planar Ge cell using the above structure and a 750 Å thick SiO single layer AR coating was only 28.7 mA/cm². From the external quantum efficiency of this cell, shown in Fig. 4, it is evident that this device has a poor current collection at the surface, indicating a need for surface passivation.

We first tried growing a very thin (less than 100 Å) chemical oxide on a Ge cell with a thin porous layer on the emitter surface. This resulted in severe UV instability. We have been able to essentially eliminate this instability as well as remarkably improve the cell performance by adding a wet chemical step of stabilizing this oxide layer.

After stabilizing the thin chemical oxide using a wet chemical treatment, for a cell made from a Ge structure identical to the one in Figs. 3 and 4, a record high short circuit current density of 55.5 mA/cm² was measured at NASA LeRC under AM0, 25°C conditions. The external quantum efficiency of this cell is shown in Figure 5 and its spectral response in Figure 6. Note the significantly improved short-wavelength response, indicating excellent collection at the surface. The n^+pp^+ Ge cells had a total area (defined by deep etching - about 5 μm into the base, using a mesa etching mask) of 1 cm². After the chemical treatment the chemical oxide layer became stable and the UV instability was significantly reduced. The chemical reactions of all three wet chemical processes, namely porous Ge growth, oxide growth, and stabilizing of the oxide are compatible with the Au-based front and back cell contacts.

From our preliminary results, it is obvious that treated chemical oxides grown on Ge front cell surface after the front grid metallization can be used not only for surface passivation, but as an effective first layer AR coating as well.

Concentrator Silicon Solar Cells

The only high efficiency concentrator solar cells available to us for this preliminary experiment were some Vertical MultiJunction (VMJ) Si solar cells, provided by PhotoVolt, Inc. The biggest contributor to efficiency loss in the Si VMJ cell structure is the fact that its illuminated and back surfaces are high recombination surfaces with exposed junctions which are difficult to passivate by means of thermal oxidation. This is because thermal oxidation needs a temperature that is higher than the temperature at which the stack is alloyed together. Additionally, as known for these cells, degradation by nonionizing (subbandgap) radiation (as far as the insulators tantalum pentoxide and silicon nitride are concerned) makes the cell performance parameters decrease significantly with time, especially if UV or near UV radiation are not completely absorbed by the cover glass and/or encapsulant.

On some Si VMJ cells with Ta₂O₅ as an AR coating, after 1 hour exposure to high intensity (about 50 mW/cm²) near UV light, the drop in the performance parameters was as high as 20%. After the exposure, the cell performance parameters completely recovered after only about 30 minutes, which suggests that fast surface states at the Ta₂O₅/Si interface were responsible for the performance parameters drop. After removing the Ta₂O₅ layer, passivating the surfaces using a chemically grown thin film SiO-based layer, the cell performance parameters increased by as much as 50%. Additionally, no UV degradation was observed even after exposure to the aforementioned halogen light for as long as 5 hours. In fact, for some cells, with similar surface treatments, measurements performed in the PV branch at NASA LeRC under AM0, 25°C conditions, showed even a small increase in performance parameters after prolonged light exposure.

CONCLUSIONS

In summary, we show in this paper that using simple, cost-effective room temperature wet chemical techniques to grow passivating layers on the front surface of Ge, Si and InP and GaAs based solar and TPV cells, it is possible to reduce reflection and very significantly improve current collection near the illuminated surface. Based on our results we suggest that replacing the presently used passivating/window layers of high efficiency homo- and heterojunction III-V based space solar cells with stable ultrawide bandgap chemically grown oxide layers will increase both the BOL and EOL efficiencies while decreasing the fabrication cost and increasing the yield of space solar cells. We are confident that through a relatively short R&D effort, stable chemically grown oxides with good passivating and optical properties can be cost effectively and reproducibly grown prior to or after the front metallization step for any other space and terrestrial solar cell and TPV cell configurations.

References

- [1] J. Joseph, Y. Robach, G. Hollinger, P. Ferret and M. Pitval, "The Passivation of InP by $\text{In}(\text{PO}_3)_3$ for MISFET Applications," Proc. 1st Int'l IPRM Conf., 1989, p.268.
- [2] C. Wilmsen, "Physics and Chemistry of III-V Compound Semiconductor Interfaces," Plenum Press, New York, 1985.
- [3] Maria Faur, Mircea Faur, D.T. Jayne, M. Goradia and C. Goradia: "XPS Investigation of Anodic Oxides Grown on p-type InP", Surface and Interface Analysis, 15, p 641, 1990.
- [4] P. Jenkins, M. Goradia, Mircea Faur, S. Bailey and Maria Faur, "Measurement of Surface Recombination Velocity on Heavily Doped Indium Phosphide," Proc. 21st IEEE PVSC, 1990, p.399.
- [5] Mircea Faur, Maria Faur, P. Jenkins, M. Goradia, S. Bailey, D. Jayne, I. Weinberg and C. Goradia, "Study of Surface Passivation of InP," Surface and Interface Analysis, 15, 745 (1990)
- [6]. Mircea Faur, Maria Faur, D.J. Flood, D.J. Brinker, I. Weinberg, C. Goradia and M. Goradia, "Low Carrier Removal Rates and Annealing Behavior of Thermally Diffused $p^+n(\text{Cd,S})$ InP Structures After 10^{13}cm^{-2} , 3 MeV Proton Irradiation", Proceedings at the 23rd IEEE Photovoltaic Specialists Conference, KY, May 10-14, 1993, p.1437.
- [7]. Mircea Faur, Maria Faur, D.T. Jayne, S. Bailey and M. Goradia, "Etchant for Chemical Thinning of InP and its Application in the Fabrication of InP Diffused Junction Solar Cells", Surface and Interface Analysis, 21, 110 (1994).
- [8]. Mircea Faur, Maria Faur, D.J. Flood, D.J. Brinker, C. Goradia, S. Bailey, I. Weinberg, M. Goradia, D.T. Jayne, J. Moulot and N. Fatemi, "Effective First Layer Antireflective Coating on InP Solar Cells Grown by Chemical Oxidation", Proceedings of the 6-th Int'l Conference on Indium Phosphide and Related Materials, Santa Barbara, California, March 28-31, 1994, p.492.
- [9] Mircea Faur, Maria Faur, D.J. Flood, D.J. Brinker, C. Goradia, N.S. Fatemi, P.P. Jenkins, D.M. Wilt, S. Bailey, M. Goradia and J. Moulot, "Status of Diffused Junction p^+n InP Solar Cells for Space Applications", Proceedings of the XIII Space Photovoltaic Research and Technology Conference, June 14-16, 1994, pp. 63-79.
- [10] J. Moulot, Mircea Faur, Maria Faur, C. Goradia, M. Goradia and S. Bailey, "Three-Layer Antireflecting Coating for High Efficiency InP Solar Cells," Proceedings of the 14th Space Photovoltaic Research and Technology Conference, Oct. 24-26, 1995, p.142.
- [11] J. Moulot, Mircea Faur, Maria Faur, C. Goradia, M. Goradia, S. Alterovitz and S. Bailey, "New Three-Layer Antireflection/Surface Passivation Coating for High Efficiency III-V Compound Solar Cells," Proceedings of the 8th Int'l Conference on Indium Phosphide and Related Materials, Schwabisch Gmund, Germany, April 21-25, 1996.

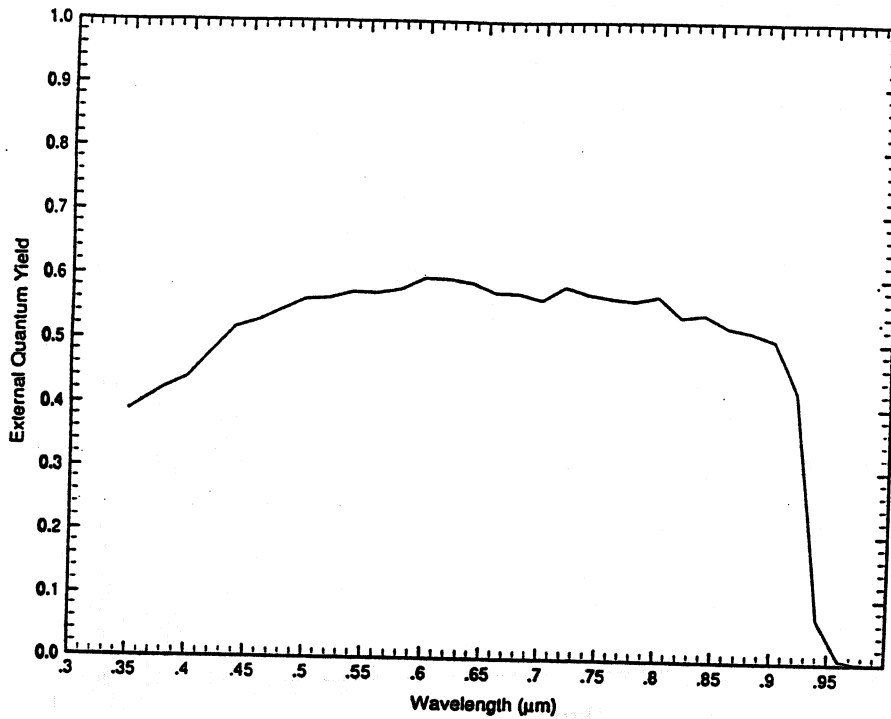


Fig. 1. Typical EQY plot of a diffused junction $p^+n(\text{Cd,S})\text{InP}$ cell with a thin (~ 30 nm) chemically grown $\text{In}(\text{PO}_3)_3$ -rich oxide as an AR coating. Overall reflectivity: $\sim 30\%$. Emitter thickness: $\sim 0.45\mu$

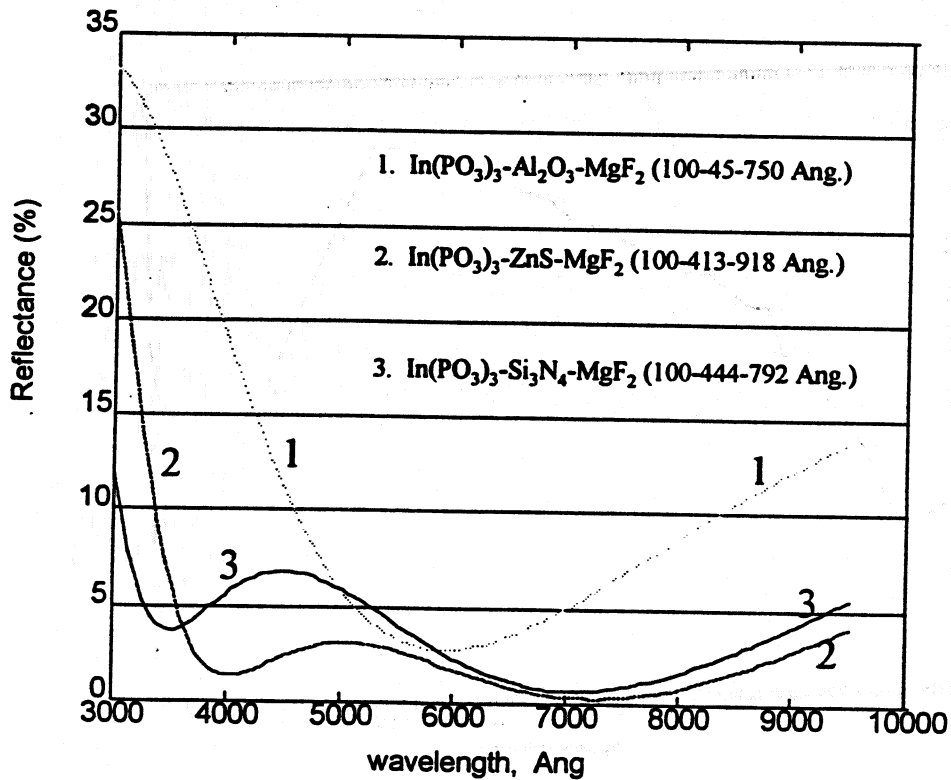


Fig. 2. Surface reflectance of p^+n InP solar cell with optimized 3-layer AR coatings using the passivating $\text{In}(\text{PO}_3)_3$ -rich chemically grown oxide as the first layer.

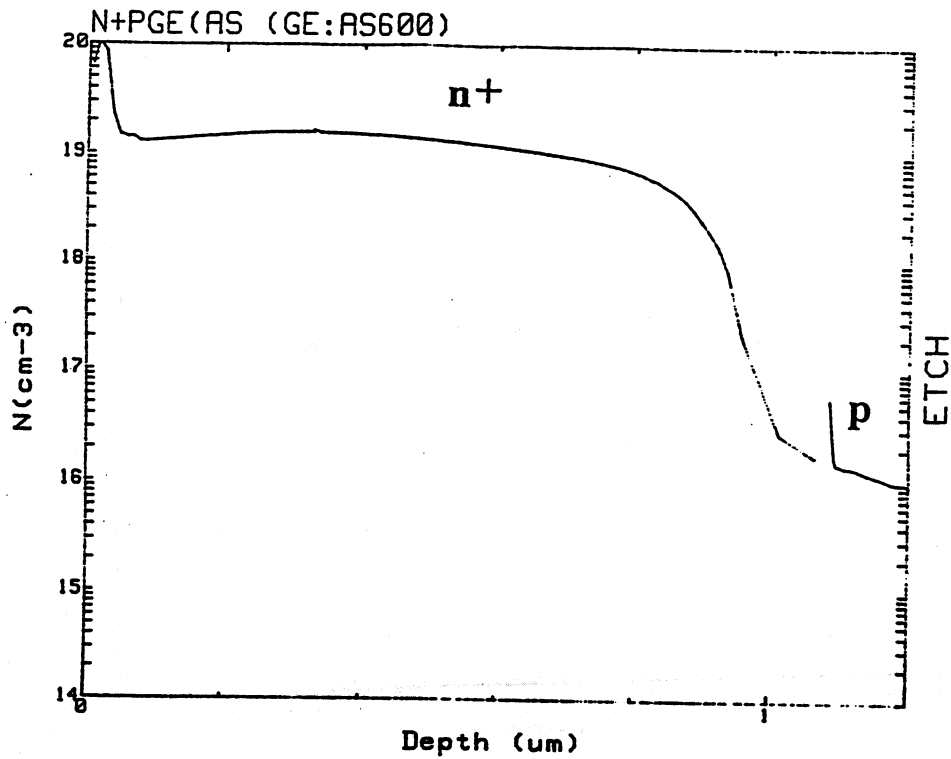


Fig. 3. EC-V net majority carrier concentration depth profile at the front of a n^+pp^+ Ge diffused structure.

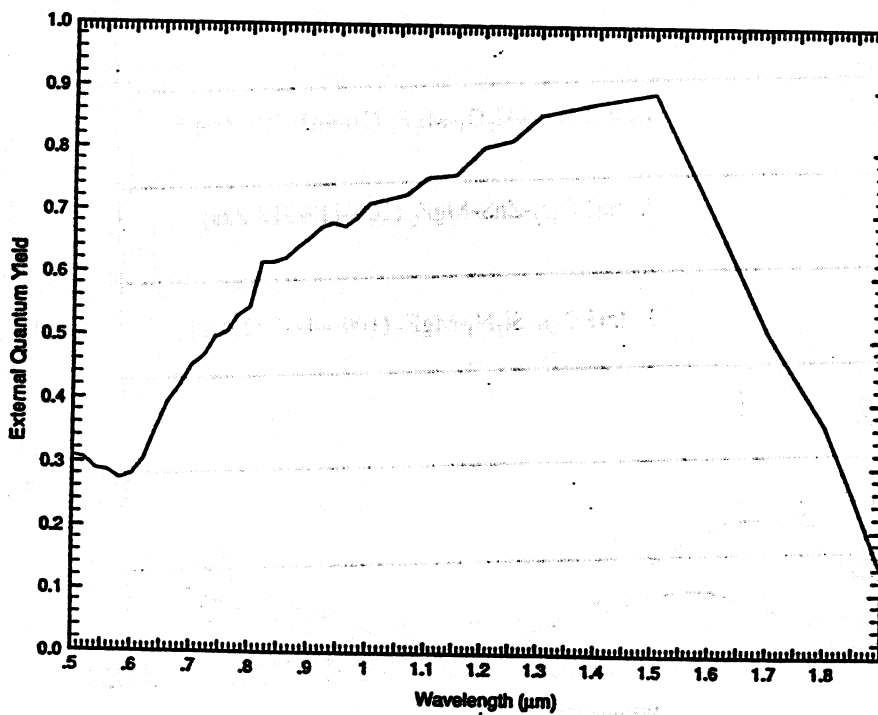


Fig. 4. External quantum efficiency of a planar n^+pp^+ Ge cell fabricated on a structure identical to the one in Fig. 3.

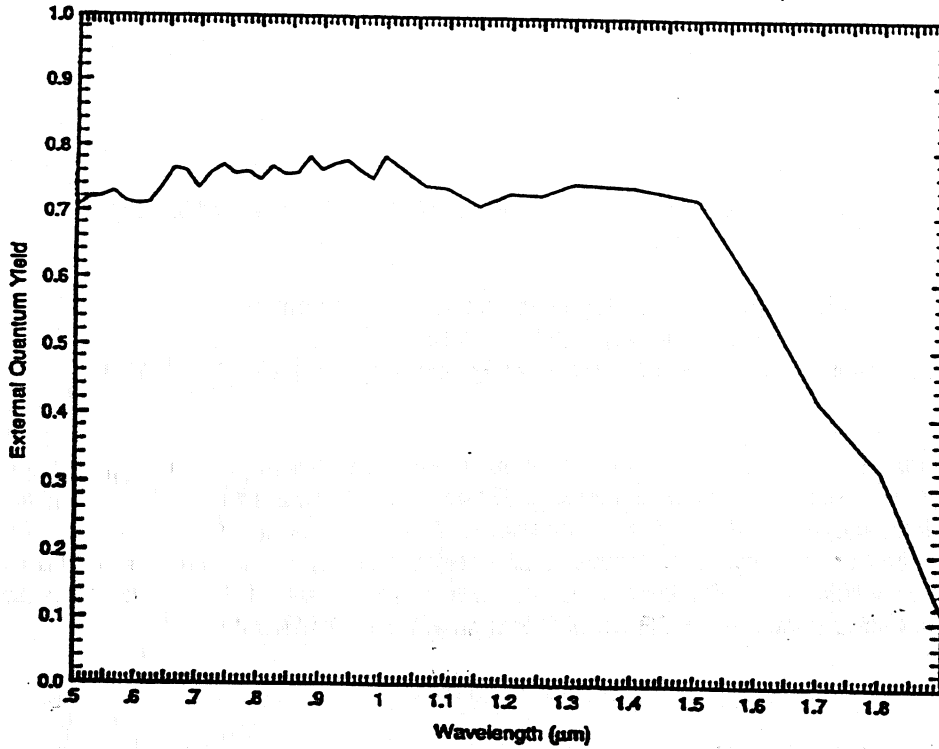


Fig. 5. External quantum efficiency of a planar n^+pp^+ Ge cell fabricated on a structure such as in Fig. 3. after passivating and stabilizing the porous layer.

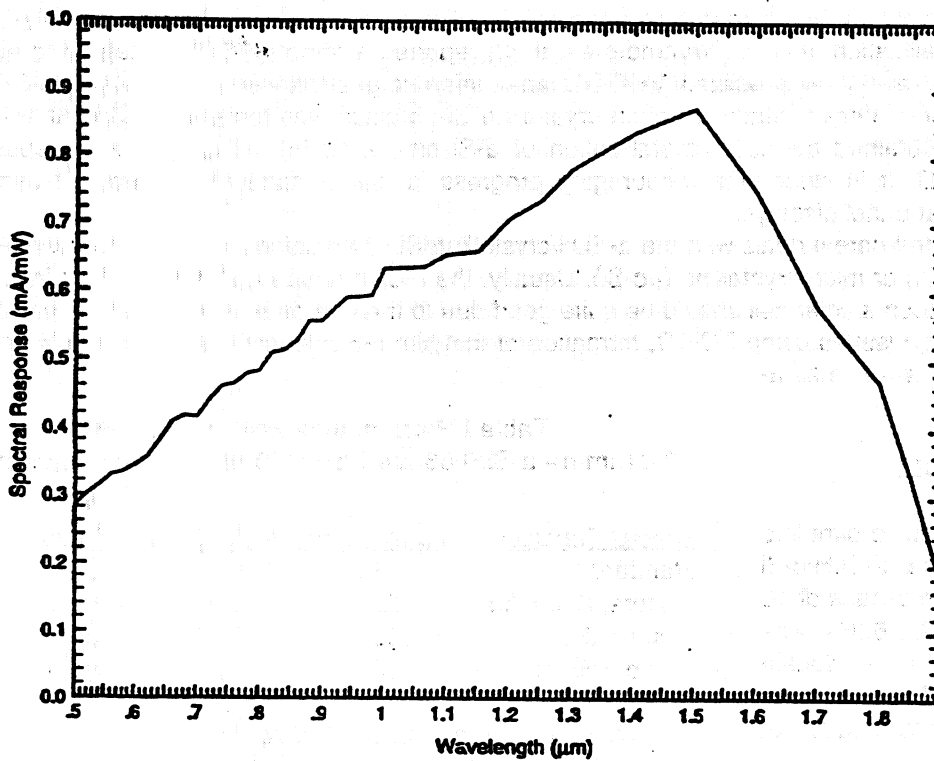


Fig.6. Spectral response of the n^+pp^+ Ge cell in Fig. 5.

LIGHT WEIGHT, THIN-FILM Si HETEROJUNCTION SOLAR CELLS

W.A. Anderson, B. Jagannathan and E. Klementieva
 State University of New York at Buffalo
 Department of Electrical and Computer Engineering, Amherst, NY 14260

Abstract. This approach to a thin-film Si solar cell combines theoretical analysis, growth of thin-film crystalline Si (c-Si) and deposition of amorphous Si (a-Si:H) to form the heterojunction. The PC-1D model predicts a potential efficiency of > 16% for a Si thickness of 10 μm . Liquid phase growth (LPG) of the base-layer c-Si gave carrier mobility of $100\text{cm}^2/\text{V}\cdot\text{s}$ and lifetime of 8 μs . Microwave electron cyclotron resonance (MECR) deposition of a-Si:H onto a c-Si wafer gives over 10% photovoltaic conversion efficiency. Work continues to combine MECR with LPG to give a thin-film Si solar cell.

INTRODUCTION

The increased use of satellites for communications makes cost of solar cells a greater concern than in the past. One way to reduce cost is to reduce the thickness of the cell. Both reduced weight and lower solar cell cost become attractive. Progress is being made on several fronts in the area of thin film Si photovoltaics. Researchers in Germany have introduced the "Micromorph" cell, in which they use very high frequency glow discharge (VHF-GD) to produce microcrystal hydrogenated Si ($\mu\text{c-Si:H}$) [1]. They report a 10.7% efficiency on an a-Si:H/ $\mu\text{c-Si:H}$ cell. Tanaka et. al. [2] report an a-Si/poly-Si cell having a 9.2% efficiency. The poly-Si was made using solid phase crystallization of a-Si. Miyamoto et. al. [3] reported a remote PECVD method to obtain poly-Si on glass. N. Beck et. al. [4] also utilized VHF-GD and different gas dilutions to achieve $\mu\text{c-Si:H}$ with drift mobilities up to $3\text{ cm}^2/\text{V}\cdot\text{s}$. Very recently, ultrathin crystalline Si on glass was formed by CVD at 1000°C [5]. Si films have also been obtained by laser crystallization of a-Si on plastic [6]. The a-Si was deposited at low temperature by PECVD. It is clear that encouraging progress is being made in the area of thin film Si for photovoltaics and for flat panel displays.

The work reported herein deals with the a-Si:H/crystalline-Si (c-Si) solar cell, where the crystalline Si may be nanocrystalline (nc-Si) or microcrystalline ($\mu\text{c-Si}$). Usually, the c-Si is p-type and the a-Si:H is layered n/i-type. Radiation hardness of such a solar cell should be quite good due to the use of a-Si:H [7] and thinner c-Si [8]. This paper will address design issues using PC-1D, formation of thin film c-Si, deposition of the a-Si:H and prospects for future advancement of the a-Si:H/c-Si solar cell.

Table I Performance Predicted by PC1D
 0.01 μm n+ a-Si/0.08 μm i a-Si/ 10 μm p c-Si/ 0.1 μm p+ c-Si

PC-1D MODEL

PC-1D was used to simulate the performance of the a-Si:H/c-Si solar cell having an Si thickness of 10 μm . An efficiency of 16.3% was predicted with use of a double antireflection coating. Table I shows the variation in photovoltaic output under various assumptions.

Special Condition	J_{sc} (mA/cm ²)	V_{oc} (V)	Fill Factor	Efficiency (%)
Standard	31.2	0.56	0.78	13.6
Texture, 3 μm , 55°	32.0	0.55	0.79	13.8
μ_H in i = 0.5	33.0	0.56	0.79	14.6
L_o in p = 85 μm	33.4	0.60	0.80	16.3

* $N_A = 4 \times 10^{15} \text{ cm}^{-3}$, double A/R coating, BSR, μ_H in i = $0.1 \text{ cm}^2/\text{V}\cdot\text{s}$, L_o in p = 10 μm

Interface recombination was introduced at the a-Si:H/c-Si interface to simulate the condition which we view as the cause for reduced efficiency. This condition of recombination velocity of $8 \times 10^7 \text{ cm/s}$ for electrons and $1 \times 10^5 \text{ cm/s}$ for holes reduced internal quantum efficiency by 20% and photovoltaic power by even more than we experimentally observed as shown in Figure 1. Increasing a-Si thickness to above 500 Å caused severe reduction in the UV portion of the quantum efficiency plot.

EXPERIMENTAL METHODS

Liquid Phase Growth (LPG) of c-Si

This study was an attempt at forming a polycrystalline Si on a foreign substrate using a relatively low temperature process. Depositions were done in a diffusion-pumped high vacuum system. A liquid nitrogen cold finger assists in achieving a base pressure in the low 10^{-7} Torr range. A filament evaporation source deposits the solvent metal prior to sputtering of the Si by d.c. magnetron from a 2" target. Typically, a polished Mo substrate, coated with SiO_2 , is first coated with a 50-500nm layer of Sn while heated to about 400°C, or at 650°C for the In/Ti prelayer. In future use, the Mo would be replaced by a suitable plastic for reduced weight. Ti is used as a wetting agent to allow full wetting of the substrate surface by the liquid In layer. This is followed by the Si deposition in 2 mTorr of 5% H_2 in Ar at a rate of 1 micron per hour with the substrate at about 600°C. During deposition, a metal-Si melt is formed which is kept saturated in Si by the sputter gun. This liquid layer remains on the surface and leaves behind a poly-Si film. Chemical etching later removes the metal-Si residue and exposes the poly-Si layer. Films have been grown with thickness ranging from less than one micron to about 6 microns. The structure is shown in Figure 2. More details have been previously published [9,10].

MECR Deposition of a-Si:H

Thin film silicon growth by a microwave plasma discharge (operated in an ECR condition) in a $\text{SiH}_4/\text{Ar}/\text{H}_2/\text{He}$ type mixture addresses the need for obtaining microcrystalline Si (mc-Si) films with lower defect density at a higher rate of deposition and amorphous Si (a-Si) films with improved stability. The technique permits electrodeless deposition of silicon films at higher plasma density compared to the rf PECVD.

The schematic of the deposition system is shown in Figure 3. It consists of a Pyrex cross, mated to a quartz tube within a resonant cavity. The magnetron tube is mounted directly on the cavity, which is a rectangular Al waveguide. The input power to the magnetron can be continuously varied up to 1000 W. The two permanent magnets (885 Gauss) provide the ECR condition in the resonant cavity. The plasma is excited in a background gas (H_2 , He or Ar) in the quartz tube and the process gases (2% SiH_4/He or 2% SiH_4/Ar) are fed at the front end of the quartz tube. A 2" stainless steel block with heater and thermocouple serves as the substrate holder. The chamber is pumped by a diffusion pump, and has a base pressure of $< 10^{-6}$ Torr. A cold trap is used to reduce backstreaming and reduce water vapor. Growth of mc-Si has been achieved in both $\text{SiH}_4/\text{Ar}/\text{H}_2$ and $\text{SiH}_4/\text{He}/\text{Ar}/\text{H}_2$ type mixtures at low substrate temperatures of 300 - 400°C at operating pressures of 1-10 mTorr. Amorphous silicon films have also been prepared with these gas combinations at temperatures of 250 °C and pressures of 40 mTorr.

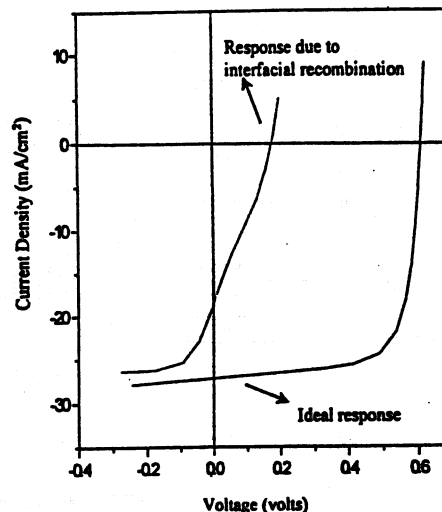


Fig. 1 Effect of interfacial recombination using PC-1D code for the a-Si:H/10µm thick c-Si.

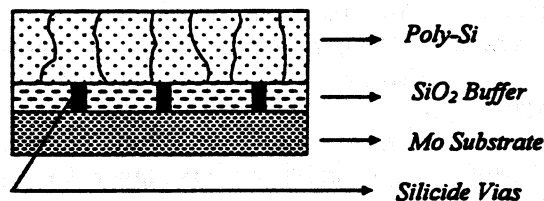


Fig. 2 Cross-section of thin-film poly-Si and substrate.

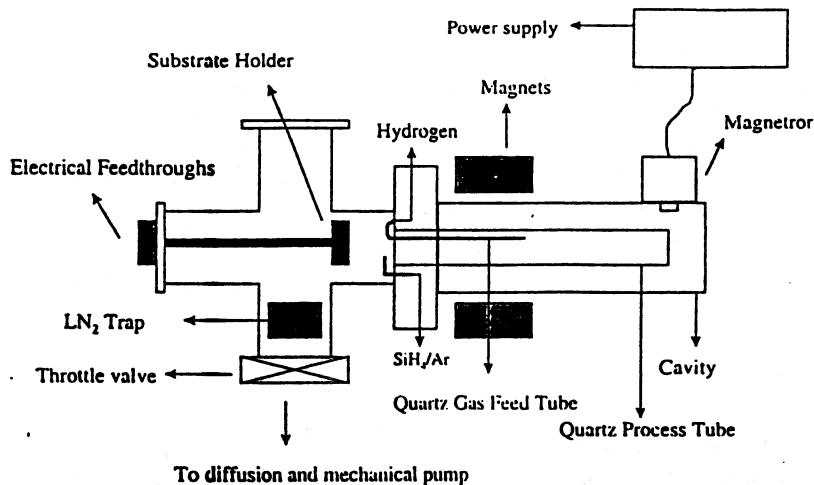


Fig. 3 MECR deposition system.

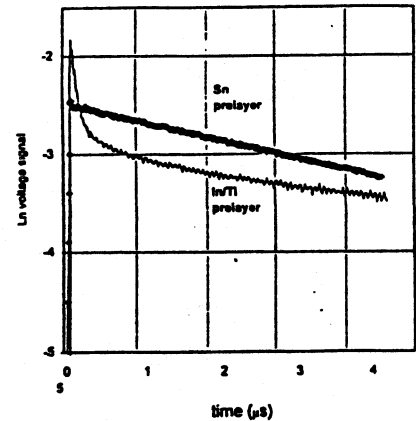


Fig. 4 Lifetime data for μ c-Si films comparing Sn to In/Ti prelayers.

EXPERIMENTAL RESULTS

Liquid Phase Growth of c-Si

Films using the In/Ti prelayer exhibit large grain size ($> 20 \mu\text{m}$), carrier mobility up to $100 \text{ cm}^2/\text{V-s}$, a preferred (111) orientation and carrier lifetime of $0.3 \mu\text{s}$, which is lower than desired due to contamination by Ti. Films using the Sn prelayer have a grain size of about $1 \mu\text{m}$, carrier mobility up to $100 \text{ cm}^2/\text{V-s}$, no preferred orientation and carrier lifetime of $8 \mu\text{s}$. Figure 4 shows the carrier lifetime data, taken by R.K. Ahrenkiel at NREL. Clearly, the films made with the In/Ti prelayer have 2 mechanisms, one of which we feel is caused by the Ti impurity. Figure 5 shows that the Sn-prelayer film responds well to hydrogenation with carrier mobility increased to $160 \text{ cm}^2/\text{V-s}$.

Data in Table II show the electrical properties comparing Sn to In/Ti pre-layers. Ti, as a wetting agent, causes electrical properties to deteriorate. Ti must be replaced in future work if In is to be used as the solvent.

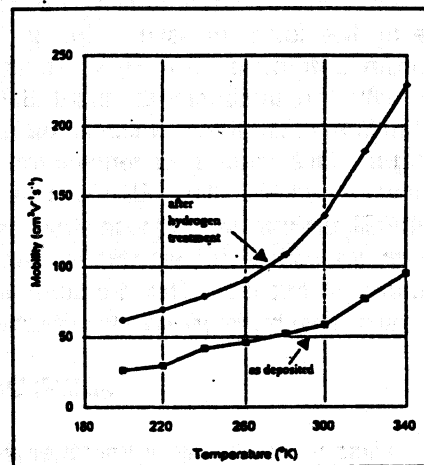


Fig. 5 Carrier mobility for μ c-Si films using an Sn prelayer.

MECR Deposition of a-Si:H and μ c-Si

The growth of microcrystalline silicon (mc-Si) by the H_2 dilution of $2\% \text{SiH}_4$ (balance of either Ar or He) by an ECR-CVD process has been examined. Variations in structural and electrical properties of thin films have been evaluated with respect to growth parameters, mainly, H_2 dilution (defined here as $R_{\text{H}} = \text{H}_2 \text{ content}/(\text{total gas content})$), substrate temperature, input power and total pressure. Most of the films discussed here were deposited at 10 mTorr total pressure.

Table II. Properties of LPG Thin Film Silicon

	Sn Prelayer	In/Ti Prelayer
Growth temperature (°C)	~ 600	~ 600
Conductivity type ^(a)	N	P
Grain size (μm)	≤ 1	20 or more
Grain orientation	mixed	(111)
Dark conductivity (Ω-cm) ⁻¹	1 - 10	0.1 - 2
Carrier mobility (cm ² V-s)	60 @300K	100 @300K
Carrier mobility (cm ² V-s) after hydrogenation	140 @300K	100 @300K
Lifetime (μs) ^(b)	~ 8	~ 0.3 ^(c)

(a) Controlled by source;
 (b) Measured at NREL;
 (c) Limited by Ti in film

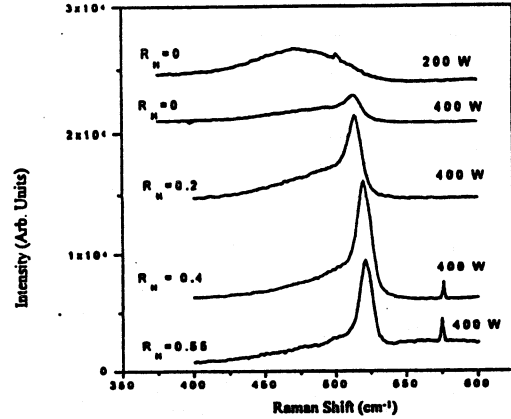


Fig. 6 Raman spectra of MECR-Si with different power and H-dilution.

Structural Properties

Figure 6 shows the Raman spectra for H₂ dilution of 2% SiH₄/Ar, as it is varied from 0 to 0.55, at a substrate temperature of 300 °C, and an input power of 400 W. The dilution at a R_H of 0.55 corresponds to a condition of almost equal amounts of Ar and H₂ in the system. The films are seen to crystallize even at R_H of zero. Completely amorphous films are obtained when the input power is lowered to 200 W. As the H₂ content in the plasma increases, the amorphous contribution in the Raman spectra at 480 cm⁻¹ and the shoulder at 503 cm⁻¹ decrease, and for R_H levels of 0.55, only a sharp crystalline TO peak is apparent. By analysis of the Raman spectra, it was found that ~45% of the film crystallizes when no H₂ is present, however, the grain sizes are only ~30 Å. With increasing R_H, the grain sizes and crystalline fraction increases. For R_H levels of 0.55, 70% of the film crystallizes at grain sizes between 200-300 Å.

Electrical Properties

Table III shows the dark/ photoconductivity (σ_D/σ_{PH}) of the best films deposited by this method. The amorphous films were deposited at 40 mTorr and a substrate temperature of 250 °C, while the mc-Si films have been deposited at 400 °C and a R_H of 0.55. Using He as the carrier gas results in films with very good σ_{PH} that also show a higher conduction activation energy compared to the films deposited with Ar, implying lower defect densities in such films. This is also seen for the mc-Si films. In the case of the mc-Si films, for films deposited at 400 °C, carrier transport was found to be thermally activated over many orders of magnitude, but the films deposited at 300 °C showed two transport mechanisms.

Table III Dark/Photoconductivity of Some ECR-CVD Films

Film Type	2% SiH ₄ Carrier	σ_D (S/cm)	σ_{PH} (S/cm)	ΔE_{act} (eV)
Amorphous	Ar	8x10 ⁻⁶	7x10 ⁻⁶	0.53
Amorphous	He	4x10 ⁻⁶	8x10 ⁻⁵	0.80
Microcrystalline	Ar	3x10 ⁻⁶	9x10 ⁻⁶	0.30
Microcrystalline	He	6x10 ⁻⁶	1x10 ⁻⁵	0.49

Devices

Heterostructure solar diodes with a-Si/crystalline silicon (c-Si) type structures were fabricated. The a-Si film was typically 300-400 Å thick. Figure 7 shows the photovoltaic characteristics of the cells. The cells made by ECR-CVD deposition of a-Si:H were not as good as ones using sputtered a-Si:H.

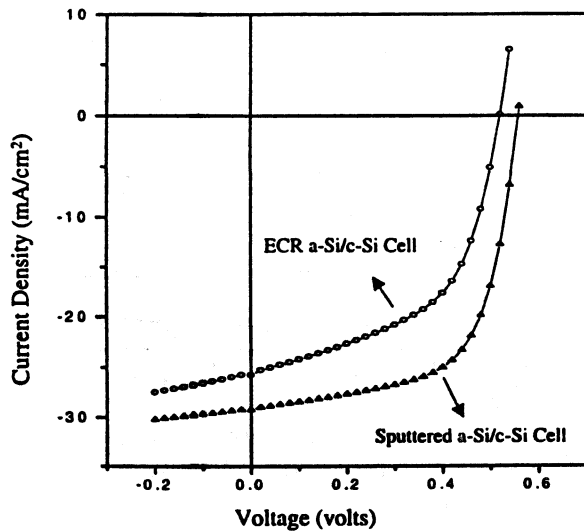


Fig. 7 Photovoltaic results for a-Si:H/c-Si wafer using 100 mW/cm² illumination, without an A/R coating.

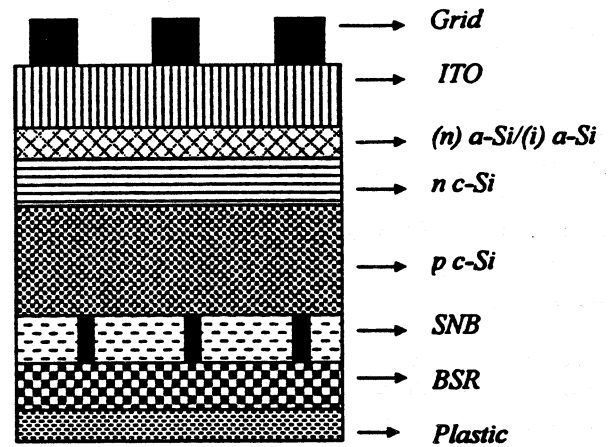


Fig. 8 Proposed design of a thin-film Si solar cell.

For sputtered a-Si:H/p-type crystalline Si, $V_{oc} = 0.55V$, $J_{sc} = 30 \text{ mA/cm}^2$, $FF = 0.67$, and efficiency = 10.9%, without an A/R coating.

DISCUSSION

The a-Si:H/c-Si thin film solar cell has a potential efficiency of >16%, based on PC-1D modeling. This work has explored the growth of thin-film c-Si using a liquid phase growth (LPG) in conjunction with a DC magnetron sputter source. Use of an Sn melt to promote LPG has led to film thickness exceeding 6 μm , carrier mobility of 100 $\text{cm}^2/\text{V-s}$ (160 $\text{cm}^2/\text{V-s}$ after hydrogenation), and carrier lifetime of 6 μs . On the negative side, film non-uniformity has hindered the fabrication of large-area solar cells. Solution of this problem might lie in use of a rotating substrate, introduction of a better buffer layer to improve wetting of the liquid phase or a seeding technique to control uniform nucleation.

Microwave electron cyclotron resonance (MECR) deposition of the a-Si:H has been quite successful. Films may be a-Si or nc-Si, by adjusting substrate temperature. Control of hydrogen dilution provides films of lesser hydrogen content which may improve upon light-induced degradation normally seen in a-Si:H. Solar cells fabricated using MECR-deposited a-Si:H/c-Si wafer have produced a 10% efficiency. The efficiency is limited by the a-Si/c-Si interface. We are exploring a solution to this problem utilizing hydrogenation and/or introduction of a thin nc-Si transition region between a-Si:H and c-Si. A more complex-solution would alter the structure to a *tandem* cell using (n-i-p) a-Si:H/(n-p)c-Si. This would remove the junction from the a-Si:H/c-Si interface.

At some point, the MECR process will be applied to the LPG thin film to give a truly thin-film Si solar cell. Such a design is given in Figure 8 and includes a stable nucleating barrier (SNB).

CONCLUSIONS

PC-1D modeling of the a-Si:H/c-Si thin film solar cell predicts a potential efficiency > 16%. The liquid phase growth (LPG) process gives a thin Si film having good electrical properties and grain sizes up to 20 μm or more. Improved uniformity is required which may be achievable by altering the buffer layer and/or wetting agent. MECR deposition of a-Si:H and nc-Si has produced quite promising films, the properties of which are easily controlled by process variables. Hydrogen dilution results in films having less incorporated hydrogen which may be more stable. MECR deposition of a-Si:H onto c-Si gave cells with an efficiency of 10%. Once LPG is improved, the MECR process can be used to complete the solar cell. A possible structure is shown in Figure 8 [11].

REFERENCES

1. J. Meier, S. Dubail, R. Platz, P. Torres, U. Kroll, J.A. Anna Selvan, N. Pellaton Vaucher, ch. Hof. D. Fischer, H. Keppner, R. Flückiger, A. Shah, V. Shklover, K.-D. Ufert, "Towards High-Efficiency Thin-Film Silicon Solar Cells with the 'Micromorph' Concept", Preprint of the 9th PVSEC, Miyazaki, Nov. 11-15, 1996, Japan.
2. M. Tanaka, S. Tsuge, S. Kiyama, S. Tsuda and S. Nakano, "Fabrication of Polycrystalline Si Thin Film for Solar Cells", Materials Research Society (MRS) Fall Meeting, Boston, Dec. 2-6, 1996.
3. Y. Miyamoto, A. Miida and I. Shimizu, "Epitaxy-Like Growth of Polycrystalline Silicon on the Seed Crystallites Grown on Glass", MRS Fall Meeting, Boston, Dec. 2-6, 1996.
4. N. Beck, P. Torres, J. Fric, Z. Remes, A. Poruba, Ha Stuchlikova, A. Fejfar, N. Wyrsh, M. Vanecek, J. Kocka and A. Shah, "Optical and Electrical Properties of Undoped Microcrystalline Silicon Deposited by the VHF-GD with Different Dilutions of Silane in Hydrogen", MRS Fall Meeting, Boston, Dec. 2-6, 1996.
5. R. Brendel, R.B. Bergmann, P. Lölgen, M. Wolf and J.H. Werner, "Ultrathin Crystalline Silicon Solar Cells on Glass Substrates", *Appl. Phys. Lett.*, 70, 390 (1997).
6. P.M. Smith, P.G. Carey and T.W. Sigmon, "Excimer Laser Crystallization and Doping of Silicon Films on Plastic Substrates", *Appl. Phys. Lett.*, 70, 342-344 (1997).
7. J.R. Woodyard and J.S. Payson, "Radiation Resistance Studies of Amorphous Silicon Films", *Space Photovoltaic Research and Technology Conference*, NASA-Cleveland, April 18-21, 1988.
8. M.W. Walkden and A.A. Dollery, "Omnidirectional Proton Irradiation of Thin and Thick Solar Cells", *16th IEEE Photovoltaic Specialists Conference*, San Diego, Sept. 27-30, 1982.
9. R.L. Wallace and W.A. Anderson, "Thin Film Polycrystalline Si by CS Solution Growth Technique", *MRS Fall Meeting*, Boston, Nov. 28-Dec. 2, 1994.
10. R.L. Wallace and W.A. Anderson, "Solution Grown Polysilicon for Photovoltaic Devices", *25th IEEE Photovoltaic Specialists Conference*, Washington, DC, May 13-17, 1996.
11. W.A. Anderson, B. Jagannathan and R. Wallace, "A Thin-Film Si Solar Cell: Deposition, Fabrication, and Design", *First Conference on Future Generation Photovoltaic Technologies*, Denver, CO, Mar. 24-26, 1997.

NOVEL SI SOLAR CELL FOR SPACE POWER APPLICATIONS

by

Dr. Henry Brandhorst and Hayden Hontgas
Center for the Commercial Development of Space Power and Advanced Electronics
Space Power Institute
Auburn University
Auburn, AL 36849-5201

Abstract: This paper presents evidence that a high efficiency (~18%), radiation tolerant (~GaAs) n-p silicon solar cell for space power applications can be developed.

It is estimated that 50% to 75% of all commercial satellites now under construction will be equipped with solar cells from III-V elements such as GaAs. But, the cost of a single crystal GaAs solar cells is as much as eight times the price of silicon cells. By fabricating the GaAs cell on a Ge substrate, costs have dropped to only two to three times the cost of Si solar cells. Theory suggests that the addition of small amounts ($\sim 10^{17}/\text{cm}^3$) of Ge into the silicon lattice in the bulk region can decrease the base minority carrier mobility leading to significant Voc increases. The mobility decrease reduces J_0 and should not greatly affect J_{sc} , thus leading to increased efficiency. PC1D simulations show agreement with these presumptions. The base resistivity ($\sim 10\text{-}100 \Omega\text{-cm}$) of the cell allows it to retain good radiation resistance. Because the cell is basically Si, it can be produced at a lower cost per cell than present GaAs space solar cells yet possessing similar efficiency and radiation tolerance.

Introduction -

The idea presented in this paper is to show theory and simulation results that suggest a silicon (Si) based n-p solar cell for space power applications may be produced that is competitive in performance characteristics with GaAs solar cells. Recent theoretical studies indicate that $\text{Si}_{1-x}\text{Ge}_x$ may be used with conventional doping schemes to achieve improvement in presently available Si solar cells. It is believed that through the introduction of material such as germanium into the solar cell structure, characteristics such as power-conversion efficiency and radiation hardness equivalent to that of gallium-arsenide (GaAs) solar cells can be achieved.

It is estimated that 50% to 75% of all commercial satellites now under construction will be equipped with solar cells from III-V elements such as GaAs. But, the cost of a single crystal GaAs solar cells is as much as eight times the price of silicon cells [1]. By fabricating the GaAs cell on a Ge substrate, costs have dropped to only two to three times the cost of Si solar cells. Therefore, development of a silicon-based solar cell with equivalent GaAs performance characteristics will offer significant additional cost reduction for satellite solar cells.

Theory -

The fundamental rationale for this research is to reduce the reverse saturation current of the diode by reducing the electron mobility within the PV cell bulk without significantly affecting the minority carrier diffusion length. This effectively increases the open-circuit voltage and may provide good power-conversion efficiency (up to 18%), while maintaining a relatively high resistivity ($\sim 10 \text{ W-cm}$) base, which ensures good radiation hardness. The governing solid-state equations are as follows:

In general, the reverse saturation current is given by [2] -

$$J_0 = \frac{qD_e n_i^2}{L_e N_A} + \frac{qD_h n_i^2}{L_h N_D}$$

Where D_e and D_h are the minority carrier electron and hole diffusivity, respectively. N_A and N_D are the p-region and n-region doping concentrations, respectively. L_e and L_h are the electron and hole diffusion lengths, respectively. The intrinsic carrier concentration is n_i , and q is the electric charge.

The open-circuit voltage is given by [2] -

$$V_{oc} = \left(\frac{kT}{q}\right) \ln\left(\frac{J_L}{J_0} + 1\right)$$

Where,

k = Boltzmann's constant

T = temperature

J_L = light generated current density

Using the Einstein relationship [2] -

$$D_{e,h} = \frac{kT\mu_{e,h}}{q}$$

where $\mu_{e,h}$ = minority electron or hole mobility, and the definition of diffusion length [2] -

$$L_{e,h} = \sqrt{D_{e,h}\tau_{e,h}}$$

where $\tau_{e,h}$ = minority electron or hole lifetime, and combining these relationships, one obtains -

$$V_{oc} = \frac{kT}{q} \ln\left(\frac{J_L}{n_i^2(\sqrt{qkT})(1/N_A \times \sqrt{\mu_e/\tau_e} + 1/N_D \times \sqrt{\mu_h/\tau_h})} + 1\right)$$

For 10 W-cm n-p cells, J_0 is dominated by the contribution from the base region. Therefore, we can simplify this relationship to obtain -

$$V_{oc} = \frac{kT}{q} \ln\left(\frac{J_L}{n_i^2(\sqrt{qkT}) \times 1/N_A(\sqrt{\mu_e/\tau_e})} + 1\right)$$

Thus, by inspection, it is clear that for a fixed base lifetime, mobility reductions in the base lead directly to V_{oc} increases. However, J_L depends on diffusion length and mobility so care must be taken not to adversely impact diffusion length while reducing mobility. This has the effect of increasing the maximum power output of the cell so long as J_L is not greatly reduced.

Maintaining a high resistivity (~10 W-cm) p-region leads to high radiation hardness. Recent theoretical

work [3] has shown that introduction of germanium into p-type silicon ($\text{Si}_{1-x}\text{Ge}_x$) doped to levels less than $10^{19}/\text{cm}^3$ can significantly decrease electron mobility. Germanium is an ideal additive in Si, being isoelectronic with Si as well as being infinitely soluble.

Simulations -

PV cell simulation software called PC1D[4] was used to perform simulations to determine the effect of lowering the minority carrier mobility in the p-type base region of a silicon solar cell. Figure 1 shows the structure of the simulated cell. The simulations were performed by applying a 1 micron region of low electron mobility at the junction and gradually increasing the thickness of this region until it made up the entire base. The total cell thickness was maintained at 150 microns. Simulations were performed for eleven different values of electron mobility. An optical coating was applied to the surface, internal reflectance, base contact and emitter contact were enabled and an exterior rear reflectance was set to 70%. The emitter was maintained at 0.5 micron and n-doped with a gaussian profile with a peak of $3 \times 10^{19}/\text{cm}^3$. The cell background doping was maintained at $10 \Omega\text{-cm}$ with a bulk recombination of $206 \mu\text{s}$. The cell was excited with the AM0 spectrum.

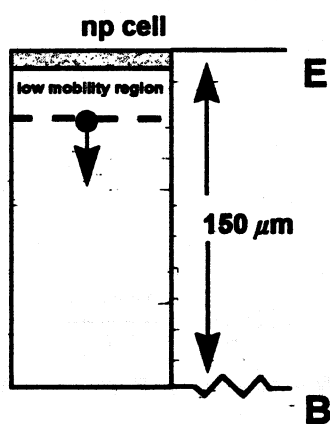


Figure 1. Cell structure.

Figures 2 and 3 show the simulation results for open-circuit voltage and short-circuit current. These results show the trend of increased open-circuit voltage and short-circuit current, and therefore efficiency, with decreased electron mobility in the p-type base.

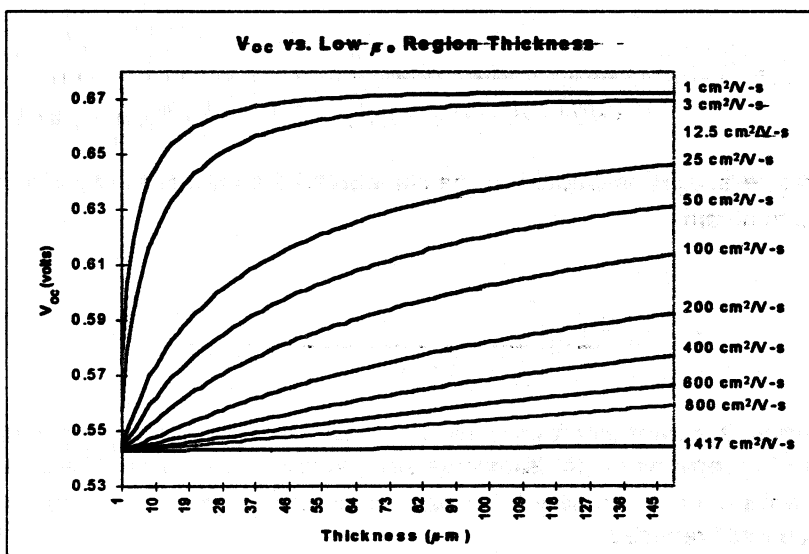


Figure 2. V_{oc} vs low μ_e region thickness for different electron mobilities.

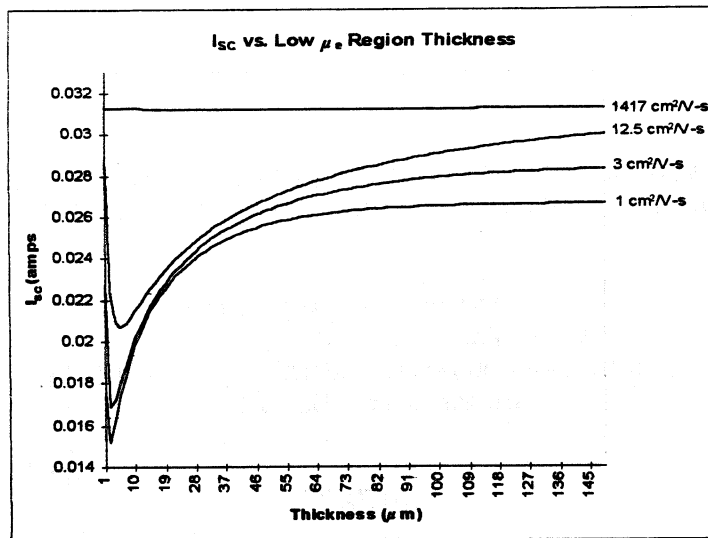


Figure 3. I_{sc} vs low μ_e region thickness for different electron mobilities.

References -

- [1] Marie Meyer and Robert A Metzger, "Flying High: The Commercial Satellite Industry Converts to Compound Semiconductor Solar Cells," *Compound Semiconductor*, Nov/Dec 1996, vol. 2, Num. 6, pp. 22-23.
- [2] Martin A. Green, *Solar Cells: Operating Principles, Technology and System Applications*, Chapter 4, The University of New South Wales, Kensington, New South Wales, 1992.
- [3] L. E. Kay and T. W. Tang, "Monte Carlo Calculation of Strained and Unstrained Electron Mobilities in $Si_{1-x}Ge_x$ Using an Improved Ionized-Impurity Model," *J. Appl. Phys.*, vol. 70, pp. 1483-1488, 1 August 1991.
- [4] Paul A. Basore, Donald A. Clugston, "PC1D Version 4 for Windows: From Analysis to Design," Center for Photovoltaic Devices and Systems, University of New South Wales, Sydney, Australia, May 1996.

PLASMA-ENHANCED PULSED LASER DEPOSITION OF WIDE BANDGAP NITRIDES FOR SPACE POWER APPLICATIONS¹

G.E. Triplett, Jr. and S.M. Durbin
Department of Electrical Engineering
Florida A&M University / Florida State University
Tallahassee, Florida 32310

ABSTRACT

The need for a reliable, inexpensive technology for small-scale space power applications where photovoltaic or chemical battery approaches are not feasible has prompted renewed interest in high-efficiency radioisotope-based energy conversion devices. Although a number of devices have been developed using a variety of semiconductors, the single most limiting factor remains the overall lifetime of the radioisotope battery. Recent advances in growth techniques for ultra-wide bandgap III-nitride semiconductors provide the means to explore a new group of materials with the promise of significant radiation resistance. Additional benefits resulting from the use of ultra-wide bandgap materials include a reduction in leakage current and higher operating voltage without a loss of energy transfer efficiency. This paper describes the development of a novel plasma-enhanced pulsed laser deposition system for the growth of cubic boron nitride semiconducting thin films, which will be used to construct pn junction devices for alphavoltaic applications.

INTRODUCTION

Alphavoltaic Device Concept

There are a number of space power applications where sufficient quantities of solar photons are not available, and chemical-based battery technology is not an optimum choice. As a result, there has been renewed interest recently in the concept of a radioisotope based battery, which is a potential alternative to solar and chemical based technologies. The concept has been described by a number of authors [1-5], and reviewed in detail by Olsen [6]. The basic idea consists of capturing highly energetic particles (such as those emitted from various radioisotopes) by a semiconductor device capable of converting the particle energy to electrical energy. Perhaps the most significant demonstration of the concept to date used silicon pn junction diodes with Pm-147 as a source of beta particles to obtain peak powers of 400 μ W in a physical package suitable for pacemaker applications [6]. The functionality of such a device is presently limited by tradeoffs resulting from the damage threshold of the semiconductor material versus the amount of available energy per particle, as well as the stopping power of the material for a specific particle type and energy. Concentrating on absorbing MeV-range alpha particles can theoretically lead to a higher energy conversion efficiency due to the comparatively large stopping power of most semiconductors for such particles, but this simultaneously leads to a probable reduction in overall device lifetime [7]. Therefore, in order to provide both the necessary output power levels and overall system lifetime, a suitable semiconductor with the required degree of radiation tolerance must be identified.

For the radioisotopes of interest, the energy of a single alpha particle is on the order of several MeV (5.5 MeV if using Am-241). Therefore, the bandgap energy of the semiconductor is largely irrelevant from a particle absorption standpoint. In fact, a single particle has sufficient energy to generate hundreds of thousands of electron-hole pairs or more. From a device perspective, then, a larger bandgap energy is preferred, as it will lead

¹ This work was supported by NASA under grant number NAG3-1971.

to a reduction in reverse leakage current and a higher value for the maximum attainable open circuit voltage. A larger bandgap energy also implies the potential for better radiation resistance due to generally stronger bond strengths. Rybicki, et. al. have demonstrated a SiC-based alphavoltaic battery, and although they found a significant initial power output, a degradation of 58% after 100 hours of exposure to a 5 millicurie Am-241 sample was observed [7]. In order to realize an alphavoltaic device with a useful lifetime, then, it is necessary to look to materials with even greater radiation resistance.

Cubic Boron Nitride

There exist a number of ultra-wide bandgap materials which, until recently, have been regarded more as insulators than actual semiconductors. Among these, diamond and the cubic phase of boron nitride exhibit a number of interesting properties beyond bandgap energies on the order of 6 eV, including hardness and good thermal conductivity (table 1). Although diamond appears to be an attractive candidate, especially as it has been found to be reasonably radiation-tolerant, so far efforts to obtain n-type diamond in particular have not yet produced the desired material [8,9]. In contrast, amphoteric doping has been possible in bulk samples of cubic boron nitride (formed by high temperature, high pressure techniques) for some time using beryllium and silicon [10]. In fact, reference [10] describes the fabrication of a blue/ultraviolet emitting pn junction fabricated from cubic boron nitride, strongly suggesting the potential for successfully fabricating a pn junction diode from the material for use in a high-energy betavoltaic or alphavoltaic application.

Table 1. Selected properties of h-BN, c-BN and diamond.

Property	hexagonal BN	cubic BN	Diamond
Density (g/cm ³)	2.26	3.45	3.52
Melting Point (K)	-	> 3000	3800
Lattice Constant (Å)	c=2.5, a = 6.661	3.615	3.567
Hardness (kg/mm ²)	-	9000	10000
Stiffness (10 ¹¹ dyne/cm ²)	33	71	-
Energy (eV)	3.63	6.4	5.45
Rel. Dielectric Constant	3.8	7.1	5.5
Doping Capabilities	-	n-type, p-type	p-type

OVERVIEW OF CUBIC BORON NITRIDE FILM GROWTH

Although fabrication of bulk cubic boron nitride is relatively straightforward (it is available commercially in powder form for example, at approximately \$25/gram), single phase thin films of cubic boron nitride still remain elusive despite numerous attempts using a variety of growth techniques [11-28]. Both chemical and physical vapor deposition techniques have been employed, both with and without some type of ion source. Many authors have reported the existence of the cubic phase of boron nitride in films grown by these and related methods, but there is no strong evidence that any cubic material has been obtained without the use of simultaneous ion bombardment, either pure N₂ or nitrogen-containing mixtures. Of all the methods discussed in the literature, the most popular seems to be ion-assisted pulsed laser deposition [17-23], which has produced some of the most convincingly cubic-containing films to date. However, there are no reports of actual nucleation of 100% cubic boron nitride, largely due to the extraordinary lattice mismatch between the film and the (001) silicon substrates commonly employed. Instead, the interfacial layer is almost always reported to be amorphous or at best a mixture of amorphous and turbostratic phases of boron nitride. However, there are reliable reports of films containing at least some fraction of the cubic phase, indicating that the cubic phase is formed some time after film nucleation.

Reference 24 describes a mechanism whereby the crucial parameter determining whether a film is cubic or not is actually the momentum of the bombarding ions. The fact that a number of groups have reported a relatively sharp threshold in terms of the bombarding ion energy (and hence the ion momentum) required to obtain

cubic as opposed to purely hexagonal films lends support to this explanation. Furthermore, almost all ion-assisted reports (mostly Kauffman-type ion sources) mention that resputtering of the film is observed if the ion energy is further increased, so that a window of ion energy exists in which it is possible to obtain cubic-containing films. There still exists some question as to the exact mechanisms at work, but compressive stress induced by ion bombardment is consistent with the fabrication techniques employed to form bulk samples of cubic boron nitride. However, although it is clear that ion bombardment plays a role in the formation of the cubic phase, it is also clear that some type of activated nitrogen is required in order to grow stoichiometric films, as the binding energy of molecular nitrogen is 9.9 eV. Substrate temperatures sufficient to disassociate the nitrogen are impractical, so an alternative is required.

Another difficulty encountered in duplicating reported techniques for successful growth of mostly cubic boron nitride thin films is that there exist a number of complications in almost every type of characterization measurement employed. The result is a great deal of skepticism with regard to whether thin films ($< 1000 \text{ \AA}$) on substrates with enormous lattice mismatch to cubic boron nitride (e.g. silicon, the most commonly employed substrate) possess more than a small fraction of cubic sp^3 bonded material. Although infrared measurements frequently suggest the presence of sp^3 bonded BN, there also exists a wurtzitic phase of BN that is also sp^3 bonded. Perhaps the most detailed description of such difficulties is given in reference 27, which suggests that many reports of cubic boron nitride films are in error, in part because of similarities between the signature features of the hexagonal and cubic phases, as well as interactions involving the silicon substrate that can lead to the incorrect conclusion that the cubic BN phase is present. The authors of reference 27 even point out that some of their own work incorrectly led to the conclusion that cubic boron nitride had been deposited, due to contamination of the sample with copper, which is closely lattice matched to cubic boron nitride. Thus, it will likely be necessary to achieve a distinctly high quality single phase film of cubic boron nitride that can be characterized by luminescence-based techniques in order to unambiguously establish a technique as successful.

In order to achieve device-quality p- and n-type single-phase thin layers of cubic boron nitride, it is unlikely that the phase conversion/compressive strain/ion bombardment approach will prove sufficient. Even if nearly 100% of the film could be converted to the cubic phase, the extremely high defect density resulting from both ion bombardment and severe lattice mismatch between the film and typical substrate choices will make the realization of efficient devices impossible. Beyond such critical issues, it should also be pointed out that the film growth techniques described result in amorphous or polycrystalline morphologies characterized by grain sizes typically on the order of 100 \AA , which can also seriously reduce device efficiency through grain boundary transport effects. In order to realize practical devices, a different approach is clearly required. In this work, a pulsed laser deposition system has been modified to incorporate an inductively coupled nitrogen plasma source capable of delivering atomic nitrogen to the surface of the growing film, in contrast to ionized molecular nitrogen. The necessary boron flux is provided through ablation of a pure boron target by a pulsed ultraviolet-wavelength laser.

PLASMA-ENHANCED PULSED LASER DEPOSITION

Technique Description

Pulsed laser deposition (PLD) is a common technique for growth of a variety of thin film materials, including insulating coatings, superconducting ceramics and semiconductors. Depending on deposition parameters (especially substrate temperature), amorphous, polycrystalline or single-crystal epitaxial layers may be formed. The basic technique consists of mounting a target inside a vacuum chamber in proximity to a heated substrate. The target is evaporated by focusing a laser beam through a window, usually with the target rotated to prevent cratering and to maximize the target life (Figure 1). Initially PLD was accomplished using Q-switched Nd:YAG lasers, which typically provide $\sim 10\text{-}100 \text{ mJ}$ in a pulse of approximately 10 ns duration, delivering on the order of megawatts of optical power to the ablation target. However, infrared lasers such as the Nd:YAG ($\lambda = 1064 \text{ nm}$) ablate the target through a thermal process, which is typically characterized by a nontrivial amount of particulate expulsion that can seriously affect the film morphology. It is now common practice to employ an ultraviolet wavelength laser such as an ArF or XeCl excimer ($\lambda = 193 \text{ nm}$ and 308 nm , respectively) or even a frequency tripled or quadrupled Nd:YAG laser ($\lambda = 355 \text{ nm}$ and 266 nm , respectively). The ultraviolet wavelengths appear to ablate many targets through a more electronic (i.e. bond-breaking) process rather than a purely thermal process, resulting in significantly reduced particulate damage to the growing film. Although it is essentially a

physical vapor deposition technique, PLD presents a number of interesting opportunities for enhanced chemical interaction at the substrate, as the vapor plume leaving the ablation target is frequently associated with a plasma, especially if there is any interaction between the plume and the incoming laser beam. The introduction of reactive gases or dense plasmas other than those generated by the laser ablation process can be also be used in PLD, providing the opportunity for unique types of non-equilibrium film growth processes.

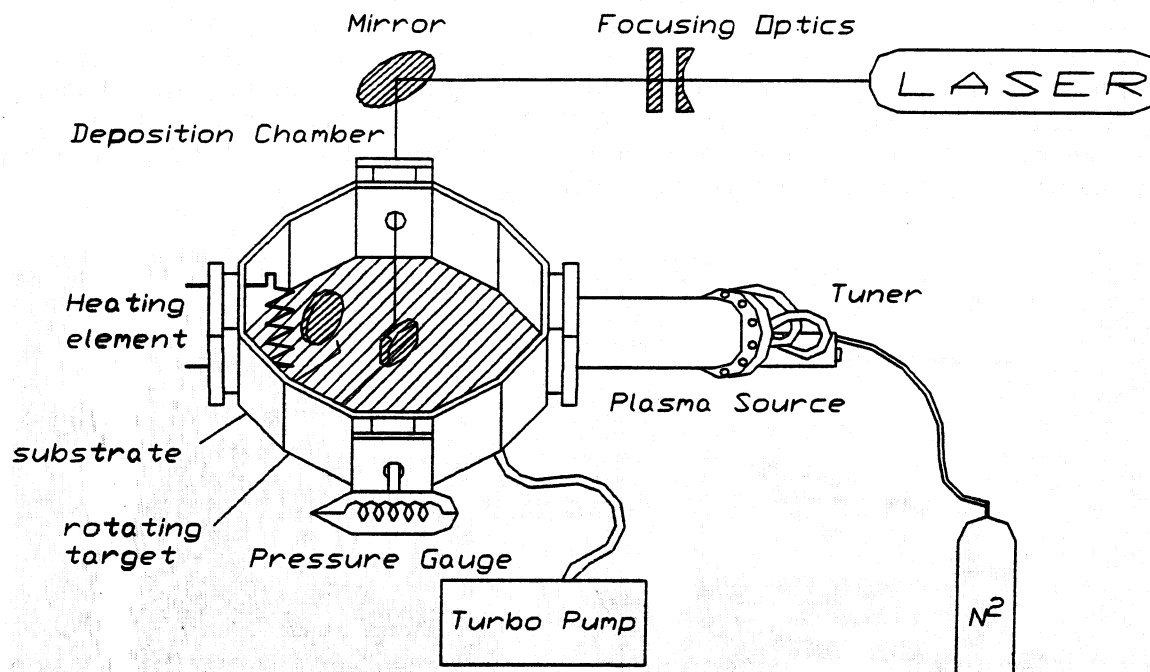


Figure 1: Schematic of plasma-enhanced pulsed laser deposition system.

Chamber Description/ Experimental Setup

Although a number of groups have attempted laser-based techniques for growth of cubic boron nitride, only ion-assisted methods seem to be successful, at least from a reproducibility standpoint. In all cases, however, the actual process seems to be a conversion of the growing film from non-cubic phases to some type of partially-cubic mixed-phase material, most likely in response to ion bombardment. Recent comparison studies of molecular beam epitaxy (MBE) growth of GaN material using different types of nitrogen sources suggest that an alternative may be possible. Hughes, et. al. recently compared an electron cyclotron resonance (ECR) plasma source and an inductively coupled RF plasma source under similar conditions to determine which source is better suited to growth of high-quality GaN [28]. As part of the study, the emission spectra from both plasma sources were measured using a monochromator [28]. Results of the measurements indicate that the ECR source produces a plasma that contains a large fraction of excited states of both neutral and ionized molecular nitrogen, but very little atomic nitrogen (at least under the power levels and N₂ flow rates employed) [28]. In direct contrast to this, excited states of atomic nitrogen were observed using the RF source, and no evidence of molecular nitrogen ions was found [28]. The conclusion of the study (based on characterization of the GaN films) was that the RF source was superior to the ECR source, most likely due to the ability of the source to deliver atomic nitrogen to the growing film.

Based on the MBE-based GaN literature, an existing PLD vacuum chamber was modified to include an EPI model EPI-RF-450-G-N UNI-Bulb N₂ RF plasma source (Figure 2). Since the EPI source was designed for use in an MBE system, it was necessary to modify the configuration in order to install the unit on the PLD chamber. In particular, an external sleeve was required over the plasma source to accommodate the 12.5" in-vacuum length of the unit and to match the 4.5" conflat plasma source flange to the 2.75" conflat flange on the PLD chamber. Also, a tantalum extension tube (Figure 3) was mounted on the plasma source to direct the plasma

into the PLD chamber and towards the substrate assembly. A capacitive tuning unit is then mounted directly on the end of the plasma source, and is used to provide impedance matching between the 600 W 13.56 MHz RF power supply and the plasma source. Operation of the plasma source consists of first pumping down the chamber to $\sim 1 \times 10^{-6}$ Torr base pressure using a turbomolecular pump, and then introducing 99.9995% purity N_2 gas through a leak valve mounted on the plasma source. The RF power supply is dialed to a setpoint of 200 W, and the tuning unit is used to adjust for any impedance mismatch. If the plasma does not ignite at that point, the flow rate of N_2 must be temporarily increased. Once a plasma has been established, there exists an appreciable impedance mismatch, as the plasma now acts as a lossy secondary inductance coupled to the plasma source coils. Typical chamber pressures during the presence of a high-brightness plasma are on the order of 5×10^{-6} to 1×10^{-4} Torr. The most dramatic visual effect is the intense orange glow emanating from the plasma source, in contrast to the purplish glow observed in capacitively-coupled RF and ECR nitrogen plasmas. According to the spectroscopic analysis in reference 28, the orange plasma corresponds to excited states of atomic nitrogen, and the purple glow in other N_2 plasmas corresponds to the 1st negative transitions of N_2^+ molecular ions.



Figure 2: Photograph of PLD system modified to include nitrogen plasma source. The tuning unit used to minimize reflected power is shown unmounted and off to the left in the photo.

The source of boron for growth of BN films is a 99.9% purity 1" diameter x 0.25" thick boron target mounted on a rotating holder. This is one of the advantages to using PLD as opposed to thermal evaporation techniques such as MBE: low vapor pressure targets such as boron can be evaporated easily without the need for high-temperature sources. The rotation of the target prevents cratering where the laser is focused, and increases the lifetime of the target. The laser presently used is a frequency quadrupled ($\lambda = 266$ nm) Spectra Physics model DCR3G Nd:YAG laser, which is also capable of operation at 1064, 532 and 355 nm. The ultraviolet lines (266 and 355 nm) are preferable for laser ablation, in that the target is ablated more smoothly and less particulate emission is obtained than with infrared lines. Up to 80 mJ per pulse (~ 5 ns for the 266 nm line) can be focused through the laser port window onto the target to obtain a boron flux. The heated substrate is parallel to the target, with the distance adjustable from about 1.5 to 4". At present, there is no means of measuring the boron or atomic nitrogen

fluxes in-situ, so they must be estimated by measuring the film thickness after growth. With the plasma source on-line, present efforts are directed towards initial depositions of BN films, and characterization by Xray diffraction, FTIR, SEM and optical spectroscopy. Once adequate material quality is obtained, the next phase is to explore both in-situ and ex-situ means of doping the layers in order to form pn junction diodes for testing under alpha and beta particle irradiation.

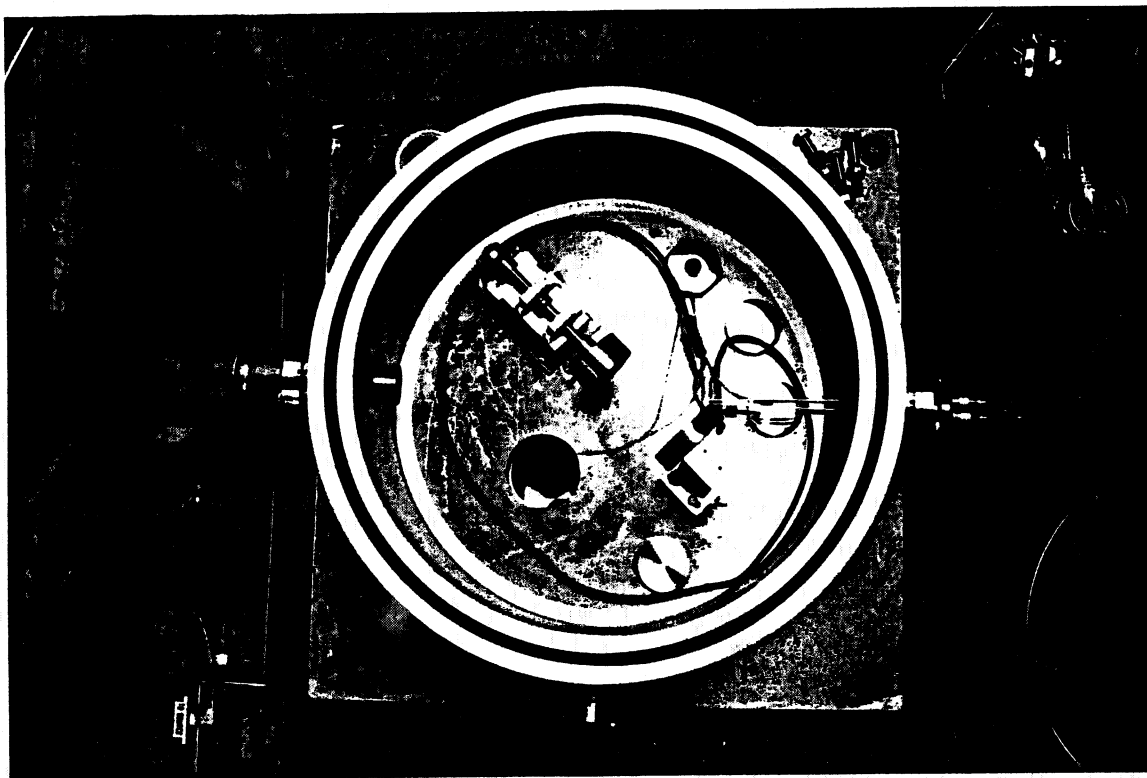


Figure 3: Interior view showing tantalum extension tube used to direct plasma flow. The substrate mounting assembly and target rotator are not in growth position, where the extension tube lines up with the substrate.

SUMMARY

In order to effectively implement the concept of an alphavoltaic device, it is necessary to develop the capability to fabricate devices with a significant degree of radiation resistance. The best possible approach is to utilize a material with an inherent ability to withstand the expected radiation environment, such as cubic boron nitride. Additional benefits of cubic boron nitride based devices include a reduction in leakage current and large open circuit voltages as a result of the ultra-wide bandgap (~6.4 eV). Previous attempts to obtain high-quality single phase thin films of the material have resulted in mixed phase or amorphous films, with any cubic content resulting from compressive strain induced by ion bombardment. An alternative approach to cubic boron nitride film growth is proposed, in which atomic nitrogen is provided directly to the substrate in what is termed plasma-enhanced pulsed laser deposition. The non-equilibrium growth inherent to PLD in conjunction with atomic nitrogen is expected to provide the means to directly nucleate the cubic phase in order to obtain device-quality semiconductor material.

REFERENCES

- [1] W.G. Pfann and W. Van Roosbroeck, "Radioactive and photoelectric p-n junction power sources", *Journal of Applied Physics* 25 (1954), p. 1422.
- [2] P. Rappaport, J.J. Joferski and E.G. Linder, "The electron-voltaic effect in germanium and silicon p-n junctions", *RCA Review* 17 (1956), p. 100.
- [3] H. Flicker, J.J. Loferski and T.S. Elleman, "Construction of a promethium-147 atomic battery", *IEEE Transactions on Electron Devices* ED-11 (1964), p. 2.
- [4] L.C. Olsen, "Betavoltaic energy conversion", *Energy Conversion* 13 (1973), p. 117.
- [5] L.C. Olsen, "Advanced betavoltaic power sources", *Proceedings of the 9th Intersociety Energy Conversion Engineering Conference* (1974), p. 754.
- [6] L.C. Olsen, "Review of betavoltaic energy conversion", *Proceedings of the 12th Space Photovoltaics Research & Technology Conference*, Cleveland, OH (June 1992), p. 256.
- [7] G. Rybicki, C. Vargas-Aburto and R. Uribe, "Silicon carbide alphavoltaic battery", *Proceedings of the 25th IEEE Photovoltaics Specialists Conference*, Crystal City, VA (May 1996), p. 93.
- [8] H. Hofsäss, M. Dalmer, M. Restle and C. Ronning, "Substitutional phosphorus doping of diamond by ion implantation", *Journal of Applied Physics* 81 (1997), p. 2566.
- [9] R. Roychoudhury, E.J. Charlson, T. Stacy, M. Hajsaid, E.M. Charlson and J.M. Meese, "Growth and characterization of phosphorus doped diamond films using trimethyl phosphite as the doping source", *Journal of Applied Physics* 81 (1997), p. 3644.
- [10] O. Mishima, K. Era, J. Tanaka and S. Yamaoka, "Ultraviolet light-emitting diode of a cubic boron nitride pn junction made at high pressure", *Applied Physics Letters* 53 (1988), p. 962.
- [11] J.J. Pouch and S.A. Alterovitz, ed., Synthesis and Properties of Boron Nitride, *Materials Science Forum*, Volumes 54 & 55 (1990), Trans Tech Publications, Ltd., Brookfield, VT.
- [12] T. Ichiki and T. Yoshida, "Growth of cubic boron nitride films by low-pressure inductively coupled plasma enhanced chemical vapor deposition", *Japanese Journal of Applied Physics* 33 (1994), p. 4385.
- [13] P. Lin, C. Deshpandey, H.J. Doerr, R.F. Bunshah, K.L. Chopra and V. Vankar, "Preparation and properties of cubic boron nitride coatings", *Thin Solid Films* 153 (1987), p. 487.
- [14] H.Hofsass, C. Ronning, U. Griesmeier, M. Gross, S. Reinke and M. Kuhr, "Cubic boron nitride films grown by low energy B+ and N+ ion beam deposition", *Applied Physics Letters* 67 (1995), p. 46.
- [15] O. Tsuda, Y. Yamada, T. Fujii and T. Yoshida, "Preparation of cubic boron nitride films by radio frequency bias sputtering", *Journal of Vacuum Science and Technology A* 13 (1995), p. 2843.
- [16] R. Clarke, C.A. Taylor, G.L. Doll, and T.A. Perry, "New developments of epitaxial cubic boron nitride and diamond films on silicon", *Diamond and Related Materials* 1 (1992), p. 93.
- [17] W. Pflöging, T. Klotzbucher, D.A. Wesner, E.W. Kreutz, "Structure and chemical composition of BN thin films grown by pulsed-laser deposition", *Diamond and Related Materials* 4 (1995), p. 370.

- [18] M.S. Athwal, A. Mele, and E.A. Ogryzlo, "Techniques for depositing DLC films by pulsed laser ablation of organic solids", *Diamond and Related Materials* 1 (1992) p. 731.
- [19] T.A. Friedmann, P.B. Mirkarami, D.L. Medlin, K.F. McCarty, E.J. Klaus, D.R. Boehme, H.A. Johnsen, M.J. Mills, D.K. Ottesen and J.C. Barbour, "Ion-assisted pulsed laser deposition of cubic boron nitride films", *Journal of Applied Physics* 76, (1994), p. 3088.
- [20] G.L. Doll and J.A. Sell, "Growth and characterization of epitaxial cubic boron nitride films on silicon", *Physical Review B* Vol. 43 (1991), p. 43.
- [21] T. Klotzbucher, W. Pflöging, D.A. Wesner, M. Mergens, E.W. Kreutz, "Structural and chemical characterization of BN thin films deposited onto Si(100) and graphite substrates by pulsed laser deposition", *Diamond and Related Materials* 5 (1996), p. 525.
- [22] F. Qian, V. Nagabushnam and R.K. Singh, "Pulsed laser deposition of cubic boron nitride films on silicon substrates", *Applied Physics Letters* 63 (1993), p. 317.
- [23] G. Reisse, S. Weissmantel, B. Keiper and A. Weber, "Properties of pulsed laser deposited boron nitride films", *Applied Surface Science* 108 (1997), p. 9.
- [24] D.J. Kester and R. Messier, "Phase control of cubic boron nitride thin films", *Journal of Applied Physics* 72 (1992), p. 504.
- [25] K. Kaneda and K. Shibata, "A comparison of the effects of RF plasma discharge and ion beam supply on the growth of cubic boron nitride films formed by laser physical vapor deposition", *Japanese Journal of Applied Physics* 33 (1994), p. 266.
- [26] H. Xin, X. Shi, C. Lin, W. Xu, L. Zheng and S. Zou, "Phase evolution in boron nitride thin films prepared by a dc-gasdischarge assisted pulsed laser deposition", *Thin Solid Films* 293 (1997), p. 17.
- [27] K.F. McCarty, M.J. Mills, D.L. Medlin and T.A. Friedmann, Comment on "Growth and characterization of epitaxial cubic boron nitride films on silicon", *Physical Review B* 50 (1994), p. 8907.
- [28] W.C. Hughes, W.H. Rowland, Jr., M.A.L. Johnson, S. Fujita, J.W. Cook, Jr., J.F. Schetzina, J. Ren and J.A. Edmond, "Molecular beam epitaxy growth and properties of GaN films on GaN/SiC substrates", *Journal of Vacuum Science and Technology B* 13 (1995), p. 1571.

InGaAs/InP MONOLITHIC INTERCONNECTED MODULES (MIM) FOR THERMOPHOTOVOLTAIC APPLICATIONS

David M. Wilt
NASA Lewis Research Center
Cleveland, Ohio 44135

Navid S. Fatemi, Phillip P. Jenkins, Victor G. Weizer, and Richard W. Hoffman, Jr.
Essential Research, Inc.
Cleveland, Ohio 44122

David A. Scheiman
NYMA, Inc.
Brook Park, Ohio 44142

Christopher S. Murray and David R. Riley
Westinghouse Electric Corporation
West Mifflin, PA 15122

Abstract

There has been a traditional trade-off in thermophotovoltaic (TPV) energy conversion development between system efficiency and power density. This trade-off originates from the use of front surface spectral controls such as selective emitters and various types of filters. A monolithic interconnected module (MIM) structure has been developed which allows for both high power densities and high system efficiencies. The MIM device consists of many individual indium gallium arsenide (InGaAs) devices series-connected on a single semi-insulating indium phosphide (InP) substrate. The MIMs are exposed to the entire emitter output, thereby maximizing output power density. An infrared (IR) reflector placed on the rear surface of the substrate returns the unused portion of the emitter output spectrum back to the emitter for recycling, thereby providing for high system efficiencies.

Initial MIM development has focused on a 1 cm² device consisting of eight series interconnected cells. MIM devices, produced from 0.74 eV InGaAs, have demonstrated $V_{oc} = 3.2$ volts, $J_{sc} = 70$ mA/cm² and a fill factor of 66% under flashlamp testing. Infrared (IR) reflectance measurements ($>2 \mu\text{m}$) of these devices indicate a reflectivity of $>82\%$. MIM devices produced from 0.55 eV InGaAs have also been demonstrated. In addition, conventional p/n InGaAs devices with record efficiencies (11.7% AM0) have been demonstrated.

Introduction

In thermophotovoltaic energy conversion, an emitter is heated to incandescence and a photovoltaic device is placed in view of the emitter to convert the radiant energy into electrical energy. Research in TPV has been renewed recently, due to the development of new emitter, filter and photovoltaic cell technology. Most current efforts in TPV research have concentrated on using front surface spectral control elements such as selective emitters^[1] or graybody emitters combined with plasma, dielectric or dipole filters^[2, 3] in order to improve system efficiency to the 20–40% range predicted by theory^[4].

The front-surface spectral control approach tends to produce systems with low power density (W/cm²). Selective emitters, for example, have demonstrated in-band emittances which range from 0.7 to 0.8,^[5] with efficiencies of ~40% (i.e. 40% of the emitted energy is convertible by the photovoltaic device). In order to

recuperate the non-convertible energy, filters are used to reflect the long-wavelength photons back to the selective emitter. Unfortunately, there are no filters available which provide both 100% transmission in the usable wavelength region and 100% reflection everywhere else. Thus, a selective emitter emittance of 0.8, coupled with a typical filter transmission of 80% leads to a reduction in the power density of 36%. This is an expensive loss, particularly given the cost of TPV cells. Grey body emitter based systems have similar power density problems.

A different approach involves the use of rear-surface spectral controls. Using this technique, the entire radiant output from the emitter is incident upon the photovoltaic (PV) device, thereby providing high output power densities. Photons which the PV device is unable to convert pass through the cell structure, reflect off of a rear reflector and are returned to the emitter for recycling. Researchers have developed TPV cells which utilize low-doped substrates and reflective rear contacts to provide photon recycling^[6, 7]. Other researchers have developed series-interconnected, monolithic cells for laser, fiber-optic and TPV applications^[8, 9]. We are developing a cell which combines the advantages of both of these approaches.

The Monolithic Interconnected Module or MIM consists of series-connected indium gallium arsenide (InGaAs) devices on a common, semi-insulating indium phosphide (InP) substrate (Fig. 1). An infrared reflector is deposited on the rear surface of the InP substrate to reflect photons back toward the front surface of the cell. This provides a second pass opportunity for photons capable of being converted by the cell. In addition, long wavelength photons are returned to the emitter for "recycling", improving the system efficiency.

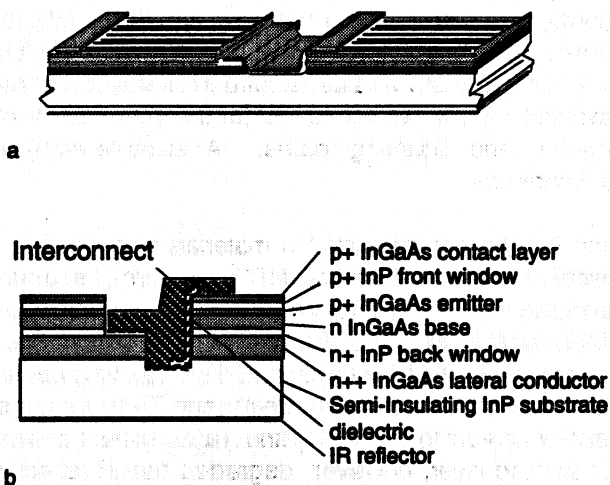


Figure 1.—a) 3-dimensional view of two cells of a MIM. b) a cross-sectional view of a MIM showing the individual layers and interconnect scheme.

The MIM design offers several advantages compared to conventional TPV cell designs. First, small series-connected cells provide high voltages and low currents, thereby reducing I^2R losses. In addition, the small size of the cells allow an array to be comprised of series/parallel strings rather than a single series-connected string of larger cells. This should improve the reliability of the TPV module since the failure of a single cell would not debilitate the entire array. Second, the MIM design maximizes output power density since losses associated with front-surface spectral controls are eliminated.

Third, the rear surface of the device is not electrically active, therefore the cell may be directly bonded to the substrate/heat sink without concern for electrical isolation. This greatly simplifies the array design and improves the thermal control of the cells. Fourth, the array may easily be designed with differing cell sizes to reduce view factor losses and losses associated with non-uniform emitter temperatures. Last, photons which are weakly absorbed have the possibility of multiple passes through the cell structure. This feature is particularly important for lattice-mismatched devices, where poor minority carrier diffusion length can be partially offset by making the cell thin, forcing the carrier generation to occur closer to the p/n junction.

Materials Development

The MIM structures were deposited in a horizontal, low-pressure organo-metallic vapor phase epitaxy (OMVPE) reactor described elsewhere^[10]. The precursor materials were trimethyl indium (TMIn), trimethyl gallium (TMGa), arsine, phosphine, diethyl zinc (DEZn) and silane for p and n doping respectively. Several test growths were conducted to determine the compositional, thickness and doping uniformity of InGaAs across the 2-in. diameter substrate. Secondary electron microscopy analysis indicates the thickness variation was $\pm 3\%$ in the axial direction and $\pm 9\%$ in the perpendicular direction (exclusive of a 5-mm wide region at the perimeter of the substrate). These results were consistent from run to run. Double crystal x-ray rocking curve measurements indicated a variation in InGaAs composition of $\pm 0.7\%$ (relative) in the axial direction and $\pm 0.4\%$ (relative) in the perpendicular direction. This compositional uniformity was reproducible from run to run, although we did observe a variation in the absolute composition of $\pm 0.5\%$ In. This was attributed to a variation in the transport efficiency of the TMIn source.

Hall measurements were conducted for both n-type (Si doped) and p-type (Zn doped) InGaAs to map the doping distribution over the 2-in. diameter substrates. The results indicate a variation of $\pm 14\%$ in the axial direction and $\pm 42\%$ in the perpendicular direction for the n-type material and $\pm 2\%$ in the axial direction and $\pm 4\%$ in the perpendicular direction for the p-type material. The p-type result is consistent with the compositional and thickness uniformity observed for this sample. The variation observed for the n-type material in the perpendicular direction is believed to be due to enhanced SiH₄ cracking caused by the close proximity of the hot chamber walls. We are examining the use of alternative dopants or modified reactor geometry to reduce this variation.

The MIM device requires dielectric isolation for the interconnect. Three different dielectrics were tested for their suitability. The three materials were e-beam evaporated Ta₂O₅, spin on glass (SOG) and plasma-enhanced chemical vapor deposited (PECVD) Si₃N₄. A test structure was developed to characterize the deposited material for dielectric constant, resistivity and breakdown strength, as well as to test for the presence of pin hole defects. Both the Ta₂O₅ and SOG contained many pinholes and shunting paths. A suitable layer of Si₃N₄ was developed which demonstrated a resistivity of $>10^{10}$ ohm-cm.

Several different contact and IR reflector metallization materials were tested. The important requirements for these materials were: 1) low specific contact resistance (10^{-6} ohm-cm²) for both n and p-type InGaAs, 2) good adhesion between the metallization and the InP, InGaAs and the dielectric, and 3) good IR reflection ($>95\%$) for the IR reflector material. The initial tests were conducted with the Au-Ge-Au contacts used in our planar cell development^[11]. This material provided excellent contact resistivity and IR reflectivity, but had poor adhesion to the dielectric. We also tested Ag-Au, Cr-Au and Ti-Au and found that the Cr-Au and Ti-Au demonstrated acceptable resistivity (mid 10^{-6} ohm-cm²) as well as excellent adhesion to the Si₃N₄ and Ta₂O₅ dielectric films and is being used for the MIM contacts. The addition of the Cr sticking layer, however, degraded the IR reflectivity. The devices reported here utilized an Au IR back surface reflector (BSR).

Device Design

A p/n cell configuration (Fig. 1) was chosen for several reasons. First, the free carrier absorption for n-type InGaAs is significantly lower than for p-type, as will be addressed in the following section. Thus, the p/n configuration minimizes the areal density of holes, making it optimum in terms of optical recuperation. Second, the MIM design requires a thick rear conductor layer to conduct current the length of the device (laterally), to reach the back contact/interconnect. The p/n configuration takes advantage of the 25x higher mobility for n-type InGaAs in this conductor layer, reducing the resistive losses.

Finally, an increase in the optical bandgap of the n⁺⁺ conductor layer material (see below) permits the use of a thin base region. Bandedge photons which are not absorbed in the base region are able to pass through the n⁺⁺ layer without being absorbed. These photons reflect off the rear reflector and have a second chance of being absorbed in the base region.

Initial device configurations for both 0.74 and 0.55 eV InGaAs MIM's illuminated by a 1200 °K blackbody were developed (Fig. 2). The thickness' and doping levels of the lateral conduction layers and emitter layers were chosen to limit the resistive losses to 1% for each layer. The base thickness (2 microns) was intentionally produced for incomplete absorption in a single pass in order to take advantage of the BSR.

The optical efficiency of the 0.74 eV MIM device (long wavelength reflectivity) was modeled by determining the free carrier absorption (FCA) for both n- and p-type InGaAs as a function of dopant type, level, thickness and wavelength. Calibration samples with doping levels ranging from 5×10^{18} to $3 \times 10^{19} \text{ cm}^{-3}$ were fabricated on semi-insulating InP substrates. Absorption measurements were conducted using a spectrophotometer for the near IR (1–3 μm) and an FTIR for the mid IR (3–10 μm).

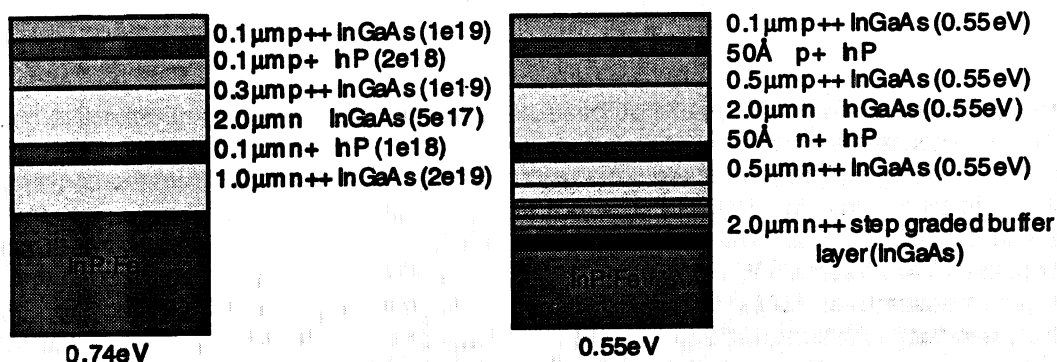


Figure 2.—0.74 and 0.55 eV device structures for operation with a 1200 K blackbody.

The spectrophotometer absorption data (Fig.3) shows several interesting features. First, the absorption for p-type material is significantly higher than for n-type material. Second, the n-type material has an apparent bandgap which is significantly higher (0.3 eV) than the equivalent composition p-type material. This shift in absorption is due to a Burstein-Moss shift.

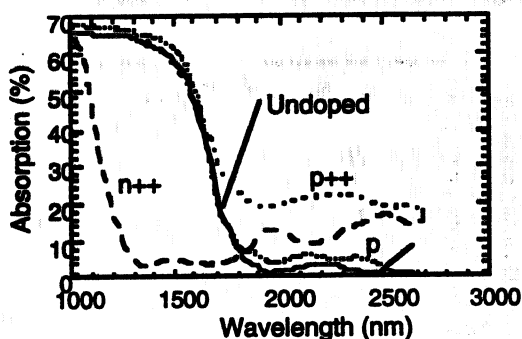


Figure 3.—Absorption data for $\text{In}_{0.55}\text{Ga}_{0.45}\text{As}$ with various doping types and densities.

Device Performance

Conventional planar p/n InGaAs devices were produced using the active cell layers shown in Figure 2a (note: the emitter doping was reduced to $1 \times 10^{18} \text{ cm}^{-3}$ for these devices) in order to verify the basic material quality. The I-V curve shown in Figure 4 demonstrates the quality of the baseline devices. The efficiency (11.7% AM0) represents a record for 0.74 eV p/n InGaAs. Calculations indicate that reducing the grid shadowing from the 16% on the test device to the 5% normally used in AM0 devices would increase the efficiency to >13%, a record for any 0.74 eV InGaAs (p/n or n/p).

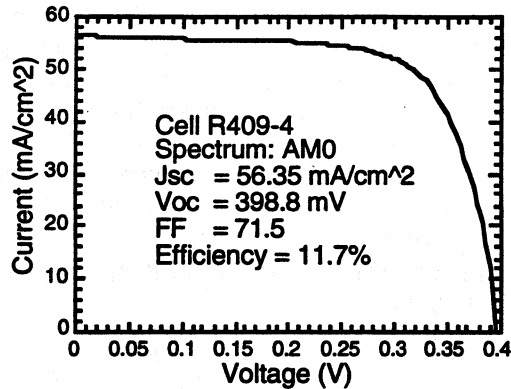


Figure 4.—I-V curve for baseline p/n cell

The external quantum efficiency for a 0.74 eV baseline device with a dual layer anti-reflective coating is shown in Figure 5. As was stated earlier, the base region was intentionally grown thin so that the effect of the BSR would be demonstrated. It was initially puzzling to observe the high bandedge photoresponse from the conventional cell (with no BSR). Optical modeling indicates that only 62% of the bandedge photons (1600 nm) are absorbed in the thin base region, assuming a single pass. Thus, the internal QE could not be greater than 62%. At 1600 nm the baseline device demonstrated a 74% internal QE (66% external QE, 10% reflection). The transmission characteristic of a n⁺ InP substrate was measured at 1600nm and indicated >45% transmission (not corrected for absorption and reflection). Thus, bandedge photons are able to reach the back contact, which is a very reflective, non-alloyed Au based contact. It is believed that this contact acts as a BSR, reflecting the bandedge photons back toward the active cell region. Our past p/n devices had all utilized a sintered contact, which forms a highly absorbing Au₂P₃ compound at the semiconductor/metal interface. The QE characteristics of these devices did not demonstrate this enhanced bandedge photoresponse.

A negative aspect of this feature is that the reflection is diffuse in nature. Thus non-convertible photons may be totally internally reflected and add to the thermal load of the cell. A benefit of the diffuse reflection is that convertible photons will generally have a longer path length in the active cell layers, improving the probability for absorption. Given the high absorption coefficient for InGaAs, this is a marginal benefit.

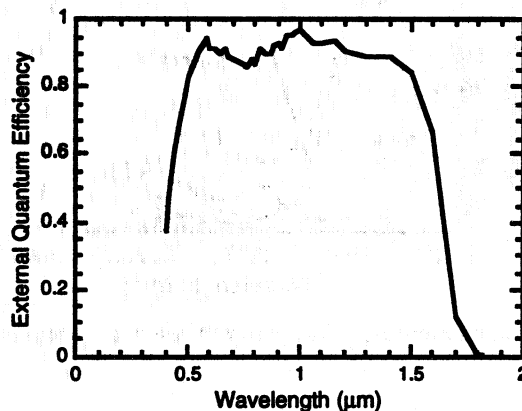


Figure 5.—External quantum efficiency for the 0.74 eV baseline InGaAs device.

The I-V curve for a 0.74eV MIM device is shown in Figure 6 under flashlamp testing. The data indicates an average voltage of 400 mV per cell. This particular device was produced prior to the development of the high quality Si₃N₄ dielectric and, therefore, is not expected to demonstrate optimum performance. The external QE curve for the 0.74eV device is shown in Figure 7 (without an anti-reflective coating). The QE data represents the aggregate worst

response from across the entire device, given the series interconnected nature of the MIM design. This device is expected to produce 48.5 mA when illuminated by a 1200 K blackbody emitter with a view factor of 1.

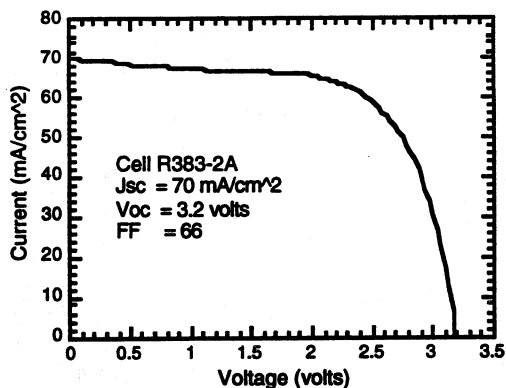


Figure 6.—I-V characteristic of 0.74 eV MIM under flashlamp testing (10 °C).

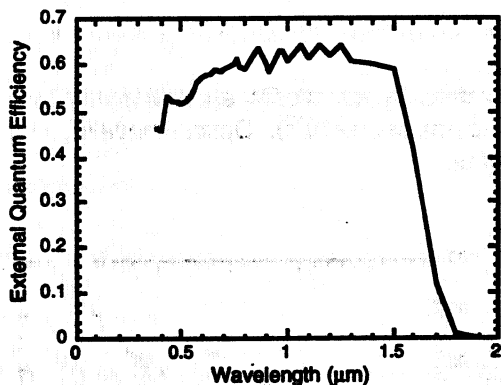


Figure 7.—External QE OF 0.74 eV MIM device without anti-reflective coating.

A 0.55 eV MIM was produced to determine if there were any unforeseen difficulties or problems in producing a MIM from lattice mismatched material. Figure 8 shows the I-V characteristic of a 0.55 eV MIM under AM0 testing. As with the 0.74 eV device reported above, this cell was produced prior to the optimization of the dielectric material. Unfortunately, this device was destroyed prior to I-V testing at higher injection levels.

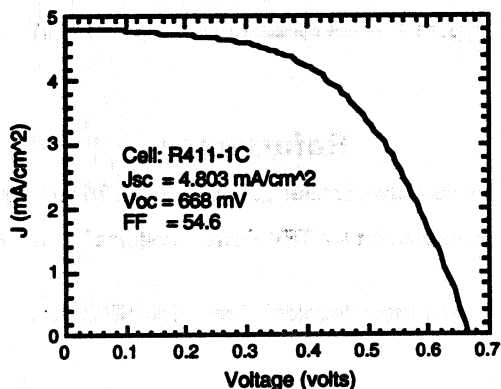


Figure 8.—AM0 I-V characteristic of 0.55 eV MIM (no AR).

Figure 9 shows the external QE characteristic for the 0.55 eV MIM (without AR). Given the rudimentary nature of the buffer layer used to produce this device and the limited development of the cell layers, the results were very promising.

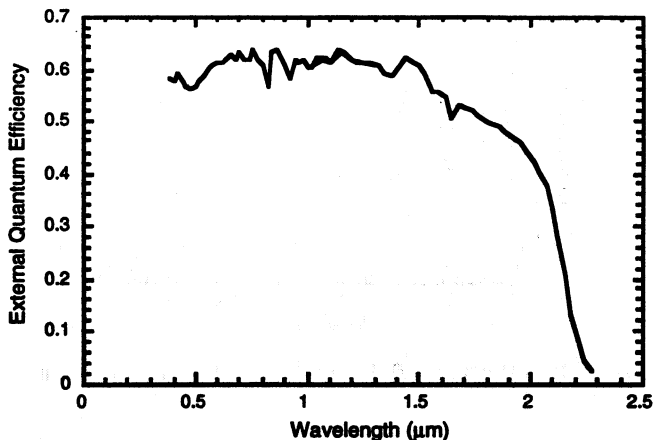


Figure 9.—External QE of 0.55 eV p/n MIM without AR.

Figure 10 shows the measured reflectivity for a 0.74 eV MIM device (without an AR coating). This particular device had a 3 μm LCL and a low doped emitter (1×10^{18}). Optical modeling suggests that IR reflectivity's of >90% are possible with optimized device structures.

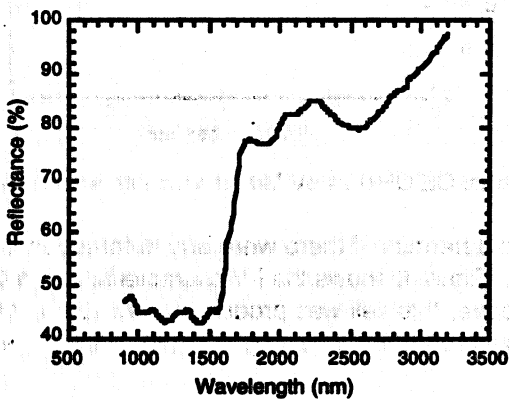


Figure 10.—IR reflectance of 0.74 eV MIM.

References

1. Chubb, D.L. and Lowe, R.L., "Thin-Film Selective Emitter", *J. Appl. Phys.* **79** (9), 1993, pp. 5687–5698.
2. Wilt, D.M., et al., "InGaAs PV Device Development for TPV Power Systems", 1st NREL Conf. on TPV Gen. of Elect., 1994, AIP 321, pp. 210.
3. Home, W.E., et al., "IR Filters for TPV Converter Modules", Proc. 2nd NREL Conf. on TPV Gen. of Elect., 1995, AIP 358, pp. 35.
4. Woolf, L.D., *Solar Cells* **19**, 19 (1986).

5. Chubb, D.L., et.al., "Review of Recent TPV Research at Lewis Research Center", Proc. 14th SPRAT Conf, 1995, NASA CP-3324, pp. 191.
6. Charache, G.W., et.al., "Thermophotovoltaic Devices Utilizing a Back Surface Reflector for Spectral Control", Proc. 2nd NREL Conf. on TPV Gen. of Elect., 1995, AIP 358, pp. 339.
7. Iles, P.A. and Chu, C.L., "TPV Cells with High BSR", Proc. 2nd NREL Conf. on TPV Gen. of Elect., 1995, AIP 358, pp. 361.
8. Wojtczuk, S., "Multijunction InGaAs Thermophotovoltaic Power Converter", Proc. 14th SPRAT Conf, 1995, NASA CP-3324, pp. 223.
9. Spitzer, M.B., et.al., "Monolithic Series-Connected Gallium Arsenide Converter Development", Proc. IEEE 22nd PVSC, (1991), pp. 142-146.
10. Wilt, D.M., et al., "Monolithically Interconnected InGaAs TPV Module Development", Proc. IEEE 25th PVSC, (1996), pp. 43-48.
11. Wilt, D.M., et.al., "High Efficiency InGaAs Photovoltaic Devices for TPV Power Systems", Appl. Phys. Lett. 64 (18), 1994.

Modeling of $\text{In}_{0.52}\text{Ga}_{0.48}\text{As}/\text{In}_x\text{Ga}_{1-x}\text{As}$ ($x>0.6$) Multiquantum Well Thermophotovoltaic Converter

I. Serdiukova, A. Freundlich

Space Vacuum Epitaxy Center, University of Houston, Houston Texas 77204

Abstract.

In this work the performance of a new thermophotovoltaic converter is investigated. Strained narrow band gap $\text{In}_x\text{Ga}_{1-x}\text{As} / \text{In}_{0.52}\text{Ga}_{0.48}\text{As}$ ($x>0.6$) multiple quantum wells (MQW) are introduced within the intrinsic region of a conventional $\text{In}_{0.52}\text{Ga}_{0.48}\text{As}$ p-i-n cell lattice matched to InP. An appropriate choice of well /barrier thickness and number of wells in the i-region maintains the pseudomorphism and lattice matching to InP. In principle, the presence of narrow band gap wells extends photon absorption up to that of confined energy states in wells.

The device characteristics such as open circuit voltage (V_{oc}), short circuit current (I_{sc}) and Spectral Response, have been calculated for 1000 to 1500 K black body emitter as a function of In composition, well/barrier thickness and number of wells in the MQW region (e.g. see figures). It is shown that the insertion of these narrow bandgap well extends the spectral response toward the infrared. A rough estimate shows that 20-40% of the incident power is available for conversion by such a MQW device for a 1500 K blackbody. The short circuit current I_{sc} of the p-i($\text{In}_x\text{Ga}_{1-x}\text{As} / \text{In}_{0.52}\text{Ga}_{0.48}\text{As}$ MQW)-n cell may therefore be substantially increased compared to that of a baseline p/n $\text{In}_{0.52}\text{Ga}_{0.48}\text{As}$ cell. Device open circuit voltage remains comparable (The voltage drop associated with increased dark current in MQW is compensated by the operation at a higher current).

In summary, for a typical low temperature TPV the strained p-i($\text{In}_x\text{Ga}_{1-x}\text{As} / \text{In}_{0.52}\text{Ga}_{0.48}\text{As}$ MQW)-n cells conversion efficiency is predicted to exceed twice that of its conventional counterpart.

Introduction.

A strong renewed interest in TPV in 1990's is due to recent developments in principal TPV system components. After have been proposed in 1960's,⁽¹⁾ a large number of investigations in 1960's-1980's was concentrated ⁽²⁾ on silicon or germanium TPV cells and high-temperature radiators (1500-2000 C°); current trend is toward lower radiator temperatures ^(3, 4), which necessitates the development of the low band gap (0.4-0.7 eV) TPV devices and efficient below band gap spectral control techniques.

Among materials with band gap energies in the range 0.5-0.8 eV, fit for the efficient conversion of radiant energy from heat sources in the temperature range 1200-1500 K, two materials, InGaAs (0.55 and 0.75 eV) and GaSb (0.72 eV), have been extensively studied. InP based strained 0.55 eV InGaAs devices produce higher currents, but suffer open circuit voltage losses compared to lattice matched 0.75 eV InGaAs. The MQW cell approach intends to avoid a strong coupling between an open circuit voltage and a short circuit current of a single solar cell. We realize this approach in the 0.75 InGaAs based Multi-Quantum-Well (MQW) solar cell (InP substrate). It combines the benefits of having higher current and voltage output and a relatively low strain.

Modeling.

Our model includes a thermal radiation source and low band gap MQW cell. Since it was meant to be general, it omits details like optical filter or reflector. The reflection coefficient of the cell itself has also been neglected. All calculations for the cell were done for the room temperature.

The dependence of critical thickness on composition for a single epitaxial layer and MQW is compared on Figure 1.

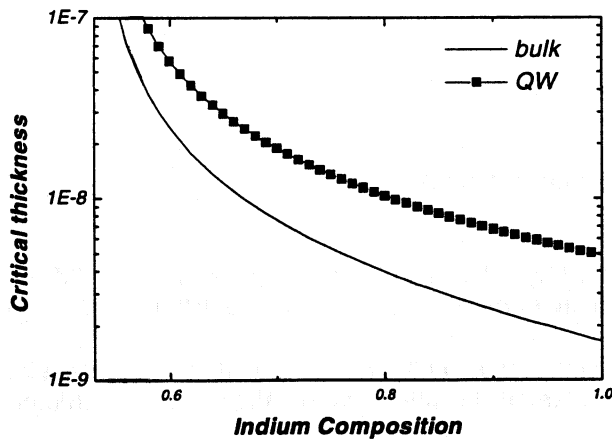


Figure 1. Critical thickness, m, vs. Indium Composition in $\text{In}_x\text{Ga}_{1-x}\text{As}$. For the single layer it was assumed that strain is equal to the half of misfit, $\varepsilon = f/2$.

Critical number of periods.

For the estimate of the maximum number of periods in MQW, the whole stack of layers is treated as a single epitaxial layer with the average lattice constant. The estimate of such a number of periods shows that it would be possible to realize structures with up to 10 period, but it would be necessary to use strain balancing to substantially increase this number.

Modeling of strain modifications to band structure.

For the modeling of MQW region, the strain induced modifications of (001) InGaAs band structure were modeled using parameters of ref. 7

The unstrained ternary compound band gap was interpolated from the binary components. Then, Van der Walle's 'model solid' theory⁽⁹⁾ was closely followed in describing the strain dependence of the valence and conduction band edges. The effective masses for heavy, light holes and electrons in unstrained material were linearly interpolated from GaAs and InAs values.

The modifications of the light hole and electron effective masses induced by strain along the quantification axis of the quantum well should also be taken into account in the calculation.^(9, 10) This was followed for the electron, but neglected for the light hole, since the well for it is shallow and its states are resonant with the barrier energy.

MQW absorption coefficient.

The calculation of the MQW structure absorption coefficient is based on the determining the confinement energies of the electrons and holes in quantum wells and Fermi's golden rule estimation of the absorption rate.

The confined energies of the electrons and holes are computed within a one-band model, since it can be shown that in the present case the correction from band non-parabolicity to the confined energies can be neglected.

The exciton binding energies are calculated using the method of ref.11 and parameters of ref.12. Following the calculation of confined energy levels, the absorption coefficient is calculated from Fermi's golden rule⁽¹³⁾. First three confined energy states and excitonic effects for the ground state were accounted for.

MQW spectral response.

The MQW region contribution to the photocurrent depends on the diffusion length of the majority carriers, photogenerated in a well. This diffusion length is expressed as $L = \mu F \tau$, where F

Radiation source.

We model a thermal radiation source as a broadband blackbody emitter at temperatures 1000-1500 K. The blackbody emission is described by Planck's distribution of photons by energy E , which gives the following formula for the photon flux in the unit energy:

$$\phi_{bb} = \frac{1}{4\hbar^3 \pi^2 c^2} \frac{E^2}{\left(\exp\left(\frac{E}{kT_B}\right) - 1 \right)}, \quad (1)$$

where k is Boltzmann's constant and T_B is black body temperature.

Modeling of TPV cell .

Strained narrow band gap $\text{In}_x\text{Ga}_{1-x}\text{As} / \text{In}_{0.52}\text{Ga}_{0.48}\text{As}$ ($x > 0.6$) multiple quantum wells (MQW) are introduced within the intrinsic region of a conventional $\text{In}_{0.52}\text{Ga}_{0.48}\text{As}$ p-i-n cell lattice matched to InP.

Since InAs lattice constant is bigger than GaAs, the well InGaAs material is undergoing compressive strain. This necessitates the consideration of strain modification to band structure and critical thickness in strained structures.

Strain limitations on thickness.

Single Layer.

The lattice misfit during the heteroepitaxy imposes critical thickness limitation on the well thickness and number of periods which can be grown before the relaxation occurs. The critical thickness is estimated by equating the force exerted by misfit strain and tension in the misfit line. For a single epitaxial film on a substrate of an infinite thickness, the critical thickness h_c can be found by solving the following equation ^(5,6) :

$$h_c = \frac{b}{8\pi f} \frac{(1 - \nu \cos^2 \alpha)}{(1 + \nu) \cos \lambda} \left(\ln \frac{h_c}{b} + 1 \right). \quad (2)$$

It had been assumed in the derivation that the maximum value of the strain ϵ is equals to lattice misfit f .

Here ν is the Poisson ratio, b is a magnitude of Burgers vector of dislocation, λ is the angle between the slip direction and that direction in the film plane which is perpendicular to the line of intersection of the slip plane and the interface; α is the angle between the dislocation line and its Burgers vector. In our case these parameters have the following values:

$$|b| = \frac{a}{\sqrt{2}}, \quad \cos \alpha = \cos \lambda = 1/2.$$

The calculation of a critical thickness versus epitaxial layer composition gives a dependence, illustrated by Figure1.

To avoid relaxation, a single epitaxial $\text{In}_x\text{Ga}_{1-x}\text{As}$ layer thickness has to be less than the critical value. Consequently, to achieve a relaxation free growth of a single epitaxial $\text{In}_x\text{Ga}_{1-x}\text{As}$ film of a certain thickness, the composition x should be contained within $x=0.53$ and the critical value.

Critical thickness in MQW.

For the growth of a MQW region, other critical thickness considerations arise. For the QW period comprising of a strained well and an unstrained barrier, there is a limitation of a well thickness in a period and on the number of well/barrier periods in MQW structure.

Well critical thickness.

Since the well material strain is partially accommodated by the barrier, the well material critical thickness in the MQW is higher than for a single epitaxial layer ⁽⁶⁾ :

$$L_w^c = \frac{b}{2\pi f} \frac{(1 - \nu \cos^2 \alpha)}{(1 + \nu) \cos \lambda} \left(\ln \frac{L_w^c}{b} + 1 \right). \quad (3)$$

is a perpendicular electric field in MQW, created by the ionized impurities at the junction, μ is the carrier mobility and τ its recombination time.⁽¹⁴⁾

The effective carrier mobility for perpendicular transport in microstructures is related to different processes.^(15, 16, 17)

Most importantly, the effective mobility depends on both thermionic emission,¹⁵ which dominates when the barrier is thick; and multi hopping⁽¹⁶⁾ when the barrier is thin (phonon-assisted tunneling). Using the method of references 15 and 16, we can theoretically estimate the effective mobility of carriers (electrons and holes) versus barrier and well widths, electric field, and temperature.

Following the modeling of MQW solar cell⁽¹⁸⁾, we estimate diffusion length of carriers in the intrinsic zone (x) as $L_e = 1e^{-9} \cdot F$ and $L_b = 4e^{-9} \cdot F$ for the regions where quasi-Fermi level is close to the valence ($x_i = x_i N_a / (N_a + N_d)$) or conduction ($x_c = x_i N_d / (N_a + N_d)$) band, respectively; F is the electric field in the intrinsic region in V/cm. For the typical electric field of 15 kV/cm in the MQW region of a solar cell, this would give 0.15 and 0.6 micron diffusion length each.

The spectral response of i(MQW) zone, obtained by solving the continuity equation, ref. 14, is expressed as:

$$J_i(E) = (1-R) \cdot \left[\frac{\alpha(E) \cdot L_e}{\alpha(E) \cdot L_e - 1} (e^{-x_{i1}/L_e} - e^{-\alpha(E)x_{i1}/L_e}) + \frac{\alpha(E) \cdot L_b}{\alpha(E) \cdot L_b + 1} (e^{-x_{i2}/L_b} (1 - e^{-(\alpha(E)+1/L_b)x_{i2}/L_b})) \right] \quad (4),$$

where $\alpha(E)$ is the spectral distribution of the absorption coefficient of the MQW, x is intrinsic region thickness (defined as the total thickness of all the MQW periods in the region). R is the front-side reflection coefficient.

Figure 2 represents a normalized spectral response of a 20 period 90/190 Angstrom well/barrier MQW solar cell, 90% Indium in the well.

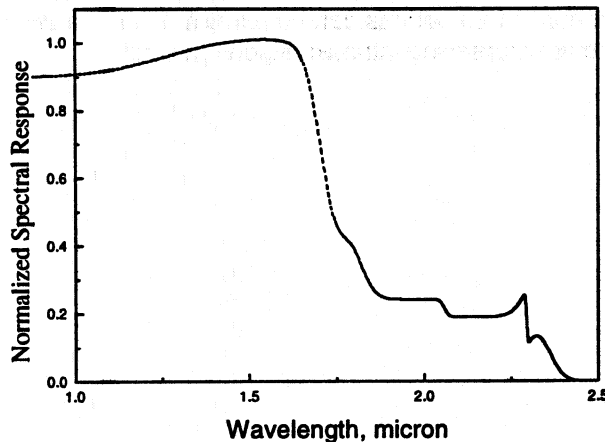


Figure 2. Normalized Spectral Response of a MQW solar cell vs. Wavelength, [micron].

MQW cell dark current.

We have considered several mechanisms contributing to the dark current of a p-i(MQW)-n photodiode:

- A diffusion current I_s due to majority carriers having diffused through the junction and recombining in the opposite quasi-neutral region⁽¹⁹⁾
- A generation-recombination (GR) current⁽¹⁹⁾ associated with Shockley-Read-Hall recombination levels, related to impurities in the depletion and intrinsic regions.

The GR current consists of contributions from bulk (I_{GRB}) and MQW regions (I_{GRI}) and is expressed

$$I_{GR} = I_{GRB} + I_{GRI} \text{ where } I_{GRB,I} = \frac{qn_{R,I}W_{B,I}}{\tau_{eff,B,I}} \quad (5).$$

W is a region thickness, τ_{eff} is the effective generation-recombination carrier lifetime which is directly dependent on the material quality and impurity density. The effective GR lifetime in MQW region becomes much smaller than in the bulk because of high recombination center density due to multiple interfaces and residual doping. A rapid increase in GR dark current due to MQW region is therefore predictable. For this modeling we assume $\tau_{eff,B} = 1 \mu s$ and $\tau_{eff,I} = 0.1 \mu s$.

- A tunneling current due to the probability of band-to-band tunneling of carriers through the junction⁽²⁰⁾

This current, usually neglected in moderately doped diodes, becomes significant in a MQW under an electric field. This effect becomes more noticeable due to reduced band gap of a MQW region and is also influenced by the barrier width.

Results of calculations.

The device characteristics such as open circuit voltage(Voc), short circuit current (Isc) and Spectral Response, have been calculated for 1000 to 1500 K black body emitter as a function of In composition, well/barrier thickness and number of wells in the MQW region (e.g. see figures). It is shown that the insertion of these narrow band gap well extends the spectral response toward the infrared. A rough estimate shows that 20-40% of the incident power is available for conversion by such a MQW device for a 1500 K blackbody. The short circuit current I_{sc} of the p-i(In_xGa_{1-x}As / In_{0.52}Ga_{0.48}As MQW)-n cell may therefore be substantially increased compared to that of a baseline p/n In_{0.52}Ga_{0.48}As cell.

Isc vs number of periods.

Ideally, the introduction of QW periods in the intrinsic region increases photocurrent (see Figure 3). However, the saturation reached at around 20 periods can be explained by a decrease in the electric field and carrier collection due to the increasing intrinsic region thickness.

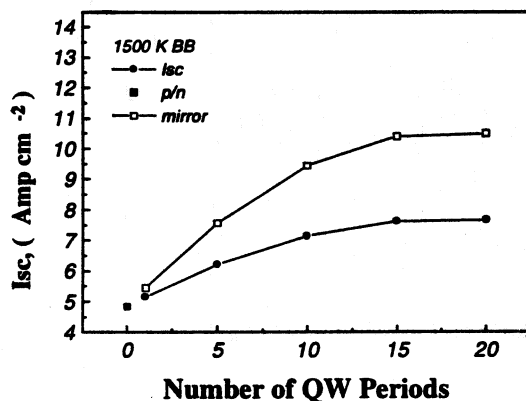


Figure 3. Short circuit current, [A/cm²], vs. the number of periods, for a 60/220 Angstrom well/barrier QW period, 90% Indium in the well.

Since in our calculations for the sake of comparison we fix the total period thickness at 0.028 micron, this conclusion should be valid for well of different thickness, provided this fixed period thickness.

Isc vs composition.

The calculation of short current versus InGaAs composition in the well showed a substantial growth with increasing In concentration. Figure 4 illustrates such a dependence for 20 periods with 90/190 Angstrom in well/barrier.

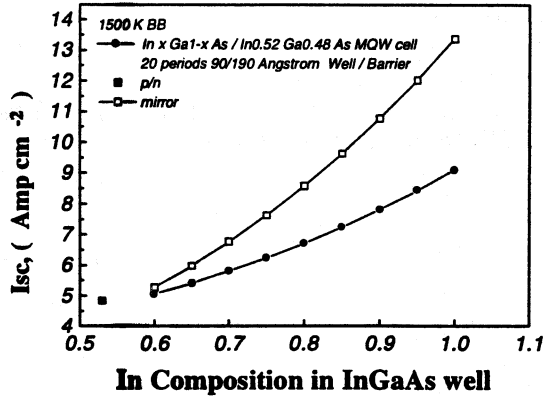


Figure 4. Short circuit current, [A/cm²], vs. Indium composition in InGaAs well, for a 90/190 Å well/barrier period MQW cell.

Ideally, almost twofold increase in Isc can be obtained by having introduced i-MQW region with strained In_xGa_{1-x}As layers into conventional p/n In_{0.52}Ga_{0.48}As solar cell.

Voc vs. composition.

The open circuit voltage of a MQW cell is expected to be less than that of a baseline cell because of the dark current increase due to MQW region. However, our calculations showed higher, but comparable, Voc for the MQW cells, increasing with In composition in wells. This is because the voltage drop associated with dark current in MQW is compensated by the operation at a higher current due to increased photoabsorption.

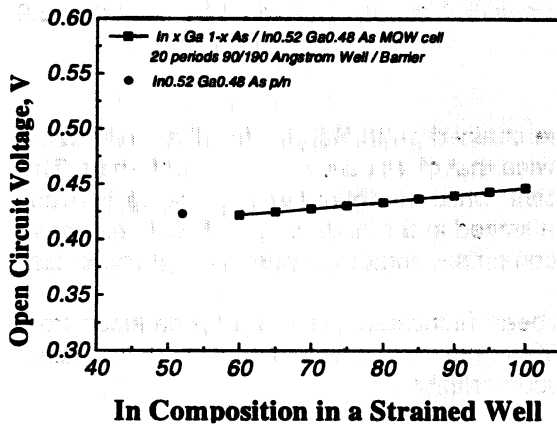


Figure 5. Open Circuit Voltage, [V], vs. Indium composition in InGaAs well.

The Figure 5 shows our results for a MQW solar cell with 20 periods of 90/190 Angstrom in well/barrier and radiation from a 1500 K blackbody.

Overall, the projected efficiency of this MQW cell (9% for 1500 K blackbody) can be twice as high as that of a single p/n In_{0.52}Ga_{0.48}As solar cell (4.5%).

We have presented the results calculated for 1500 K blackbody. We would like to give a more complete picture by adding that for a 0.75 eV band gap p/n cell about 3% of the power of a 1000 K

blackbody is emitted above its band gap; this ratio increases to 16% for a 1500 K, and 35% for a 2000 K blackbody. Assuming no transparency and recombination losses, it leads to a theoretical efficiency limit of 2%, 13% and 26 %. For a 0.47 eV band gap, which is close to the excitonic absorption edge of a strained 90 angstrom InAs well with $\text{In}_{0.82}\text{Ga}_{0.48}\text{As}$ barriers, this figures are 20%, 48% and 67 %, respectively. The upper efficiency limit would be 16%, 34% and 42%.

Strain limitation on photoabsorption and short circuit current.

For the assessment of the best achievable absorption edge of a MQW structure, we plotted the QW confined energy vs. well thickness for different In composition. We estimated the QW critical thickness as that for a single layer with half the strain of it. This estimate is in between values for the single layer and QW layer, as done in ref. 5.

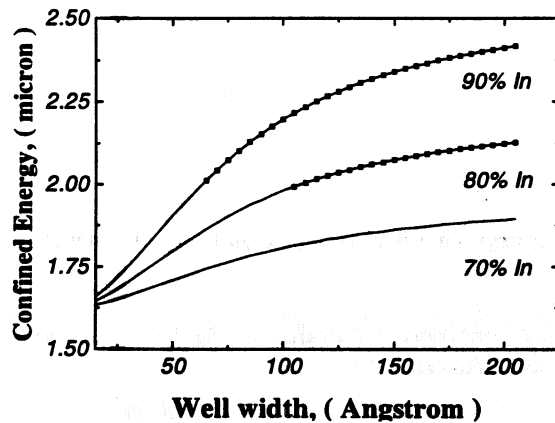


Figure 6. QW Confined energy, [micron], vs. well width, [Angstrom], for 70%, 80%, 90% $\text{In}_x\text{Ga}_{1-x}\text{As}$.

With 90% Indium composition and 6 nm well, almost 2.0 micron (1.97) confinement energy can be reached. Such a cell with 20 periods is projected to have 6.8% conversion efficiency. If we return to the calculations of a short circuit current, we can state that 90 A well is close to the critical thickness for 82% In. So with the 90 Angstrom well thickness we would be limited to 6.9 Amp/cm² and 5.9% efficiency.

Conclusions.

Ideally, for a typical low temperature TPV the strained p-i($\text{In}_x\text{Ga}_{1-x}\text{As}$ $\text{In}_{0.82}\text{Ga}_{0.48}\text{As}$ MQW)-n cells conversion efficiency is predicted to exceed twice that of its conventional counterpart. This is achieved through increase in the short circuit current, while no degradation of the open circuit voltage is predicted. However, we could expect to be limited in the number of QW periods grown without relaxation. It is possible to avoid strain limitation on the number of periods by using $\text{In}_x\text{Ga}_{1-x}\text{As}$, $x < 0.53$, to balance the well strain.

First strained MQW TPV cell structure has been fabricated. As could be deduced from the X-Ray characterization data, a 15 period 60/300 Angstrom well/barrier with 0.79 Indium composition in the well successfully maintained pseudomorphism.

References.

1. B. D. Wedlock, "Thermo-Photo-Voltaic conversion", Proceedings of the IEEE 51, 694 (1963).
2. R. Swanson, "Silicon Photovoltaic Cells in TPV Conversion", EPRI Research Project ER-1272, (1979).
3. 1st NREL Conference on the Thermophotovoltaic Generation of Electricity, Copper Mtn., CO, AIP Conf. Proc. 321 (1994).

4. 2nd NREL Conference on the Thermophotovoltaic Generation of Electricity, Colorado Springs, CO, AIP Conf. Proc. 358 (1995).
5. J. W. Matthews and A. E. Blakeslee, *J. of Crystal Growth* **27**, 118, (1974).
6. R. People and J. C. Bean, *Appl. Phys. Lett.* **47**, (3), 322, (1985).
7. M P C M Krijn, *Semicond. Sci. Technol.* **6**, 27-31 (1991).
8. C. G. Van de Walle, *Phys. Rev. B* **39** (3), 1871, (1989).
9. J. Leymarie, C. Monier et al., *Phys. Rev. B* **51** (19), 13274, (1995).
10. R. People and S. K. Sputz, *Phys. Rev. B* **41**, 8431 (1990).
11. R. P. Leavitt and J. W. Little, *Phys. Rev. B* **42**, 11774 and 1184 (1990).
12. *Properties of lattice matched and strained Indium Gallium Arsenide*, 1993 INSPEC (ed. London).
13. G. Bastard, *Wave mechanics applied to Semiconductor heterostructures*, ed. Les editions de Physique.
14. R. P. Leavitt and J. L. Bradshaw, *Appl. Phys. Lett.* **59** (19), 1991.
15. H. Schneider and K. Klitzing, *Phys. Rev. B* **38**, 6160 (1988).
16. D. Calecki, J.F. Palmier, A. Chomette, *J. of Physics C* **17**, 5017 (1984). See also J. F. Palmier, H. Le Person, C. Minot, A. Chomette, A. Regreny, D. Calecki, *Superlattice and microstructures*, **1**, 1 (1985).
17. X. L. Lei, N. J. M. Horing and H. L. Cui, *Phys. Rev. Lett.* **66**, 3277 (1991). See also X. L. Lei, N. J. M. Horing, H. L. Cui and K. K. Thornber, *Phys. Rev. B*, **48**, 5366 (1993).
18. P. Renaud, M.F. Vilela, A. Freundlich, A. Bensaoula and N. Medelci *et al.* in *1994 IEEE First World Conference on Photovoltaic Energy Conversion*, V II, p.1787, (1994).
19. J. M. Sze, *Physics of Semiconductor Devices*, ed. Wiley-Intersciences, (1985).
20. S. R. Forrest, R. F. Leheny, R. E. Nahorny, and M. A. Pollack, *Appl. Phys. Lett.* **37**, 322 (1980).

LOW BANDGAP, HIGH BANDGAP, AND ALTERNATIVE CONVERSION DEVICES AND TECHNOLOGY WORKSHOP SUMMARY

**Navid S. Fatemi
Essential Research, Inc.
Cleveland, OH**

**Alex Freundlich
University of Houston
Houston, TX**

About 20 people attended this workshop. The focus of the workshop was on technologies that utilize low bandgap or high bandgap photovoltaic (PV) cells. Their use in conventional multijunction tandem solar cell structures was, however, not considered. Instead, the applications for these cells in the context of newer and emerging technologies were considered. These technologies were identified as: thermophotovoltaics (TPV), alphavoltaics, betavoltaics, and planar high temperature photovoltaics. Three broad mission scenarios were discussed. These were earth orbit and near earth missions (~ 1 A.U.), near sun missions ($\ll 1$ A.U.), and missions to the outer planets of the solar system ($\gg 1$ A.U.).

Thermophotovoltaics

TPV systems, in general, utilize emitters which operate at temperatures of $\leq 2000^\circ\text{C}$. Low bandgap (Eg) PV cells are, therefore, used to match the spectral output power distributions of these emitters. PV cells with bandgaps in the range of 0.5-1.1 eV are suitable candidates for TPV applications.

The general consensus was that only two types of TPV technologies are suitable for space applications: radioisotope thermophotovoltaics (RTPV) and solar thermophotovoltaics (STPV). The TPV emitter temperature in an RTPV system is about 1100°C , whereas, the emitter temperature in an STPV is system-dependent, but is generally greater than 1200°C .

In an RTPV system, the fuel which provides the heat to a TPV emitter is a Pu-based radioisotope. As a result, an RTPV system can be used for missions where the solar flux is prohibitively low (i.e., $\gg 1$ A.U.) for conventional PV systems to be practical. The relatively long half-life of the radioisotope fuel also accommodates the long duration of these missions

(>10 years). Since NASA's future spacecrafts are envisioned to be much smaller than their historic counterparts, accommodating the relatively large radiator required to reject excess heat from an efficient RTPV system, however, can be a challenge for spacecraft designers.

For earth orbit and near earth missions where solar insolation is relatively high (~1.4 kW/m²), an STPV system can be an alternative to conventional planar or concentrator PV systems. In an STPV system, concentrated solar radiation is used to provide heat to the TPV emitter. Like conventional PV systems, STPV is still a passive power generating system. Yet it has some of the advantages of the solar dynamic power systems, such as less concentrator pointing accuracy requirements, and thermal energy storage capability for night orbits.

Several components already developed for solar dynamic power systems, can also be used for the STPV system. The Stirling dish concentrator mirror (up to 15,000X concentration) and thermal energy storage systems are examples of these components. A thermal storage unit, comprised of phase change salts or bulk silicon, can be an efficient alternative to electrochemical batteries. In addition, such an energy storage unit should, in theory, have a far greater life span than batteries.

One point that was made in regard to non-PV powered satellites, in general, was that the conventional wing-like solar panels, usually symmetrically positioned on two sides of the satellite, act as mass inertial references for the satellite. Since TPV systems will eliminate this inertial reference, they will force the designers of satellites to rethink this issue. It was also agreed that the most important drivers for space-based systems will be the total system power-to-weight (W/kg) ratio and efficiency. Both RTPV and STPV systems are envisioned to show conversion efficiencies approaching 20%.

The low bandgap PV cells which may be used in these TPV systems will probably be one or more of the following technologies: InGaAs, GaSb, GaInSb, GaInAsSb, Si, and Ge, with bandgaps in the range of 0.5-1.1 eV. With the exception of InGaAs, currently all others are only available in a conventional format of p/n junction residing on a conducting substrate. The InGaAs is also available in the monolithic integrated module (MIM) format. This format enables the use of rear surface spectral control in a TPV converter, via the use of an IR transparent semi-insulating InP substrate and a metallic back surface reflector.

Alphavoltaics and Betavoltaics

Higher bandgap cells, in the range of 1.8-6.0 eV, are generally thought to be suitable for α - and β -voltaic applications. The power level requirements for these systems are thought to be rather small, in the range of 100's of μ W. As such, they are envisioned to have niche applications, such as self-powered digital electronic components.

The biggest obstacle in developing such systems is thought to be the electronic damage PV cells will incur due to the high levels of radiation emitted by α and β sources. Pm^{147} , Sr^{90} , Tl^{204} , tritium (H^3), and Ni^{63} were identified as possible sources for β -voltaic systems. Am^{241} was identified as a source for α -voltaic systems. It was noted that H^3 and Ni^{63} were being studied more intensely than other β sources, and that Ni^{63} is a rather expensive source.

Because of the large radiation damage PV cells are likely to experience in these systems, the following unconventional PV cell technologies are being considered: diamond, cubic BN, SiC, and (Ga, Al)N. No n-type doped material exists for diamond, however, and although c-BN is a very promising material, it is still in its early stages of development. p/n junctions and small area devices such as UV detectors, lasers, and LEDs, however, do exist for SiC or Ga and Al nitrides. As such they are very attractive candidates for use with future α - and β -voltaic systems. A note of caution was also raised that conventional radiation tolerant PV cells such as InP will probably not be able to handle the very large radiation doses emitted by these systems effectively.

Planar Large Area PV systems

Another interesting application for large bandgap PV cells was raised during the workshop. They are at least two near sun missions (i.e., $\ll 1$ A.U.) proposed by NASA (JPL) and the European Space Agency: the solar probe and the mercury missions. The PV cells in an environment so close to the sun will experience large solar fluxes and very high operating temperatures ($\geq 400^\circ\text{C}$). As a result, PV cells will be needed that can withstand these conditions.

Large solar flux presents a problem with heat rejection at the cell level in a high temperature ambient environment. The high cell operating temperature presents several problems with material decomposition, enhanced metal-semiconductor interactions, and the rate of reverse saturation current (J_0) increase with temperature.

Because of the above conditions, larger bandgap materials should be more suitable candidates than smaller bandgap cells. Conventional large bandgap III-V cells such as GaAs and InP, however, will likely have problems with material decomposition and excessive metal-semiconductor interactions.

The one material that was identified by the group as a possible candidate for near sun missions was SiC. Although, to our knowledge no large area SiC solar cells has ever been fabricated, SiC UV detectors do exist that are stable in the temperature range of 400 - 600°C .

Conclusions

Three different technologies for low and high bandgap cells were discussed in the workshop. They were thermophotovoltaics (TPV), alphavoltaics, betavoltaics, and planar high temperature photovoltaics. Three broad mission scenarios were also considered. These were earth orbit and near earth missions (~1 A.U.), near sun missions (<<1 A.U.), and missions to the outer planets of the solar system (>>1 A.U.).

THE ROSSI X-RAY TIMING EXPLORER (XTE) SOLAR ARRAY ANOMALY

Edward M. Gaddy, Robert Kichak, and Lee Niemeyer
Goddard Space Flight Center, Greenbelt, MD 20771

Richard Stegeman
Jackson and Tull, Seabrook, MD 20706

ABSTRACT

The XTE was launched December 30, 1995. Shortly after launch, it became apparent that the solar array was not performing as expected. On leaving shadow, the array exhibited many discontinuous drops in current output. The size of each of these drops was consistent with the loss of a part of a cell. The current decreases could not be caused by the loss of an entire cell or an entire circuit. This meant that the array may have had numerous cracked solar cells that opened as the array got warmer. Studies performed on the array's qualification panel suggest that the cell cracks may have been caused by extensive tap testing performed on the array and that these cracks were undetectable at room temperature using usual inspection methods.

CONFIGURATION

The XTE's solar array is such that it is always oriented to the sun except when the spacecraft is slewing from one "target" to another. Figure 1 shows that the XTE solar array is divided into eight circuits. Six of these circuits are each contained completely on a single solar panel. The other two, circuits four and eight, are each divided on three panels. Each circuit is further subdivided into nine strings of silicon solar cells. Six of these strings have 100 cells in series and three have 103 cells in series. The strings comprising each circuit are paralleled at the most positive and negative cell. Each cell's size is 3.92 centimeters by 5.70 centimeters. The cells are fixed to aluminum face sheet substrates with CV 2568. The circuits are wired into the spacecraft as depicted in Figure 2; and, their voltages and currents are monitored as shown.

Figure 2 shows that each of the eight circuits feeds into the spacecraft independently. As the battery charges during the sunlit portion of the orbit, the spacecraft needs less current. This current control is accomplished by partially and then sequentially completely shorting out one circuit after another, with circuit eight shorting first. For example, soon after coming into sunlight circuit eight is shorted, circuit seven is partially shorted, and the remaining circuits are fully on line. Sometime thereafter circuits eight, and seven are shorted, circuit six is partially shorted and the other circuits are fully on line; etc.

ARRAY PERFORMANCE

Figures 3 and 4 respectively show the voltage across and the current produced by circuits five and four during the sunlit portion of orbit five. The performance of circuit five is normal in all respects. The voltage rises rapidly across the circuit when it comes into sunlight. It then reaches the battery voltage and is clamped to battery voltage through the diode. The voltage rise continues at a slower rate as the battery is charged. The rise in voltage stops when the battery hits its voltage limit. The voltage then holds steady for about seven minutes. Subsequently, it decreases suddenly. This is due to the power system shorting out the circuit which is no longer needed to maintain the battery at constant voltage. The circuit voltage stays at about 0.6 volt until

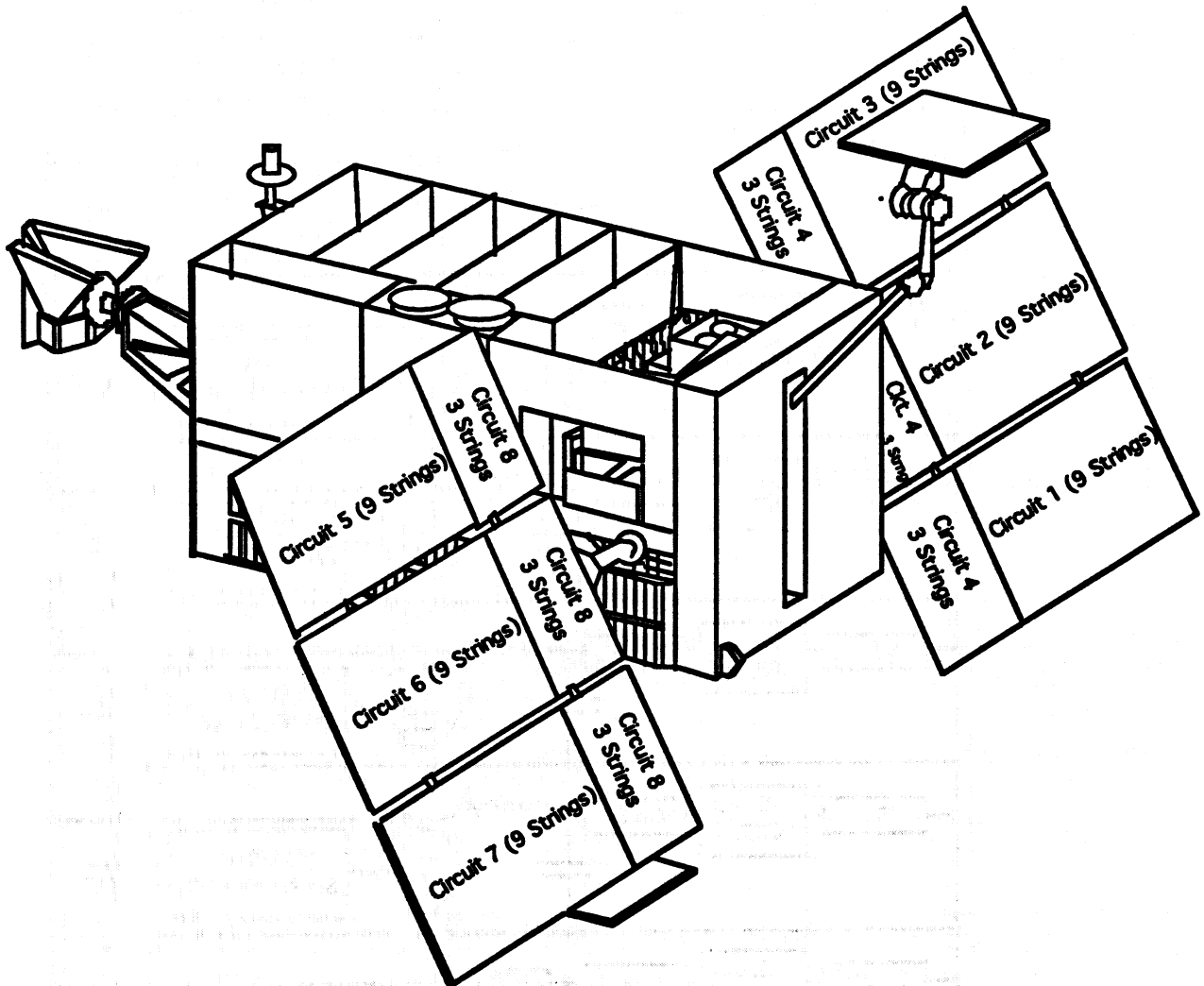


Figure 1
The XTE Spacecraft and Solar Panels

the spacecraft begins to enter darkness. At this point, there is insufficient power to maintain battery voltage, and the power system electronics takes the short off circuit five and its voltage again rises.

The current from circuit five rises rapidly as the circuit comes into sunlight. It then rises more slowly. This second rise is due to two effects. First the array is approaching and then going over the terminator about ten minutes into the orbit. This event corresponds to an increase in the array current due to earth albedo. Second, the array produces more current because its temperature is rising. The current then drops and rises again as the spacecraft crosses the terminator again at about 55 minutes. The shorting of the circuit to about 0.6 volts at about 17 minutes shows little effect on the current. This is because the operating voltage of the circuit is well to the short circuit side of the current versus voltage curve knee. There is nonetheless an effect. It cannot be seen in Figure 3, but a barely perceptible increase in current occurs every time the circuit is shorted. We will contrast the increase to the increase in the malfunctioning circuit four later.

Circuit four performance, shown in Figure 5, is abnormal. For the first nine minutes or so in the sunlit portion of the orbit, the circuit is performing as expected. Then the current from the circuit drops discontinuously. It then recuperates and then drops suddenly again and then again. This occurs while the voltage on the circuit steady. The only explanation is that the circuit current versus voltage characteristic is

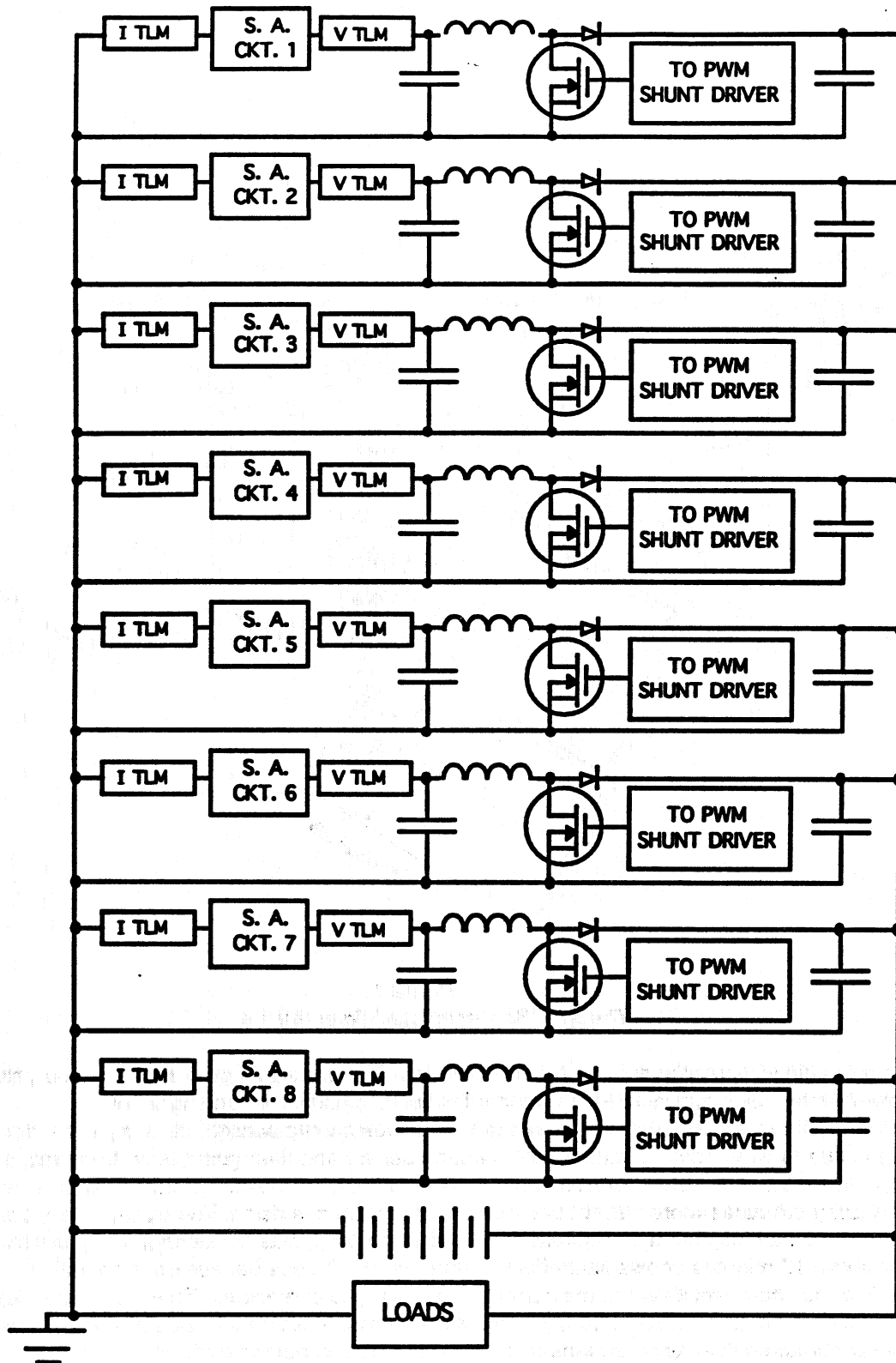


Figure 2
Simplified Schematic of the XTE Power System

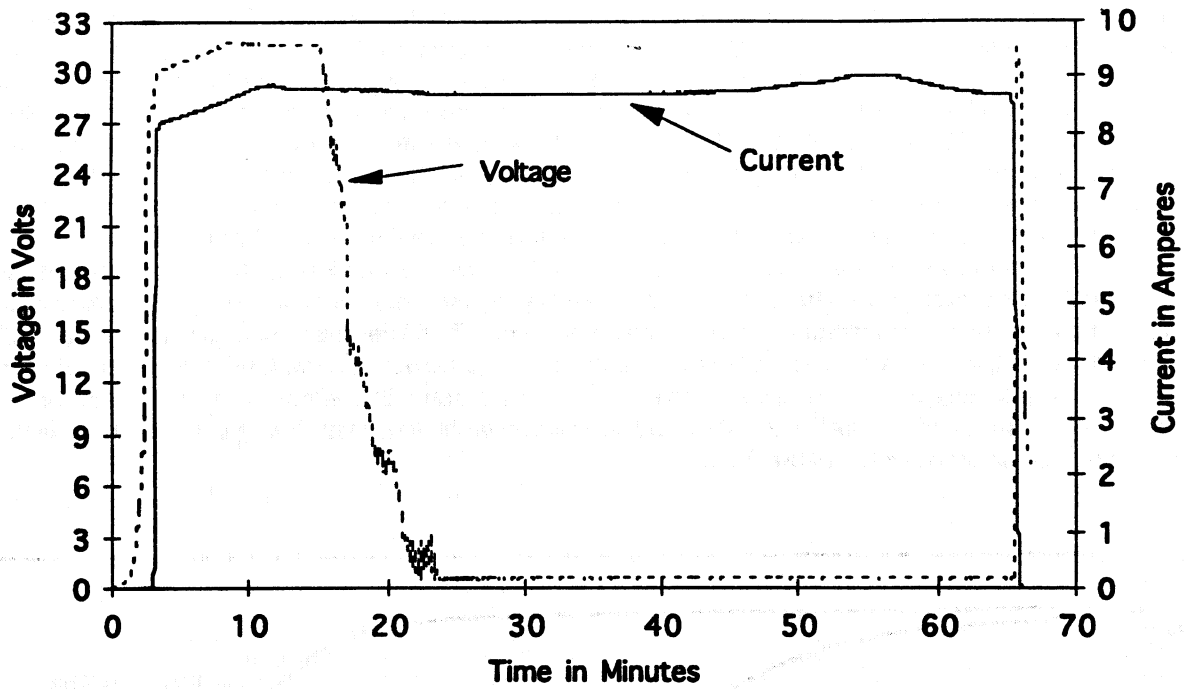


Figure 3
Module Five Voltage and Current Versus Time for Orbit Five

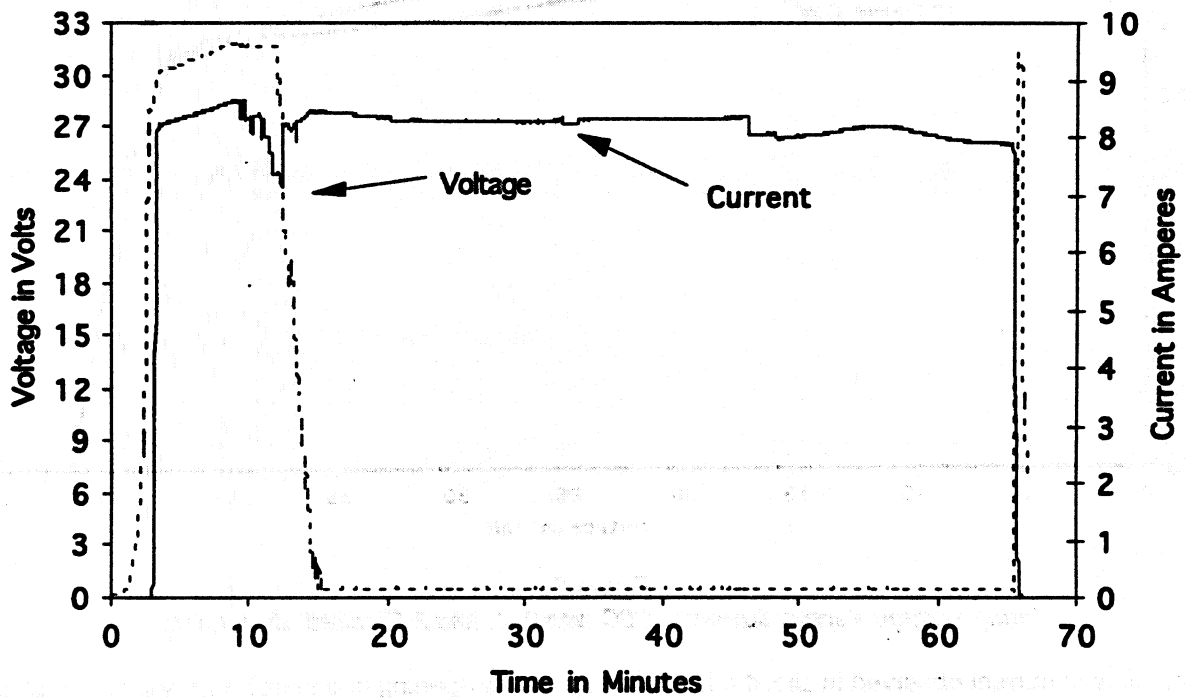


Figure 4
Module Four Voltage and Current Versus Time for Orbit Five

changing anomalously and discontinuously. The current decreases discontinuously until about thirteen minutes after coming into sunlight when the circuit is shorted out by the spacecraft electronics. At this point the current rises quite suddenly. Normally, the current is expected to rise very slightly with decreasing voltage, as with circuit five, but not nearly as much as it does with circuit four. Seven of the eight circuits showed anomalies similar to those in circuit four. Circuits 1 through 8 showed maximum orbital degradations of approximately 5%, 14%, 18%, 22%, 0%, 20%, 4%, and 15%. The total average loss was much smaller.

Circuit four performance, and the performance of the other malfunctioning circuits, is explained by Figure 5 which shows the I-V curve of one of the circuit's strings with none, one and two cracked solar cells. Each cell is cracked such that the maximum amount of cell that can be lost is lost. The Figure was generated by measuring the reverse bias performance of the XTE solar cells, extrapolating what their current versus voltage characteristics would be with a "maximum" cell crack, and then simulating string performance. A complex example of such a "maximum" crack is shown in Figure 7. If the crack were any further to the "left" both pieces of the cell would be connected into the circuit by the parallel redundant interconnects and the cell would function as if it were in a single piece. Such a crack would have little effect on the overall output. If the crack were any further to the "right", the cell would lose somewhat less than the approximate 1/3 it loses with the worst case crack depicted in the Figure.

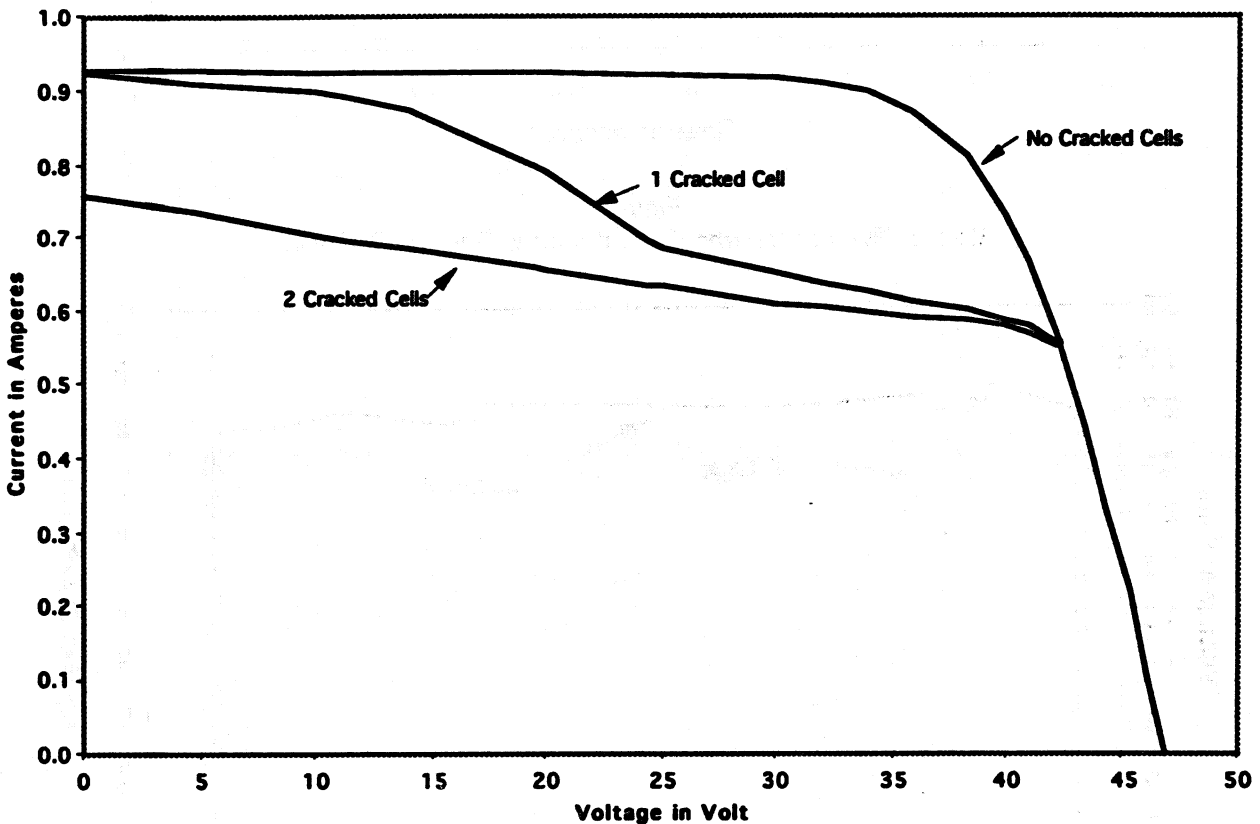


Figure 5
String Voltage Versus Current at 70C with 0, 1, and 2 Cracked Solar Cells

The decrease in current observed in circuit 4 is caused by cracks opening in one cell after another in different strings, dropping the current by about 0.3 amperes in a given string each time a cell opens. Furthermore, the effect of the cracks is not observed at short circuit current if only one cracked cell is present in a single string; but is present with two or more cracks in a string. This explains the current recovery in circuit four after it is shorted. Apparently, some of the strings have just one crack. It also explains how the current recovery is not

complete. If any of the strings in circuit four have more than two cracked solar cells, the current will not recover.

The possibility that there are completely open strings in the circuits was explored. This is easy to eliminate as it would cause current decreases on the order of 0.9 amperes. Current decreases that large are not seen in any of the circuits.

TEST OF THE XTE QUALIFICATION PANEL

Because of the array's unexpected performance in space, the XTE qualification panel was used to help determine the cause. Prior to array delivery, the qualification panel underwent extensive testing including exposure to thermal vacuum cycles, thermal cycles at ambient pressure and an acoustic environment. The panel showed no anomalous behavior due to these exposures. However, all the evaluations of the panel were performed at room temperature. When the panel was flash tested at elevated temperatures, subsequent to the XTE's launch, the panel showed an anomalous I-V curve, see Figure 6. At elevated temperature, a crack was clearly seen that could lead to the anomalous performance, see Figure 7.

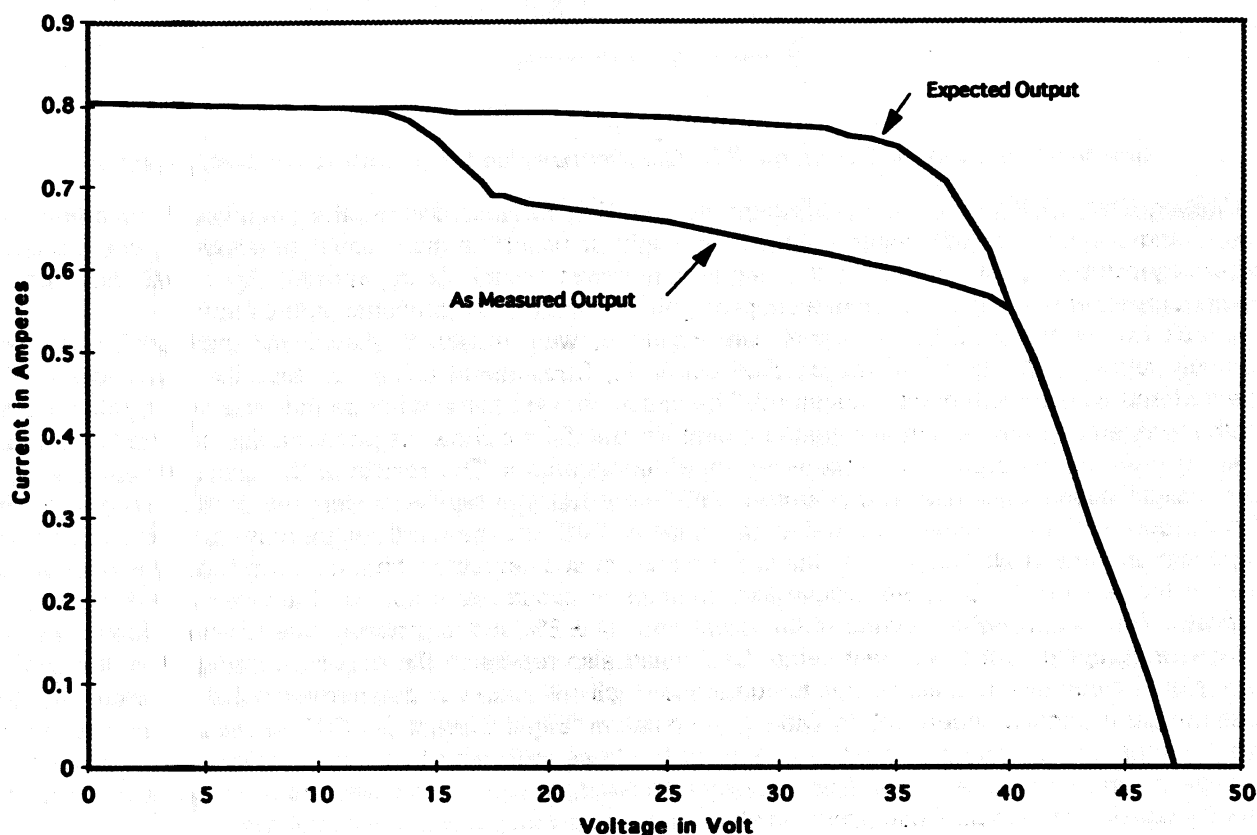


Figure 6
XTE Qualification Panel Circuit One I-V Curve at 70C

However, the crack in the solar cell was such that only one of its four branches could be seen at room temperature with the usual methods the cell manufacturer, Spectrolab, and GSFC use to inspect for cracks. This suggested the possibility that the XTE array was launched with cracked cells that could not be seen. The plausibility of this was increased because the flight panels were extensively and repeatedly tapped tested to check for delaminated substrates. Further inspections were carried out on the qualification panel to determine the conditions under which the crack could be seen, and also, to further determine if tap testing, bending, or

heating could cause cell cracks that were not visible at room temperature. These last two items were performed because the flight panels were bend tested and were subjected to high temperatures in bake out.

The panel was reinspected at Goddard using two methods: infrared light and a stereo microscope with normal light. The cracks in the solar cell were not detected using infrared equipment despite several approaches that were tried. Using a stereo microscope, the GSFC located the "vertical" part of the crack at 7X. This vertical crack actually consists of a small series of 45 degree zigzags that on the whole proceed vertically, not unexpected for a silicon solar cell crack as the zigzags follow the crystalline "planes" in the silicon. The other cracks were not visible using this method until the cell was heated to "45 to 50C" with a heat gun at which temperature they were plainly visible.

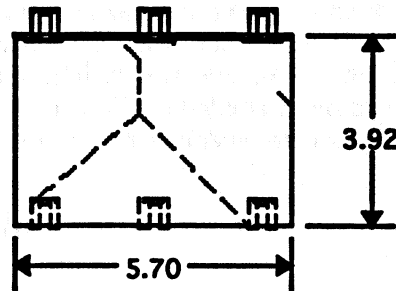


Figure 7

Sketch of the Cracked Cell on the XTE Qualification Panel, Dimensions in Centimeters

Subsequently, GSFC sent the qualification panel to Spectrolab and to another organization to determine if they could see the "cracks" under either infrared light or using the more usual stereoscopic examination. Neither organization picked up the crack using the stereomicroscope. Using infrared, Spectrolab did identify, at room temperature, an anomaly whose shape slightly resembled two branches of the crack.

Circuit two of the qualification panel, see Figure 8, was inspected, electrically measured, and then vigorously tapped. (Circuit 1 had the cracked cell in it.) Subsequent to the tap test, the panel was again inspected and its electrical output measured. The circuit showed some damage that was visually detectable at both room temperature and at elevated temperature, but did not show the phenomenon of a crack that was hidden at room temperature but visible at elevated temperatures. The results of the electrical test, Table I, show a slight power decrease at 28C and at 70C. Note that the results designated as 28C were actually taken at room ambient temperature and extrapolated to 28C, the standard temperature at which solar cells and panels are evaluated. Because of one of the results of subsequent testing, a fairly substantial increase in power at the last test at 28C, we believe that changes in circuit two output on the order of $\pm 5\%$ are not significant. This is somewhat outside of the usual error of $\pm 2\%$ and is probably due to an unknown error in the measuring equipment or our test setup. Or it could also represent the actual performance of the circuit which might be somewhat unstable due to numerous small cell cracks or deteriorated solder after the thermal cycles the panel circuits underwent. In Table I, the notation "Slight Current Cut Off" means that the circuit two current versus voltage curve is a bit too sharp at the knee indicating that one or more cells is producing slightly less current than the others. This is a very mild example of the anomalous curve in Figure 5; but is not generally considered a fault. It can occur simply because a low output cell is in circuit two.

Subsequently, circuit two was tapped using a harder tap than previously. It is not conceivable that the Spectrolab technicians would have tapped the flight panels with such force. Numerous cover cracks and several cell cracks were noted both at room temperature and at elevated temperatures, but there was no evidence of cracks that were "hidden" at room temperature but otherwise visible. Table I provides electrical results at 28C and 70C.

Subsequent to these measurements, the qualification panel was subjected to a "bend" test, the purpose of which was to closely replicate the "bend" tests of the flight array. These tests made certain that the "fixes" for the delaminations on the flight panels worked and verified that there were no additional areas on the panels that might delaminate that had not already delaminated. (Some of the flight panel substrates had delaminated in thermal vacuum exposure). Table I again shows that at both 28C and 70C, there was no significant change in electrical output and visual inspection showed no additional cracks.

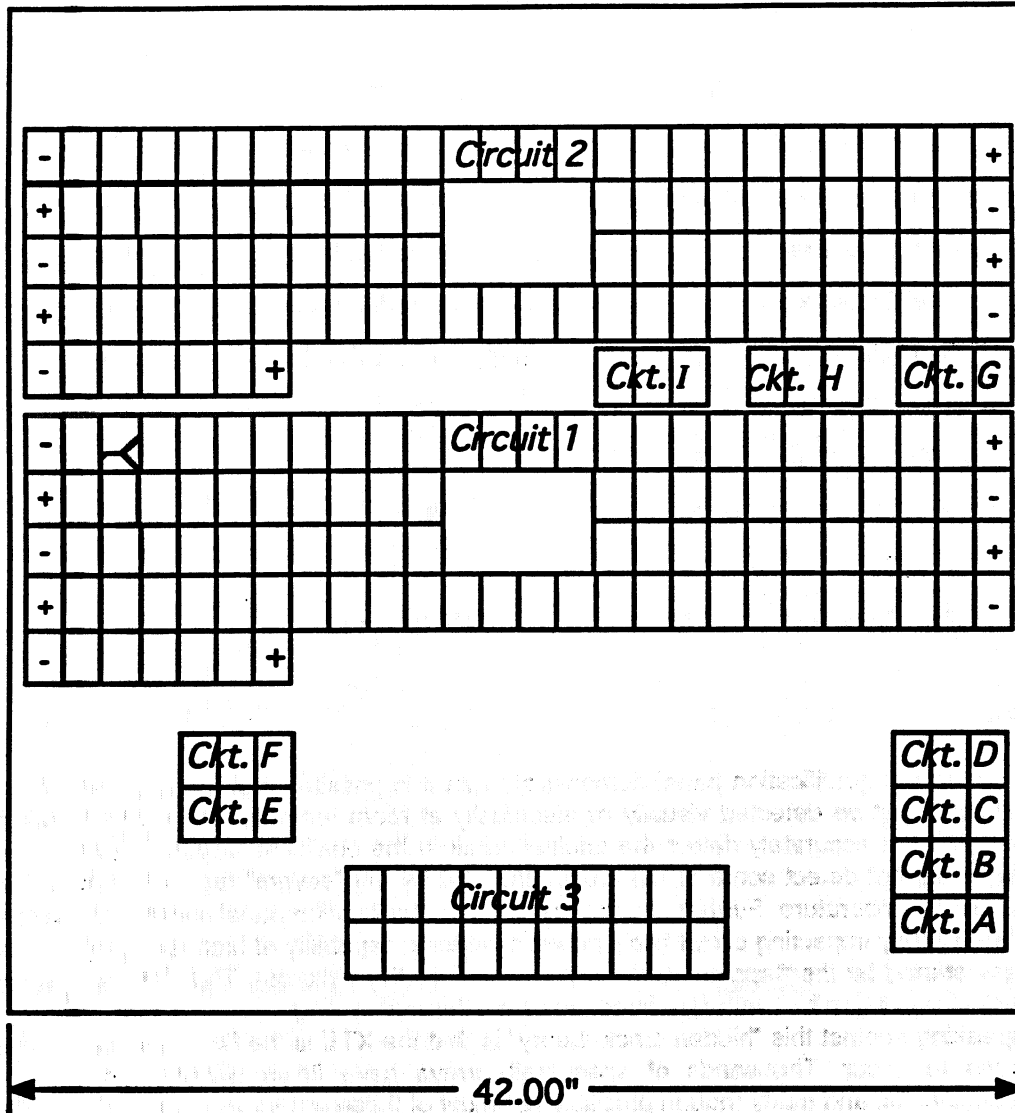


Figure 8
Sketch of the XTE Qualification Panel

As a last environmental exposure, the qualification panel was thermal cycled twice in vacuum between ambient temperature and a nominal 110C with two hour soaks at the extreme temperatures. The panel reached a maximum of 111.9C. Subsequent to this test there was no degradation at room temperature electrical testing, see Table I; but, there was a greater than 50% degradation at high temperatures and a mimicking of the electrical signature of the original crack on the XTE solar panel.

In addition, ten cells in circuit two were inspected with a hood and with the naked eye after the thermal cycle test. A large number of cracks that could not be seen prior to the test were visible. An inspection of the ten cells with a stereo microscope at room temperature and at 70C showed a very large proportion of the cracks visible at 70C that were not visible at 28C.

Table 1
Electrical Output of Qualification Panel Circuit 2

Condition	Temp.	Curve Shape	Power Output (W)
Pre Tap Test	28	Slight Current Cut Off	42.5
Post First Tap Test	28	Sight Current Cut Off	42
Post Second Tap Test	28	Slight Current Cut Off	41.3
Post Bend Test	28	Slight Current Cut Off	40.2
Post Bake Test	28	Slight Current Cut Off	44.6
Pre Tap Test	70	Good	32.2
Post First Tap Test	70	Good	31.8
Post Second Tap Test	70	Good	31.7
Post Bend Test	70	Good	29.7
Post Bake Test	70	Cell Reversed	14.8

CONCLUSIONS

The tests run on the qualification panel demonstrate that it is possible that the array was launched with cell cracks that could not be detected visually or electrically at room temperature. Three organizations and several people could not accurately detect the original crack in the qualification panel at room temperature. Additionally, we could not detect some of the cracks induced by the "severe" tap test at room temperature, but could at elevated temperature. Further, thermal cycling the qualification panel seemed to make the hidden cracks worse by severely impacting circuit two's power producing capability at high temperature. Perhaps the cracks were only started by the "tapping" and then "finished" by the bake out. The flight panels underwent a similar sequence of tapping, albeit with less force, and then thermal cycling.

The fact speaking against this "hidden crack theory" is that the XTE is the first time such a phenomenon has been known to occur. Thousands of spacecraft arrays have flown without showing evidence of undetected cracked cells, and many though probably not most of these arrays were tap tested. There are two possible explanations. The first is that the XTE substrates delaminated in test and this resulted in numerous tap tests to the panels' cells, certainly far more than is usual. The second is that the XTE had unusually good telemetry on it. This allowed detection of signatures that definitely had to be cell cracks. Had the XTE had more typical telemetry it only would have been known that the array output was somewhat low, probably not enough to be concerned about.

RECOMMENDATIONS

We recommend that future flight solar panels undergo a visual inspection and an electrical output test at elevated temperatures. The electrical output test need not precisely determine the power output of the array but just the I-V curve shape. This test found the defect on the XTE qualification panel when room temperature tests did not. In addition, a similar test run on a NOAA K qualification panel found failed cell to interconnect connections, when room temperature testing did not. Fortunately the inspection and the test are inexpensive and quickly performed.

Secondly, we recommend that tap testing solar panels, usually performed to determine whether or not they have a delaminated area, be replaced by other less stressful testing. This testing could include acoustic transmittance through the panel, which is really quite equivalent to a tap test, a suction test where the cells

are pulled with a known force and observed for undue motion, or a pressure test where the cells are gently pushed with known force and observed for undue motion.

IN-ORBIT PERFORMANCE OF HS-376HP GaAs/Ge SOLAR ARRAYS

Richard E. Daniel, Steven W. Gelb, Joseph S. Powe and Joel A. Schwartz
Hughes Space and Communications Company
El Segundo, California 90245

Abstract

The first two commercial communications satellites using gallium-arsenide on germanium (GaAs/Ge) solar arrays were launched in January and November of 1996. The spacecraft, named HS-376HP M1 and M2, were built by Hughes Space and Communications Company. In this paper, we present the in-orbit performance data collected from both spacecraft. These data are compared with predictions generated by Hughes' solar array prediction model. The results show that the in-orbit power output of both M1 and M2 arrays exceed the minimum power predictions from launch through the present time. When compared to nominal case predictions, the in-orbit power for M1 falls approximately 1.7% below the prediction and the in-orbit power for M2 is approximately 0.4% above the prediction. These results are comparable to previous studies on Hughes silicon solar arrays showing agreement with prediction to within approximately 2%. We assess the differences between M1 and M2 solar arrays, the effect of balloon standards, the measurement uncertainty, and the accuracy of the prediction model.

Introduction

In recent years, the spacecraft industry has experienced a dramatic transition with the introduction of higher efficiency solar arrays, primarily using gallium-arsenide on germanium (GaAs/Ge) solar cells [1]. In the commercial satellite industry, the use of GaAs/Ge solar cells was impeded for several years by the high cost of these devices. However, progress in GaAs/Ge manufacturing technology, as well as the demand for higher power spacecraft, has now made the use of GaAs/Ge solar cells on commercial spacecraft both feasible and desirable [2].

The first two commercial communications satellites with GaAs/Ge solar arrays were launched in January and November of 1996. The spacecraft, named HS-376HP M1 and M2, were built by Hughes Space and Communications Company (HSC) [2]. In-orbit data from spacecraft telemetry are now available on both M1 and M2. In this paper, we assess the in-orbit performance of these arrays and validate the testing and analysis used in generating performance predictions.

Solar Array Description

The HS-376HP spacecraft, illustrated in Figure 1, are both Hughes HS376 model spin-stabilized spacecraft. The solar array consists of two cylindrical solar panels as shown in Figure 1. The solar panels were built by Spectrolab Inc. and delivered to HSC for systems integration. The introduction of GaAs/Ge solar cells on this spacecraft significantly increased the power generation capability of the solar panel. As a result, GaAs/Ge solar cell technology has made a major contribution to the longevity of this product line.

The solar cell assemblies used on HS-376HP consisted of large area GaAs/Ge solar cells manufactured by Spectrolab, Inc.. Five solar cell sizes were used, ranging in area from 20.0 cm² to 22.9 cm². The average solar cell thickness was 140 μm, prior to installing coverglass. The coverglass was 150 μm thick CMG, manufactured by Pilkington Space Technology [3]. The coverglass included a front surface antireflective (AR) coating and a back surface infrared reflective (IRR) coating. The IRR coating was used to minimize the spacecraft temperature by reflecting wavelengths of light too long to be converted into current by the solar cell. Coverglass was bonded to the solar cells using Dow Corning 93-500 adhesive.

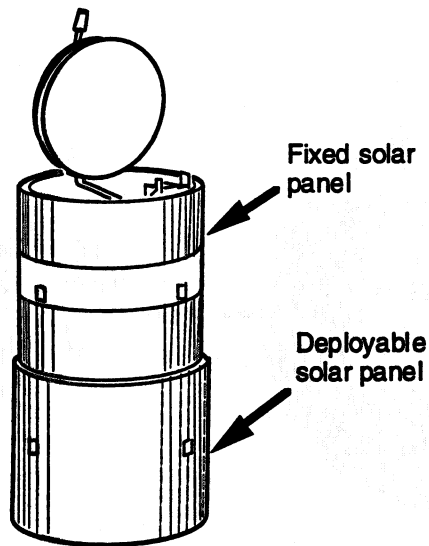


Figure 1. HS-376HP Solar Array

Solar cells were connected into circuits using 25 μm thick silver mesh interconnects. The interconnects were installed by welding to the front ohmic contact of the solar cell and soldering to the backside of the adjacent cell. Each circuit consisted of either 36, 37 or 38 cells in series, depending on the location of the circuit on the array. Temperature predictions for different portions of the array were used to determine the expected cell voltage at end-of-life (EOL); the number of cells in series was then chosen to optimize power output at an EOL bus voltage of 29.3 V.

Electrical output was measured for each solar cell assembly prior to connection into solar cell circuits. This data was used to assign cells of a given output to particular circuits and assign circuits to particular locations on the solar array. The designated locations were chosen to minimize ripple in the spacecraft bus

voltage, induced by the array as the spacecraft spins. Predicted ripple, defined as the difference between average and minimum available power, was less than 1% for both M1 and M2 solar arrays.

The generic HS376 electrical power system is described in reference [4]. To summarize briefly, the spacecraft bus voltage is regulated using an array of tap limiters which shunts excess power from the solar array to ground. When the payload is extracting full power, all limiters are non-conducting. When excess power is available (at the bus voltage), a subset of the limiters regulates using bipolar transistors in the active gain mode. If these limiters saturate, another subset begins to regulate in active gain. To minimize heat dissipation in the limiters, each solar cell circuit is "tapped" by a limiter at a point between two cells in the circuit; for HS-376HP, this point is 10 cells above spacecraft ground.

Spacecraft telemetry includes the bus voltage, bus current and tap limiter current. These data are used to calculate the telemetered in-orbit power, as described below.

Prediction Methodology

Solar array performance predictions were generated using the HSC solar array prediction model. Figure 2 presents an overview of the prediction model's functions. As shown in the figure, the model incorporates a large number of input variables which are needed to predict performance. The inputs include the detailed solar cell characterization data generated by HSC and reported in reference 2. These data include the effects of radiation exposure, temperature and angle of incident light on solar cell current-voltage (I-V) curves.

The detailed design data for the HS-376HP solar panels are used to generate predictions specifically for HS-376HP. These include the layout of solar cell circuits on the panels, I-V curves for isolation diodes and estimated voltage drops in the wire harness. Power output is predicted at the minimum EOL bus voltage; for M1 and M2, this voltage is 29.3 V. The model allows any number of failed (non-conducting) circuits to be assumed in the prediction; for M1 and M2, one failed circuit is required for predictions of minimum power. However, to assess the accuracy of the prediction methodology, we also include a calculation with no failed circuits, as discussed below.

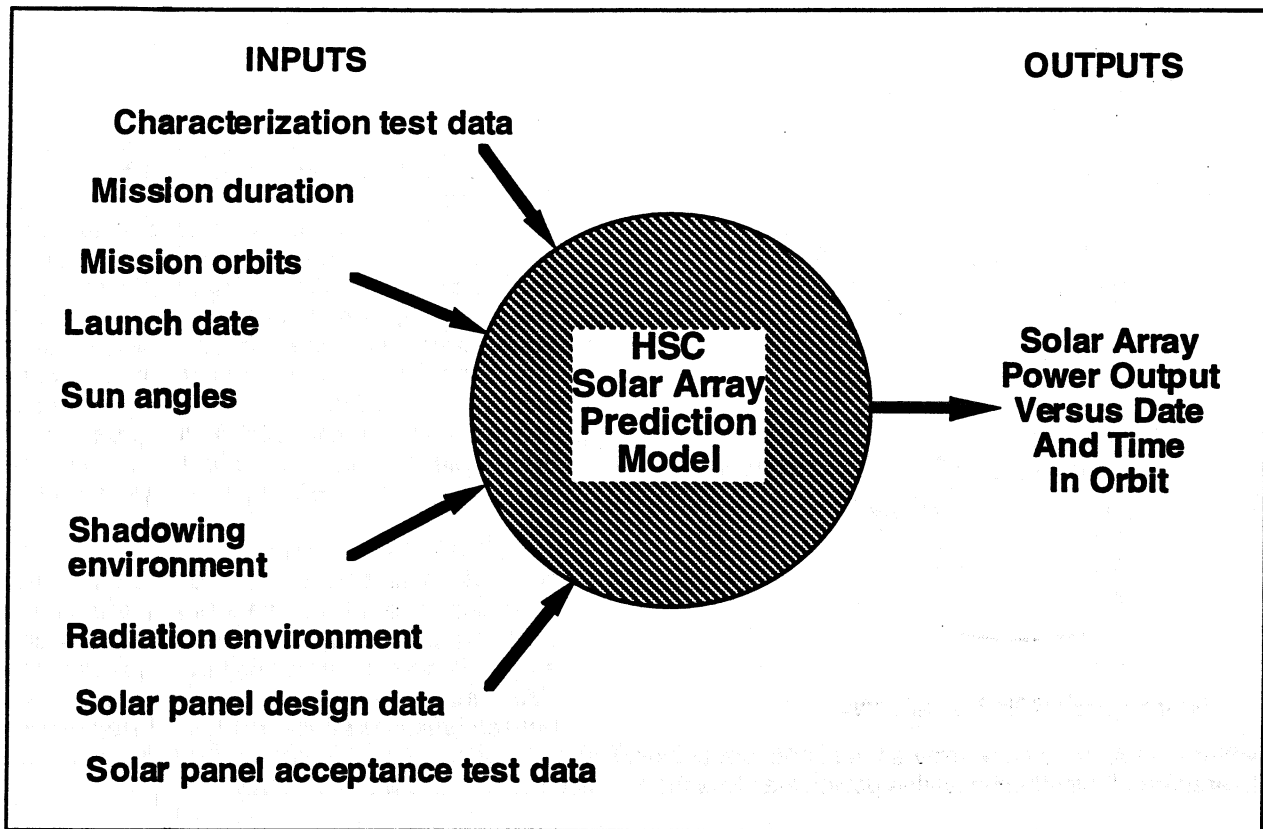


Figure 2. Solar array performance prediction methodology

The design data also include temperature predictions for various portions of the array. Temperature predictions vary as a function of the time of year and location on the panels. For example, the fixed panel in Figure 1 tends to have higher temperatures, due to heat from the internal payload. However, during winter solstice, the deployable panel temperatures increase, due to sunlight on the panel backside. After the spacecraft is launched, telemetry from temperature sensors located on the array can be used as inputs to the model. This allows the accuracy of the model to be assessed while excluding the effect of deviations from predicted thermal behavior.

Inputs to the power prediction model also include the space radiation environment. For predictions, the model uses the AE8 and AP8 trapped radiation environments [5,6] and either the 20th or 22nd solar cycle [7] for solar flare protons (provided by the National Oceanic and Atmospheric Administration Space Environment Laboratory). For M1 and M2, the 20th solar cycle is used, since the spacecraft was designed prior to completion of the 22nd cycle. Relevant details of the mission, such as the mission duration, orbit and launch date are used to reduce the radiation environment to an equivalent fluence of 1 MeV electrons [8]. HS-376HP is a geosynchronous mission with a design life of 15 years. Since both spacecraft were launched near the solar cycle minimum, the expected solar proton fluence corresponds to a single solar cycle. After the spacecraft is launched, actual solar flare data may be used as model inputs, to assess the model's accuracy while excluding the effect of short-term fluctuations in solar activity.

The prediction model accounts for the effects of different angles of incident light on solar panel output. As the spacecraft revolves around the sun, the nominal sun angle to the spacecraft varies from 0 degrees in equinox to 23.5 degrees in solstice periods. However, on HS376 series spacecraft, there are additional angle of incidence effects, since the solar array is cylindrical and spinning. As a result of the spacecraft configuration, the angles of incident light on any solar cell circuit vary from the nominal sun angle to 90 degrees during any rotation. Furthermore, the angle of incidence effects are a function of radiation exposure [9]. Hence, the prediction model calculates the effects of angle of incidence on each solar cell circuit as a function of date and time in orbit. The aggregate effect on the solar array I-V curve is then generated for each day of the mission. After the spacecraft is launched, actual telemetry on

spacecraft pointing may be used as input data, to assess the effects of any deviation from the nominal expected sun angle on solar array performance.

Another important aspect of the prediction model is the ability to include losses due to shadowing of the array. For M1 and M2, the fixed panel in Figure 1 is subjected to partial shadowing under normal operating conditions. The shadow is cast by a mechanical part, located behind the antenna dish in Figure 1, and extends over an area of the fixed panel which varies with the season. The maximum length of the shadow occurs at summer solstice and is expected to reach 3 inches down from the top of the panel. However, the precise dimensions of the shadow are only estimated, since the part which casts the shadow is wrapped in a thermal blanket. The prediction model includes the nominal losses due to solar cell shadowing, as a function of time, based on the expected shadowing pattern.

Finally, the solar panel acceptance test results are used as input data. For M1 and M2, these data were taken by Spectrolab, Inc. using a large area pulsed-xenon solar simulator (LAPSS). The measured I-V curves, at ambient temperature and AM0, for each solar cell circuit are used to establish the initial electrical output of the solar array. Therefore, the model predictions are absolute power predictions, in watts, based on ground test data.

The output of the prediction model is the solar array power versus date and time in orbit, as shown in Figure 2. To generate the prediction, the model determines the beginning-of-life (BOL) power from the LAPSS data, corrected to predicted operating temperatures and sun angles using the characterization and design information. Characterization data and the radiation environment are then used to generate power predictions throughout the life of the spacecraft. This methodology has been in use at HSC for approximately 20 years [10], with periodic refinements made to the algorithms and the database.

Comparison Of Predicted And Telemetered Performance

To obtain a meaningful comparison between predicted and telemetered data, we have found it useful to generate two types of prediction data [10], shown in Table I. First, we generate minimum power predictions, which represent the model outputs generated prior to launch. As such, they are required to include some conservative factors such as one failed circuit. They also include a loss factor for the ripple effect discussed above. As shown in Table I, they are based on (nominal) predicted temperatures and the nominal predicted solar proton fluence. Next, we generate "in-orbit predictions". As shown in Table I, the in-orbit predictions assume no failed circuits, no ripple factor, are adjusted for telemetered temperatures and sun angles, and use actual solar flare data.

Comparison of telemetered power output with the minimum power predictions is used to assess our process for generating predicts prior to launch. Comparison with the in-orbit predictions is used to assess the accuracy of the prediction methodology using completely nominal inputs and excluding, as far as possible, the uncertainty in the thermal predictions, fluctuations in solar activity and any deviation from the expected spacecraft attitude. In-orbit predicts are therefore referred to as the most "nominal case".

To calculate the available power from telemetry, we multiplied the telemetered bus voltage by the current from the solar array. The solar array current was taken as the sum of the telemetered bus current and the telemetered tap limiter current. Implicit in this approach is the assumption that the tap limiter current is available at the bus voltage. Also implicit is the assumption that the bus voltage is close to the minimum bus voltage of 29.3 V. The uncertainty associated with this calculation and with the telemetry itself is discussed below.

The comparison between the predicted and telemetered data for M1 is shown in Figure 3. As shown in the figure, the measured power exceeded the minimum power prediction throughout the mission; the average difference was 1.4%. The measured power was below the in-orbit prediction throughout the mission; the average difference was -1.7%.

The comparison for M2 is shown in Figure 4. As shown in the figure, the measured power exceeded the minimum power prediction throughout the mission; the average difference was 3.4%. The measured power was very close to the in-orbit predict throughout the mission; the average difference was 0.4%.

The comparisons in Figures 3 and 4 show generally close agreement between measured and predicted data. As expected, the minimum power predictions were slightly conservative. The in-orbit predictions were within 2% of the actual power on both spacecraft. Hence, the inherent accuracy of the model appears to be approximately $\pm 2\%$; this result is very similar to previous results for silicon solar arrays [10].

Table 1. Prediction Model Inputs

	Minimum Power Predict	In-Orbit Predict
Initial I-V curves	LAPSS data	LAPSS data
<i>Failed circuits</i>	<i>One failed circuit</i>	<i>No failed circuits</i>
<i>Ripple factor</i>	<i>Based on LAPSS data</i>	<i>None</i>
<i>Temperatures</i>	<i>Nominal predictions</i>	<i>Adjusted using telemetered temperature data</i>
<i>Sun angle</i>	<i>Nominal prediction</i>	<i>Telemetered data</i>
Electron environment	AE8	AE8
<i>Solar proton environment</i>	<i>20th solar cycle (M1 and M2)</i>	<i>Actual flare data</i>
Optical degradation	2%	2%
Radiation degradation profile	Characterization data	Characterization data
Temperature coefficients	Characterization data	Characterization data
Angle of incidence effects	Characterization data	Characterization data
Shadowing	Predicted shadow pattern	Predicted shadow pattern
Wire harness loss	Estimated	Estimated
Isolation diode loss	Nominal	Nominal
Operating voltage	29.3 V (M1 and M2)	29.3 V (M1 and M2)

* Note: Italics indicate where minimum power predicts and in-orbit predicts use different inputs.

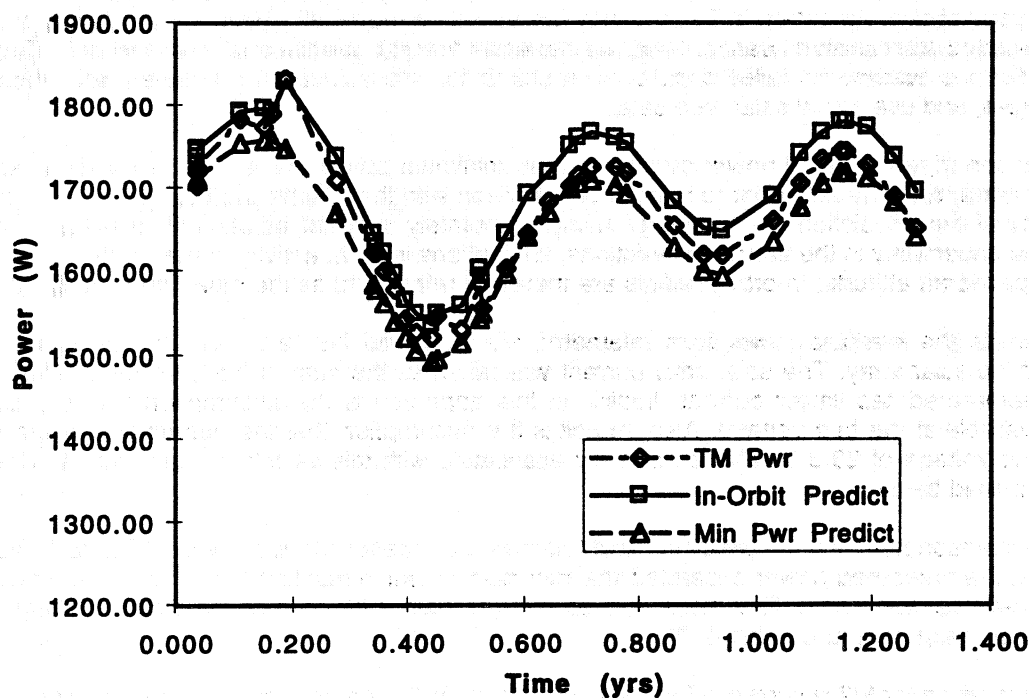


Figure 3. Comparison of predicted and telemetered power for M1 solar array

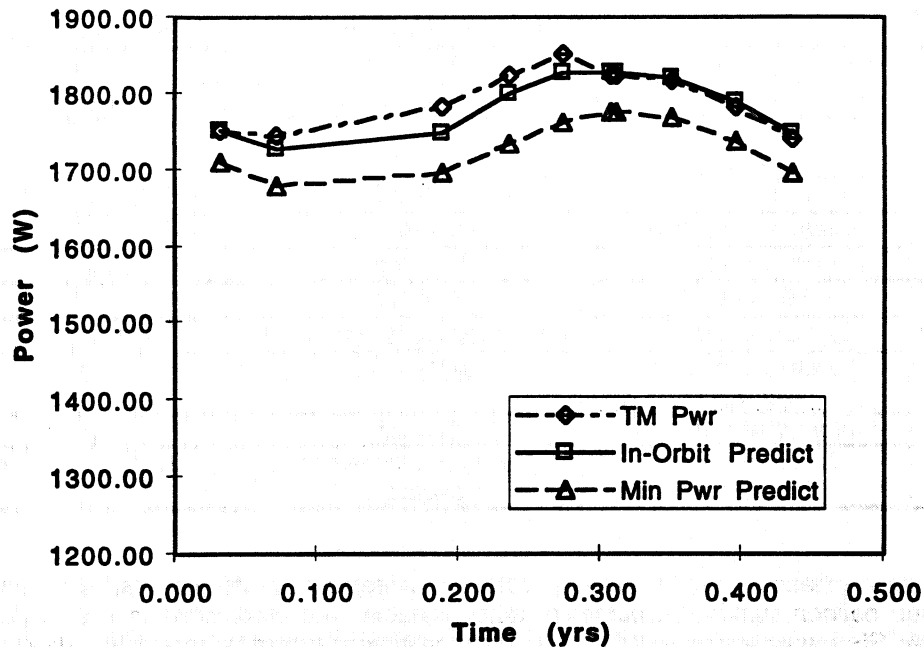


Figure 4. Comparison of predicted and telemetered power for M2 solar array

Some differences between the M1 and M2 spacecraft are apparent. The BOL power of M2 was higher than M1; both the LAPSS and telemetered data showed this difference. In addition, during the mission, the M1 performance agreed more closely with the minimum power predictions and the M2 performance agreed more closely with the in-orbit predictions. However, the M2 spacecraft was launched more recently than M1. As a result, it appears to be too early to obtain a definitive comparison between M1 and M2. As the mission proceeds, additional data should provide a more meaningful comparison.

Uncertainty Analysis

Several uncertainties affect the predictions and the measurements presented above. To analyze the accuracy of the above comparisons and to help in further refining our prediction model, a detailed uncertainty analysis was initiated. A summary of the key uncertainties is shown in Table II. The table includes uncertainties which can affect both telemetered power and predicted power. The uncertainties affecting telemetered power include both measurement errors and assumptions made in calculating available power from the telemetry. For errors affecting predicted power, only measurement errors (e.g. LAPSS calibration) are included.

Table II includes both random and systematic errors. The random errors are not expected to affect the average results when a large number of measurements are taken. However, a few potential systematic errors were also identified. Two systematic errors affect the telemetered power. These are 1) the assumption that the tap limiter current is available at the bus voltage and 2) use of the measured bus voltage to calculate available power. These assumptions are valid when the payload is extracting close to full power. When the solar array has significant excess power, the tap limiter assumption results in an overestimate of the available power and the array voltage assumption results in an underestimate of the available power. For both M1 and M2, the power usage has been close to maximum after a couple of months following launch. As a result the estimated error for each of these effects is less than 0.2%. Future work will include improvements to the calculation to reduce these uncertainties.

Table II. Uncertainty Analysis

	Uncertainty	Random/Systematic	Estimated Error
Uncertainty in telemetered power	Bus voltage telemetry	Random	±0.02%
	Bus current telemetry	Random	±0.5%
	Tap limiter current telemetry	Random	±0.01%
	Tap limiter voltage	Systematic	≤ 0.2% (M1 and M2)
	Solar array voltage	Systematic	≥ -0.2% (M1 and M2)
	Sun angle telemetry	Random	Negligible
Measurement uncertainty affecting predicted power	LAPSS fluctuation	Random	±1%
	LAPSS calibration	Systematic for each panel	±1%
	Balloon standard accuracy	Systematic	≤ 1.4%
	Temperature telemetry	Random	In work
	Shadow pattern uncertainty	Systematic for each spacecraft	±1% at summer solstice

Table II also lists the measurement errors with potential systematic effects on predicted power. Of these, we identified balloon standard accuracy as a key variable. The predictions in Figures 3 and 4 were based on LAPSS measurements with the LAPSS calibration traceable to a 1994 balloon flight (JPL standard #94-101). In general, we expect that the uncertainty resulting from balloon standard accuracy will diminish as additional balloon flights are conducted. For example, a more recent balloon standard (#96-155), flown in 1996, resulted in a lower calibration value for the LAPSS. The 1996 value was lower than the 1994 value by 1.4%; hence, there is the possibility that the LAPSS spectrum was 1.4% higher than AM0. If this is the case, then the M1 power would fall below the in-orbit prediction by 0.3% and the M2 power would exceed the in-orbit prediction by 1.8%. This difference between the two balloon standards was also analyzed using spectral response measurements; however, the spectral response data were inconclusive. Nevertheless, the question will be answered by additional measurements taken on upcoming balloon flights and comparison with in-orbit data, including the data from M1 and M2.

Based on the uncertainties described above, we expect that the predictions and in-orbit data should agree, on average, to within approximately 2%. To date on HS-376HP, the data have validated our expectation. Future work will focus on further reducing the model uncertainties, continuing to build the GaAs/Ge performance database, and assessing the prediction model capabilities in a variety of missions.

Summary

The first two commercial communications satellites with GaAs/Ge solar arrays were launched in January and November of 1996. In-orbit solar array performance data from both spacecraft were compared with predictions from Hughes' solar array prediction model. The results show that the in-orbit power of both arrays exceeded the pre-launch predictions throughout the mission. When compared to in-orbit, or nominal case, predictions, the M1 power was approximately 1.7% below the prediction and the M2 power was approximately 0.4% above the prediction. These results are comparable to previous studies on Hughes silicon solar arrays showing agreement with prediction to within approximately 2%.

References

- [1] P.A. Iles and F. Ho, Technology Challenges For Space Solar Cells, 1994 IEEE First World Conference On Photovoltaic Energy Conversion Vol. II, IEEE, p. 1957, 1994.
- [2] M.R. Brown, C.A. Garcia, G.S. Goodelle, J.S. Powe, J.A. Schwartz, Characterization Testing Of Measat GaAs/Ge Solar Cell Assemblies, Progress In Photovoltaics - Research and Applications, Vol. 4 no. 2, John Wiley and Sons, p. 129, 1996.

- [3] **Infra Red Reflective Coverglasses: The Next Generation**, K. Mullaney, G.M. Jones, C.A. Kitchen, D.P. Jones, IEEE 22nd Photovoltaic Specialists Conference, IEEE, 1991, p. 1593, 1991.
- [4] **P. Gorian, J. Jordan, T. Chao, Spacecraft Power And Electronics, 1985 IRECON International 20th International Electronics Convention & Exhibition of the Institution of Radio and Electronics Engineers Australia, Digest of Papers, v. 1, Inst of Radio & Electronics Engineers Australia, p 365-368, 1985.**
- [5] **J.I. Vette, The AE8 Trapped Electron Model Environment, NSSDC/WDC-A-R&S 91-24, 1991.**
- [6] **D.M. Sawyer and J.I. Vette, AP8 Trapped Proton Environment for Solar Maximum and Solar Minimum, NSSDC/WDC-A-R&S 76-06,1976**
- [7] **E.G. Stassingolopoulos and J.H. King, An Empirical Model Of Energetic Solar Proton Fluxes With Applications To Earth Orbiting Spacecraft, NASA GSFC X-601-72-489, 1972.**
- [8] **B. E. Anspaugh, GaAs Solar Cell Radiation Handbook, JPL Publication 96-9, Jet Propulsion Laboratory, 1996.**
- [9] **D.R. Burger, R.L. Mueller, G. Goodelle, J. Powe, J. Schwartz, Angle Of Incidence Corrections for GaAs/Ge Solar Cells with Low Absorptance Coverglass, Proceedings Of The 25th IEEE Photovoltaics Specialists Conference, IEEE, p. 243, 1996.**
- [10] **S.W. Gelb and L.J. Goldhammer, In-Orbit Performance of Hughes HS-393 Solar Arrays, Proceedings of the 22nd IEEE Photovoltaic Specialists Conference, IEEE, 1991.**

SCARLET SOLAR ARRAY SYSTEM STUDY FOR HIGH POWER GEO SPACECRAFT

Brian R. Spence, P. Alan Jones, Mike I. Eskenazi, David M. Murphy
AEC-Able Engineering Company, Inc.
Goleta, California 93117

ABSTRACT

In response to market demand for increased GEO satellite capability, commercial spacecraft manufacturers will require significantly higher power solar arrays to meet future mission requirements. As satellite and solar array capability increases the demand for high power array systems which are both cost and performance competitive becomes more crucial. Conventional rigid panel planar arrays, although suitable in the past, are cost and performance prohibitive for these new applications. The Solar Concentrator Array with Refractive Linear Element Technology (SCARLET) represents an attractive solution for meeting these new high power requirements. When compared to conventional planar arrays, SCARLET provides substantially lower cost and higher deployed stiffness, competitive mass, better producibility, and affordable use of high efficiency multi-junction cells. This paper compares cost/performance characteristics of the SCARLET array to conventional planar arrays for high power GEO spacecraft applications. High power SCARLET array configurations are described, and inherent spacecraft and array level cost/performance benefits are presented.

INTRODUCTION

As satellite and solar array capability increase, the demand for higher power array systems which are both cost and performance competitive is becoming more crucial. Recent projections from leading GEO spacecraft manufactures indicate that solar array power requirements will climb from the 8 kW - 10 kW ranges of today to 15 kW - 20 kW within five years, and up to 30 kW within the next decade.¹ Meeting these new aggressive applications requires consideration of an alternative array technology which minimizes performance/cost impacts at the spacecraft system level.

The Solar Concentrator Array with Refractive Linear Element Technology (SCARLET) offers an attractive solution for meeting these new high power requirements. When compared to conventional planar arrays, SCARLET provides substantially lower cost, competitive mass, higher deployed stiffness, better producibility, and affordable use of high efficiency multi-junction cells.

To address the benefits of the SCARLET solar array, when compared to conventional systems for high power GEO spacecraft applications, a trade study evaluation was performed. Parameters considered include array and spacecraft system level cost, mass, and deployed stiffness. It will be shown that SCARLET represents a low-risk, high-payoff, solution for high power GEO applications when compared to conventional rigid panel array systems.

GENERAL GEO SOLAR ARRAY BACKGROUND

Rigid multi-panel conventional planar arrays have long been the array of choice for GEO spacecraft applications. The rigid multi-panel design leverages successful past flight heritage and, as such, is ideally suited for conservative/risk sensitive applications. Panel materials, photovoltaics, and mechanism subsystems have evolved over the years to produce array level end-of-life specific powers between 40-50 W/kg. These systems have performed admirably since their inception. The basic structural platforms have maintained an ability to provide GEO spacecraft manufacturers with power growth capability to meet today's end-of-life power needs of 8-10 kW.

Due to the enormous demand for increased GEO spacecraft capability, satellite manufactures are aggressively developing next generation spacecraft designs which operate larger more efficient payloads and employ improved systems for radiating waste heat. As such, these enhanced spacecraft configurations both require and can tolerate higher power generating capabilities. As power systems grow beyond 10 kW, and up to 20-30 kW, the limitations of conventional rigid multi-panel solar arrays for meeting these new requirements are being realized. In general, a conventional system adapted for a higher power application becomes larger, heavier, or significantly more expensive. This results in notable performance and/or cost impacts for the GEO spacecraft producer.

A number of modifications can be incorporated to adapt a conventional array for a high power application. The most common approach is a simple changeout of photovoltaics to a higher efficiency cell, such as high efficiency Silicon, GaAs/Ge, or more expensive multi-junction GaInP₂/GaAs/Ge. Incorporation of such advanced photovoltaics does increase specific power, but carries with it a significant increase in array cost.

Another technique for increasing power is to incorporate additional panels onto each wing. Unfortunately, this adaptation poses many structural and spacecraft attitude control system concerns. Adding panels to a wing increases kinematic complexity which affects deployment authority and reliability. A suitable qualification program is generally required to minimize risk of the modified design.

As a wing becomes longer its deployed stiffness degrades approximately as the cube of its length. Therefore, the longer the wing the greater the burden it places on a spacecraft's ability to efficiently perform attitude and control maneuvers. Additionally, some spacecraft attitude and control system designs actually limit the number of panels that can be deployed. This deficiency may drive a system designer to consider completely alternative wing configurations which position the array center of gravity closer to the spacecraft to enable more precise spacecraft attitude and control response.

Many of the above modifications are being considered by commercial spacecraft manufacturers as a short-term solution to increase power. As spacecraft capability and power needs continue to increase, performance and cost competitive pressures will begin to drive array selection. This process will likely result in the slow demise of the conventional rigid panel array in favor of a highly efficient array technology, such as SCARLET, which can cost-effectively employ high efficiency photovoltaics.

ANALYTICAL SCOPE

SCARLET and conventional GaAs/Ge planar array systems for GEO spacecraft applications were configured and analyzed for powers ranging from 8-20 kW EOL. Array system level costs and mass properties were calculated for each array type and configuration. Depending upon the array's mass, an additional cost savings/penalty valued at \pm \$58,000/kg was applied to each configuration accordingly to determine a spacecraft system level cost.² Finite Element Models

(FEM) were used to determine the deployed first mode fundamental frequency for each array type and size.

Array costs were calculated for each system based upon pricing for a 25-shipset (50-wings) multiple-buy procurement over a 5-year duration. Array costs for the conventional GaAs/Ge planar systems are based on actual costs from numerous industry sources (commercial and government) which have been substantiated through several current buyers. For confidentiality reasons, raw array costs for these systems cannot be provided in this paper.

CONVENTIONAL RIGID PANEL GEO ARRAY DESCRIPTION

To model the performance of a conventional high power array system for this trade study an ABLE PUMA system, as shown in Figure 1, was configured and analyzed to represent the current state-of-the-art. Wing configurations ranged from four to seven panels per wing. Panel size, thickness, stowed volume, and number of tie-down points are consistent with typical GEO solar array systems. Photovoltaics consisted of 19% efficient single junction GaAs/Ge solar cells. It is important to note that state-of-the-art multi-junction GaAs/Ge solar cells were not considered for conventional arrays in this analysis because of their excessive costs and limited maturity. Substrate materials consisted of 1.00-inch-thick aluminum honeycomb core at a 1.6 lb/ft³ density with graphite/cyanate ester facesheets integrated with localized reinforcements at high stress regions.

Mass properties of the 8-kW class planar design is based on a specific power of approximately 49 W/kg EOL at 15-years Equinox. Mass properties for the remaining planar wing configurations, up to 20 kW, were calculated in detail to account for the additional number of panels and support structure.

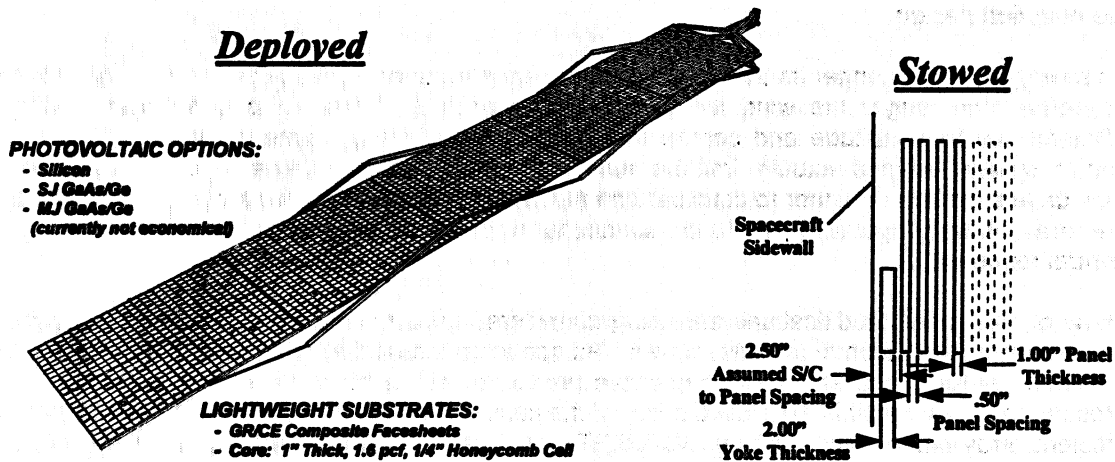


Figure 1. Conventional GEO Rigid Panel Array (ABLE PUMA Array Shown for Illustrative Purposes)

SCARLET GEO ARRAY DESCRIPTION

The SCARLET array modeled in this analysis has been configured especially for GEO spacecraft applications. These systems accommodate conventional single axis sun tracking with standard alpha pointing tolerances of ± 3 degrees. Additionally, these SCARLET systems include an outboard facing planar panel to provide stowed power and on-orbit tumble recovery power. Descriptions of SCARLET sub-systems and hardware can be found in the provided references.^{3,4}

The SCARLET GEO array is shown in Figure 2. The array consists of a hybrid configuration in which each wing is composed of multiple SCARLET panels with an integrated outboard conventional planar panel. Panel size and number of tie-down points are consistent with typical GEO array systems.

The SCARLET optics and cell modules are similar to, and based on, the New Millennium DS1 SCARLET II flight design. Structural platforms modeled in this analysis included both a standard substrate design, which yields conventional stowed packing efficiencies, and a modified substrate design, which produces a significantly reduced stowed stack height. Each structural platform type incorporates locking shear-tie features which effectively couple the lens frame and cell substrate elements together to produce a deployed section with appreciable structural depth and greater deployed stiffness.

The SCARLET cell options modeled include both GaAs/Ge and multijunction GaInP₂/GaAs/Ge. It is important to note that multijunction GaInP₂/GaAs/Ge photovoltaics were modeled in the analysis for SCARLET designs only, since SCARLET enables an affordable implementation. Because fewer and smaller cells are required by SCARLET the cost impacts and cell yield concerns with employing advanced photovoltaics becomes negligible. Additionally, under SCARLET's ~7.5 X concentration, cell shunt defects become insignificant allowing low performing 1.0 AM0 shunt-defected multijunction cells to be utilized rather than scraped, further increasing yield which translates into reduced cost. The outboard planar panel can be populated with a variety of cell options, but for this analysis proven high efficiency Silicon photovoltaics were modeled.

ANALYSIS RESULTS

SCARLET and conventional planar array analysis results for specific power, deployed stiffness, array level costs, and spacecraft system level costs are discussed in the following paragraphs.

Specific power as a function of EOL power for each array system and configuration are shown in Figure 3. Figure 3 shows that the SCARLET system provides better specific power than the conventional planar array at all power levels. Understandably, SCARLET's economical use of advanced multijunction photovoltaics provides higher specific powers than the GaAs/Ge arrays. The highest specific power was achieved with the SCARLET modified substrate design populated with multijunction cells.

SCARLET and conventional planar array analysis results for deployed first mode frequency are shown in Figure 4. Typically, a suitable deployed first mode requirement for GEO spacecraft ranges between 0.05 Hz to 0.1 Hz, depending upon bus attitude control system capability.

Figure 4 shows that deployed stiffness of the SCARLET designs are significantly higher compared to conventional planar arrays. This is because SCARLET uses an innovative coupling between the lens frame and cell substrate panel which increases the sectional moment of inertia to produce a significantly stiffer deployed structure. As Figure 4 shows, the SCARLET designs meet

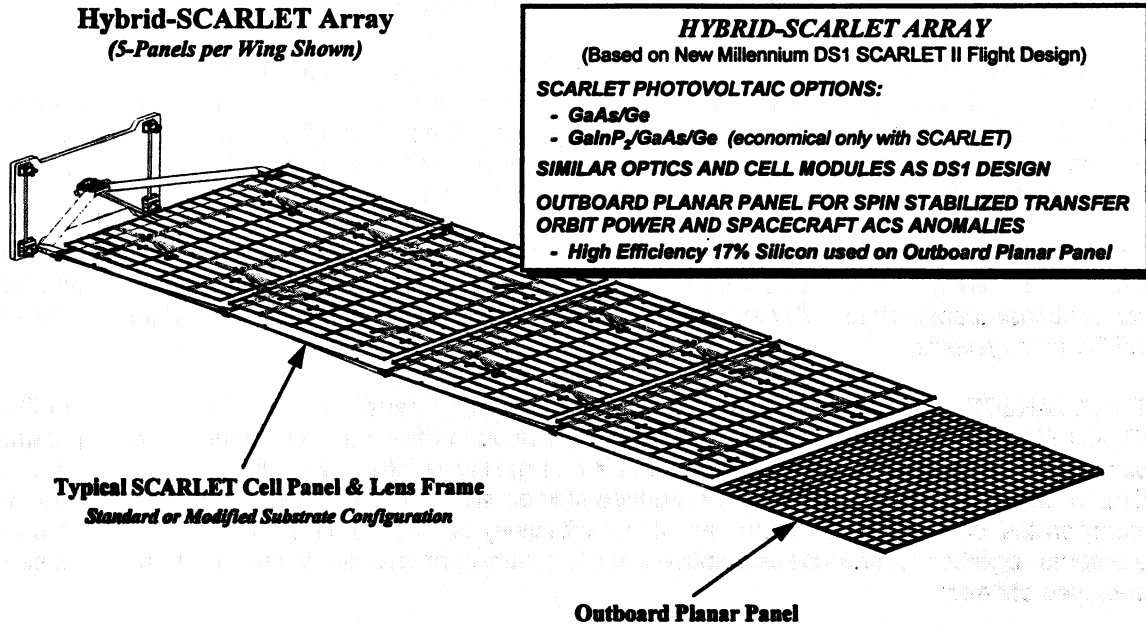


Figure 2. GEO SCARLET Solar Array

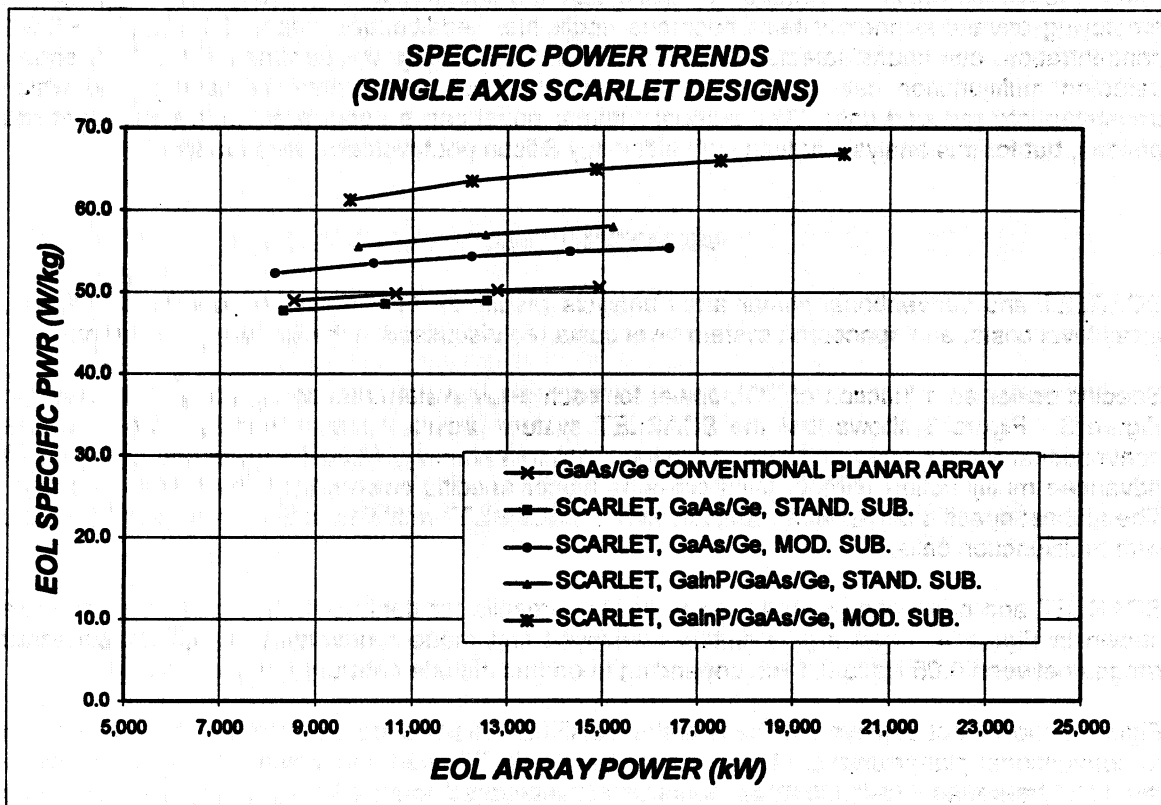


Figure 3. Specific Power Comparison

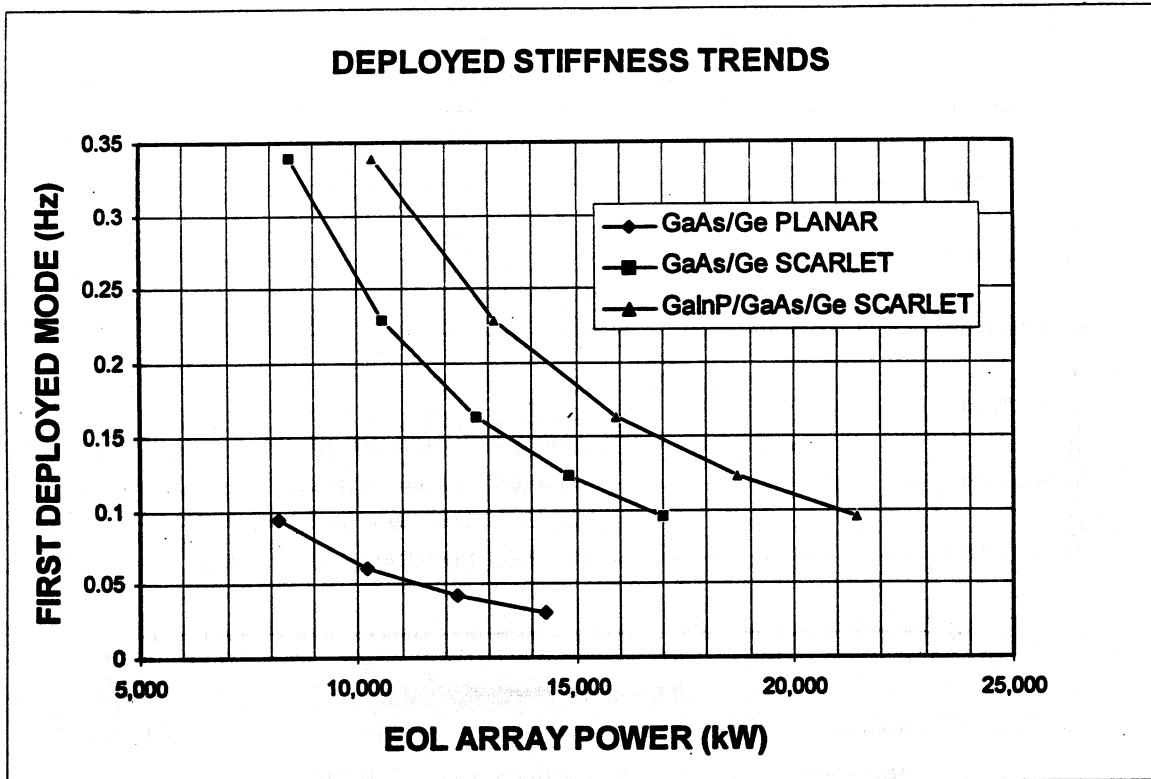


Figure 4. Deployed Stiffness Comparison

the deployed stiffness requirements by a large margin and will not impact existing spacecraft attitude and control systems for higher power arrays. In contrast, the conventional planar array drops below 0.05 Hz deployed first mode for systems larger than ~ 11 kW EOL. The lower deployed stiffness of the conventional planar array will impact the spacecraft attitude control system. SCARLET's higher stiffness will save significant fuel weight and cost over mission life.

Figure 5 depicts array level cost savings for a SCARLET system when compared to a GaAs/Ge planar array over a 25-shipset procurement. The curves displayed in Figure 5 clearly show that conventional GaAs/Ge planar designs are not cost competitive when compared to SCARLET. As an example, a 15 kW EOL SCARLET system produces an array level cost savings between ~ \$9M to \$10M per spacecraft. In some cases, this cost savings represents a 10% reduction in overall spacecraft cost.

Figure 6 depicts spacecraft level cost savings for a SCARLET system when compared to a GaAs/Ge planar array over a 25-shipset procurement. The spacecraft level cost savings curves shown in Figure 6 account for array level costs and an applied mass savings/penalty valued at +\$58,000 per kg, adjusted appropriately depending on a system's mass.² The curves displayed in Figure 6 clearly show that conventional GaAs/Ge planar designs are not cost competitive when compared to SCARLET, at any power range. Again, as an example, a 15 kW EOL SCARLET system produces a spacecraft level cost savings between ~\$11M to \$13M per spacecraft.

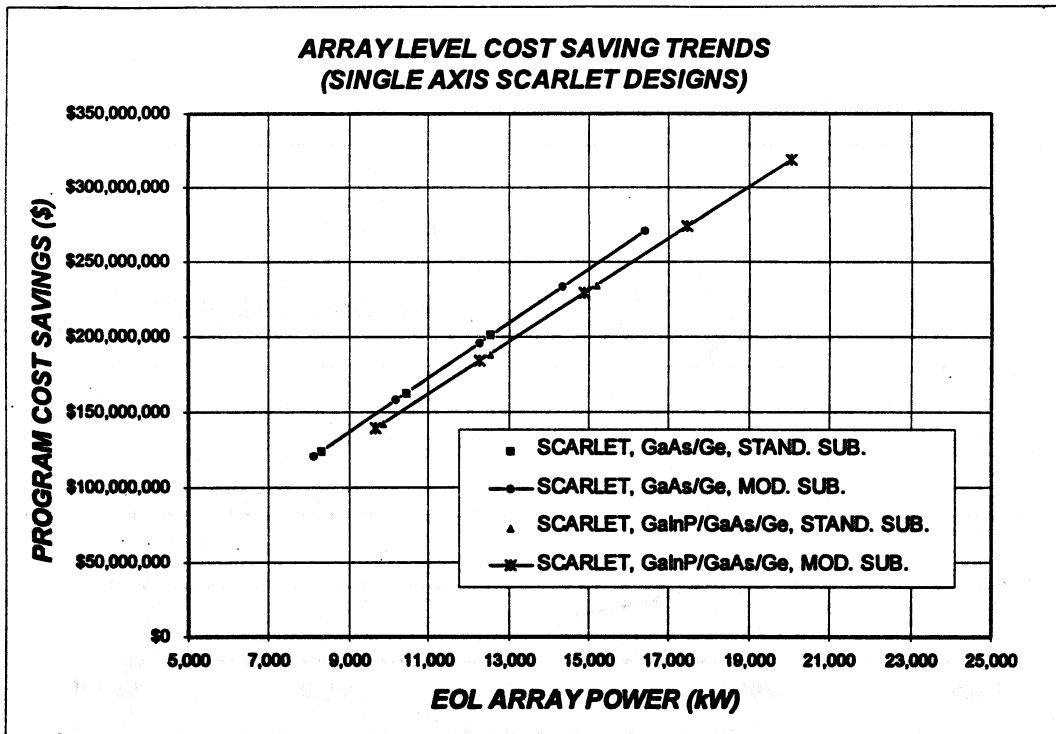


Figure 5. Array Level Cost Savings with SCARLET

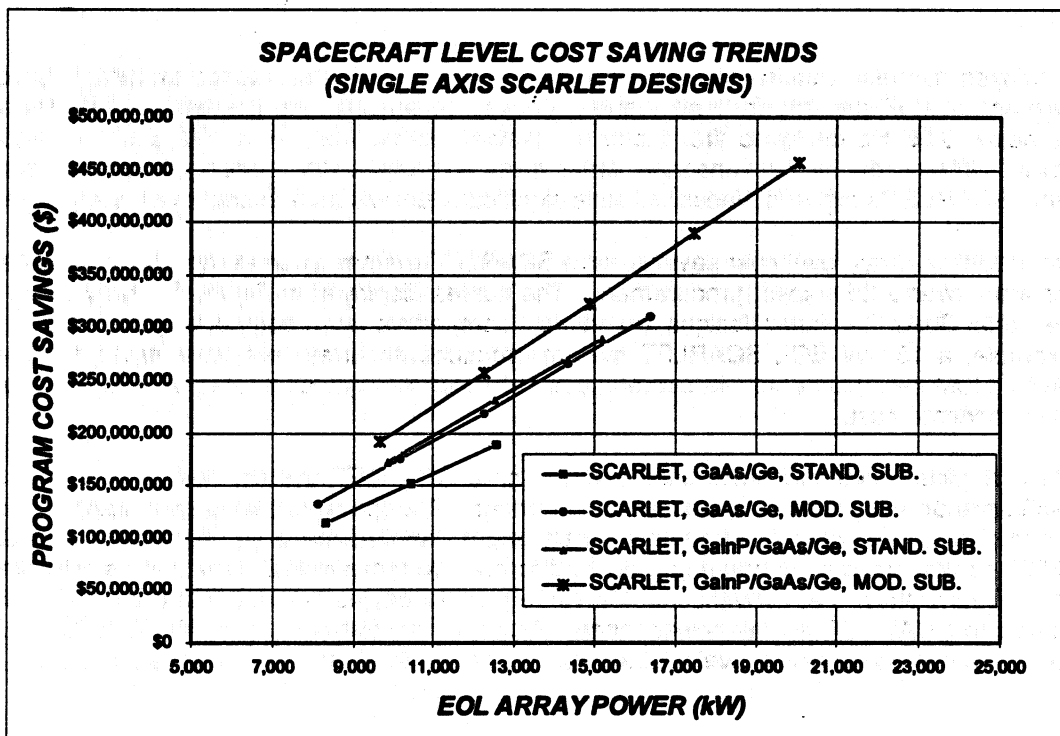


Figure 6. Spacecraft Level Cost Savings with SCARLET

CONCLUSIONS

Conventional GaAs/Ge planar solar arrays are not cost or performance competitive for high power GEO spacecraft applications when compared to SCARLET systems. Conventional planar systems exhibit significant cost, mass, and deployed stiffness impacts to the spacecraft which significantly affect overall system performance and cost competitiveness. SCARLET systems provide an attractive alternative for meeting these aggressive high power requirements. When compared to conventional GaAs/Ge planar arrays, SCARLET systems provide substantial cost savings. Cost savings for a 15 kW EOL SCARLET array are estimated between ~ \$9M to \$10M at the array level, and ~ \$11M to \$13M at the spacecraft level. Additionally, SCARLET systems have superior specific power ranging up to 67 W/kg EOL. SCARLET also provides a significantly higher deployed stiffness which mitigates the impacts to an existing spacecraft attitude and control system. SCARLET provides more cost-effective power growth accommodation by the implementation of multijunction GaInP₂/GaAs/Ge cells. Further performance gains can be achieved through the implementation of the modified substrate design which produces an extremely high stowed packing density. Unlike other concentrator designs, SCARLET's innovative linear Fresnel optics can accommodate standard single axis tracking systems which eliminates the impacts to existing bus designs. SCARLET's unique hybrid configuration which incorporates an outboard facing planar panel provides mission dependent stowed transfer orbit and deployed tumbling anomaly power. Finally, because of SCARLET's ~7.5 X concentration, the currently impacted solar cell manufacturing base is leveraged because fewer and smaller cells are required. Risk mitigation through ongoing programs and ABLE IR&D activities facilitate SCARLET's implementation as a low risk high-payoff array solution for high power GEO spacecraft applications.

REFERENCES

1. McVey, M., "Commercial Space System Practices," Presentation at the 15th Annual Space Power Workshop, 1997.
2. Wong, R. (TRW) "Space Mission Analysis and Design," Chapter 20 titled: Cost Modeling, 2nd Edition.
3. Jones, P. A. et al, "SCARLET: A High-Payoff, Near-Term Concentrator Solar Array," Proceedings of the 16th American Institute of Aeronautics and Astronautics ICSSC Conference, 1996.
4. Allen, D. M. et al, "The SCARLET Light Concentrating Solar Array," Proceedings of the 25th IEEE Photovoltaics Specialist Conference, 1995.

Balloon and Lear Jet Testing of SCARLET Modules and Cells

Michael I. Eskenazi & David M. Murphy
AEC-ABLE Engineering Co., Inc.
Goleta, California 93117

Bruce E. Anspaugh & Robert L. Mueller
Jet Propulsion Laboratory
Pasadena, California 91109

Dave Brinker
NASA Lewis Research Center
Cleveland, Ohio 44135

Mark J. O'Neill
ENTECH, Inc.
Keller, Texas 76248

Abstract

This paper presents test results from SCARLET (Solar Concentrator Array with Refractive Linear Element Technology) experiments performed on several Lewis Research Center Lear jet flights and two JPL balloon flights. The tests were performed in support of the BMDO sponsored SCARLET II program, which is building a 2.6 kW SCARLET solar array to supply the primary power for the JPL New Millennium Deep Space 1 Mission. The experiments involve TECSTAR dual junction GaInP₂/GaAs/Ge cells flown bare and under two different types of SCARLET lenses. The two types of lenses tested were a developmental design consisting of monolithic THV fluoroplastic and the current baseline flight design consisting of ceria-doped microsheet and silicone. Measured lens and total module efficiencies are presented and the flight data is compared to various solar simulator test results.

Introduction and Background

SCARLET, as shown in Figure 1, is a concentrator solar array for space applications which uses linear refractive concentrator lenses to focus sunlight onto spaced rows of solar cells. For a given power level, the SCARLET optical system reduces the required solar cell area by approximately a factor of seven. The decreased cell area significantly reduces solar array cost and weight especially in high radiation environments where thick cell coverglass is required.

The BMDO Innovative Science and Technology Program is funding AEC-ABLE Engineering Co., Inc. (ABLE) to design and manufacture a 2.6 kW SCARLET solar array for NASA's first New Millennium Deep Space flight, called "DS1," which will be launched in July, 1998. The DS1 SCARLET solar array is shown in Figures 2 and 3. ABLE's

primary subcontractors on the DS1 SCARLET program are TECSTAR, who is supplying dual junction GaInP₂/GaAs/Ge cells, and ENTECH who is supplying the linear Fresnel concentrator lenses. Fabrication of the DS1 SCARLET solar array wings is nearing completion. Power verification and environmental testing is to start in June 1997 with array delivery to JPL for spacecraft integration occurring in December 1997.

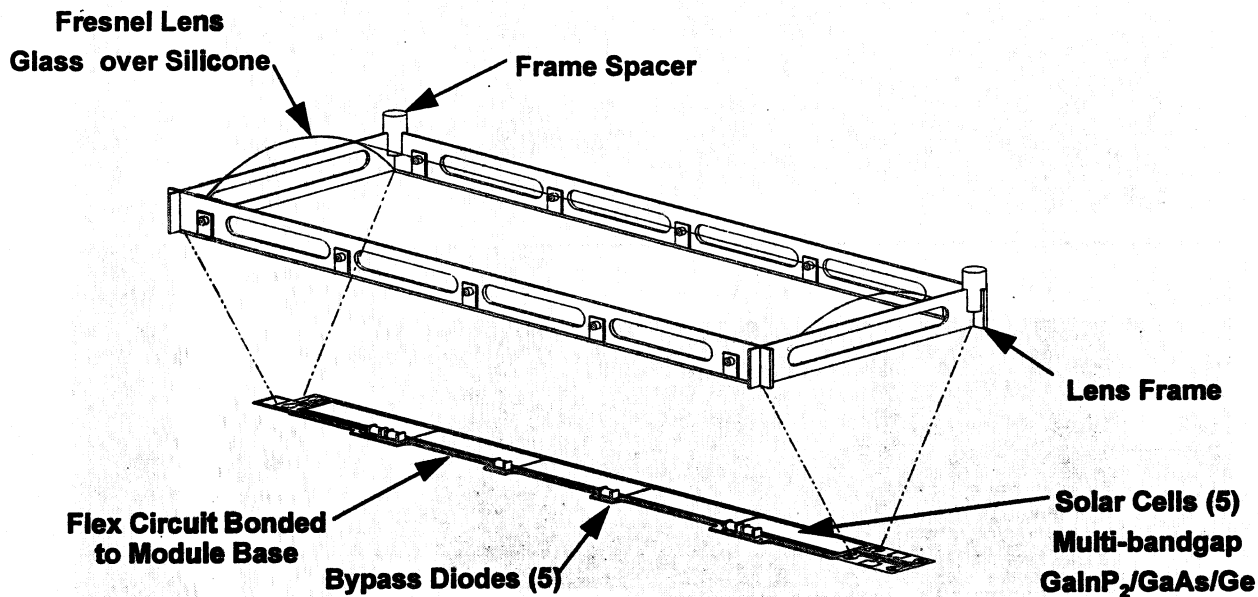


Figure 1. SCARLET Power Module - Building Block of the SCARLET Solar Array

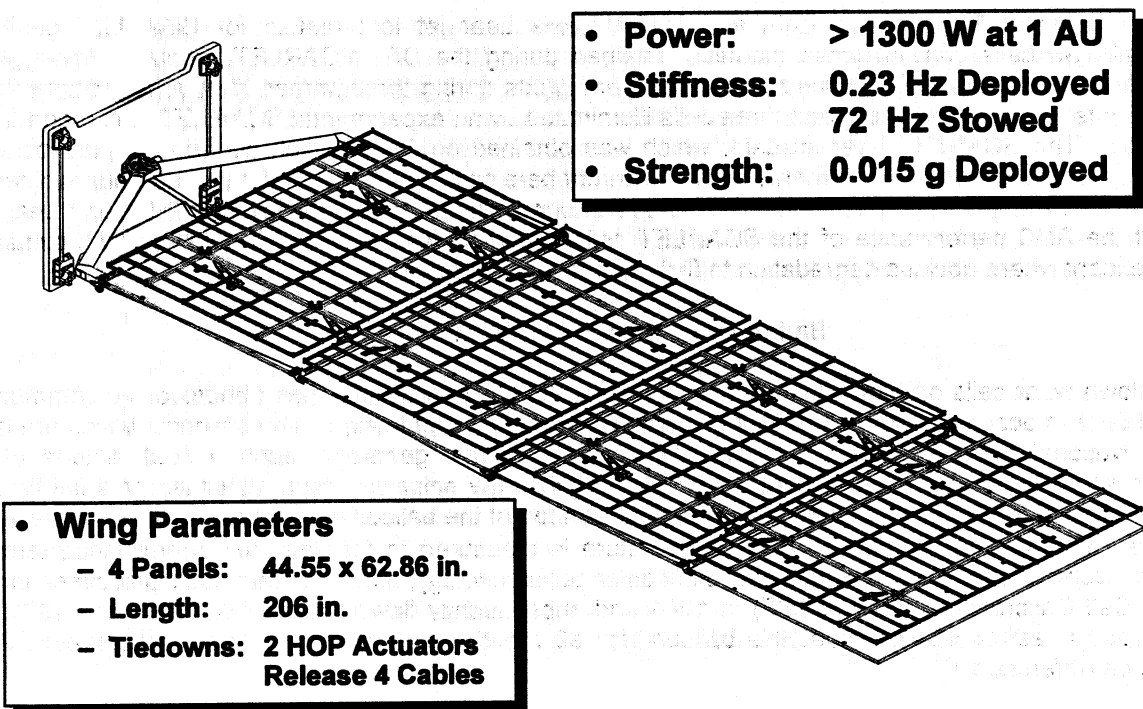


Figure 2. DS1 SCARLET Solar Array Wing

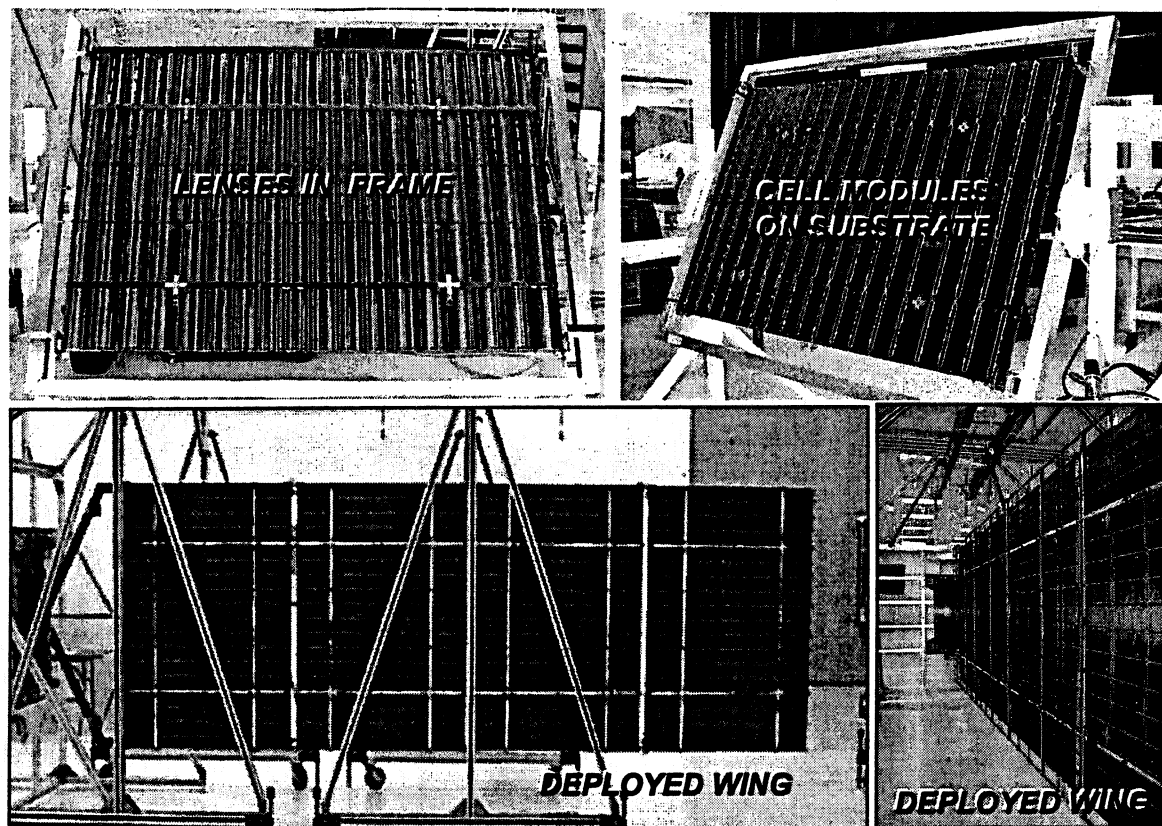


Figure 3. Photographs from DS1 SCARLET Solar Array Wing Manufacturing and Deployment Testing

This paper presents JPL balloon flight and NASA Lewis Lear jet test results for SCARLET dual junction GaInP₂/GaAs/Ge cells and lens/cells modules obtained during the DS1 SCARLET program. The SCARLET balloon flight data, which was obtained on two different flights during the summer of 1996, consists of IV curve measurements for three bare cells and three cells illuminated by an experimental SCARLET lens made from THV fluoroplastic. The SCARLET Lear jet data, which was obtained on flights which occurred during the winter of 1996/1997, consists of I_{sc} measurements for five different bare cells and I_{sc} and IV curve data for two cells under a DS1 flight-like ceria-doped microsheet/DC 93-500 silicone lens. Overall, the balloon flight and Lear jet data show that the AM0 performance of the SCARLET cells and modules tested are consistent with simulator test results – except where obvious degradation to flight test articles occurred.

Balloon Flight Solar Cell Measurements

JPL has flown solar cells on high altitude balloons since 1963 to provide the space photovoltaic community AM0 calibrated cells to accurately set solar simulator intensity during ground testing. The balloons, which are launched from the National Scientific Balloon Facility in Palestine, Texas, generally reach a float altitude of around 120,000 ft where the balloon remains for several hours while the solar cell data, either I_{sc} or a full IV curve, is collected. The solar cells are mounted to a sun tracker on top of the balloon which points normal to the sun within ±1 degree. The solar cell mounting plate temperature is measured to facilitate cell performance temperature correction. Comparison of a wide cross section of solar cell technology, flown on the shuttle Discovery as a part of the Solar Cell Calibration Facility (SCCF) in 1984 and subsequently flown on the JPL balloon in 1985 showed nearly identical results verifying that the balloon, for all practical purposes, is a true measure of AM0 cell performance (reference 1).

SCARLET Balloon Flight Data

The SCARLET balloon flight data, which was obtained on two different flights during the summer of 1996, consists of IV curve measurements for three bare cells and three cells illuminated by an experimental SCARLET lens made from THV fluoroplastic. The TECSTAR dual junction GaInP₂/GaAs/Ge SCARLET cells flown on the balloon were manufactured during an engineering development program in which 100 cells (4.2 x 1.14 cm) were delivered with a lot average efficiency of 24.2% at 7.5X AM0 uniform illumination. The primary purpose of the balloon flight test was to provide calibration cells for DS1 SCARLET ground testing. The secondary objective was to measure AM0 performance of SCARLET power modules utilizing an experimental THV lens.

Bare Cell Data

The three bare SCARLET cells were flown on the JPL balloon launched on June 10, 1996. A summary of the flight and pre-flight JPL LAPSS data for these cells, corrected to 28 °C, is shown in Tables 1 and 2. Temperature corrected IV curves from the beginning and end of the flight for cells 96-308 and 96-346 are shown in Figure 4. The average cell parameters during flight were calculated from 152 different IV curves measured over approximately a 3 hour period. Two of the three bare cells showed reduced fill factors and efficiencies in flight compared to the pre-flight JPL LAPSS. Cell 96-138 appears to have been severely damaged, as indicated by its very poor fill factor and efficiency measured in flight. Cell 96-346 showed modest fill factor and efficiency reduction raising questions about its condition. Cell 96-308 performed similarly on both the pre-flight LAPSS and in-flight tests making this cell the best cell for SCARLET ground test calibration until the flight-build cells are calibrated on the 1997 balloon flight.

Table 1. Bare SCARLET Cell Pre-flight JPL LAPSS and Balloon Flight Data Summary - 1 Sun Data

BARE CELL No.	LAPSS		BALLOON		LAPSS		BALLOON		Voc (V)	
	Efficiency (%)	Fill Factor (%)	Efficiency (%)	Fill Factor (%)	Efficiency (%)	Fill Factor (%)	Efficiency (%)	Fill Factor (%)	Pre-flight	Flight
96-138	22.1%	12.5%	0.80	0.58	68.43	68.97	2.425	1.8626		
96-308	21.8%	21.7%	0.81	0.80	67.44	68.51	2.423	2.3761		
96-346	22.0%	21.1%	0.80	0.78	68.16	67.91	2.423	2.3803		

Table 2. Difference Between Pre-flight JPL LAPSS Data and Balloon Flight Data for Bare Cells

BARE CELL No.	EFFICIENCY		FILL FACTOR		Isc (mA)		Voc (V)	
	Δ	(%)	Δ	%	Δ	(%)	Δ	(%)
96-138	-0.096	-43.44	-0.22	-27.50	0.541	0.79	-0.562	-23.19
96-308	-0.001	-0.46	-0.01	-1.23	1.067	1.58	-0.047	-1.94
96-346	-0.009	-4.09	-0.02	-2.50	-0.255	-0.37	-0.043	-1.76

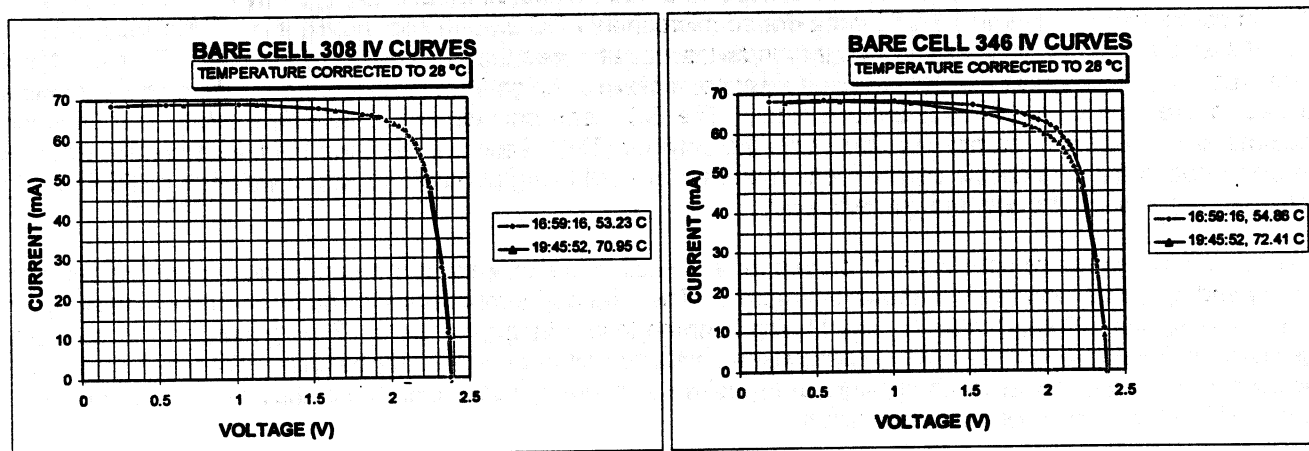


Figure 4. Bare SCARLET Cell IV Curves from June 10, 1996 JPL Balloon Flight

A post-flight investigation at ABLE has determined the most likely reason for the damage to cells 96-138 and 96-346 was due to reverse bias encountered either during ground or flight testing. Bypass diodes were not installed on the bare cells because before the flight it was not known that various pieces of test equipment, like LAPSS electronic loads, could produce enough transient reverse bias to damage the cells. This was an important lesson learned and incorporated on subsequent cell and module testing.

Balloon Flight SCARLET Lens/Cell Module Data

A SCARLET lens module, consisting of three individually wired cells under a single monolithic THV fluoropolymer lens measuring 7.50 x 3.43 inches, was flown on the August 8, 1996 balloon flight. Figure 5 is a photograph of the SCARLET balloon flight module mounted to the solar tracker during ground testing. The line of focused light on the solar cells created by the SCARLET lens is readily seen in the photograph.

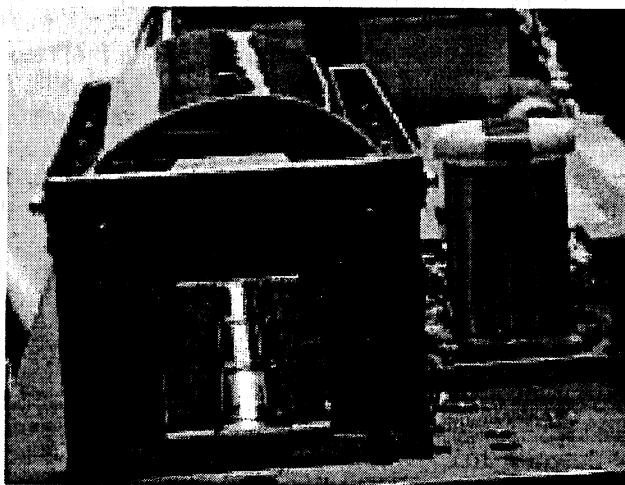


Figure 5. SCARLET Balloon Flight Module on Solar Tracker During Ground Testing

The three cells under the lens were individually wired so that IV curves could be measured separately for each one. A Resistance Temperature Device (RTD) was located in the baseplate under the middle cell (96-304). The measured baseplate temperature was used to calculate the cell junction temperature which is used to adjust cell performance to 28 °C.

The SCARLET balloon flight module THV prototype lens was measured by ENTECH to have an efficiency of only 80%. In comparison, the average DS1 ceria-doped microsheet / DC 93-500 silicone flight lens efficiency is 89.5%. The THV lens was used on the balloon flight module because it was the only DS1-sized SCARLET lens available at the time. The switch to microsheet / silicone lenses, a proven design from previous programs, came after it was too late to prepare a lens for the balloon flight. The DS1 lens change was made to alleviate manufacturing problems and radiation tolerance concerns with the polymer (THV, Teflon, Tefzel, etc.) lenses originally explored. It is worth noting that monolithic polymer lens materials are still being pursued for future versions of SCARLET to decrease cost and weight and improve efficiency.

The raw (non-temperature corrected) IV curves for each cell in the concentrator module obtained at the beginning and the end of the balloon flight is shown in Figure 6. The time and temperature for each IV curve is shown in the legend in the plots. Note, that both I_{sc} and V_{oc} became lower during the flight. The reduction in V_{oc} is easily explained by the negative cell voltage temperature coefficient and the higher temperature at the end of the flight. However, since I_{sc} increases with temperature (positive temperature coefficient), I_{sc} should have been *higher* at the end of the flight compared to the beginning.

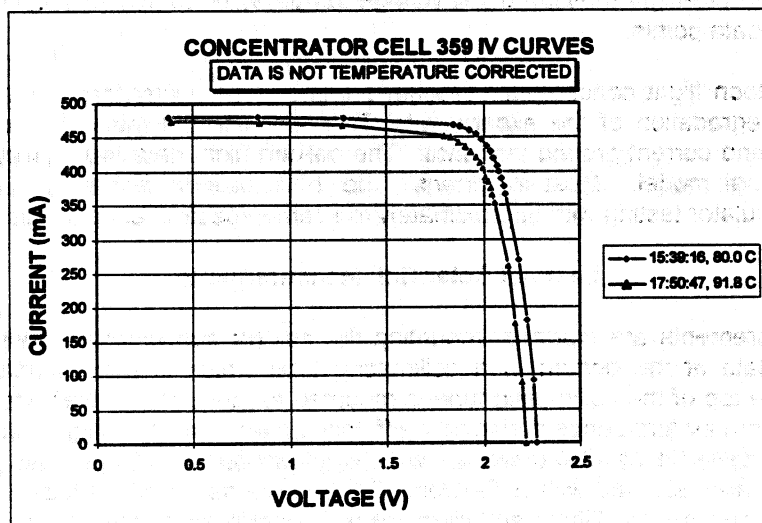
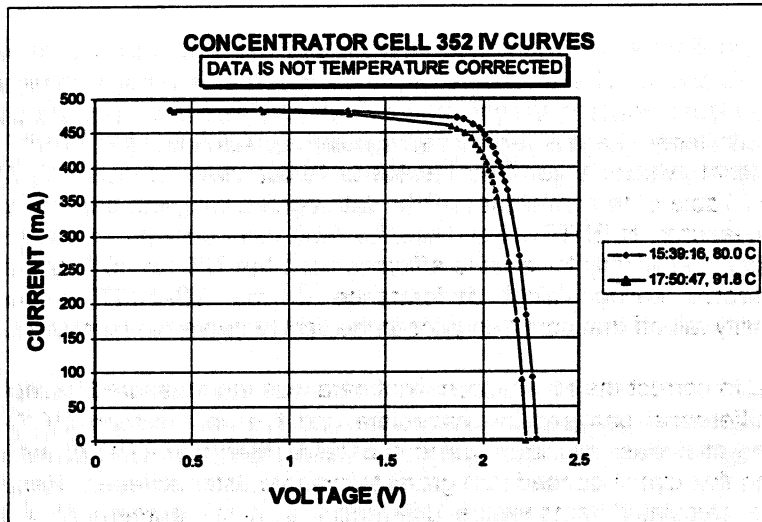
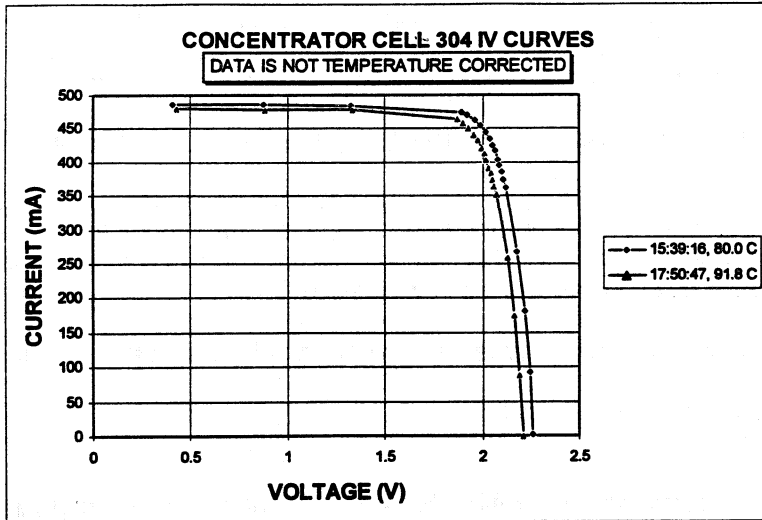


Figure 6. Concentrator Module Cell IV Curves from Beginning and End of Flight - Not Temperature Corrected

As shown in Figure 7, when voltage and current are temperature corrected, using the JPL measured cell temperature coefficients, no variation in Voc with temperature is observed, but the variation in Isc and thus maximum power becomes larger. In fact as shown in Figure 8, temperature corrected Isc steadily decreased for all cells as a function of flight time most likely indicating a steady reduction in light flux on the cells during flight. The consistency of temperature corrected Voc indicates that the temperature correction is quite accurate.

The exact cause of the light intensity reduction is still not known because unfortunately the balloon payloads on this flight, including the solar cells, descended through a thunderstorm and landed in a muddy field - coating the concentrator module with mud and ruining it. This made post flight analysis somewhat difficult. However, reasons for the performance decrease have been postulated and include:

1. Contamination on lens and cells from outgassing of plywood lens supports installed just prior to flight or from some other source.
2. Rapid lens darkening caused by UV radiation
3. Lens thermal distortion

Further investigation will be performed to explain this result if THV or similar material is pursued as a future SCARLET lens material.

A summary of the balloon in-flight and pre-flight JPL LAPSS data for the concentrator module cells, corrected to 28 °C, is shown in Tables 3 and 4. The flight data presented are the first measurements made during the flight because they represent the least reduction in light intensity. Module efficiency was calculated using an illuminated area equal to the lens width times the cell length and a solar constant of 1367 W/m². The SCARLET module efficiency on the balloon flight, which ranged from 19.0% to 19.5% was 1.5 % to 4.7 % less than the pre-flight LAPSS data. As shown in Table 5, the pre-flight LAPSS data agreed well with performance predictions based on the 80% lens efficiency measured at ENTECH and the 7.5 AM0 cell performance measured at TECSTAR. The balloon flight data correspond to slightly lower lens efficiencies in the 78% to 80% range. The most likely cause for the lower than expected balloon flight performance of the SCARLET concentrator module is the aforementioned light intensity fall-off that occurred prior to the first IV curve measurement.

The cell temperature used to correct the raw balloon flight data was the measured baseplate temperature plus the calculated temperature differential between the baseplate and the cell junction (15.6 °C). The baseplate-to-junction temperature differential was calculated using a detailed thermal model of the balloon flight cell carrier which consists of a Kapton flex circuit bonded to a graphite/cyanate ester stiffener. Results of this calculation are shown in Figure 9. The calculated temperature differential is in fair agreement with that derived from the measured cell Voc and the pre-flight measured cell voltage temperature coefficients - which ranged from 17.2 °C to 18.0 °C for all 65 flight data points.

While the SCARLET balloon flight concentrator produced slightly less power than expected, most likely due to contamination induced degradation of the experimental THV lens, it otherwise appears that the flight data is consistent with previous and current ground test data. The balloon flight data has helped validate and refine the SCARLET receiver thermal model. Most importantly, the 1996 balloon flights produced calibrated cells for SCARLET array solar simulator testing with approximately the same spectral response as the DS1 flight cells.

Lear Jet Solar Cell Measurements

Lear jet solar cell measurements are made by mounting the cell (or concentrator module) on a 3-inch-square, temperature-controlled plate at the bottom of a collimating tube which is approximately 20 inches long and 6 inches in diameter. The top of the collimating tube is mounted to the fuselage wall beneath an external shutter which protects the cells from air turbulence during take off, landing and low level flight. During cell measurements the protective shutter is opened, illuminating the cell with direct unfiltered sunlight. Sun pointing is controlled by the pilot. Lear IV curves are recorded with a Tektronix 370A curve tracer controlled with a Grid 386 computer. Timing of the curves with regards to altitude and illumination is controlled by the copilot. Cell Isc measurements are made on the Lear jet by loading each cell with a precision resistor (0.1 ohms in this case) and measuring the voltage drop across the resistor.

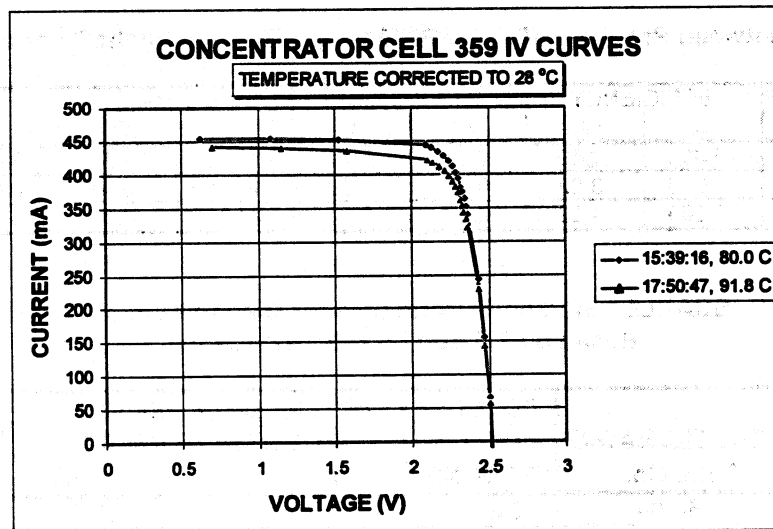
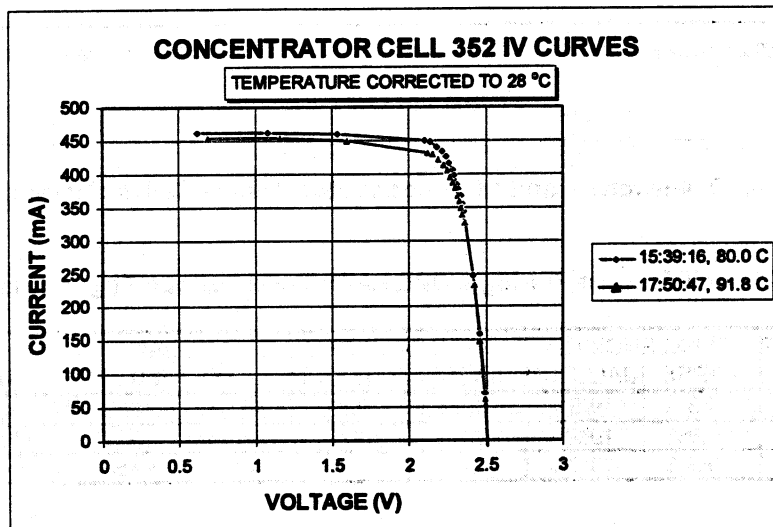
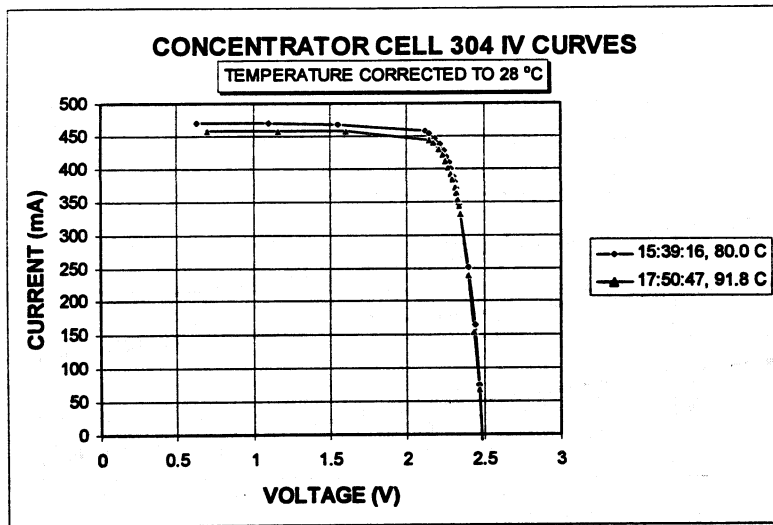


Figure 7. Concentrator Module Cell IV Curves from Beginning and End of Flight -Temperature Corrected

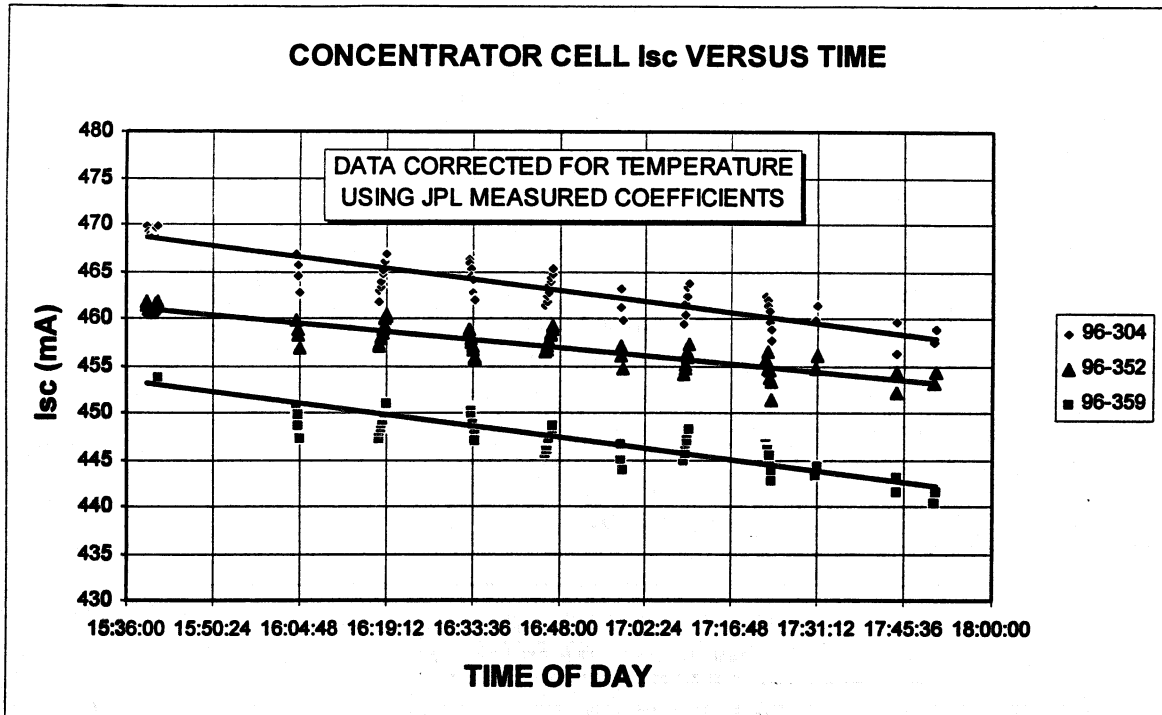


Figure 8. Downward Trend of Concentrator Module Cell I_{sc} Versus Time

Table 3. SCARLET Module Pre-flight JPL LAPSS and Balloon Flight Data Summary

CONCENTRATOR CELL No.	EFFICIENCY (%)		FILL FACTOR		I _{sc} (mA)		V _{oc} (V)	
	LAPSS	BALLOON	LAPSS	BALLOON	LAPSS	BALLOON	LAPSS	BALLOON
96-304	19.8%	19.5%	0.82	0.83	481.73	469.6	2.493	2.485
96-352	19.8%	19.2%	0.82	0.83	476.04	461.7	2.530	2.508
96-359	19.9%	19.0%	0.81	0.83	481.51	453.7	2.536	2.522

Table 4. Difference between Pre-flight JPL LAPSS Data and Balloon Flight Data for SCARLET Module

CONCENTRATOR CELL No.	EFFICIENCY		FILL FACTOR		I _{sc} (mA)		V _{oc} (V)	
	Δ	(%)	Δ	%	Δ	(%)	Δ	(%)
96-304	-0.003	-1.52	0.01	1.22	-12.130	-2.52	-0.008	-0.32
96-352	-0.006	-3.03	0.01	1.22	-14.340	-3.01	-0.022	-0.87
96-359	-0.009	-4.52	0.02	2.47	-27.810	-5.78	-0.014	-0.55

Table 5. SCARLET Module Performance for Different Lens Efficiencies Based on 7.5 Sun LAPSS Test Results

CONCENTRATOR CELL No.	TECSTAR LAPSS (7.5 SUNS)	28 °C MODULE EFFICIENCY AT LENS EFFICIENCY:		
		78%	80%	90%
96-304	24.49%	19.1%	19.6%	22.0%
96-352	24.53%	19.1%	19.6%	22.1%
96-359	24.47%	19.1%	19.6%	22.0%

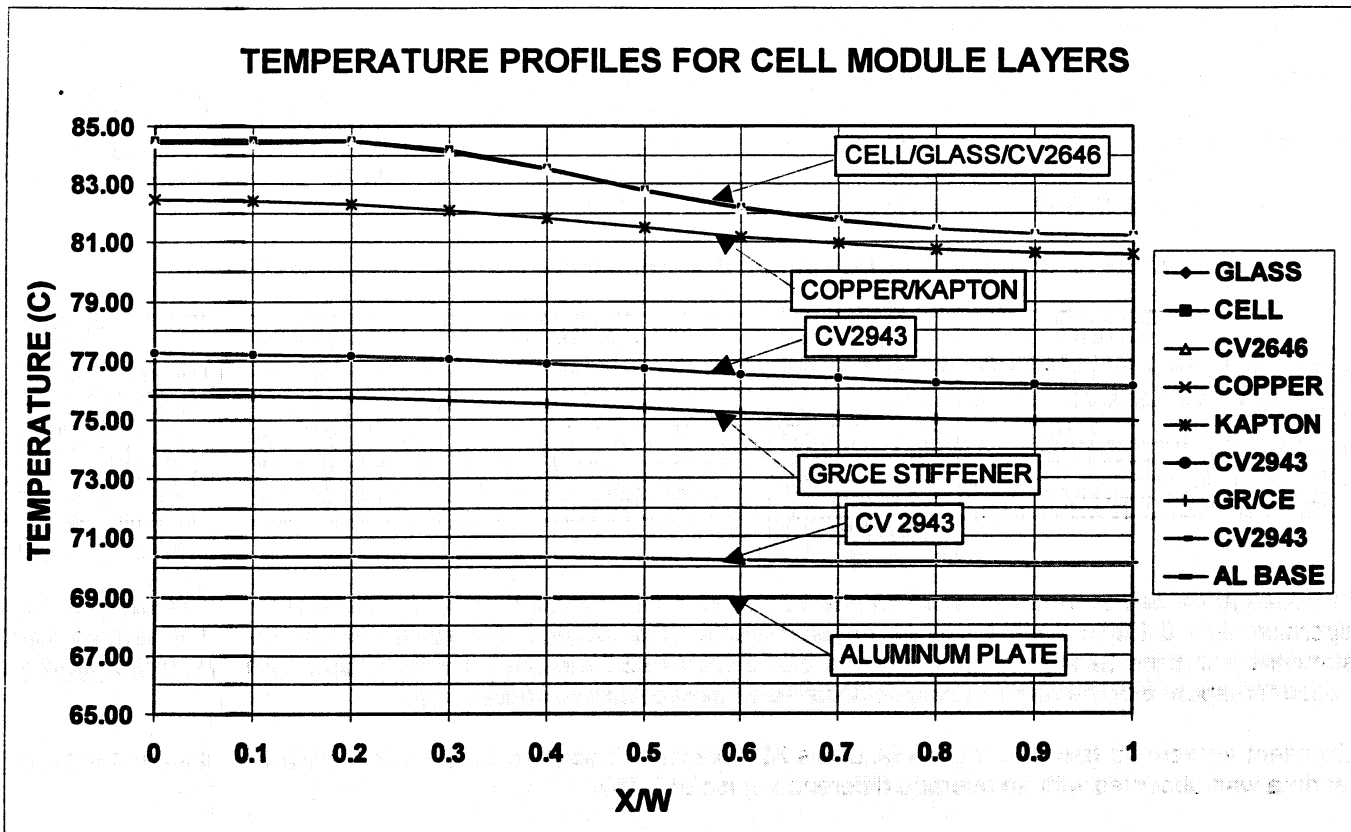


Figure 9. Balloon Flight Cell Carrier Thermal Analysis Results (x/w = 0 corresponds to the cell centerline (line of symmetry) and x/w = 1 is the cell edge)

Data is taken at several altitudes starting at a peak altitude of typically 48,000 ft. Barometric pressure is continually monitored and the equation:

$$\text{Air Mass} = P / (P_0 \cos(L-D))$$

where

- P = pressure
- P₀ = standard sea level pressure = 14.69 psia
- L = latitude 45° north in our case
- D = declination angle (which varies daily)

is used to determine the air mass of each data point. A Langley plot of log(Isc) versus air mass is made and the AM0 Isc is determined by extrapolation. Typically the Isc measured at peak altitude is greater than 95% of the AM0 Isc, so the extrapolation to AM0 is small.

Lear Jet SCARLET Data

The SCARLET Lear jet data, which was obtained on flights which occurred during the winter of 1996/1997, consists of Isc measurements for five different bare SCARLET cells and Isc and IV curve data for two cells under a DS1 flight-like, ceria-doped microsheet/DC 93-500 silicone lens. The SCARLET cells flown on the Lear jet were obtained from early DS1 production runs. For various process related reasons the TECSTAR production cells, which measure 4.06 x 1.12 cm, are generally lower performing than the engineering development SCARLET cells (flown on the JPL balloon flight the previous summer), with an average lot efficiency of 22.7% at 7.5X AM0 uniform

The cell Isc measurements taken with the JPL LAPSS (pulsed xenon arc source with Schott GG-395 UV filter (reference 2), GaAs calibration cell) were lower on average than the Lear jet data by about 2%.

The major significance of this data for the DS1 SCARLET program is that it suggests that the SCARLET cell AM0 power may have been *slightly* overrated (~2%) by TECSTAR's simulator. This is because TECSTAR used Hoffman 10 Isc to correct the 7.5 X AM0 LAPSS performance data for each flight cell. This was necessary because balloon flight calibration cells of the *exact* spectral response of the DS1 production cells were not available during LAPSS testing so calibration using the Hoffman 10, which has a spectrum that matches AM0 better than the LAPSS, was thought to be the best alternative. Two cells, representative of the DS1 flight build, are being calibrated on the JPL balloon flight this June and will enable more accurate measurement of the DS1 array power.

Lear Jet Lens Optical Efficiency

The DS1 SCARLET lenses consist of a silicone Fresnel lens bonded to a ceria doped microsheet superstrate which provides structural support and UV radiation protection. ENTECH successfully built, tested and delivered on time 800 lenses (includes 80 spares) for the DS1 SCARLET program with an average measured optical efficiency of 89.5%.

The DS1 SCARLET lenses are 3.36 inches wide by 8.38 inches long and focus light onto a 5 solar cell receiver. For Lear jet testing short lenses, 2.0 inches long, illuminating a single cell were manufactured to fit in the collimating tube. A photograph of the Lear jet SCARLET test module is shown in Figure 11.

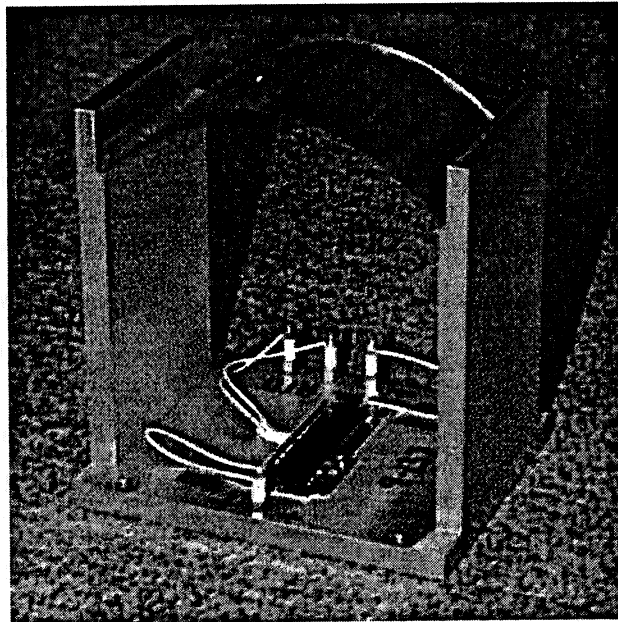


Figure 11. SCARLET Module for Lear Jet Testing

Lens efficiency, for flight-like DS1 SCARLET lenses, was measured in near AM0 sunlight during the Lear jet tests to validate the lens efficiency measurements made during lens manufacturing. Good agreement was found.

Since solar cell Isc varies in direct proportion to light intensity, the measurement of SCARLET cell Isc both bare and lens illuminated allows for the calculation of lens optical efficiency through the equation:

$$\text{Lens efficiency} = (I_{sc_L} / I_{sc_B}) * (W_{cell} / W_{lens})$$

Where

- I_{scL}** = Lens illuminated cell short circuit current
- I_{scB}** = Bare cell short circuit current
- W_{cell}** = Active cell width (does not include bus bars) = 0.402 inches
- W_{lens}** = Lens aperture width = 3.22 inches

Applying this equation to the Lear jet data obtained for cell 9-132 a lens efficiency of 88.5% is calculated. This compares very favorably to the 89% lens efficiency measured for this lens during in-process acceptance testing at ENTECH where a collimated tungsten light source and a flight-like cell receiver are used.

Unfortunately the Lear jet winter flight season ended before cell 8-132 could be flown bare (it had already been flown with a lens). However, using the NASA Lewis X25 bare cell I_{sc} and the Lear jet cell-with-lens I_{sc} for cell 8-132, a lens efficiency of 94.0% was calculated. The NASA Lewis X25 bare cell I_{sc} is used because it matches the Lear jet results best for these cells. This Lear jet lens efficiency for module 8-132 is significantly higher than the 90% lens efficiency measured during acceptance testing at ENTECH due to experimental uncertainties.

The Lear jet test results for the two SCARLET modules suggest the AM0 lens efficiency is approximately the same or perhaps slightly more than measured during acceptance testing at ENTECH.

Conclusion

Several successful SCARLET experiments with both bare cells and lens/cell modules were completed on both the JPL balloon, during the summer of 1996, and the NASA Lewis Lear jet, during the winter of 1997. Generally, agreement between the flight data and the several different types of solar simulators used, which include the X25, Hoffman 2, Hoffman 10 and LAPSS, is good - except in the cases where obvious degradation occurred in flight. The Lear jet test results for five bare SCARLET cells suggest the DS1 SCARLET flight cells may produce slightly less power in space than predicted by the Hoffman 10. The Lear jet test results for the two SCARLET modules suggest the AM0 lens efficiency for the DS1 ceria-doped microsheet / DC 93-500 lenses is approximately the same or perhaps slightly more than measured during acceptance testing at ENTECH.

References

1. Anspaugh, B. E. and Weiss, R. S., Results of the 1996 JPL Balloon Flight Solar Cell Calibration Program, JPL Publication 97-5, December 1996.
2. Mueller, R. L., The Large Area Pulsed Solar Simulator (LAPSS), JPL Publication 93-22, Rev. A., July 1994.

CONTRIBUTION OF LOW ENERGY PROTONS TO THE DEGRADATION OF SHIELDED GaAs SOLAR CELLS IN SPACE

G.P. Summers

**Naval Research Laboratory, Code 6615, Washington, DC 20375, and
Department of Physics, University of Maryland Baltimore County, Baltimore, MD 21228**

**S.R. Messenger and E.A. Burke
SFA, Inc., Largo, MD 20774**

**M.A. Xapsos and R.J. Walters
Naval Research Laboratory, Code 6615, Washington, DC 20375**

INTRODUCTION

There are several reasons to be concerned about the effect of low energy protons on the performance of solar cells in space. First, the measured differential energy spectra for protons both trapped in the Van Allen belts and emitted during solar proton events increase monotonically as the energy decreases from a maximum of several hundred MeV to the lowest energies considered (typically ~0.1 MeV). Second, the displacement damage caused by protons generally increases with decreasing energy and reaches a maximum near the threshold for atomic displacement, which is typically a few hundred eV. For example, the displacement damage produced by a 400 eV proton is three orders of magnitude larger than that produced by a 10 MeV proton in a thin layer of material. Although it is possible to use coverglass to shield against incident low energy protons, the coverglass also has the effect of slowing down higher energy protons, so that there is actually a spectrum of protons entering the active region of the cell with energies ranging from hundreds of MeV down to zero. Experiments using monoenergetic beams confirm that low energy protons produce severe degradation to solar cells [1,2]. The question arises, then, what fraction of the total degradation produced in solar cells in actual space environments will be produced by protons with energies much lower than typically used in ground testing, e.g., several MeV. A related issue is to determine the appropriate proton energy to use in a single ground test that will best simulate the effect of space protons.

In this paper, we address these questions using the example of widely-used GaAs cells. In order to calculate a typical example we chose an incident spectrum corresponding to a circular, 5000 km orbit. However, the results are similar for other orbits and even for the effects of solar proton events. We first describe a quantity called displacement damage dose which can be used to correlate the damage produced by different energy protons. We then calculate the slowed-down differential spectra for protons penetrating several thicknesses of silica coverglass. From this the cumulative fraction of the total displacement damage produced in the cell can be determined as a function of increasing proton energy, for both the slowed-down and the incident spectra. Finally, we show the contribution that protons in different energy ranges make to the overall degradation of the cell efficiency over the course of a particular mission lifetime.

DIFFERENTIAL DISPLACEMENT DAMAGE DOSE

We have shown in papers at previous conferences both here and elsewhere that the effect of different energy protons (and electrons) on the photovoltaic properties of solar cells can be quantitatively correlated using a calculable quantity called displacement damage dose, D_d [3,4]. D_d is determined by integrating the product of the differential energy spectrum of the incident protons and the nonionizing

energy loss (NIEL) in the target material. D_d is the displacement damage equivalent of ionizing dose, in which the quantity equivalent to the collision stopping power is NIEL. When the radiation-induced degradation of a photovoltaic property of a solar cell such as conversion efficiency is plotted against D_d , a single characteristic curve is obtained, which represents the response of the cell to protons of all energies. The characteristic curve for GaAs cells has been presented previously in reference 4. The displacement damage dose approach gives a conceptually straightforward way of quantifying the energy dependence of proton-induced damage in solar cells.

In order to calculate D_d in the active region of a covered GaAs cell, we need to determine both the slowed-down spectrum of protons that have traversed the coverglass and the NIEL for protons in GaAs. The latter has been calculated previously and we will not discuss it further here [5]. We base the calculation of the slowed-down proton spectrum on an approach first described by Haffner [6] and Burrell [7]. The proton is assumed to follow a straight line path through the coverglass and to have an energy at any point in the path determined by the range. Haffner [6] used a simple power function to describe the energy dependence of the range, $R(E)$, which fits the data well down to ~ 0.1 MeV. A lower energy limit of 0.1 MeV in the slowed-down spectrum is appropriate for modelling ionization effects, but for displacement damage it is necessary to follow the protons down to the threshold for atomic displacements, which is ~ 200 eV for GaAs. We, therefore, use an expression consisting of the sum of two power functions which fits the range data much better at lower energies, i.e.,

$$R(E) = AE^a + BE^b \quad (1)$$

where A , a , B , and b are constants. Fig. 1 shows a fit of Eq. (1) to experimental measurements of the energy dependence of the range of protons in silica as compiled by Ziegler et. al. and tabulated in the computer code SRIM96 [8].

Since for every proton there is a one to one correspondence between the incident energy, E , and the energy, ϵ , after passing through a certain thickness of silica, an incident spectrum $g(E)$ will be reduced to a slowed-down spectrum $f(\epsilon)$ given by,

$$f(\epsilon) = g(E) \frac{dE}{d\epsilon} \quad (2)$$

where $dE/d\epsilon$ can be obtained from Eq. (1). In space, the incident spectrum represented by $g(E)$ actually contains an isotropic distribution of protons ranging in energy from a few eV up to several hundred MeV. Evaluation of Eq. (2) for a real case, therefore, involves some complexity because protons emerging through the coverglass with a particular energy will initially have possessed a range of energies depending on the angle of incidence. For purposes of calculation, the coverglass is represented by a semi-infinite slab of silica. There is, of course, a lower, cut-off energy which is determined by those protons that travel perpendicularly to the coverglass and which have, therefore, the shortest range.

In order to calculate a specific example, we used a differential fluence spectrum taken from the NASA space proton model AP8MAX [9] corresponding to five years in a circular orbit with an altitude of 5000 km and an inclination of 60° . The results of the calculations are shown in Fig. 2 for three representative coverglass thicknesses, i.e., 3, 12, and 30 mils, respectively. Fig. 2 shows that the thicker coverglasses tend to harden the spectrum slightly, but that the energy dependence of the calculated distributions are approximately independent of coverglass thickness below ~ 1 MeV. The curve labelled "Uncovered" shows the incident spectrum. At high energies, this curve differs by a factor of two from the "slowed-down" curves because only those protons incident on the top of the coverglass are taken into account in the calculation.

The product of the slowed-down spectra shown in Fig. 2 and the NIEL for protons in GaAs [4] give the differential displacement damage doses deposited in a shielded GaAs cell after five years in orbit. These curves are shown in Fig. 3, again for coverglass thicknesses of 3, 12, and 30 mils. The area under one of these curves gives the total displacement damage dose deposited over the course of the mission. However, it is the cumulative fraction of this total dose as a function of increasing proton energy that is the result we are looking for.

Before we present this result, however, it is worth noting that the dose deposited throughout the whole active volume of the cell varies very little from the curves shown in Fig. 3, which specifically show the dose just below the coverglass. The reason is that the total active region of a GaAs cell is only a few micrometers thick compared to the thickness of the coverglass, which for the cases considered here range from 75 - 750 micrometers. The slowed down spectra, and the differential dose curves calculated from them in Fig. 3, will therefore vary very little for protons travelling a few additional micrometers in GaAs. Calculations confirm that this is indeed the case. Fig. 3 therefore shows the differential dose deposited throughout the cell by the protons that penetrate the respective coverglasses, including those protons that actually stop.

CUMULATIVE FRACTION OF D_d

Figure 4 shows the cumulative fraction of the displacement damage dose deposited as a function of slowed-down proton energy for the three different coverglass thicknesses, using the curves in Fig. 3. Figure 4 shows several interesting features. It can be seen that the curves all have the same general shape, with slightly more of the damage being produced by lower energy protons as the coverglass becomes thinner. In all cases, however, a relatively small fraction of the damage, and hence the resulting degradation in cell efficiency, comes from protons with energies $< \sim 0.1$ MeV or > 10 MeV. To take a specific example of a cell shielded by 12 mils of coverglass, only $\sim 20\%$ of the damage results from protons with energies $< \sim 0.1$ MeV and only $\sim 7\%$ of the damage results from energies > 10 MeV, even though the incident spectrum includes protons with energies > 400 MeV. It should be recalled that these results include protons that actually stop in the cell. Even though such particles individually produce substantial damage, in total they contribute relatively little to the total cell degradation.

Figure 5 shows the cumulative fraction of the damage produced as a function of the incident proton energy. In this case, there is a minimum energy required for a proton to penetrate the coverglass into the cell. For example, 3 mils of silica is sufficient to stop all protons with energies less than 2.7 MeV. Figure 5 shows that nearly all of the damage is produced by a small range of proton energies. For a cell shielded by a 12 mil coverglass, more than 90% of the damage is produced by protons with energies between 6 and 12 MeV. Furthermore, it can be seen that incident protons with energies > 20 MeV contribute almost none of the damage.

Figure 6 presents the results shown in Fig. 4 in terms of the predicted degradation that would occur in cell efficiency over the course of a five year mission in a 5000 km orbit. Since maximum shielding would be required in such a harsh environment, we show results for a cell protected by a 30 mil coverglass. Note that the abscissa in Fig. 6 has the units of dose rather than the more familiar units of fluence. The abscissa can be converted to a corresponding fluence of monoenergetic protons by dividing by the appropriate value of NIEL. We have shown as separate curves in Fig. 6 the contribution to the total degradation at any point in the mission due to slowed-down protons in four different energy ranges, i.e., 0 - 0.1, 0.1 - 1, 1 - 10, and 10 - 400 MeV. It can be seen that only $\sim 15\%$ of the degradation come from the range containing the lowest energy protons, whereas $\sim 50\%$ comes the 1 - 10 MeV range.

The highest energy protons are also relatively unimportant. We emphasize that these ranges refer to proton energies throughout the active region of the cell. For example, it is not correct to interpret the lowest energy range as including only those protons that stop in the emitter of the cell, because essentially the same slowed-down spectrum is present in the junction and the base.

CONCLUSIONS

It is important to perform ground radiation testing that simulates as closely as possible the conditions devices will encounter in space. The results presented here show that unshielded GaAs devices can be irradiated with monoenergetic, unidirectional protons in the 1 - 10 MeV range and the results will be representative of shielded devices in space environments containing protons with energies up to hundreds of MeV.

It has been shown previously [4] that the characteristic degradation curve can be determined as a function of D_d from measurements made with only one proton energy. Space solar cells have traditionally been tested using 10 MeV protons. However, the results presented here shows that this will usually be at the upper end of the optimum energy range for testing and will generally give no better

information about the performance in space than could be obtained using protons with a lower energy, e.g., 3 MeV, which are generally much cheaper to use.

REFERENCES

- [1] B.E. Anspaugh, *Proceedings of the twenty-second IEEE Photovoltaic Specialists Conference* (IEEE, New York, 1992), p.1593.
- [2] D.M. Scott and D.C. Marvin, *Proceedings of the twenty-third IEEE Photovoltaic Specialists Conference* (IEEE, New York, 1994), p.1338.
- [3] G.P. Summers, E.A. Burke, and M.A. Xapsos, *Radiation Measurements*, 24, 1 (1995).
- [4] G.P. Summers, R.J. Walters, M.A. Xapsos, E.A. Burke, S.R. Messenger, P. Shapiro and R. Statler, *Proceedings of the First IEEE World Conference on Photovoltaic Energy Conversion* (IEEE, New York, 1994), p. 2068.
- [5] G.P. Summers, E.A. Burke, P. Shapiro, S.R. Messenger and R.J. Walters, *IEEE Trans. in Nucl. Sci.*, 40, (1993), p.1372.
- [6] J.W. Haffner, *Radiation and Shielding In Space*, (Academic Press, New York, 1967).
- [7] M.O. Burrell, *Proceedings of the Second Symposium on Protection against Radiations in Space*, (NASA, Publication SP-71, 1964).
- [8] J.F. Ziegler, J.B. Biersack, and U. Littmark, *The Stopping and Range of Ions in Solids, Vol. I*, (Pergammon Press, New York, 1985).
- [8] J.F. Ziegler, J.B. Biersack, and U. Littmark, *The Stopping and Range of Ions in Solids, Vol. I*, (Pergammon Press, New York, 1985).
- [9] D.M. Sawyer and J.I. Vette, *NASA Publication NSSDC/WDC-A-R&S 76-06* (1976).

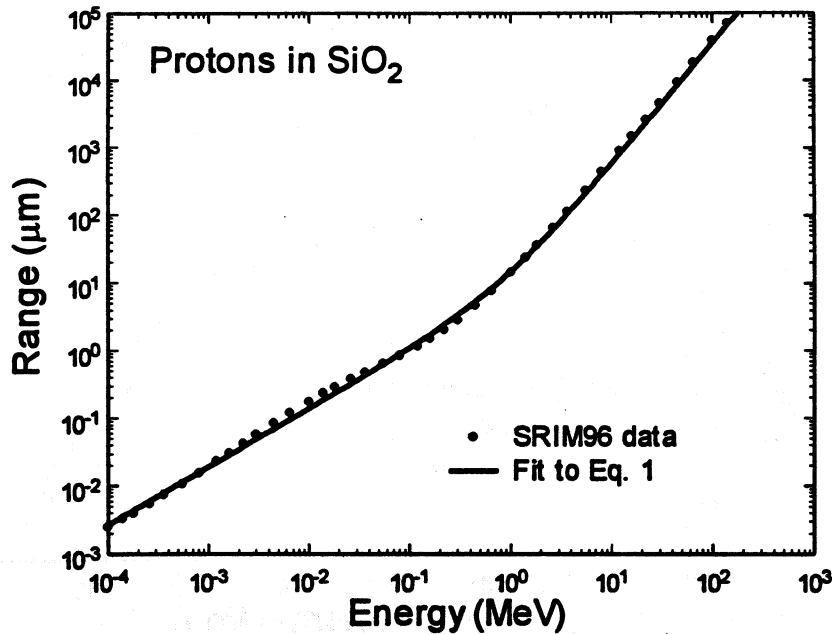


Fig. 1. The range of protons in silica as a function of energy. The data points are taken from SRIM96 [8]. The line is a least squares fit of Eq.(1) to the data.

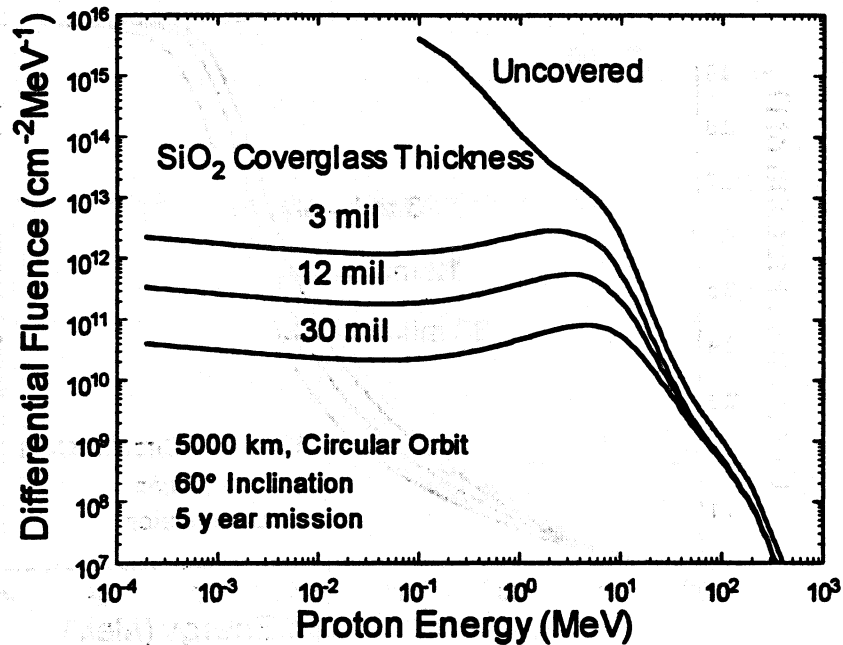


Fig. 2. Differential proton fluence taken from AP8MAX corresponding to 5 years in a 5000 km circular orbit, with 60° inclination. The curve labeled "Uncovered" corresponds to the isotropic incident spectrum. The other curves show slowed-down spectra after the incident spectrum has passed through semi-infinite slabs of silica having thicknesses of 3, 12 and 30 mils, respectively.

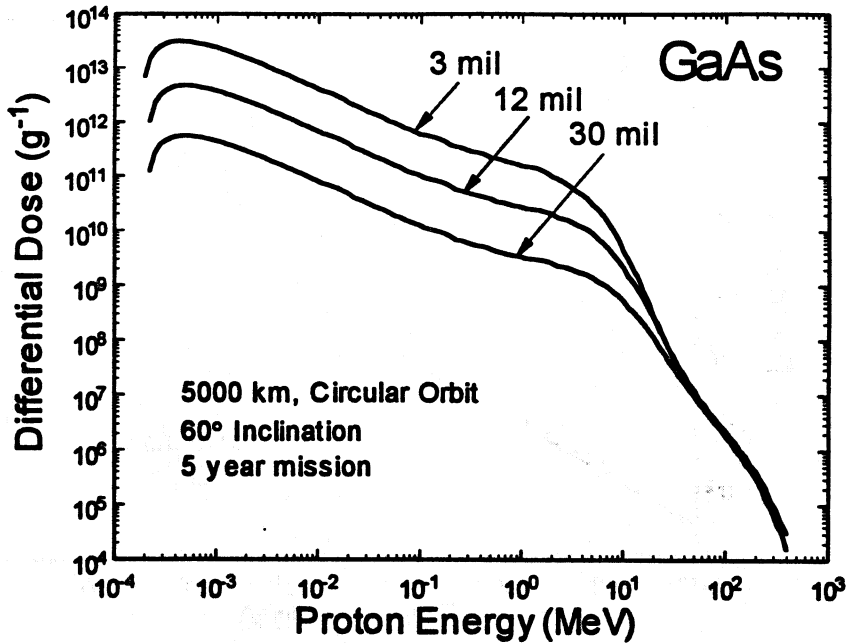


Fig. 3. Differential displacement damage dose, D_d , in GaAs as a function of silica coverglass thickness after 5 years in 60° inclination, circular 5000 km orbit.

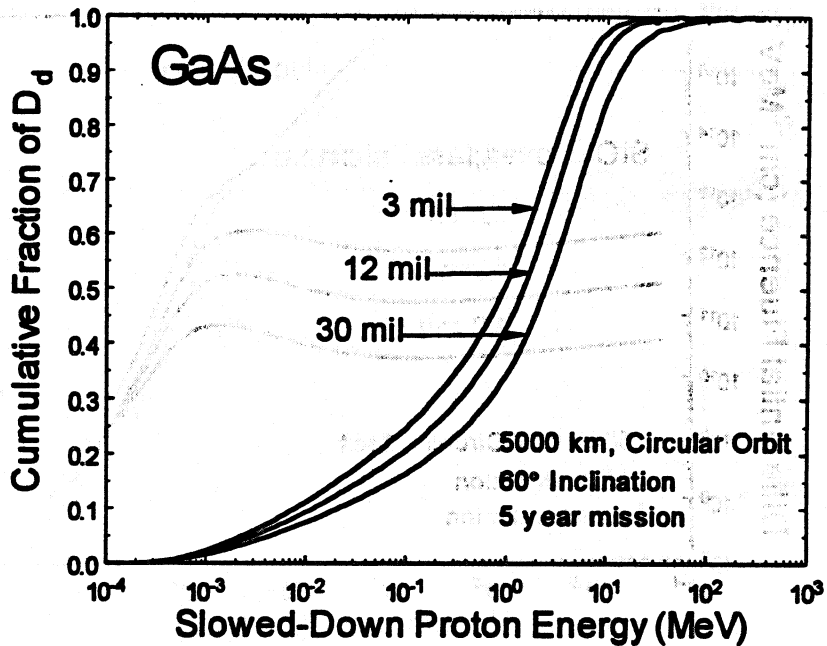


Fig. 4. Energy dependence of the cumulative fraction of the displacement damage dose, D_d , in GaAs due to slowed-down protons in a 60° inclination, circular 5000 km orbit after passing through silica coverglasses of thickness 3, 12, and 30 mils, respectively.

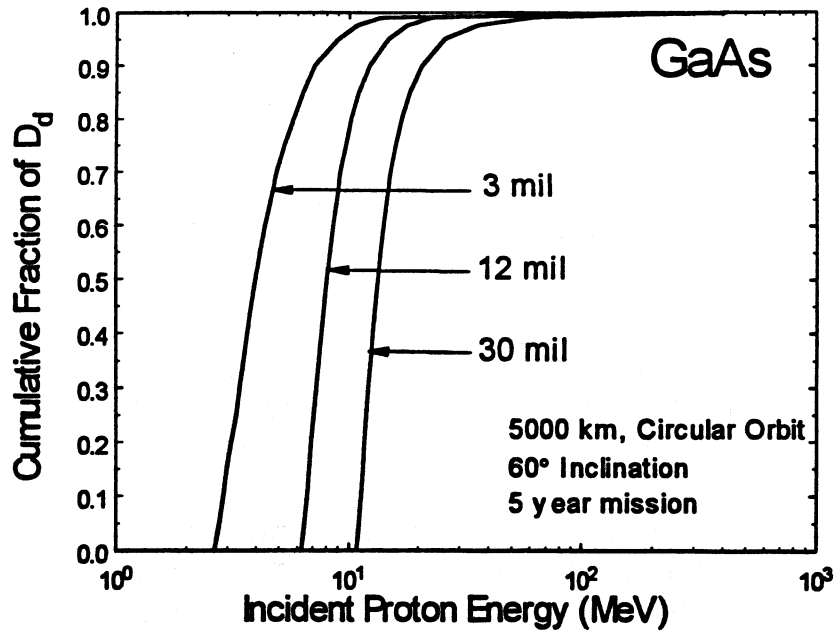


Fig. 5. Energy dependence of the cumulative fraction of the displacement damage dose, D_d , in GaAs due to incident protons in a 60° inclination, circular 5000 km orbit after passing through silica coverglasses of thickness 3, 12, and 30 mils, respectively.

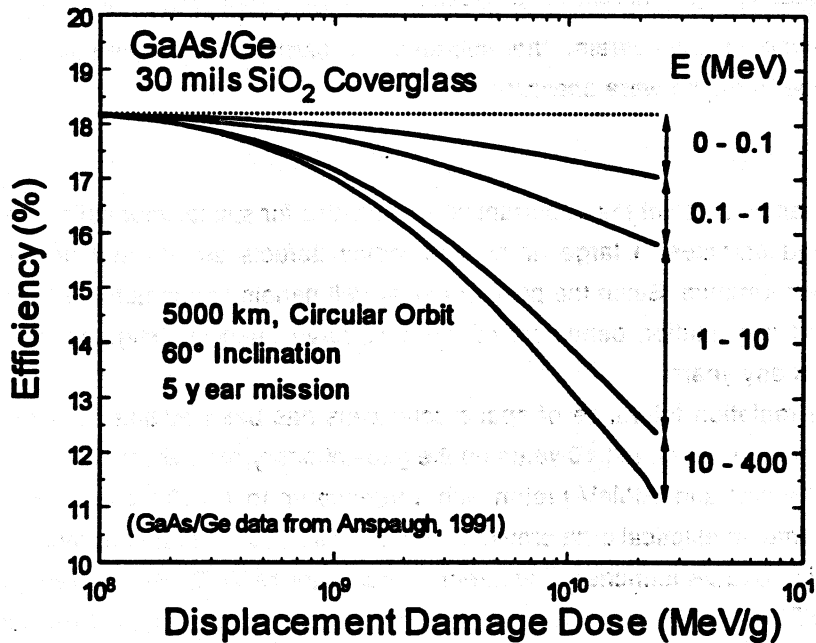


Fig. 6 The contribution of slowed-down protons in the energy ranges 0 - 0.1, 0.1 - 1, 1 - 10 and 10 - 400 MeV, respectively, to the total predicted degradation over five years of GaAs solar cells shielded by 30 mils coverglass, operating in a 60° inclination, circular, 5000 km orbit.

DEGRADATION PROPERTIES OF LARGE FLUENCE IRRADIATED SPACE SILICON BSR CELLS

Tadashi HISAMATSU and Sumio MATSUDA
National Space Development Agency of Japan (NASDA),
2-1-1 Sengen, Tsukuba City, Ibaraki 305, Japan

Tetsuya NAKAO and Yusuke MATSUMOTO
Advanced Engineering Services (AES) Corporation,
1-6-1 Takezono, Tsukuba City, Ibaraki 305, Japan

We have already reported the anomalous degradation of large fluence irradiated space silicon BSFR cells. In this paper, we present the data obtained for BSR cells. As a result, it was found that BSR cells showed similar anomalous degradation behavior in large fluence regions. Hall effect measurements were performed to the irradiated p-type silicon wafers, the decrease of carrier density and following conduction-type conversion from p-type to n-type were observed.

1. Introduction

Radiation tolerance is one of the important characteristics for space solar cells. When a space solar cell is exposed to charged particles, a large amount of lattice defects are formed and it results in a gradual degradation of cell performance. Since the power of solar cell panels dominates the life of artificial satellites, radiation damage and degradation behaviors of the cells have been investigated and published by many research workers for many years.

Generally, the radiation tolerance of space solar cells has been evaluated under conditions derived from the radiation exposure more than 10 years on the geostationary orbit of satellites: 1MeV electrons with a fluence up to 1×10^{16} e/cm² and 10MeV proton with a fluence up to 1×10^{13} p/cm². However, an accidental injection of a satellite into an elliptical orbit provided an opportunity to evaluate the radiation tolerance in larger fluence region. That is, NASDA launched Engineering Test Satellite VI (ETS-VI) on August 28, 1994 by an H-II rocket. However, ETS-VI could not be placed in the planned geostationary orbit because of a failure in the liquid-fueled apogee engine[1]. As a result of strenuous endeavors, ETS-VI was placed in an elliptical orbit instead. Since this orbit passes through the Van Allen belt, ETS-VI's solar panels were exposed to unprecedented amounts of radiation, and the out-put power decreased rapidly. To estimate the life of this satellite, it became necessary to estimate the obtained power of solar panels.

The solar cells on ETS-VI were 50 μ m thick Si BSFR (back surface field and reflector) cells manufactured by SHARP Corporation[2]. Using this type cells, we conducted 1MeV electron irradiation tests with a fluence up to 1×10^{17} e/cm² and 10MeV proton irradiation tests with a fluence up to 3×10^{14} p/cm² in cooperation with Takasaki Laboratory of the Japan Atomic Energy Research Institute (JAERI). As a result of these tests, we found the anomalous degradation of the cell performance which could not be predicted with previous data in the proton irradiation as well as in the electron irradiation. Figure 1 shows the relationship

between the remaining factors of cell performance (normalized electrical performance) and the incident radiation fluence obtained by these tests[3]. The anomalous degradation is characterized by a slight increase of short circuit current I_{sc} (at fluence of about 3×10^{16} e/cm² for electrons, about 2×10^{13} p/cm² for protons) and a sudden drop of maximum power P_{max} (at fluence of about 7×10^{16} e/cm² for electrons, about 1×10^{14} p/cm² for protons).

This anomalous degradation is of great interest in understanding the degradation mechanism of Si solar cells and the effect of irradiation on silicon materials. Moreover, it may also provide us with new aspects for developing future radiation tolerant space solar cells. In order to clarify this anomalous degradation in detail and understand the degradation mechanism of Si solar cells in all fluence regions, NASDA established a committee chaired by Dr. H. Okamoto in Osaka University and started the research in various aspects in the autumn of 1995. We have already reported the electrical properties of the degraded BSFR cells and proposed the models for explaining this anomalous degradation [4-7].

In this paper, we present the electrical properties of the other basic type cell: the BSR cell. The dark I-V and C-V characteristics of the BSR cells irradiated with 10MeV protons with a fluence exceeding 1×10^{13} p/cm² and irradiated with 1MeV electrons with a fluence exceeding 1×10^{16} e/cm² are presented. We also present the results of Hall effect measurement of the irradiated silicon substrates and discuss.

2. Experimental

Measured cell samples were 2×2 cm² 200 μ m thick Si BSR cells. Figure 2 (a) shows the structure of the cell. A thin n⁺ layer (about 0.15 μ m) was formed by a phosphorous diffusion on a p-type CZ Si single crystal substrate (boron-doped, about 10 Ω cm, (100) plane). Metallurgical electrodes were deposited on each side and an anti-reflective coating was deposited on the incident surface. The structural-difference from BSFR cell (Fig.2(b)) was the absence of the rear p⁺ (back surface field) layer. The initial conversion efficiency of BSR cell sample was about 13-14 % (AM0, 28°C).

For Hall effect measurements, the specimen with ohmic contacts was made of p-type Si wafer which was used as a cell substrate. Ohmic contacts were formed before irradiation.

Proton and electron irradiations were carried out at JAERI Takasaki. Both 1 MeV electrons and 10 MeV protons have ranges long enough to pass through the cells. The fluence rate was about 4×10^{10} p/cm² · sec for 10 MeV protons and about 1×10^{13} e/cm² · sec for 1 MeV electrons. Measurements were carried out after annealing for stability at 60°C for 24H.

Dark I-V and C-V measurements were performed at room temperature. For I-V measurements, we obtained the series resistance R_{se} in high-voltage regions of I-V curves and calculated the voltage drop due to the R_{se} . For C-V measurements, we varied the measurement frequency from 1KHz to 1MHz.

Hall effects were measured with Van der Pauw method in room temperature using Hall Effect Measurement System HL5500 by Bio-Rad Laboratories Inc.. Applied magnetic flux density was 5,200 gauss[8].

3. Results and Discussion

3.1 Degradation Behavior

Figure 3 shows the degradation curves of BSR cells. It was found that the BSR cells showed similar anomalous degradation behavior which was found with BSFR cells in large fluence regions, though we were short of proton irradiation data.

3.2 I-V Characteristics

Figure 4 shows the forward dark I-V characteristics of 1MeV electron irradiated samples. The plots of black symbols represent the raw data ; white symbols represent the corrected data of voltage drops due to R_{se} .

Considerable changes in the plotted data can be seen with the increase of fluence. Similar data were obtained for 10MeV proton irradiated samples. From the intersection with current-axis we got a saturation current I_0 , and from the slope we got a diode factor n .

Figure 5 shows the fluence dependence of the saturation current density I_0 . The I_0 increased gradually with an increase of fluence and became more than three orders of magnitude greater than the initial value (I_0 of the unirradiated cell) at about $1 \times 10^{14} \text{ p/cm}^2$ for 10MeV protons and about $1 \times 10^{17} \text{ e/cm}^2$ for 1MeV electrons. The diode factors (n values) were preserved at about 1.0-1.2 in spite of the increase of fluence, however, they became about 1.4 at $1 \times 10^{14} \text{ p/cm}^2$ for 10MeV protons and about $1 \times 10^{17} \text{ e/cm}^2$ for 1 MeV electrons. Figure 6 shows the fluence dependence of the series resistance R_{se} . Similar to I_0 , the R_{se} increased extremely with increased fluence and became more than one order of magnitude greater than the initial value.

3.3 C-V Characteristics

In C-V measurements, similarly to BSFR cells, a measurement frequency dependence (lowering the frequency from 1MHz to 1KHz caused a slight increase in capacitance) was seen for the large fluence irradiated cells. This suggests that a large amount of carrier traps were induced by large fluence irradiation. Since the voltage dependence of capacitance became small for the measurement of large fluence irradiated cells at a high frequency, we used a measurement frequency of 1KHz for C-V measurements. We plotted the capacitance C in $1/C^2$ -V plots, all data points of measured samples were approximately on a straight line (see in Fig. 7). From the $1/C^2$ -V plots, we evaluated the diffusion voltage V_d and the carrier density p .

Figure 8 shows the fluence dependence of the diffusion voltage V_d . A decrease of V_d with an increase of fluence was found in the fluence region exceeding about $1 \times 10^{13} \text{ p/cm}^2$ for 10MeV protons and about $1 \times 10^{16} \text{ e/cm}^2$ for 1MeV electrons. Figure 9 shows the fluence dependence of carrier density p of the cell substrates. The carrier density of the n^+ region of samples was assumed to be $5 \times 10^{19} / \text{cm}^3$. The carrier density of unirradiated cells agreed with the one of the cell substrate. The carrier density p decreased with an increase of fluence, however, a bit higher carrier density were obtained at $1 \times 10^{17} \text{ e/cm}^2$ for 1MeV electrons. Figure 10 shows the fluence dependence of depletion layer width W_d calculated from no-biased capacitance. The W_d increased with an increase of fluence, however, smaller widths were obtained at $1 \times 10^{17} \text{ e/cm}^2$ for 1MeV electrons.

3.4 Hall measurements

Figure 11 shows the fluence dependence of carrier density derived from Hall effect measurements. It was confirmed that the carrier density decreased with the increase of fluence. Moreover, from the direction of Hall voltage, the conduction-type conversion from p-type to n-type was found at $1 \times 10^{17} \text{ e/cm}^2$ of 1MeV electron irradiation. It agrees with the fact that the EBIC signal was observed only near the interface of substrate and p^+ -BSF layer in 10MeV proton $1 \times 10^{14} \text{ p/cm}^2$ irradiated BSFR cells[9]. It must be the carrier compensation with radiation-induced defects. Thus, the separated data in Fig.9 and 10 at $1 \times 10^{17} \text{ e/cm}^2$ for 1MeV electron irradiation are seemed to be n-type data. Why the data of sample irradiated electron by $1 \times 10^{17} \text{ e/cm}^2$ showed the straight line of $1/C^2$ -V, in spite of the conversion of sample structure from n^+p to n^+n ? We consider the reason as follows. The position of Fermi-level seems to be fixed at the interface of p-type silicon rear surface and deposited metal (Al-BSR) in cell production process. The carrier density decreases due to the irradiation, however, the position dose not move, and it forms a depletion region between the Si rear surface and the metal. The C-V characteristic of this depletion region must be measured. We etched off the rear surface metal partially and confirmed the decrease of capacitance.

Figure 12 shows the fluence dependence of carrier mobility derived from Hall effect measurements. The decrease of hole mobility from $3 \times 10^{16} \text{ e/cm}^2$ to $7 \times 10^{16} \text{ e/cm}^2$ of electron irradiation seems to be attributed to the ionized impurity scattering of electron-induced defects. The mobility at $1 \times 10^{17} \text{ e/cm}^2$ in electron irradiation,

which we believe a n-type data, is similar to the estimated value with Irvin's data [10]. We intend to obtain more data and examine the conduction mechanism of large fluence irradiated silicon in detail.

In conclusion, it became clear that the BSR cells showed similar anomalous degradation behavior and electrical properties which was found with BSFR cells in large fluence regions. This phenomenon should be explained mainly by the theory proposed for BSFR cells. That is, the slight increase of I_{sc} is attributed to a transient increase of collection efficiency for photo-generated carriers by depletion width broadening and the sudden drop of P_{max} is attributed to a decrease of the carrier density and an increase of the resistivity of p-substrate due to majority carrier trapping by radiation-induced defects. To confirm the decrease of carrier density, Hall effect measurements were performed to the irradiated Si wafers. The decrease of carrier density and following conduction-type conversion from p to n were observed.

- [1] H.Kitahara, S.Tanaka, Y.Kanamori and T.Itoh: "Engineering Test Satellite VI's Experiment Results," 46th International Astronautical Congress, Oct.2-6, 1995, Oslo, Norway.
- [2] S.Matsuda, T.Matsutani, T.Saga and A.Suzuki: "Development of Ultrathin Si Solar Cells," 17th IEEE Photovoltaic Specialists Conference, (1984), p123-127.
- [3] Y.Yamamoto, O.Kawasaki, S.Matsuda and Y.Morita: "Radiation Effects of Solar Cells for Space Use," Proceeding of the European Space Power Conference, Poitiers, France, 4-8 September 1995, esa SP-369, (1995), p573-578.
- [4] T.Hisamatsu, O.Kawasaki, S.Matsuda, T.Nakao and Y.Wakow: "Radiation Degradation of Large Fluence Irradiated Space Silicon Solar Cells", Technical Digest of 9th International Photovoltaic Science and Engineering Conference, Nov.11-15 1996, Miyazaki, Japan, p633-634.
- [5] M.Yamaguchi, S.J.Taylor, S.Matsuda and O.Kawasaki: "High-energy and High-fluence Proton Irradiation Effects in Silicon Solar Cells," J.Appl.Phys., Vol.80, (9),1 November 1996, p4916-4920.
- [6] M.Yamaguchi, S.T.Taylor, M.-J.Yang, S.Matsuda, O.Kawasaki, T.Hisamatsu: "Analysis of Radiation Damage to Si Solar Cells under High-Fluence Electron Irradiation," Jpn. J.Appl. Phys. Vol.35 (1996) pp.3918-3922.
- [7] T.Ohshima, Y.Morita, I.Nashiyama, O.Kawasaki, T.Hisamatsu, T.Nakao, Y.Wakow and S.Matsuda: "Anomalous Degradation of Silicon Solar Cells Subjected to High-Fluence Irradiation," 33rd Annual International Nuclear and Space Radiation Effects Conference, Indian Wells, California, July 15-19, 1996, G-2.
- [8] L.J. van der Pauw: "A Method of Measuring Specific Resistivity and Hall Effect of Discs of Arbitrary Shape," Philips Res. Rept. 13 (1958) 1.
- [9] M.Imaizumi, S.J.Taylor, M.Yamaguchi, S.Matsuda, O.Kawasaki and T.Hisamatsu: "Type Conversion in P-type Base Layer of Si Space Solar Cells Induced by High Energy Particle Irradiation", Extended Abstracts (The 44th Spring Meeting, 1997); The Japan Society of Applied Physics and Related Societies, 30p-B-5, p.764 (in Japanese).
- [10] S.M.Sze and J.C.Irvin: "Resistivity, Mobility, and Impurity Levels in GaAs, Ge, and Si at 300K," Solid State Electron., 11, 599 (1968).

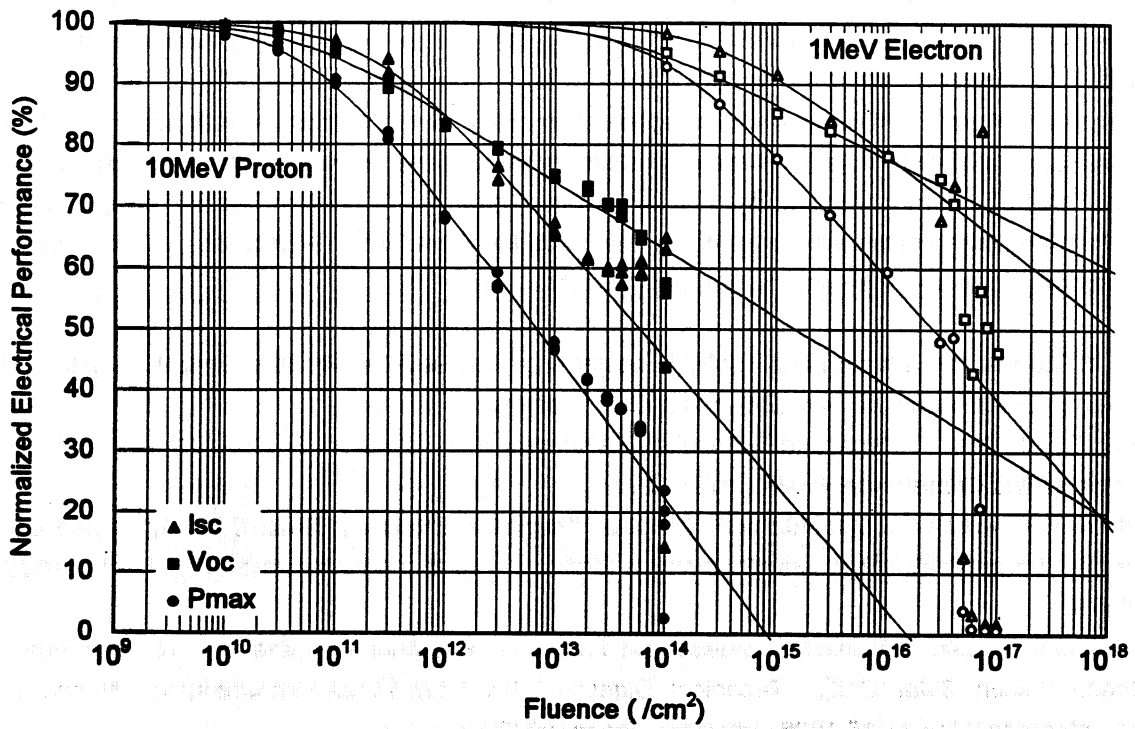


Fig. 1. Normalized electrical performance versus fluence for Si BSFR Solar cells[3].
(black symbols:10MeV proton, white symbols:1MeV electron)

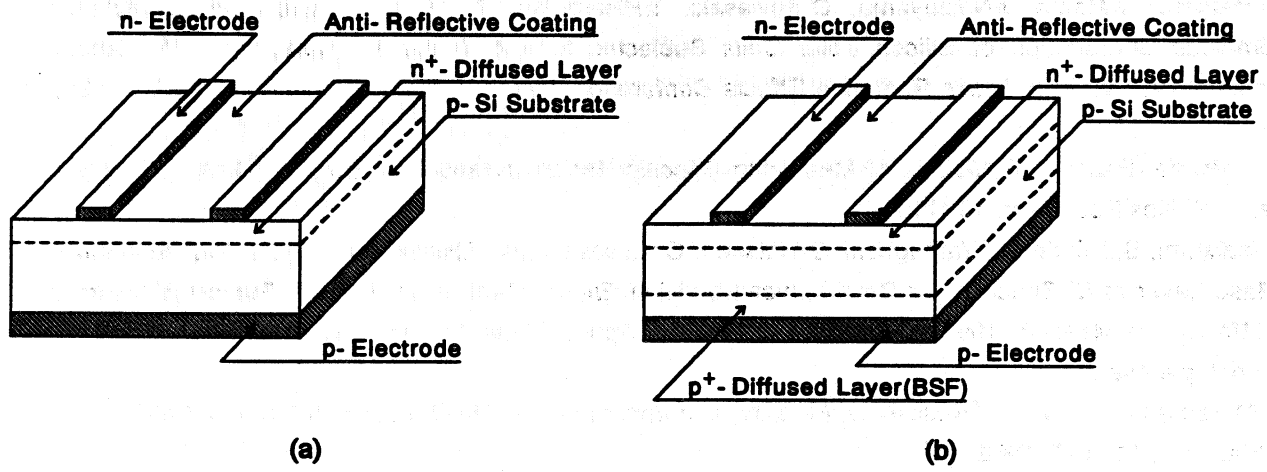


Fig.2 Cell Structure: (a) BSR Cell (b)BSFR Cell.

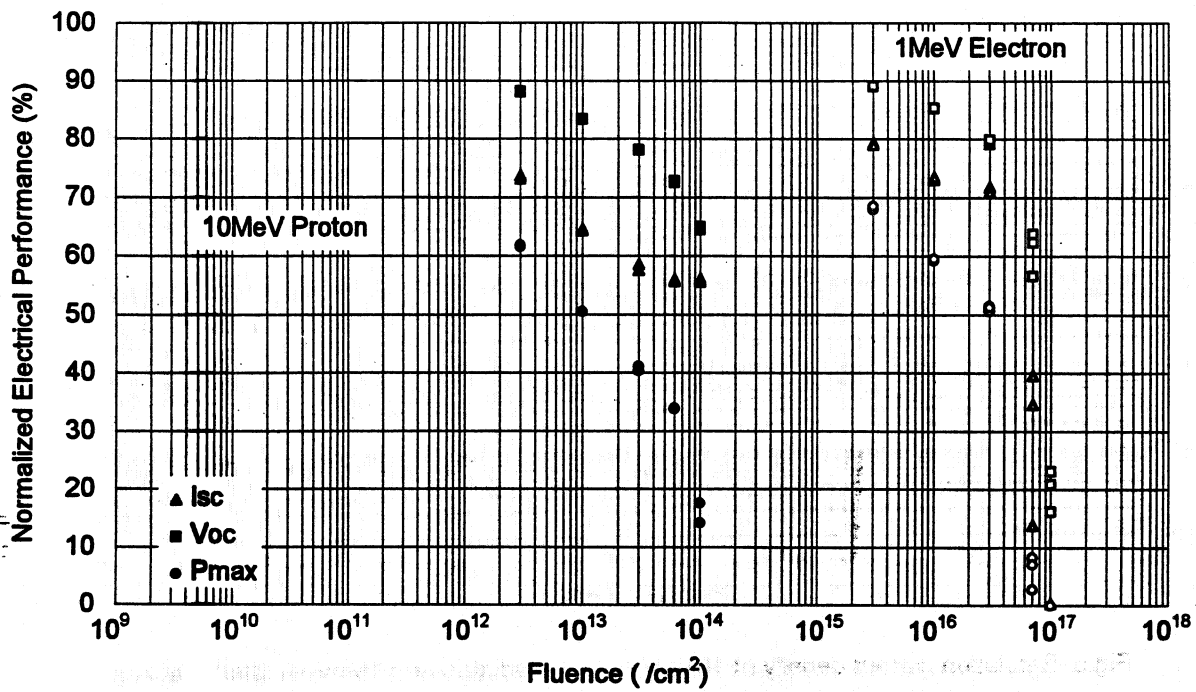


Fig.3 Normalized electrical performance versus fluence for Si BSR Solar cells.

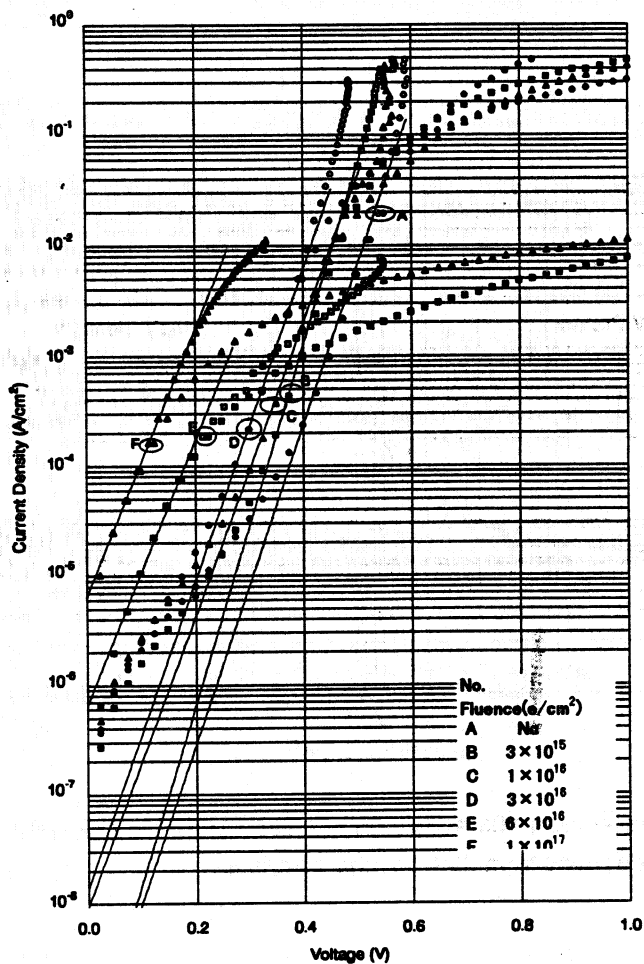


Fig.4 Dark I-V characteristics of 1MeV electron irradiated BSR cells (forward).

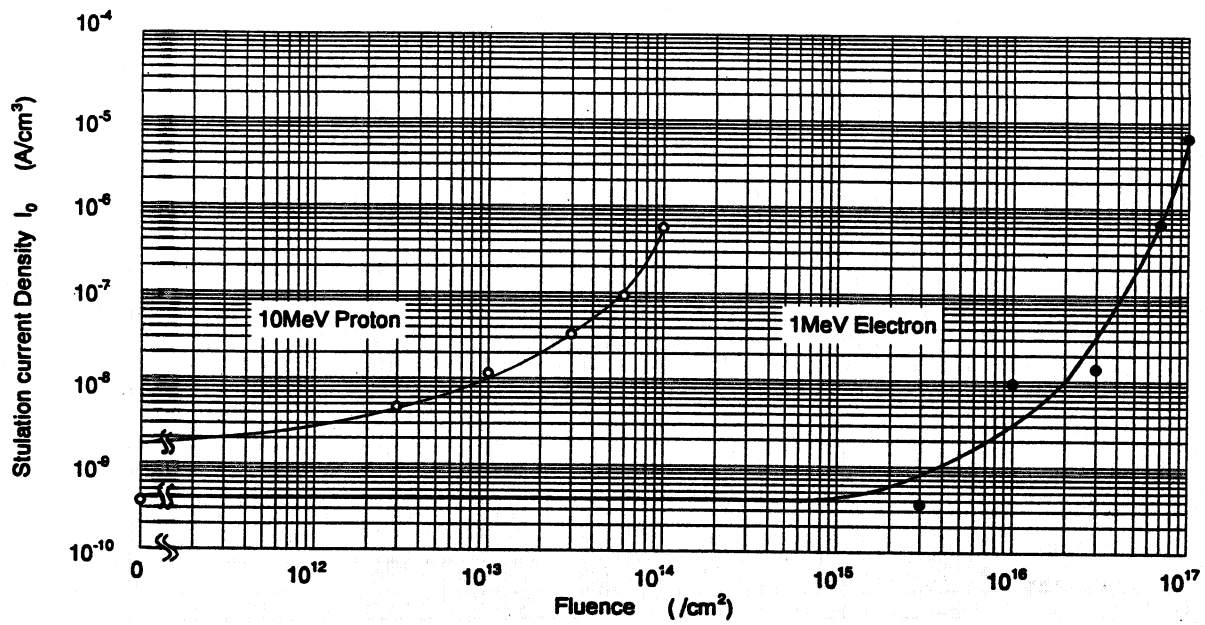


Fig.5 Saturation current density of 10MeV proton irradiated and 1MeV electron irradiated BSR cells derived from dark I-V characteristics.

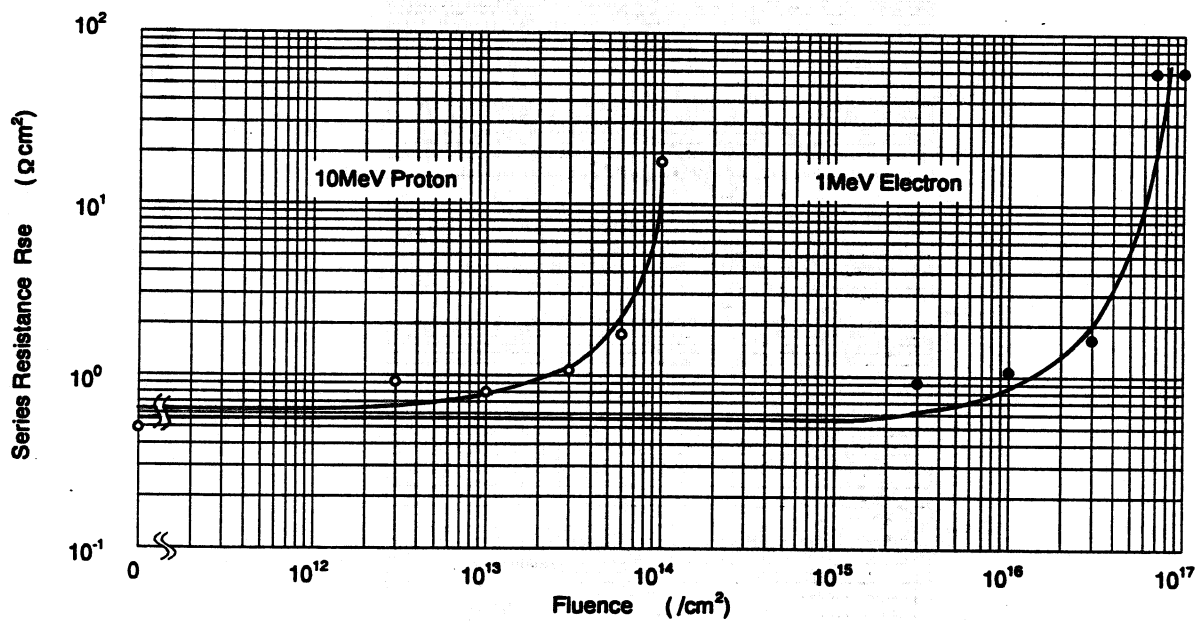
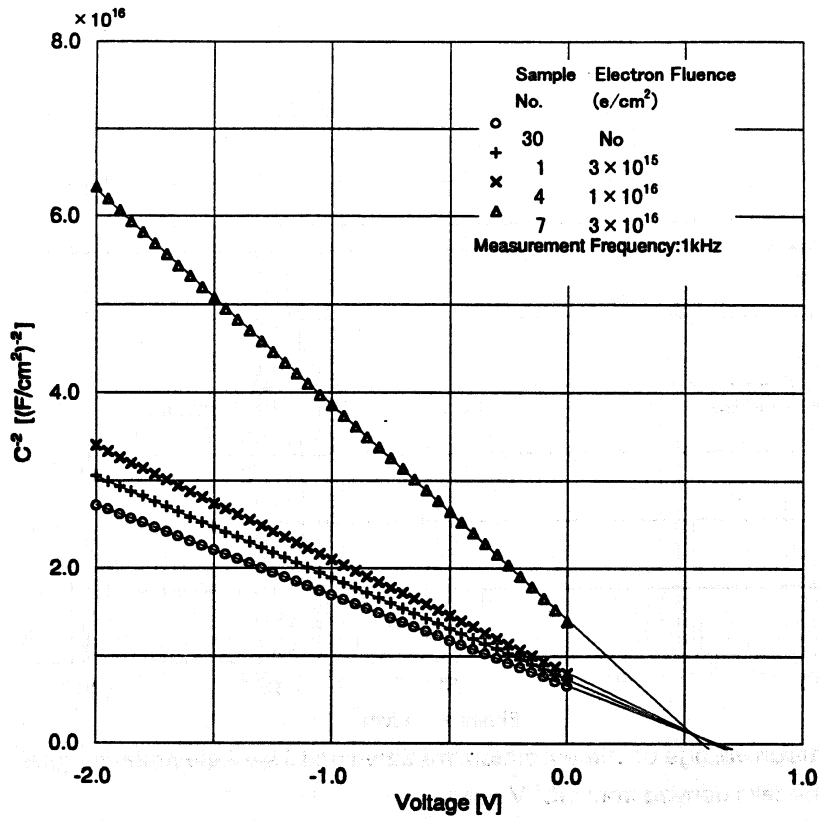
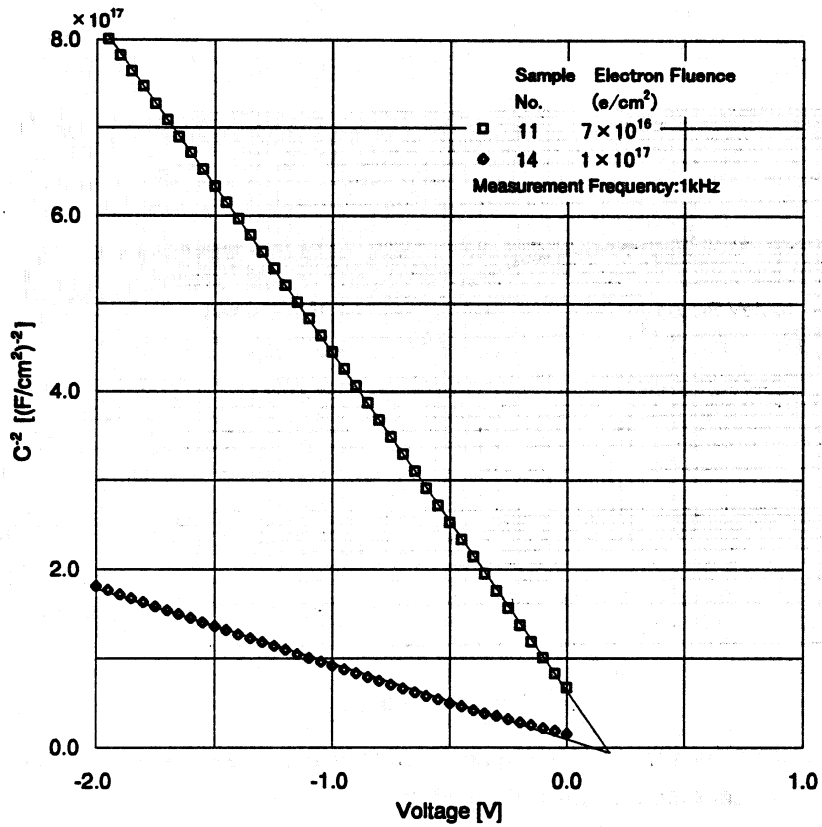


Fig.6 Series resistance of 10MeV proton irradiated and 1MeV electron irradiated BSR cells derived from dark I-V characteristics.



(a)



(b)

Fig.7 $1/C^2$ versus V plots of 1MeV electron irradiated BSR cells.

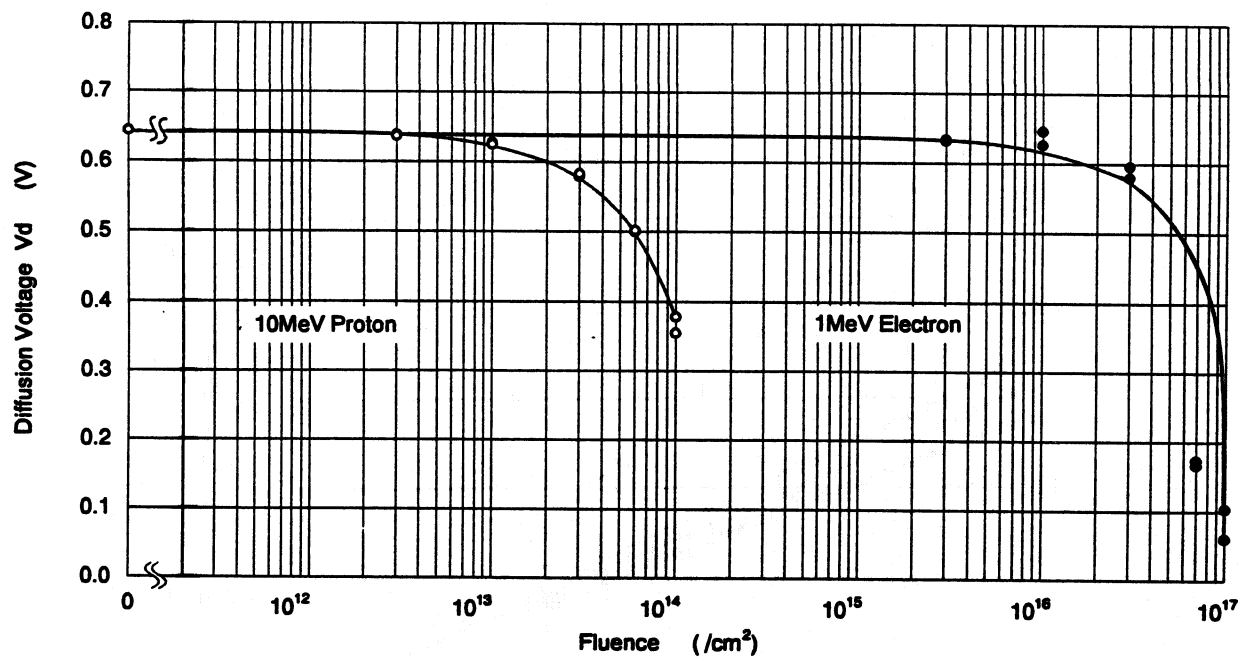


Fig.8 Diffusion voltage of 10MeV proton irradiated and 1MeV electron irradiated BSR cells derived from $1/C^2$ -V plots.

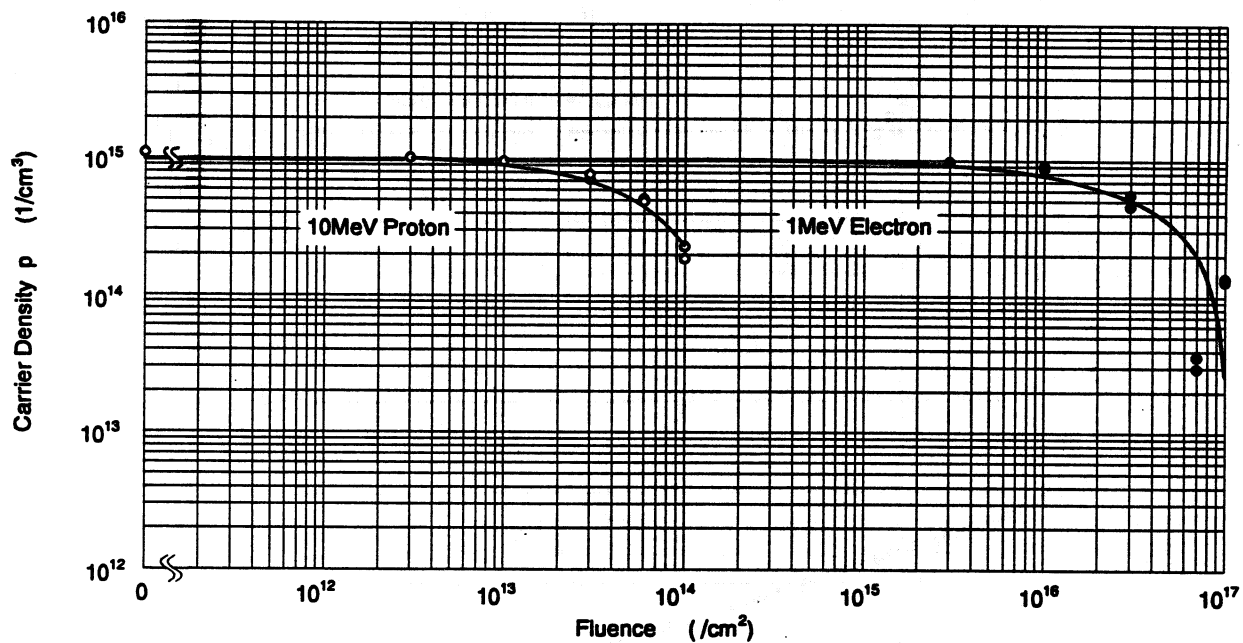


Fig.9 Carrier density of 10MeV proton irradiated and 1MeV electron irradiated BSR cells derived from $1/C^2$ -V plots.

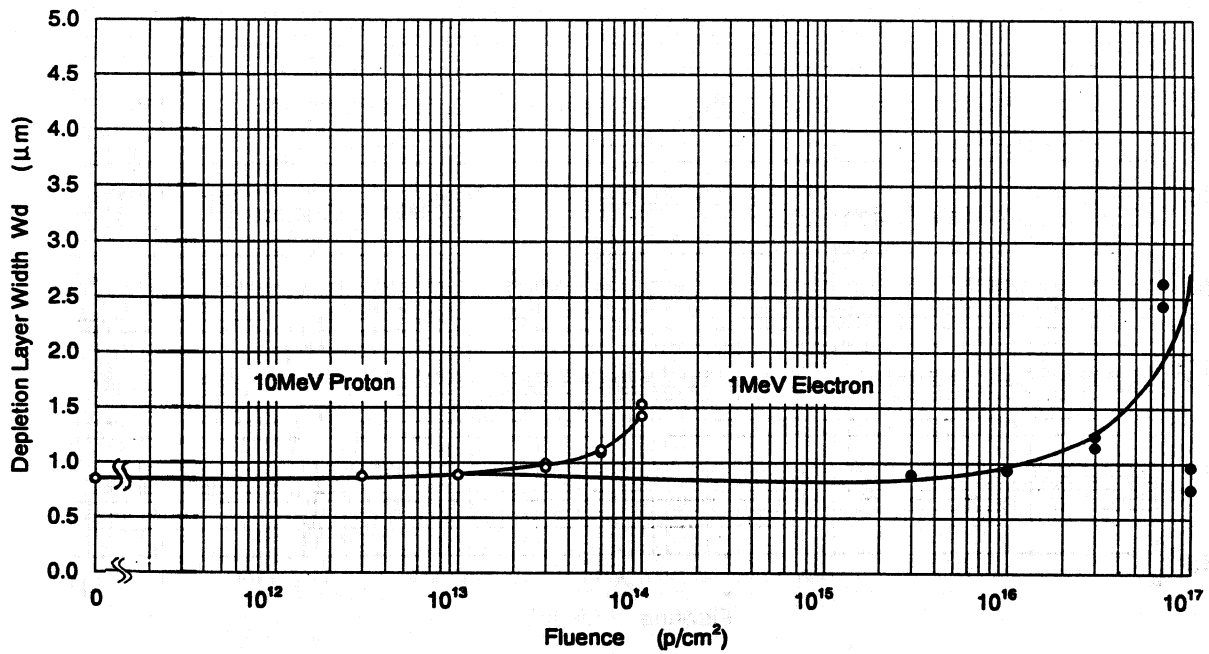


Fig.10 Depletion layer widths of 10MeV proton irradiated and 1MeV electron irradiated BSR cells derived from capacitance with no bias.

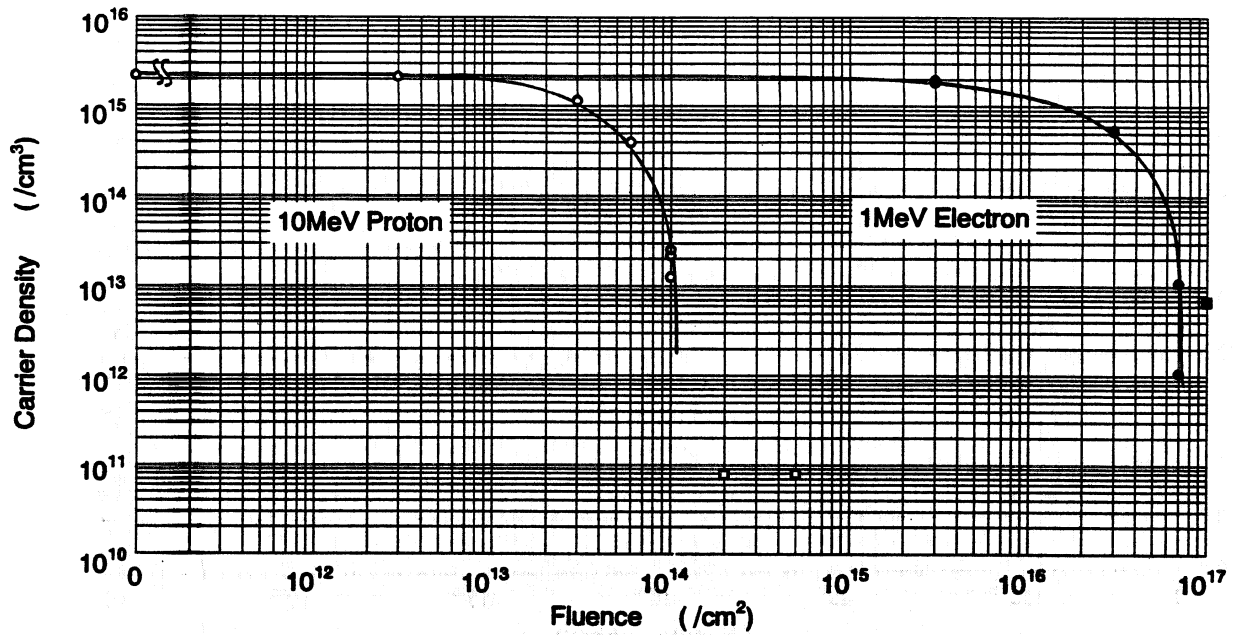


Fig.11 Carrier Density of 10MeV proton irradiated and 1MeV electron irradiated Si wafer derived from Hall measurements at room temperature.
 (circular symbols:p-type, square symbols:n-type)

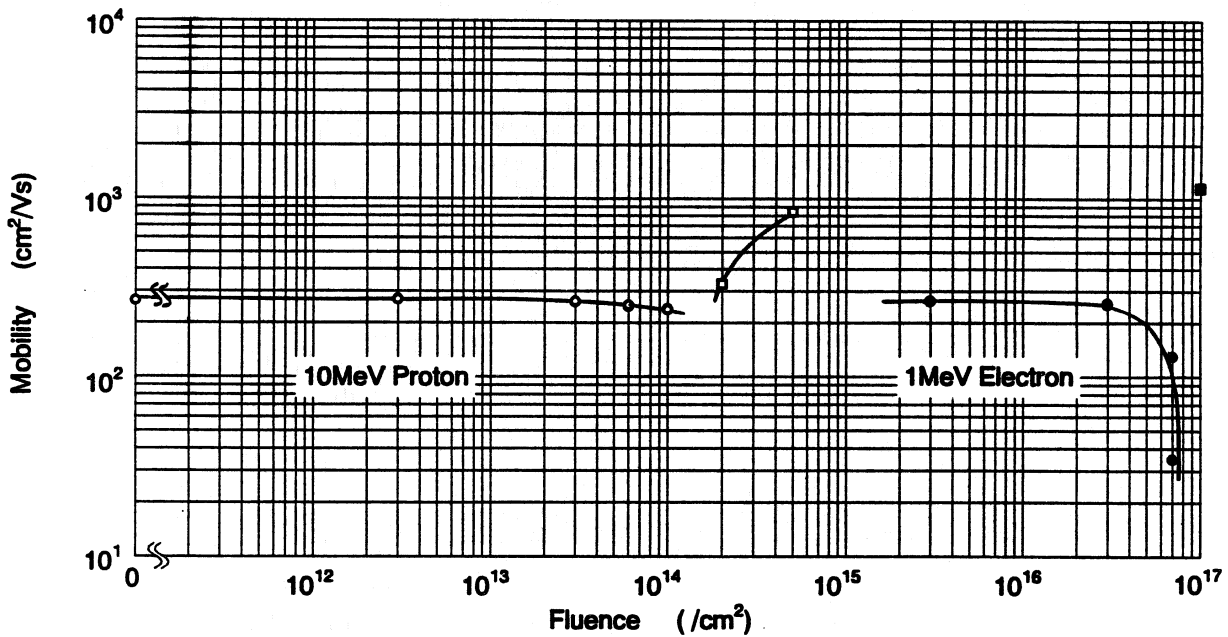


Fig.12 Mobility of 10MeV proton irradiated and 1MeV electron irradiated Si wafer derived from Hall measurements at room temperature.
 (circular symbols:p-type, square symbols:n-type)

THE EFFECT OF LARGE SOLAR PROTON EVENTS ON GaAs SOLAR CELL EFFICIENCY

M.A. Xapsos^{*}, S.R. Messenger^{*}, R.J. Walters^{*}, G.P. Summers^{*†} and E.A. Burke^{*}

^{*}Naval Research Laboratory, Washington, DC

[†]SFA, Inc., Landover, MD

^{*}University of Maryland Baltimore County, Baltimore, MD

INTRODUCTION

In geosynchronous orbits, radiation damage to solar cells results almost entirely from the outer trapped radiation belt (trapped electrons) and from solar proton events. The latter are the focus of this paper. Solar proton events occur randomly throughout the 7 active years of a typically 11 year solar cycle. The sizes of these events are known to vary by many orders of magnitude. Thus, the largest events within each active period are expected to contribute most of the proton dose absorbed by solar cells. Detailed measurements of solar proton events have been made for the last four solar cycles (19-22). Figure 1 shows the total > 10 MeV proton fluence for each cycle, along with the corresponding fluence of the largest event in each cycle. The sources of these data are given in the following section. Solar cycle 19 was the most active of the four. During this period, the largest event in at least the last 40 years occurred - the November 1960 event. The > 10 MeV fluence of this event was $3.2 \times 10^{10} \text{ cm}^{-2}$, and was about 45% of the fluence of the entire cycle. The first 6 active years of cycle 20 were rather quiet. However, the well-known August 1972 event occurred in the final active year. The > 10 MeV fluence of this event accounted for half of the cycle's total. Cycle 21 was the quietest of the last four cycles. The largest event during this period was $2.9 \times 10^9 \text{ cm}^{-2}$. Subsequently, solar cycle 22 turned out to be a rather active cycle, and had a > 10 MeV fluence total which exceeded that of cycle 21 by more than a factor of 3. The largest event occurred in October 1989, and accounted for 35% of the total of cycle 22.

It is important to understand the effects of very large solar proton events, which can significantly degrade solar cell properties over a time period that is very short (hours to days) compared to a satellite lifetime. In this paper, the probability of occurrence of these large events is described using established methods of extreme value statistics. The effect of such events on the efficiency of widely used GaAs solar cells is then described. Finally, this is compared to the efficiency degradation due to all events in solar cycle 22, as well as that of the electron environment in geosynchronous orbit.

A recent analysis of the general solar activity of cycle 23 forecasts that it will be similar to cycle 22 [1]. This is based on studies of common indicators of solar and geomagnetic activity. Thus, an assessment of the effects of cycle 22 on solar arrays should be quite useful for predicting the effect of cycle 23. The 7 active year period of cycle 23 is expected to extend from mid-1997 to mid-2004 [1].

EXTREME SOLAR PROTON EVENTS

As discussed above, detailed data of solar proton event fluences exists for the last 4 solar cycles. The methods for detecting solar protons have changed over this time period. It is therefore important to use a data base that is as self-consistent as possible. Shea and Smart have put great efforts into compiling such lists of events [2], and our data base is, to a large extent, based on their work. The event fluence data we have used is taken from Shea and Smart for cycles 19-21 [2]. For cycle 22, we have used data from the *GaAs Solar Cell Radiation Handbook* [3], supplemented with data from NOAA [4].

We have previously found that extreme value theory is useful for describing large solar proton events [5], and have applied such results to characterize degradation of silicon solar cells [6]. Details of the theory are found in references 5-8. Applicability of extreme value theory is often determined by plotting an ordered data set of the largest annual events on extreme value probability paper to see if it is linear. This is shown in Figure 2 using our updated data base. It is seen that the theory describes the data very well for > 10 MeV event

fluences that exceed about $5 \times 10^8 \text{ cm}^{-2}$. The straight line shown in the Figure is a regression fit to the extreme value type I cumulative distribution of maximum events, given by [8]

$$F(x) = \exp(-\exp[-\alpha(x - u)])$$

The quantity x is the natural logarithm of the event fluence, and α and u are fitting parameters. The regression fit resulted in $\alpha = 0.980 \pm 0.023$ and $u = 20.87 \pm 0.03$.

Once the cumulative distribution is obtained, it is straight forward to project this result to longer periods of time [5]. Figure 3 shows the probability that the largest solar proton event in a solar cycle exceeds a given $> 10 \text{ MeV}$ fluence. For example, note that this probability for exceeding $3 \times 10^{10} \text{ cm}^{-2}$ is about 25%. The data base shows this has occurred once in the last four solar cycles.

Now that the various probabilities of extreme events are known, the next step is to determine the proton energy spectrum. It is well known that the energy spectrum of solar proton events, when transformed to a magnetic rigidity spectrum, follows an exponential behavior [9]. We have determined that this description is valid over the proton energy range of 1 to 80 MeV for the 12 largest events of cycle 22. These include all of the events of cycle 22 that fall within the fluence range that is described by our extreme value model, i.e. events with a $> 10 \text{ MeV}$ fluence that exceeds $5 \times 10^8 \text{ cm}^{-2}$. Summing these 12 spectra gives the average spectrum of a large event in cycle 22. This average is also described by an exponential in magnetic rigidity. Expressed directly as a function of proton energy, and normalized to a $> 10 \text{ MeV}$ fluence of $1 \times 10^{10} \text{ cm}^{-2}$, the average differential distribution of a large event in cycle 22, in units of $\text{cm}^{-2}\text{MeV}^{-1}$, is given by

$$N(E) = 1575 \times 10^9 \left(\frac{E + 938.3}{R} \right) \exp\left(\frac{-R}{60.8} \right)$$

where the magnetic rigidity, R , is related to the proton energy, E , as follows:

$$R = \sqrt{E^2 + 1876.6E}.$$

The units of R are MV, and those of E are MeV. This spectrum can be adjusted to an event with a different magnitude by direct scaling. Those familiar with the magnetic rigidity description will recognize that the characteristic rigidity, R_0 , has a value of 60.8 MV.

The above description of the average differential distribution of a large event is displayed in Figure 4. The magnitude shown corresponds to the 50% confidence level of the largest event that is expected to occur in a solar cycle. This was obtained from Figure 3. Also shown in Figure 4 are the results of transport calculations through coverglass thicknesses of 3, 12 and 30 mils. The transport calculation is a modified version of that given by Haffner [9], and is described in detail in these proceedings [10]. The calculations must be carried out down to a threshold for producing atomic displacements - around 200 eV. Note that the effect of increasing the coverglass thickness is to harden the event spectrum that reaches the device.

COMPARISON TO THE TOTAL CYCLE 22 FLUENCE AND THE ELECTRON ENVIRONMENT

In order to directly compare the effect of the large solar proton event shown in Figure 4 with that of all events in cycle 22 and with the electron environment, the following procedure was used. The proton spectrum that emerges through a given coverglass thickness was first converted to an equivalent 10 MeV proton fluence using nonionizing energy loss values in GaAs [11]. The 10 MeV proton fluence was then converted to a 1 MeV equivalent electron fluence using the empirically established factor for GaAs solar cell efficiency degradation found in reference 3. These results are shown in Figure 5 as a function of coverglass thickness for the largest event in a cycle at the 50% confidence level, and for all events in cycle 22. The former amounts to about 22% of the latter for all coverglass thicknesses.

Results for the electron environment in geosynchronous orbit, obtained from reference 3, are also shown in Figure 5 for a 7 year period. For the reason given in this reference, the exposure in the electron belts at these altitudes is weakly dependent on longitude. What is shown in Figure 5 is simply the average value for the various given longitudes. An interesting feature of Figure 5 is that with decreasing coverglass thickness, the effect of solar proton events becomes more important relative to the electron environment. Another way to

view this is that increasing the coverglass thickness is more effective for shielding against solar proton events than against the electron environment.

Finally, the effect of these radiations on GaAs/Ge solar cells is shown in Figure 6 as a function of coverglass thickness. Here data for normalized maximum power given in the *GaAs Solar Cell Radiation Handbook* [3] was used. The results shown are for the largest expected event in a solar cycle at the 50% confidence level, all events in solar cycle 22, and all events plus the electron environment for the 7 active year period. It is seen that for a 10 mil coverglass, the single large event will reduce the normalized maximum power to about 0.98. For this same thickness, all cycle 22 events will reduce it to about 0.95. All cycle 22 events plus the 7 year electron environment will reduce it to 0.91.

CONCLUSIONS

We have assessed the probabilities of occurrence of large solar proton events during the recently beginning 7 active year period of solar cycle 23. There is about a 55% chance that the largest event during this cycle will have a > 10 MeV fluence in excess of $1 \times 10^{10} \text{ cm}^{-2}$. Although such events are rare, they can cause a sudden power loss in a solar array. The general solar activity of cycle 23 is expected to be similar to cycle 22. Thus, during the 7 active years of the upcoming cycle, the effect of all solar proton events on a GaAs/Ge solar array with 10 mil coverglass, as determined from 1 MeV equivalent electron fluences, is expected to be 50 to 60% of the effect of the electron environment in geosynchronous orbit. Such a solar array is therefore expected to have a normalized maximum power of about 0.91 by the middle of the year 2004.

REFERENCES

- [1] J.A. Joselyn, J. Anderson, H. Coffey, K. Harvey, D. Hathaway, G. Heckman, E. Hildner, W. Mende, K. Schatten, R. Thompson, A.W.P. Thomson and O.R. White, Summary of Panel Findings for Solar Cycle 23 Project, Boulder, CO, Sept. 1996.
- [2] M.A. Shea and D.F. Smart, "A Summary of Major Solar Proton Events", *Solar Phys.* **127**, 297-320 (1990).
- [3] B.E. Anspaugh, *GaAs Solar Cell Radiation Handbook*, JPL Publication 96-9, July 1996.
- [4] *Solar Geophysical Data, No. 603 -Part II*, pp.28-31, published by NOAA, Boulder, CO, Nov. 1994.
- [5] M.A. Xapsos, G.P. Summers, P. Shapiro and E.A. Burke, "New Techniques for Predicting Solar Proton Fluences for Radiation Effects Applications", *IEEE Trans. Nucl. Sci.* **43**, 2772-2777 (1996).
- [6] G.P. Summers, M.A. Xapsos and E.A. Burke, "Application of Extreme Value Statistics to the Prediction of Solar Flare Proton Effects on Solar Cells", Proceedings of the 25th IEEE Photovoltaics Specialists Conference, pp.289-292 (1996).
- [7] E.J. Gumbel, *Statistics of Extremes*, Columbia University Press, NY, 1958.
- [8] A.H-S. Ang and W.H. Tang, *Probability Concepts in Engineering Planning and Design, Vol. I - Basic Principles*, John Wiley & Sons, NY, 1975.
- [9] J.W. Haffner, *Radiation and Shielding in Space*, Academic Press, NY, 1967.
- [10] G.P. Summers, S.R. Messenger, E.A. Burke, M.A. Xapsos and R.J. Walters, "Contribution of Low Energy Protons to the Degradation of Shielded GaAs Solar Cells in Space", this proceedings.
- [11] G.P. Summers, E.A. Burke, P. Shapiro, S.R. Messenger and R.J. Walters, "Damage Correlations in Semiconductors Exposed to Gamma, Electron and Proton Radiations", *IEEE Trans. Nucl. Sci.* **40**, 1372-1379 (1993).

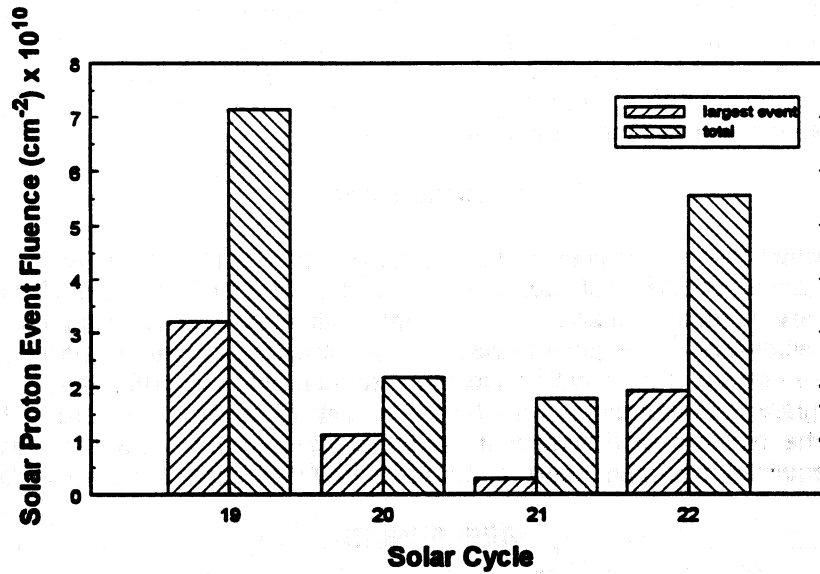


Figure 1. Single largest event and total > 10 MeV proton fluences for solar cycles 19-22.

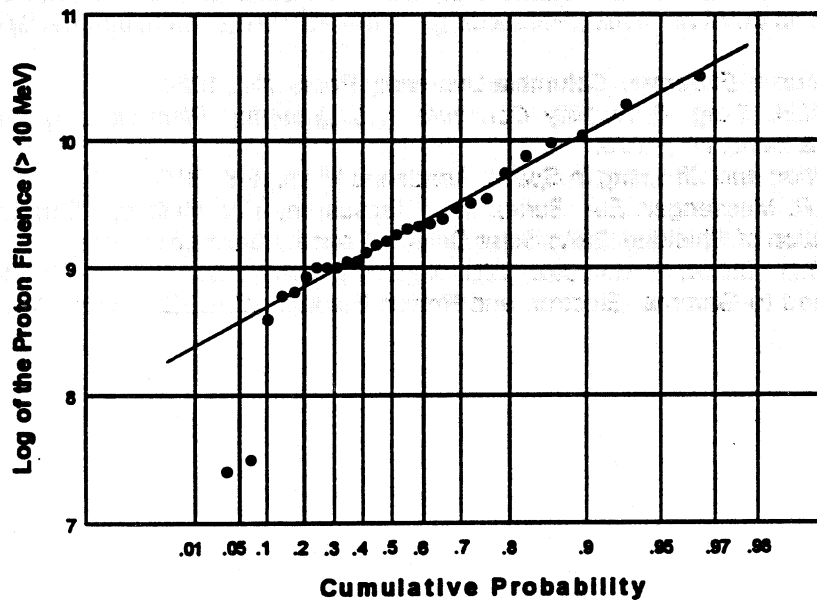


Figure 2. Extreme value probability plot of the largest annual solar proton events for the active years of solar cycles 19-22. The straight line is a regression fit to the data. See text.

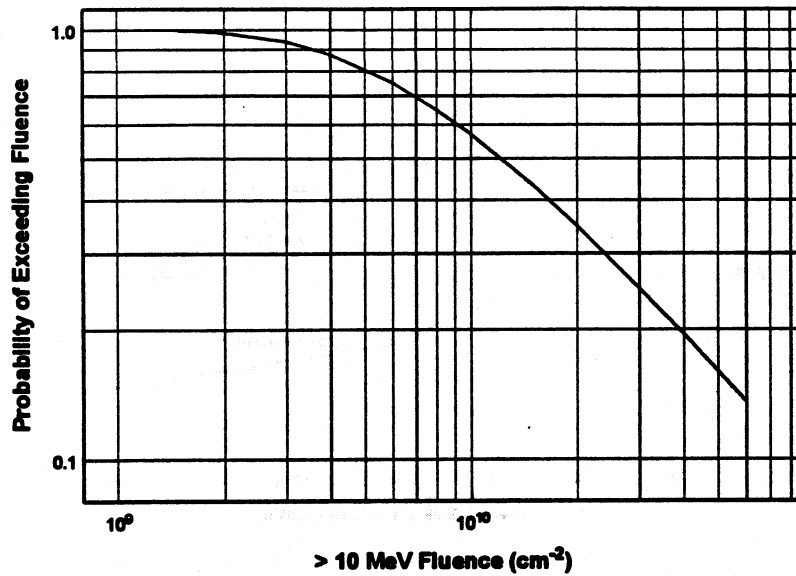


Figure 3. Probability that the largest event in a solar cycle exceeds a given fluence of > 10 MeV protons.

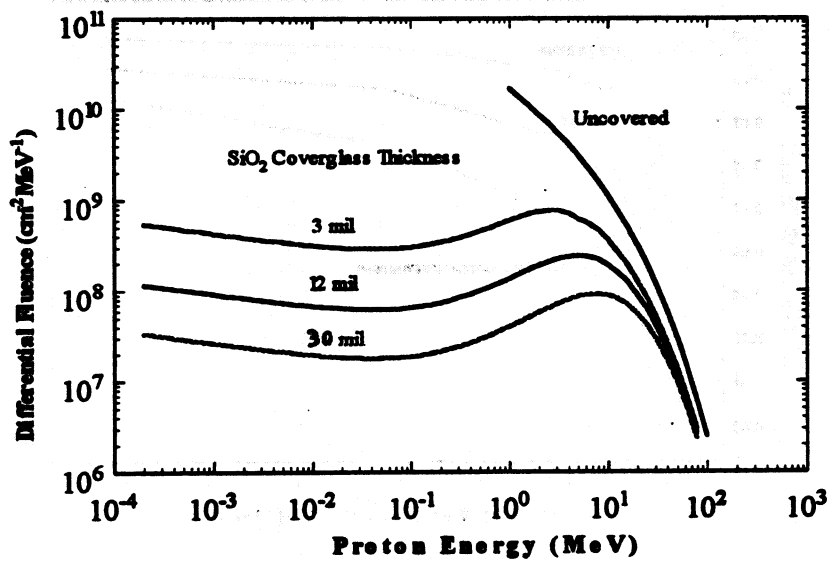


Figure 4. The effect of transport through different coverglass thicknesses on the average differential energy spectrum of a large solar proton event in cycle 22. The initial spectrum is well described by an exponential in magnetic rigidity. See text.

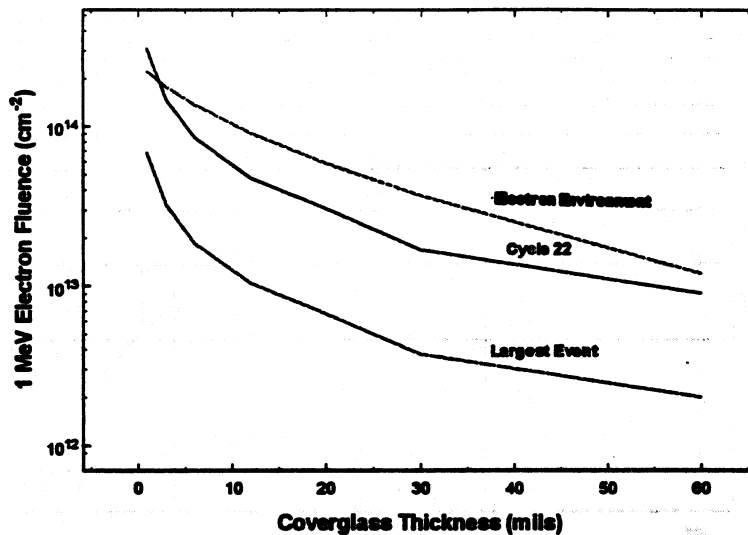


Figure 5. Damage equivalence in GaAs solar cells, expressed in terms of a 1 MeV equivalent electron fluence, for the expected largest solar proton event in a solar cycle, all events in solar cycle 22, and the electron environment in geosynchronous orbit. Results are shown as a function of coverglass thickness.

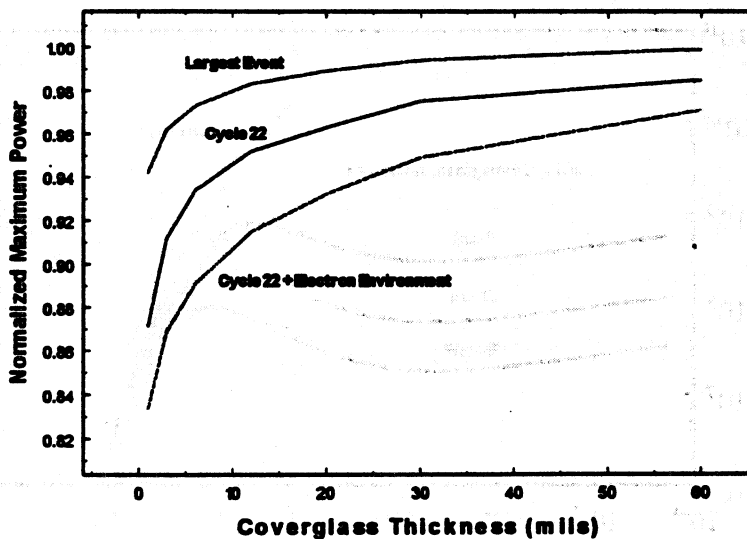


Figure 6. The effect of the radiation environment in geosynchronous orbit on the normalized maximum power of GaAs solar cells. Shown as a function of coverglass thickness is the effect of the largest expected solar proton event in a solar cycle, the effect of all events in cycle 22, and the effect of all events in cycle 22 plus the electron environment for a 7 year period.

Evidence For Enhanced UV Degradation to Cracked Coverslides

Andrew Meulenberg
Matra Marconi Space
Toulouse, France
and

J. Brower, M. Kruer, and C. M. C. Toporow
TRW
Redondo Beach, California

Summary

A TRW UV test of 1000 ultraviolet solar hours (UVSH) on 2x3 cm silicon solar cells with cracked coverslides has been completed and analyzed. The results indicate that the presence of cracks on the solar cell coverslides will increase the UV degradation (~1% per crack in short-circuit current at 1000 UVSH). However, the increase in degradation from the cracked coverslides is less than the overall losses from UV to the array. The predicted worst-case increase in UV degradation due to a large crack is ~50% of the 4% predicted for uncracked cells at end-of-life (~10 years). Considering the test results and a reasonable percentage of cracked cells, the array degradation from UV on the cracks is well within the 1% array power margin generally provided for such effects.

Introduction

Traditionally, solar-cell-assembly UV-acceptance tests require that there be less than 2% UV degradation at 1000 UVSH. A TRW UV Test was set up to establish that cracked coverslides would not cause a great increase in the solar-array degradation due to solar UV. It was recognized that a limited (engineering) test would not provide sufficient data to accurately predict long-term degradation. However, such a test would identify anomalously large degradation (such as found in an early ESTEC test, Reference 1), if it existed. A rough analysis of the effects of decreasing short-circuit current of a single cell in an array is required to understand the implications of this test and its results

Analysis of the TRW UV Experiment

The total population of 2x3 cm cells tested and acceptable for analysis in this program is small (2 bare cells, 1 covered without cracks, 2 covered with 1 crack, and 1 covered with 2 cracks). Nevertheless, the trends are consistent in the two measurement techniques used to identify the effects of cracked cells on UV degradation and, by comparison with higher precision UV degradation experiments, are capable of being extrapolated to a >10 year mission in space. The first technique is described in detail below. The second technique for determining UV degradation to the cells with cracked coverslides (in the appendix) provides relative measurements only. However, the precision in the second technique is better because of the more numerous measurements.

The principal technique for determining the UV degradation is a standard test utilizing a UV source and an accurate solar simulator. The UV source is for long-term exposure to simulate the degrading portion of the solar spectrum. The solar simulator (a Spectrolab X25 in this case) is used to determine the actual effects of the exposure. Short-circuit current (I_{sc}) measurements were made prior to exposure and at 400 and 1000 UVSH. Figure 1 displays the relative degradation (raw data) after UV exposure. The 6 cells acceptable to the test

requirements are displayed. Three cells in one (base 2) of the three vacuum chambers were eliminated from the database as a consequence of possible contamination in the system (a very common problem in this type of test). The cell notation indicates the vacuum chamber and cell location (e.g., 3,1 means base 3 and position 1). The symbols and lines in the figure are an attempt to maintain the logic imposed by the coverslide condition (no cover = fully dotted lines, no cracks = unbroken line, one crack = single-dotted line, and two cracks = double-dotted line).

The variation in degradation between the 400 and 1000 UVSH points ($\leq \pm 0.5\%$) is larger than statistical variations within measurements on the same day, but not uncommon for systematic variations in measurements with solar simulators over different days. The actual degradation at these points should be close, with the 1000 UVSH point displaying greater degradation. The data for one vacuum system (base 1) at 1000 UVSH was accumulated over 10 repeated operations to test reproducibility of the positioning and short-term stability of the X25 simulator. Since the base 3 cell data follows the base 1 trend very well, it is felt that the 1000 UVSH data has the best precision of the 3 UVSH measurements. The accuracy must depend on the long-term reproducibility of the X25.

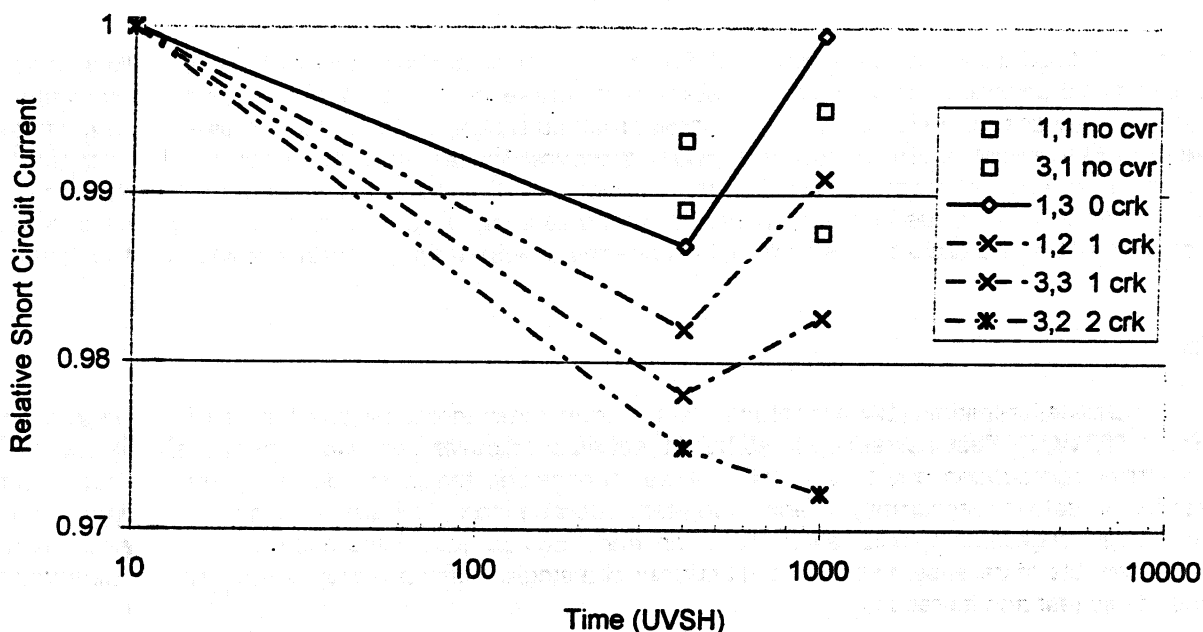


Figure 1. UV Degradation data as a Function of Equivalent UV Sun hours for Silicon Solar Cells Without Coverslides and With Uncracked and Cracked Coverslides.

Several points are clear from Figure 1. First, cracks do increase the UV degradation to solar cell Isc. In all cases, the cells with cracked coverslides degraded more than did the cells with no, or with uncracked, coverslides. Second, when a trend line is drawn averaging the 400 and 1000 UVSH points for each cell, the cell with 2 cracks in its coverslide degrades about twice as much as the cells with a single crack in their coverslides (relative to the degradation of the cell with no crack in its coverslide). Third, from these data, there is no way to predict how the cells will degrade under extended UV exposure from this limited data set.

Analysis of the UV Experiment

To address the point about long-term degradation, we have superimposed the test data on a curve from a recent extended UV test (Reference 2) with INTELSAT-6 solar cells used as controls (2x6 cm planar-surface silicon cells cut into 2x2 cm pieces) in Figure 2. The points on the curve represent the many times at which data were

taken (the actual data is scattered about the curve, the curve fitting algorithm and error analysis is described in Reference 3). Clearly an accurate projection, to beyond 10 years in orbit, requires the extensive test such as that performed in references 2 and 3. Nevertheless, this new test has pointed out an effect that had not been mentioned before – edge degradation. It has been suspected for many years that partial recovery of UV degradation upon exposure to air has been a result of oxygen diffusing through the coverslide adhesive from the edges. Therefore, the edges could (and should) be related to at least a portion of the UV degradation to solar cell assemblies.

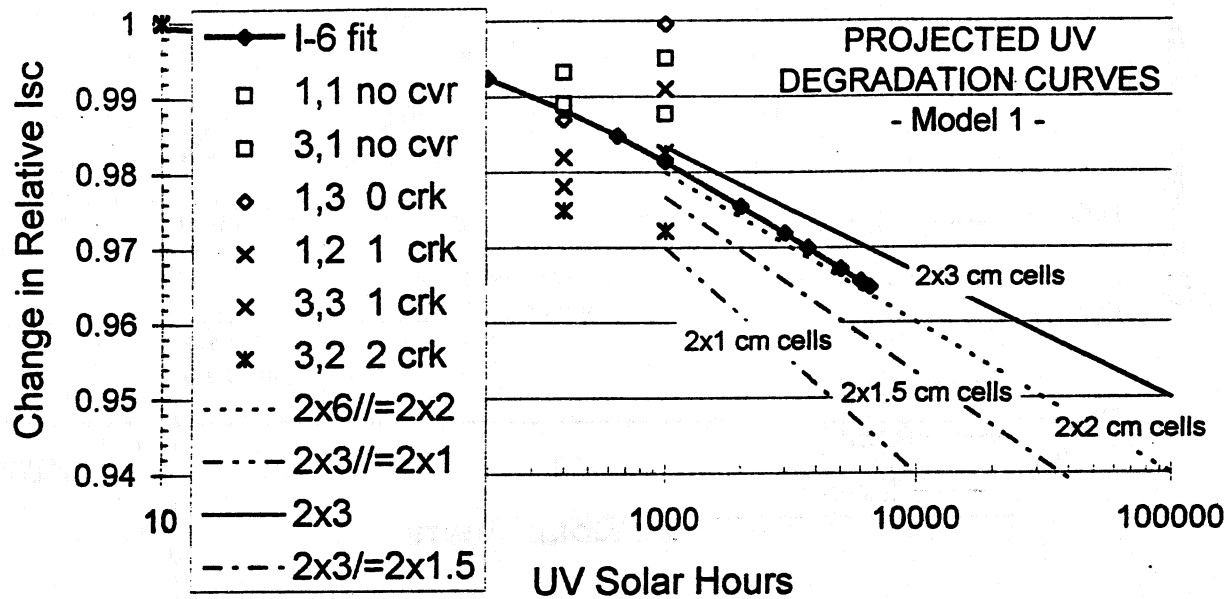


Figure 2. Figure 1 Data Superimposed on Data for 2x2 cm INTELSAT-6 Silicon Solar Cells. Projected lines are based on model 1 described in text.

With the recognition that edges effect UV degradation, a simple model is proposed to quantify this effect. A 2x3 cm cell has 10 cm of edge for 6 cm² of area. If the coverslide is cracked, then the 2x3 cm cell becomes equivalent to two 2x1.5 cm cells (notation in the figures are for 2x3// to represent a 2x3 cm cell cut twice or having a coverslide with 2 fractures). A 2x1.5 cm cell has 7 cm of edge for 3 cm² of area. Similarly, 2 cracks in a 2x3 cm cell gives the equivalent edge to area ratio of a 2x1 cm cell (i.e., 6 cm of edge for 2 cm² of area). This model is displayed in the projected degradation area of Figure 2. Since this model does not fit the presented data particularly well, a second model is proposed – a cut or coverslide break, after bonding, is twice as sensitive to UV as is a normal edge.

This second, more conservative, model fits the data quite well considering the limitations in systematic error and statistics. The 2x3 cm cell line goes through the center of data for the uncovered cells and the 2x3 cm cells with uncracked coverslide. The 2x2// cm cell line is fitted to the I-6 cell data (these were 2x2 cm pieces cut from 2x6 cm cells). This line indicates less degradation than that to the 2x3 cm cells with a single crack in the coverslide. The 2x1 cm cell line now fits the data for a 2x3 cm cell with one crack in the coverslide. While model 2 is still simple, it represents the data of both the earlier and present experiments and the message is clear. **The increase in UV degradation to a solar cell's Isc, near end-of-mission (100,000 UVSH = 11.4 years), is > 2% per 2 cm crack on a 2x3 cm cell.** The effect on larger cells is proportional to the crack length and inversely proportional to the cell area. Therefore, a crack across the narrow dimension of a 2x6 cm coverslide will introduce > 1% more degradation than that experienced by a 2x6 cm cell with an uncracked coverslide. A similar crack in a 4x6 cm coverslide will introduce >2% more degradation.

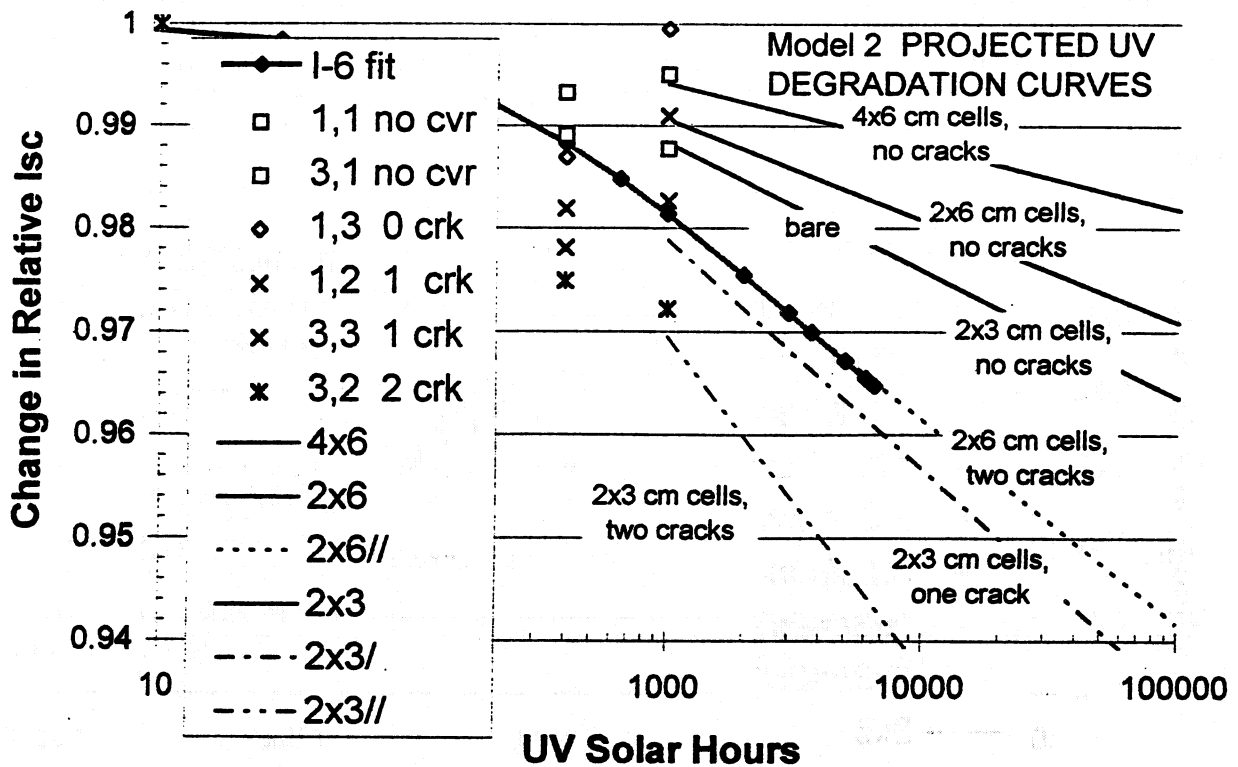


Figure 3. Figure 1 Data Superimposed on Data for INTELSAT-6 Cells (2x2 cm cells cut from 2x6 cm cells). Projected lines are based on model 2 described in text.

The experimental data and Model 2 results are seen in Table 1 (values in parentheses are modeled, projected, or interpolated). The projected values are based on the assumption that the differences will continue to grow and on the data from earlier (more detailed) experiments for coverslides with no cracks.

TABLE I. PERCENT DEGRADATION OF 2x3 cm SOLAR CELL Isc

Coverslide	0 UVSH	400 UVSH	1000UVSH	> 10 years UV
none	0	0.8 (0.6)	0.8 (1.2)	(~ 3 - 4%)
no cracks	0	1.3 (0.6)	0.1 (1.2)	(3 - 4)
1 crack	0	2 (1.4)	1.4 (2.1)	(6 - 7)
2 crack	0	2.5 (2)	2.8 (3)	(> 9)
INTELSAT-6 cell data (twice-cut 2x6 cm cells)	0	1.2	1.8	(6)

Implications for Solar Arrays

While the data and modeled results indicate a significant degradation in the Isc of individual solar cells with cracked coverslides, the practical implications of the present effort to a solar array are actually positive. First, large cells, which are most likely to experience coverslide cracking during solar-array panel assembly, testing, and launch, are the least affected by such cracks. Second, the actual UV degradation of large cells with intact coverslides is less than that of smaller cells. Third, most coverslide cracks are not as large as those tested in

this program and the Isc degradation depends upon the net coverslide crack length. Therefore, a large cell, with a single crack in its coverslide, will likely experience less UV degradation than would a small cell with no cracks.

The affect of a single coverslide crack on a solar cell string can vary from negligible to minor. Cells combined in a string are generally from a single grade. If the cell grades vary by 1% in current at a given voltage, the effect of coverslide cracks can alter the end-of life cell performance by a single grade. Since the variation in string performance at EOL is near the maximum power point, a 1% loss in cell Isc will result in $\geq 1\%$ loss in cell Pmax and a string loss of 1% divided by the number of cells in the string. Clearly, the increased loss of 1-2% in one cell (or even from 10 cells) of a 100 cell string is not of concern (~0.02% per cracked coverslide). However, if multiple cracks on a single cell were permitted, that cell could be operating well below its EOL Pmax and therefore the loss to the EOL string performance could be on the order of 1%.

Conclusion

Experimental data, on modern solar cells and adhesives with cracked coverslides, indicate that full-width cracks can increase the long-term UV degradation to a cell Isc by $> 2\%$ per crack per cell over a 10 year mission. The impact on a solar array end-of-life power output would depend upon the number of cracks per solar-cell string, the current of the cells with cracked coverslides relative to the string current, the number of cells per string, and the load voltage relative to the max-power point of the string.

With the above assumptions and models and a permitted population of cracked cells (~2%), the end-of-life power degradation to a solar array from cracked coverslides would be on the order of 0.04%. If a higher percentage of cracked coverslides is assumed or if multiple full-width cracks per coverslide are permitted, the predicted degradation will increase correspondingly.

References:

1. J. C. Larue, "Testing of CTS solar cell covers with hairline cracks," ESRO Memo TEC/JCL/0015/js, January 9, 1974
2. A. Meulenberg, "Space Qualification of IR-Reflecting Coverslides for GaAs Solar Cells" Proceedings of the 14th Solar Photovoltaic Research and Technology (SPRAT) Conference, NASA/LeRC, Cleveland, OH, 10/95.
3. A. Meulenberg, "UV Testing of Solar Cells: Effects of Anti-Reflective Coating, Prior Irradiation, and UV Source" Proceedings of the 12th SPRAT Conference NASA/LeRC, Cleveland, OH 1992.

APPENDIX: Relative Degradation of Solar Cell Isc Under UV Source Illumination

TRW monitored the short-circuit current of the test cells while under the UV source illumination. The purpose of this exercise was to confirm the extended UV exposure of the cells. However, long periods of illumination with UV exposure also provided a means of determining the relative degradation of the various coverslide configurations while eliminating the effects of statistical error in measurement (~ 4000 measurements). While the UV source is not a good spectral match to air mass zero (AM0), this problem will only affect absolute degradation determination, not the relative degradation.

Figure A1 is the results of the Isc data over 900 UVSH. These data have been normalized to remove effects of light source variations with time. The normalization is performed by dividing the Isc values of the different cells by the average Isc of all 3 sets of cells. The breaks in the curves result from spectral and intensity shifts (125, 361, and 400 UVSH) of the UV source and from physical shifts of the 3 vacuum systems for measurement (400 UVSH). Since, the average value is the normalization factor at each point, some cells will show an increase in relative Isc and others a decrease. Again, such normalization will affect absolute and not relative measurements.

The X25 solar simulator will provide absolute values of the UV degradation when measured with one sun AM0. However, because of the limited number of measurements (a few measurements at 0, 400 and 1000 UVSH), the statistical and systematic errors are a problem. The Isc data from the UV source will provide better relative measurements because of the hundreds of measurements per time period studied (only a few of which are shown in figure A1). The numerous data points will reduce the statistical errors by $N^{1/2}$. Therefore, instead of a standard deviation of $\sigma = 0.3\%$ per measurement period (e.g., 400 UVSH), we can obtain a standard deviation of the mean $\sigma_m < 0.03\%$ per measurement period (e.g., 200 - 400 UVSH).

While the relative Isc of all of the cells with cracked coverslides consistently degrade beyond the 125 UVSH mark, the cells in chamber 2 (i.e., 2.1, 2.1 and 2.3) all degrade more than the others in the 0 - 125 UVSH time frame. This anomalous degradation was the reason for rejecting this set of data. Nevertheless, the relative data from this set is consistent at later times with the 2-crack cell degrading and the bare and no-crack cells not degrading.

Summary of Solar Cell Isc Data under the UV-Source

The 2 crack cells degraded the most; 1 crack cells next; and perhaps covered cells degrade more than bare cells. These conclusions confirm the results of the X25 measurements. Cracks in solar cell coverslides increase the observed UV degradation to Isc.

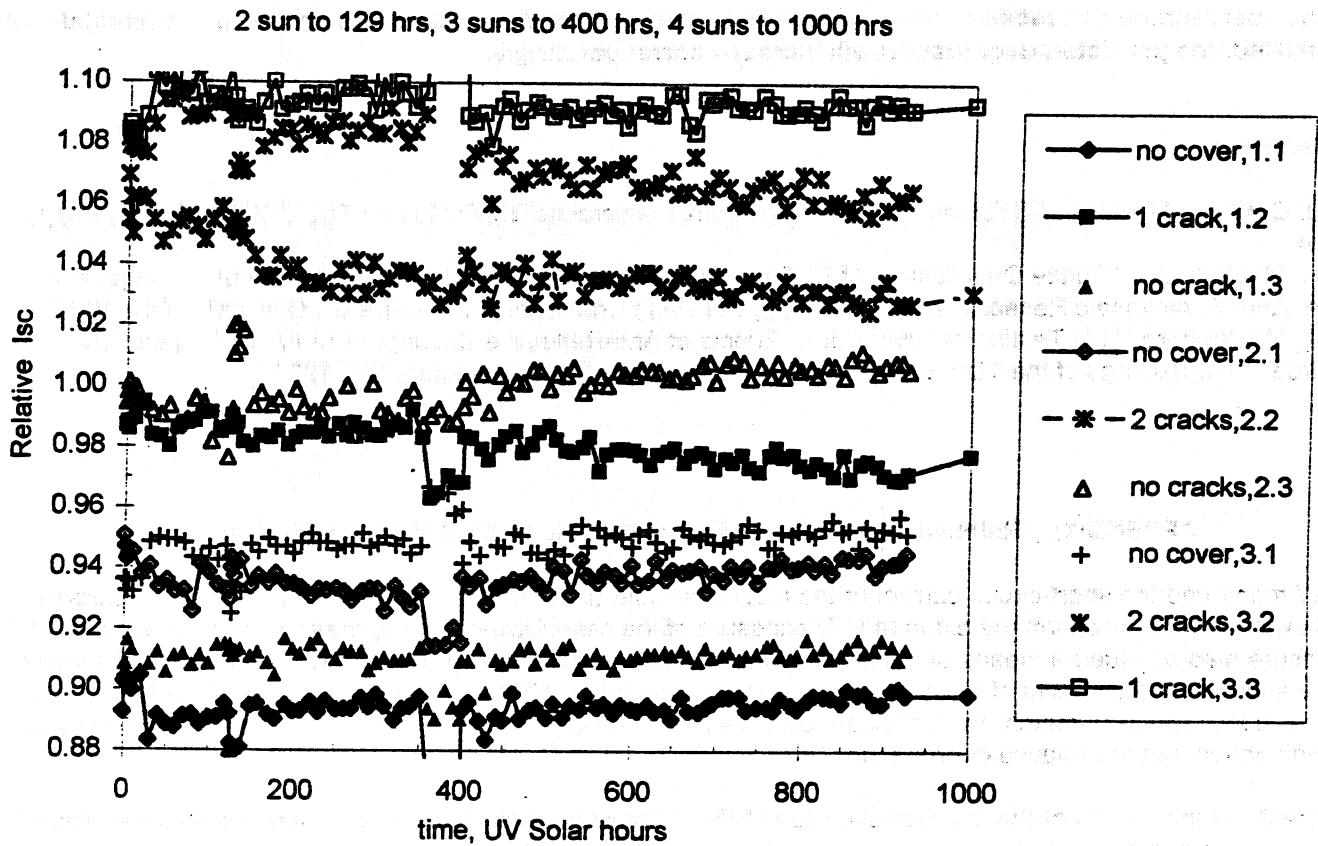


Figure A1. Normalized Isc of Test Cells under UV Illumination Source.

NASCAP MODELING OF GEO SATELLITES - SPACECRAFT CHARGING IS BACK!

R. Chock, D.C. Ferguson and D.B. Snyder
NASA Lewis Research Center
Cleveland, OH 44135

ABSTRACT

During the last few years of Solar Minimum, GEO spacecraft charging design practices may have become lax because of a paucity of spacecraft charging events. Unfortunately, this has also been the time of great changes in spacecraft design, because of the new emphases on higher power arrays and lower costs. Also unfortunate is the fact that spacecraft charging may lead to failures of solar array strings, panels, or entire spacecraft. One way to prevent satellite failures due to spacecraft charging events is to simulate the effects with a charging code, such as the venerable NASCAP/GEO code. We will discuss the use of NASCAP on the ACTS satellite as well as a newer application dealing with typical recent spacecraft charging anomalies.

BACKGROUND

In the late 1970's and early 1980's, it was commonplace for satellites in geosynchronous Earth orbit (GEO) to undergo mysterious sudden failures. For instance, the Marecs-A communications satellite suffered the loss of much of its solar power during its demonstration news conference. The suspected culprit in these failures was the space environment, and this was confirmed when detailed calculations using spacecraft charging codes such as NASCAP/GEO and laboratory experiments using high fidelity simulations of the GEO environment showed that geomagnetic substorms could lead to sudden differential charging of spacecraft surfaces, followed by large electrical discharges which, when coupled into the spacecraft or solar array interiors, could lead to electronics upsets or failures.

Completion of the NASCAP/GEO computer code in 1984, and simultaneous publication of the Design Guidelines for Assessing and Controlling Spacecraft Charging (Purvis et al, 1984, hereafter called the Spacecraft Charging Guidelines), gave spacecraft designers powerful tools to prevent spacecraft charging and the electrical discharges associated with it. NASCAP/GEO made it possible to make detailed geometrical models of spacecraft and "fly" them in severe substorm conditions inside laboratory computers, thereby making it possible to evaluate the spacecraft charging that would occur and to predict problems before they occurred. The Spacecraft Charging Guidelines gave engineering rules of thumb for materials, geometries, and construction techniques which could be used to prevent charging before the expensive GEO spacecraft were built and launched. Although not perfect, these codes and guidelines have been used by a decade of spacecraft designers with generally positive results. The incidence of spacecraft charging related failures has dropped dramatically.

However, geomagnetic substorms are more common and more severe during the times of solar sunspot maximum. The last maxima were in 1980 and 1989, and we are now just past the time of solar minimum. The next maximum is forecast to be in 1999 or 2000. It is believed that this maximum will rival the last two maxima, which were abnormally strong (Joselyn et al, 1997). That means that for the last several years, spacecraft charging conditions have been somewhat benign, and we are now headed for an upswing in solar activity. Also, the last several years, with the new demands for lower cost, lighter, more

powerful communications satellites, have seen the introduction of several new satellite designs, using larger, lighter and more efficient solar arrays, spacecraft bodies made of new composite materials, and new high voltage spacecraft buses. Many of the older engineers who used the Spacecraft Charging Guidelines and NASCAP/GEO during the previous solar cycle maximum have retired or moved upstairs, and the need to prevent spacecraft charging has seemed less urgent. These are very dangerous times for new GEO satellite designers, whose satellites must survive the coming solar maximum.

BASIC SPACECRAFT CHARGING PHYSICS

All spacecraft surfaces in GEO will tend on very short timescales (micro- to milli-seconds) to balance the positive ion and negative electron currents impacting on the spacecraft. Any imbalance will lead to charged surfaces, which will act to repel the charging species and attract the species of opposite charge, thereby discharging the surface. However, insulators tend to local current balance, whereas conductors, which are typically tied together by the spacecraft ground structure and must therefore be at or near the same potential, will tend toward global current balance. In some cases, this may lead to high differential voltages between adjacent spacecraft conductors and insulators. The ambient plasma in GEO is typically of very low density, meaning that the normal, thermal currents of ions and electrons are quite small. Unlike the LEO plasma, which actively tries to maintain all spacecraft surfaces at the same potential, the GEO plasma cannot be relied upon to instantly discharge charged surfaces. GEO spacecraft will tend toward an equilibrium potential which is slightly to moderately negative of the surrounding plasma, because the incoming rapid electrons at zero potential will overbalance the slow moving ions. Current balance is thus achieved when the electrons are being repelled, somewhat. The equilibrium potential (floating potential) will be that which is just repelling a majority of the electrons, and thus depends on the average impacting electron energy.

One of the factors that are important in determining the charge on GEO spacecraft surfaces is the photoelectric effect, wherein UV sunlight can liberate electrons from some surfaces, and keep them from charging highly negative. At the plasma densities typical of GEO, the photoelectric effect can lead to local electron emission currents greater than the thermal plasma currents. Another effect is secondary electron emission. If an electron within a certain energy range hits a surface, more than one electron may be liberated. As strange as it may seem, it is thus possible for a positive surface to charge more highly positive when it attracts electrons from the adjacent ambient plasma. Backscattered electrons can also impinge on spacecraft surfaces. Still another effect has to do with the "plasma sheath" around a spacecraft. Beyond a certain distance, the spacecraft's potentials will be screened from its surroundings by a rearrangement of the positive and negative charges in its vicinity. In GEO, it is possible for parts of the spacecraft sheath to extend far enough to "bottle-up" or prevent the surroundings from discharging certain surfaces. Such an effect is called a potential barrier. Sometimes, the conductivity of insulators is increased somewhat by impinging sunlight, a property called photoconductivity. Yet another factor is "snapover". Here, secondary electrons emitted from a surface when it is bombarded by high energy electrons hop across the surface, effectively making it a funnel for current to adjacent conductors. In order to determine the potentials to which surfaces will come in a real-life GEO satellite situation, the current balance equations must be solved simultaneously with the electrostatic potential distribution, a problem for which NASCAP/GEO was invented.

Spacecraft surfaces can charge to high potentials when high energy particles impinge on them (as in geomagnetic substorms, when changes in Earth's magnetosphere can accelerate particles to tens of thousands of electron volts). Above about +100 V, some surfaces produce more secondary electrons than impinge on them, and may charge to a potential where this is no longer the case, some few thousands of volts positive with respect to the ambient plasma. Surfaces which don't emit more secondaries than primary electrons can charge highly negative in a flux of high energy electrons, because the floating potential must rise to the point where most of the incoming electrons are repelled. And, if conducting surfaces are shaded, the photoelectric effect can't help discharge them. It is possible for an entire satellite to charge to high potentials relative to its environment. This is called absolute charging. A more

dangerous situation is when adjacent surfaces charge to very different potentials. This is called differential charging.

Arcs can occur when dielectric materials are asked to stand off potential differences greater than their breakdown voltage. Solar arrays can arc when the cells are at potentials more negative than about 200 V with respect to the surfaces of their coverslides. If high voltage solar arrays or power system wiring use flexible kapton substrates or insulation, then once an arc occurs, the kapton may pyrolyze and produce a conductive path to allow the power source to continue the arc, shorting out an entire power system circuit. And, conductor-insulator junctions can arc at differential potentials of a few hundred volts. The situation seems too complex to allow for many generalizations.

Nevertheless, the Spacecraft Charging Guidelines have some important recommendations to make. First, it is recommended that all possible spacecraft surfaces be coated with conducting material and grounded together. This will absolutely prevent any large differential potentials from existing on the surfaces. The coating material does not have to be highly conducting, but nearly perfect insulators (such as Kapton and Teflon) will not prevent differential charging. Teflon is not a good photoconductor, either, so that impinging sunlight will not allow potential equalization. It may be possible to use electron guns or plasma generating devices to discharge high spacecraft potentials. This solution is being used on the International Space Station, for example. Another tack is to prevent electrical discharges, if they occur, from disrupting satellite electronics. One recommendation is to shield all electronic components inside a Faraday cage, to prevent space plasma and radiated noise from entering. Electrical filtering may be used to protect circuits from the rapid transients associated with electrical discharges. These filters must be capable of filtering out the highest arc currents expected (sometimes in the 10's to 100's of amp range). One recommendation not in the Guidelines is to avoid the use of kapton insulation in high voltage circuits where arcs may occur for any reason. But perhaps the best recommendation is to use NASCAP/GEO to predict, find, and eradicate the problem areas before starting spacecraft buildup.

AN EXAMPLE - THE ACTS SATELLITE

The ACTS satellite is in many ways typical of today's modern communication satellite in GEO. It is a 3-axis stabilized box-shaped body, with large solar panels extending from its sides, and antennae mounted on the box. The solar arrays may be moved around alpha joints and, along with control of the body orientation, this allows for a favorable (normal) solar incidence. The ACTS satellite was analyzed for spacecraft charging by Joel Herr (1991). Much of what follows is taken from his paper.

As may be seen in Figure 1, two of the sides of the ACTS body are covered with Optical Solar Reflector (OSR). OSR has a thin coating of silica, a non-conductive material. Thermal control is maintained over much of the spacecraft surface by the use of a metallized multi-layer insulation thermal blanket. In addition to being conductive, these surfaces also have high photoemission, a source of free electrons which may help discharge surfaces.

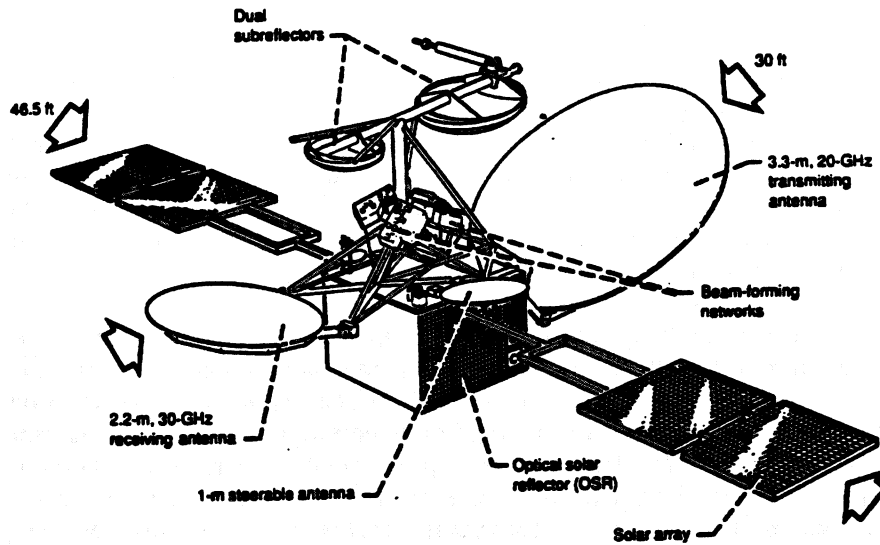


Figure 1. The ACTS satellite.

In Figure 2, we see the NASCAP/GEO model of ACTS, which was used to do the calculations for a spacecraft charging analysis by Herr (1991). In producing the model, it was assumed that the metallized multi-layer insulation was covered with grounded Indium Tin Oxide, a conductive coating, and that conductive paint (cpaint) was used on the antennae. The areas of silver interconnects and silica coverslides were adjusted to represent the approximate areas on the real spacecraft.

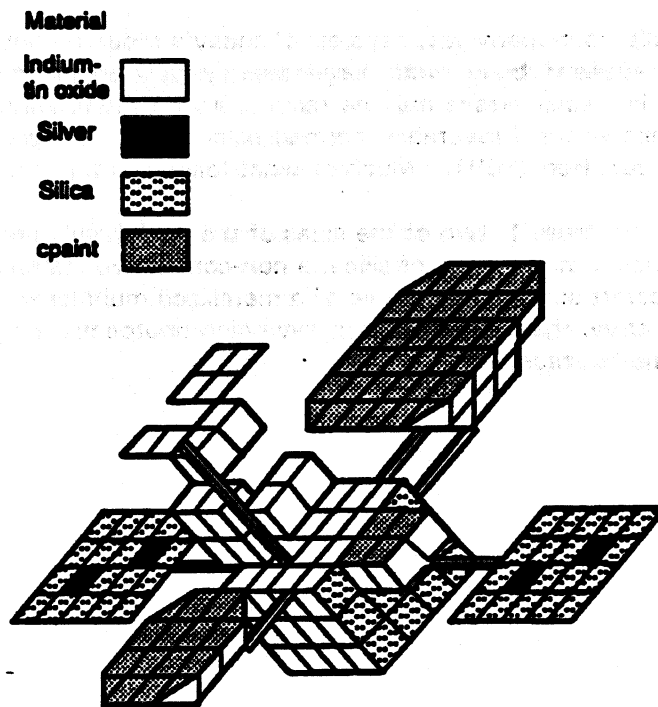


Figure 2. NASCAP/GEO model of the ACTS satellite.

In Figure 3, the potential contours calculated by NASCAP/GEO (Herr, 1991) are shown for a time shortly after ACTS comes out of eclipse, the time most likely for differential charging to develop. Here, it is easy to see the potential barriers which have developed over the solar arrays, and could lead to discharges.

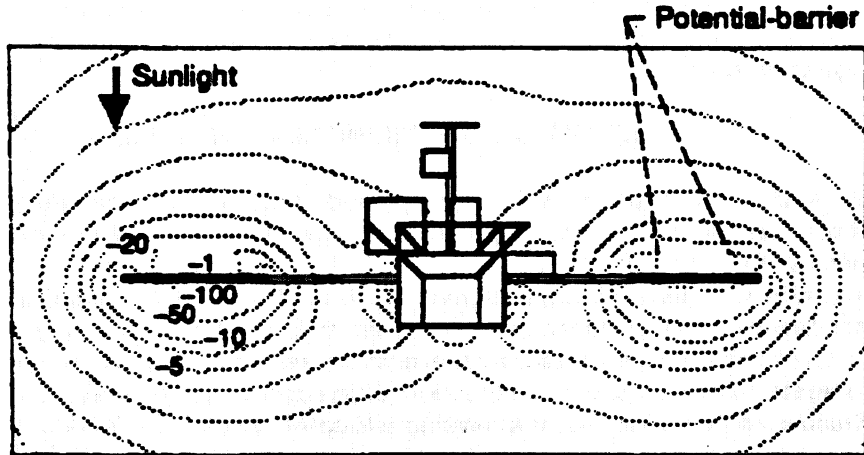


Figure 3. Potential barriers have formed over the ACTS solar arrays.

Finally, Figure 4 shows the time history of differential charging on ACTS calculated by NASCAP/GEO (Herr, 1991) for an eclipse period and shortly thereafter. Here we see that an assumed punchthrough (dielectric breakdown) discharge threshold is exceeded on the array substrate for times about an hour after emergence from eclipse under the conditions assumed for this analysis.

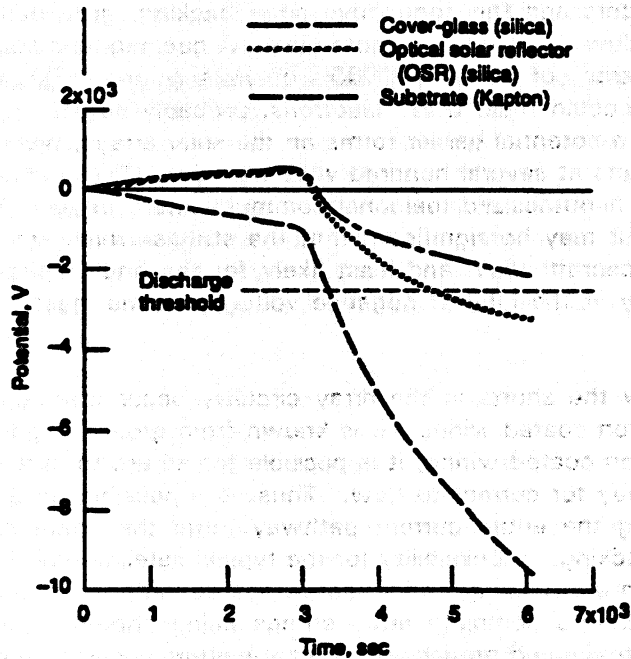


Figure 4. Time history of charging, NASCAP/GEO calculations, ACTS satellite (Herr, 1991).

These figures are presented not as a criticism of the ACTS satellite, but to show the kinds of analyses it is possible to do with NASCAP/GEO. For further details on the ACTS analyses, see Herr (1991).

It is imperative that the materials and material thicknesses used in the NASCAP/GEO analysis of a spacecraft accurately reflect the true spacecraft. In the case of the ACTS satellite, the analysis was done by a person not directly connected with the ACTS project, who found it difficult to find out the details of the geometries and materials used on ACTS from project personnel. They apparently believed that the NASCAP/GEO analyses could be used by ACTS opponents to find fault with the spacecraft, and might lead to its funding demise. As it turns out, some features of ACTS were found to be advantageous in preventing spacecraft charging (such as the use of highly photoemissive materials on the spacecraft body) and the analysis showed that they would make spacecraft charging only a minor problem for ACTS, if a problem at all. Other spacecraft are not so lucky.

A CASE TYPICAL OF RECENT GEO ANOMALIES

Recently, GEO spacecraft have started suffering sudden shorts in their power system circuitry, leading to the loss of some spacecraft power. The general design of these satellites is similar to the ACTS satellite above, but with some significant differences. First of all, the array area is significantly greater, in keeping with the trend toward higher and higher power GEO satellites. This is important not so much for the total area, but that the array wings extend to very great distances from the body, and are outside the range of the photoemitted electrons generated on the body materials. Secondly, the array string voltages are higher, again to negate losses in power distribution efficiency on large arrays at low voltages. The array substrate are flexible kapton, and the array wiring is kapton insulated. Thirdly, the backbias bypass diodes on the solar array strings, originally incorporated to prevent string damage when parts of a string were shadowed, have been eliminated, even though they also provided some arcing protection. Finally, many materials are being used which have no counterparts in the NASCAP/GEO databases, so their charging properties are essentially unknown. All of these factors may be important in the typical recent anomaly, presented below.

To the best of the limited analysis that has been done to date, it appears that photoemission on the solar cell coverslides is enough to keep the coverslides at the local plasma potential, whenever they are in sunlight. The array conductors and the conductive array backing, grounded at the negative end to the structure, respond to and follow the spacecraft potentials. A geomagnetic substorm suddenly showers the satellite with numerous electrons of 100's to 1000's of volts energy. The spacecraft body responds by taking on a potential which could repel these electrons, probably several hundred volts negative of the surroundings. At this point, a potential barrier forms on the solar arrays, with the coverslides at near zero, and the cells and interconnects at several hundred volts negative. These conditions can lead to arcing on the solar arrays, and it was hypothesized (personal communication, Snyder, 1997) that this has occurred on GEO spacecraft arrays. It may be significant that the strings which are damaged are typically those farthest away from the spacecraft body, and least likely for the body's photoemitted electrons to reach them. The parts of the array at the highest negative voltage are the most likely places for the arcing to occur.

It is not known how the shorts in the array circuitry occur after the initial arcs, but a possible hypothesis involves the kapton coated wiring. It is known from ground experiments that if a high voltage source is connected to kapton coated wiring, it is possible for an arc to pyrolyze the kapton in its vicinity, providing a continued pathway for current to flow. Thus, it is possible for an arc to propagate along the kapton-coated wire, charring the entire current pathway, until the entire circuit is shorted at near its source. This is called arc-tracking. A possibility for the typical satellite now being discussed is that an arc at the solar array can lead to arc-tracking on its kapton coated wiring, and the high voltage array supplies the necessary current, leading to complete array strings being shorted (personal communication, Katz, 1997). Backbias bypass diodes would probably prevent the short circuit scenario during an arc, leading to increased array viability after arcing. The exact details of any scenario depend on the details of spacecraft design. However, the lessons are clear. NASCAP/GEO analysis should come first, before finishing satellite construction, and certainly before launch. In the typical case given above, several mitigating strategies could be followed. The structure could incorporate lots of photoemissive material in the solar direction, so that the body charge could bleed off. The solar cell coverslides could be coated with conductive material

(Indium Tin Oxide, for example), and grounded to the structure, so that the differential potentials causing the arc could not develop. Or, the high voltage wiring could be been insulated with another, less volatile, insulator.

At the present time, NASCAP/GEO is available through COSMIC, the NASA software distributor, or for different platforms, through its developer, Federal Division of Maxwell Laboratories in San Diego, California. It is hoped that it can be modified, for new spacecraft materials, new geometries, and new computers, by the Photovoltaic and Space Environments Branch at the NASA Lewis Research Center. One of the desperately needed steps is to attain laboratory measurements of the photoemission, photoconductivity, and secondary electron emission characteristics of new spacecraft materials to incorporate into the NASCAP/GEO database. A NASCAP/GEO analysis of a GEO satellite will cost less than one man year of time and money, and may save a \$100 million satellite from failure.

REFERENCES

Herr, Joel (1991), "A Charging Study of ACTS Using NASCAP," NASA CR 187088.

Joselyn, J.A. et al (1997), "Panel Achieves Consensus Prediction of Solar Cycle 23," EOS, 78 (20), p. 205.

Purvis, C.K., Garrett, H.B., Whittlesey, A.C., and Stevens, N.J. (1984), "Design Guidelines for Assessing and Controlling Spacecraft Charging Effects," NASA TP 2361.

SOLAR CELL CALIBRATION AND MEASUREMENT TECHNIQUES

Sheila Bailey, Dave Brinker, Henry Curtis, *Phillip Jenkins, †Dave Scheiman
NASA Lewis Research Center
MS 302-1
Cleveland, Ohio 44135

*Essential Research, Inc.
Cleveland, Ohio 44135

† NYMA
Cleveland, Ohio 44135

ABSTRACT

The increasing complexity of space solar cells and the increasing international markets for both cells and arrays has resulted in workshops jointly sponsored by NASDA, ESA and NASA. These workshops are designed to obtain international agreement on standardized values for the AMO spectrum and constant, recommend laboratory measurement practices and establish a set of protocols for international comparison of laboratory measurements. A working draft of an ISO standard, WD15387, "Requirements for Measurement and Calibration Procedures for Space Solar Cells" was discussed with a focus on the scope of the document, a definition of primary standard cell, and required error analysis for all measurement techniques. Working groups addressed the issues of Air Mass Zero (AM0) solar constant and spectrum, laboratory measurement techniques, and the international round robin methodology. A summary is presented of the current state of each area and the formulation of the ISO document.

INTRODUCTION

The expanding choice of space solar cells from worldwide vendors has focused attention on the need for an internationally recognized standard value of the Air Mass Zero (AM0) solar constant and spectral intensity distribution and the primary set of standards and protocols to establish equitable comparisons of laboratory measurements around the world. To achieve this universality of calibration and laboratory measurements NASA Lewis Research Center's Photovoltaic Branch initiated a series of workshops jointly sponsored by the National Aeronautics and Space Administration (NASA), the European Space Agency (ESA), and the National Space Development Agency of Japan (NASDA). The First international Workshop on Space Solar Cell Calibration and Measurement Techniques took place in Honolulu, Hawaii in December of 1994 and was attended by thirty-four participants from Japan, the United States and Europe representing not only the space agencies but industry as well (Brinker et al, 1995). The Second Workshop took place in Madrid, Spain in September of 1995 with twenty-five participants, expanding to include China. The Third Workshop occurred at Tsukuba, Japan in November of 1996 with thirty-five participants. There were three established working groups: A. AM0 Solar Constant and Spectrum; B. Laboratory Measurements Techniques; C. International round Robin Methodology. The current draft of the International Organization for Standardization (ISO) standard, WD 15387 was presented by Mr. Kiyota of SHARP Corporation. Dr. Cuquel of CNES presented the CNES balloon flight calibration system and Mr. Scheiman of NASA Lewis Research Center (LeRC) presented the JPL balloon flight calibration method and the LeRC aircraft calibration method. Dr. Bucher of the Fraunhofer Institute discussed the Institute fur Solare Energiesysteme (ISE) Photovoltaic (PV) Charts.

ISO 15387

Terrestrial solar cell standards are governed by the International Electrotechnical Commission (IEC), specifically the technical committee number 82: Solar Photovoltaic Energy System. However, it was decided that space solar cell standards would fall under the auspices of ISO technical committee number 20: Aircraft and Space Vehicle, sub committee number 14: Space Systems and Operation. Japan proposed ISO standardization of space solar cell calibration at a meeting in 1994 and submitted the first working draft in 1996 with input from the International Workshop participants and other interested parties. The ISO and IEC standards can be compared in the topics

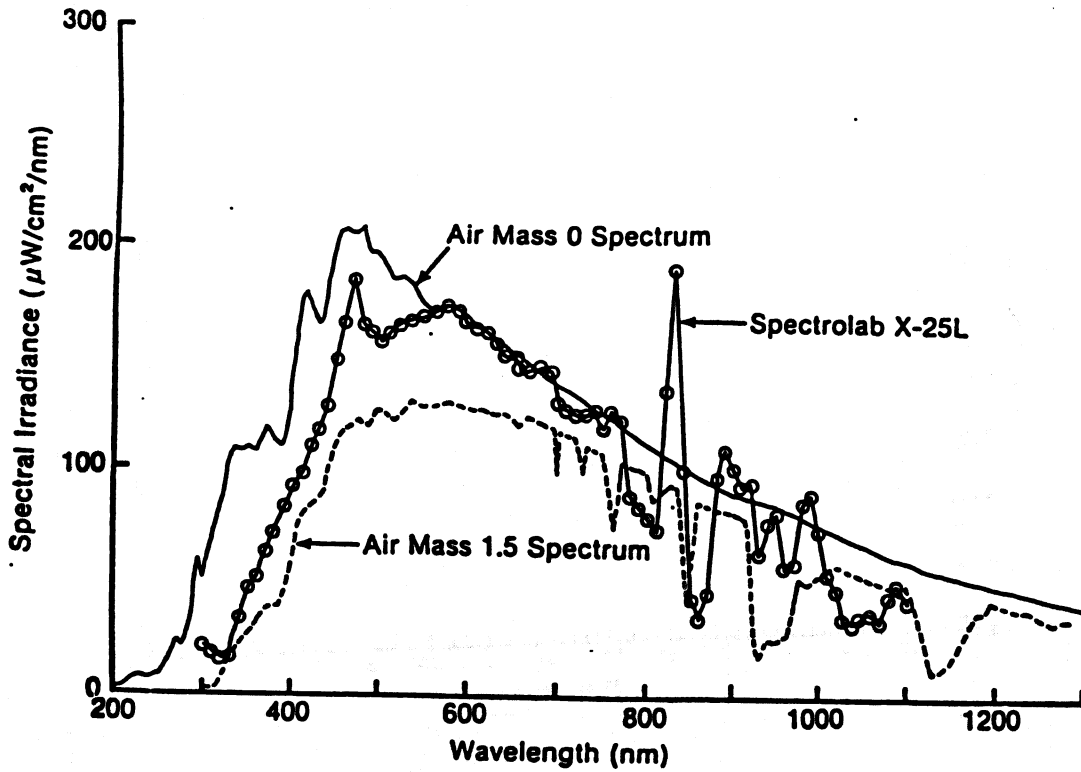


FIG. 1. AIR MASS 0 AND 1.5 SPECTRUM AND SPECTROLAB X-25L SPECTRUM

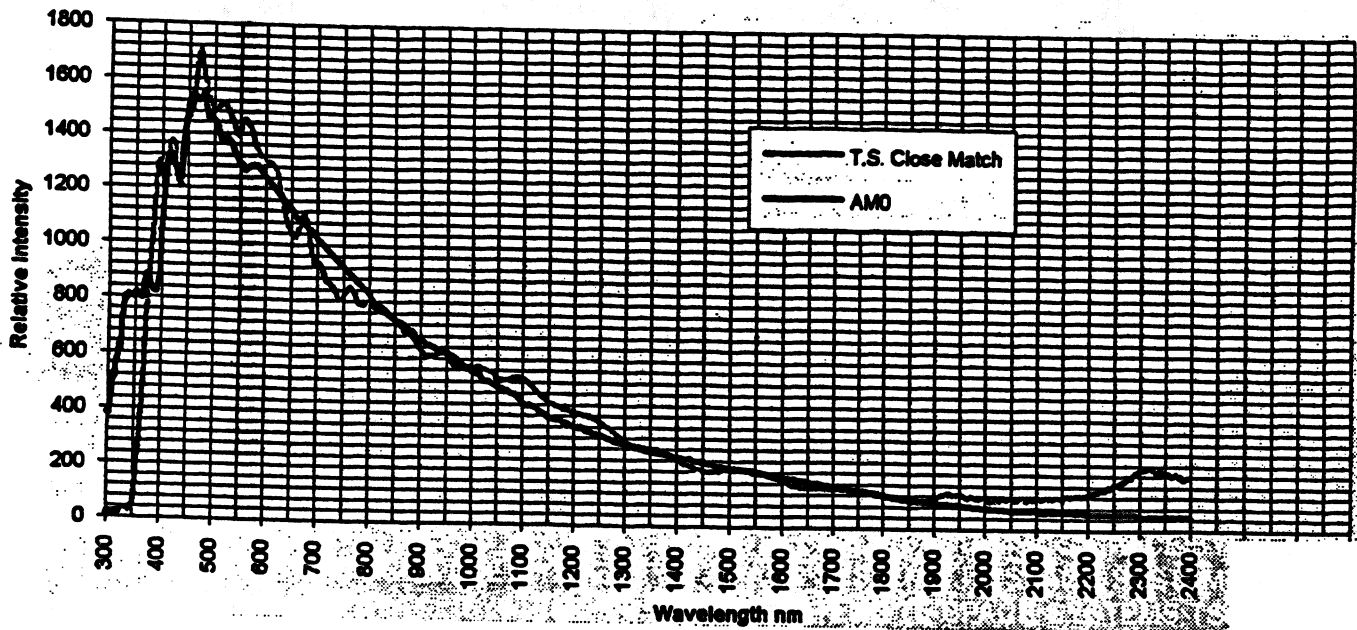


FIG. 2. TS SPACE SYSTEMS MULTIPLE SOURCE SIMULATOR

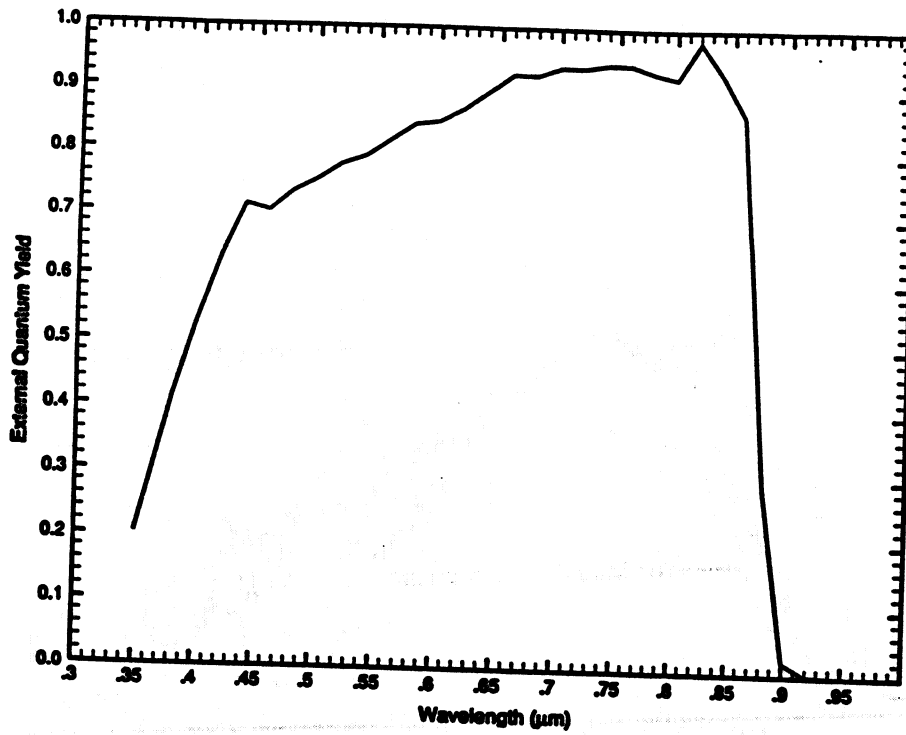


FIG. 3. SPECTRAL RESPONSE OF A GaAs/Ge SOLAR CELL

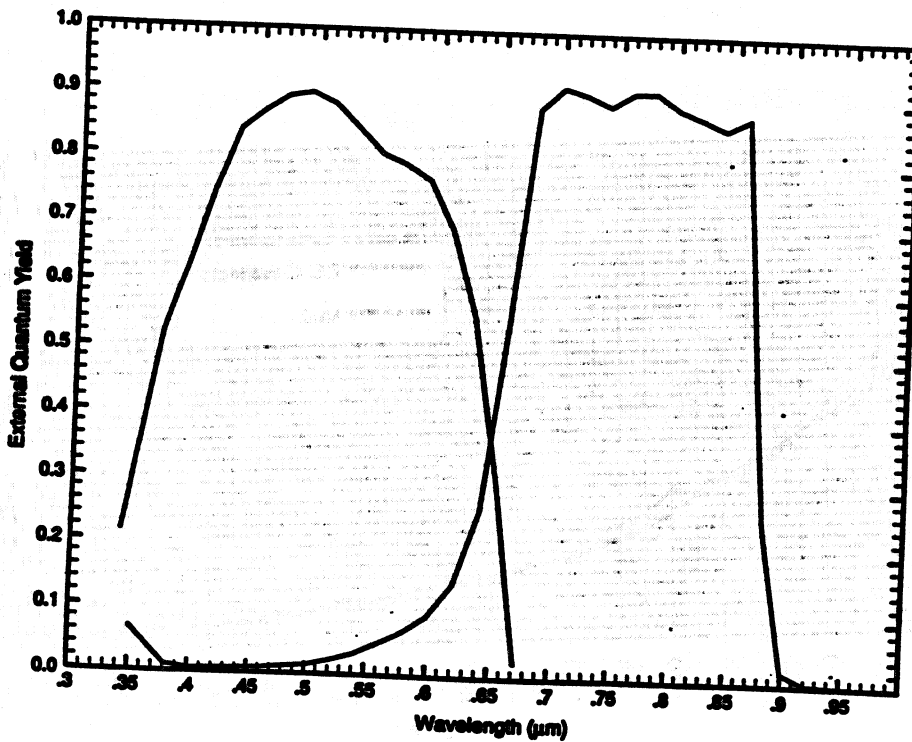


FIG. 4. SPECTRAL RESPONSE OF A GaInP/GaAs/Ge SOLAR CELL

which are addressed by each set of standards: requirements for reference solar cells (IEC 904-2), measurement principles for space solar cells with reference to the extraterrestrial solar spectral irradiance data (IEC 903-3), computation of spectral mismatch error introduced in the testing of the solar cells (IEC 904-7), guidance for the spectral measurement of a solar cell (IEC 904-8), solar simulator performance requirements (IEC 904-9), calibration methods for primary reference solar cell (IEC 82-101), methods of spectral distribution measurement for the light source (ASTM and JIS standards), measurement of current-voltage (I-V) characteristics (IEC 904-1), procedures for temperature and irradiance corrections to measured I-V characteristics of crystalline silicon solar cells (IEC 891). The scope of the ISO document is restricted to single-junction crystalline space solar cells. The AM0 standard solar cell would record the type of calibration spectrum (extraterrestrial: JPL high-altitude balloon (36.6 km), CNES high-altitude balloon (36.6 km), space shuttle or space station (500 km); direct sunlight: NASA Lewis high-altitude aircraft (15.4 km); ground level sunlight: global sunlight, direct normal sunlight; synthetic sunlight: solar simulator or differential spectral response (if applicable)). The calibration results will be repeatable within a standard deviation of $\pm 1\%$. The solar constant, which is slightly variable, is accepted to be $1367 \text{ Wm}^2 \pm 7 \text{ Wm}^2$. The standard temperature test condition is $25 \pm 1^\circ\text{C}$. The following data are recorded: identification number, type solar spectrum, cell manufacturer, material type, type of cell package, calibration organization, site and date of calibration, method of calibration, radiometer or standard lamp characteristics (where applicable), AM0 standard solar cell identification (for simulator calibration, where applicable), simulator characteristics, type of temperature sensor, relative spectral response, temperature coefficient of short-circuit current, calibration value (AW^{-1}m^2), and claimed accuracy (with a description of error analysis). The final version of the working draft ISO 15387 will be discussed at the 4th International Workshop in October of 1997 at NASA Lewis Research Center.

WORKING GROUP: AM0 SOLAR CONSTANT & SPECTRUM

The values identified above were accepted for cell temperature, spectrum, and solar constant corresponding to the most recent cavity measurement in space. It was agreed to solicit "a letter of agreement" from all space calibration agencies in order to reach common reporting conditions; to collect reports of the calibration procedures and a detailed error analysis of all procedures. The following institutions agreed to use the standard measurement conditions (pending completion of current contracts specifying 28°C rather than 25°C): NASA, JPL, NASDA, ESA, CNES, CAST, DRA, NREL, Japanese Space Solar Cell Calibration Committee, INTA-Spasolab, HIREC, WYMA, Space System Loral, Essential Research, Hughes, TecStar.

WORKING GROUP: LABORATORY MEASUREMENTS TECHNIQUES

Single light source simulators, commonly used in laboratories and by commercial vendors, are accurate for single junction gallium arsenide (GaAs) and silicon (Si) solar cells within an experimental error of approximately 1%. The spikes of the Xenon light source of the X25 Spectrolab Single Source Simulator, for example, (see Fig. 1) can become a significant source of error for multi-junction cells unless carefully filtered. Recently, a filtered dual source simulator has become available (see Fig. 2) which provides a closer matched AM0 spectrum. The spectral response of a GaAs/Ge single junction cell can be seen in Fig. 3 and a GaInP/GaAs/Ge dual junction cell can be seen in Fig. 4. It should be noted that both spectrally tunable solar simulators and subcell standards for multi-junction cells will be required to obtain $\pm 1\%$ accuracy. A dual beam pulse solar simulator for module and array testing would be difficult to develop, the more probable option would be a suitably filtered design. A color filter bias light method has been used and verified with three junction devices (Bucher et al, 1995). A proposal has been submitted to NASA from the Photovoltaic and Space Environments Branch at NASA Lewis and the Ohio Aerospace Institute to utilize the international space station as a solar cell calibration and measurement facility.

WORKING GROUP: INTERNATIONAL ROUND ROBIN METHODOLOGY

The first international round robin of solar cell calibration was established following the 1st International Workshop. There were 12 samples (4 each from NASA, ESA, and NASDA) which would be measured by NASA, ESA, NASDA and the Chinese Academy of Space Technology (CAST) and then reflown at NASA. These samples were silicon cells, GaAs cells, and high efficiency silicon cells. The first round robin is complete. These cells will now be cycled through other organizations, e.g. DRA, JPL, NREL, ISE, etc. Measurement data will be reported at the 26th IEEE-PVSC in October of 1997.

A second round robin of Si and GaAs solar cells was proposed with NASA, JPL, and CNES providing the cells, 2 cells each; 1 Si and 1 GaAs. They would be measured at NASA Lewis then sent to CNES and JPL. These extraterrestrial measurements are anticipated to be available for publication at the 2nd World Conference on

Photovoltaic Energy Conversion in July of 1998. After the extraterrestrial measurements the cells would be measured by NASA and DRA in a solar simulator, CAST by direct sunlight, and ESA-Spasolab by global sunlight with ISE to be determined. It was agreed to begin a round robin of GaInP/GaAs/Ge dual junction cells, not to compare results, but to assess measurement techniques for multi-junction cells.

CONCLUSION

The three International Workshops held since 1994 have involved eight countries, government organizations and corporations. They have provided a forum for discussion regarding the ISO 15387 standards, achieved agreement on the standardized values of the AM0 solar constant and spectral intensity distribution, established a set of protocols for making interlaboratory comparison measurements, initiated round robin cell calibration series, and addressed the complicated issue of multi-junction solar cell measurements. The 4th International Workshop on Space Solar Cells will be held at NASA Lewis Research Center, October 6th - 9th, 1997. For further information contact Dave Brinker (Phone: 216-433-2236, Fax: 216-433-6106, dbrinker@lerc.nasa.gov).

REFERENCES

Brinker, D.J., Curtis, H.B., Flood, D.J., Jenkins, P., Scheiman, D.A., "A Summary of the International Workshops on Space Solar Cell Calibration and Measurement Techniques", *Space Photovoltaic Research and Technology Proceedings*, 186-190, (1995).

Bucher, K. and Kunzelmann, "The FhG-ISE PV Charts: Assessment of PV Device Performance", *13th European Photovoltaic Solar Energy Conference Proceedings*, 2352-2357, (1995).

MEASUREMENT OF N-TYPE 6H SiC MINORITY-CARRIER DIFFUSION LENGTHS BY ELECTRON BOMBARDMENT OF SCHOTTKY BARRIERS

S. M. Hubbard, M. Tabib-Azar
Case Western Reserve University; Dept. of Elect. Eng. & Applied Physics
Cleveland, OH

S. Bailey, G. Rybicki, P. Neudeck
NASA Lewis Research Center
Cleveland, OH

R. Raffaele
Florida Institute of Technology; Dept. of Physics & Space Science
Melbourne, FL

Minority-Carrier diffusion lengths of n-type 6H-SiC were measured using the electron-beam induced current (EBIC) technique. Experimental values of primary beam current, EBIC, and beam voltage were obtained for a variety of SiC samples. This data was used to calculate experimental diode efficiency vs. beam voltage curves. These curves were fit to theoretically calculated efficiency curves, and the diffusion length and metal layer thickness were extracted. The hole diffusion length in n-6H SiC ranged from $0.93 \pm 0.15 \mu\text{m}$ to $1.37 \pm 0.20 \mu\text{m}$.

1. Introduction

Silicon Carbide (SiC) has been recognized for its excellent mechanical properties for over 150 years. It has only been in the past 2 decades that its electronic properties have been explored [1]. With increasing need for high temperature sensors and high power electronics, SiC promises to be one of the premiere semiconductors of the next century.

The main thrust of research into SiC in the past two decades has been to exploit its high breakdown field and high thermal conductivity. These two physical properties make SiC ideal for high power and high temperature application, respectively. Additionally, SiC's wide bandgap (3.0 eV for 6H) makes it an attractive material for blue/UV sensors and emitters. In fact, all of the above devices are commercially available.

In spite of all the progress made in SiC crystal growth and device fabrication [2], much research remains in order to lower the current levels of defect and micropipe density in SiC. It has only been since 1989, through the use of the modified Lely seeded sublimation technique, that large area, low defect

density substrates became available [3]. Crystal growth of SiC is still a budding technology, much work remains if acceptable high quality electronic grade SiC is to be produced.

Minority-Carrier diffusion length is an important parameter in the electrical characterization of semiconductor materials. It describes the mean length that a carrier will travel before recombining with the opposite type of carrier. The minority-carrier diffusion length can be related to minority-carrier lifetime using the familiar relation:

$$L = \sqrt{D * \tau} \quad (1)$$

where D is the diffusion coefficient given by the Einstein relation [4] and τ is the carrier lifetime.

The carrier lifetime is of critical importance in evaluation and computer simulation of devices. It is used in the calculations of leakage current and non-ideal diode characteristics. It is also necessary for calculating amplification factors, turn on, and turn off times in Bipolar Junction Transistors (BJT). Additionally, open-circuit voltages and short circuit

currents in solar cells are calculated based on the values of diffusion lengths and lifetimes. In order to evaluate potential uses of SiC in solar cells, semiconductor lasers, BJTs, etc., the researcher must have some knowledge of the minority-carrier lifetime.

Additionally, lifetimes/diffusion lengths can give us some handle on the material quality. Large amounts of defects create recombination centers, thereby reducing the effective diffusion length. Measurement of diffusion length in SiC could be useful in gauging the effect of large micropipe [2] densities on the electrical properties of the material.

In this work, we have used the Electron Beam Induced Current (EBIC) technique in order to measure the diffusion length. Our particular method was first developed by Wu & Wittry in 1978 [5]. This method calls for the bombardment of Schottky barriers, or shallow p-n junctions, by electrons of varying energy (Figure 1). By assuming a Gaussian excitation distribution of electron-hole pairs within the material, Wu&Wittry were able to arrive at a theoretical model of collection efficiency vs. applied beam voltage. By comparing our experimental collection efficiency with this model, we were able to extract the diffusion length. Because the material surface lies underneath the metal layer, surface recombination velocity does not effect our experiments. The Wu & Wittry method is an excellent way to measure the smaller diffusion lengths typical of SiC.

II. Theory

A. Wu & Wittry method (planer configuration)

In the configuration shown in Figure1, the electron beam is exposed to a metal-semiconductor junction. As the beam voltage is raised, the center of the excitation distribution will move deeper into the sample. The excess carriers will diffuse toward the junction, where they are collected. The collected current I_{sc} will depend primarily on the range of the generated carriers and the diffusion length of the minority carriers.

The experimental collection efficiency e is given by:

$$e = \frac{I_{sc}}{qG} \quad (2)$$

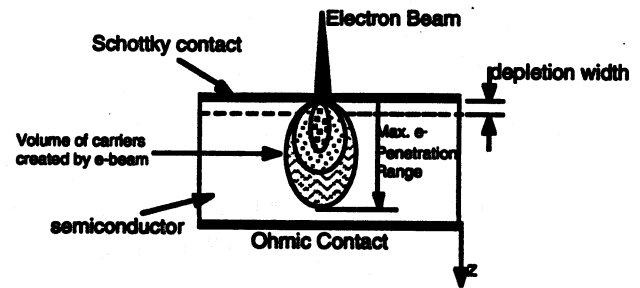


Fig. 1. Drawing of the experimental EBIC technique in the planer junction configuration. The collection efficiency of the Schottky diode is measured as a function of beam voltage.

where I_{sc} is the collected EBIC current, G is the total generation rate, and q the electronic charge. The generation rate is given by [5]:

$$G(\text{sec}^{-1}) = 1000 \frac{V_o i_{beam}}{qE} \left(1 - \eta \frac{\bar{V}}{V_o}\right) \quad (3)$$

where, V_o is the incident beam voltage in kV, i_{beam} the beam current in Amperes, E the mean energy to create one electron-hole pair in eV, η is the fraction of backscattered electrons, and \bar{V} the mean energy of backscattered electrons. The value of η at 20keV was calculated for SiC using an empirical formula cited in Goldstein [6]:

$$\eta_{SiC} = 0.134 \quad (4)$$

Goldstein shows that the η value changes slightly from a 10keV to a 50 keV beam voltage. This change is extremely small for lower atomic numbers, therefore, the above η value for SiC is assumed constant for our calculations.

The mean energy of backscattered electrons was determined using a simplified expression proposed by Sternglass [7]:

$$\bar{V} = (0.45 + 2 * 10^{-3} Z) V_o \quad (5)$$

where Z is the average atomic number of the sample ($Z=10$ for SiC). Our calculated backscattered correction factor $\left(1 - \eta \frac{\bar{V}}{V_o}\right)$ for SiC was 0.93.

Because SiC is 70% Si by weight, we expect our backscatter correction to be near the value of 0.9 given for Si [5].

The hole-electron pair generation energy ϵ has been measured for a variety of materials over the past 50 years. The data has shown that this energy is linearly related to the bandgap [8]. Ehrenberg and Gibbons [9] have given this relation as:

$$\epsilon = 2.1E_g + 1.3 \quad (6)$$

where E_g is the bandgap. We have used this relation in all our calculations.

The theoretical collected current actually depends on the sum of two currents, I_d and I_b . I_d is the current due to carriers generated in the depletion region, while I_b is the current due to carriers generated in the bulk of the semiconductor. By assuming a collection probability near unity inside the depletion layer, Wu and Wittry have derived expressions for I_d and I_b [5].

The theoretical collection efficiency can be written as:

$$e = \frac{|I_c|}{qG} = \frac{|I_d + I_b|}{qG} \quad (7)$$

The above equation in functional form is:

$$e = f(R, L, Z, w) \quad (8)$$

Where R is the maximum range of electrons, L the diffusion length, Z the metal layer thickness, and w the depletion layer width. The following range-energy function was developed by Wittry and Kyser [10]:

$$R = 2.56 * 10^{-3} \left(\frac{V_o}{30}\right)^{1.7} \text{ g/cm}^2 \quad (9)$$

This range-energy equation is one of a number of range-energy relations given in the literature (Grun, Everhart-Hoff, etc.) [8]. Wu & Wittry have successfully applied this equation to both Si and GaAs [5]. Therefore, we have decided to use it in all of our calculations. The depletion width w was calculated using the doping concentration of the material [4]. We then used a nonlinear fit routine in Mathematica 3.0 to fit our experimental data to the theoretical equation using Z and L as free parameters. Figure 2 shows a set of theoretical collection efficiency curves for a Pd/SiC diode.

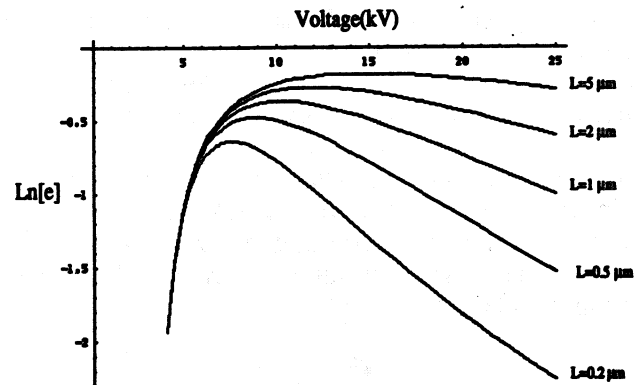


Fig. 2 Theoretical EBIC curves for Pd/SiC Schottky diodes. The metal layer thickness was taken to be 300Å, and the depletion layer width, 1000Å.

III. Experimental

A. Sample Preparation

Samples of n-type 6H SiC were obtained from NASA Lewis Research Center. We would like to extend our thanks to Gary Hunter for providing us with these samples. All samples were Nitrogen doped n/n+ 6H SiC grown by CVD[8]. The top n side of each sample was a highly polished Si face. The bottom n+ side was a rough polycrystalline face.

Samples 1636 and 2419 were first cleaned in concentrated HCl for 1 minute. Following this they were dipped in buffered HF, then deionized water. After drying with nitrogen, they were placed in a diffusion pumped vacuum evaporator. After reaching a base pressure of $1.2 * 10^{-6}$ Torr, Ti wire was thermally evaporated using a tungsten boat source. The thickness of the Ti film was monitored using a digital quartz-crystal thickness monitor.

The monitor was previously calibrated by evaporating approx. 1000Å of Ti, then measuring the thickness using a DekTak profilometer. After calibration, the thickness monitor was within $\pm 100\text{Å}$ of the actual thickness.

After metallization, a pattern of varying diode sizes was laid down using reverse photolithography. The excess Ti was etched away using very dilute HF. A final cleaning was performed by cleaning in a beaker of acetone, then propanol. Samples 18202F & G were fabricated by Gary Hunter at NASA Lewis Research Center [NASA Technical Memorandum 107255]. These samples were also cleaned with acetone and propanol before use.

Ohmic contacts to the Ti samples were made by evaporating 3000Å of Al on the back of the samples using the vacuum evaporator. The Pd samples had back side ohmic contacts made by Al sputtering.

All samples were analyzed using standard IV measurement techniques. A Keithly 236 High Current Source Unit was used to take the IV data. The IV data was analyzed using the following equation [11]:

$$I = I_0 \left[\exp\left(\frac{qV}{\eta kT}\right) - 1 \right] \quad (10)$$

where η is the ideality factor and I_0 is the saturation current. The barrier height was calculated from the following relation [11]:

$$I_0 = SA^*T^2 \exp\left[-\frac{\phi_B}{kT}\right] \quad (11)$$

Where S is the diode area, T the temperature, A^* the modified Richardson constant, and ϕ_B is the barrier height.

Values for our samples are reported in Table I. Values for samples with Pd contacts (18202F-G) show extremely small saturation currents and large barrier height. These barrier heights were much larger than for the Ti/SiC samples. This was expected due to the difference in the relative work functions for Ti (≈ 4.3 eV) and Pd (≈ 5.2 eV).

In the Ti samples (1636/2419), the saturation current was much larger. These diodes were observed to conduct immediately upon forward bias. This may be due in part to barrier height lowering and/or large tunneling currents. Fortunately, very near the origin, these diodes exhibit almost ideal behavior.

Table I. IV Analysis of our samples.

Sample	η	I_0 (Amps)	ϕ_B (eV)
1636A	1.04	$7.32 \cdot 10^{-9}$	0.66
1636B	1.06	$4.33 \cdot 10^{-9}$	0.68
18202F	1.23	$8.21 \cdot 10^{-21}$	1.42
18202G	1.08	$8.21 \cdot 10^{-21}$	1.42
2419	0.97	$3.14 \cdot 10^{-9}$	0.69

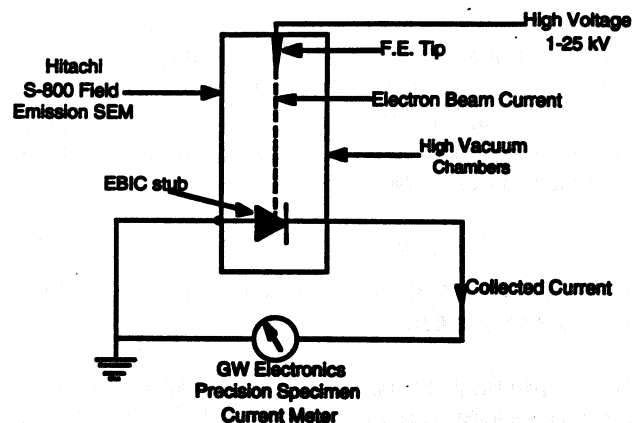


Fig. 3. Schematic of the experimental setup.

B. Instrumentation

A Hitachi S-800 Scanning Electron Microscope was used for electron bombardment. All measurements were made at room temperature and in a reasonably high vacuum (10^{-5} - 10^{-6} Pa). The EBIC was collected using a special EBIC sample stub. A sharp copper clip was attached to the top of the diode. The clip itself was attached to a insulated ring around the sample stub. This ring was contacted by a lever arm on the sample stage. Through the use of a coaxial feedthrough, the top side of the diode was connected to a GW Electronics Precision Specimen Current Meter. The beam current was measured in a similar manner using a standard Faraday cage. Figure 3 shows the experimental schematic.

C. Results

Most of the results of our experiments show good agreement with theory. These results are shown in Figures 4-7 and summarized in Table II. Figures 4-5 show a good agreement between theory and experimental data. Our measured values of diffusion length ranged between 0.93 to 1.37 μm for a variety of doping densities. The extracted metal thickness' were within experimental error, $\pm 10\%$, of our expected values.

Samples 1636A and B were two different dots on the same wafer. The dots were approximately 2.5 mm apart. The results show no change in the diffusion length. This illustrates one of the advantages of the technique, the ability to measure diffusion lengths on different diodes over the 2-dimensional plane of the wafer. We will be extending this study in the near future to obtain a

more detailed map of diffusion length over the surface of the sample.

Samples 18202F and G do not show any significant differences in L , although they have different doping densities. Part of our future study will be to measure L for a wide variety of doping densities.

Samples 2419 (Figure 7) illustrates one of the limitations of this technique. This sample had a much larger leakage current (100 nA at -0.1 V) than either 1636 (<5 nA at -0.1V) or 18202 (<100 pA at -0.1 V). This large reverse leakage will subtract from actual EBIC causing our measured EBIC to deviate significantly from predicted values. It was not surprising that the 2419 data did not fit theory as well as expected.

By curve fitting our experimental data to our theoretical curves, we were able to extract the minority-carrier diffusion lengths of n-type 6H SiC. Good agreement between theory and experiment was observed. The diffusion lengths of our samples ranged from 0.93 to 1.37 μm . These values have an estimated accuracy of better than $\pm 20\%$. The extracted values of our metal layer thickness were well within range of our expected values, providing further evidence of the accuracy of the technique. Some of the limitations of the technique were seen with very leaky diodes, but overall, this technique appears to be an excellent way to measure the smaller diffusion lengths typical of SiC.

III. Conclusion

Table II. Results of experiment.

Specimen	Type	Carrier Conc.	Ohmic Contact	Schottky Contact	Extracted Metal Thickness	Expected Metal Thickness	Depletion Width	Diffusion Length L_p	Error +/-
1636 A	n/n+	1.35×10^{17}	Al	Ti	1563 Å	1500 Å	500 Å	1.28 μm	0.15 μm
1636 B	"	"	"	"	1519 Å	"	"	1.25 μm	0.15 μm
18202F	n/n+	1.65×10^{17}	Al	Pd	304 Å	300 Å	800 Å	0.98 μm	0.15 μm
18202G	n/n+	6.75×10^{16}	Al	Pd	407 Å	300 Å	1280 Å	0.93 μm	0.25 μm
2419	n/n+	6.14×10^{16}	Al	Ti	1292 Å	1500 Å	735 Å	1.37 μm	0.25 μm

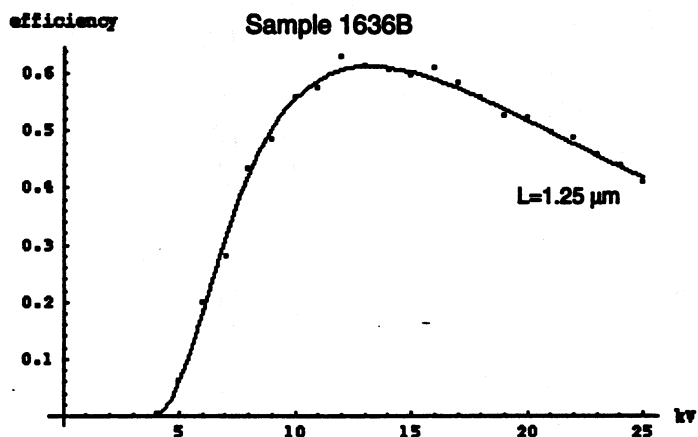


Fig 4. EBIC collection efficiency vs. beam voltage for Sample 1636 A and B. The dots are experimental data for 1636B. Data for 1636A was almost identical, and is not shown here.

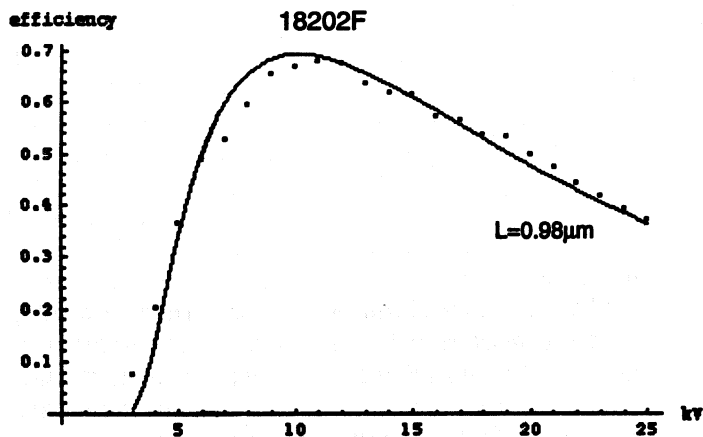


Fig 5. EBIC collection efficiency vs. beam voltage for Sample 18202F.

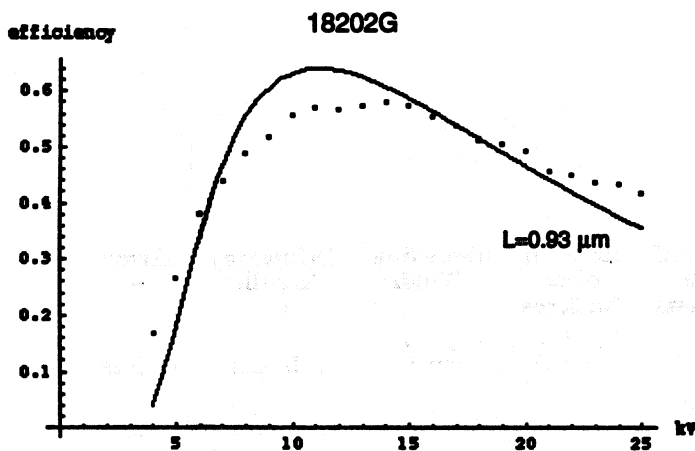


Fig 6. EBIC collection efficiency vs. beam voltage for Sample 18202G.

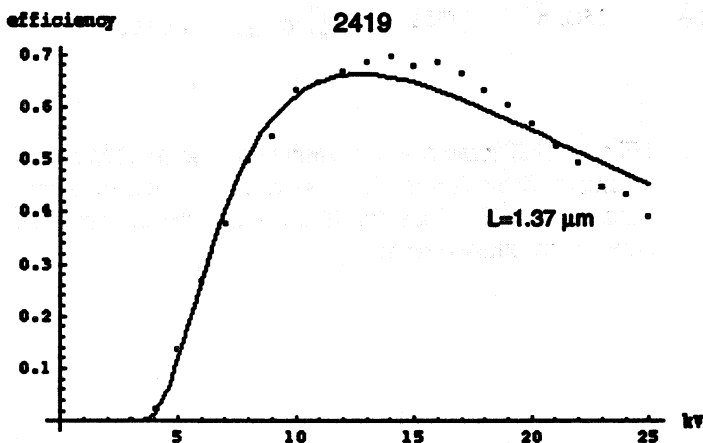


Fig 7. EBIC collection efficiency vs. beam voltage for Sample 2419.

References

¹ H. Morkoc, S. Strite, G.B. Gao, M.E. Lin, B. Sverdlov, M. Burns, *J. Appl Phys.* **76**, 1363(1994).

² P. Neudeck, "<http://www.lerc.nasa.gov/WWW/SiC/SiCReview.html>" (1997).

³ Cree Research, Inc., 2810 Meridian Parkway, Suite 176, Durham, NC 27713.

⁴ S.M. Sze, *Physics of Semiconductor Devices* (2nd ed., Wiley-Interscience, New York, 1981).

⁵ C.J. Wu, D.B. Wittry, *J. Appl. Phys.* **49**, 2827 (1978).

⁶ J. I. Goldstein, D.E. Newbury, P. Echlin, D.C. Joy, C. Fiori, E. Lifshin, *Scanning Electron Microscopy and X-Ray Microanalysis* (Plenum Press, New York, 1981), Chap. 3.

⁷ Sternglass, E.J., *Phys. Rev.* **95**, 345(1954).

⁸ D.B. Holt, D.C. Joy, *SEM Microcharacterization of Semiconductors* (Academic Press, London, 1989), Chap. 6.

⁹ W. Ehrenberg, D.J. Gibbons, *Electron Bombardment Induced Conductivity and Its Applications* (Academic Press, London, 1981).

¹⁰ D.B. Wittry, D.F. Kyser, *J. Appl. Phys.* **38**, 375 (1967).

¹¹ B.L. Sharma, *Metal-Semiconductor Schottky Barrier Junctions and their Applications* (Plenum Press, New York, 1984).

HIGH CONCENTRATING GaAs CELL OPERATION USING OPTICAL WAVEGUIDE SOLAR ENERGY SYSTEM¹

T. Nakamura and J. A. Case
Physical Sciences Inc.
San Ramon, CA 94583

M. L. Timmons
Research Triangle Institute
Research Triangle Park, NC 27711

ABSTRACT

This paper discusses the results of the concentrating photovoltaic (CPV) cell experiments conducted with the Optical Waveguide (OW) Solar Energy System. The high concentration GaAs cells developed by Research Triangle Institute (RTI) were combined with the OW system in a "fiber-on-cell" configuration. The cells' performance was tested up to a solar concentration of 327. Detailed V-I characteristics, power density and efficiency data were collected. It was shown that the CPV cells combined with the OW solar energy system will be an effective electric power generation device.

OPTICAL WAVEGUIDE (OW) SOLAR ENERGY SYSTEM

In the OW Solar Energy System, solar radiation is collected by the concentrator which transfers the concentrated solar power to the OW transmission line consisting of low-loss optical fibers. The OW transmission line transmits the high intensity solar radiation to the thermal reactor for thermochemical material processing. By making use of an efficient OW transmission line, solar energy can be utilized for material processing not possible with conventional solar power systems. In the NASA program which Physical Sciences Inc. (PSI) completed recently, a ground test model of the OW solar energy system was developed and tested for performance characterization (1). A schematic representation of the system is given in Figure 1. The ground test model consists of a concentrator array, the OW transmission line, and the solar thermal reactor. A photo of the ground test model is given in Figure 2.

OPTICAL WAVEGUIDE PHOTOVOLTAIC POWER GENERATION EXPERIMENT

One of the important capabilities of the OW System developed in this program is that it can generate electric power when it is not used for material processing. A concentrating CPV is an ideal device for the optical waveguide system because the highly concentrated solar radiation can be effectively coupled to the CPV cells as shown in Figure 3. The concentrated solar radiation is defocused at the end of the optical fiber to provide optimum radiation intensities for the CPV cell. This "fiber-on-cell" configuration allows the small scale, high concentration CPV to operate at high efficiencies. Another important advantage of this power generation concept is that the quantity of the photovoltaic (PV) cells can be reduced significantly, allowing use of more expensive and efficient PV cells for the power generation system. The purpose of this experiment is to

¹Supported by NASA/JSC under contract NAS9-19105.

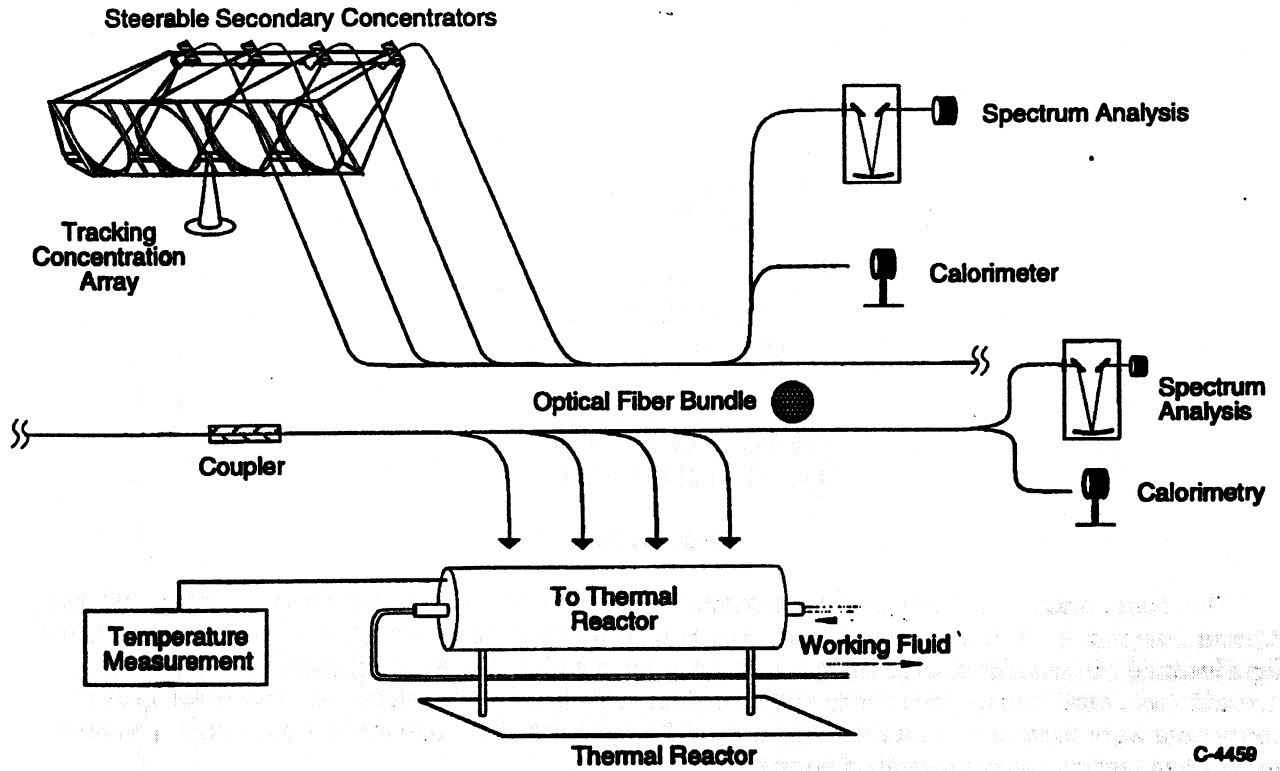


Figure 1. Schematic representation of the subscale ground test model of the OW solar energy system.

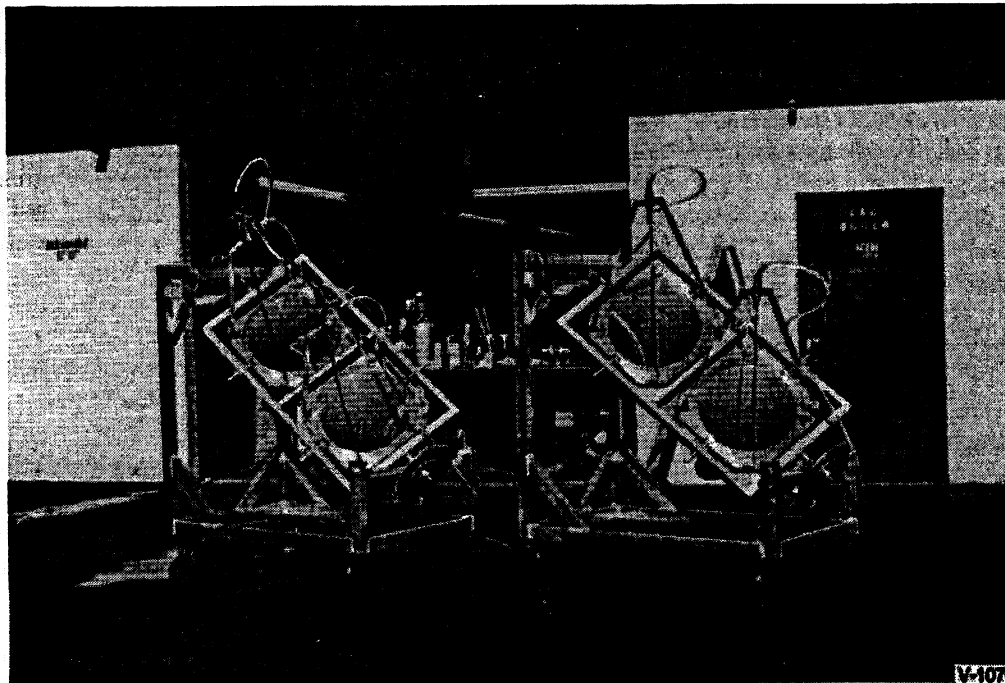
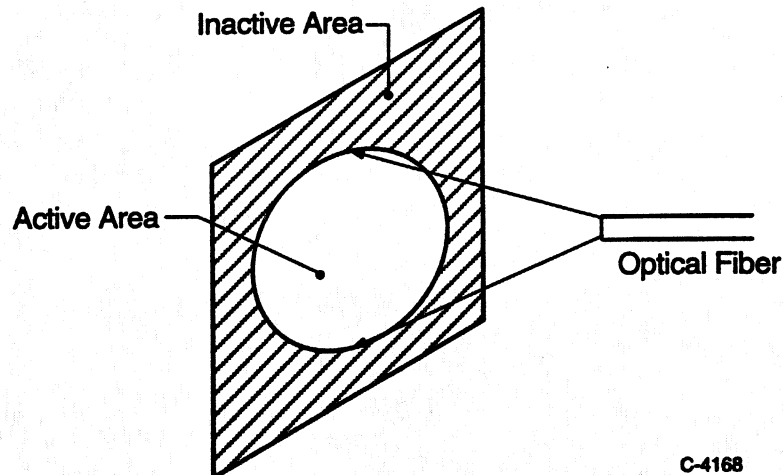


Figure 2. Photograph of the subscale ground test model of the OW solar energy system.



C-4168

Figure 3. Fiber-on-cell coupling of optical fiber and concentrating photovoltaic cell.

demonstrate the feasibility of the OW photovoltaic power generation, and to identify technology issues associated with the power generation system.

Photovoltaic Cell (PV) Characteristics

The PV cell used in the present experiment was the GaAs cell prepared by Dr. Michael L. Timmons, Semiconductor Materials Research Department, Research Triangle Institute (RTI). The GaAs cell (about 0.5×0.5 cm in size) has a circular aperture area of 0.16 cm^2 . With the electric contact grid partially blocking the front surface of the cell, the active area becomes 0.14 cm^2 . The cell has p-on-n polarity with the back side connected to the substrate acting as ground or negative potential. Positive voltage is produced at the top surface. Figure 4 shows a photograph of the cell soldered on a copper plate. This cell, when illuminated with 1-sun AM0 Xe-lamp solar simulator, produces a short circuit current of 200 mA, the open circuit voltage being 1.1 V. The fill factor for the cells are greater than 0.8. The efficiency of the cell under the 40 ~ 50 suns AM0 solar simulator light was measured to be 16% based on the aperture area (0.16 cm^2), and 18.5% based on the active area (0.14 cm^2).

We have tested a total of seven PV cells. Each cell was soldered to a copper plate ($4 \times 4 \times 3/16$ in.) which acted as a heat sink. A single or multiple optical fibers were placed at the PV cell such that the solar flux filled the aperture of the cell as shown in Figure 5. We utilized both 3-ft and 2-m cables for the power generation experiment. For each experiment, solar power from the optical fiber(s) was measured by the thermopile calorimeter (Coherent 210). The output power characteristics of the PV cell were measured by changing the load resistor. During the test the copper plate temperature was constant at room temperature. Of the seven PV cells we tested, #3 cell appeared to be defective, and #5 and #7 cells showed low open circuit voltage when tested at 1-sun. Consequently, data for these cells were not discussed in this paper.

Solar Spectral Characteristics

Figure 5 compares the solar spectra in space (2) and the solar spectra on the ground at Air Mass Two (AM2). Spectral distribution of the direct solar insolation at the test site was not measured. We believe, however, that the spectra at the test site will be somewhat higher than the AM2 spectra. As shown in the figure, the solar spectra in space (AM0) contains a higher percentage of the spectra for $\lambda < 0.87 \mu\text{m}$ than that of AM2. The wavelength $\lambda = 0.87 \mu\text{m}$ (1.43 eV) corresponds to the bandgap cut-off of the GaAs cell. We may expect from this fact that the efficiency of the GaAs cell when exposed to the terrestrial 1-sun will be lower than the value measured with the solar simulator (AM0) light.

The spectral intensity distribution of the fiber output is shown in Figure 6. These data were taken using a 10-m long fiber at 2 p.m. on May 31, 1995. The vertical axis of Figure 6 shows "relative" spectral intensity reduced from the silicon detector voltage output with appropriate corrections for: 1) higher order blocking filter transmission;

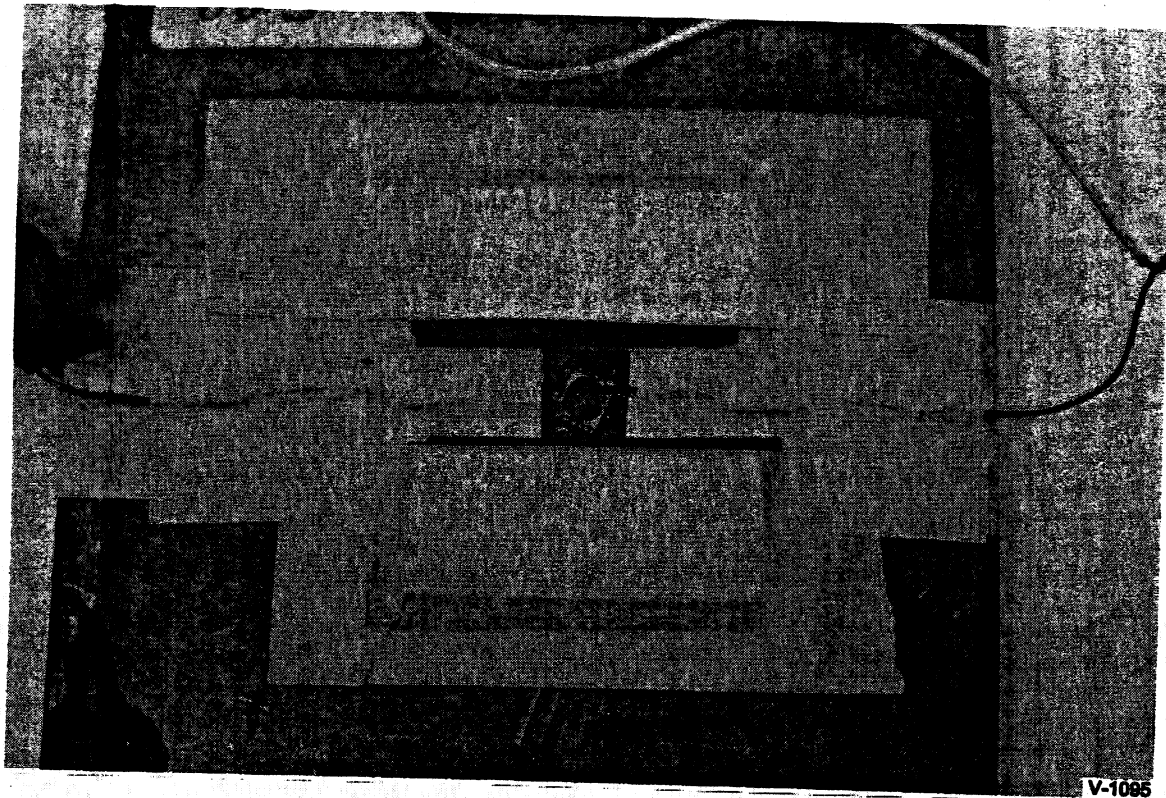


Figure 4. The RTI GaAs cell soldered on the copper substrate.

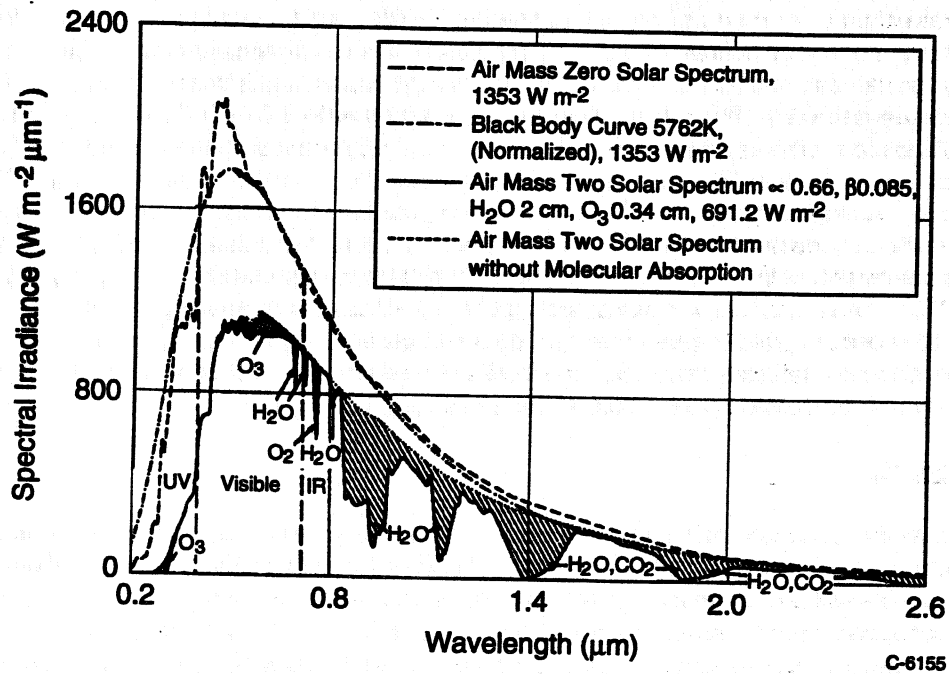


Figure 5. Comparison of AM0 and AM2 solar spectra, showing the various atmospheric absorption bands in AM2.

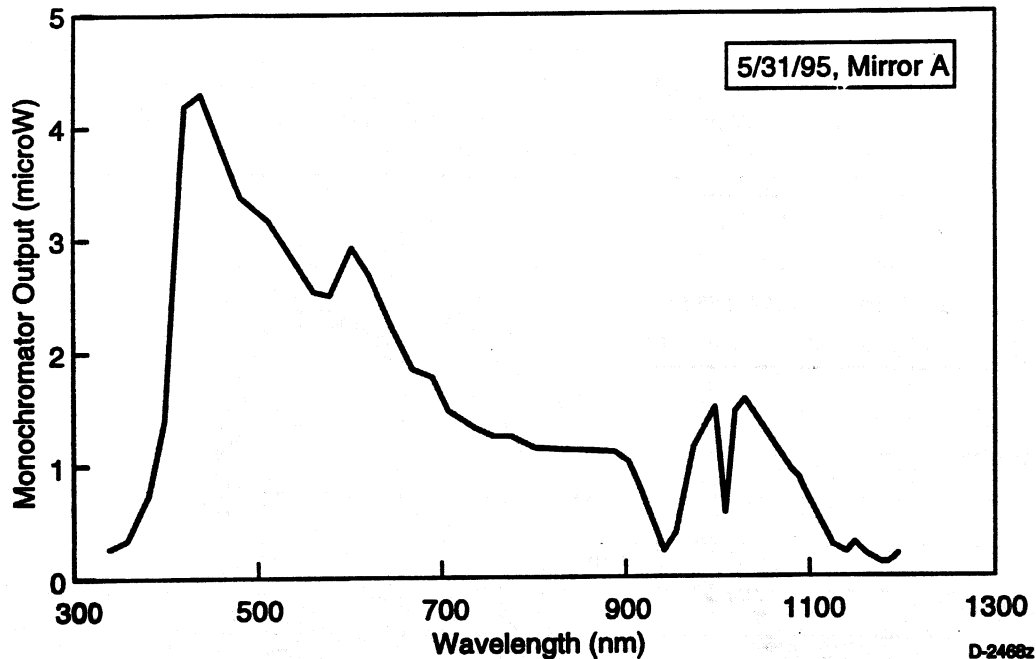


Figure 6. Spectral intensity distribution of the optical fiber output.

2) grating efficiency; and 3) silicon detector responsivity. There is a distinct "dip" in intensity between 900 and 1000 nm which is due to absorption by atmospheric water vapor and by the -OH ions in the fiber material. The intensity distribution curve in Figure 6 shows that the solar spectra of the optical fiber output contains a sufficient amount of photon intensity of interest to photovoltaic power generation ($\lambda < 0.87 \mu\text{m}$).

EXPERIMENTAL RESULTS

Power Generation With the Direct 1-Sun

Prior to the high concentration experiment we conducted the direct 1-sun exposure experiments. For these measurements, the cells were exposed to the direct sun without using the optical fibers. The voltage-current (V-I) characteristics of the cells for the direct 1-sun exposure were taken. The solar flux intensities at the test site were 847 to 885 W/m^2 . The solar powers which fell on the cell based on the cell aperture area (0.16 cm^2) were 0.0135 to 0.0141 W. The open circuit voltage for some cells was anomalously low. This is likely due to the leakage path somewhere in the cell circuit. However, when the solar intensity is increased, the open circuit voltage improves towards 1.1 V as will be shown later.

In Figure 7, the efficiency of the cell is plotted as a function of the cell potential. Except for cell #1, the peak efficiency takes place at the cell voltage of 0.7 - 0.8 V. The peak efficiency ranges from 11 to 13%. The efficiency values shown here are based on the cell aperture area (0.16 cm^2). As discussed before, the RTI cells were tested with AM0 solar simulator lighting to yield an efficiency of 16%. This 3 to 5% difference may be attributed to difference in spectral distribution between the AM0 flux and the flux on the ground, or to the non-ideal cell preparation process for this particular experiment.

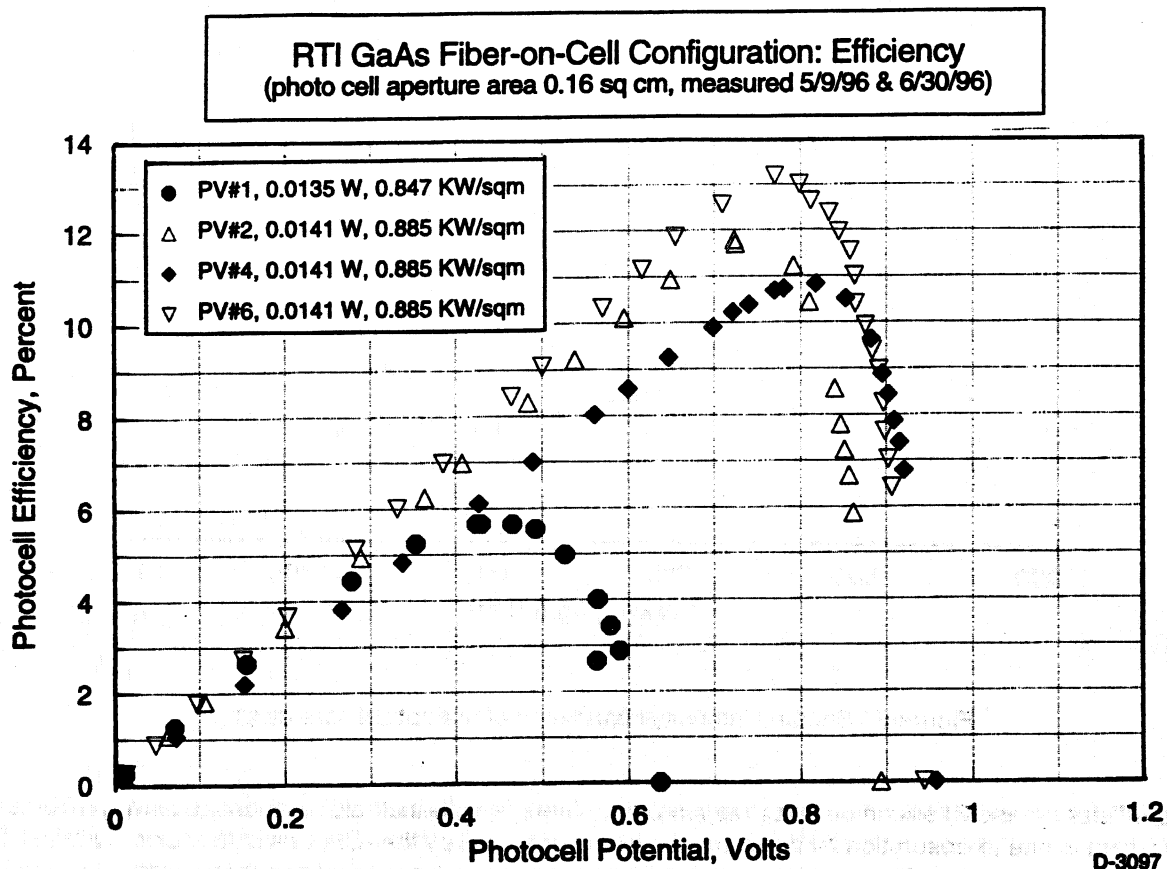


Figure 7. The efficiency-voltage characteristics of the four RTI GaAs cells at the direct 1-sun.

Power Generation With High Concentration Solar Flux from the Optical Waveguide

Figure 8 shows the V-I characteristics of the cell #1 as they were illuminated with the high intensity solar flux from the optical fiber. The solar power input to the cell, listed on the figure legend in the middle column at the right of the cell number, was measured by a thermopile calorimeter. The intensity of the solar flux, listed on the right column of the legend, was calculated using the optical fiber power output, and the solar cell aperture area (0.16 cm²). The open circuit voltage (V_{op}) is constant at 1.1 V regardless of the solar flux intensity, while the cell current increases with solar flux intensity.

The power output of cell #1 as the function of cell voltage is given in Figure 9. The solar flux intensity to cell #1 is 288 kW/m², or 320 suns based on 880 W/m² on the ground. The corresponding cell output is 0.53 W. This is a remarkable high power capability for this small GaAs cell.

The efficiency-voltage characteristics of cell #1 for various flux intensities is given in Figure 10. The open circuit voltage (V_{op}) of cell #1 recovers from its anomalous value of 0.63 to 1.1 V as the flux intensity is increased. The maximum efficiency for cell #1 is 12% at high flux intensities.

RTI GaAs Fiber-on-Cell Configuration: V-1 Characteristics
 (photo cell aperture area 0.16 sq cm, measured 5/7/96)

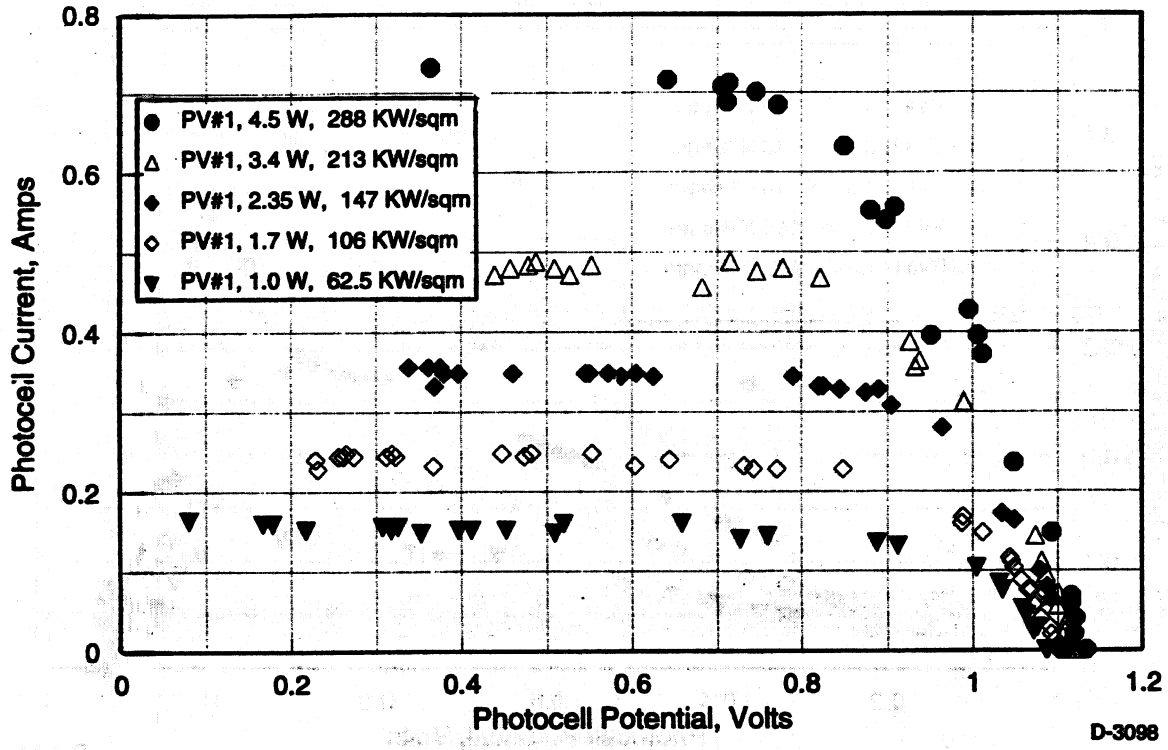


Figure 8. The voltage-current characteristics of the RTI GaAs cell #1 for high intensity solar flux.

RTI GaAs Fiber-on-Cell Configuration: Power Output
 (photo cell aperture area 0.16 sq cm, measured 5/7/96)

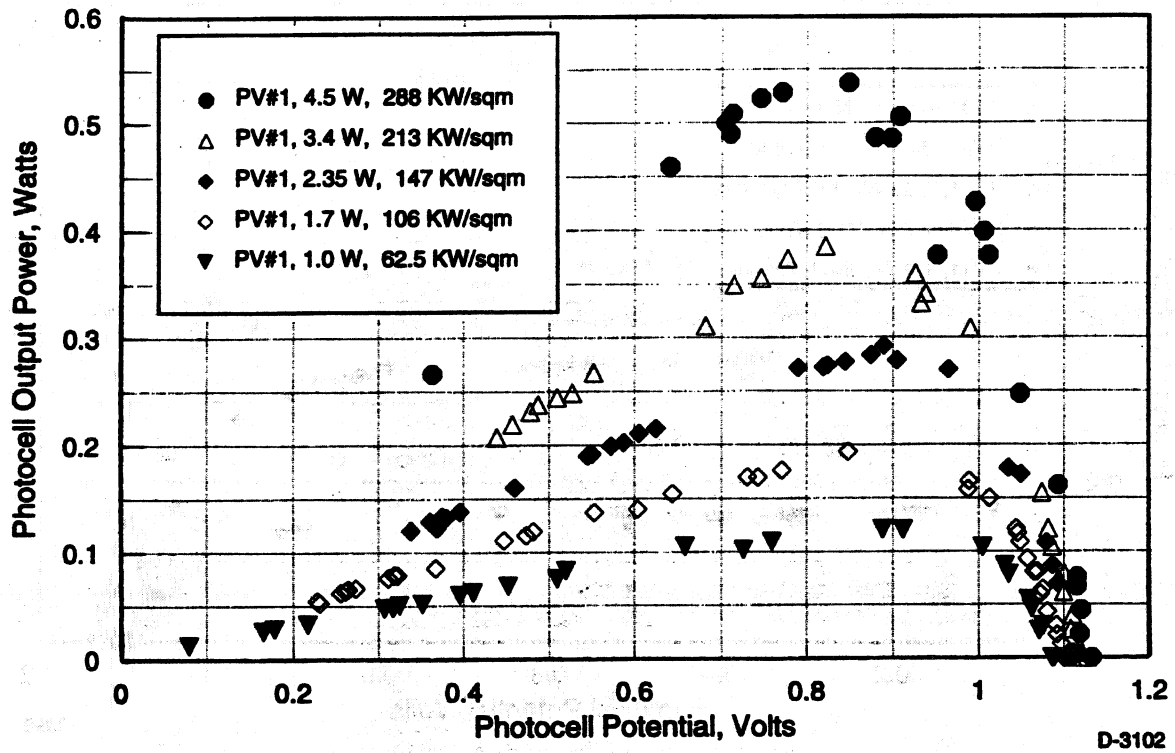


Figure 9. The cell power output versus cell voltage for the RTI GaAs cell #1.

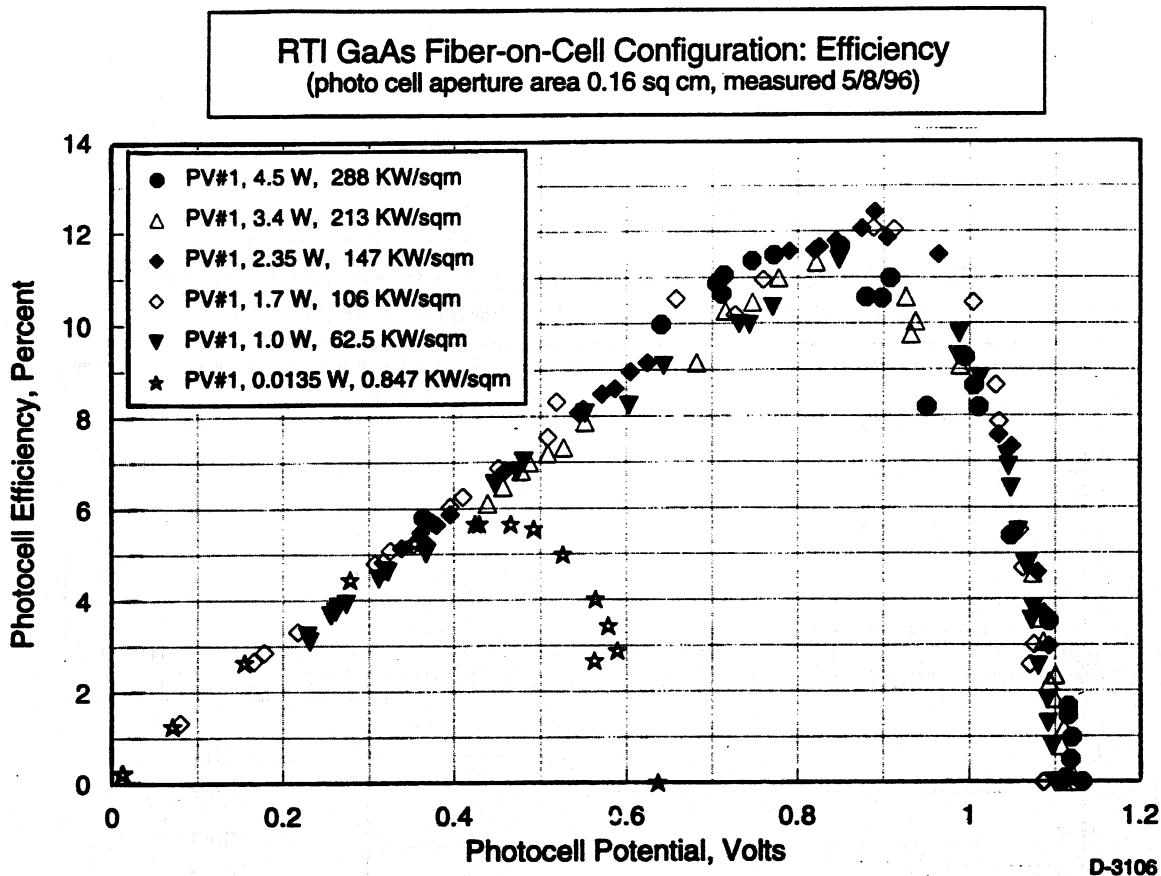


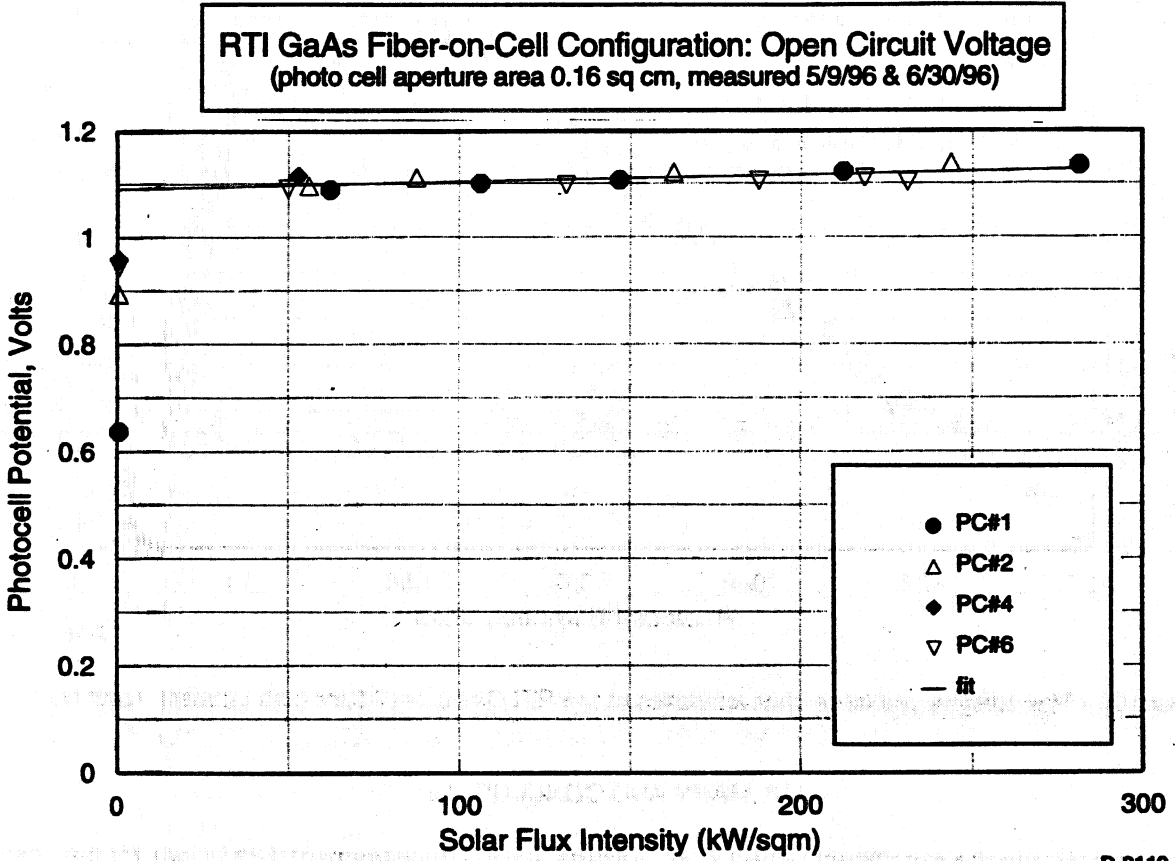
Figure 10. The efficiency-voltage characteristics of the RTI GaAs cell #1 for high intensity solar flux.

SUMMARY AND CONCLUSION

Having reviewed the experimental results, we will organize the measurement data to look for the answers to the following questions: (1) will the cell output increase with the solar flux intensity, and (2) what will be the power generation efficiency as solar flux intensity increases?

The answer to the first question is given in Figures 11 through 13. The open circuit voltage (V_{op}) of the RTI GaAs cells is plotted against the solar flux intensity in Figure 11. The V_{op} for the direct 1-sun exposure is much lower than 1.1 V. However, as the solar flux density is increased, V_{op} goes up to 1.1 V and increases steadily as the solar flux intensity increases. The data shows this tendency very clearly. The short circuit current (I_{sc}) of the RTI GaAs cell is plotted against the solar flux density in Figure 12. This is another very clear data plot: all data points line up neatly. The plot shows that the short circuit current increases linearly with the solar flux intensity.

In Figure 13, the cell electric power output is plotted against the solar flux intensity over the cell aperture area (0.16 cm²). The plotted data show that the slope is linear with no indication of saturation. The highest solar flux intensity is 288 kW/m² which corresponds to 213 suns in space (1.35 kW/m²) or 327 suns on the ground (880 W/m² at the test site). The maximum solar power input to the cell was 4.5 W. At this power range we did not observe any thermal or electrical problems. We expect that the cell will perform properly for higher solar power input, possibly up to 10 W per cell (470-suns in space).



D-3110

Figure 11. The open-circuit voltage of the RTI GaAs cells versus solar flux intensity.

RTI GaAs Fiber-on-Cell Configuration: Short Circuit Current
 (photo cell aperture area 0.16 sq cm, measured 5/9/96 & 6/30/96)

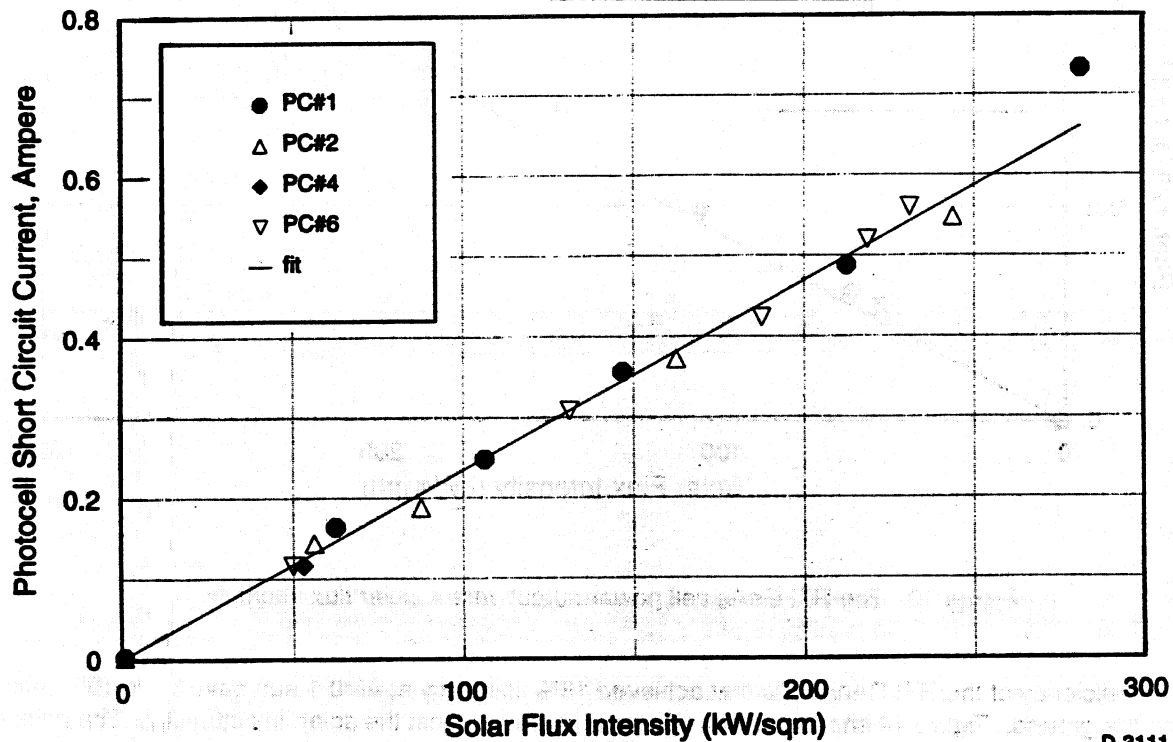


Figure 12. The short-circuit current of the RTI GaAs cells versus solar flux intensity.

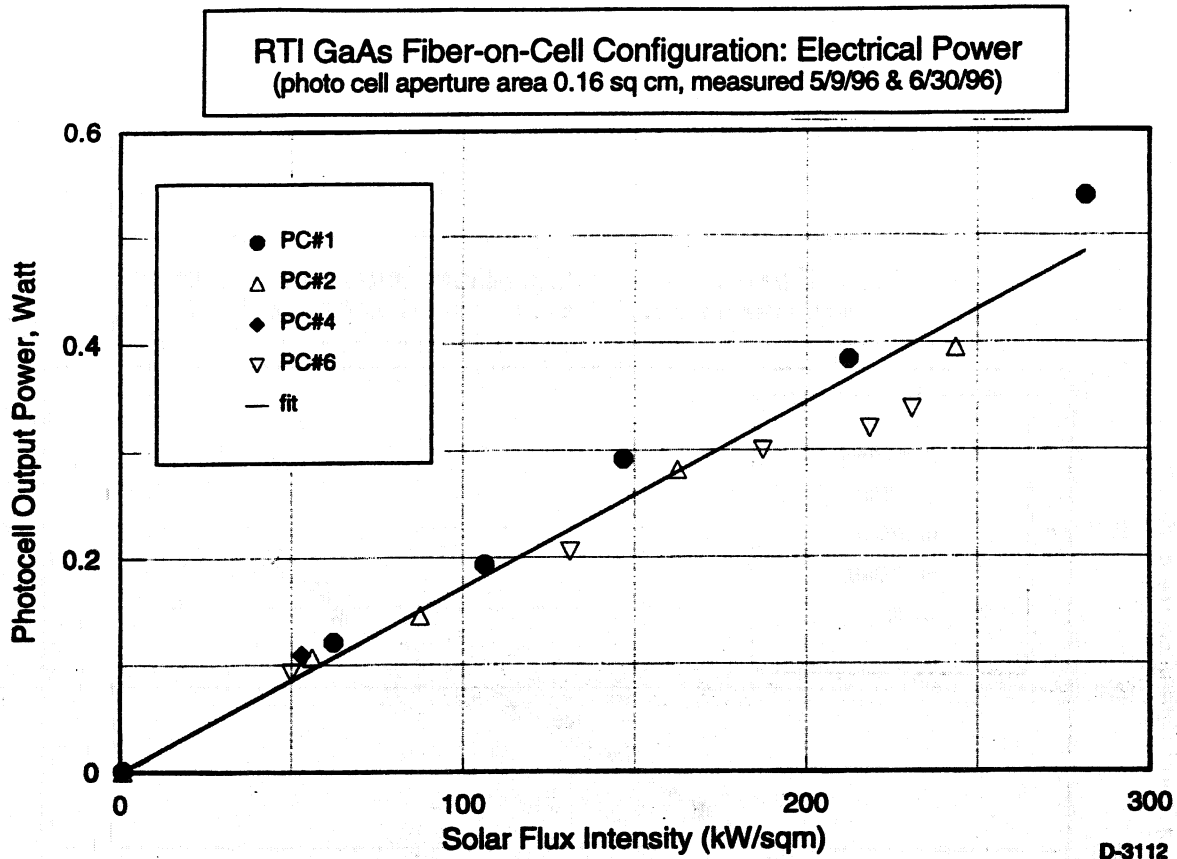


Figure 13. The RTI GaAs cell power output versus solar flux intensity.

The efficiency of the RTI GaAs cells that achieved 16% efficiency at AM0 1-sun gave 11 to 13% efficiency at 1-sun on the ground. Figure 14 shows the cell efficiency plotted against the solar flux intensity. The efficiency decreases slowly as the solar flux intensity is increased. We believe that the decrease in efficiency is due to imperfect coupling between the fiber and the cell, not to fundamental limitations of the semiconductor performance. We noticed that as the optical fiber end is fixed over the cell aperture, part of the solar flux "spilled" over the aperture area. With a proper coupling method such as with a reflective collimator, flux spill-over will be minimized. In this case, we expect that the cell efficiency will be constant. We must take note that, contrary to commonly accepted theory, the present experimental results do not show an increase in cell efficiency as solar input flux increases. We do not have an explanation for this at present.

The foregoing discussions lead us to the following conclusions. The high concentration GaAs cells when combined with the OW system will be an effective power generation device. The high power density implies a small size PV cell array which is attractive from cost and weight aspects. Furthermore, as the OW system can switch the solar power from the material processing plant to the electric power generation facility and vice versa, the PV power generation device can become an integral part of the lunar material processing plant.

The OW system can take advantage of the advanced PV cell which can operate at higher efficiency. The current experiment was conducted only for one type of GaAs cell with a moderate efficiency value. Power generation at a higher efficiency is possible and is desirable from a system engineering point of view.

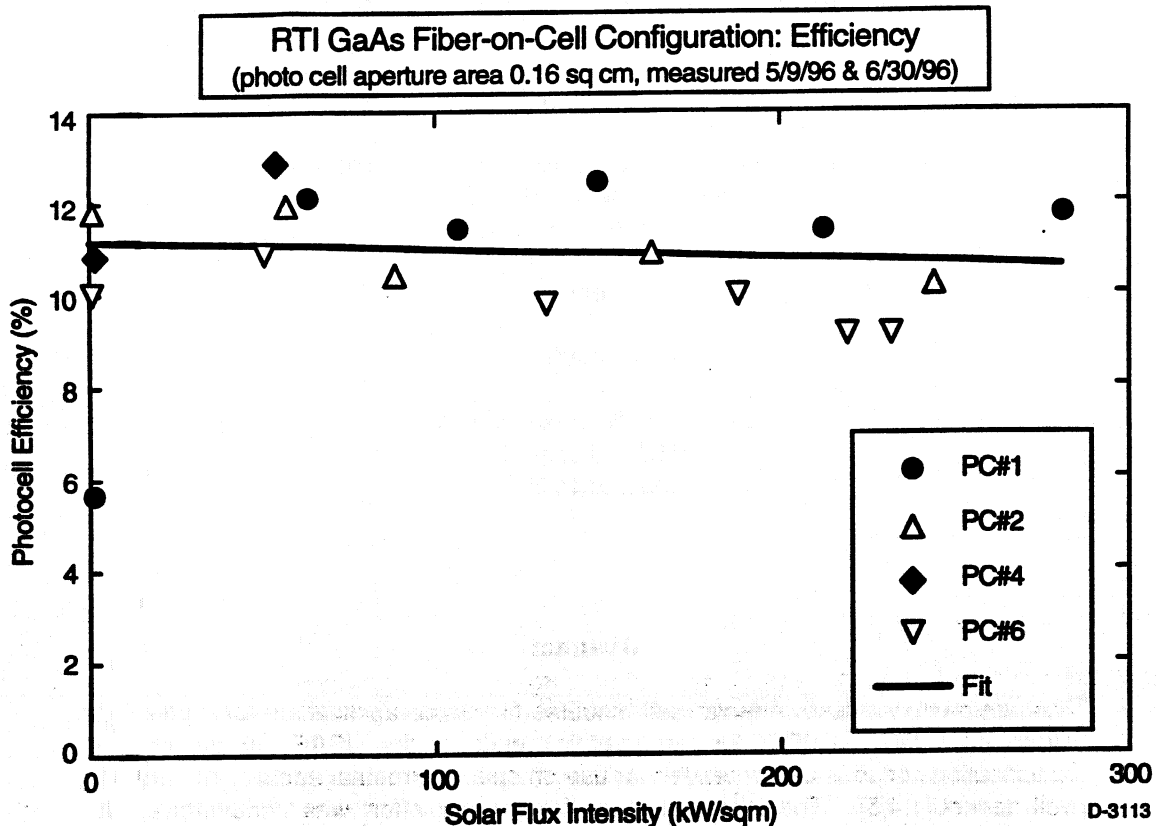


Figure 14. The efficiency of the RTI GaAs cell versus solar flux intensity.

REFERENCES

1. Nakamura, T., J.A. Case, and C.L.Senior, "Optical Waveguide Solar Energy System for Lunar Materials Processing", Final Report: PSI-2287/TR-1437, Submitted to NASA/JSC, August 1996.
2. Thekaekara, M. P., "Data on Incident Solar Energy" in The Energy Crisis and Energy from the Sun, Inst. Environ. Sci., Mt. Prospect, IL (1974).

SPACE QUALIFICATION TEST OF a-SILICON SOLAR CELL MODULES

Q. Kim, R.A. Lawton, S.J. Manion, J.O. Okuno, R.P. Ruiz, D.T. Vu and S.A. Kayali

Center for Space Microelectronics Technology
Jet Propulsion Laboratory
California Institute of Technology

and

F.R. Jeffrey

Iowa Thin Film Technologies
2501 N. Loop Dr.
Ames, Iowa 50010

Abstract

The basic requirements of solar cell modules for space applications are generally described in MIL-S-83576 for the specific needs of the USAF. However, the specifications of solar cells intended for use on space terrestrial applications are not well defined[1,4,5]. Therefore, this qualification test effort was concentrated on critical areas specific to the microseismometer probe which is intended to be included in the Mars microprobe programs. Parameters that were evaluated included performance dependence on: illuminating angles, terrestrial temperatures, lifetime, as well as impact landing conditions. Our qualification efforts were limited to these most critical areas of concern. Most of the tested solar cell modules have met the requirements of the program except the impact tests. Surprisingly, one of the two single PIN 2x1 amorphous solar cell modules continued to function even after the 80,000G impact tests. The output power parameters, P_{out} , FF, I_{sc} and V_{oc} , of the single PIN amorphous solar cell module were found to be, 3.14mW, 0.40, 9.98mA and 0.78V, respectively. These parameters are good enough to consider the solar module as a possible power source for the microprobe seismometer. Some recommendations were made to improve the usefulness of the amorphous silicon solar cell modules in space terrestrial applications, based on the results obtained from the intensive short term lab test effort.

Introduction

Various amorphous solar cell modules were obtained from Iowa Thin Film Technologies on July 8, 1996. These modules[2] were to be tested as part of a program to identify the qualification requirements dictated by the environmental specification[3] for solar cells in order to utilize them as a potential power source for a microseismometer, which is one of the many Mars Microprobe programs of the New Millennium project. Much of the electronics will actually be shield by some 3mm-thickness of steel, but the solar cell modules will have only minimal shielding. The purpose of this study was to develop the needed space terrestrial qualification guidelines on different types of state-of-the-art solar modules that may be applicable for use as the power source of the Mars microseismometer.

Test Results and Discussions

1. External Visual Inspection

Three major different groups of twelve (12) different kinds of samples as listed in Table I were examined and documented. No major visual defects were seen. A typical 5x1 single PIN module is shown in Figure 1.

Table I. Parts List.

Parts	Encapsulation	Serial No.	Adhesive	Operation/Comment	No. of Parts
1.	Polyester		EVA thin/0.1 mil	3V,45mA	8
2.	Polyester 1.5 mil		EVA 0.2mil		45
3.	Tefzel		EVA 18 mil	3V,90 mA	3
4.	Tefzel		EVA		4
5.	None		None	R379(4),F83-86(4)	
6.	Tefzel		EVA	3M Adhesive Foil 6x2 cells	3
7.	Tefzel		EVA	F-8257 Adhesive Foil 6x2 cells	3
8.	Tefzel		EVA	Indium/Tin Solder Paste	3
9.	Tefzel		EVA	Bismuth/Tin Solder Paste	3
10.	Tefzel		EVA	3M Adhesive Foil 12x2 Cells	5
11.	Tandem	357			5
12.	Tandem	395			5

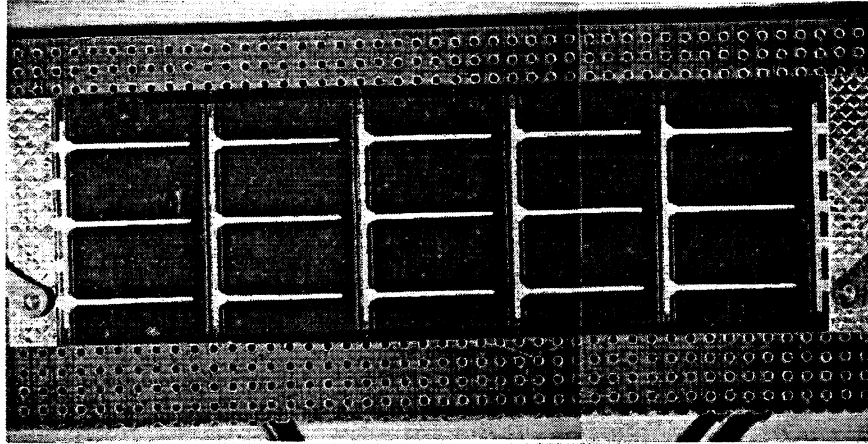


Figure 1. External Visual Inspection of a Typical 5 x 1 Single PIN Amorphous Solar Module.

2. I-V Characterization

I-V characteristic measurements of the modules in dark and light at 1/2 Martian sun (28.5 mW/cm^2) were performed as a required specification of the Mar's probe. The characteristics (Isc, Voc, Fill Factor, Output Power) of the modules agrees well with the nominal values given by the manufacturer within 5%. A typical I-V characteristics of the polyester encapsulated amorphous silicon solar cell module (MPV-P) is shown in Figure 2.

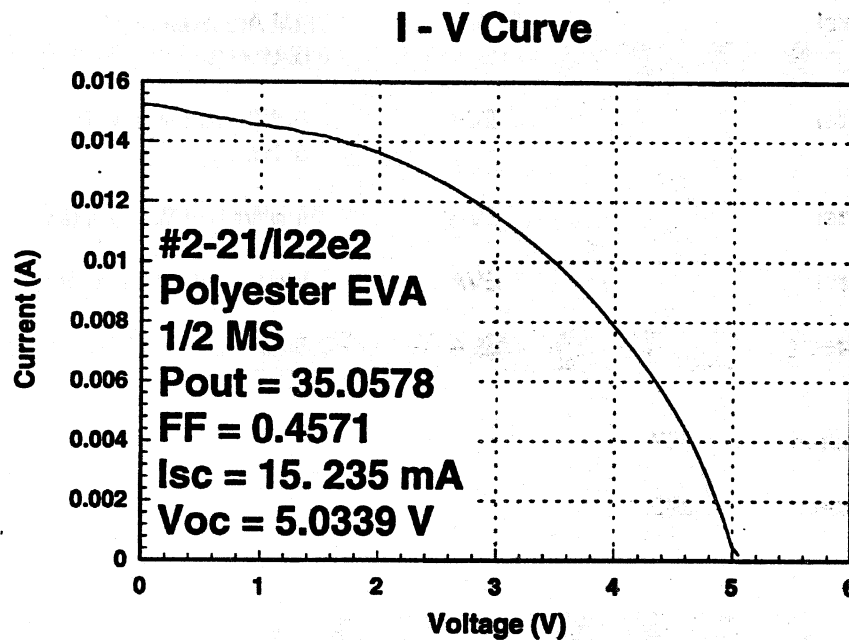


Figure 2. I-V Characteristic of a Polyester Encapsulated Amorphous Silicon Solar Cell Module.

3. Illuminating Angle Dependence

The power generation of the solar cell module depends upon the angle of the solar illumination at the microprobe landing site[3]. The maximum power output of the module was compared with the cosine of the sun's illumination angle. At 40 degrees of tilt for example, the power output was reduced to 60% (Figure 3). The output power is still high enough to supply the needed power for the seismometer.

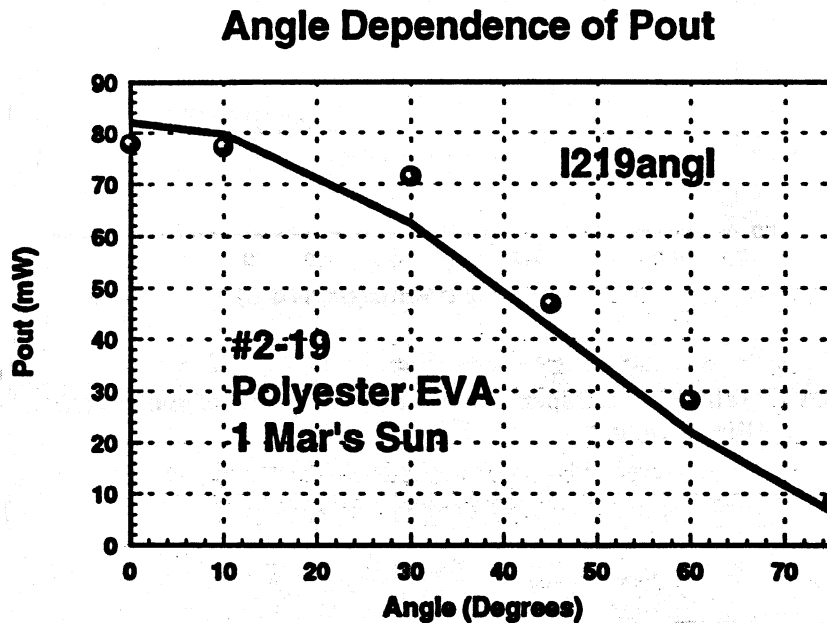


Figure 3. Angle Dependence of the Amorphous-Si Solar Module Power Output.

4. Temperature Dependence

The optimum performance of the solar module depends upon the module operating temperature. The projected range of operating temperatures for the microprobe is from -70 to +25° C. The maximum output power of a polyester encapsulated module (#2-20) was measured. The power output was reduced in a linear fashion at the lower temperature range. At -60°C, for example, the maximum output power was reduced to 58% of the output power at +25°C (Figure 4). High Temperature tests (room temperature - +150°C) were also performed. The maximum output at +150°C was reduced to 35% of the output power at +25°C (Figure 5). Note that the maximum power output decreases when the operating temperature of the solar cell module is either cooled or heated from room temperature, probably due to the amorphous nature of the silicon material.

Temperature Dependence of Pout

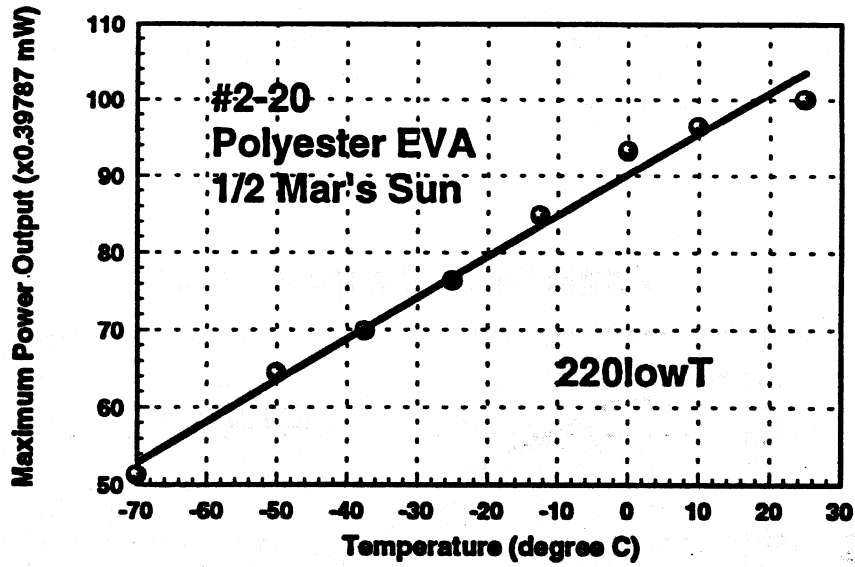


Figure 4. Temperature Dependence of the Amorphous-Si Solar Module Power Output.

Temperature Dependence of Pout

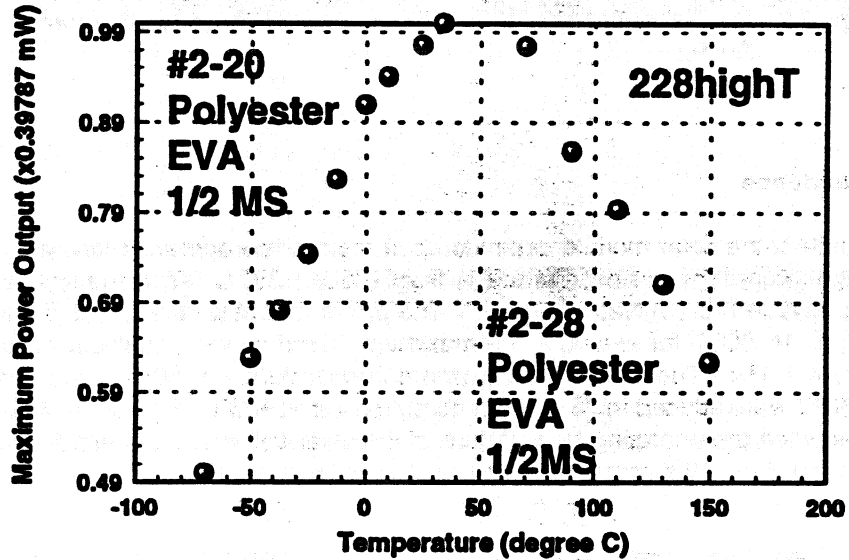


Figure 5. High Temperature Dependence of the Amorphous-Si Solar Module Power Output.

Aging of the Out Power

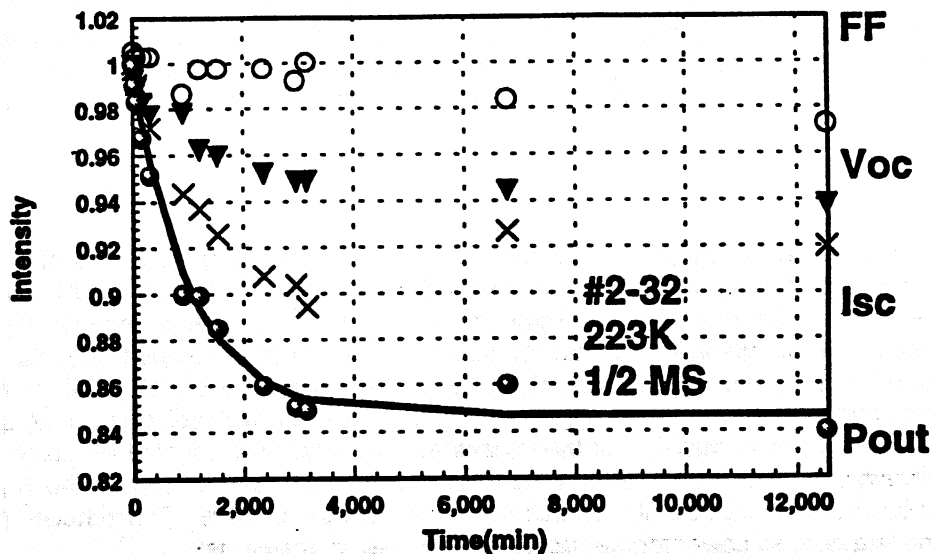


Figure 6. Illumination Time Dependence of the Amorphous-Si Solar Module Power Output at 223K.

5. Time Dependence

The demonstrated reliable lifetime of the module should exceed the required life expectancy for a ten day mission. One of the polyester encapsulated EVA modules was kept at 223K for 12,531 minutes (~9 days) under the 1/2 Martian sun. The maximum power output was down by 15% within two days in an exponential fashion and stayed at that level as shown in Figure 6. The maximum power output characteristics are similar even at 248K as shown in Figure 7. However, the power output was degraded by 12 percent.

Performance Degradation at 248K

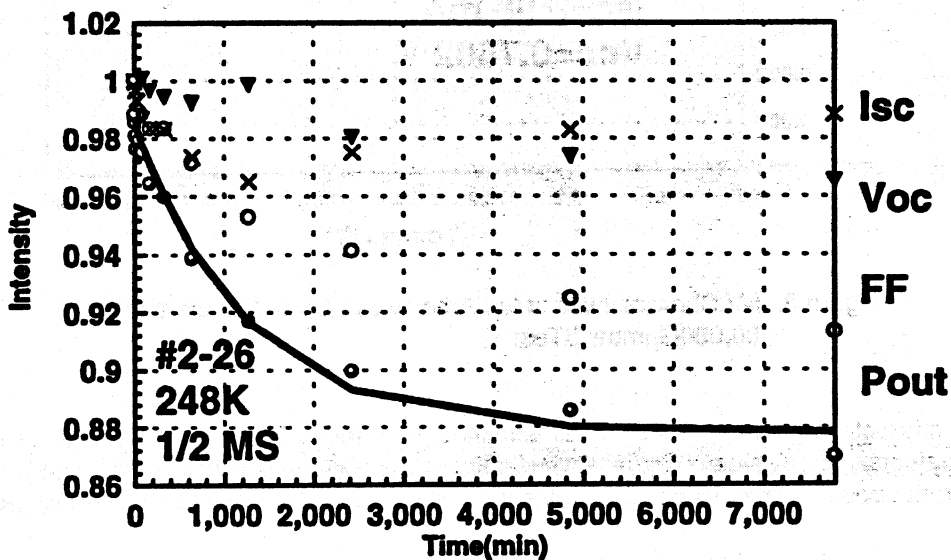


Figure 7. Illumination Time Dependence of the Amorphous-Si Solar Module Power Output at 248K.

6. Absorption of the Encapsulation EVA

One of the solar module encapsulants, Tefzel, was tested for absorption spectrum by using Fourier Transformation Spectroscopy for a baseline reference of the degradation caused by solar illumination. Reflection from the stainless steel substrate, polyester encapsulated solar cell module can be tested later as needed in order to measure the degree of degradation of the encapsulant using a reflection sample holder.

7. Impact tests

One of the most critical parameters of a solar cell as a power generating source for the microprobes is the survivability of the module after an impact landing at 80,000 Gs[3]. A series of single PIN solar cells and tandem PIN solar cells were characterized before and after application of the simulated impacts. In these tests all the samples were modified to fit into the impact test chamber. All four different tandem PIN samples were found to be electrically shorted after the applied impact, reducing the output power of those modules down to 1.7 microwatts from 35 milliwatts. Two of the single PIN cells encapsulated with polyester using EVA adhesive were also modified to 2x1 from a 5x1 matrix to fit the impact test chamber, and covered with a plastic film before the impact test. Surprisingly, one of the two tested amorphous solar cell modules survived the 80,000G impact. The maximum power output of the module at 1/2 Martian sun was reduced by 65%. This reduced power output is still sufficient to supply the needed power for the microelectronic seismometer task.

SC1LA, Light I-V, After Impact

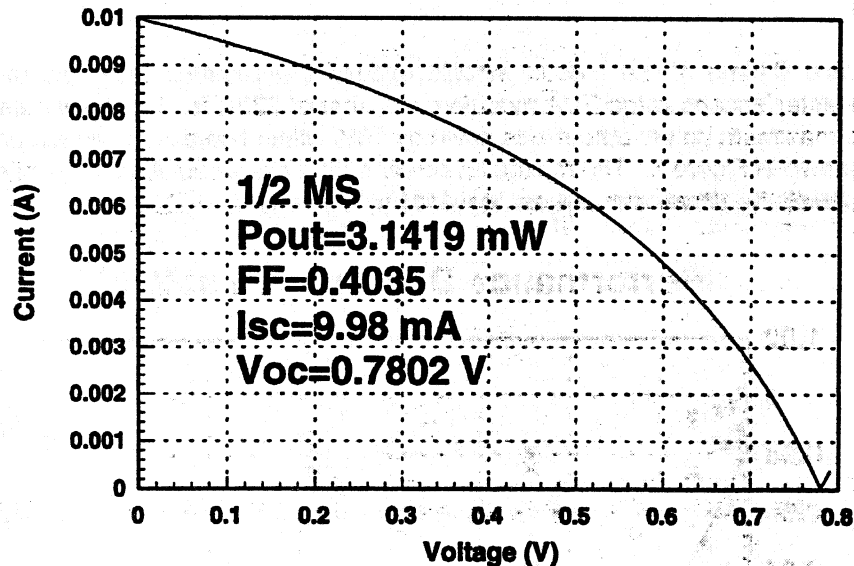


Figure 8. I-V Characteristic of the Amorphous Solar Module after the 80,000G Impact Test.

The PIN diode characteristics of the module still exhibited the needed fill factor (40%) (Figure 8) despite the fact that physical defects were visible (Figure 9) including a stain and scuffing on the front surface and some damaged silver electrodes. The device characteristics of the module before and after the impact test are listed in Table II.

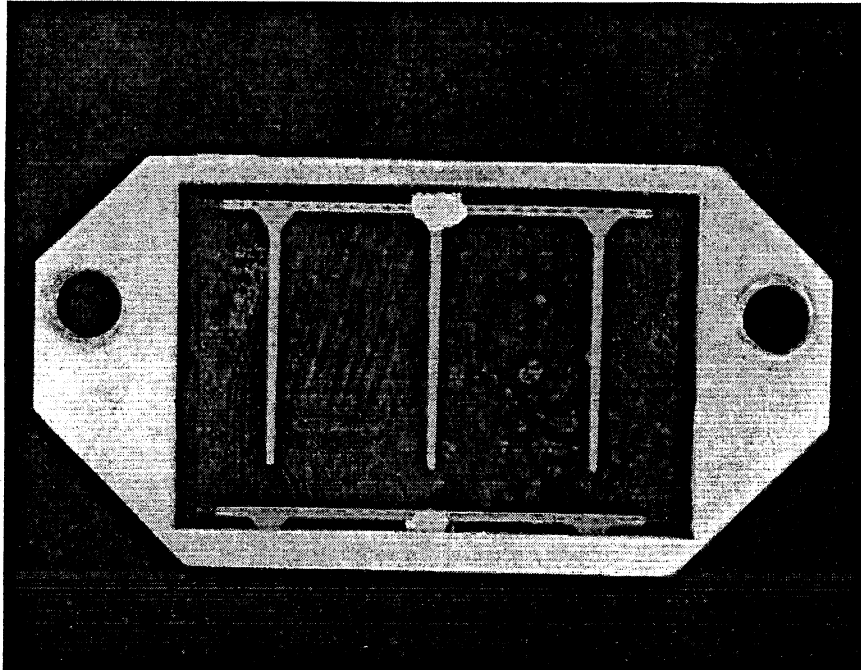


Figure 9. Visual Damage Inspection of the Impact Tested Amorphous Solar Cell.

Further impact tests of single PIN solar cell modules are in progress to improve the reliability of the module, especially in the electrical contacts.

Table II. Single Cell Impact Test Results

		$R_{sheet}(\Omega)$ At Dark	$R_{series}(\Omega)$ At 1/2 Mars Sun	$R_{shunt}(\Omega)$
Cell #1	Before	618.6	17.01	500.00
	After	25.00	24.55	220.75
Cell #2	Before	252.2	19.47	666.67
	After	26.18	26.18	11.06

8. Leakage Test

Some of the failed samples after the impact tests were photographed to find the leakage spots by using an Infrared Camera. Leakage spots were found in areas within the active cell as well as near the silver electrode grid of the failed tandem PIN solar modules as shown in Figure 10. However, no hot spots or breakdown spots were observed on single PIN solar cell modules. This may indicate that the leakage path of the failed modules

may be a short within the conductive series contact layers rather than a breakdown of the PIN cell structure. Further tests are scheduled in order to improve the electrical contacts.

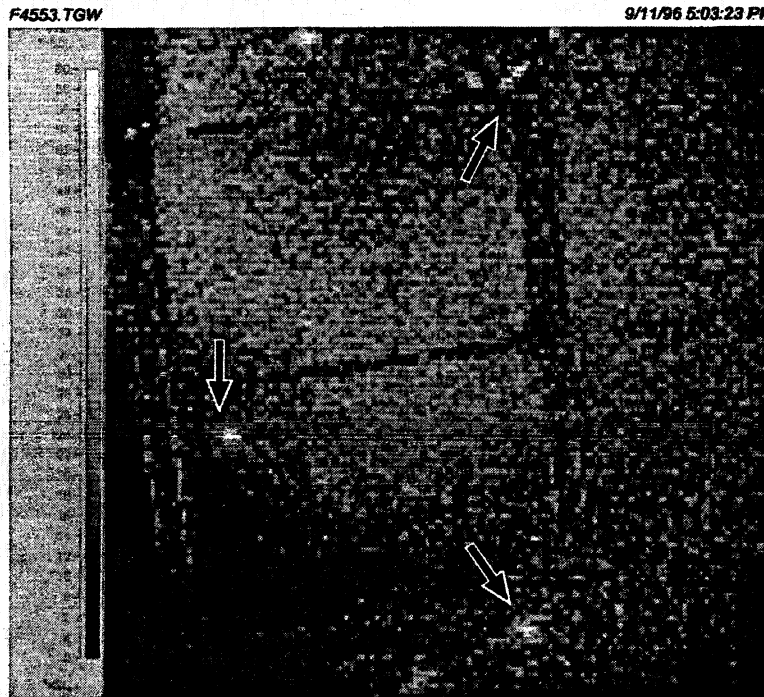


Figure 10. Possible leakage spots of a good solar module as observed by the Infrared Camera.

9. Cross Section Analysis

As a part of the effort to ascertain the manufacturer's workmanship integrity, a cross section of a single PIN structure was performed by fracturing a cell that was made brittle by immersion in liquid nitrogen. During SEM examination of cross sectioned samples, damage to the underlying dielectric isolation caused by the laser scribed grooves within the electrical contacts was revealed as a potential leakage path.

Conclusions

Most of the test qualification results obtained for the single PIN amorphous solar cell modules were satisfactory. These modules are suitable for consideration as the power source for the seismometer of the Mars microprobe. However, the electrical contacts of the module should be improved before final selection of qualified modules. Of special importance is the need to identify and test improved encapsulation materials and techniques to increase the survivability of the module against impact damage.

Additional testing is in progress to improve the conductive contacts and the protective encapsulant of the single PIN module against damage induced by the stress of high velocity impact anticipated for the Mars microprobe application.

Acknowledgments

The authors appreciate the assistance of the JPL calibration laboratory for their work to determine the one Martian sun (58 mW/cm^2) calibration of the ELH illumination source used in this study. This work was supported by a grant of JPL-204-56005. The research described in this paper was carried out by the Jet Propulsion Laboratory, California Institute of Technology, under a contract with the National Aeronautics and Space Administration. Reference herein to any specific commercial product, process, or service by the trade name, trademark, manufacturer, or otherwise, does not constitute or imply endorsement by the United States Government or the Jet Propulsion Laboratory, California Institute of Technology.

References

- [1]. E. L. Royal, and J. W. Lathrop, "Determining Terrestrial Solar Cell Reliability", Proceedings of Workshop Held at Clemson University, Clemson, South Carolina, May 1-2, 1980.
- [2]. F. R. Jeffrey, D. P. Grimmer, S. A. Marthens, K. Abudagga, M. L. Thomas, and M. Noak, "Polyimide Based Amorphous Silicon Solar Modules", Twelfth Space Photovoltaic Research and Technology (SPRAT XII) Conference, p. 88, NASA Lewis Research Center, 1993.
- [3]. R. Payton, "Environmental Requirements Document, Mars Surveyor Program", Internal Document, Lockheed Martin Astronautics.
- [4]. Fourteenth Space Photovoltaic Research and Technology (SPRAT XIV) Conference, Cleveland, Ohio, October 1995.
- [5]. Proceedings of the 25th Photovoltaic Specialist Conference, Washington, D.C., May 1996.

Exploring PV on the Red Planet:

Mars Array Technology Experiment and Dust Accumulation and Removal Technology

Geoffrey A. Landis¹, Cosmo Baraona, David Scheiman², and David Brinker
NASA Lewis Research Center
Photovoltaics Branch, mailstop 302-1
21000 Brookpark Rd.,
Cleveland, OH 44135

Abstract

The environment on the surface of Mars is different in several critical ways from the orbital environment in which space solar arrays normally operate. Some important differences are:

- (1) low intensity, low temperature operation
- (2) spectrum modified by atmospheric dust, varies with time
- (3) indirect sunlight
- (4) possibility of dust storms at some times of year
- (5) deposited dust
- (6) wind
- (7) peroxide-rich reactive soil

We are developing two experiments to test operation of solar arrays on the surface of Mars, to be flown on the 2001 Surveyor Lander mission. The Mars Array Technology Experiment (MATE) will test the operation of several types of solar cells under Mars conditions, and determine the direct and scattered solar spectrum at the surface. The Dust Accumulation and Removal Technology (DART) experiment will monitor the amount of dust deposition on a target solar cell, measure the characteristics of the dust, and test the feasibility of dust removal.

1. Introduction

Over the next ten years, Earth is launching an assault on the planet Mars. Starting with Pathfinder [1] and Mars Global Surveyor, which arrive at Mars this year, there will be at least two spacecraft sent to explore the Red Planet during each launch opportunity for the next decade, leading, perhaps, toward a human mission early in the next century.

The single most important resource required for operation of robotic and human spacecraft on Mars is energy. Power is required for all phases of a mission, for scientific instrumentation, communication, transportation, life-support (for human missions), and for propellant production (for missions manufacturing propellant from Mars resources), including atmospheric collection and compression, thermal and electrical requirements for processing, and requirements for liquefaction and storage of cryogenic fuels.

For proposed missions in the next decade, the power source will be solar arrays. The power system will be the major constraint on the landing site latitude, on how much propellant can be produced, and on how long during each day and during which Mars seasons propellant can be produced. For this reason, it is important to use advanced, high-efficiency/low-mass solar array technology. However, issues related to the operation of advanced solar array technology on the surface of Mars have to be resolved.

Operation of solar arrays on the surface of Mars has been a research area at NASA Lewis for the last eight years. A result of initial studies of solar array operation on Mars [2-7] which determined that solar power systems are, in fact, feasible on the surface of Mars, solar arrays were chosen for the Pathfinder [1] lander and rover mission, which will be the first mission to operate on solar power on the surface of Mars.

The Pathfinder mission includes an instrument to measure the deposition rate of dust onto the Rover [8-10]. This will give us our first look at the effect of dust deposition on solar arrays on Mars.

¹ Ohio Aerospace Institute, Brook Park, OH

² Nyma, Inc., Brook Park, OH

There are major unknowns about the operation of solar arrays on Mars due to the lack of "ground truth" information. Long-term performance of advanced photovoltaic cell and array hardware in the hostile Mars environment is not known, and cannot be adequately tested on Earth.

To answer these questions, we have designed two experiment packages to fly on the Mars-2001 Surveyor Lander. This mission, to launch in April 2001, will arrive on Mars in January 2002. The primary science mission is to deliver a rover vehicle to the surface of Mars; after this science objective is accomplished, the mission will be devoted to technology experiments. One of these technology objectives is to test technologies required for production of rocket propellant using the Martian atmosphere as a resource; this will be tested with the MIP (Mars In-Situ Propellant) package. The MATE and DART experiments will be flown part of the MIP package.

A conceptual rendering of the spacecraft is shown in figure 1.

The MATE experiment (Mars Array Technology Experiment) is designed to test performance of advanced solar cells under Mars conditions, verify solar-cell operation after long-term exposure to the Mars environmental conditions, in order to qualify solar arrays for Mars, and obtain measurements of parameters of the Mars solar environment most important to solar cell performance, in order to reduce the uncertainty in solar array performance prediction.

The DART experiment (Dust Accumulation and Removal Technology) is designed to quantify dust deposition from the Mars atmosphere, measure the properties of settled dust, and test a method of clearing the dust from the array.

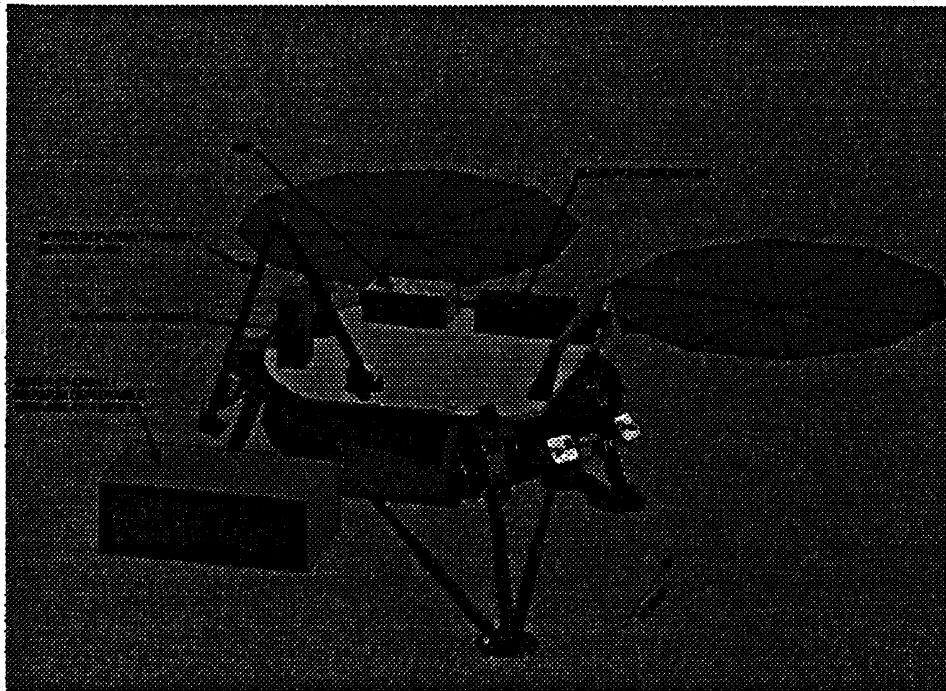


Figure 1: Conceptual design of the Mars-2001 Surveyor Lander spacecraft, featuring foldable circular solar arrays. The MATE and DART experiment packages will be in the "MIP" box on the surface of the lander.

2. Solar Cell Operation on Mars

The Mars environment is different in several critical ways from the orbital environment in which space solar arrays normally operate. Some important differences are:

- (1) low intensity, low temperature operation
- (2) spectrum modified by dust; spectrum may change with time of day and year
- (3) indirect sunlight (i.e., scattered light)
- (4) presence of dust storms at some times of year
- (5) deposited dust
- (6) wind
- (7) peroxide-rich reactive soil

1. Low Temperature

Orbital solar arrays typically operate at temperatures between 50 and 100 Celsius. For this reason, a cell technology is usually selected to have a low coefficient of temperature degradation. On Mars, however, the temperature is lower than the standard test temperature, rather than higher. This means that a high temperature coefficient is desirable, since this actually leads to higher efficiency at Mars temperatures than at test temperature. This shifts the technology choice toward lower bandgap materials and away from higher bandgap materials.

Temperature coefficients are also highly dependent on spectrum, and depend on the detailed shape of the spectrum near the energy bandgap of the material. They are almost impossible to measure with simulated sunlight.

The combination of low intensity and low temperature is a condition known as "LILT", which can lead to anomalous degradation of cell efficiency. It is important to verify that the technology chosen is tested against LILT phenomena.

2. Spectrum

The solar spectrum on the surface of Mars is modified by the atmospheric dust, making it blue-deficient, and enriched in red and IR compared to the orbital ("Air Mass Zero") spectrum. This will change the technology choice to make materials which respond most to the red and IR more desirable than cells responding to the blue end of the spectrum. The spectrum modification is minimum when the dust thickness is lowest, at high sun angles (mid-day, low latitude operation), and for low atmospheric dust content (northern hemisphere summer). The spectrum modification is maximum when dust thickness is highest, at low sun angles (early and late in the day, operation at high latitudes) and when the atmospheric dust is high (northern hemisphere winter). It is most important to have high efficiency when the solar intensity is low. Many systems, for example, are limited not by the average power, but have an operational limit determined by how soon after sunrise the power reaches high enough levels to begin operation. Thus, spectral shifting is more important than average power level numbers might suggest.

Another difficulty is that future high-efficiency cells will use tandem junctions, which require a current matching of several sub-cells of different materials. This matching is highly dependent on details of the spectrum. The variation of the spectrum with time of day and time of year may result in unacceptable degradation due to current mismatch; this is very difficult to predict based on laboratory tests, since it is very sensitive to the details of the spectrum. For example, a high-efficiency GaAs/Ge tandem cell developed in 1987 turned out to be unusable because of current mismatch. The test results were excellent under simulated sunlight, but the performance was poor when test conditions approached actual AMO conditions.

These two effects imply that a critical measurement for determining solar performance on Mars is the operational performance of cells of different bandgaps. It would be desirable to measure this as a function of temperature, sun angle, and atmospheric dust content.

Unfortunately, the Pathfinder and Surveyor-98 landers use only a single type of solar cell, GaAs. The Pathfinder operational lifetime is also too short to make the required measurements, especially as it lands well before perihelion, and probably won't see high-dust loadings. Surveyor-98 lands in very high latitudes (inside the Martian antarctic circle) and never sees high sun angles or increased temperatures. Thus, the solar operational information we get from these two missions will be important in that it will verify operation of solar arrays on Mars, but will not be badly insufficient to use for design of future large power systems which will operate for long periods on the Martian surface.

A selection of technologies chosen to specifically generate this information would be single-junction cells of a range of bandgaps. It would also be desirable to add dual-junction and triple-junction cells to directly determine

the operation of tandem cells on Mars. In principle the performance of dual and triple junction cells can be analyzed by determining the performance of the individual semiconductor elements, but it is desirable for qualification of the full array to be able to reference results from tests of a complete tandem stack.

3. Indirect sunlight.

Since the sky of Mars scatters light, the sunlight comes from a range of angles, rather than in a straight line from the sun. The primary implication of this for solar cell technology is that it means that concentration technologies (such as mirrors or lenses) will be much less effective than planar technologies which accept light from a wide range of angles, and the efficiency of concentration devices will be worst at the highest dust loadings, when efficiency is most critical. It also means that physical spectrum-splitting devices, such as prisms or gratings, will probably be not be effective on Mars, since they generally require collimated light to function.

The indirect sunlight also has implications for array design, choice of tracking, fixed-tilt, or horizontal array orientation, and fresnel reflection from the coverglass.

These effects are known. While it is important in selection of technology, information from Viking, Pathfinder, and Surveyor are likely to be sufficient. Given limited resources; we do not expect to require an experiment on the MIP experiment to test these effects.

4. Dust Storms

The seasonal dust storms are discussed earlier in terms of their effect on the solar spectrum. We believe that it is a very important to measure power production during a global storm for cells of different materials, since we expect that the best materials for producing power during a global storm may be considerably different from the technology best suited for operation during clear periods. Thus, we would very much like the experiment to have a duration at least to perihelion (northern winter).

5. Settled Dust

The atmosphere of Mars contains a considerable load of suspended dust. This dust deposits out of the atmosphere and onto any flat surface; the time scale for this settling has been measured to be on the order of 100 days. For example, observations by the Viking lander showed dark-colored surfaces being coated with a covering of dust, attributed to particles deposited from dust storms, over a time-scale of a hundred days to a few hundred days [11,12].

This is potentially the major lifetime limiting factor for a solar power system on any Mars mission which is required to last for longer than a 100 day mission, unless a technique is developed to periodically remove the dust. The issue of dust settling has been analyzed in detail by Landis [13,14], based on a review of the available evidence from Viking and Mariner [the Viking lander [15], with a RTG (nuclear) power system, was not subject to this limitation, however, future missions are not projected to use RTG power systems.] Table 1 shows the predicted dust deposition, based on the best available models of Mars dust settling.

The worst-case scenario is that the lander is in the settling phase of a global dust storm. There can be one, and possibly two, global dust storms per Martian year, typically occurring near perihelion (southern summer). However, in some years there are no global storms.

As can be seen, except for the case of a probe landing during a dust storm, the obscuration is not too bad for a short mission. It can be catastrophic for a long mission, unless dust removal is effected. It will be necessary to have a means to remove dust if a long-duration stay on the surface is to be achieved. Preferably, the dust removal should require little or no EVA activity by astronauts, since, even for a human mission, a Mars propellant plant will probably be operated as an unmanned vehicle launched two years before the piloted launch. A technique that requires no moving parts and is as simple as just pressing a button would be most desirable.

Case:	obscuraton (30 day mission)	obscuraton (2 yr mission)
Baseline	6.6%	77%
Best	0.5%	22%
Worst	52.2%	89%

Table 1: dust obscuration for short and long duration missions to Mars

6. Wind

Wind is an array design issue. In fact, the low atmospheric density (less than 1% of Earth pressure) on Mars means that dynamic pressures are low, which makes wind far less of a problem on Mars than on Earth. However, typical array designs for space are not designed for wind loads at all, and this must be taken as an additional array design factor. Viking measured an average wind of 2 meters per second, with a velocity of 17 meters per second exceeded less than 1% of the time.

7. Mars Soil Oxidant

Experiments on Viking [15] indicate that the soil of Mars (and presumably the dust as well) apparently contains a highly energetic oxidant, presumably produced by the action of ultraviolet light on the soil. The Viking experiments found the oxidant active in the presence of moisture. Quoting from reference 15: "The evolution of O₂ on humidification of the Martian surface samples was clearly a chemical reaction involving one or more reactive species such as ozonides, superoxides and peroxides," and later in the same reference: "The spontaneous evolution of O₂ when the Martian surface samples were humidified... suggested that the superoxides were modified by the water vapor available." Based on the fact that water was required for the oxidant to become active, since liquid water is absent on the surface of Mars we do not expect oxidant attack to be a difficulty. It would be useful to monitor long-term operation of different technologies on Mars to verify this supposition.

The atmosphere of Mars is expected to also have some presence of reactive radicals, produced by the action of ultraviolet.

In order to have good confidence in Mars array operation, we will want long-term exposure on the Mars surface to look for degradation with time. This will show that there is no unexpected synergy of operating conditions produces a degradation mechanism in the actual environment that was not predicted from lab tests. There is no substitute for operation in the actual environment.

8. Radiation environment

The radiation environment includes ultraviolet (UV) and particulate radiation (primarily high-energy protons and electrons).

The radiation environment of Mars is actually quite benign compared to the ordinary environment, since the Mars has no trapped radiation belts, and the Mars atmosphere serves as a mass shield against coronal mass-ejection ("solar flare") events. The shielding provided by the Mars atmosphere is, in fact, sufficient that we could consider flying a solar array without the conventional coverglass used for protection against radiation.

3. MATE Experiment Package

The MATE experiment (Mars Array Technology Experiment) is designed to (1) test performance of advanced solar cells under Mars conditions, (2) verify solar-cell operation after long-term exposure to the Mars environmental conditions, in order to qualify solar arrays for Mars, and (3) obtain measurements of parameters of the Mars solar environment most important to solar cell performance, in order to reduce the uncertainty in solar array performance prediction. Due to limited area and budget, only a limited set of cell types will be tested. Primary considerations in selection of cell types to test will be (1) commercial availability in the 2005+ time frame, (2) potential for high performance and/or low mass under Mars conditions, and (3) generation of information which will be widely applicable to general predictions of array performance on Mars.

MATE will be designed as a fixed flat plate with cells and instruments on surface, plus a separate electronics package. The plate will be a lightweight rigid substrate commonly used for arrays and spacecraft, either aluminum honeycomb with woven Kevlar or graphite epoxy face sheets. All sensors and diagnostics will be made in the plane of the plate, with no solar tracking. (Sun tracking would be costly and most proposed arrays for Mars do not employ this technique.) MATE's primary function is passive diagnostics, i.e. measure the performance of solar cells, light, and temperature on Mars.

A conceptual diagram of MATE is shown in figure 2.

1. Test of Individual Cells

The baseline MATE package will test two samples each of 5 different cell types. There are two samples of each type of cell for intercomparison and redundancy

Full IV curves will be run on each cell. To do this, all the cells require 4 wire connections, a front and back pair for both voltage and current. The cells can share common grounds. Based on the Mars insolation and cell sizes, currents will range from 0 to 60 mA and voltages range from 0 to 2.5 V.

These photodiodes arrays complicate the electronics package for MATE. They require start/stop and reset pulses from a computer along with a sequential timing pulses to read each element voltage. They are an off-the-shelf component. Two proposed photodiode arrays are Hamamatsu S3904 (Si) and G6890. The S3904 is currently used in a wide range of spectrometers.

Sun Position Sensor (will be part of DART package). This sun position sensor will consist of a lens mounted over a CCD array with a solar filter. The same sensor will be used to determine optical depth.

4. DART experiment package

The utility of dust removal technique on Mars may depend on the detailed properties of the surface dust, including composition, binding strength, particle size distribution, native charge, and surface chemical state. These properties cannot be adequately simulated in an Earth environment, but must be tested with actual Mars dust. It would also be desirable to demonstrate operation in the actual temperature, UV radiation, dry, low-pressure mixed-gas atmosphere (primary components: CO₂, N₂, and Ar) environment of Mars.

A survey of dust removal techniques on Mars is given by Landis [16]. The DART package is flight demonstration program to gather engineering data about the deposition rate and properties of the dust, data important to the future exploration of Mars (as well as of fundamental scientific interest), and to demonstrate the removal of dust.

The flight experiment will measure the dust deposition rate, the dust optical opacity, the solar constant on Mars and the portion of the spectrum which is important to the operation of solar cells. By improving knowledge of the operating conditions of solar cells on Mars, the uncertainty in power output for future Mars missions can be reduced. This result is quite important in selecting a site, since the amount of power available is often the limiting factor in what latitudes can be reached.

The flight demonstration package, shown in schematic in figure 3, consists of five portions. Integrated onto the upward-facing surface of the spacecraft:

- (1) Solar cells. This will include one control and two experimental solar cells.
- (2) diagnostic sensors to measure the amount of dust
- (3) plasma breakdown electrodes

In the MIP warm-electronics box:

- (4) RS-422 programmable high-voltage power supply
- (5) electronics to support sensors; spacecraft interface.

This is shown in schematic in figure 2.

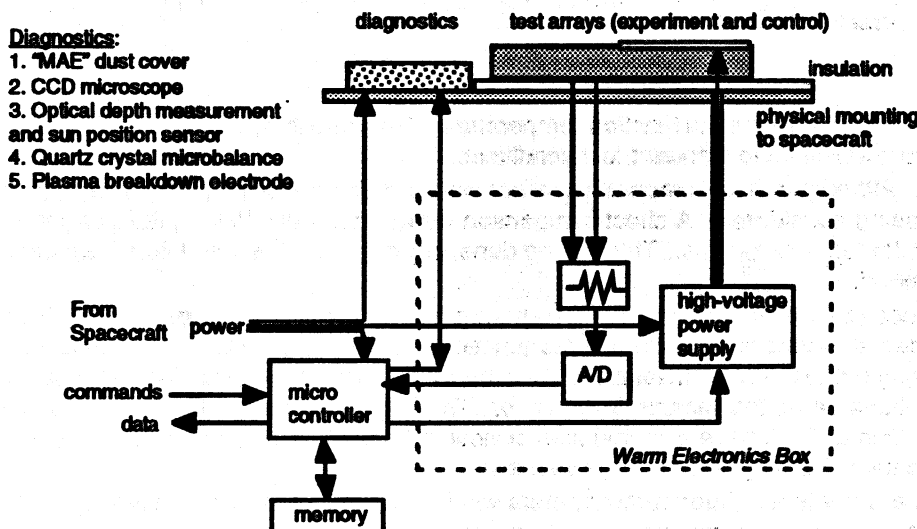


Figure 3: DART experiment package block diagram

The diagnostic sensor set will be based on the "CADO" package [17] under development at Lewis, and uses heritage from the Pathfinder "MAE" experiment [8,9]. It will also measure the amount of dust deposited, its optical opacity, and particle size, and will include an electrode set to measure the breakdown potential of the Mars

In addition to measuring the IV curve, there are three cell temperature sensors. The temperature sensor is an resistance temperature device or RTD. An RTD is a resistive device that varies linearly with temperature, it typically is 100 Ω at 0° C. These are mounted under three of the ten cells. The temperatures will be used to extrapolate the temperatures of all 10 cells. All temperature sensors can share a common ground.

2. Test of Strings

MATE will test two strings of cells, of two different cell technologies. The strings will require a full IV curve. The test will not only detect changes in the cells but evaluate the integrity of the related interconnect technology. Interconnects between cells are highly affected by thermal stresses and related fatigue. The cell types and interconnects will be based on the best viable technology of the time, and presumably one standard cell string, one thin-film string. Each string will require a 4 wire connection and can share common grounds.

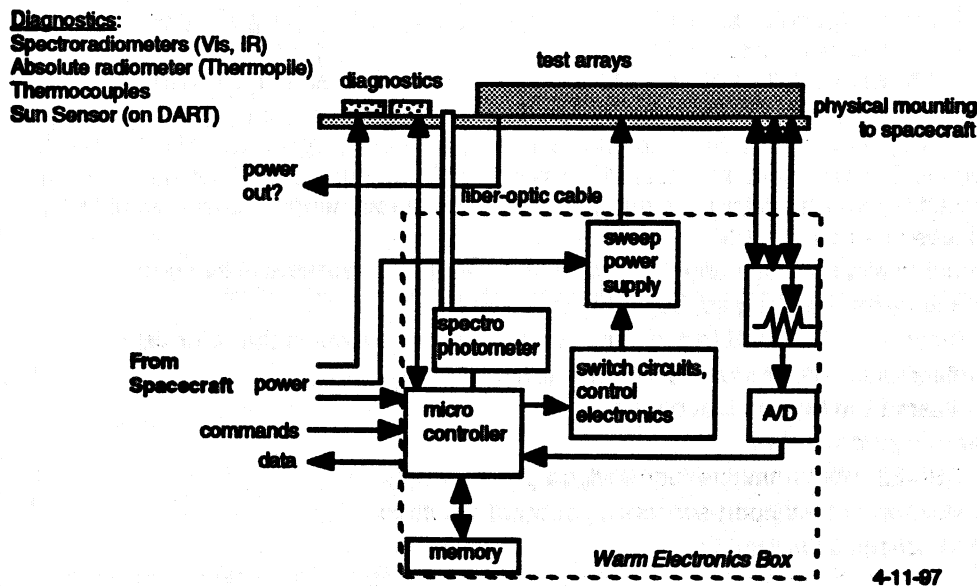


Figure 2: Conceptual block diagram of MATE components

3. Diagnostic Sensors

Temperature measurements. We will measure the junction temperature of representative cells. This is required to allow the cell performance to be normalized to standard test conditions.

Air temperature measurement. Although the air temperature is not critical to the performance of solar cells, an air temperature measurement is being considered. A direct comparison between the cell temperature and the air temperature may aid in modeling for future programs. This will be done using an RTD with additional absorptive and emissive materials as determined.

Radiometers (global and direct (as close as possible)) requiring some temperature correction. These radiometers are thermopile devices and consist of thermocouple junctions on a thin substrate. The radiometers generate a voltage which is proportional to the solar insolation. As a thermal device, the radiometers are sensitive to temperature and each unit will have an added temperature sensor. The two radiometers are used to measure both direct and global insolation. One unit will have a limited field of view to measure the direct light, the other will be shielded from direct sunlight to measure only surrounding irradiance.

Spectroradiometers (photodiode array type). Spectroradiometers will include UV/Vis/NIR and NIR to cover 300 nm to 1800 nm or more as feasible. These devices are made from three separate components. The first is the fore-optics which take in the light, this will be a fiber optic tube with a direct view of the sun from the plane of the cells and <25° field of view. Second will be a grating which splits the sunlight into its spectral components (as a prism). Third will be a photodiode array of ~ 512 elements. These three components will be used to generate a high resolution (<5 nm) spectral energy plot of the Mars sunlight. Two spectroradiometers are required because of the limitations of the gratings and photodiode array. One array will consist of Si elements which respond to 300-1100 nm light, a second array will consist of InGaAs elements and respond to 900-1800 nm. The grating and photodiode array do not need to be located on the cell plate and could be housed beneath it.

atmosphere. The diagnostic instrument set comprises:

1. "MAE" commandable dust cover (similar to the Mars Pathfinder instrument [8,9])
2. Quartz crystal microbalance (similar to the Mars Pathfinder instrument [8,9])
3. CCD microscope based on TC-255 CCD array or other focal plane detector as specified [17]
4. Optical depth measurement and sun position sensor, also based on TC-255
5. Plasma breakdown electrode

5. Conclusions

The first solar-powered spacecraft to operate on the surface of Mars are on their way to the red planet, and will land on July 4th of this year. The environment in which solar arrays will operate on Mars is quite different from the operating environment of other spacecraft power systems, and it would be valuable to characterize the operating environment, measure the operation of solar cells on Mars, and test whether deposited dust will be a problem for the long-term operation. Two experiments on the Mars-2001 Surveyor Lander, MATE and DART, are designed to accomplish these goals.

6. References

1. "Mars Pathfinder Mission and Ares Vallis Landing Site," special issue of *Journal of Geophysical Research*, Vol. 101, No. E2, Feb. 1997.
2. Appelbaum and D. Flood, "The Mars Climate for Photovoltaic System Operation," *Space Power*, Vol. 8, No. 3, 307-317 (1989); NASA Technical Memo TM-102075 (1989)
3. G. Landis and J. Appelbaum, "Design Considerations for Mars PV Power Systems," *Proceedings of the 21st IEEE Photovoltaic Specialists Conference*, May 1990, Vol. 2, 1263-1270.
4. J. Appelbaum and G. Landis, "PV Arrays for Martian Surface Power," *Acta Astronautica*, Vol. 30, 127-142 (1993); paper IAF-92-0591, 43rd IAF Congress (1992); NASA TM-105827 (1992)
5. R. Haberle, C.P. McKay, O. Gwynne, D. Atkinson, G. Landis, R. Zurek, J. Pollack and J. Appelbaum, "Atmospheric Effects on the Utility of Solar Power on Mars," *Resources of Near Earth Space*, pp. 799-818, U. Arizona Press Space Science Series (1993).
6. J. Appelbaum, G. Landis and I. Sherman, "Solar Energy on Mars: Stationary Collectors," *Journal of Propulsion and Power*, Vol. 11 No. 3, 554-561 (1995). Available as NASA TM-106321 (1993).
7. D. Burger and G. Landis, "Solar Array Corrections for the Mars Surface," presented at Case for Mars V, Boulder CO, 26-29 May 1993.
8. P. Jenkins, G. Landis, D. Schelman, M. Krasowski, and L. Oberle, "Materials Adherence Experiment: Technology," paper IECEC-97339, 32nd Intersociety Energy Conversion Engineering Conference, July 27-Aug. 1, 1997, Honolulu HI.
9. G.A. Landis and P. Jenkins, "Development of a Solar-Cell Dust Opacity Measurement Instrument for Mars Pathfinder," *Space Photovoltaics Research and Technology 1995*, NASA CP-3324, 313-319; presented at SPRAT-XIV, NASA Lewis Research Center, Oct. 24-26 1995.
10. G. Landis, P. Jenkins and G. Hunter, "Materials Adherence Experiment: Early Results," paper IECEC-97340, 32nd Intersociety Energy Conversion Engineering Conf., July 27-Aug. 1, 1997, Honolulu.
11. E.A. Guinness, C.E. Leff and R.E. Arvidson, "Two Mars Years of Surface Changes Seen at the Viking Landing Sites," *J. Geophys. Res.*, Vol. 87, B12, pp. 10051-10058 (1982).
12. R.E. Arvidson, E.A. Guinness, H.J. Moore, J. Tillman and S.D. Wall, "Three Mars Years: Viking Lander 1 Imaging Observations," *Science*, Vol. 222 No. 4623, pp. 463-468 (1983).
13. G. Landis, "Dust-Induced Degradation of Solar Arrays on Mars," *Proceedings of the 1st World Photovoltaic Energy Conversion Conference*, Hawaii, Dec. 5-9 1994, pp. 2030-2033.
14. G. Landis, "Dust Obscuration of Mars Photovoltaic Arrays," *Acta Astronautica*, Vol. 38, No. 11, 885-891 (1996). Paper IAF-94-380, 45th International Astronautical Federation Congress, Jerusalem, Oct. 9-14 1994.
15. "Scientific Results of the Viking Project", reprinted from *J. Geophysical Research*, Vol. 82, No. 28, 1977, page 4675.
16. G. Landis, "Mars Dust Removal Technology," paper IECEC-97345, 32nd Intersociety Energy Conversion Engineering Conference, July 27-Aug. 1, 1997, Honolulu HI.
17. G. Landis, P. Jenkins, J. Flatico, L. Oberle, M. Krasowski and S. Stevenson, "Development of a Mars Dust Characterization Instrument," *Planetary and Space Science*, Vol. 44, No. 11, pp. 1425-1433 (1996). Presented as paper IAF-95-U.4.09, 46th International Astronautics Federation Congress, Oslo Norway, 2-6 Oct. 1995.

Workshop III - Arcs, Sparks & Spacecraft Charging

Issues:

What levels of arcs are acceptable?

In particular what level of arc currents/time scale can Ga/As or Multijunction cells tolerate?

How do Arc Characteristics scale with Array Size?

Capacitance? Stored Energy? Finite discharge area?

Past testing has been performed on small array samples of 10's cm dimensions. We need to understand how to extrapolate observations to flight systems. Some hypotheses have been advanced on how to do this but we need to verify or modify these hypotheses.

Effects of New Materials?

Cell material, new solvents, new adhesives, conductive cover slides, new coatings, etc.

Test Methods: Cannot simply put a grounded array in an electron beam and assume this represents flight conditions. We know more about arc's than we did 10 years ago. Need to reproduce correct potential distributions, and approximate floating conditions of a satellite in space.

Effects of High voltage arrays?

LEO grounding issues, Kapton pyralization (LEO and Geo)? Other?

Who should lead/fund these efforts?

Government? *Open data, reluctance to do commercial research, under-funded.*

Flight Programs? *Cost Conscious, Off-the-shelf systems, proprietary data.*

Consortiums?

Workshop III - Arcs, Sparks & Spacecraft Charging

**What charging/arcing issues are specifically of concern to solar array designers?
(summary of short tutorial)**

EMI characteristics are determined by size of arrays, and conductivity of array structure, and bus. Dimensions contribute to frequency spectrum. High Impedance permits high Voltages, Low Impedance permits high currents.

Also large solar cell arrays present the highest capacitance to space, so they will contribute a significant Displacement Current, to a voltage transient elsewhere on the spacecraft.

As transients propagate, additional arcs may occur.

**Effects of Arcs may be mitigated by doing things spread out the pulse.
Introduce Inductance to ground and DC bus lines?**

**Conductive Black Kapton (Warning: not all black Kaptons are conductive)
alleviates many charging problems of thermal blankets.**

High Voltage arrays (100V) in Low Earth Orbit can control structure potentials, and lead to arcing elsewhere on the spacecraft. Solutions are positive or floating ground for Array power bus, large exposed conductive areas at spacecraft ground or active control techniques such as a plasma contactor (will be used for ISSA).

REPORT DOCUMENTATION PAGEForm Approved
OMB No. 0704-0188

Public reporting burden for this collection of information is estimated to average 1 hour per response, including the time for reviewing instructions, searching existing data sources, gathering and maintaining the data needed, and completing and reviewing the collection of information. Send comments regarding this burden estimate or any other aspect of this collection of information, including suggestions for reducing this burden, to Washington Headquarters Services, Directorate for Information Operations and Reports, 1215 Jefferson Davis Highway, Suite 1204, Arlington, VA 22202-4302, and to the Office of Management and Budget, Paperwork Reduction Project (0704-0188), Washington, DC 20503.

1. AGENCY USE ONLY (Leave blank)		2. REPORT DATE June 2004	3. REPORT TYPE AND DATES COVERED Conference Publication	
4. TITLE AND SUBTITLE Proceedings of the 15th Space Photovoltaic Research and Technology Conference			5. FUNDING NUMBERS WBS-22-755-04-03	
6. AUTHOR(S) Sheila Bailey, compiler				
7. PERFORMING ORGANIZATION NAME(S) AND ADDRESS(ES) National Aeronautics and Space Administration John H. Glenn Research Center at Lewis Field Cleveland, Ohio 44135-3191			8. PERFORMING ORGANIZATION REPORT NUMBER E-14260	
9. SPONSORING/MONITORING AGENCY NAME(S) AND ADDRESS(ES) National Aeronautics and Space Administration Washington, DC 20546-0001			10. SPONSORING/MONITORING AGENCY REPORT NUMBER NASA CP-2004-212735	
11. SUPPLEMENTARY NOTES Proceedings of a conference held at and sponsored by NASA Glenn Research Center, Cleveland, Ohio, June 10-12, 1997. Responsible person, Sheila Bailey, organization code 5410, 216-433-2228.				
12a. DISTRIBUTION/AVAILABILITY STATEMENT Unclassified - Unlimited Subject Category: 20 Available electronically at http://gltrs.grc.nasa.gov This publication is available from the NASA Center for AeroSpace Information, 301-621-0390.			12b. DISTRIBUTION CODE	
13. ABSTRACT (Maximum 200 words) The purpose of the SPRAT conference is to bring members of the space solar cell community together in a relatively informal conference setting to discuss recent developments in solar cell and array technology and to discuss the future directions of the field. The conference is sponsored by the Photovoltaic and Space Environmental Effects Branch at the NASA Glenn Research Center.				
14. SUBJECT TERMS Photovoltaic; Solar cells			15. NUMBER OF PAGES 288	
			16. PRICE CODE	
17. SECURITY CLASSIFICATION OF REPORT Unclassified	18. SECURITY CLASSIFICATION OF THIS PAGE Unclassified	19. SECURITY CLASSIFICATION OF ABSTRACT Unclassified	20. LIMITATION OF ABSTRACT	